

MAGNETIC SKYRMIONS  
AND  
TOPOLOGICAL DOMAIN WALLS

Inaugural-Dissertation

zur

Erlangung des Doktorgrades

der Mathematisch-Naturwissenschaftlichen Fakultät

der Universität zu Köln

vorgelegt von

Jan Müller

aus

Köln



Köln 2018

Berichterstatter: Prof. Dr. Achim Rosch  
(Gutachter) Prof. Dr. Simon Trebst  
Prof. Dr. Jairo Sinova

Tag der mündlichen Prüfung: 26. Februar 2018

# Abstract

This cumulative dissertation explores the diverse phenomena that occur in magnets, where non-collinear magnetization-textures are stabilized as a consequence of broken mirror or inversion symmetries of the material. These textures include long-ranged spirals, lattices of skyrmions, and polarized structures.

The magnetic skyrmion is the youngest and most exotic among the above mentioned textures and plays a key role in this thesis. It appears as a whirl in the magnetization that has a topological winding number but in contrast to magnetic vortices, is a local object. Since the first experimental measurement of the skyrmion lattice in 2009 it attracts massive attention both due to the novel physics that arise from the topological magnetism, and its possible consequences for information technology devices, which are summarized in the first part of this thesis.

The second part is the cumulative part, i.e., a collection of works related to this thesis, to which I contributed and that were published during the last years. In collaboration with the groups of Prof. Dr. Meier and Prof. Dr. Tokura, we observed that type-II domain walls with an unforeseen texture stabilize within the helical phase in chiral magnets. Their occurrence is explained by a simple micromagnetic model that reveals their non-trivial topology.

Upon application of a moderate magnetic field, defects nucleate in the helical phase. Within our micromagnetic model these are identified as skyrmions and we calculate their energetics and interactions. We predict the formation of characteristic clusters that are experimentally observed by our collaborators from the groups of Prof. Dr. Carbone and Prof. Dr. Rønnow.

In order to create or to unwind a skyrmion, a Bloch point is required that acts as a monopole of topological charge. This singular structure is naturally associated with a large energy barrier which should make skyrmions extremely stable. However, in collaboration with the groups of Prof. Dr. Back and Prof. Dr. Pfeleiderer we find that the time scale associated to the decay of a skyrmion is corrected by more than 30 orders of magnitude due to entropic compensation effects.

If not by Bloch points, the skyrmion number can be changed smoothly and without singularities via the edges of the system. This is the result of a theoretical study, where we analyzed the non-reciprocal spectrum of magnons that are bound to the twisted magnetization at an edge.

The edge-instability provides a possible filling mechanism for the two-lane racetrack which is a shift register memory that requires a decent density of skyrmions. We calculate the energy potentials for various three-dimensional nanostructures that yield an energy potential which is suitable for the two-lane layout. Furthermore, we show that the skyrmion motion in such complicated systems is still compatible with the simplistic Thiele equation for current driven skyrmions.

Finally, in collaboration with the group of Prof. Dr. Zhou we show that also the motion of spin-wave driven skyrmions can be described within the Thiele picture and that it can be considered a driving mechanism for skyrmions in nanostructures.

The third part reviews the theoretical models, explains the most important methods that

were used and adds unpublished work to this thesis. We show that within the micromagnetic model a surface reconstruction occurs in the helical phase. Moreover, investigations of phase diagrams for tilted magnetic fields predict distorted skyrmion phases and anisotropic skyrmion interactions. Furthermore, we study the distortion of spin-torque driven skyrmions in collaboration with the group of Dr. Everschor-Sitte. We find an instability of the skyrmion which sets a speed limit for the motion, except if the Gilbert damping  $\alpha$  and the ratio  $\beta$  for the non-adiabatic spin-transfer-torque are equal. However, at even higher current densities, the micromagnetic model again stabilizes a heavily distorted skyrmion in a broad current range before this solution collapses.

# Kurzzusammenfassung

Diese kumulative Dissertation untersucht die vielfältigen Phänomene, die in Magneten auftreten, in denen nicht-kollineare Magnetisierungs-Texturen als Folge von gebrochenen Spiegel- oder Inversionssymmetrien des Materials stabilisiert werden. Zu diesen Texturen gehören langreichweitige Spiralen, Gitter von Skyrmionen und polarisierte Strukturen.

Das magnetische Skyrmion ist das jüngste und exotischste unter den oben genannten Texturen und spielt eine Schlüsselrolle in dieser Arbeit. Es erscheint als Wirbel in der Magnetisierung, der eine topologische Windungszahl hat, aber im Gegensatz zu magnetischen Wirbeln ein lokales Objekt darstellt. Seit der ersten experimentellen Messung des Skyrmion-Gitters im Jahr 2009 erregt es massive Aufmerksamkeit, sowohl aufgrund der neuartigen physikalischen Phänomene, die sich aus dem topologischen Magnetismus ergeben, wie auch wegen seiner möglichen Folgen für Geräte der Informationstechnologie, wie im ersten Teil dieser Arbeit zusammengefasst.

Der zweite Teil ist der kumulative Teil, d.h. eine Sammlung von Arbeiten im Zusammenhang mit dieser Arbeit, zu der ich beigetragen habe und die in den letzten Jahren veröffentlicht wurden. In Zusammenarbeit mit den Arbeitsgruppen von Prof. Dr. Meier und Prof. Dr. Tokura konnten wir beobachten, dass sich innerhalb der Helixphase bei chiralen Magneten Typ-II-Domänenwände mit einer unvorhergesehenen Textur stabilisieren. Ihr Auftreten wird durch ein einfaches mikromagnetisches Modell erklärt, das ihre nicht-triviale Topologie offenlegt.

Bei Anlegen eines moderaten Magnetfeldes bilden sich Defekte in der Helixphase. Innerhalb unseres mikromagnetischen Modells werden diese als Skyrmionen identifiziert und wir berechnen ihre Energetik und Wechselwirkungen. Wir prognostizieren die Bildung von charakteristischen Clustern, die von unseren Kollegen aus den Gruppen von Prof. Dr. Carbone und Prof. Dr. Rønnow experimentell beobachtet werden.

Um ein Skyrmion zu erzeugen oder zu entknoten, wird ein Blochpunkt benötigt, der als Monopol der topologischen Ladung fungiert. Diese singuläre Struktur ist natürlicher Weise mit einer großen Energiebarriere verbunden, die Skyrmionen extrem stabil machen soll. In Zusammenarbeit mit den Arbeitsgruppen von Prof. Dr. Back und Prof. Dr. Pfeleiderer stellen wir jedoch fest, dass die Zeitskala, die mit dem Zerfall eines Skyrmions verbunden ist, durch entropische Kompensationseffekte um mehr als 30 Größenordnungen korrigiert wird.

Wenn nicht durch Blochpunkte, so kann die Skyrmionenzahl über die Kanten des Systems kontinuierlich und ohne Singularitäten verändert werden. Dies ist das Ergebnis einer theoretischen Studie, in der wir das nicht-reziproke Spektrum von Magnonen analysiert haben, die in der verdrehten Magnetisierung an einer Kante lokalisiert sind.

Die Instabilität an der Kante bietet einen möglichen Füllmechanismus für den zweispurigen Racetrack – einem Schieberegisterspeicher, der eine mäßige Dichte an Skyrmionen erfordert. Wir berechnen die Energiepotentiale für verschiedene dreidimensionale Nanostrukturen, die ein Energiepotential ergeben, das für den zweispurigen Aufbau geeignet ist. Darüber hinaus zeigen wir, dass die Bewegung des Skyrmions in solch komplizierten Systemen immer noch mit der vereinfachenden Thiele-Gleichung für stromgetriebene Skyrmionen kompatibel ist.

Schließlich zeigen wir in Zusammenarbeit mit der Gruppe von Prof. Dr. Zhou, dass auch die Bewegung von spinwellengetriebenen Skyrmionen im Thiele-Bild beschrieben werden kann und

dass dies als möglicher Antriebsmechanismus für Skyrmionen in Nanostrukturen in Betracht gezogen werden sollte.

Der dritte Teil bespricht die theoretischen Modelle, erklärt die wichtigsten Methoden, die verwendet wurden, und fügt unveröffentlichte Arbeiten zu dieser Arbeit hinzu: Wir zeigen, dass innerhalb des mikromagnetischen Modells eine Oberflächenrekonstruktion in der Helixphase stattfindet. Untersuchungen von Phasendiagrammen für mäßige Magnetfelder zeigen verzerrte Skyrmion-Phasen und anisotrope Skyrmion-Wechselwirkungen. Darüber hinaus untersuchen wir die Verzerrung von spinstromgetriebenen Skyrmionen in Zusammenarbeit mit der Gruppe von Dr. Everschor-Sitte. Wir finden eine Instabilität des Skyrmions, die eine Geschwindigkeitsbegrenzung festlegt, außer wenn die Gilbert-Dämpfung  $\alpha$  und das Verhältnis  $\beta$  für das nicht-adiabatische Spin-Transfer-Torque gleich sind. Bei noch höheren Stromdichten stabilisiert das mikromagnetische Modell jedoch wieder ein stark verzerrtes Skyrmion in einem weiten Strombereich, bevor auch diese Lösung zusammenbricht.

# Contents

<b>Abstract</b>	<b>iii</b>
<b>Kurzzusammenfassung</b>	<b>v</b>
<b>I. Introduction</b>	<b>1</b>
<b>1. Spirals, skyrmions, and topology</b>	<b>3</b>
1.1. Non-collinear magnetism . . . . .	3
1.2. Topological winding numbers . . . . .	4
1.2.1. A mathematical introduction . . . . .	4
1.2.2. Topological winding numbers in magnetism . . . . .	5
1.2.3. The skyrmion number on a lattice . . . . .	6
1.3. Twists in d=1: Spiral, helical, and the conical phases . . . . .	6
1.3.1. Coplanar spin spirals: Spirals and helices . . . . .	7
1.3.2. Escape through the third dimension: The conical phase . . . . .	8
1.4. Skyrmions: From nuclear physics to condensed matter . . . . .	8
1.4.1. Skyrmions in all areas of physics . . . . .	8
1.4.2. The zoology of $\mathbb{S}^2$ magnetic skyrmions . . . . .	9
1.4.3. Early prediction of magnetic skyrmions . . . . .	11
1.4.4. First experimental confirmation in MnSi . . . . .	12
1.4.5. Skyrmions in more materials . . . . .	13
1.5. A new field emerges: Skyrmionics . . . . .	17
1.5.1. Skyrmions on a racetrack . . . . .	17
1.5.2. The creation of topological particles . . . . .	18
1.5.3. The interactions of skyrmions . . . . .	19
1.5.4. Pushing skyrmions . . . . .	19
1.5.5. Other applications with skyrmions . . . . .	21
1.5.6. Experimental state of the art . . . . .	21
<b>2. Outline of the thesis</b>	<b>23</b>
<b>II. Publications</b>	<b>27</b>
<b>3. Topological domain walls in helimagnets</b>	<b>29</b>
3.1. Introduction . . . . .	29
3.2. Classification of experimentally observed domain walls . . . . .	31
3.3. Theoretical analysis of energetics . . . . .	33
3.4. Topology of domain walls . . . . .	34
3.5. Discussion . . . . .	35

3.6.	Bibliography . . . . .	36
3.7.	Supplementary Text . . . . .	39
3.7.1.	Experimental Methods . . . . .	39
3.7.2.	Theoretical considerations . . . . .	41
3.7.3.	Bibliography . . . . .	47
3.7.4.	Supplementary Figures . . . . .	47
<b>4.</b>	<b>Magnetic skyrmions and skyrmion clusters in the helical phase of <math>\text{Cu}_2\text{OSeO}_3</math></b>	<b>61</b>
4.1.	Introduction . . . . .	61
4.2.	Single skyrmions in a helical phase . . . . .	63
4.3.	Interactions and cluster formation . . . . .	64
4.4.	Experiments . . . . .	65
4.5.	Conclusions . . . . .	66
4.6.	Bibliography . . . . .	67
4.7.	Supplemental Material . . . . .	70
4.7.1.	Micromagnetic Simulations . . . . .	70
4.7.2.	Experimental details . . . . .	73
4.7.3.	Fluctuation of helical and skyrmion domains . . . . .	73
4.7.4.	Skyrmions in a ferromagnetic background . . . . .	75
4.7.5.	Phase diagram . . . . .	75
4.7.6.	Bibliography . . . . .	75
<b>5.</b>	<b>Entropy-limited topological protection of skyrmions</b>	<b>77</b>
5.1.	Introduction . . . . .	77
5.2.	Results . . . . .	79
5.3.	Discussion . . . . .	82
5.4.	Materials and methods . . . . .	85
5.4.1.	Crystal growth and sample preparation . . . . .	85
5.4.2.	Magnetic imaging . . . . .	86
5.5.	Bibliography . . . . .	86
5.6.	Supplementary Materials . . . . .	90
5.6.1.	Image processing for the skyrmion decay measurements . . . . .	90
5.6.2.	Evaluation of intermediate states . . . . .	92
5.6.3.	Scaling analysis of activation energies . . . . .	93
5.6.4.	Bibliography . . . . .	94
<b>6.</b>	<b>Edge instabilities and skyrmion creation in magnetic layers</b>	<b>95</b>
6.1.	Introduction . . . . .	95
6.2.	Magnons at the edge of a chiral magnet . . . . .	97
6.2.1.	The free energy functional . . . . .	97
6.2.2.	The magnetization at the edge of the layer . . . . .	99
6.2.3.	Effective magnon Hamiltonian . . . . .	101
6.2.4.	Bound magnon edge modes . . . . .	102
6.2.5.	Phase diagram and instabilities of the metastable FP state . . . . .	105
6.3.	Edge instability and creation of skyrmions . . . . .	107
6.4.	Discussion . . . . .	110
6.5.	Bibliography . . . . .	111

---

<b>7. Magnetic Skyrmions on a Two-Lane Racetrack</b>	<b>115</b>
7.1. Introduction . . . . .	115
7.2. Potentials and landscapes . . . . .	117
7.3. Operation of a two-lane racetrack . . . . .	119
7.4. Summary . . . . .	121
7.5. Methods . . . . .	122
7.5.1. Model and units . . . . .	122
7.5.2. Micromagnetic simulations . . . . .	122
7.5.3. Calculation of the potentials . . . . .	123
7.5.4. Thiele analysis . . . . .	123
7.6. Bibliography . . . . .	124
<b>8. Shape-dependence of the barrier for skyrmions on a two-lane racetrack</b>	<b>127</b>
8.1. Introduction . . . . .	127
8.2. The Model . . . . .	128
8.3. Barriers and potentials . . . . .	130
8.3.1. Comparison of the different barriers . . . . .	130
8.3.2. Smeared out edges . . . . .	132
8.4. Summary . . . . .	132
8.5. Bibliography . . . . .	133
<b>9. Motion of skyrmions in nanowires driven by magnonic momentum-transfer forces</b>	<b>135</b>
9.1. Introduction . . . . .	135
9.2. Results . . . . .	136
9.2.1. Skyrmion trajectories for longitudinal and transverse driving by spin waves	136
9.2.2. Thiele approximation . . . . .	138
9.2.3. Damping dependence of the skyrmion motion . . . . .	140
9.2.4. Steady-state motion for transverse driving . . . . .	141
9.3. Summary . . . . .	144
9.4. Appendix. Micromagnetic modeling . . . . .	145
9.5. Bibliography . . . . .	146
<b>III. Further Work</b>	<b>149</b>
<b>10. Theoretical models and methods</b>	<b>151</b>
10.1. Atomistic Heisenberg model . . . . .	151
10.2. Micromagnetic model . . . . .	153
10.2.1. Derivation from symmetry considerations . . . . .	153
10.2.2. The isotropic bulk chiral magnet . . . . .	153
10.2.3. The isotropic two-dimensional magnet . . . . .	154
10.2.4. Connection to atomistic model . . . . .	155
10.3. Dynamics of magnetization . . . . .	156
10.3.1. The Landau-Lifshitz-Gilbert equation . . . . .	156
10.3.2. Spin-torques for the manipulation of magnetic textures . . . . .	157
10.3.3. The Thiele equation of motion . . . . .	158
10.4. System of reduced units . . . . .	159

10.5. Micromagnetic simulations . . . . .	161
10.5.1. A simple discretization of space and time . . . . .	161
10.5.2. Infinite damping for energy minimization . . . . .	162
10.5.3. Higher order discretization: Better accuracy, less runtime. . . . .	163
10.5.4. The implementation of boundary conditions at the surface . . . . .	165
<b>11. Surface reconstructions in the helical phase</b>	<b>171</b>
11.1. Motivation . . . . .	171
11.2. A convenient twist at the surface . . . . .	172
11.3. Reconstruction for the 90° scenario . . . . .	174
<b>12. Tilted fields</b>	<b>177</b>
12.1. Motivation . . . . .	177
12.2. Computing phase diagrams: The simplex minimization . . . . .	178
12.3. One-dimensional systems . . . . .	180
12.4. Two-dimensional systems . . . . .	181
12.4.1. Phase diagram . . . . .	181
12.4.2. Skyrmion interactions . . . . .	182
12.5. Thin films of chiral magnets . . . . .	184
12.5.1. A first atomistic approach . . . . .	185
12.5.2. The continuous thin film . . . . .	186
<b>13. Speed-limits for skyrmions</b>	<b>189</b>
13.1. Motivation . . . . .	189
13.2. Implementation of a co-moving frame . . . . .	190
13.2.1. The moving frame of reference . . . . .	190
13.2.2. The reduced set of parameters . . . . .	190
13.2.3. Thiele revisited . . . . .	191
13.3. Bimeron instability for current-driven skyrmions . . . . .	192
13.4. Current-stabilized shooting star skyrmions . . . . .	193
<b>IV. Summary</b>	<b>195</b>
<b>V. Bibliography</b>	<b>203</b>
<b>VI. Appendix</b>	<b>223</b>
<b>14. Discretization of derivatives</b>	<b>225</b>
14.1. Getting the prefactors . . . . .	225
14.2. Symmetric discretizations . . . . .	226
14.3. Asymmetric discretizations . . . . .	227
14.4. Asymmetric discretizations with boundary conditions . . . . .	229
<b>15. German patent application for a memory device based on skyrmions</b>	<b>233</b>

<b>Acknowledgments</b>	<b>xiii</b>
<b>Anhänge gemäß Prüfungsordnung</b>	<b>xv</b>
Anhang zur Eigenbeteiligung an den Publikationen . . . . .	xvii
Erklärung . . . . .	xix



Part I.  
Introduction



# 1. Spirals, skyrmions, and topology

Whether in the compass in the early ages of mankind or in the hard disk drives that provide the vast quantities of memory that nowadays information technology demands: magnetism is a ubiquitous phenomenon with numerous applications in our everyday life. The comparatively young skyrmion, in turn, adds with its topologically non-trivial structure a new flavor to this extensively studied field.

On the following pages, we will shortly introduce non-collinear magnetism and in particular helimagnetism which in contrast to the maybe more prominent hard-axis magnetism opens the door for the novel magnetic textures that are studied in this thesis. After defining topological winding numbers for magnetic textures in Sec. 1.2, where we orient after Ref. [1], we can discuss the one-dimensional modulated phases in Sec. 1.3 and review the very short history of magnetic skyrmions in Sec. 1.4 and Sec. 1.5.

An summary of the theoretical model and the methods that are used throughout the thesis is provided in part III.

## 1.1. Non-collinear magnetism

A rough categorization of magnetism by the different possible orders of the spins is the separation into *collinear* and *non-collinear magnetism*.

Collinear magnetism refers to magnetic orders where the spins align in a common direction, as it is the case in ferromagnetism, see first panel in Fig. 1.1.1. But also in antiferromagnetism the spins align along a common direction, though with different signs on distinct sublattices, as well as in ferrimagnetism, where the amplitude of the spin can differ on sublattices but still a common axis determines the orientation of the spins.

The direct opposite to the collinear magnetism with its global quantization axis for the spin is the paramagnet, second panel in Fig. 1.1.1, where the direction of the spin is random on

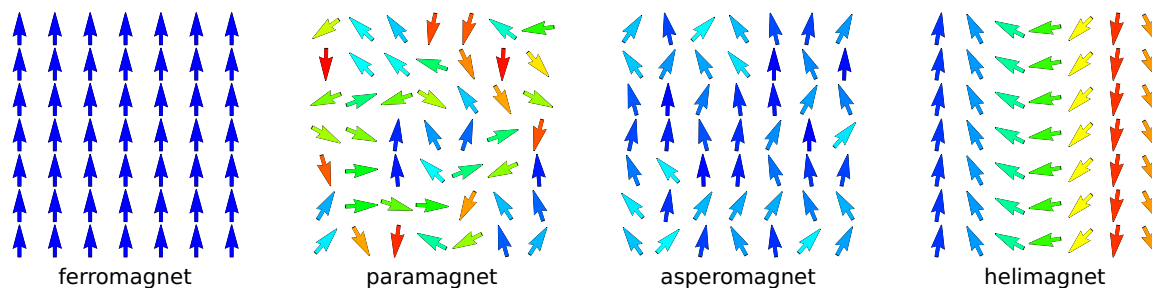


Figure 1.1.1.: Two-dimensional sketch of classes of spin-configurations as labeled according to Hurd's categorization in Ref. [2]. The color denotes the vertical component of the spin (arrow). The helimagnetic texture (right) rotates in the plane perpendicular to the propagation vector but is here, for simplicity, sketched in a two-dimensional projection. See also Fig. 1.3.4 for the difference between a helix and a normal spiral.

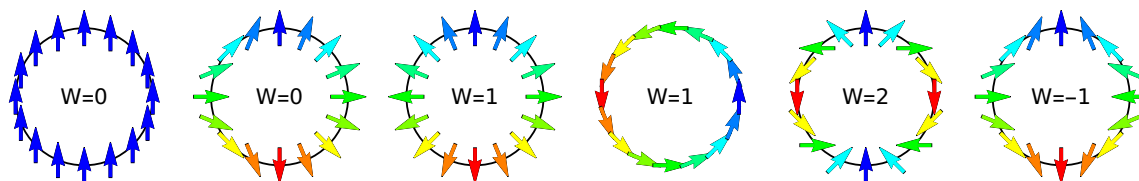


Figure 1.2.2.: Graphical representation of maps  $\mathbf{u} : \mathbb{S}^1 \subset \mathbb{R}^2 \rightarrow \mathbb{S}^1 \subset \mathbb{R}^2$  with different winding numbers as indicated in the panels. The color code denotes the vertical component of the arrows.

every site. A subcategory of the paramagnet is the asperomagnet, see Ref. [2], third panel in Fig. 1.1.1, which is characterized by also a random alignment of the spins with the tendency to align with a global axis.

The helimagnet, which itself represents a subcategory of the asperomagnet, is in a sense the prime example for non-collinear magnetism as the quantization axis turns steadily from site to site. Notably, in the setups that we consider in the following, the twist is unidirectional and the handedness is fixed by the symmetry-broken underlying atomic lattice via spin-orbit coupling [3–6]. The simplified representation in the right panel of Fig. 1.1.1 does not strictly show a helix as this requires a third dimension for the spin, see Fig. 1.3.4. In contrast to the helimagnetic state, the here shown coplanar spin-spiral does not require broken inversion symmetry in the lattice but instead a broken mirror symmetry [7, 8] which fixes the rotary plane and also the handedness.

## 1.2. Topological winding numbers

### 1.2.1. A mathematical introduction

Let us consider a smooth self-map  $\mathbf{u}$ , which assigns to every point on a the sphere another point on a sphere,  $\mathbf{u} : \mathbb{S}^d \rightarrow \mathbb{S}^d$ . The winding number  $\mathcal{W} \in \mathbb{Z}$  measures how often the mapping  $\mathbf{u}$  covers the image space  $\mathbb{S}^d$  taking the orientation into account.

$$\mathcal{W}(\mathbf{u}) = \frac{\text{oriented area of } \mathbf{u}(\mathbb{S}^d)}{\text{area of } \mathbb{S}^d} \quad (1.2.1)$$

We can represent such maps  $\mathbf{u}$  graphically by using that  $\mathbb{S}^d = \{\mathbf{x} \in \mathbb{R}^{d+1} : |\mathbf{x}| = 1\} \subset \mathbb{R}^{d+1}$ , i.e. we can draw a sphere in  $(d+1)$ -dimensional space which is covered by a smooth field of normalized  $(d+1)$ -dimensional arrows. For simplicity, we only draw a discrete set of these arrows. Alternatively or in addition, a smooth color-code can be used. Fig. 1.2.2 shows such a representation for  $d = 1$  and various winding numbers. Configurations with the same winding number are *topologically equivalent*, meaning that they can be transformed into each other via smooth deformations of the map  $\mathbf{u}$ . As an example, the second mapping in Fig. 1.2.2 can be transformed smoothly into the first mapping by rotating first the arrow on the south pole until it points parallel to its neighbors. Then, the three arrows at the bottom are rotated until they resemble the arrows on the equator. If iterated, this deformation yields the polarized texture of the first panel. Also, the third and fourth panel show equivalent textures. By simply rotating the arrows clockwise, panel three transforms smoothly into panel four. Here, it becomes clear that the orientation of the mapping is important as it distinguishes between positive and negative winding numbers: there is no smooth connection between panel six and

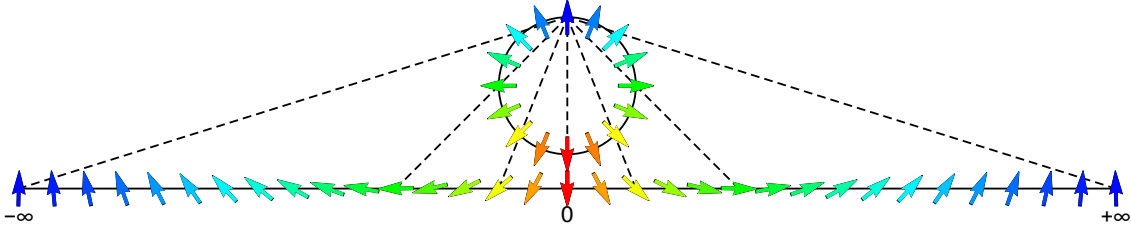


Figure 1.2.3.: Graphical representation of a map  $\mathbf{u} : \mathbb{S}^1 \rightarrow \mathbb{S}^1$  with winding number  $\mathcal{W}(\mathbf{u}) = 1$  and its stereographic projection  $f : \mathbb{S}^d \rightarrow \mathbb{R}^d \cup \{\infty\}$  to  $\hat{n} : \mathbb{R}^d \cup \{\infty\} \rightarrow \mathbb{S}^d \subset \mathbb{R}^{d+1}$ . The color code denotes the vertical component of the arrows.

three.

### 1.2.2. Topological winding numbers in magnetism

In a classical continuum theory of magnetism, the magnetization in  $d$ -dimensional (flat) space is represented as a smooth and normalized vector field  $\hat{n} : \mathbb{R}^d \rightarrow \mathbb{S}^{d'} \subset \mathbb{R}^{d'+1}$ . Note that in general  $d \neq d'$ , i.e. some systems may be described as a chain of Heisenberg spins ( $d = 1$ ,  $d' = 2$ ) whereas others may be Ising spins in a bulk volume ( $d = 3$ ,  $d' = 0$ , where  $\mathbb{S}^0 := \mathbb{Z}_2$ ). Since the edge of the considered volume breaks the smoothness condition of the magnetization, we also include  $\pm\infty$ . Then, we can find a stereographic projection  $f : \mathbb{S}^d \rightarrow \mathbb{R}^d \cup \{\infty\}$  which defines a smooth bijective map from the sphere to a flat volume. Fig. 1.2.3 shows a sketch of this mapping for  $d = 1$ . With this projection we have established a connection to the smooth self-map  $\mathbf{u}$  and the winding number defined there, see Eq. 1.2.1. It follows immediately that the magnetization

$$\hat{n} : \mathbb{R}^d \cup \{\infty\} \rightarrow \mathbb{S}^{d'} \subset \mathbb{R}^{d'+1} \quad (1.2.2)$$

can only have a non-trivial winding number  $\mathcal{W}(\hat{n}) \in \mathbb{Z}$  for  $d = d'$ . This winding number can be calculated by evaluating Eq. 1.2.1 with the help of the pull-back  $\omega(\hat{n}) := \hat{n}^* \omega_0$ . Since we have defined the magnetization in Cartesian coordinates  $\{x_1, x_2, \dots, x_d\}$ , the standard volume form is  $\omega_0 = dx_1 \wedge \dots \wedge dx_d$  and the pull-back takes the simple form

$$\omega(\hat{n}) = \det(\hat{n} | D\hat{n}) = \det \left( \hat{n} \left| \begin{array}{c} \frac{\partial \hat{n}}{\partial x^1} \\ \vdots \\ \frac{\partial \hat{n}}{\partial x^d} \end{array} \right. \right) dx^1 \wedge \dots \wedge dx^d. \quad (1.2.3)$$

In a later context we will refer to this pull-back as the *topological charge density* since the winding number can be considered as a conserved *topological charge*. The terms 'topological winding number' and 'topological charge' are often used equivalently. Upon integration over  $\mathbb{R}^d$ , we obtain the oriented area covered by  $\hat{n}$  and the winding number evaluates to

$$\mathcal{W}(\hat{n}) = \frac{1}{\text{area of } \mathbb{S}^{d'}} \int_{\mathbb{R}^d} \omega(\hat{n}) dx^d. \quad (1.2.4)$$

In magnetism, this still quite general formula reduces even further since only the two cases  $d = 1$  and  $d = 2$  are of particular interest.

For  $d = 1$ , the magnetization is a function  $\hat{n} : \mathbb{R} \cup \{\infty\} \rightarrow \mathbb{R}^2$  and can be represented as  $\hat{n}(x) = (\cos \phi(x), \sin \phi(x))^T$ ,  $\phi : \mathbb{R} \rightarrow \mathbb{R}$ . Taking into account that the magnetization has to be the same at both ends of the wire,  $\hat{n}(-\infty) = \hat{n}(+\infty)$ , it follows that the difference

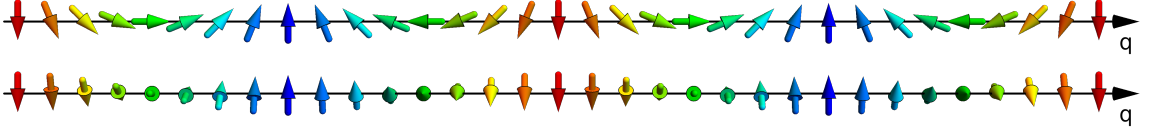


Figure 1.3.4.: Examples of coplanar spin spirals characterized by a plane normal  $\hat{v}$ . The upper chain shows a spiral with  $\hat{v} \perp \hat{q}$ . The lower chain is an example of the special case  $\hat{v} \parallel \hat{q}$  which is also referred to as *helix*.

$\Delta\phi = \phi(\infty) - \phi(-\infty)$  can only be an integer multiple of  $2\pi$ ,  $\Delta\phi = 2\pi N$  with  $N \in \mathbb{Z}$ . The winding number therefore takes the form

$$\mathcal{W}(\hat{n}) = \frac{1}{2\pi} \int_{-\infty}^{\infty} \left( \hat{n}_1 \frac{d\hat{n}_2}{dx} - \frac{d\hat{n}_1}{dx} \hat{n}_2 \right) dx = \frac{1}{2\pi} \int_{-\infty}^{\infty} \phi'(x) dx = \frac{1}{2\pi} \Delta\phi = N \in \mathbb{Z} \quad (1.2.5)$$

and in particular  $\mathcal{W}(\hat{n}) = N = 1$  for the example shown in Fig. 1.2.3.

The case  $d = 2$  evaluates the *skyrmion number* which is most important for the following discussions. For a magnetization  $\hat{n} : \mathbb{R}^2 \cup \{\infty\} \rightarrow \mathbb{R}^3$  it takes the form

$$\mathcal{W}(\hat{n}) = \frac{1}{4\pi} \int_{\mathbb{R}^2} \hat{n} \cdot \left( \frac{d\hat{n}}{dx_1} \times \frac{d\hat{n}}{dx_2} \right) d(x_1, x_2) \in \mathbb{Z}. \quad (1.2.6)$$

### 1.2.3. The skyrmion number on a lattice

Note that we often do not consider a continuous function for the magnetization but rather a discrete set of magnetization vectors on a square lattice. In this case, the derivatives in Eq. 1.2.6 can be approximated which always comes with certain errors. However, we can avoid these errors with an exact computation using the Oosterom and Strackee algorithm [9]. First, we introduce a triangulation of the two-dimensional plane, for example by dividing each square tile of the original square lattice into two triangular tiles. The triangulation must cover the whole space without triangles overlapping. Let the triangle  $\Delta_{ijk}$  be defined as the area between the sites  $\{i, j, k\}$  and  $\Omega_{ijk}$  is the solid angle spanned by the corresponding spins  $\{\hat{n}^i, \hat{n}^j, \hat{n}^k\}$  at these sites. From geometric considerations, they can be identified as

$$\tan \left( \frac{\Omega_{ijk}}{2} \right) = \frac{\hat{n}^i \cdot (\hat{n}^j \times \hat{n}^k)}{1 + \hat{n}^i \cdot \hat{n}^j + \hat{n}^j \cdot \hat{n}^k + \hat{n}^k \cdot \hat{n}^i}. \quad (1.2.7)$$

Instead of integrating over the pull-back to calculate the oriented area, we can now directly sum over the solid angles  $\Omega_{ijk}$  of all triangles  $\Delta_{ijk}$ . The skyrmion number for the magnetization on a discrete lattice then evaluates to

$$\mathcal{W} = \frac{1}{4\pi} \sum_{\Delta_{ijk}} \Omega_{ijk}. \quad (1.2.8)$$

## 1.3. Twists in d=1: Spiral, helical, and the conical phases

Most of the materials which will be discussed in the context of this work are three-dimensional bulk magnets or thin films of these. In general, the magnetization therefore is a function  $\hat{n} :$

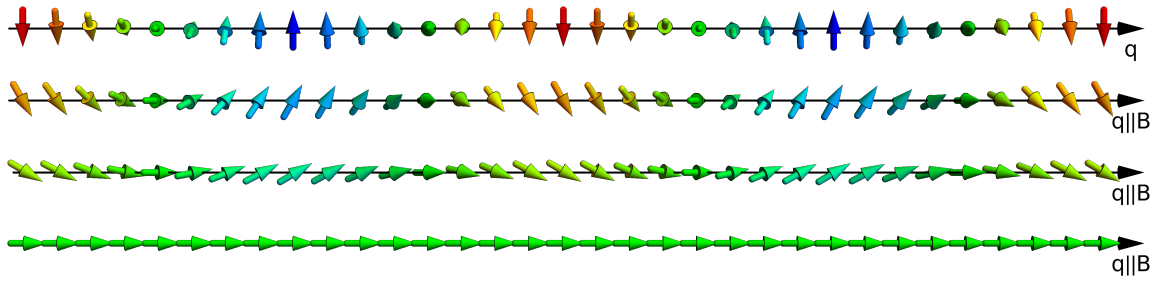


Figure 1.3.5.: Transition of the helical state (top chain) to the polarized state (bottom chain) induced by an increasing external magnetic field  $\mathbf{B}$ . The transition is continuous by tilting all spin in the direction of the field with  $\hat{q} \parallel \mathbf{B}$ . The intermediate states are conical states (the spins are on a cone with an opening in the direction  $\hat{q}$ ). From the first to second chain, rotation symmetry about  $\hat{z}$  (with  $\hat{z} \perp \hat{q}$ ) is broken and from the third to the fourth chain a rotation symmetry about  $\hat{q}$  manifests. Thus both transitions are of second order.

$\mathbb{R}^3 \rightarrow \mathbb{S}^2$  which may realize arbitrarily complicated textures. However, textures with periodic modulations in only one spatial dimension are very popular in non-collinear magnetism but also in other areas of physics such as cholesteric liquid crystals [10].

### 1.3.1. Coplanar spin spirals: Spirals and helices

Coplanar spin spirals are a prominent candidate of this class of magnetic textures. As the name suggests, upon translation in the direction  $\hat{q}$ , the spins rotate unidirectionally in a common plane defined by the normal vector  $\hat{\nu}$ . In the directions perpendicular to  $\hat{q}$ , the system is translation invariant. The direction of  $\hat{q}$  is usually pinned by anisotropies and degenerate. Two examples for such *spiral states* are shown in Fig. 1.3.4. The upper chain of arrows represents a periodic spiral comparable to the projection in Fig. 1.2.3 with  $\hat{\nu} \perp \hat{q}$ . The lower panel shows the *helical state* which is also a spiral but with the special condition that  $\hat{\nu} \parallel \hat{q}$ . The symmetry which both these spirals share is a rotation by  $\pi$  about any axis perpendicular to  $\hat{q}$ . Note that the helix is in addition invariant under  $\pi$ -rotations about  $\hat{q}$  followed by time reversal.

Dependent on the symmetries of the specific material, the one kind of rotation is favored over the other. In chiral magnets, where bulk-type DMI is the driving force for spiralization [11], helices are predicted as the thermodynamic ground state at low temperatures. This generic prediction is in agreement with a huge number of experiments on various chiral magnets, following after the indirect observation by neutron scattering on MnSi by Ishikawa *et al.* [12,13] and the direct real-space measurements by LTEM on  $\text{Fe}_{0.5}\text{Co}_{0.5}\text{Si}$  by Uchida *et al.* [14].

Moreover, in compounds where the coplanar spirals are stabilized by interfacial-type DMI, the extra symmetry of the helical state is broken by the sample, i.e. usually either by an interface [15] or by the underlying atomic lattice as in polar magnets [16].

From the optical similarity to Fig. 1.2.3 and the description now effectively being  $\hat{n} : \mathbb{R} \rightarrow \mathbb{S}^1$ , it is quite natural to also assign a winding number to these periodic states. Assuming that the magnetization at the edges is pinned, this implies that the wavelength of the spiral can only change in discrete steps. Such an incommensurate-commensurate phase transition to the finally polarized state has indeed been observed experimentally in the monoaxial chiral magnet  $\text{Cr}_{1/3}\text{NbS}_2$  by Togawa *et al.* [17–21] who applied a magnetic field in the rotary plane of the helical state,  $\hat{q} \perp \mathbf{B}$ .

### 1.3.2. Escape through the third dimension: The conical phase

However, what happens more often in standard bulk chiral magnets with isotropic DMI is that the  $\hat{q}$ -vector of the helix orientates away from the pinning directions and aligns with the applied field,  $\hat{q} \parallel \hat{\nu} \parallel \mathbf{B}$ . The magnetic field has then triggered the true  $\mathbb{S}^2$ -nature of the magnetization and the confinement to the rotary plane is broken. The new state which is generated from the helix by tilting the magnetization out of the common plane and towards  $\hat{q}$  now breaks the  $\pi$ -rotation symmetry about the axes  $\hat{z} \perp \hat{q}$ . It is called the *conical state* since the magnetization now rotates on a common cone instead of a common plane. The transition from the helical state to the conical state and finally to the polarized state is sketched in Fig. 1.3.5. This escape through the third dimension via the conical phase is long known for helimagnets and has been extensively studied theoretically and experimentally [22–24]. Note that both transitions on the way to the polarized state are second order. If the helix is for any reason not able to undergo a reorientation, arbitrary angles  $\angle(\hat{\nu}, \hat{B})$  may be realized. In this case, a study by Laliena *et al.* [25] suggests that the order of the transition depends on the angle.

However, so far this section has omitted the existence of phases with modulations in more than one spatial dimension. The power of topological concepts in magnetism comes to full glory when modulations in more dimensions are taken into account.

## 1.4. Skyrmions: From nuclear physics to condensed matter

Back in 1961, the British nuclear physicist Tony H. R. Skyrme proposed a new model for the description of the fermionic neutrons and protons in the atomic nucleus [26–28]. He introduced a non-linear sigma model which combines three bosonic pion fields into one  $SU(2)$ -valued field  $U(\mathbf{r})$ . Since  $U$  is intended to describe the interior of the nucleus, it is defined on  $\mathbb{R}^3$  but should decay sufficiently fast for  $\mathbf{r} \rightarrow \infty$ . Effectively, this means that the field  $U : \mathbb{R}^3 \cup \{\infty\} \rightarrow SU(2)$  can be rewritten as a map  $\tilde{U} : \mathbb{S}^3 \rightarrow \mathbb{S}^3$  and hence according to Sec. 1.2 topological solitons may exist. These topologically non-trivial solitons, which are associated to the protons and neutrons, are called *skyrmions*.

### 1.4.1. Skyrmions in all areas of physics

Over the time, however, an ever growing amount of localized and topologically non-trivial quasi-particles has emerged in many areas of physics and they are also treated under the name *skyrmion*. Examples range from particle physics [29–33] over quantum physics in, for example, the Hall state at half filling [34–36] or Bose-Einstein condensates [37–39] to more macroscopic systems as liquid crystals [40].

Vortices are also topological objects and already long-known in the XY-model, where they mediate a particular type of phase transition [41–43]. In magnetism, strong anisotropies may lead to a confinement of the magnetization to the two-dimensional plane and hence the magnetic moments are effectively two-dimensional, see Ref. [44] for a review. A sketch of a magnetic vortex configuration as a projection of a topologically non-trivial map  $\mathbb{S}^1 \rightarrow \mathbb{S}^1$  is shown in Fig. 1.4.6. Important is here, that the vortex in the two-dimensional plane is long-ranged and it can not unwind into a uniformly polarized background without further topological defects, e.g. an anti-vortex. The  $\mathbb{S}^1$ -winding number, see Eq. 1.2.5, for any closed path therefore counts the charges of all vortex cores in the enclosed area.

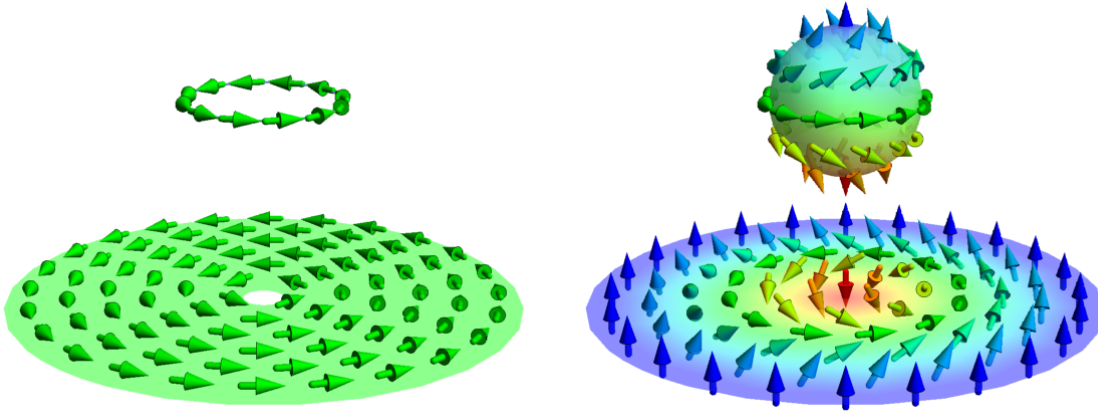


Figure 1.4.6.: Left: Representation of a *vortex* in a two-dimensional plane and its mapping to  $S^1$ , represented as a circle, compare Fig. 1.2.2. The core of the projection is left out since the texture is singular there. Right: Representation of a topologically non-trivial *combed hedgehog*  $\hat{n} : S^2 \rightarrow S^2$  in  $\mathbb{R}^3$  and its stereographic projection  $S^2 \rightarrow \mathbb{R}^2$ , the *skyrmion*.

### 1.4.2. The zoology of $S^2$ magnetic skyrmions

The *magnetic skyrmion* [45], in contrast to the magnetic vortex, is built from  $S^2$ -spins. As a consequence, it can exploit the third dimension in order to be smoothly integrated into a polarized background without the need for an anti-skyrmion. In contrast to the vortex, the skyrmion is therefore not necessarily long-ranged and, in particular, the concept of an  $S^1$ -winding number does not apply here: a closed path does not yield any information about the number of skyrmions.

The topological character of a skyrmion is visualized in Fig. 1.4.6 via the stereographic projection of the *combed hedgehog* which is a topologically non-trivial mapping  $\hat{n} : S^2 \rightarrow S^2$ , see Sec. 1.2. The skyrmion thus directly inherits the topological properties of the hedgehog. To show this property, let us consider the winding number, Eq. 1.2.6, for a circular skyrmion in a polarized background  $\hat{n}(\infty) = \hat{z}$ . This very particular choice makes the calculation easier while the result is still valid for any skyrmion that can be smoothly transformed to the circular skyrmion. Next, we choose a parametrization of the two-dimensional plane in cylindrical coordinates  $\mathbf{r} = \rho(\cos \phi, \sin \phi)^T$  and the normalized magnetization  $\hat{n}(\mathbf{r})$  with a trivial pull-back

$$\hat{n}(\mathbf{r}) = \hat{n}(\theta, n_z) = \begin{pmatrix} \sqrt{1 - n_z^2} \cos \theta \\ \sqrt{1 - n_z^2} \sin \theta \\ n_z \end{pmatrix} \quad \text{with } \theta = \theta(\phi), n_z = n_z(\rho). \quad (1.4.9)$$

The expression for the winding number then simplifies to

$$\begin{aligned} \mathcal{W}(\hat{n}) &= \frac{1}{4\pi} \int_{\mathbb{R}^2} \hat{n} \cdot \left( \frac{d\hat{n}}{dx_1} \times \frac{d\hat{n}}{dx_2} \right) d(x_1, x_2) \\ &= \frac{1}{4\pi} \int_{\mathbb{R}^2} \hat{n} \cdot \left( \frac{d\hat{n}}{d\rho} \times \frac{d\hat{n}}{d\phi} \right) d(\rho, \phi) \\ &= \frac{1}{4\pi} \int_{\mathbb{R}^2} \left( \frac{\partial \theta}{\partial \rho} \frac{\partial n_z}{\partial \phi} - \frac{\partial n_z}{\partial \rho} \frac{\partial \theta}{\partial \phi} \right) d(\rho, \phi) \end{aligned} \quad (1.4.10)$$

$$\begin{aligned}
& \text{use } \theta = \theta(\phi), n_z = n_z(\rho) \text{ and } \Delta n_z := n_z(\infty) - n_z(0) \in \{-2, 0, 2\} \\
& = -\frac{\Delta n_z}{4\pi} \int_0^{2\pi} \frac{\partial \theta}{\partial \phi} d\phi \\
& \text{use the d=1 result from Eq. 1.2.5 with } \Delta\theta/2\pi \in \mathbb{Z} \\
& = -\frac{\Delta n_z}{2} \Delta\theta \in \mathbb{Z}.
\end{aligned}$$

For the skyrmion in Fig. 1.4.6 with  $\Delta n_z = 2$  and  $\Delta\theta = 2\pi$  follows  $\mathcal{W}(\hat{n}) = -1$ . Note that the sign is sometimes redefined.

Interestingly, we have derived that with the restrictions  $\theta = \theta(\phi), n_z = n_z(\rho)$  the two-dimensional winding number for the skyrmion traces back to the one-dimensional winding number in Eq. 1.2.5. Skyrmions with other winding numbers can hence be constructed by replacing the angular dependence  $\theta(\phi)$  by any other non-trivial dependence as depicted in Fig. 1.2.2(a)-(f). The results are sketched in Fig. 1.4.7.

We can obtain trivial bubbles (a) and (b) with  $\mathcal{W} = 0$  that can be transformed smoothly into the polarized background. Skyrmions are called *Néel-type* (c) or *Bloch-type* (d) with ( $\mathcal{W} = -1$ ), dependent on the orientation of the rotary plane of the magnetization when going from the core to the outside rim. This orientation is often referred to as helicity and does not affect the winding number. A Bloch-type skyrmion with opposite helicity is shown in panel (g). Also circular higher order skyrmions (e) with ( $\mathcal{W} = -2$ ) can be constructed, or anti-skyrmions (f) with ( $\mathcal{W} = +1$ ). Note that the skyrmion is rotation invariant but has a helicity-degree of freedom, whereas the anti-skyrmion breaks rotation invariance and thus the rotation couples to the helicity. Furthermore, also upon time reversal,  $\hat{n} \rightarrow -\hat{n}$ , the winding number changes sign (h).

The result from Eq. 1.4.10 can be even used to describe more complicated textures such as the *skyrmionium* in panel (i): The center of the skyrmion of panel (d) is widened and the anti-skyrmion of panel (h) is inserted. The respective winding numbers then add to zero and the skyrmionium therefore is equivalent to a trivial bubble. The same result is obtained from Eq. 1.4.10 since  $\Delta n_z = 0$ . More generally, this construction recipe yields to the class of *target skyrmions*, i.e. skyrmion which wind by  $n\pi$  when going from the core to the rim. Special cases are the skyrmion with  $n = 1$  and the skyrmionium with  $n = 2$ .

In principle, the uniformly polarized backgrounds could also be in-plane. A skyrmion in such a background is depicted in panel (j) and has been constructed again by a stereographic projection of a hedgehog after turning it by  $90^\circ$  first. Regarding this in-plane skyrmion, the green horizontal line of rotating spins catches the eye: Cutting along this line, the skyrmion decays into two long-ranged objects called *merons*, each with  $\mathcal{W} = -1/2$ . A meron can be viewed as half a skyrmion or equally the continuous version of a vortex, which exploits the third dimension at the core. Such a meron is shown in panel (k) as a result of the projection of only the southern hemisphere of the combed hedgehog. Note that it inherits properties from both the skyrmion and the vortex. Another meron which will appear in the context of this thesis is shown in panel (l), where the Bloch-type skyrmion of panel (d) is literally cut in half. This meron then forms the one end of an elongated double domain wall string. When the double domain wall is capped by another meron, the resulting object is often referred to as a *bimeron*, which is nothing but an elongated skyrmion [46].

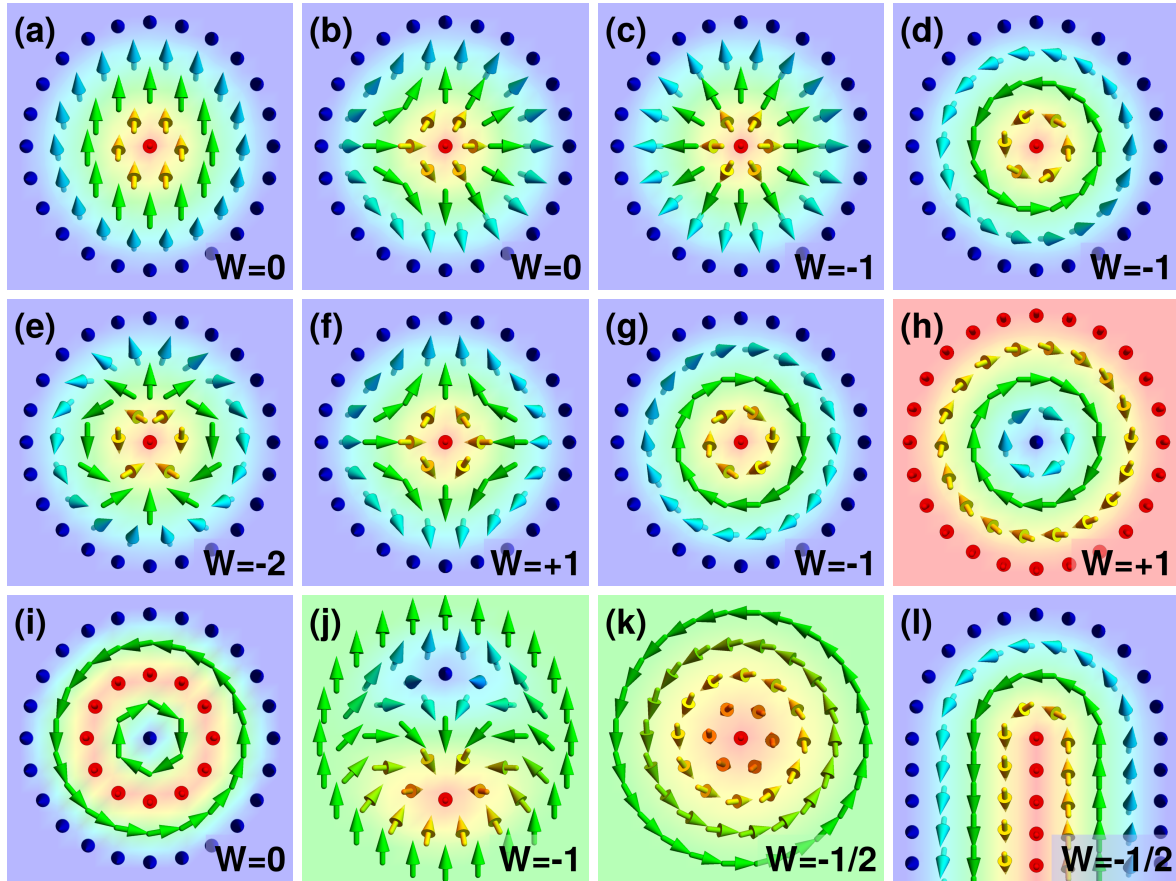


Figure 1.4.7.: Topviews on characteristic magnetic textures with winding numbers as indicated: (a) and (b) magnetic bubbles, (c) Néel-type skyrmion, (d) Bloch-type skyrmion, (e) higher order skyrmion, (f) anti-skyrmion, (g) Bloch-type skyrmions with reversed helicity, (h) Bloch-type skyrmion in opposite background, thus opposite winding number, (i) skyrmionium, (j) skyrmion in in-plane polarized background, (k) meron (vortex-like), (l) meron (half-skyrmion) as on the end of a helical string. The colorcode denotes the  $z$ -component of the magnetization. The angular components for the panels (a)-(f) are taken in the same order as they appear in Fig. 1.2.2. Details are discussed in the main text.

### 1.4.3. Early prediction of magnetic skyrmions

The first predictions of magnetic skyrmions in real materials go back to 1989 when Bogdanov and Yablonskii predicted a thermodynamically stable lattice of vortices in magnets of the crystallographic classes  $C_n$ ,  $C_{n,\nu}$ ,  $D_n$ ,  $S_4$ , or  $D_{2d}$  with  $n = 3, 4, 6$  [47] in a zero temperature model. What the early pioneers Bogdanov and Yablonskii called *vortices* should later turn out to actually be *skyrmions*. In the following years, Bogdanov and Hubert studied the stability of the triangular lattice of skyrmions and its phase boundary to the helical phase [48]. They also predicted stable isolated skyrmions [48] and calculated a repulsive character for their pairwise interaction [49]. Furthermore, they even predicted stable skyrmion-like objects with a  $n\pi$ -rotation: the *target skyrmion* and in particular the *skyrmionium* also goes back to a work by Bogdanov and Hubert in 1999 [50]. Bogdanov and Rößler then extended the candidates for skyrmion hosting materials to also thin films and multilayers where a broken inversion symmetry at the surface or interface stabilizes skyrmions [51]. Finally, in 2006, the term

*skyrmions* is first mentioned in a publication by Rößler, Bogdanov and Pfleiderer [52] who extended the models in Refs. [47–51] by a magnetization with a variable amplitude to leave no doubt that skyrmion lattices are indeed possible ground states in chiral magnets, at surfaces and in multilayer systems.

Another three years later, in 2009, the skyrmion lattice was indeed measured for the first time.

#### 1.4.4. First experimental confirmation in MnSi

It was already long-known from small angle neutron scattering (SANS) experiments, that the chiral magnet MnSi exhibits an unusual phase called *A-phase* close to the thermal phase transition to the paramagnetic state [22].

However, it was up to Mühlbauer *et al.* [53] to observe that in this phase a six-fold Bragg pattern appears in the plane perpendicular to the external field, see top panels of Fig. 1.4.8, and that it forms independently of the orientation of the crystal. They used a standard Ginzburg-Landau theoretical model [11] for the energy of a ferromagnet with broken bulk inversion symmetry. This model includes the stiffness of the magnetization  $J$ , the DMI parameter  $D$ , an external magnetic field  $\mathbf{B}$  and the Landau-parameters  $r_0$  and  $U$  to control the temperature-dependent absolute value of the magnetization  $\mathbf{M}$ :

$$\mathcal{F}[\mathbf{M}] = \int d^3r \quad r_0 \mathbf{M}^2 + J(\nabla \mathbf{M})^2 + 2D \mathbf{M} \cdot (\nabla \times \mathbf{M}) + U \mathbf{M}^4 - \mathbf{B} \cdot \mathbf{M}. \quad (1.4.11)$$

In contrast to the previous studies, however, they did not use the energy  $\mathcal{F}[\mathbf{M}]$  to determine the ground state but instead used the free energy  $\mathcal{G}$  which describes the thermodynamic ground state of the system. In dimensionless units,  $\mathcal{G}$  can be calculated from the functional integral

$$\exp(-\mathcal{G}) = \int \mathcal{D}\mathbf{M} \exp(-\mathcal{F}[\mathbf{M}]). \quad (1.4.12)$$

This integral can be approximated around the fixed points  $\left. \frac{\delta \mathcal{F}}{\delta \mathbf{M}} \right|_{\mathbf{M}_0} = 0$  to leading order (Gaussian fluctuations). The free energy of a configuration  $\mathbf{M}_0$  is then approximated as

$$\mathcal{G} \approx \mathcal{F}[\mathbf{M}_0] + \frac{1}{2} \log \det \left( \left. \frac{\delta^2 \mathcal{F}}{\delta \mathbf{M} \delta \mathbf{M}} \right) \right) \Big|_{\mathbf{M}_0} \quad (1.4.13)$$

and can be compared to the free energy of other states.

The resulting phase diagram is shown in the bottom left panel of Fig. 1.4.8. The shift of the free energy due to the Gaussian fluctuations is shown in the inset. Note that this approximation is only well defined if the corrections are sufficiently small, thus only the part of the phase diagram which is below the red dashed line should be treated seriously.

The seemingly well agreement between theory and experiment thus provides evidence that the A-phase is indeed an entropy-stabilized triangular lattice of skyrmions, see lower panels of Fig. 1.4.8. Interestingly, the model only requires a ferromagnet with broken bulk inversion symmetry and a decent magnetic field. The result can thus be considered *universal*. However, this first measurement was not only indirect but also at fairly low temperatures ( $\sim 30\text{K}$ ), finite magnetic field ( $\sim 0.2\text{T}$ ), and only in a tiny pocket in phase space.

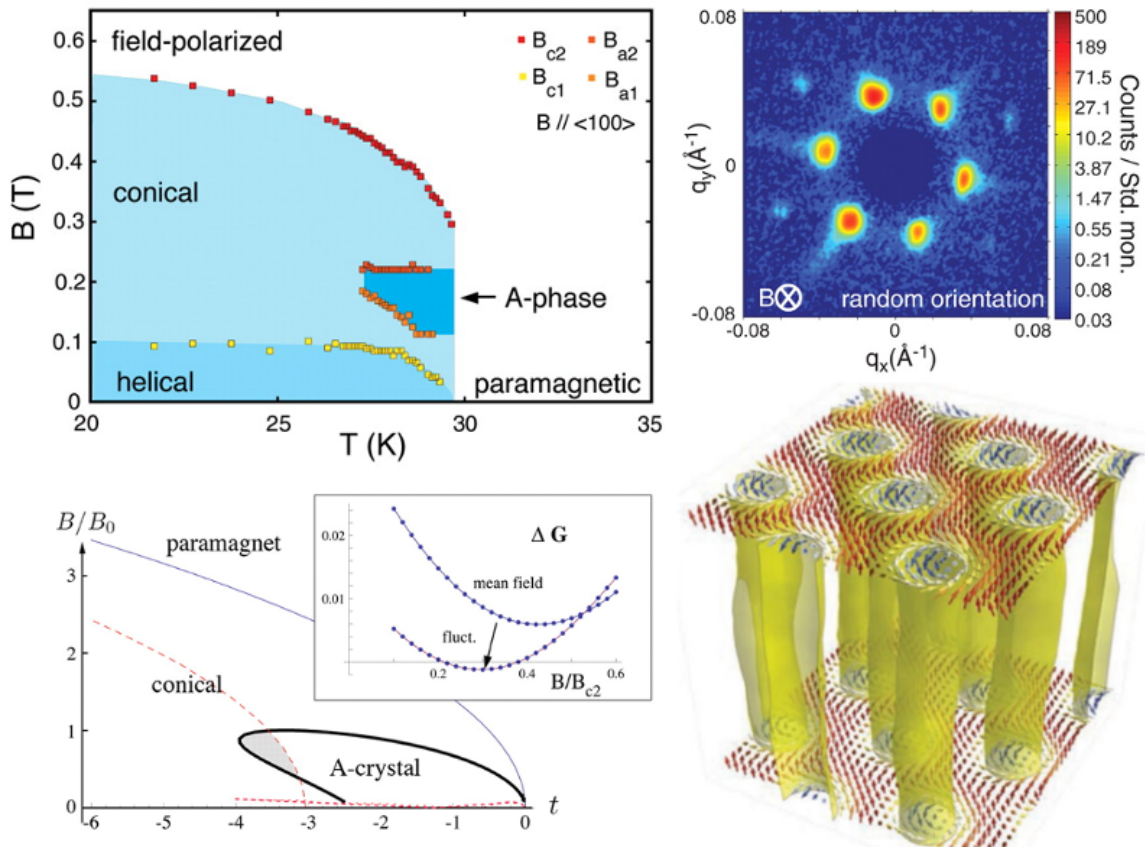


Figure 1.4.8.: The first indirect experimental observation of a skyrmion lattice in MnSi. In the B-T-phase diagram (top left panel), the A-phase was discovered early among the other phases, but could not be explained [22]. SANS measurements from 2009 [53] showed a 6-fold Bragg pattern (top right panel) in the plane perpendicular to the external field, independent of the orientation of the crystal. A theory taking into account thermal fluctuations to the level of Gaussian corrections [53] could derive a consistent phase diagram (bottom right panel). Images taken from Ref. [53]. The A-phase was identified with the skyrmion lattice. A schematic representation is shown in the bottom right panel. Image taken from Ref. [54].

### 1.4.5. Skyrmions in more materials

#### Bulk crystals

This first observation was followed by a wave of new experiments on different materials. An overview is provided in Table 1.4.1.

The list ranges from metals [53, 55–57, 67] over doped semi-conductors [64, 65] to insulators [70–75], among which FeGe comes with the highest critical temperature: a skyrmion lattice can be observed almost at room temperature. A specialty for the insulator  $\text{Cu}_2\text{OSeO}_3$  are its magneto-electric properties, which make it controllable by not only magnetic but also electric fields [72, 87–89]. In addition to these observations also magnetic [90–93] and ultra sound [94] resonance experiments were performed that report a good agreement between theory and experiment .

Additionally, in 2015 Tokunaga *et al.* [78] observed a skyrmion lattice in  $\beta$ -Mn-type Co-Zn-

## I. Introduction

material	sample	conduction	$\Delta T_{\text{sky}}/\text{K}$	$\lambda_{\text{H}}/\text{nm}$	Type	Refs.
MnSi	bulk	metal	28 - 29.5	18	Bloch	[53, 55–57]
MnSi (press.)	bulk	metal	5 - 29	18	Bloch	[58–61]
MnSi	film ( $\sim 50\text{nm}$ )	metal	$<5$ - 23	18	Bloch	[62, 63]
$\text{Fe}_{1-x}\text{Co}_x\text{Si}$	bulk	semi-metal	25 - 30	37	Bloch	[64, 65]
$\text{Fe}_{0.5}\text{Co}_{0.5}\text{Si}$	film ( $\sim 20\text{nm}$ )	semi-metal	5 - 40	90	Bloch	[66]
FeGe	bulk	metal	273 - 278	70	Bloch	[67]
FeGe	film ( $\sim 75\text{nm}$ )	metal	250 - 270	70	Bloch	[67–69]
FeGe	film ( $\sim 15\text{nm}$ )	metal	60 - 280	70	Bloch	[68]
$\text{Cu}_2\text{OSeO}_3$	bulk	insulator	56 - 58	60	Bloch	[70–75]
$\text{Cu}_2\text{OSeO}_3$	film ( $\sim 100\text{nm}$ )	insulator	$<5$ - 57	50	Bloch	[71, 76]
$\text{Co}_8\text{Zn}_8\text{Mn}_4$	bulk	metal	284 - 300	125	Bloch	[77]
$\text{Co}_8\text{Zn}_9\text{Mn}_3$	bulk	metal	311 - 320	$>125$	Bloch	[78]
$\text{Co}_8\text{Zn}_9\text{Mn}_3$	film ( $\sim 150\text{nm}$ )	metal	300 - 320	$>125$	Bloch	[78]
$\text{GaV}_4\text{S}_8$	bulk	semi-metal	9 - 13	17.7	Néel	[16]
Fe/Ir(111)	monolayer	—	$\sim 11$	$\sim 1$	Néel	[15, 79, 80]
PdFe/Ir(111)	bilayer	—	$\sim 4.2$	$\sim 1$	Néel	[15, 80–84]
(Ir/Co/Pt) <sub>10</sub>	multilayer	metal	$\leq \text{RT}$	30 – 90	Néel	[85]
Pt/CoFeB/MgO	multilayer	metal	$\leq \text{RT}$	480	Néel	[86]

Table 1.4.1.: Selection of materials that are known to host skyrmion lattices or single skyrmions. The table covers bulk materials, thin films, and layer-materials, see second column. The conductive behavior - if known - is given in the third column. The following columns provide the temperature range  $\Delta T_{\text{sky}}$  at which skyrmions were observed, the wavelength  $\lambda_{\text{H}}$  of the helical/stripe phase, and the texture of the skyrmion (compare Fig. 1.4.7). The References are listed in the last column. RT is short for room temperature.

Mn alloys. These alloys have a broken inversion symmetry in the bulk, but in contrast to the space group  $P2_13$  of the above mentioned materials they come with space groups  $P4_132$  or  $P4_332$ . Interestingly, the changed composition results in both a larger length scale of the magnetic structures but also an elevated temperature for the observation of the skyrmion lattice. Dependent on the composition ( $\text{Co}_x\text{Zn}_y\text{Mn}_z$  with  $x+y+z=20$ ), skyrmions can be observed at room temperature [77] and even above [78].

Nevertheless, what all bulk magnets have in common is the relatively small pocket in the (universal) B-T-phase diagram where the thermodynamically stable skyrmion lattice occurs. This observation is in agreement with theoretical predictions, which foot on both analytical [53, 95] and numerical studies [96](Monte Carlo).

One way to enlarge the pocket is to exploit the (topological) stability of the skyrmion: A singular and hence energetically costly spin configuration, called *Bloch point* (or also *emergent monopole*), needs to annihilate one skyrmion string or zip two skyrmions together [54, 97–99].

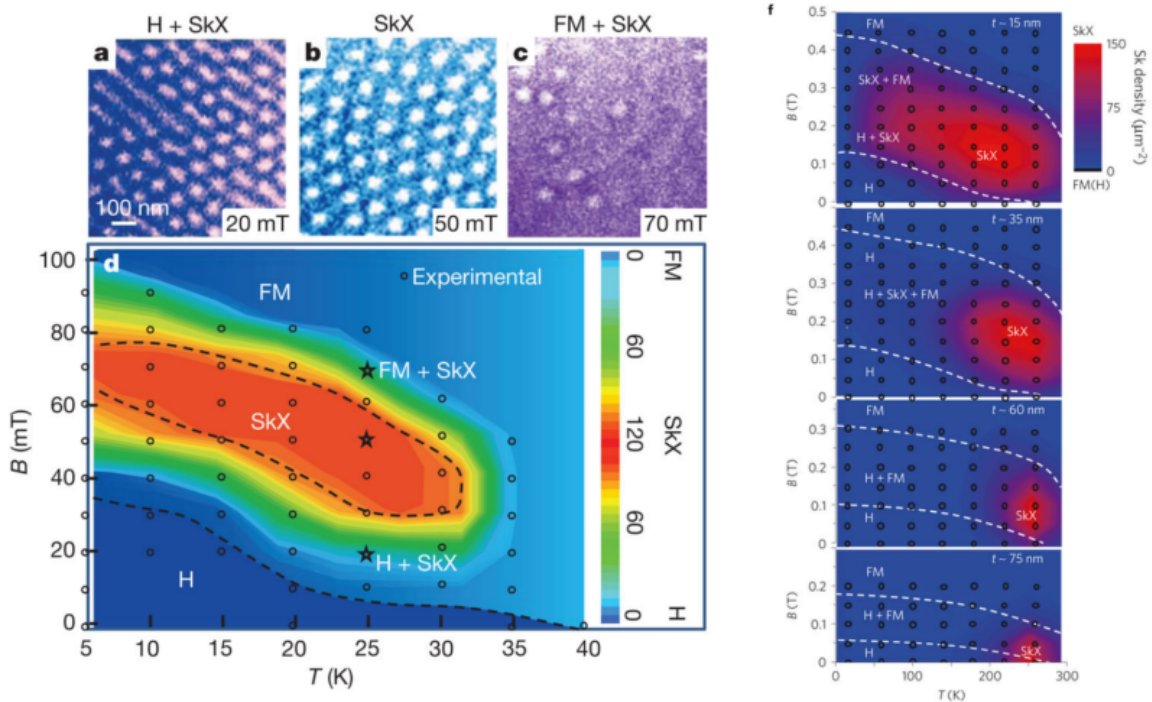


Figure 1.4.9.: Left: results from Lorentz transmission electron microscopy (LTEM) on a film ( $\sim 20$ nm) of  $\text{Fe}_{0.5}\text{Co}_{0.5}\text{Si}$ . (a-c) show the real-space images from LTEM. (d) shows the B-T-phase diagram obtained from an analysis of the images. Figure taken from Ref. [66]. Right: (f) shows the skyrmion lattice (SkX) in the B-T-phase diagram for thin films of FeGe with different thicknesses  $t$  as indicated in the panels ( $t \sim 15, 35, 60, 75$ nm). Figure taken from Ref. [68].

Upon rapid cooling, the skyrmion lattice remains metastable at lower temperatures [100] and eventually even changes from a triangular to a square lattice [77]. Note that the skyrmion lattice in this case is only metastable and thus decays into the real thermodynamic ground state. For more details, see Sec. 5.

### Thin films of bulk crystals: The importance of surfaces

A robust way to enlarge the pocket was found already in 2010, when the first real-space observation of a skyrmion lattice was achieved by Lorentz transmission electron microscopy (LTEM). This technique builds on electrons which get deflected by the magnetic texture while passing through the sample. Consequently, a transparent sample was required which could be achieved by Yu *et al.* [66] who thinned down a  $\text{Fe}_{0.5}\text{Co}_{0.5}\text{Si}$  crystal to only  $\sim 20$  nm thickness. Their observations are shown in Fig. 1.4.9(a-c).

The B-T-phase diagram, Fig. 1.4.9(d), which they could reconstruct from the LTEM images, shows a clearly enlarged area for the skyrmion lattice phase (SkX) which extends down to the lowest accessible temperatures. This observation is in agreement with theoretical calculations of two-dimensional phase diagrams [101–108], where the missing conical phase allows for an expansion of the skyrmion lattice phase space.

However, more recent studies showed that in a chiral magnet the magnetization gets an extra twist at the surface. This additional twist, which is caused by the isotropic character of the

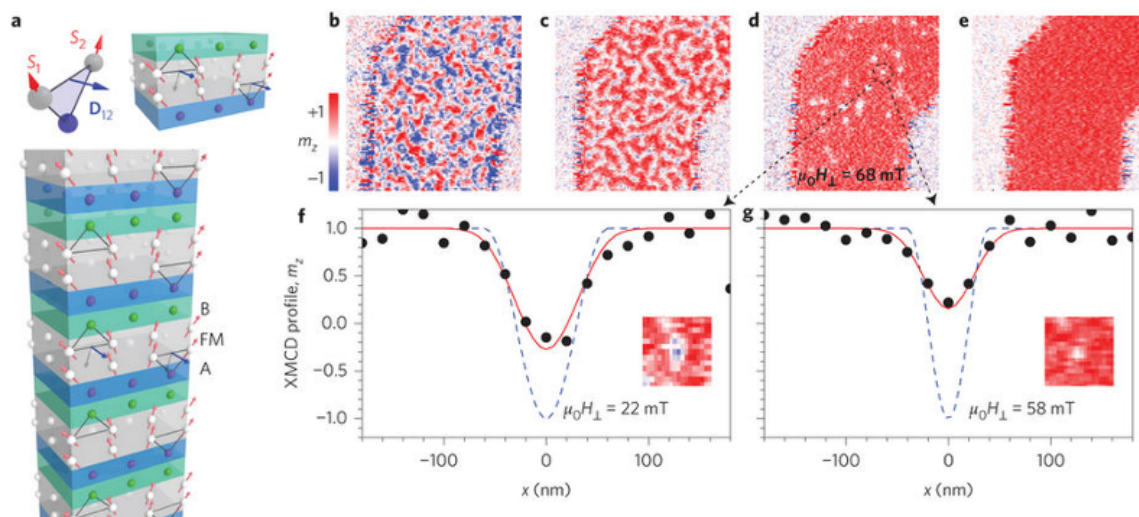


Figure 1.4.10.: (a) Schematic explanation for the source of DMI in stacked multilayers and the idea of additive DMI. (b-e) STXM images of an  $(\text{Ir}/\text{Co}/\text{Pt})_{10}$  multilayer with increasing magnetic field from (b) to (e), taken at room temperature. (f) skyrmion profiles measured by XMCD (black dots) compared to a theoretical prediction (red) which is obtained from convoluting a calculated skyrmion profile (blue dashed) with the profile of the beam. Figure taken from Ref. [85].

Dzyaloshinskii-Moriya interaction, energetically favors skyrmions and helical structures [109] and can stabilize more exotic objects at surfaces [110,111]. Since this is only an surface effect, it is only strong if the film is sufficiently thin. Upon increasing the film thickness the bulk phase diagram is recovered [110,112].

This prediction could also be confirmed in experiments on a thinned crystal of FeGe, which provided ranges of various thickness [68]. A series of B-T-phase diagrams in Fig. 1.4.9(f) shows the transition from almost two-dimensional behavior to three-dimensional bulk behavior. Other experiments on thin films have shown the variety of new effects that arise apart from the enhanced stability, e.g. the deformation of the skyrmion lattice possibly due to strain [113].

### Monolayers and chiral multilayers

The reduced dimensionality enlarges the skyrmion pocket by blocking the conical phase as its direct competitor. An orthogonal approach to the thinning down of bulk crystals is the direct growth of monolayers or thin layers of material [15,80].

In 2011, Heinze *et al.* [79] calculated with *ab initio* methods the magnetic properties of a monolayer of Fe on an Ir(111) surface. The interface between the magnetic iron monolayer and the heavy metal Iridium substrate generates a strong spin-orbit coupling in the magnetic layer and thus interfacial Dzyaloshinskii-Moriya interaction [7]. Additionally, they predicted that four-spin interactions play a crucial role in this artificial compound and thus lead to the stabilization of a square lattice of skyrmions with only a few atoms per magnetic unit cell. This theoretical prediction was accompanied by spin-polarized scanning tunneling microscopy (sp-STM) measurements of the exact material and indeed the nano-skyrmion lattice was observed.

Later experiments on bilayers of PdFe on Ir(111) showed that in these ultra-thin systems it is possible to create single skyrmions with the current from the STM tip [81] and later by only its electric field [114]. Moreover, theoretical predictions of the skyrmion profile fit nicely to the

experimentally observed skyrmions [115].

While the DMI in these ultra thin film setups is generated only at the interface, an additional layer on top of the thin layer can generate an additional source of DMI. Following this idea, materials with arbitrary skyrmions should be realizable [116]. By interlocking the magnetization through many repetitions of layers [85,117], the thermal stability could be increased such that artificially designed skyrmions at room temperature could be observed [85,117–119].

### More candidates for stable skyrmions

Summarizing this paragraph, it should be noted that more recent theoretical works also suggest stable skyrmions and lattices of those in magnets with frustrated symmetric exchange interaction [120–123] and magnets with a dominant antiferromagnetic nearest neighbor exchange [124,125]. While skyrmions in these systems are expected to have interesting properties, none have been observed until now.

## 1.5. A new field emerges: Skyrmionics

Already in the early studies of skyrmions it was realized that the topological nature of the skyrmion leaves a finger print in the Hall signal, if an electric current is applied. This characteristic signal which shows up as an additional Hall signal on top of the normal and the anomalous Hall signal, is called *topological Hall effect* [55]. However, since it is not a unique finger print of the skyrmion lattice, it has been debated whether the Hall signal alone is a good measure for the existence of a skyrmion lattice [126–128].

In the wake of measurements of the topological Hall effect on MnSi it was soon found that if small currents are combined with a magnetic field gradient or temperature gradient they can cause a rotation of the skyrmion lattice [129–133]. Stronger current densities were then found to unpin the skyrmion lattice and drag it with the current [132,134], with corrections of a skyrmion Hall effect [135]. Notably, the required current densities were 5 orders of magnitude smaller than those which are usually no unpin the vortex lattice of a type-II superconductor [132].

### 1.5.1. Skyrmions on a racetrack

The idea to using the spin degree of freedom in data storage and information technology, called *spintronics* in analogy to its more power consuming twin *electronics*, had already emerged before skyrmions were discovered [136]. With the topological aspect that comes with skyrmions, they were soon discussed as a possible candidate for magnetic storage devices [137].

The efficient manipulation of skyrmions by currents inspired ideas of using skyrmions in *racetrack type devices* as shown in Fig. 1.5.11. The racetrack layout was initially proposed by Parkin [138,139] to overcome the density limits of two-dimensional data storages by exploiting the third dimension. The racetrack is based on the more general *shift register memory* which is - most generally - a sequence of information with a specialty: Either the information or the read- and write-elements are mobile and can be shifted along the sequence.

In the racetrack memory, this is realized by a magnetic wire which is divided in a sequence of magnetic domains, see Fig. 1.5.11(A). Here the wire is additionally bent in the third dimension with the read- and write-element fixed at the point where the wire is attached, Figs. 1.5.11(C,D). Current pulses can move the domain walls via spin-transfer torque as indicated in Fig. 1.5.11(A).

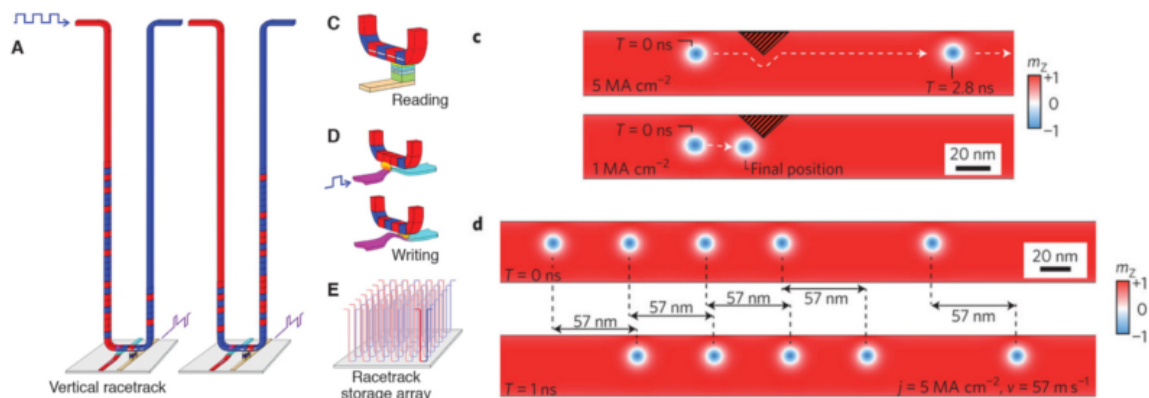


Figure 1.5.11.: Left: The domain wall racetrack as presented in Ref. [139]. (A) Sequence of magnetic domains on a bent wire. The reading element (C) and the writing element (D) are fixed while the data is moved along the wire. High storage densities can be achieved by exploiting the third dimension (E). Part of figure taken from Ref. [139]. Right: The proposal by Fert *et al.*, Ref [140], uses a chain of skyrmions with fixed distances (d) instead of magnetic domains with a fixed length. Skyrmions are mobile and may circumvent defects (c). Part of figure taken from Ref. [140].

Finally, many of these serial memories can be used in parallel which further increases the speed of operation, Fig. 1.5.11(E).

In this original proposal by Parkin, magnetic domains of equal size act as the mobile bits on the data racetrack. With the discovery of highly mobile skyrmions, Fert *et al.* [140] suggested to replace the polarized domains by sections which do have a skyrmion and sections which lack the skyrmion and are polarized, see Fig. 1.5.11(d). Current pulses can push the chain of skyrmions along the wire, which remain at their initial distance, even after a certain time has passed, compare Fig. 1.5.11(d). In addition, the point-like nature of the skyrmions allows for another degree of freedom when it comes to evading defects, see Fig. 1.5.11(c), where the skyrmion can shift within the wire, whereas a one-dimensional domain wall can not.

Furthermore, the non-trivial topology of the skyrmions has the unusual effect that their dynamics are effectively governed by the Thiele equation, which is in more detail described in Sec. 10.3.3 and serves as the basis for large-scale skyrmion simulations [45, 141–145]. As a result, the speed of skyrmions increases by a factor  $1/\alpha$  if it is pushed into the repulsive edge as compared to being pushed directly in the direction of the wire [146–150]. Here  $\alpha$  is the Gilbert damping of the magnetization which can be  $\alpha = 0.3$  in disordered metals [151] but also low as  $10^{-4}$  in insulators [152].

## 1.5.2. The creation of topological particles

Based on this proposal, many theoretical works followed [153, 154] that studied the properties of isolated skyrmions in nanostructures [155, 156]. In a parameter regime where the polarized state is usually the ground state [157], first the question arises how topological whirls can be created on demand.

Exploiting the fact that the magnetization at the edge of the wire is actually not a continuous function anymore, topological charge can be continuously induced into the wire. Following this thought, it was suggested to induce skyrmions from the edge of the wire, either by electric currents [148] or magnetic fields [154], see also Sec. 6.

Other proposals for creating skyrmions require that the energy of a Bloch point is finite, which is certainly the case in the real discrete system. Then skyrmions and anti-skyrmions can be created randomly by temperature [158] or pair-wise by currents [159], where the energetically unfavorable anti-skyrmion decays and only the skyrmion remains stable. Changes of the local magnetic properties of the material [160, 161] may also lead to the formation of skyrmions.

The lifetime of skyrmions has been studied by Monte Carlo (MC) simulations [98, 162] and with the more recently developed geodesic nudged elastic band method (GNEB) [163–165]. Measuring single skyrmions on the nano-scale has been proposed by measuring the topological Hall conductivity [166, 167] in the wire by contacts on the sides or the non-collinear magnetoresistance by contacts on the bottom and top surfaces [168].

### 1.5.3. The interactions of skyrmions

Once that skyrmions are inside the nanostructure, they interact with edges, defects, magnetic textures, and in particular also with other skyrmions. From simulations it is predicted that skyrmions are repulsive to both edges [169] and other skyrmions [49, 141, 169], see also Sec. 7.

However, this is only the case if the exchange interaction is not frustrated [120, 121]. Also, the interaction of skyrmions becomes attractive with both other skyrmions and edges if the background is not out-of-plane polarized but polarized in another direction [170, 171], see also Sec. 12, conical [172, 173], or even a helical phase, see Sec. 4.

Only more recently it was suggested to also take the surface of the racetrack into account, e.g. in the proposal in Ref. [174], where it was shown that a scratch in the surface can attract skyrmions and serve as a track without physical edges. The inverse setup is also shown to work in Sec. 7 and Sec. 8. Note that it is pointed out in Sec. 8 that the edges of the track can lose their repulsive properties if the height of the track reduces close to the edge.

### 1.5.4. Pushing skyrmions

In order to move the skyrmions along the track, the possibility of using spin-polarized currents has been discussed [146–148, 175, 176]. Note that in these scenarios the mass of skyrmions does not play any important role. It should be noted, however, that big skyrmions which usually require strong dipolar interactions can easily deform and thus have a non-negligible mass [177, 178] where DMI-stabilized skyrmions are more rigid and have a low mass [175].

Another possible way of moving skyrmions is due to their interaction with magnons. Early simulations showed that skyrmions in a temperature gradient move towards the source of heat [179] which may be interpreted as a source of magnons. More qualitative studies showed [180–184] that indeed skyrmions are attracted by the source of magnons. This principle can be used for skyrmion control in nanostructures [185] and see also Sec. 9 but note that the interaction of magnons with edges and other textures is of non-reciprocal nature [186, 187]. A more macroscopic but similar mechanism combines a tilted background field combined with an oscillatory superposition, that breaks again sufficiently many symmetries to occupy the translational mode of a skyrmion [188].

Finally, the stability of the trails that the skyrmions take has been studied. If a storage device relies on equidistant skyrmions, they should pass the same distances in the same time. In perfectly clean systems which all previous scenarios assumed, this can certainly be assumed as a fact, apart from inter-skyrmion interactions. Studies on the interaction of skyrmions and

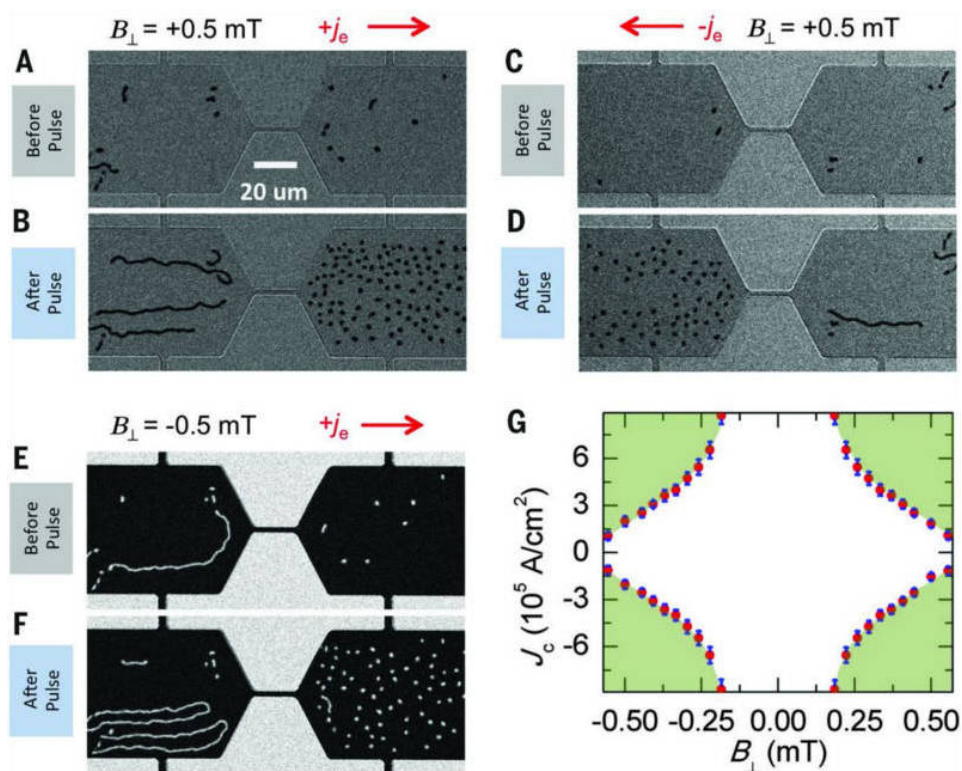


Figure 1.5.12.: Experimental observation as documented by Jiang *et al.* [199]. A trilayer composed as Ta(5 nm)/Co<sub>20</sub>Fe<sub>60</sub>B<sub>20</sub>(CoFeB)(1.1 nm)/TaOx(3 nm) was nanostructured and imaged. The areas covered by the trilayer are clearly visible in panels (E) and (F) as black regions. The smaller structures within this area are skyrmions or elongated skyrmions (bimerons). A magnetic field  $B_{\perp}$  is applied perpendicular to the trilayer. Note that in (E) and (F) the magnetic field is in the opposite direction and hence the contrast is inverted. (A), (C), and (E) show the initial states before any current is applied. (B), (D), and (F) show the magnetization after a current pulse was applied in the direction as indicated by the red arrows. As a result, skyrmions accumulate in the area to which the current points. The green areas in the phase diagram (G) indicate above which current densities  $J_c$  and fields  $B_{\perp}$  the skyrmion proliferation is observed. Figure taken from Ref. [199].

random defects such as vacancies or holes [150] or localized changes in the magnetic properties [149] showed, that the interaction of skyrmions and defects can not only show the repulsive behavior as Fig. 1.5.11(c) but might as well be attractive. In combination with the gyroscopically dominated dynamics, the motion of a skyrmion can appear unforeseen as was computed in effective particle models [45, 141–145] and simulations of tracks which consist of patches of varying anisotropy [189], as expected from experiments [190].

Other problems might also be caused by the thermal diffusion of skyrmions [175]. Here proposals suggest to divide the racetrack into parking lots by using various mechanisms, e.g., voltage gating [191–193]. Coupling layers antiferromagnetically to eliminate the complicated gyroscopic motion has been suggested for skyrmion systems [194] which is in addition known for the positive effects on the acceleration in usual domain wall racetracks [195]. Other suggestions include antiferromagnetic instead of ferromagnetic nearest neighbor exchange interaction [196–198], such that possible problems with stray fields are already eliminated.

### 1.5.5. Other applications with skyrmions

While the skyrmion racetrack is the most prominent candidate for a skyrmion-based device, other ideas include a racetrack with skyrmions and bobbars in bulk chiral magnets [200] or skyrmions and anti-skyrmions in systems with rank-1 DMI [201]. Again other memory applications suggest to exploit the under-cooled square lattice [202] or directly substitute skyrmions for the domains in the currently growing MRAM technology [203, 204].

Moreover, not only memory applications are discussed but also possible low energy logic devices which directly ground on the racetrack layout [205, 206] or which exploit the two-dimensional nature of the skyrmion lattice for reservoir computing [207]. Other ideas are rather more motivated by the similarity to magnetic vortices, e.g. a magnetic oscillator based on gyrating skyrmions [208].

### 1.5.6. Experimental state of the art

On the experimental side, skyrmionics are a challenging task due to both the small spatial dimensions and the small time scales on which skyrmions move. Time-resolved experiments are thus actually a sequence of current pulses with intermediate measurements. Here it is important that the skyrmions are sufficiently large and do not diffuse during the measurement. In such a setup the existence of a skyrmion mass could be proven [178].

Further, a technique to blow skyrmions like soap bubbles was experimentally found [209] and later theoretically analyzed [210, 211]. Also the skyrmion Hall effect was confirmed experimentally [199, 212] and skyrmions could be moved through racetracks [86, 212]. Importantly, the pinning due to defects which also cause accidental skyrmion creation and annihilation and make experiments hard to reproduce could be reduced [212] such that billion times repetitions of a skyrmion motion could be realized.

On a smaller scale, skyrmion production at the edge of a thin film of FeGe was shown experimentally [213] and at the same time predicted theoretically, see Sec. 6.

Finally, on the smallest accessible scale, measurements with spSTM were able to write and delete nanometer sized skyrmions on demand with currents [81] and later only by application of an electric field [114]. These experiments also showed that skyrmions can be measured via their non-collinear magneto-resistance [168], to which already simple STM experiments are sensitive.



## 2. Outline of the thesis

The following presentation of the scientific results of this cumulative thesis is categorized in two parts, namely the published articles in part II and the additional unpublished work in part III. For completeness, the patent application that is related to Sec. 7 is printed in the appendix, Sec. 15. A detailed introduction to the model and methods is additionally provided in the beginning of part III.

The general outline of the following sections is summarized in Fig. 2.0.1. It demonstrates, that the order in which the projects are presented in the following is chosen according to the schematic phase diagram of the two-dimensional chiral magnet, which is the heart of this thesis.

### Topological domain walls

We begin our exploration in a cubic chiral magnet without any applied magnetic field. Below the critical temperature, the thermodynamic ground state is a helix with an orientation along the  $\langle 111 \rangle$ -direction. When the crystal is cooled down from higher temperature, helical domains nucleate with nearly random orientations and expand until the crystal is fully covered in patches of helical domains. Over time, thermal fluctuations help eliminate domain boundaries by rotating some neighboring helical patches parallel, however, other helical domains are pinned and remain differently oriented. The domain walls, that can be arbitrarily complex, are now rearranged by the thermal fluctuations and eventually turn into the energetically optimal domain walls subject to the boundary condition that the helical domains remain pinned. This texture and topology of the resulting domain walls is studied in the publication in Sec. 3 which is in collaboration with the groups of Prof. Dr. Tokura and Prof. Dr. Meier. The article is published in *Nature Physics* [214].

The MFM-measurements of the magnetism on the surface of the considered FeGe crystal revealed that, surprisingly, the observed helical wavelength is precisely the same on the surface

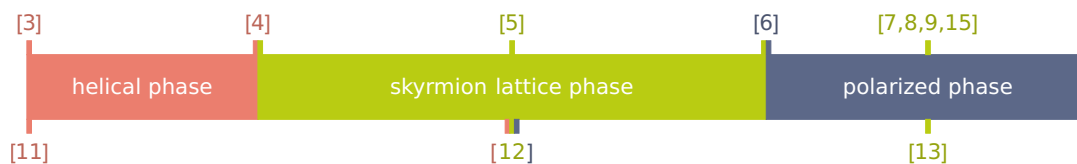


Figure 2.0.1.: Schematic representation of how the projects in the different sections are connected via the schematic phase diagram, sorted by published (above the bar) and unpublished projects (below the bar). The colors encode the thermodynamically stable phases and the also possible metastable excitations that were studied therein. Secs. 3 and 11 are located in the helical phase and Sec. 4 deals with the phase transition to the skyrmion lattice phase. In Sec. 5 the stability of the skyrmion lattice is analyzed. Sec. 6 is dedicated to the polarized phase and its stability with respect to the other phases whereas in Secs. 7, 8, 9, 13, and 15 the ground state is polarized and meta-stable skyrmion are analyzed therein. Sec. 12 covers all phases.

as in the bulk. However, the orientations of the helix on the surface and in the bulk differ. This implies that an interface has to exist underneath the surface of the crystal which separates the two helical phases of different orientation. In Sec. 11, we study this surface reconstruction phenomenon and try to find out whether it can be explained within our simple micromagnetic model.

### Skyrmions in the helix

Besides the topological domain walls between helical domains in Sec. 3 we study another kind of topological defect in the helical phase in Sec. 4 which is the skyrmion. While the skyrmion in a polarized background is now extensively studied, only little is known about isolated skyrmions in a helical background. In Sec. 4, we study the stability and the interactions of skyrmionic defects in the helical phase and how they drive the phase transition to the skyrmion lattice phase. The theoretical work is complemented with experimental LTEM measurements in collaboration with the groups of Prof. Dr. Rønnow and Prof. Dr. Carbone. The article is published in *Physical Review Letters* [215].

### Stability of skyrmions

Once that a skyrmion is established in the system, its topological winding number makes it an extremely robust object. The change of winding number requires a singular Bloch point which has a tremendously high activation energy which makes its thermal excitation very unlikely. In Sec. 5 we study the decay of a skyrmion lattice which is driven into metastable regimes to learn how the lifetime of a skyrmion depends on the free energy activation barrier of the Bloch point. This predominantly experimental work is done in collaboration with the groups of Prof. Dr. Pfeleiderer and Prof. Dr. Back and is published in *Science Advances* [216].

The unpublished work in Sec. 12 explores the stability of the skyrmion lattice phase with respect to the orientation of the external magnetic field. Since the orientation of the magnetic phases is directly correlated with the orientation of the magnetic field, the geometric confinement which arises naturally in the two-dimensional model but also thin films of a chiral magnet is expected to have a crucial effect on the thermodynamic stability of all modulated phases.

### Skyrmions in the polarized phase

For high magnetic fields or strong uniaxial anisotropy, the ground state is the uniformly polarized state except for a narrow region in the proximity of an edge: Here the system can gain energy from the Dzyaloshinskii-Moriya interaction by developing an extra twist of the magnetization. In Sec. 6 we study the spectrum of the bound magnons at this edge and find an instability that triggers the phase transition to the helical phase. Interestingly, this instability can be used to smoothly create a regular chain of metastable skyrmions close to the edge, as has also been demonstrated experimentally in Ref. [213]. Our theoretical work is published in *New Journal of Physics* [217].

The edge instability of the polarized phase offers a method to smoothly create skyrmions close to an edge without the need for a singular magnetization configuration. For storage devices that are based on the creation and annihilation of skyrmions, such as the skyrmion racetrack [140], this could be a very welcome finding. However, Sec. 7 proposes an alternative approach for a skyrmion memory device, see also the appendix 15, which works without the

need to write and erase topologically protected skyrmions but instead offers a scalable energy barrier that protects the data. In this section we also calculate the interaction of skyrmions with three-dimensional nanopatterns and test the validity of the simple Thiele approach for such heavily distorted skyrmions. The article is published in *New Journal of Physics* [218]. The following section, Sec. 8, is a peer-reviewed conference contribution [219] that extends the study of the previous section to more diverse nanostructures. In particular, the additional calculations check for the stability of the effects in Sec. 7 with respect to imperfections of the nanopattern which also includes calculations of the imperfect standard racetrack geometry.

The idea of skyrmion racetracks demands for methods for moving skyrmions efficiently but also rapidly. Two complementary methods are studied here: On the one hand, in collaboration with the group of Dr. Everschor-Sitte we follow in Sec. 13 the more traditional approach and use spin-transfer-torques to move a skyrmion. The unpublished work in this section studies the stability of the driven skyrmion as it deforms under an applied current. On the other hand, in the article in Sec. 9 we exploit the interaction of skyrmions with magnons for the manipulation of a skyrmion in a nanowire. For this study, numerical calculations have been performed in the group of Prof. Dr. Zhou which we supplement with an analysis of a magnon-driven skyrmion within the Thiele framework. The result of this collaboration is published in *New Journal of Physics* [220].



Part II.

Publications



## 3. Topological domain walls in helimagnets

P. Schoenherr<sup>1</sup>, J. Müller<sup>2</sup>, L. Köhler<sup>3</sup>, A. Rosch<sup>2</sup>, N. Kanazawa<sup>4</sup>, Y. Tokura<sup>4,5</sup>, M. Garst<sup>2,3</sup>, D. Meier<sup>1,6,7</sup>

*Topological domain walls in helimagnets*  
Nature Physics (2018)

Doi: 10.1038/s41567-018-0056-5  
Copyright 2018, Springer Nature

### Abstract

Domain walls naturally arise whenever a symmetry is spontaneously broken. They interconnect regions with different realizations of the broken symmetry, promoting structure formation from cosmological length scales to the atomic [1, 2]. In ferroelectric and ferromagnetic materials, domain walls with unique functionalities emerge, holding great promise for nanoelectronics and spintronics applications [3–5]. These walls are usually of Ising, Bloch or Néel type and separate homogeneously ordered domains. Here we demonstrate that a wide variety of new domain walls occurs in the presence of spatially modulated domain states. Using magnetic force microscopy and micromagnetic simulations, we show three fundamental classes of domain walls to arise in the near-room-temperature helimagnet iron germanium. In contrast to conventional ferroics, the domain walls exhibit a well-defined inner structure, which – analogous to cholesteric liquid crystals – consists of topological disclination and dislocation defects. Similar to the magnetic skyrmions that form in the same material [6, 7], the domain walls can carry a finite topological charge, permitting an efficient coupling to spin currents and contributions to a topological Hall effect. Our study establishes a new family of magnetic nano-objects with non-trivial topology, opening the door to innovative device concepts based on helimagnetic domain walls.

### 3.1. Introduction

In chiral magnets, the Dzyaloshinskii-Moriya interaction twists the magnetization and leads to a helimagnetic ground state. The magnetic moments periodically wind around a certain axis  $\mathbf{Q}$ , with the wavelength  $\lambda$  determined by a competition between the usual exchange interaction and the Dzyaloshinskii-Moriya interaction [8]. The overall magnetization can be visualized as

---

<sup>1</sup>Department of Materials, ETH Zurich, Zürich, Switzerland

<sup>2</sup>Institut für Theoretische Physik, Universität zu Köln, Köln, Germany

<sup>3</sup>Institut für Theoretische Physik, Technische Universität Dresden, Dresden, Germany

<sup>4</sup>Department of Applied Physics, University of Tokyo, Tokyo, Japan

<sup>5</sup>RIKEN Center for Emergent Matter Science (CEMS), Wako, Japan

<sup>6</sup>Department of Materials Science and Engineering, Norwegian University of Science and Technology (NTNU), Trondheim, Norway

<sup>7</sup>Center for Quantum Spintronics, Department of Physics, Norwegian University of Science and Technology (NTNU), Trondheim, Norway

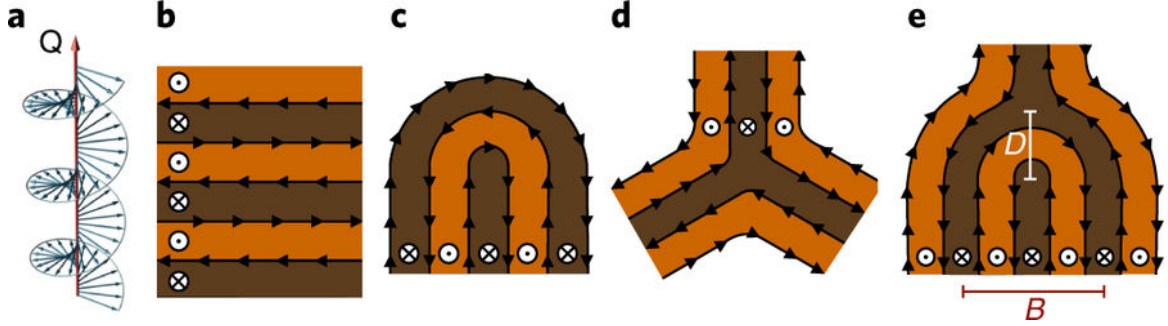


Figure 3.1.1.: Helimagnetic order and defect structures. a, Right-handed magnetic helix. b, Magnetic moments form periodic layers (black arrows) orthogonal to the helix axis  $\mathbf{Q}$ . The bright and dark areas corresponds to stray fields pointing in and out of the plane, respectively. c,  $+\pi$  disclination. d,  $-\pi$  disclination. e, Edge dislocation formed by a pair of  $+\pi$  and  $-\pi$  disclinations at distance  $D$ . The Burgers vector,  $B = 2D$ , is given by an integer multiple of the helix wavelength,  $B = n\lambda$  (here,  $n = 2$ ).

a stack of equidistant sheets with uniformly oriented moments, where the orientation rotates from one sheet to the next (Fig. 3.1.1a,b). The lamellar morphology of the chiral spin texture is thus analogous to cholesteric liquid crystals [9] and, to some extent, magnetic stripe domains [10]. However, the length scales involved are strikingly different. In helimagnets, the characteristic periodicity is up to three orders of magnitude smaller, with lamellae having nanoscopic dimensions.

Despite this difference in length scales, one may expect these systems to develop similar types of defect [11,12]. Smooth spatial variations of the helix axis  $\mathbf{Q}$  simply result in a curvature of the lamellar spin structure [13]. More pronounced variations, however, may break the periodicity and induce vortices – that is, disclinations (Fig. 3.1.1c,d). The strength of such vortices is parametrized by the winding angle of the helix axis on a path encircling the vortex core. As the helix axis is a director ( $\mathbf{Q} = -\mathbf{Q}$ ), half-integer vortices are possible with  $+\pi$  and  $-\pi$  rotations (Fig. 3.1.1c,d). Furthermore, disclinations can pair up and form edge dislocations (Fig. 3.1.1e), with the Burgers vector  $B$  quantifying the distance  $D$  between them.

We reveal the fundamental importance of disclination and dislocation defects for the formation and properties of domain walls in helimagnets, presenting such walls as a magnetic analogue to grain boundaries in liquid crystals. A wide variety of functional helimagnetic domain walls with non-trivial topology is observed, including the vortex domain walls suggested recently [14]. Using magnetic force microscopy (MFM), we study domain walls in the near-room-temperature chiral magnet iron germanium (FeGe;  $T_N = 278$  K). FeGe single crystals are grown by chemical vapour transport and their phase purity (B20) is confirmed by powder X-ray diffraction (see Methods and Supplementary Fig. 3.7.5 for details). For our MFM studies, (100)- and (110)-oriented samples with a thickness of  $\approx 500\mu\text{m}$  are cut and chemo-mechanically polished with silica slurry, yielding flat surfaces with a roughness of about 1 nm. MFM is sensitive to the out-of-plane component of the magnetic stray field, and helimagnetic order manifests as a stripe-like pattern of bright and dark lines in the MFM scans in Fig. 3.1.2a-c (corresponding topography images are presented in Supplementary Fig. 3.7.9). The periodicity of the pattern is  $\lambda = 70\text{nm}$ , matching with previous bulk data [15]. However, we find equivalent values of  $\lambda$  on (100)- and (110)-oriented surfaces, which indicates that  $\mathbf{Q}$  preferentially lies within the surface plane. This orientation is different from the bulk, where  $\mathbf{Q}$  orients along the  $\langle 100 \rangle$  direction.

The MFM data thus reflect a surface-anchoring of  $\mathbf{Q}$  implying a surface reconstruction of magnetic order [16] – that is, formation of magnetic surface domains with in-plane  $\mathbf{Q}$ . Furthermore, the measured statistical orientational distribution of  $\mathbf{Q}$  is almost flat with a slight tendency to point along a  $\langle 100 \rangle$  direction (if present) within the surface plane. The observations indicate that the surface domains are largely independent of both the crystallographic orientation and bulk magnetism.

Most interestingly, the MFM scans reveal helimagnetic domain walls with a complex, but well-defined inner structure. Their structure crucially depends on the angle  $\angle(\mathbf{Q}_1, \mathbf{Q}_2)$  enclosed between the helix axes of the adjacent domains as defined and summarized in Fig. 3.1.2. Based on our data we distinguish curvature walls (type I, Fig. 3.1.2a), zigzag disclination walls (type II, Fig. 3.1.2b) and dislocation walls (type III, Fig. 3.1.2c).

### 3.2. Classification of experimentally observed domain walls

Walls of type I occur for the smallest angles  $\angle(\mathbf{Q}_1, \mathbf{Q}_2) \lesssim 85^\circ$  and exhibit a smooth, continuous rotation of the helix axis from  $\mathbf{Q}_1$  to  $\mathbf{Q}_2$  (Fig. 3.1.2a). Type II walls display a characteristic zigzag pattern of alternating  $\pm\pi$  disclinations. They arise for intermediate  $\angle(\mathbf{Q}_1, \mathbf{Q}_2)$  (Fig. 3.1.2b) and induce distortions in the helimagnetic spin structure that extend over micrometre-sized distances away from the wall. Type III walls form for large  $\angle(\mathbf{Q}_1, \mathbf{Q}_2)$ , involving an abrupt transformation from  $\mathbf{Q}_1$  to  $\mathbf{Q}_2$  (Fig. 3.1.2c). On closer inspection, type III walls can be identified as a chain of magnetic edge dislocations.

The length of domain walls (type I to III) can reach several micrometres, exceeding the characteristic length scale of the helical structure,  $\lambda$ , by two orders of magnitude. Individual walls can also change their type and thereby adapt to local variations of  $\angle(\mathbf{Q}_1, \mathbf{Q}_2)$ . An example is seen in Fig. 3.1.2c, where a dislocation wall (type III) turns into a curvature wall (type I). To evaluate pinning effects, we image domain walls before and after heating above  $T_N$  and also record their response to magnetic fields as exemplified in Supplementary Fig. 3.7.8. The data show that domain walls tend to appear in similar positions after cooling, which we attribute to the presence of structural defects at the surface or in surface-near regions. The pinning is overcome by transiently applying a moderate magnetic field (50mT in Supplementary Fig. 3.7.8), reflecting that the effect is weak. Most importantly, we observe that domain walls reappear with a different spin texture after annealing. This change shows that defects act as pinning centres for domain walls, but they do not govern their magnetic structure. Furthermore, we observe an additional constant, non-dipolar background in our MFM images wherever the helimagnetic spin structure is distorted (see bright contrast in Fig. 3.1.2). Whether this background originates from, for example, quadrupolar magnetic fields [17] or other low-symmetry phenomena remains to be demonstrated.

Most importantly for this study, the observation of the three types of domain wall strikingly corroborates the analogy between chiral magnets and cholesteric liquid crystals, where such domain walls have been observed too [18–20]. This universality emphasizes that the domain wall formation is governed by the inherent topology arising from the lamellar structure, being independent of the involved length scales and microscopic properties.

Figure 3.1.2d presents a quantitative analysis of more than 90 measured domain walls. The larger angle  $\alpha$  enclosed by the domain wall and one of the helix axes  $\mathbf{Q}_i$ , measured within the triangle defined by  $\mathbf{Q}_1$  and  $\mathbf{Q}_2$  (Fig. 3.1.2a-c), is plotted as a function of  $\angle(\mathbf{Q}_1, \mathbf{Q}_2)$ . The data show that, at the surface,  $\mathbf{Q}$  is oriented in all directions, resulting in a broad spectrum of angles

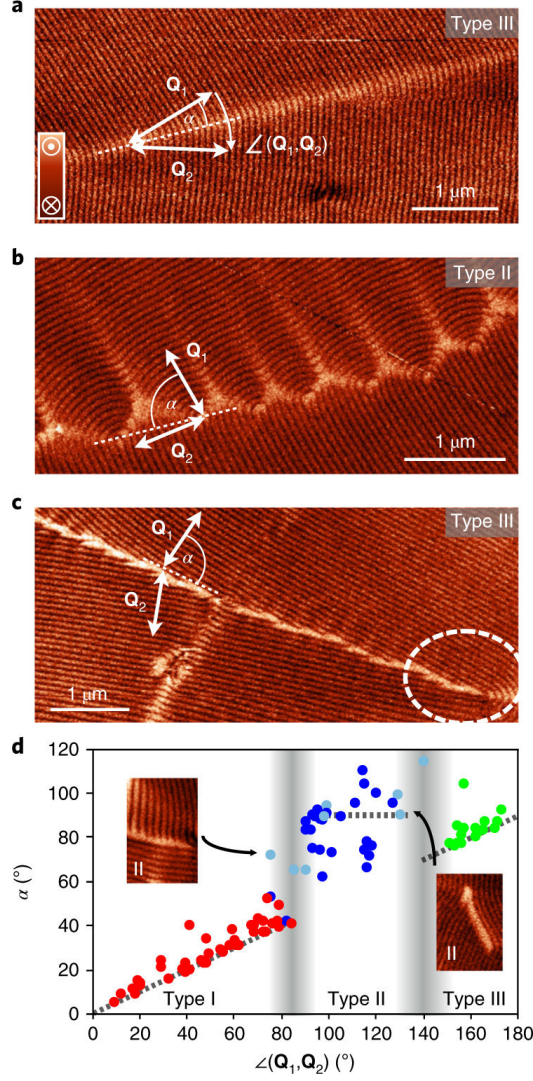


Figure 3.1.2.: Helimagnetic domain walls in FeGe. (a) Curvature wall (type I). (b) Zig-zag disclination wall (type II). (c) Dislocation wall (type III). The MFM data is obtained at 260 – 273 K. (d) Quantitative analysis of the domain wall angle  $\alpha$  (see (a)-(c)) as function of the angle between  $\mathbf{Q}_1$  and  $\mathbf{Q}_2$  ( $\angle(\mathbf{Q}_1, \mathbf{Q}_2)$ ). The plot reveals three distinct stability regimes for type I (red), type II (blue), and type III (green) walls. Special type II walls (light-blue) occur in the transition regions (see inset images) as explained in detail in the main text. Within the marked region in (c) (white dashed contour) the wall changes from type III to type I.

$0^\circ \leq \angle(\mathbf{Q}_1, \mathbf{Q}_2) \leq 180^\circ$ . Type I walls dominate for angles  $\lesssim 85^\circ$  (red dots), type II walls are realized approximately between  $85^\circ$  and  $140^\circ$  (blue dots) and type III walls for angles  $\gtrsim 140^\circ$  (green dots). Figure 3.1.2d reflects that structure and orientation of the walls are interlinked. For walls of type I and III, the angle  $\alpha$  follows the bisecting line ( $\alpha = \frac{1}{2}\angle(\mathbf{Q}_1, \mathbf{Q}_2)$ ). In contrast, type II walls have a tendency to orient parallel to one of the  $\mathbf{Q}_i$ , so that  $\alpha = 90^\circ$ . Close to the transition regions around  $85^\circ$  and  $140^\circ$ , we occasionally observe a special case of type II walls. This subgroup of walls exhibits a minimal distance  $D = \lambda/2$  between  $\pm\pi$  disclinations (light-blue dots) as previously observed [7] and discussed theoretically [14]. Bisecting domain

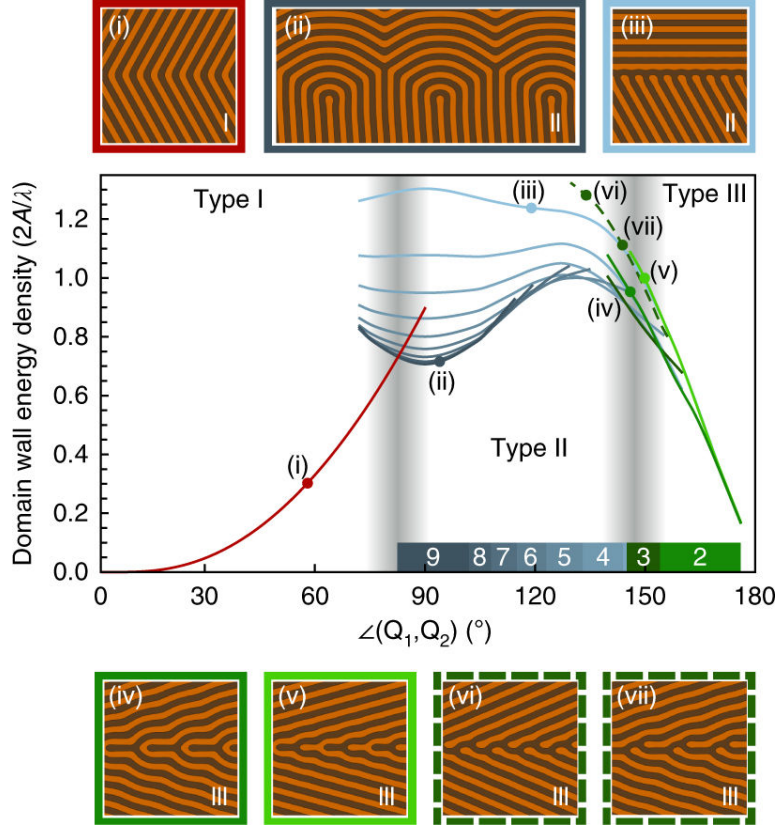


Figure 3.3.3.: Micromagnetic domain wall simulations. (a) type I, (b,c) type II, and (d-g) type III walls. The graph shows that type I walls are lowest in energy density for small angles  $\angle(\mathbf{Q}_1, \mathbf{Q}_2)$ . Type II walls stabilize for intermediate angles. As  $\angle(\mathbf{Q}_1, \mathbf{Q}_2)$  increases, type II walls with smaller defect distance  $D$  become energetically favorable (blue, numbers in units of  $\lambda/2$ ). For larger angles, type III walls with continuous stripes ( $B = 3\lambda$  (dark green line),  $2\lambda$  (d) and  $\lambda$  (e)) are most stable. The associated Burgers vector varies with  $\angle(\mathbf{Q}_1, \mathbf{Q}_2)$  (green, numbers in units of  $\lambda$ ).

walls as well as zigzag structures were also anticipated in ref. [14].

### 3.3. Theoretical analysis of energetics

To understand the relation between the orientation of a wall and its topological magnetic structure, we perform two-dimensional micromagnetic simulations (see also Supplementary Information). We determine the energy density for various domain walls as function of  $\angle(\mathbf{Q}_1, \mathbf{Q}_2)$  on a finite-size system extending up to a cutoff distance  $L = 12\lambda$  away from the wall (Fig. 3.3.3). The calculations reveal that type I walls (Fig. 3.3.3(i)) are lowest in energy for small angles  $\angle(\mathbf{Q}_1, \mathbf{Q}_2)$  (red line in Fig. 3.3.3). Type II walls with  $\alpha = 90^\circ$  (Fig. 3.3.3(ii)) become energetically favourable as  $\angle(\mathbf{Q}_1, \mathbf{Q}_2)$  exceeds  $85^\circ$ , which is in excellent agreement with the experimental data (Fig. 3.1.2d).

The blue lines in Fig. 3 correspond to the energies of type II walls with varying distance  $D$  between  $\pm\pi$  disclinations. The energy of a pair of  $+\pi$  and  $-\pi$  disclinations grows logarithmically with  $D$  (ref. [9]) so that for an angle  $\angle(\mathbf{Q}_1, \mathbf{Q}_2) = 90^\circ$  the energy per length of the type II domain wall scales as  $\log D/D$ . As a consequence, domain walls with large  $D$  are in principle

preferred energetically (see Supplementary Information). To account for the finite  $D$  observed in the MFM images, we consider a finite cutoff length  $L$  in our simulations ( $L = 12\lambda$ , that is,  $D = 9\lambda/2$  in Fig. 3.3.3). For angles  $\angle(\mathbf{Q}_1, \mathbf{Q}_2)$  that deviate from  $90^\circ$ , the arrangement of disclinations is elastically distorted with an energy cost that grows quadratically with the deviation  $\angle(\mathbf{Q}_1, \mathbf{Q}_2) - 90^\circ$ , but linearly with  $D$ . As the angle  $\angle(\mathbf{Q}_1, \mathbf{Q}_2)$  increases, type II walls with smaller  $D$  are therefore energetically favoured until a defect distance of  $D = 4\lambda/2$  is reached, which marks the transition from type II to type III walls. Type II walls with minimal defect distance ( $D = \lambda/2$ , Fig. 3.3.3(iii)) are more costly than other configurations. Their high energy cost is in agreement with their rareness in our MFM data and their tendency to occur in transition regions (light-blue dots in Fig. 3.1.2d).

At around  $145^\circ$ , walls of type III become energetically less costly than type II walls ( $D = 3\lambda/2$ ). Different micromagnetic wall structures are possible, all with similar energy (Fig. 3.3.3(iv-vii)). Within our numerical accuracy, a chain of serially aligned edge dislocations, first with a Burgers vector  $B = 3\lambda$  (see Supplementary Information) and then with  $B = 2\lambda$  (Fig. 3.3.3(iv)), is lowest in energy. Towards larger angles, type III walls with  $B = 2\lambda$  and  $B = \lambda$  (Fig. 3.3.3(v)) become almost degenerate. In addition, more complex domain wall structures with slightly higher energy arise (Fig. 3.3.3(vi,vii)). Consistent with the small energy difference, a large variety of type III walls is observed experimentally (see also Supplementary Fig. 3.7.7), and the micromagnetic structure frequently changes along the wall (Fig. 3.1.2c).

### 3.4. Topology of domain walls

Aside from their intriguing magnetic textures, the domain walls may also carry a topological skyrmion number, which fundamentally distinguishes them from classical magnetic stripe domains and other lamellar structures. In general, the topology of a magnetic structure is identified via the topological charge density  $\rho_{\text{top}} = \frac{1}{4\pi} \hat{M}(\partial_x \hat{M} \times \partial_y \hat{M})$  for the unit vector field of the magnetization  $\hat{M}$  defined within the  $(x, y)$  plane [21]. A single skyrmion with the magnetization pointing downwards at its centre and a topological charge  $W = \int dx dy \rho_{\text{top}} = -1$  is depicted in Fig. 3.4.4a. The same charge is obtained if the structure is embedded in a topologically trivial helimagnetic background as illustrated in Fig. 3.4.4b. However, this embedded skyrmion is equivalent to a pair of edge dislocations with a Burgers vector  $B = \lambda$  (Fig. 3.4.4c,d). The dislocation with  $B = \lambda$  can thus be interpreted as a single meron, that is, a half-skyrmion, which carries charge  $W = -\frac{1}{2}$ . The sign reflects the orientation of the magnetization at the meron core. Straightforward generalization of this argument (see Supplementary Information for details) yields a general relation between the topological charge of a dislocation and its Burgers vector

$$W_{\text{disloc.}} = \frac{s}{2} \text{mod}_2 \left( \frac{B}{\lambda} \right) \quad (3.4.1)$$

where  $\text{mod}_2$  is the modulo 2 operation, and the sign,  $s = \pm 1$ , is determined by the orientation of  $\hat{M}$  at the dislocation centre.

To obtain the topological charge for domain walls, one has to add the charges of dislocations or, alternatively, pairs of  $\pm\pi$  disclinations contained within the wall. This leads to the conclusion that type I and type III walls with continuous stripes have zero topological charge (Fig. 3.3.3(i,iv,v)). However, the type III walls of Fig. 3.3.3(vi,vii) with broken stripes have a finite charge  $W$ . Similarly, type II walls can have a zero or finite charge  $W$  (see also Fig. 3.4.4e). An odd dimensionless distance  $2D/\lambda$  between  $\pm\pi$  disclinations leads to  $W \neq 0$  and an even

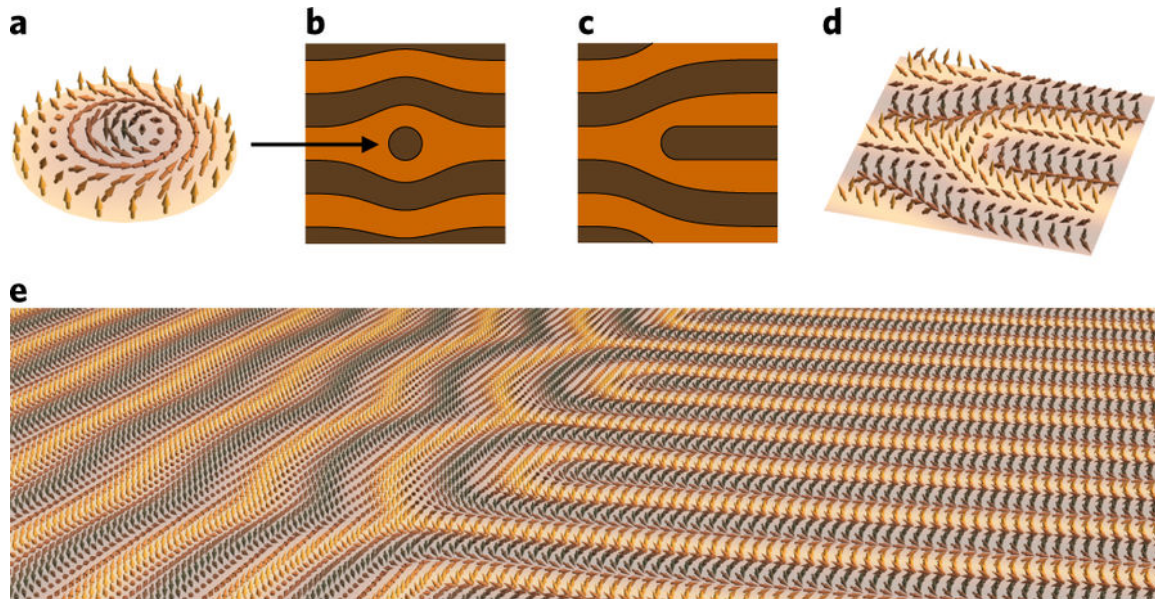


Figure 3.4.4.: Magnetic edge dislocation with nonzero skyrmion charge. (a) Magnetic skyrmion with topological charge  $W = -1$ , (b) Cartoon of a skyrmion embedded in a helimagnetic background, (c,d) Cartoon and spin configuration of an edge dislocation with Burgers vector  $B = \lambda$ , i.e., a meron with  $W = -\frac{1}{2}$ . (e) Illustration of the spin structure of a type II domain wall with  $D = 3\lambda/2$ .

distance to  $W = 0$ . Such topological textures with a finite charge  $W \neq 0$  are in general expected [21,22] to give rise to an emergent electrodynamics for electrons and magnons and to contribute to a topological Hall effect [23–26].

### 3.5. Discussion

Our results reveal a new class of magnetic spin textures with non-trivial topology and establish a striking analogy between topological domain walls in chiral magnets and defect networks in mesoscopic liquid crystals. The walls naturally arise when cooling the sample below  $T_N$  as domains nucleate and grow, and it can be expected that they also profoundly influence macroscopic properties. Enabled by their chiral magnetic microstructure, the walls can carry a finite topological charge and, hence, couple efficiently to spin currents, which is to be demonstrated in future experiments. The walls and their building blocks, the magnetic disclinations and dislocations, are probably associated with long lifetimes that play a key role for the a.c. susceptibility and general relaxation dynamics in helimagnets [27,28]. In particular, they might be crucial for previously observed melting processes [29,30] and the pressure-induced non-Fermi liquid behaviour [31–33]. The observations apply to chiral magnets in general and reveal a large variety of topologically non-trivial magnetic nano-objects – beyond skyrmions [21,34,35] – extending the field of topology-based spintronics into the realm of helimagnetic domain walls.

#### Methods

Methods, including statements of data availability and any associated accession codes and references, are available at <https://doi.org/10.1038/s41567-018-0056-5>.

### 3.6. Bibliography

- [1] I. Chuang, R. Durrer, N. Turok, and B. Yurke, *Cosmology in the laboratory: defect dynamics in liquid crystals*, *Science* **251**, 1336-1342 (1991).
- [2] A. del Campo and W. H. Zurek, *Universality of phase transition dynamics: topological defects from symmetry breaking*, *Inter. J. Mod. Phys. A* **29**, 1430018 (2014).
- [3] G. Catalan, J. Seidel, R. Ramesh, and J. F. Scott, *Domain wall nanoelectronics*, *Rev. Mod. Phys.* **84**, 119-156 (2012).
- [4] S. S. P. Parkin, M. Hayashi, and L. Thomas, *Magnetic Domain-Wall Racetrack Memory*, *Science* **320**, 190-194 (2012).
- [5] E. Salje and H. Zhang, *Domain boundary engineering*, *Phase Transit.* **82**, 452-469 (2009).
- [6] X. Z. Yu, Y. Onose, N. Kanazawa, J. H. Park, J. H. Han, Y. Matsui, N. Nagaosa, and Y. Tokura, *Real-space observation of a two-dimensional skyrmion crystal*, *Nature* **465**, 901-904 (2010).
- [7] X. Z. Yu, N. Kanazawa, Y. Onose, K. Kimoto, W. Z. Zhang, S. Ishiwata, Y. Matsui, and Y. Tokura, *Near room-temperature formation of a skyrmion crystal in thin-films of the helimagnet FeGe*, *Nat. Mater.* **10**, 106-109 (2011).
- [8] P. Bak and M. H. Jensen, *Theory of helical magnetic structures and phase transitions in MnSi and FeGe*, *J. Phys. C* **13**, L881 (1980).
- [9] P. G. de Gennes and J. Prost, *The Physics of Liquid Crystals*, Clarendon: Oxford, 1993.
- [10] A. Hubert and R. Schäfer, *Magnetic Domains: The Analysis of Magnetic Microstructures*, Springer: Berlin, Heidelberg, 2009.
- [11] M. Kléman, *Magnetic singularities in helimagnet crystals*, *Philos. Mag.* **22**, 739-749 (1970).
- [12] M. Seul, L. R. Monar, L. O’Gorman, and R. Wolfe, *Morphology and local structure in labyrinthine stripe domain phase*, *Science* **254**, 5038 (1991).
- [13] M. Uchida, N. Nagaosa, J. P. He, Y. Kaneko, S. Iguchi, Y. Matsui, and Y. Tokura, *Topological spin textures in the helimagnet FeGe*, *Phys. Rev. B* **77**, 184402 (2008).
- [14] F. Li, T. Nattermann, and V. L. Pokrovsky, *Vortex domain walls in helical magnets*, *Phys. Rev. Lett.* **108**, 107203 (2012).
- [15] B. Lebech, J. Bernhard, and T. Freltoft, *Magnetic structures of cubic FeGe studied by small-angle neutron scattering*, *J. Phys. Condens. Matter* **1**, 6105 (1989).
- [16] F. N. Rybakov, A. B. Borisov, S. Blügel, and N. S. Kiselev, *New spiral state and skyrmion lattice in 3D model of chiral magnets*, *New J. Phys.* **18**, 045002 (2016).
- [17] A. Yagil, A. Almoalem, A. Soumyanarayanan, A. K. C. Tan, M. Raju, C. Panagopoulos, and O. M. Auslaender, *Stray field signatures of Néel textured skyrmions in Ir/Fe/Co/Pt multilayer films*, *Arxiv e-print* (2017), arXiv:1705.07608.
- [18] Y. Bouligand, *Dislocations in Solids*, (ed. F. R. N. Nabarro) Ch. 23 (North-Holland Publishing Company, New York, NY, 1983).
- [19] Y. Bouligand, *Recherches sur les textures des états mésomorphes. 3. Les plages à éventails dans les cholestériques*, *J. Phys. Fr.* **34**, 603-614 (1973).
- [20] Y. Bouligand, *Recherches sur les textures des états mésomorphes. 4. La texture à plans et la morphogénèse des principales textures dans les cholestériques*, *J. Phys. Fr.* **34**, 1011-1020 (1973).
- [21] N. Nagaosa and Y. Tokura, *Topological properties and dynamics of magnetic skyrmions*, *Nat. Nanotech.* **8**, 899-911 (2013).
- [22] M. Garst, *Topological Structures in Ferroic Materials*, (ed. J. Seidel) Ch. 2 (Springer, Berlin, Heidelberg, 2016).
- [23] A. Neubauer, C. Pfleiderer, B. Binz, A. Rosch, R. Ritz, P. G. Niklowitz, and P. Böni, *Topological Hall Effect in the A Phase of MnSi*, *Phys. Rev. Lett.* **112**, 186602 (2009).

- 
- [24] T. Schulz, R. Ritz, A. Bauer, M. Halder, M. Wagner, C. Franz, C. Pfleiderer, K. Everschor, M. Garst, and A. Rosch, *Emergent electrodynamics of skyrmions in a chiral magnet*, Nat. Phys. **8**, 301-304 (2012).
- [25] C. Schütte and M. Garst, *Magnon-skyrmion scattering in chiral magnets*, Phys. Rev. B **90**, 094423 (2014).
- [26] M. Mochizuki, X. Z. Yu, S. Seki, N. Kanazawa, W. Koshibae, J. Zang, M. Mostovoy, Y. Tokura, and N. Nagaosa, *Thermally driven ratchet motion of a skyrmion microcrystal and topological magnon Hall effect*, Nat. Mater. **13**, 241-246 (2014).
- [27] A. Bauer, A. Chacon, M. Wagner, M. Halder, R. Georgii, A. Rosch, C. Pfleiderer, and M. Garst, *Symmetry breaking, slow relaxation dynamics, and topological defects at the field-induced helix re-orientation in MnSi*, Phys. Rev. B **95**, 024429 (2017).
- [28] A. Dussaux, P. Schoenherr, K. Koumpouras, J. Chico, K. Chang, L. Lorenzelli, N. Kanazawa, Y. Tokura, M. Garst, A. Bergman, C. L. Degen, and D. Meier, *Local dynamics of topological magnetic defects in the itinerant helimagnet FeGe*, Nat. Commun. **7**, 12430 (2016).
- [29] M. Janoschek, M. Garst, A. Bauer, P. Krautscheid, R. Georgii, P. Böni, and C. Pfleiderer, *Fluctuation-induced first-order phase transition in Dzyaloshinskii-Moriya helimagnets*, Phys. Rev. B **87**, 134407 (2013).
- [30] H. Wilhelm, M. Baenitz, M. Schmidt, U. K. Röckler, A. A. Leonov, and A. N. Bogdanov, *Precursor phenomena at the magnetic ordering of the cubic helimagnet FeGe*, Phys. Rev. Lett. **107**, 127203 (2011).
- [31] C. Pfleiderer, S. R. Julian, and G. G. Lonzarich, *Non-Fermi-liquid nature of the normal state of itinerant-electron ferromagnets*, Nature **414**, 427-430 (2001).
- [32] R. Ritz, M. Halder, M. Wagner, C. Franz, A. Bauer, and C. Pfleiderer, *Formation of a topological non-Fermi liquid in MnSi*, Nature **497**, 231-234 (2013).
- [33] P. Pedrazzini, H. Wilhelm, D. Jaccard, T. Jarlborg, M. Schmidt, M. Hanfland, L. Akselrud, H. Q. Yuan, U. Schwarz, Y. Grin, and F. Steglich, *Metallic state in cubic FeGe beyond its quantum phase transition*, Phys. Rev. Lett. **98**, 047204 (2007).
- [34] A. Fert, V. Cros, and J. Sampaio, *Skyrmions on the track*, Nat. Nanotech. **8**, 152-156 (2013).
- [35] R. Wiesendanger, *Nanoscale magnetic skyrmions in metallic films and multilayers: a new twist for spintronics*, Nat. Rev. Mater. **1**, 16044 (2016).

## Acknowledgement

We thank M. Fiebig for direct financial support. The work at ETH was supported by the Swiss National Science Foundation through grants 200021-149192 and 200021-137520. L.K. and M.G. were supported by SFB 1143 'Correlated Magnetism: From Frustration To Topology' and DFG grant GA 1072/5-1. J.M. and A.R. were supported by SFB 1238 (Kontrolle und Dynamik von Quantenmaterialien). J.M. also acknowledges support from the Deutsche Telekom Stiftung and Bonn-Cologne Graduate School of Physics and Astronomy BCGS. N.K. acknowledges funding through the JSPS Grant-in-Aids for Scientific Research (S) No. 24224009 and for Young Scientists (Start-up) No. 26886005. D.M. thanks the Research Council of Norway (FRINATEK project no.263228) and the Norwegian University of Science and Technology (NTNU) for financial support.

## Author contributions

P.S. conducted the MFM experiments supervised by D.M.; J.M. performed the two-dimensional micromagnetic simulations supervised by M.G. and A.R.; N.K. grew the FeGe single crystals

under supervision of Y.T.; P.S., J.M., L.K., M.G. and D.M. classified the domain walls; M.G. and L.K. defined the skyrmion charge of edge dislocations; P.S., J.M., L.K., M.G. and D.M. wrote the paper; M.G. and D.M. supervised the work. All authors discussed the results and contributed to their interpretation.

### Competing financial interests

The authors declare no competing interests.

### Additional information

**Supplementary Information** is available for this paper at <https://doi.org/10.1038/s41567-018-0056-5>.

**Reprints and permissions information** is available at [www.nature.com/reprints](http://www.nature.com/reprints).

**Correspondence and requests for materials** should be addressed to M.G. or D.M.

**Publisher's note:** Springer Nature remains neutral with regard to jurisdictional claims in published maps and institutional affiliations.

### Methods

**Sample growth.** FeGe single crystals were grown by chemical vapour transport from FeGe B35 powder with I<sub>2</sub> (20 mg) in an evacuated quartz tube. The tube was mounted in a heated three-zone furnace for 1 month with a thermal gradient of 560 °C to 500 °C. This leads to the growth of 0.5 × 1 × 1 mm<sup>3</sup> large B20 FeGe crystals at the lower temperature side. The B20 crystal structure was confirmed by powder X-ray diffraction (see Supplementary Fig. 3.7.5) and surfaces for MFM imaging were oriented using Laue diffraction.

**Data availability.** The data that support the plots within this paper and other findings of this study are available from the corresponding authors upon request.

## 3.7. Supplementary Text

In this supplement, we provide details about the experimental methods and present more examples of observed domain wall configurations. The analysis of the experimental data is discussed in detail. Moreover, we describe our micromagnetic simulations and analyze the results. The distance between disclinations within type II zig-zag disclination walls is compared between theory and experiment. Finally, a detailed discussion of the topological charge attributed to dislocations is presented, and the charge of various domain walls is specified.

### 3.7.1. Experimental Methods

#### Sample preparation

FeGe single crystals were grown by chemical vapour transport from FeGe B35 powder with I2 (20 mg) in an evacuated quartz tube. The tube was mounted in a heated three-zone furnace for 1 month with a thermal gradient of 560° C to 500° C. This leads to the growth of  $0.5 \times 1 \times 1 \text{ mm}^3$  large B20 FeGe crystals at the lower temperature side. The B20 crystal structure was confirmed by Laue diffraction. For our magnetic force microscopy studies, samples with (100)- and (110)-oriented surfaces were cut and chemo-mechanically polished with silica slurry, yielding flat surfaces with roughness of  $\approx 1 \text{ nm}$ . Powder X-ray diffraction patterns of FeGe show that all peaks can be assigned to the B20 structure of FeGe with no indication of impurity phases (Fig. 3.7.5).

#### Magnetic force microscopy - MFM

For our MFM measurements we used magnetic coated tips with a tip radius  $\lesssim 50 \text{ nm}$  (Nanosensors, PPP-MFMR, resolution  $< 50 \text{ nm}$ ). Imaging was performed in two-pass mode. First the topography was recorded in semi-contact. In the second pass the magnetic response was detected with a fixed tip-surface distance of about 30 nm. The magnetic tips were operated at their resonance frequency of 75-77 kHz and with a scan speed of  $2 - 3.5 \mu\text{m s}^{-1}$  to achieve optimal image resolution of 10 – 15 nm. All MFM images were measured in a commercially available scanning probe microscope (NT-MDT) using a home-built cooling holder. This cooling holder is based on a water-cooled three-stage peltier element and reaches temperatures down to 260 K, giving us access to the helimagnetic phase of FeGe ( $T_N = 278 \text{ K}$ ). Low water flow rates were used in order to reduce noise from vibrations due to the water cooling cycle. Additionally, the measurements were performed in a dry nitrogen environment (humidity below 1 %) to avoid ice formation on the sample surface.

#### Examples of observed domain wall configurations

In Fig. 3.1.2 of the main text, typical examples of the three types of domain walls are shown. Figure 3.7.6a and c present the same walls but on a larger scanning area ( $\sim 6 \mu\text{m} \times 6 \mu\text{m}$ ). Panel b shows a different example of a type II wall, and it covers the whole length of the wall including its beginning and end. In comparison to type I and III, the width of type II walls is relatively large. It consists of the extent of the zig-zag pattern itself as well as the  $\mu\text{m}$ -sized distortions emanating from the  $-\pi$  disclinations affecting the regular stripe pattern of the  $\mathbf{Q}_1$  domain in panel b.

Besides these representative domain walls, there is a wide variety of domain walls observed by our MFM measurements. Figure 3.7.7 identifies some of the subtypes for the three domain wall categories. Panel a shows a curvature wall with a large angle  $\angle(\mathbf{Q}_1, \mathbf{Q}_2)$  enclosed by the helix axes of the two domains that splits into two type I walls with smaller angles. In panel b a type II wall with its characteristic zig-zag pattern meets a type III dislocation wall seen in the upper right corner. Panel c and d show irregular type II domain walls. Note that there exist helimagnetic stripes that can be continuously followed from one domain to the other resulting in a deviation of the domain wall angle  $\alpha$  from  $90^\circ$ . In panel e the domain wall angle  $\alpha$  of a type III dislocation wall varies along the wall. In general, one can distinguish type III walls with continuous and discontinuous stripe patterns, see in the main text Fig. 3.3.3(iv),(v) and (vi),(vii), respectively. Whereas in Fig. 3.7.7f and g the type III walls contain regions with continuous stripes, the dark stripes in panel h are all discontinuous.

To verify that the domain wall topology is governed by magnetic interactions rather than structural defects, Fig. 3.7.8a-d show a representative set of scans (MFM + topography) documenting the response of a domain wall to thermal annealing and magnetic fields. Before and after heating above  $T_N$  the domain wall arises in a similar area. A closer inspection of Fig. 3.7.8a,c reveals, however, that the wall topology has changed. Furthermore, we observe that the wall does not reappear when we transiently field-align the spin system ( $0 \text{ mT} \rightarrow 50 \text{ mT} \rightarrow 0 \text{ mT}$ ). We thus conclude that the domain wall topology does not depend on structural defects (also see topography images in Fig. 3.7.9 corresponding to the magnetic images in Fig. 3.1.2 of the main text). Structural or crystallographic defects, however, co-determine where domain walls form. As domain walls coincide only occasionally with anomalies visible in AFM, we conclude that both surface defects and defects in surface-near regions contribute to the pinning.

### Statistical analysis of domain walls

**Domain wall angle  $\alpha$**  In Fig. 3.1.2d of the main text, the relation between the domain wall angle  $\alpha$  and the angle  $\angle(\mathbf{Q}_1, \mathbf{Q}_2)$  enclosed by the helix axes of the two domains is analysed. Each point in this diagram corresponds to a single wall. The lengths of the walls varies between  $\approx 1 - 21 \mu\text{m}$ . Arrow bars reflect the accuracy of the angles extracted from the MFM images, that is, better than  $\pm 5^\circ$ . For domain walls of type I and III the variance of the experimentally observed values around the bisecting line  $\alpha = \frac{1}{2}\angle(\mathbf{Q}_1, \mathbf{Q}_2)$  is relatively small. The type I curvature walls are free of defects so that they are expected to relax easily in order to assume their energetically most stable configuration. Similarly, the dislocations within a type III wall are able to arrange themselves by a climbing motion to yield an optimal domain wall angle [28], which does not involve the crossing of a topological barrier. In contrast, the variance of the data related to type II walls is comparatively large which will be discussed in detail in the following section.

**Statistical analysis of type II zig-zag disclination walls** In order to evaluate the micromagnetic domain wall structure of walls of type II, we performed the following statistical analysis. Consider a type II wall oriented such that the  $+\pi$  defects are located below the  $-\pi$  defects, see Fig. 3.7.10a. Then, we define for the  $i^{\text{th}}$   $+\pi$  disclination of the wall the integers  $x_i$  and  $y_i$  measuring the distance to the adjacent  $-\pi$  disclination to the left- and right-hand side, respectively, in units of  $\lambda/2$ . The average of these values over a single domain wall are denoted by  $\bar{x}$  and  $\bar{y}$ .

The mean distance between adjacent disclinations within a single wall is then given by  $D = \frac{\lambda}{2} \frac{\bar{x} + \bar{y}}{2}$ . The dependence of  $D$  on  $\angle(\mathbf{Q}_1, \mathbf{Q}_2)$  is discussed in Section 3.7.2 and compared to theory, see Fig. 3.7.16. Error bars for each domain wall are given by the standard deviation and depend on the domain wall length. The domain wall lengths used in our statistical analysis vary from 3 to 44  $\pi$  defects (average length of 14  $\pi$  defects per wall).

The distance between  $\pm\pi$  disclinations fluctuates within a wall as can be seen in Fig. 3.7.10a. In order to quantify these fluctuations, we consider in Fig. 3.7.10b the difference  $\bar{x} - \bar{y}$  for each wall. We find that the mean  $\langle \bar{x} - \bar{y} \rangle \approx -0.1$  averaged over all walls is basically zero with a standard deviation  $\sigma_{\bar{x} - \bar{y}} \approx 3.5$  indicated by the grey shaded region in panel b.

In the main text, we introduced the domain wall angle  $\alpha$  whose definition was given in Fig. 3.1.2 of the main text. The dependence of the experimentally determined  $\alpha$  as a function of  $\angle(\mathbf{Q}_1, \mathbf{Q}_2)$  was discussed in Fig. 3.1.2d of the main text. The domain wall angle  $\alpha$  is related to  $\bar{x}$  and  $\bar{y}$  by the formula

$$\alpha = \frac{\pi}{2} + \arctan \left( \frac{(\bar{x} - \bar{y}) \sin \angle(\mathbf{Q}_1, \mathbf{Q}_2)}{\bar{x} + \bar{y} + (\bar{x} - \bar{y}) \cos \angle(\mathbf{Q}_1, \mathbf{Q}_2)} \right). \quad (3.7.2)$$

It follows that for a symmetric type II wall with  $\bar{x} = \bar{y}$  the domain wall angle is  $\alpha = 90^\circ$ . On average this holds approximately as  $\langle \bar{x} \rangle \approx \langle \bar{y} \rangle$ . Moreover, for a zero average  $\langle \bar{x} - \bar{y} \rangle = 0$  the standard deviation of  $\alpha$  is simply given by

$$\sigma_\alpha = \frac{|\sin \angle(\mathbf{Q}_1, \mathbf{Q}_2)|}{2d(\angle(\mathbf{Q}_1, \mathbf{Q}_2))} \sigma_{\bar{x} - \bar{y}} \quad (3.7.3)$$

where  $d(\angle(\mathbf{Q}_1, \mathbf{Q}_2))$  is the average of  $(\bar{x} + \bar{y})/2$  over domain walls at a given  $\angle(\mathbf{Q}_1, \mathbf{Q}_2)$ . This implies a standard deviation  $\sigma_\alpha$  ranging approximately between  $20^\circ$  and  $38^\circ$  for angles  $\angle(\mathbf{Q}_1, \mathbf{Q}_2)$  between  $90^\circ$  and  $130^\circ$ . This is consistent with the observation in Fig. 3.1.2d of the main text.

The above analysis of the experimental data indicates that zig-zag disclination walls prefer a domain wall angle  $\alpha = 90^\circ$ . For this reason, we limited our micromagnetic simulations of type II walls to this value of  $\alpha$ . The relatively large standard deviation  $\sigma_\alpha$  is related to the fact that the relaxation of a type II wall with  $\alpha \neq 90^\circ$  requires a specific rearrangement of disclinations which is however inhibited by a topological barrier.

### 3.7.2. Theoretical considerations

#### Micromagnetic simulations of helimagnetic domain walls

For a quantitative comparison with experiment, we performed micromagnetic simulations of various domain wall structures of helimagnetic order. In FeGe the magnetic exchange is predominant followed by a significantly weaker Dzyaloshinskii-Moriya interaction. This leads to a variation of the magnetization on a length scale substantially larger than the atomic unit cell. This allows for a continuum description in terms of a continuous vector field  $\mathbf{n}(x, y)$  of unit length  $|\mathbf{n}| = 1$  representing the orientation of the magnetization vector. From the experiments we know that the pitch of the helix is aligned parallel to the surface so that we restrict ourselves, for simplicity, to an effective two-dimensional simulation within the surface plane. We consider a minimal model in terms of the free energy functional

$$F[\mathbf{n}] = \int d^2\mathbf{r} \left( A(\partial_\alpha \mathbf{n}_i)^2 + \mathcal{D} \varepsilon_{i\alpha j} \mathbf{n}_i \partial_\alpha \mathbf{n}_j \right) \quad (3.7.4)$$

where indices  $i, j = x, y, z$  sum over all components of the magnetization while the spatial index  $\alpha = x, y$  is confined to the two-dimensional plane.  $\varepsilon_{i\alpha j}$  is the totally antisymmetric tensor with  $\varepsilon_{xyz} = 1$ .  $A$  is the exchange stiffness and  $\mathcal{D}$  is the Dzyaloshinskii-Moriya interaction. For simplicity, we neglect dipolar interactions and magnetic anisotropies.

The helimagnetic ground state of Eq. 3.7.4 is given by  $\mathbf{n}(\mathbf{r}) = \mathbf{e}_1 \cos(Q\mathbf{e}_3\mathbf{r} + \varphi) + \mathbf{e}_2 \sin(Q\mathbf{e}_3\mathbf{r} + \varphi)$  where  $\mathbf{e}_3$  is lying within the plane, the orthonormal unit vectors obey  $\mathbf{e}_1 \times \mathbf{e}_2 = \mathbf{e}_3$ , and the helix wavelength is given by  $\lambda = 2\pi/Q$  with the wavevector  $Q = \mathcal{D}/(2A)$ . The phase  $\varphi$  can be chosen arbitrarily as it is a zero mode, i.e., the energy does not depend on its choice. The helix axis  $\mathbf{Q}$  is determined by  $\mathbf{e}_3$ . Note that the helix is invariant with respect to a  $\pi$ -rotation of the three orthonormal vectors around  $\mathbf{e}_1$  (for  $\varphi = 0$ ), i.e.,  $\mathbf{e}_1 \rightarrow \mathbf{e}_1$ ,  $\mathbf{e}_2 \rightarrow -\mathbf{e}_2$ ,  $\mathbf{e}_3 \rightarrow -\mathbf{e}_3$ . The helix axis  $\mathbf{Q}$  is thus only defined up to a sign so that it is effectively a director field allowing for half-integer vortices, in particular,  $\pm\pi$  disclinations.

After measuring energy and length in dimensionless units,  $\tilde{F} = F/(2A)$  and  $\tilde{r} = rQ$ , the theory (3.7.4) is parameter-free. This implies that the energy of a particular domain wall between two helimagnetic regions is exclusively determined by geometric factors: the relative angle between the two domains and the angle defining the orientation of the wall, denoted in the main text by  $\angle(\mathbf{Q}_1, \mathbf{Q}_2)$  and  $\alpha$ , respectively, (see Fig. 3.1.2 of the main text).

We determine the energy of various domain wall configurations numerically using micromagnetic simulations of the Landau-Lifshitz-Gilbert equation

$$\partial_t \mathbf{n} = -\mathbf{n} \times \mathbf{B}_{\text{eff}} + \alpha_G \mathbf{n} \times \partial_t \mathbf{n} \quad (3.7.5)$$

with the dimensionless effective magnetic field  $\mathbf{B}_{\text{eff}} = -\delta\tilde{F}/\delta\mathbf{n}$ , and the dimensionless time  $t$ . The continuous field  $\mathbf{n}$  is discretized with the help of classical Heisenberg spins on a square lattice with lattice spacing  $a \approx 0.024\lambda$ . Derivatives are approximated by finite differences, and the total grid is rectangular with  $N_x \times N_y$  sites. The Gilbert damping is chosen within the range  $\alpha_G \in [0.1, 0.8]$ .

We choose the domain wall to be aligned with the  $x$ -axis. Anticipating periodic domain walls, we employ periodic boundary conditions along the  $x$ -axis enforcing a periodicity of the wall which is commensurate with the size  $N_x$ . The boundary conditions along the other two edges are fixed and chosen such that the resulting spin configuration corresponds to magnetic helices with orientations  $\mathbf{Q}_1$  and  $\mathbf{Q}_2$  with certain phases  $\varphi_1$  and  $\varphi_2$ . Moreover, the angles  $\angle(\mathbf{Q}_1, \mathbf{Q}_2)$  and  $\alpha$  have to be restricted to specific values so that the two boundary helices are commensurate with the chosen system size.

The interface between these two helimagnetic domains is first initialized with a magnetization profile that implements the corresponding topology of the wall. Afterwards the system evolves according to Eq. 3.7.5 and relaxes the implemented magnetization yielding the energy. In order to obtain the energy  $\tilde{E}_{dw}$  attributed to the domain wall, the energy of the perfectly ordered helimagnetic state is subtracted. Small systematic errors might arise here from anisotropy energies due to the discretization on a quadratic lattice. Note that the result for the domain wall energy does not depend on the choice of phases,  $\varphi_1$  and  $\varphi_2$ , as the wall can adapt its position along the  $x$ - and  $y$ -axes.

Preferably, the distance between the domain wall and the boundaries,  $L$ , should be chosen large enough such that the fixed boundary configurations do not significantly influence the energetics. We observe that the finite size scaling substantially depends on the type of wall under consideration and, in particular, on the width of the wall. The energy converges with increasing  $L$  the slower the larger the width of the domain wall.

A slow convergence is especially observed for type II walls which possess a large width for  $\angle(\mathbf{Q}_1, \mathbf{Q}_2) \approx 90^\circ$ . As an example with particularly strong finite-size correction, we present in Fig. 3.7.11 a single period of such a wall with disclinations separated by  $D = 9\lambda/2$  after full numerical optimization for three different system sizes. Similar to Fig. 3.1.1 of the main text, we only show a binary representation of the full helimagnetic structure where bright and dark stripes represent regions where the local magnetization possesses a component that points out or into the plane, respectively. The distance  $L$  between the upper fixed boundary and the domain wall interface corresponds to 12, 15, and 20 helix wavelengths  $\lambda$  for panels a, b, and c, respectively. The deformation of the helix arrangement induced by the  $-\pi$  disclination extends rather far away from the wall, which is also observed experimentally, see Fig. 3.7.6b. This leads to a relatively strong dependence of the energy density on the system size  $L$ , see Fig. 3.7.14a, amounting to differences of 14% for the configurations shown in Fig. 3.7.11. In contrast, for walls with a comparatively smaller width as shown in Fig. 3.7.12 and 3.7.13 the finite-size corrections are substantially smaller for the same values of  $L$ , see Fig. 3.7.14b and c, with a difference in energy density of 6% and 0.6%, respectively. As the evaluation of domain wall energies is computationally demanding, we limit ourselves in the main text to a comparison of energies for a system size of  $L = 12\lambda$ . The precise transition angles between the various walls and details of the spectrum might thus alter in the thermodynamic limit of very large systems, see also the discussion in Section 3.7.2. However, we expect that the qualitative features remain unaffected.

The micromagnetic simulations are nevertheless in remarkably good agreement with our experimental findings. This is noteworthy because our two-dimensional simulations do not only neglect dipolar interactions but also do not account for the additional twist of the magnetization on the surface of a three-dimensional bulk helimagnet which arises from the Dzyaloshinskii-Moriya interaction [1, 2]. The helix gains additional energy from such surface twists that also influence the energetics of domain wall configurations within the surface plane. In fact, we believe that the energy gain from such surface twists is responsible for the surface anchoring of the helix axes observed in our experiments on FeGe. Moreover, we neglected magnetocrystalline anisotropies in our theoretical treatment, that tend to align the helix along crystallographic directions. It is known [15] that as a function of temperature these anisotropies change sign in FeGe at  $T \approx 230K$  so that, by coincidence, they are particularly small at the temperature of our measurements. As a result, helices feel only a very weak crystallographic potential, which, we believe, explains the broad distribution of helix orientations observed in our experiments.

### Domain wall configurations

In Fig. 3.3.3 of the main text, the numerically obtained energy density and various domain wall configurations were presented for a system size of  $L = 12\lambda$ . In Fig. 3.7.15 we again show this energy spectrum and an extended set of real space configurations. Panels a to l show a series of energetically minimal domain wall structures as a function of increasing angle  $\angle(\mathbf{Q}_1, \mathbf{Q}_2)$ . The zig-zag disclination walls in panel c to h are distinguished by a decreasing distance  $D$  between  $\pi$  and  $-\pi$  disclinations starting from 9 and ending with 4 in units of  $\lambda/2$ . The extent of the various type II walls as a function of  $\angle(\mathbf{Q}_1, \mathbf{Q}_2)$  is indicated by the blue shaded boxes right above the  $x$ -axis in Fig. 3.7.15. Upon increasing  $\angle(\mathbf{Q}_1, \mathbf{Q}_2)$  further, one first observes the type III wall of panel i containing a chain of serially aligned edge dislocations with Burgers vector  $B = 3\lambda$ . This is followed by a chain of dislocations with Burgers vector  $B = 2\lambda$  whose separation increases with further increasing  $\angle(\mathbf{Q}_1, \mathbf{Q}_2)$  as indicated in panel j, k and l. Within

our numerical accuracy, we find that the wall containing a chain of dislocations with  $B = \lambda$  shown in panel t always has a slightly higher energy than  $B = 2\lambda$  although the energies approach each other very closely for large  $\angle(\mathbf{Q}_1, \mathbf{Q}_2)$ . Panels m to s show further configurations that possess a higher energy than the domain wall ground states.

### Distance between $\pm\pi$ disclination defects within type II domain walls: theory vs. experiment

The blue shaded boxes above the  $x$ -axis in Fig. 3.7.15 indicate in which regime of angles  $\angle(\mathbf{Q}_1, \mathbf{Q}_2)$  type II zig-zag disclination walls with a certain distance  $D$  between  $\pm\pi$  disclinations are expected to be most stable. In Fig. 3.7.16, this theoretical result for a series of special values of  $\angle(\mathbf{Q}_1, \mathbf{Q}_2)$  (red and green circles) is compared with  $D$  obtained from a statistical analysis of experimentally observed zig-zag disclination walls (blue and light blue triangles), see Section 3.7.1. Theoretically, only type II walls with a constant distance  $D$  between defects are considered whereas in the experiment the distance between disclinations fluctuates within the wall giving rise to the error bars. The vertically grey-shaded areas again indicate approximately the transition region towards type I and type III walls for smaller and larger values of  $\angle(\mathbf{Q}_1, \mathbf{Q}_2)$ , respectively. Within these transition regions type II walls with small distances  $D \gtrsim \lambda/2$  are observed which are represented by the light blue triangles. Theoretically, we find however that such walls have a relatively large energy. The configurations with larger distances  $D$  are found to possess a smaller energy and they are more frequently observed (blue triangles). Consistently in the experimental as well as the theoretical data, the distance  $D$  is maximal for  $\angle(\mathbf{Q}_1, \mathbf{Q}_2) \approx 90^\circ$ , and it decreases for smaller and larger values of  $\angle(\mathbf{Q}_1, \mathbf{Q}_2)$ . The precise theoretical values of  $D$  increase with increasing system sizes; the red and green dots were obtained for  $L = 12\lambda$  and  $L = 20\lambda$ , respectively, see the discussion in Section 3.7.2. Domain wall configurations up to  $2D/\lambda = 10$  have been simulated; the distance  $D$  of the optimal configuration probably exceeds this value for  $L = 20\lambda$  close to  $\angle(\mathbf{Q}_1, \mathbf{Q}_2) \approx 90^\circ$ . Whereas the qualitative trend agrees between theory and experiment, it seems that the asymptotics for  $L \rightarrow \infty$  quantitatively overestimates the experimentally determined values of  $D$ . This might hint at the presence of an intrinsic cutoff length, or it indicates that contributions neglected in our numerical simulations are important for a full quantitative agreement, see the discussion at the end of Section 3.7.2.

### Energetics of type II domain walls

Perhaps the most striking experimental and theoretical result is the stabilization of type II domain walls with large periodicity  $D$  for angles close to  $\alpha \sim 90^\circ$  and a sequence of transitions where  $D$  is reduced for increasing  $\alpha$ , see Fig. 3.7.15 (blue shaded bar in the upper panel). In the following, we will therefore explain the numerical finding using analytic arguments.

The energy of a pair of  $\pi$  and  $-\pi$  disclinations grows logarithmically,  $\log D$ , with their distance  $D$ . The energy per length of the wall is then proportional to  $\log D/D$  and decreases for increasing  $D$  so that zig-zag type II walls with large distances  $D$  are energetically preferred ( $\angle(\mathbf{Q}_1, \mathbf{Q}_2) \approx 90^\circ$ ). More precisely, this argument only holds for an infinitely large system,  $L = \infty$ . For a finite system size  $L$  (see section 3.7.2) there is an additional contribution to the energy density proportional to  $D^2/L$  which stabilizes a solution with finite, but large  $D$ , see Fig. 3.7.18.

For angles  $\angle(\mathbf{Q}_1, \mathbf{Q}_2)$  that slightly differ from  $90^\circ$ , the arrangement of disclinations within the type-II domain wall is distorted from the symmetric configuration found for  $\angle(\mathbf{Q}_1, \mathbf{Q}_2) = 90^\circ$ .

This leads to an elastic distortion energy that is proportional to the square of the displacement  $D(\angle(\mathbf{Q}_1, \mathbf{Q}_2) - \pi/2)$ . The resulting change of the domain wall energy per length can be estimated to be

$$\Delta e \approx c \frac{A}{\lambda^2} D(\angle(\mathbf{Q}_1, \mathbf{Q}_2) - \pi/2)^2. \quad (3.7.6)$$

This describes the numerical data reasonable well for small deviations  $\pm 20\%$  in particular for larger distances  $D$  as demonstrated in Fig. 3.7.18. A simultaneous fit to our data results yields for the numerical prefactor  $c \approx 0.13$ . According to Eq. 3.7.6, the energy per length of the type-II domain wall increases proportional to  $D(\angle(\mathbf{Q}_1, \mathbf{Q}_2) - \pi/2)^2$ . As a consequence, defect configurations with large  $D$  are successively suppressed when the domain wall angle  $\angle(\mathbf{Q}_1, \mathbf{Q}_2)$  increases.

### Topological charge of a dislocation

The topological skyrmion charge density is defined by  $\rho_{\text{top}} = \frac{1}{4\pi} \mathbf{n}(\partial_x \mathbf{n} \times \partial_y \mathbf{n})$ . A finite topological charge gives rise to an emergent electrodynamics in the interplay of electron spin currents or magnon currents with a magnetic texture [4, 23, 24, 26], see N. Nagaosa et al. [21] and M. Garst [5] for reviews. We can attribute a well-defined topological charge to any localized magnetic texture provided that its associated charge density decays sufficiently fast with increasing distance  $\rho = \sqrt{x^2 + y^2}$  so that the two-dimensional integral  $\int dx dy \rho_{\text{top}}$  converges.

This is for example not the case for disclinations. This is best illustrated for a  $2\pi$  disclination that we can approximate with the parametrization

$$\mathbf{n}_{2\pi}(\vec{r}) = (\sin \phi \sin(\theta_0 - Q\rho), -\cos \phi \sin(\theta_0 - Q\rho), \cos(\theta_0 - Q\rho)) \quad (3.7.7)$$

where  $\vec{r} = \rho(\cos \phi, \sin \phi)$ . We consider the cases  $\theta_0 = \pi$  and  $\theta_0 = 0$  for which the magnetization at the disclination core points down and up, respectively, see Fig. 3.7.19. Its topological charge density

$$\rho_{\text{top}}^{2\pi} = -\frac{Q}{4\pi\rho} \sin(\theta_0 - Q\rho) \quad (3.7.8)$$

only decays as  $1/\rho$ , and, as a result, its topological charge is not well-defined. This is reflected in the fact that the integral over the topological density depends on the integration area even for large  $\rho$ . The integral over the area of a circle around the origin with radius  $m\pi/Q$  yields zero for even integer  $m$ . For odd integer  $m$  the resulting topological charge is  $-1$  for  $\theta_0 = \pi$  and  $+1$  for  $\theta_0 = 0$ .

The topological charge of a dislocation, however, is well-defined because its topological charge density decays faster than  $1/\rho$  as the two  $\pm\pi$ -disclinations screen each other at long distances. For its determination we invoke the concept of topological, i.e., continuous transformations. First, consider the pristine helix which varies only along a single direction in space, so that its topological charge density is exactly zero. As a result, the total charge integrated over a large area also vanishes. This remains true after applying a topological transformation of the helix by elastically deforming it within a locally confined area, see Fig. 3.7.20. Whereas the deformed configuration in Fig. 3.7.20b will have a finite local topological charge density, its total charge integrated over the full area remains zero.

Now let us distort the helix locally like in Fig. 3.7.20b and insert a locally confined  $2\pi$  disclination of radius  $m\pi/Q$ . This leads to magnetic textures as shown, for example, in Fig. 3.7.21a, c, e, and g. It follows that the total topological charge of the whole magnetic texture is deter-

mined by the embedded  $2\pi$  disclination only, and it is 0 for even  $m$  and  $\pm 1$  for odd  $m$  where the sign depends on the orientation of the magnetization at the disclination core. However, the resulting texture can be alternatively identified as a helix containing two dislocations of the type shown in panels b, d, f, and h, with Burgers vector  $B = m2\pi/Q = m\lambda$ . By symmetry, it follows that each of them must carry half of the total charge. This yields the formula for the topological charge of a dislocation given in the main text

$$W_{\text{disloc.}} = s \frac{1}{2} \text{mod}_2 \frac{B}{\lambda}. \quad (3.7.9)$$

The sign  $s$  is determined by the magnetization at the associated  $2\pi$  disclination core with  $s = -1$  for a magnetization pointing downwards and  $s = +1$  for a magnetization pointing upwards.

### Topological charge of helimagnetic domain walls

After having clarified the topological charge of a single dislocation, we now turn to the discussion of topological charges of various domain walls. In order to determine the total charge of a domain wall we can add the charges of dislocations contained within it. As we consider only periodic domain walls, we can limit ourselves to a discussion of the topological charge associated with their primitive unit cell that we denote by  $w$ , see Fig. 3.7.22 for various examples.

The topological charge of curvature walls vanishes because these walls can be continuously transformed to plain helices by straightening out their lamellar pattern. Non-zero topological charges can only appear for topologically non-trivial walls of type II and III.

All type II walls contain a single  $\pi$  and  $-\pi$  disclination per primitive unit cell separated by a distance  $D$ . Such a pair of disclinations is topologically equivalent to a dislocation with Burgers vector  $B = 2D$ , see Fig. 3.1.1 of the main text. So we can conclude that the charge of type II walls per primitive unit cell is given by  $w = \frac{s}{2} \text{mod}_2 \frac{2D}{\lambda}$  where  $s = 1$  if the magnetization at the core of the  $\pi$  disclination points up (bright) and  $s = -1$  if it points down (dark). As a result, we obtain an even/odd effect for type II walls as shown in Fig. 3.7.22a-i representing such walls with decreasing values of  $D$ . For example in panel h the distance between the disclinations is a single helix wavelength,  $D = \lambda$ , so that  $w = 0$ , whereas in panel i it is only half a helix wavelength,  $D = \lambda/2$ , and  $w = \frac{1}{2}$ .

For the discussion of the topological charge of type III dislocation walls we distinguish between situations where their lamellar stripes are broken or not. If they remain unbroken like in Fig. 3.7.22j-m, which also includes the ground state configurations for large angles  $\angle(\mathbf{Q}_1, \mathbf{Q}_2)$ , their total topological charge always vanishes. In this case, the lamellar stripes, similar to curvature walls, can be straightened out and transformed to plain helices. The same result is obtained by adding the charges of dislocations within such type III walls. For example, in Fig. 3.7.22j-l the dislocations both possess a Burgers vector that is an even integer multiple of  $\lambda$  so that  $w = 0$ . In panel k and m, the Burgers vector is an odd integer multiple of  $\lambda$  but the primitive unit cell contains two dislocations with opposite magnetizations at their cores (one bright and one dark). The finite charges of these two dislocations therefore compensate each other so that again  $w = 0$ .

A finite topological charge, however, might be obtained for type III walls with broken stripes like in the examples shown in Fig. 3.7.22n and o. They both possess two dislocations per primitive unit cell where each carries a charge  $\frac{1}{2}$  resulting in  $w = 1$ .

### 3.7.3. Bibliography

- [1] M. N. Wilson, E. A. Karhu, D. P. Lake, A. S. Quigley, S. Meynell, A. N. Bogdanov, H. Fritzsche, U. K. Rößler, and T. L. Monchesky, *Discrete helicoidal states in chiral magnetic thin films*, Phys. Rev. B **88**, 214420 (2013).
- [2] S. Rohart and A. Thiaville, *Skyrmion confinement in ultrathin film nanostructures in the presence of Dzyaloshinskii-Moriya interaction*, Phys. Rev. B **88**, 184422 (2013).
- [3] J. Iwasaki, A. J. Beekman, and N. Nagaosa, *Theory of magnon-skyrmion scattering in chiral magnets*, Phys. Rev. B **89**, 064412 (2014).
- [4] F. Jonietz, S. Mühlbauer, C. Pfleiderer, A. Neubauer, W. Münzer, A. Bauer, T. Adams, R. Georgii, P. Böni, R. A. Duine, K. Everschor, M. Garst, and A. Rosch, *Spin Transfer Torques in MnSi at Ultralow Current Densities*, Science **330**, 1648-1651 (2010).
- [5] M. Garst, *Topological Structures in Ferromagnetic Materials*, Ch. 2 (Springer, Basel, 2016).

### 3.7.4. Supplementary Figures

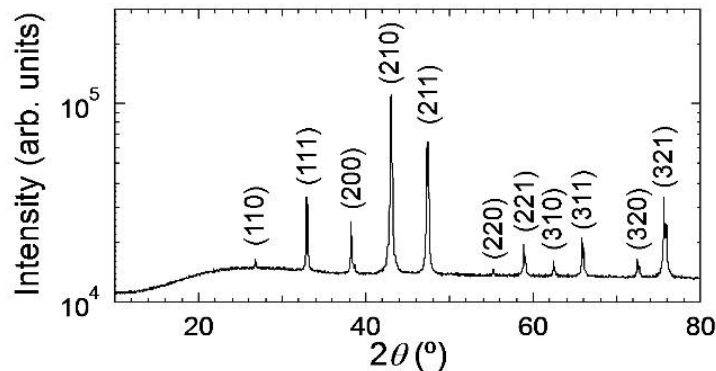


Figure 3.7.5.: Powder X-ray diffraction pattern of FeGe. All peaks are assigned according to the B20 structure of FeGe with no indication of impurity phases.

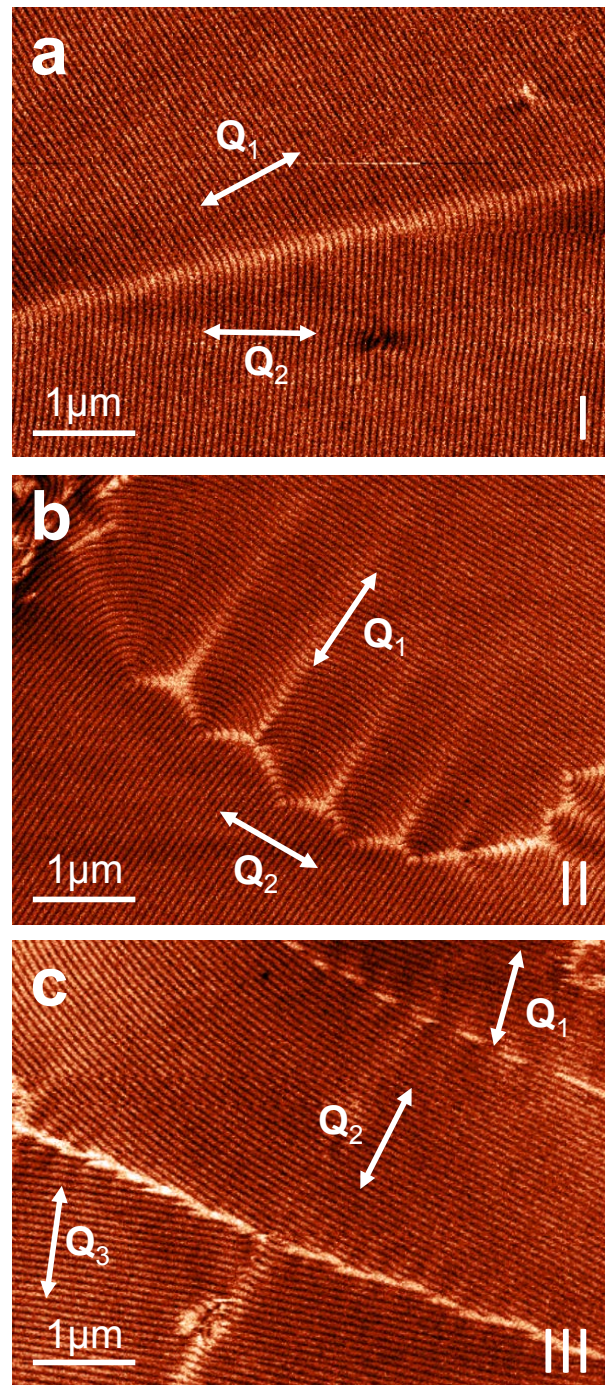


Figure 3.7.6.: MFM images of the three main domain wall configurations. In comparison to type I and III, the width of domain walls of type II is relatively large comprising micrometer-sized distortions due to  $-\pi$  disclinations.

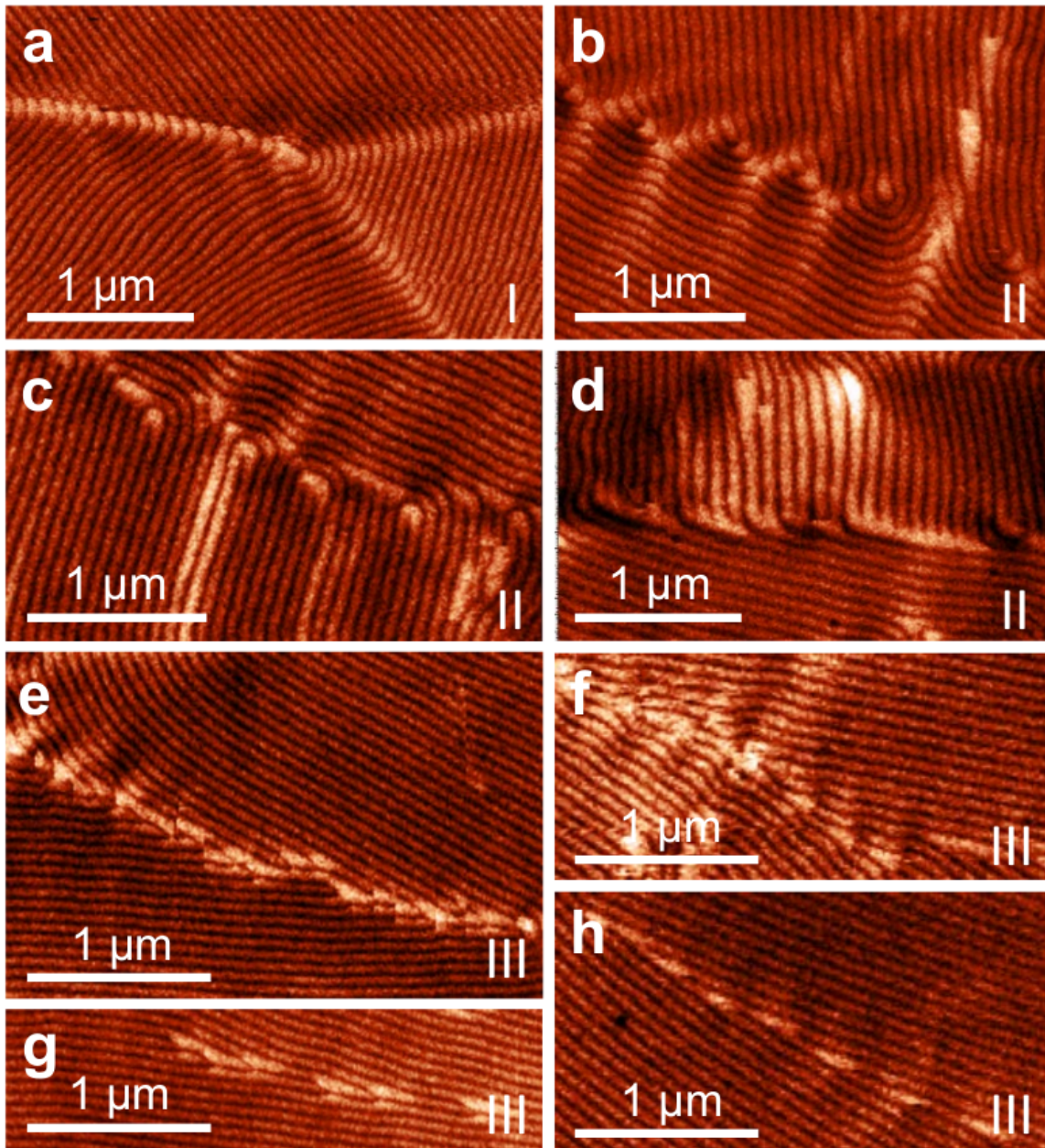


Figure 3.7.7.: Domain wall configurations in FeGe. The number of domain walls reflects the high variety of domain wall subtypes.

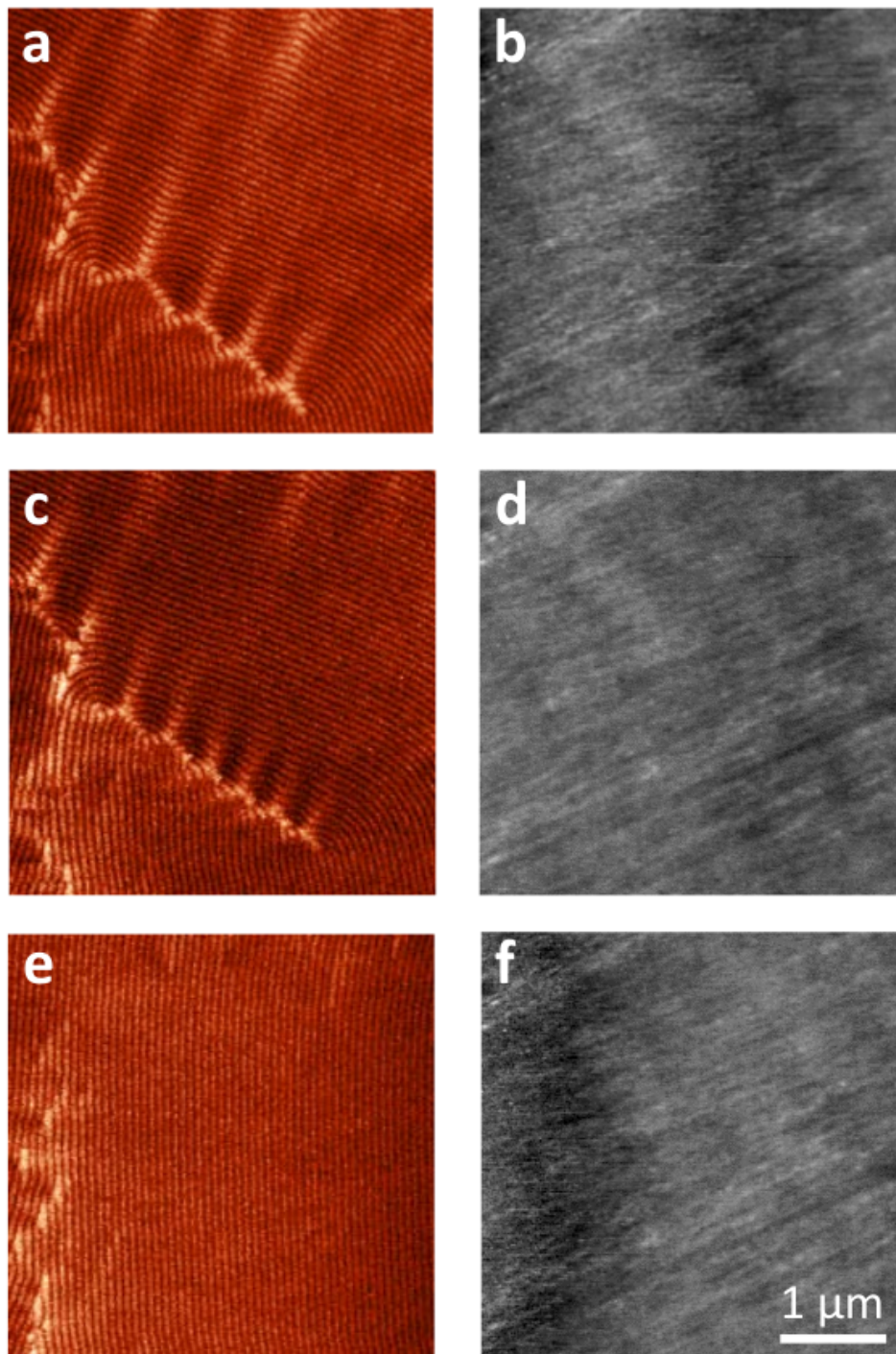


Figure 3.7.8.: Domain wall evolution under temperature and magnetic field changes. MFM images and topography scans gained at the same position on FeGe after initial cooling (a), after temporarily heating above  $T_N$  (c), and after application of a magnetic field (50 mT) (e). Corresponding topography images reveal no significant features in the region where the domain wall is observed (gray scale from  $-0.5\text{nm}$  -  $1\text{ nm}$ ).

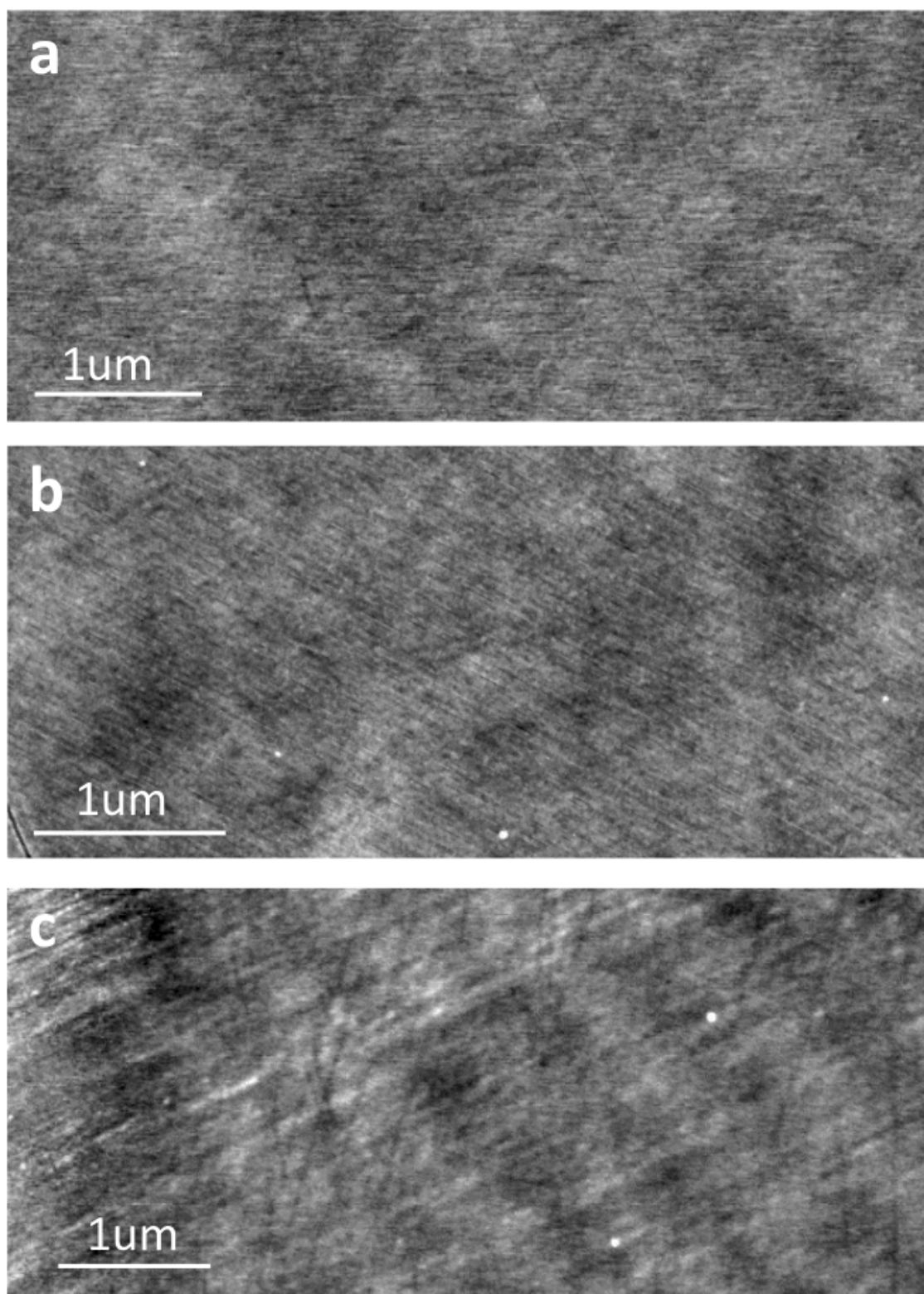


Figure 3.7.9.: Topography images to Fig. 3.1.2 of main text. Topography images show the same area as Fig. 3.1.2 of the main text. Gray scale corresponds to  $-0.4\text{nm} - 0.6\text{ nm}$  (dark to bright).

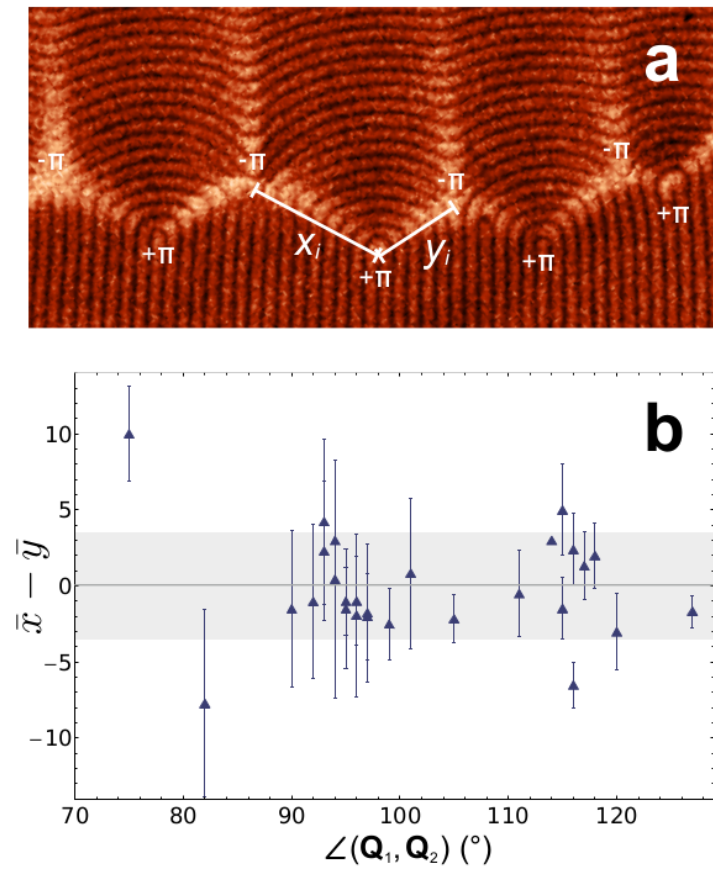


Figure 3.7.10.: Inner structure of type II domain walls. Panel a displays a representative MFM image of a type II domain wall with a zig-zag chain of  $\pm\pi$  disclinations. The distances between those defects are measured by  $x$  and  $y$  in units of  $\lambda/2$ . In panel (b), the difference between  $x$  and  $y$  averaged over each domain wall is shown as a function of  $\angle(\mathbf{Q}_1, \mathbf{Q}_2)$  for 27 experimentally observed type II walls. The grey area indicates the corresponding standard deviation.

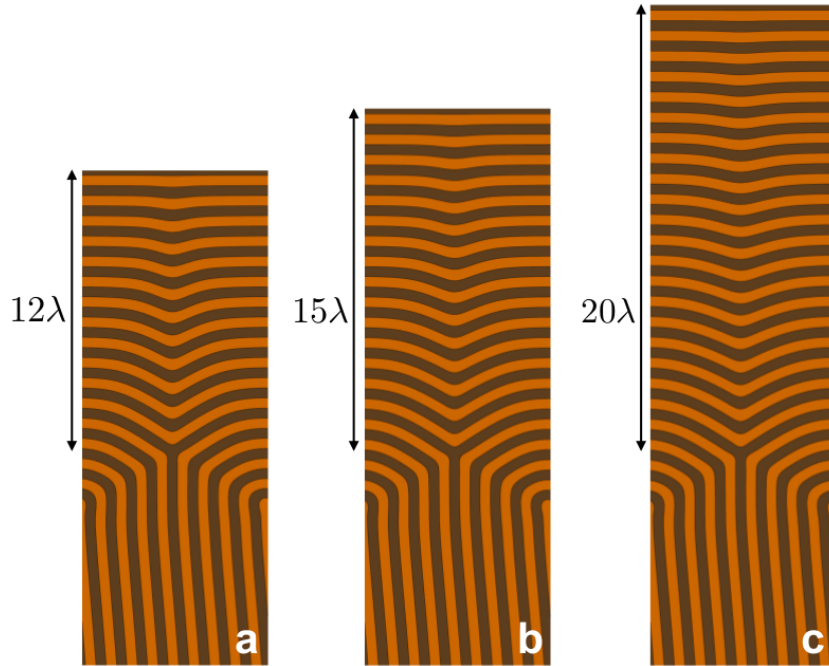


Figure 3.7.11.: Micromagnetic simulations of a type II domain wall for different system sizes. Optimized helimagnetic texture with a type II zig-zag disclination wall with  $\angle(\mathbf{Q}_1, \mathbf{Q}_2) = 94^\circ$  and a distance  $D = 9\lambda/2$  between disclinations for three different system sizes with fixed boundary conditions at the lower and upper edge. A single period of the wall is shown where bright and dark stripes represent regions where the magnetization points out or into the plane, respectively. For all three setups the number of sites along the wall was  $N_x = 378$ . The number of sites perpendicular to the wall is  $N_y = 1008, 1134, 1344$  and the distance between the upper boundary and the domain wall interface is  $L = 12, 15, 20\lambda$ , respectively, for panel (a), (b), and (c).

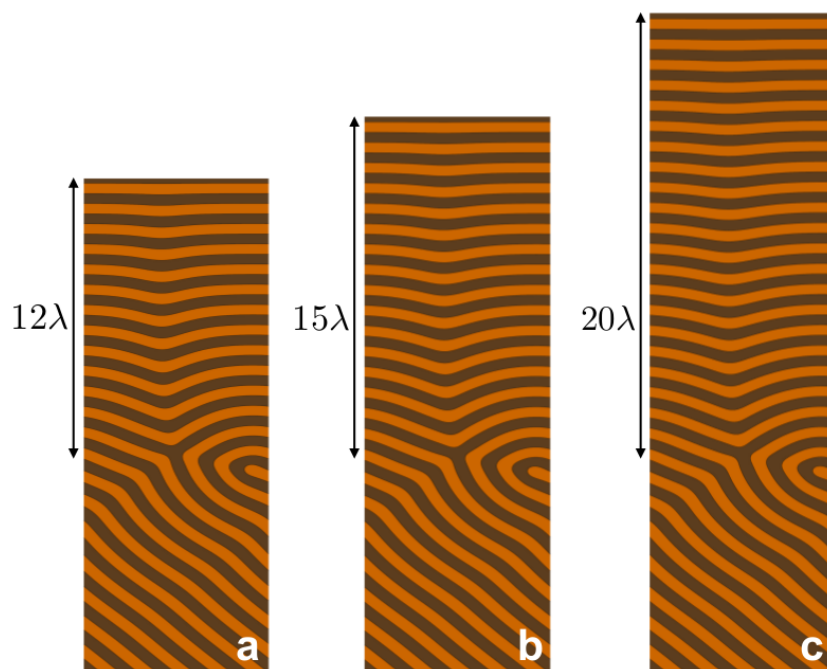


Figure 3.7.12.: Micromagnetic simulations of a type II domain wall with larger angle for different system sizes. Optimized helimagnetic texture with a type II zig-zag disclination wall like in Fig. 3.7.11 but for  $\angle(\mathbf{Q}_1, \mathbf{Q}_2) = 134^\circ$  and  $D = 5\lambda/2$ . The number of sites along the wall is  $N_x = 295$ , and perpendicular to the wall they possess the same values as in Fig. 3.7.11.

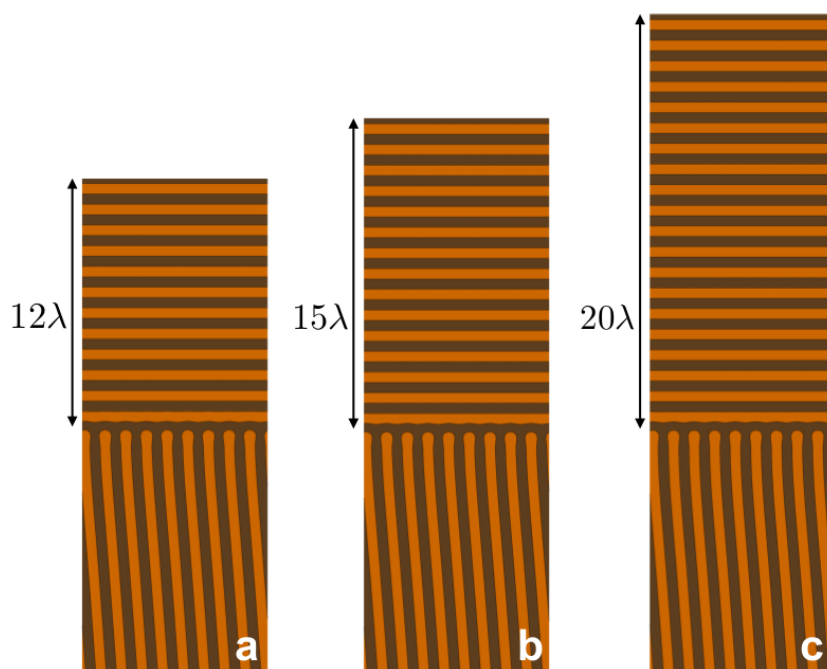


Figure 3.7.13.: Micromagnetic simulations of a type III domain wall for different system sizes. Optimized helimagnetic texture with a type II zig-zag disclination wall like in Fig. 3.7.11 with  $\angle(\mathbf{Q}_1, \mathbf{Q}_2) = 94^\circ$  and  $D = \lambda/2$ . The number of sites are the same as in Fig. 3.7.11.

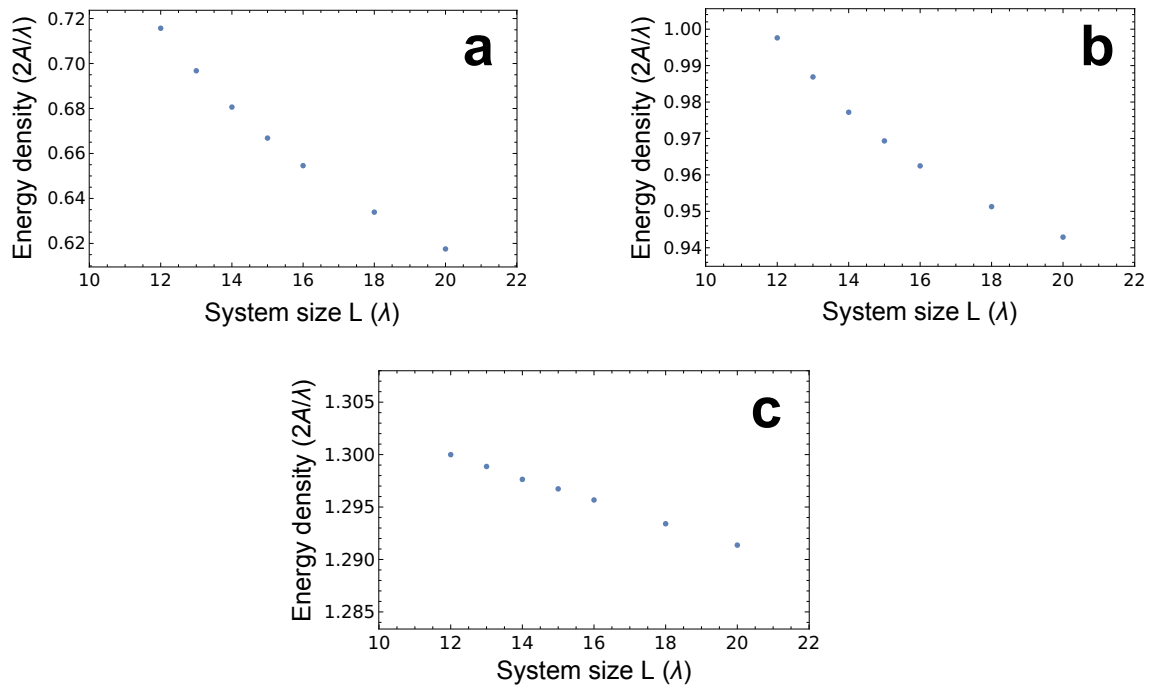


Figure 3.7.14.: Finite size scaling of the domain-wall energy density. Finite size scaling of the domain wall energy density for the three examples shown in Fig. 3.7.11, Fig. 3.7.12 and Fig. 3.7.13 displayed in panel (a), (b), and (c), respectively.

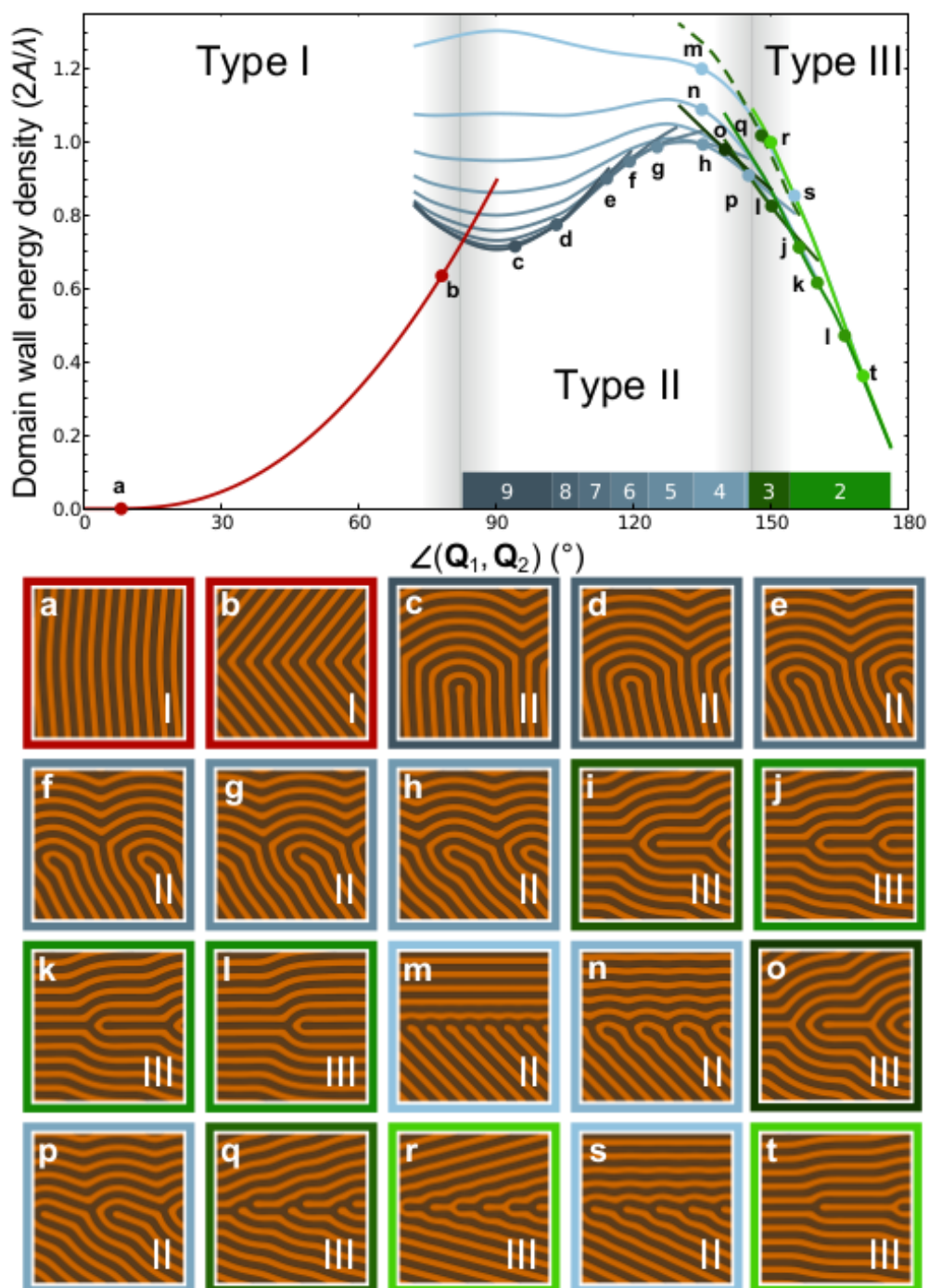


Figure 3.7.15.: Domain-wall energy density. Energy densities were obtained with the help of micromagnetic simulations for a system size  $L = 12\lambda$  as shown in Fig. 3.3.3 of the main text. The blue and green shaded boxes above the x-axis refer to properties of domain walls with lowest energies for a given angle  $\angle(\mathbf{Q}_1, \mathbf{Q}_2)$ . The blue shaded boxes indicate the separation  $D$  of disclinations within type II walls in units of  $\lambda/2$ , and the green shaded boxes indicate the Burgers vector of serially aligned edge dislocations within type III walls in units of  $\lambda$ . Panels (a) to (l) represent a series of domain wall ground states as a function of increasing angle  $\angle(\mathbf{Q}_1, \mathbf{Q}_2)$ . Panel (m) to (t) show domain wall configurations with higher energies.

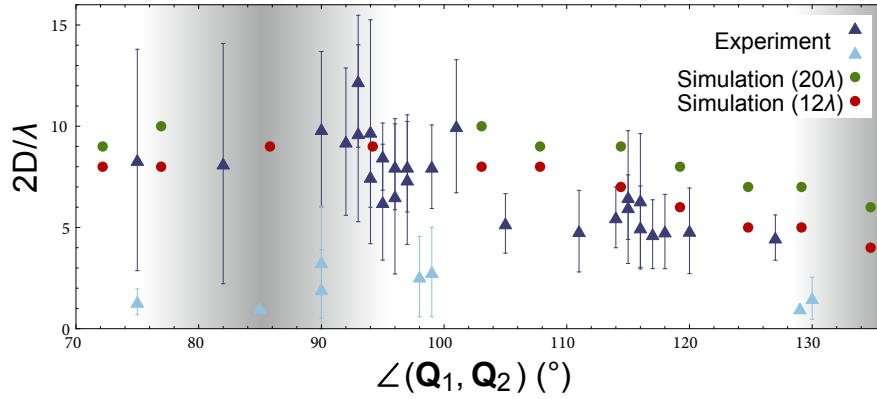


Figure 3.7.16.: Experimental and theoretical distances between  $\pi$  and  $-\pi$  disclinations within type II domain walls. Experimental values (light blue and blue triangles) are obtained in Section 3.7.2. Theoretical values for special values of  $\angle(\mathbf{Q}_1, \mathbf{Q}_2)$  are shown for two implemented system sizes  $L = 12\lambda$  (red circles) and  $L = 20\lambda$  (green circles).

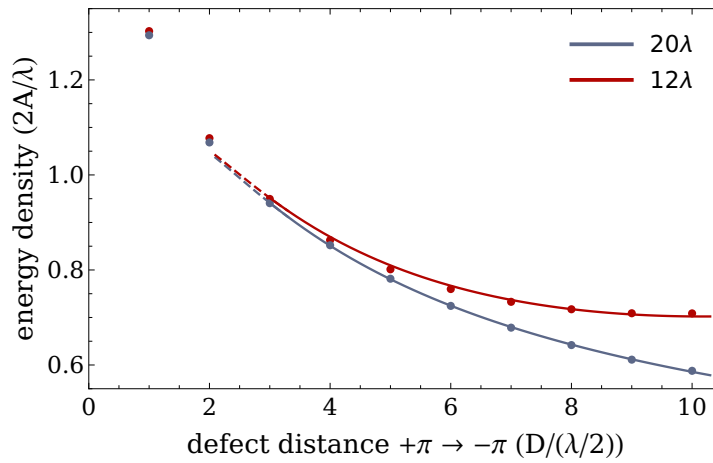


Figure 3.7.17.: Type-II-domain-wall energy density with  $\angle(\mathbf{Q}_1, \mathbf{Q}_2) = 90^\circ$  vs. defect distance  $D$ . Energy densities were obtained with the help of micromagnetic simulations for system sizes  $L = 12\lambda$  (red dots) and  $L = 20\lambda$  (blue dots) as illustrated in panel (a) and (c) of Figs. 3.7.11-3.7.13, respectively. The value for a type-II domain wall with  $\angle(\mathbf{Q}_1, \mathbf{Q}_2) = 90^\circ$  is obtained by interpolating the data from nearby angles  $\angle(\mathbf{Q}_1, \mathbf{Q}_2) \neq 90^\circ$ . The data for  $D \leq 3\lambda/2$  and  $L = 20\lambda$  is fitted by the function  $f(x) = 0.214 + 1.27\log(1.85x)/x$  with  $x = D/(\lambda/2)$  (blue line) as explained in the text of Sec. 3.7.2. For the smaller system size  $L = 12\lambda$  (red line) an additional quadratic correction  $\Delta f(x) = 0.0012x^2$  is necessary to describe the numerical data.

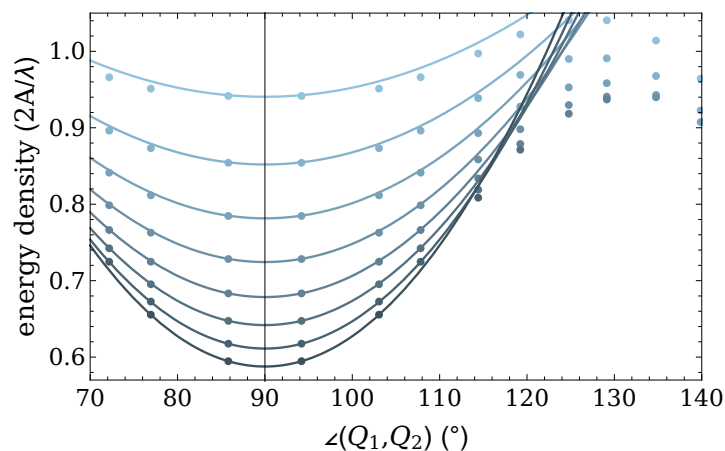


Figure 3.7.18.: Type-II-domain-wall energy density for  $\angle(\mathbf{Q}_1, \mathbf{Q}_2) \neq 90^\circ$ . Energy densities (blue dots) were obtained with the help of micromagnetic simulations for system sizes  $L = 20\lambda$  for various angles  $\angle(\mathbf{Q}_1, \mathbf{Q}_2)$  between the helical domains. The color encodes the distance  $D$  between nearest  $\pi$  and  $-\pi$  defects, ranging from  $D = 3\lambda/2$  (light blue dots) to  $D = 10\lambda/2$  (dark blue dots). A fit to Eq. 3.7.6 (solid lines) accounts for the initial quadratic dependence close to  $\angle(\mathbf{Q}_1, \mathbf{Q}_2) \approx 90^\circ$  yielding the numerical factor  $c \approx 0.13$ .

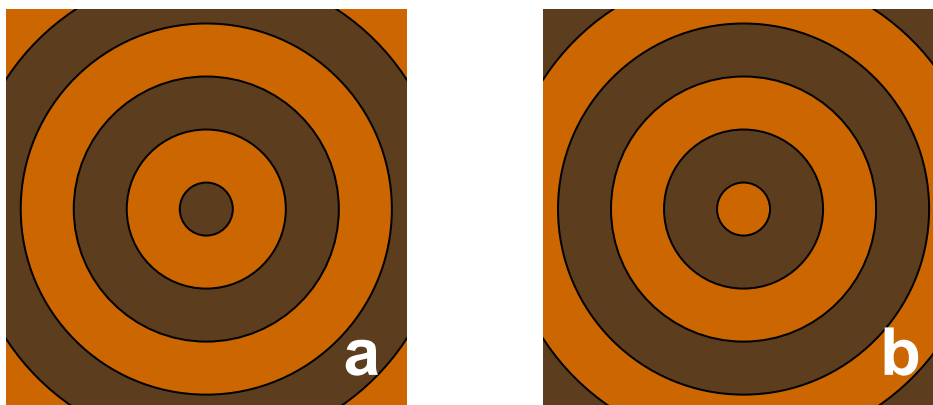


Figure 3.7.19.: Illustrations of  $2\pi$  disclinations.  $2\pi$  disclinations with (a) a dark center corresponding to a magnetization pointing down ( $\theta_0 = \pi$  in Eq. 3.7.7) and (b) a bright center corresponding to a magnetization pointing up ( $\theta_0 = 0$  in Eq. 3.7.7). These are only illustrations and not configurations optimized by micromagnetics.

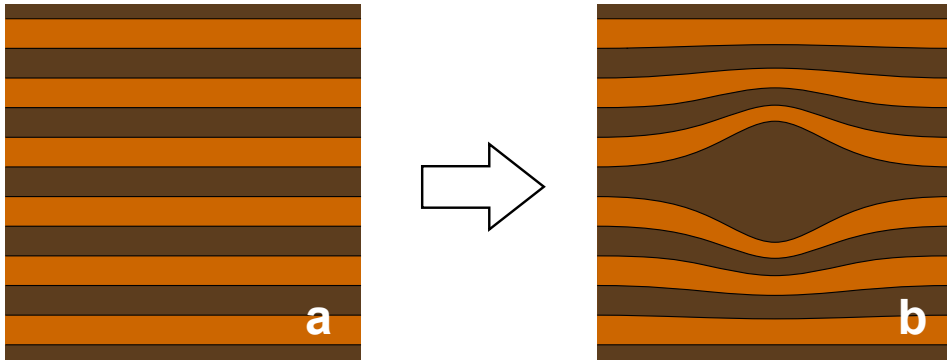


Figure 3.7.20.: Elastic deformation of the helimagnetic structure. The pristine helix (a) and the elastically deformed configuration (b) both possess vanishing total topological charge. These are only illustrations and not configurations optimized by micromagnetics.

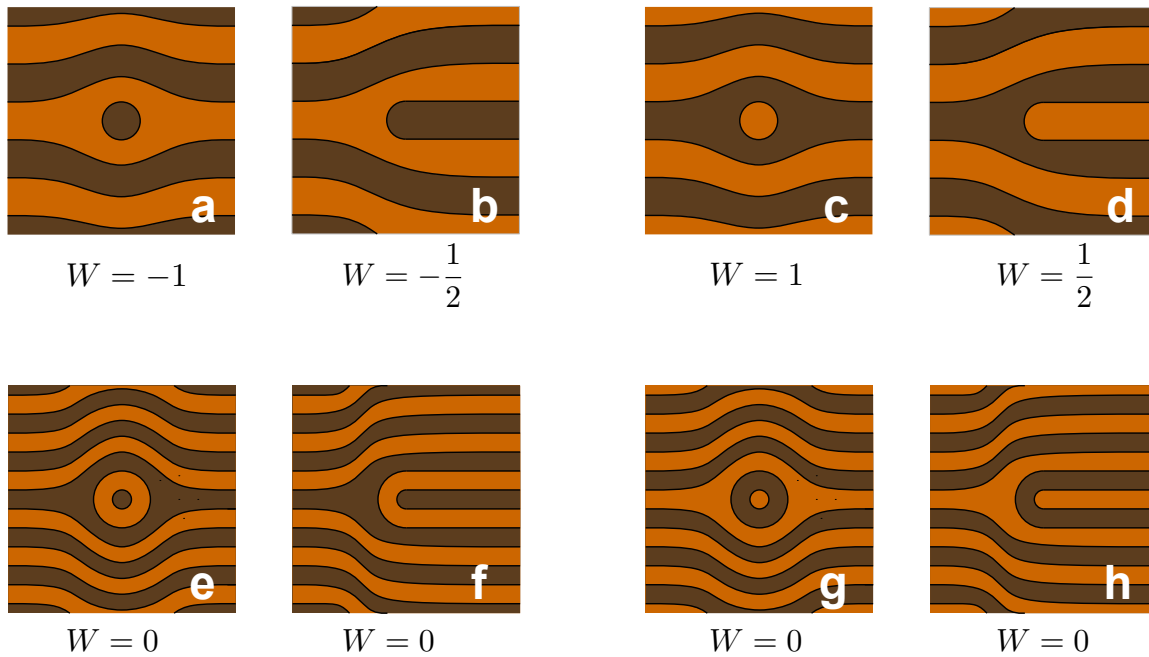


Figure 3.7.21.: Visual derivation of the total topological charge for a dislocation. A  $2\pi$  disclination with finite radius  $m\pi/Q = m\lambda/2$  embedded in a magnetic helix structure can be interpreted as two dislocations with Burgers vector  $B = m\lambda$  each carrying a charge  $W$  defined in Eq. 3.7.9. (a) and (c) show an embedded  $2\pi$  disclination with radius  $\lambda/2$ , i.e., a skyrmion where the magnetization at the core is pointing downwards (dark) and upwards (bright) resulting in a total topological charge  $W = -1$  and  $W = 1$ , respectively. The corresponding dislocations in (b) and (d) each possess half this value of the topological charge. In contrast, the total topological charge of an embedded  $2\pi$  disclination with radius  $\lambda$  and of its associated dislocations vanishes, see panel (e-h). These are only illustrations and not configurations optimized by micromagnetics.

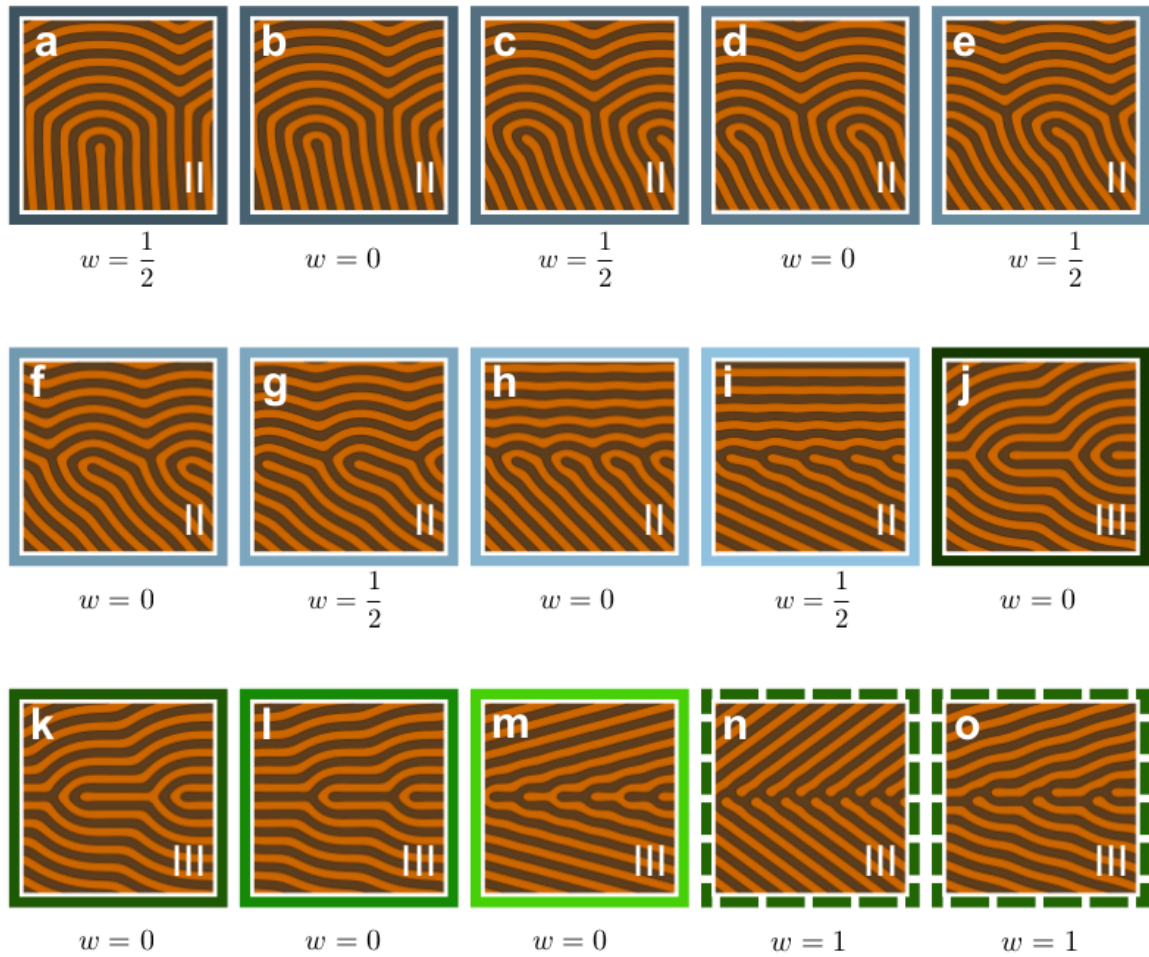


Figure 3.7.22.: Topological charge for all domain wall types. Examples of periodic domain walls and total topological charges  $w$  associated with their primitive unit cell. Note that the panels display a region of the walls that is larger than the extent of a single primitive unit cell.

## 4. Magnetic skyrmions and skyrmion clusters in the helical phase of $\text{Cu}_2\text{OSeO}_3$

Reprinted article with permission from

Jan Müller<sup>1</sup>, Jayaraman Rajeswari<sup>2</sup>, Ping Huang<sup>3</sup>, Yoshie Murooka<sup>2</sup>, Henrik M. Rønnow<sup>3</sup>, Fabrizio Carbone<sup>2</sup>, and Achim Rosch<sup>1</sup>

*Magnetic skyrmions and skyrmion clusters in the helical phase of  $\text{Cu}_2\text{OSeO}_3$*

Physical Review Letters 119, 137201 (2017)

Doi: 10.1103/PhysRevLett.119.137201

Copyright 2018 by the American Physical Society.

### Abstract

Skyrmions are nanometric spin whirls that can be stabilized in magnets lacking inversion symmetry. The properties of isolated skyrmions embedded in a ferromagnetic background have been intensively studied. We show that single skyrmions and clusters of skyrmions can also form in the helical phase and investigate theoretically their energetics and dynamics. The helical background provides natural one-dimensional channels along which a skyrmion can move rapidly. In contrast to skyrmions in ferromagnets, the skyrmion-skyrmion interaction has a strong attractive component and thus skyrmions tend to form clusters with characteristic shapes. These clusters are directly observed in transmission electron microscopy measurements in thin films of  $\text{Cu}_2\text{OSeO}_3$ . Topological quantization, high mobility and the confinement of skyrmions in channels provided by the helical background may be useful for future spintronics devices.

### 4.1. Introduction

In crystals lacking inversion symmetry, subtle relativistic interactions lead to the formation of exotic spin textures [1–4]. For example, in chiral magnets such as  $\text{Cu}_2\text{OSeO}_3$ , ferrimagnetically ordered spins spontaneously cant to form helices with a pitch of 60 – 70 nm [5–7]. Upon applying a tiny magnetic field, lattices of stable magnetic whirls emerge [6, 8–13]. Because of the nanometer confinement and sensitivity to electromagnetic control, these magnetic structures have potential for new spintronic devices.

In particular, the spin direction of a magnetic skyrmion wraps once around the unit sphere. This implies that the spin configuration cannot be continuously deformed to another magnetic state, i.e., skyrmions are topologically protected particles [9, 14]. Therefore, they can be created and destroyed only by singular magnetic configurations [15]. Furthermore, for sufficiently small

---

<sup>1</sup>Institute for Theoretical Physics, University of Cologne, D-50937 Cologne, Germany

<sup>2</sup>Laboratory for Ultrafast Microscopy and Electron Scattering (LUMES), Institute of Physics, EPFL, CH-1015 Lausanne, Switzerland

<sup>3</sup>Laboratory for Quantum Magnetism (LQM), Institute of Physics, EPFL, CH-1015 Lausanne, Switzerland

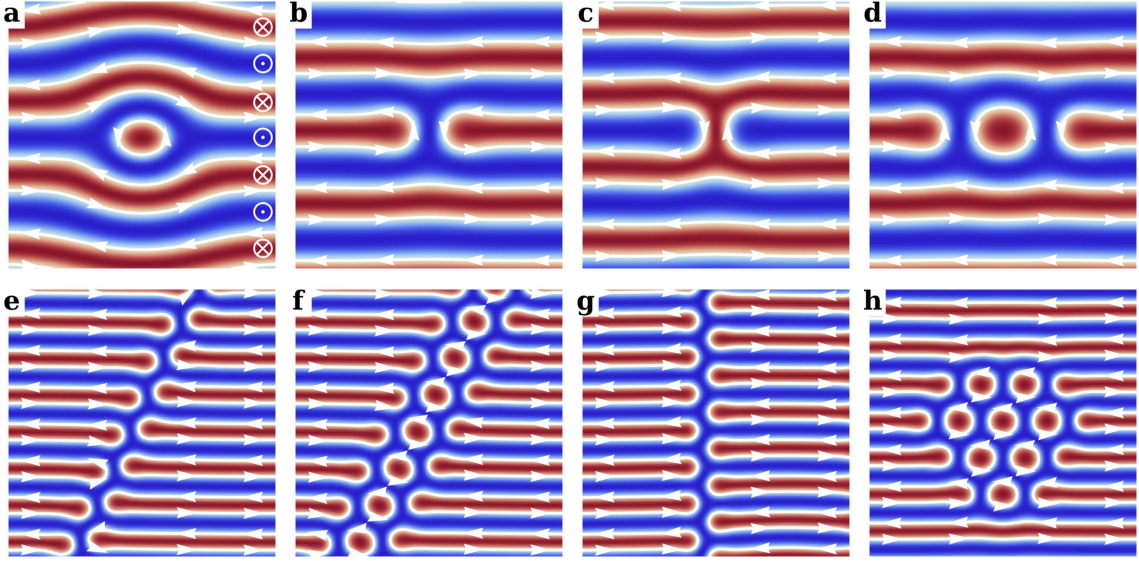


Figure 4.1.1.: Skyrmions in the helical phase ( $B = 0.2B_0$ ). The color code denotes the out-of-plane component of the magnetization as shown in (a). The in-plane component is sketched by white arrows. (a) and (b) are topologically equivalent single skyrmion states with winding number  $-1$  that can be smoothly transformed one into the other. The energy of the H-shaped skyrmion (b) is, however, much lower compared to the “interstitial” skyrmion of panel (a). In (c) an antiskyrmion with opposite winding number is shown. Because of attractive interactions, two skyrmions form a dimer bound state with winding number  $-2$ , shown in panel (d). (e-h) are multiskyrmion bound states, see text.

temperatures and magnetic fields, skyrmions can have practically an infinite lifetime [16]. As a very smooth magnetic configuration, skyrmions couple only weakly to local defects [17, 18]. Instead, they couple extremely well to external forces. In metals and heterostructures, skyrmions can be manipulated by small electric or thermal currents [18–21] while in magnetoelectric insulators they can be manipulated dissipationlessly with electric fields [22–25], heat currents [21, 26], and laser pulses [27, 28]. Furthermore, skyrmions are repelled from the edges of nanostructures and react very fast to external control [29–32].

From the application perspective, research has mainly focused on the manipulation of skyrmions in a ferromagnetic background. For example, it has been suggested to build memory devices [33] based on skyrmions arranged in a nanowire where information is encoded in the distance between skyrmions. Alternative designs use nanostructures with lanes for skyrmions where the information is stored in the lane number [34].

An interesting alternative is to consider skyrmions in a helical background. This problem, first studied by Ezawa [35], has, up to now, received little attention. Such states naturally occur when the phase transition from the skyrmion crystal phase to the helical phase is investigated [15, 36]. We argue that four major properties distinguish skyrmions in a helical background from their cousins in a ferromagnetic environment: (i) Skyrmions naturally move along the tracks defined by the helical order. Currents perpendicular to these naturally formed tracks are expected to drive skyrmions to very high speeds especially in materials with low Gilbert damping [18, 29, 37]. (ii) In the helical phase, skyrmions are metastable even for vanishing magnetic field. In contrast, skyrmions in the ferromagnetic state require either a sufficiently

strong external magnetic field or sufficiently strong easy-axis anisotropy to guarantee local stability [35,38,39]. (iii) While in the ferromagnetic state only one type of skyrmion is preferred by the background magnetization [40], in the helical phase skyrmions and antiskyrmions can coexist moving on different tracks in the helical background. (iv) While the skyrmion-skyrmion interaction is typically repulsive in the ferromagnetic case [31, 41], there are strong attractive components in the helical phase which naturally lead to the formation of skyrmion dimers and larger skyrmion clusters. Recently, clusters of skyrmions were also predicted [42] in a conical background. Leonov *et al.* [43] studied experimentally the hysteretic behavior in this regime and the formation of multidomain patterns. After submission of this Letter, a study by Loudon *et al.* [44] reported the observation of skyrmion clusters within the conical phase. Other works suggest attractive skyrmions in a fully polarized background only if an additional frustrated exchange [45] is taken into account. Also clusters in a homogeneous background have been measured under strong geometrical confinement [46]. In a helical background, however, the attractive interaction intrinsically arises from the helical modulations and thus no additional extensions of the minimal model are required.

In the following, we will first describe the theory of skyrmions in the helical phase, their interactions, and the formation of clusters of skyrmions. Energies and magnetic fields will be measured in units of  $E_0$  and  $B_0$ , respectively. These are set by the exchange coupling and the critical field stabilizing the ferromagnet, see the Supplemental Material [47]. To observe these clusters experimentally, we acquired real space and real time movies of the helical-skyrmion phase transition in a thin film of  $\text{Cu}_2\text{OSeO}_3$  using Lorentz transmission electron microscopy (LTEM) [47]. The movies reveal the nucleation of skyrmions in the helical background and their tendency to arrange in clusters of different configurations.

## 4.2. Single skyrmions in a helical phase

To investigate the energetics of skyrmions in a helical background, we performed micromagnetic simulations; see the Supplemental Material [47]. Figure 4.1.1 depicts the different skyrmion configurations: top panels represent single skyrmions and the characteristic skyrmion dimer. Bottom panels show the different multiskyrmion cluster configurations. While the “interstitial” skyrmion in panel (a) resembles the well-known skyrmion in a ferromagnetic background, the H-shaped skyrmion of panel (b) can be viewed as a bound state of two half-skyrmions (merons) defined by the ends of a helical strip, also referred to as a *meron pair* in Ref. [35]. An anti-skyrmion (panel (c)) with opposite winding number can be obtained by time reversal. Panel (d) represents the formation of a two-skyrmion dimer bound state due to the presence of attractive interactions. Plots of the winding number densities show that the skyrmions are indeed well localized, see Supplemental Material [47].

Figure 4.2.2(a) shows the energetics of four configurations of skyrmions (solid lines) and the corresponding antiskyrmions (dashed lines). Blue and red lines represent the energetics of the interstitial and the H-shaped configuration, respectively, and the green lines describe the dimer state. The H-shaped state requires much less distortion of the helical background lattice and has a significantly lower energy than the interstitial state. However, both states have the same winding number [35, 47] and can be smoothly deformed into each other. For  $B = 0$ , skyrmions and antiskyrmions are degenerate but since each skyrmion configuration carries a finite magnetization, they split linearly in the magnetic field. Above a critical field  $B_s^c$  the energy of a single skyrmion becomes negative with respect to the pure helical background

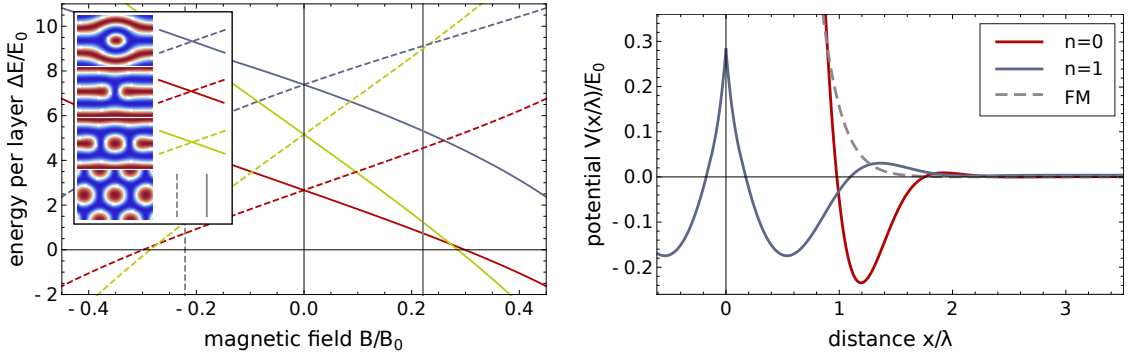


Figure 4.2.2.: Energetics of the skyrmion configurations and effective interaction potentials. Left: The H-shaped skyrmion of Fig. 4.1.1(b) has always a much lower energy (red) than the “interstitial” skyrmion of Fig. 4.1.1(a) (blue). The energy (light green) of the dimer (2-skyrmion bound state), Fig. 4.1.1(d), is slightly lower than the energy of two separate skyrmions due to attractive interactions. The thermodynamic phase transition to the skyrmion lattice is indicated with vertical lines (gray). Dashed lines show the energies of the corresponding antiskyrmion states. Right: Interaction potentials at  $B = 0.2B_0$  of two skyrmions on the same track ( $n = 0$ ) and on neighboring tracks ( $n = 1$ ) as a function of their distance ( $\lambda$  is the wavelength of the helix at  $B = 0$ ). For comparison, also the purely repulsive potential of two skyrmions in a polarized background at  $B = 1B_0$  is shown (FM). Skyrmion-dimer and dimer-dimer interactions can to a good approximation be obtained by adding monomer-monomer potentials; see Supplemental Material [47].

implying that above this field the system energetically favors the proliferation of skyrmions. The exact critical field for the phase transition to the skyrmion lattice is, however, slightly lower due to attractive interactions between skyrmions (explained below).

By translational symmetry it costs no energy for a single skyrmion to move parallel to the track defined by the helical background. In contrast, a huge energy barrier of several exchange coupling constants (per layer of the material) prohibits the motion to the parallel lane as can be estimated from the large energy value of the interstitial skyrmion configuration. This confinement has also important consequences for the velocity of the skyrmion when it is driven by a spin current perpendicular to the confining walls where we assume that the helix is pinned by disorder. In a ferromagnet, the skyrmion would flow in the direction of the spin current with a velocity of the order of  $v_s$ , the velocity characterizing the spin current [48]. Instead, the helical background acts as a confining potential [17, 18, 29, 34, 37] and, accordingly, one finds a velocity of the order of  $v_s/\alpha$ , if  $v_s$  has a component perpendicular to the track. Here  $\alpha$  is the Gilbert damping constant, which can be smaller than  $10^{-2}$  in insulating materials like  $\text{Cu}_2\text{OSeO}_3$  [49, 50]. This effect is somehow similar to a sailing boat which can obtain velocities larger than the velocity of the wind: in this analogy the keel of the boat takes over the role of the helical background.

### 4.3. Interactions and cluster formation

Skyrmion-skyrmion interactions determine the collective behavior of skyrmions and the nature of phase transitions. Attractive interactions, for example, induce the formation of bound states and clusters and render the phase transition into the skyrmion phase to be of first order. To investigate collective skyrmion states in the helical background, we calculate [47] the skyrmion-

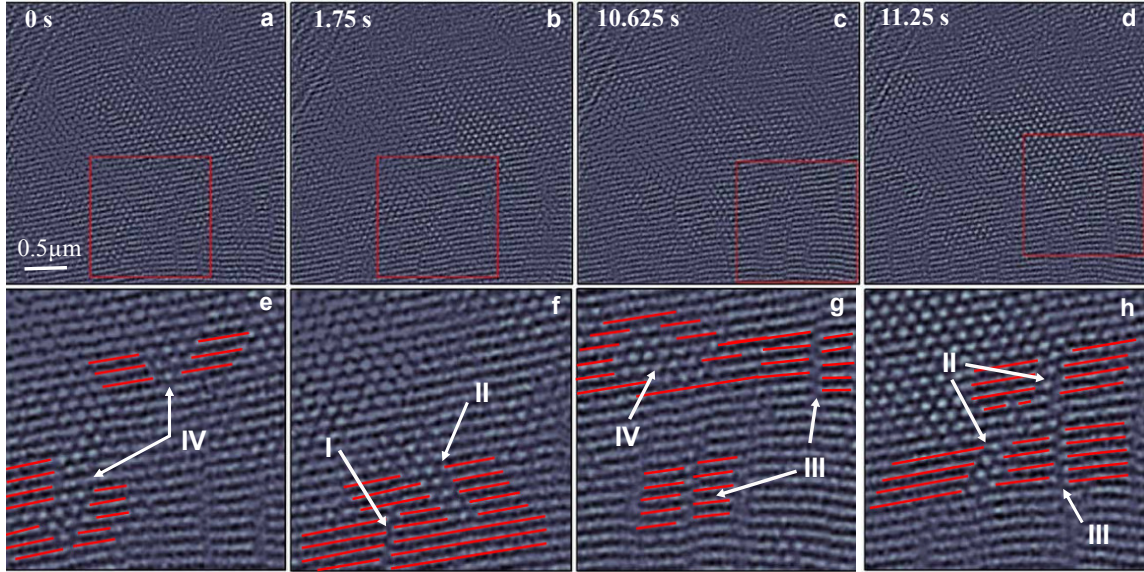


Figure 4.3.3.: Real-space cryo-Lorentz images reveal the coexistence of skyrmion and helical phases. Several types of skyrmion clusters, I - IV, can be identified corresponding to the simulated structures shown in Fig. 4.1.1(e-h).

skyrmion interaction potential  $V_i(R)$  for two skyrmions in the H-type configuration and the results are shown in Fig. 4.2.2(b). Red and blue solid lines describe the potential for skyrmions on the same track and on neighboring tracks, respectively. In both cases, the interaction is characterized by a weak long-ranged repulsion and a much stronger short ranged attraction. This leads to the formation of a bound state of two skyrmions, the dimer state depicted in Fig. 4.1.1(d). For comparison, we also show the interaction potential for two skyrmions in a polarized background [31, 41] (gray dashed line). Note that this potential is purely repulsive, which is in sharp contrast to the situation in a helical background. The attractive potential in the helical background is strongest when the two skyrmions are on the same track ( $n = 0$ ). Remarkably, the attractive potential on neighboring tracks,  $-0.175E_0$ , is only about 25% lower than on the same track,  $-0.234E_0$ . The minimal energy is thereby obtained for a relative displacement of the two skyrmions of about half the helical wavelength either to the right or to the left. The attractive skyrmion-skyrmion interaction implies that it is energetically favorable to form clusters of skyrmions. Their energy can be estimated with high accuracy by adding the interaction potential of neighboring skyrmions. For  $B = 0.2B_0$ , for example, we obtain from this simple estimate  $-0.469$ ,  $-0.584$ ,  $-4.67E_0$  for the binding energy of three skyrmions in the same track, three skyrmions distributed on two tracks, and a 12-skyrmion cluster shown in Fig. 4.1.1(h). These values can be compared to  $-0.482$ ,  $-0.581$ ,  $-4.60E_0$  obtained from direct minimization. We have checked that similar results hold for  $B = 0.4B_0$ .

## 4.4. Experiments

To experimentally detect the different skyrmion configurations predicted above, we have investigated a 110 nm thin plate of  $\text{Cu}_2\text{OSeO}_3$ . The magnetic textures were imaged using a cryo-LTEM, see methods in the Supplemental Material. The applied magnetic field and tem-

perature of the sample were held constant at 33 mT and 13 K, respectively, such that the system is close to the phase transition between the helical and the skyrmion phase. We recorded several movies and analyze here a selected movie of 100 frames with an integration time of 125 ms per frame. We observe a coexistence of helical and skyrmion domains which fluctuate with time, see Supplemental Material [47]. Fig. 4.3.3(a-d) represents a  $3.3 \times 3.3 \mu\text{m}^2$  zoom of the total  $5.7 \times 5.7 \mu\text{m}^2$  micrograph at four different time points. One can clearly identify large regions dominated either by skyrmion crystals or the helical phase. The interesting feature here is the appearance of smaller clusters of skyrmions inside the helical phases. For clarity, we show a zoom of the real-space images marked by red squares in the lower panels (Fig. 4.3.3(e-h)). To highlight the different configurations of skyrmions, some of the helical regions are marked in red.

We can identify several frequently occurring defect clusters that can be related to the theoretical states shown in Fig.4.1.1(e)-(h). The configurations I forming a line of skyrmions correspond to the state shown in Fig. 4.1.1(e). Also lines of dimers, compare Fig. 4.1.1(f), are often found and labeled by II in Fig. 4.3.3. Averaging over several such configurations of I and II, we find that the angle between the defect orientation and the ordering vector of the helix is given by  $23.5 \pm 1.5^\circ$  for a line of skyrmions and  $25.2 \pm 1^\circ$  for a line of dimers. This can be compared to  $24^\circ$  and  $26^\circ$  obtained within our simulations. We also find one further type of defect marked by III in Fig. 4.3.3 which cannot be interpreted as a bound state of skyrmions in a given helical background. Instead, in this “zipper” configuration the helical background on one side is shifted by half a lattice period. A simulation of such a structure is displayed in Fig. 4.1.1(g). In our simulation the binding energy per skyrmion for this configuration is lowered by approximately  $0.1E_0$  compared to the skyrmion line of Fig. 4.1.1(e) which implies that long defects of type I may transform into defects of type III. Furthermore, we observe all types of irregularly shaped clusters denoted by IV in Fig. 4.3.3. It is instructive to compare the formation of skyrmions in the helical and the ferromagnetic state. In the latter case, skyrmion-skyrmion interactions are repulsive [31,34,41] and therefore no formation of skyrmion clusters is expected. We have checked this by performing experiments at magnetic fields of 100 to 150 mT, where only skyrmions in a ferromagnetic background occur. As expected, no cluster formation was observed by us; see the Supplemental Material [47].

We also observe regions where the image is blurred at the location of defects. We believe that this effect arises from the motion of defects. Assuming a Gilbert damping of the order of  $10^{-2}$ , we estimate the 1D diffusion constant of a cluster of  $n$  skyrmions [47] in the absence of defects to be of the order of  $\frac{1}{n}10^{-9} \text{m}^2/\text{s}$ . Within the capturing time of a frame of our movie (125ms) a freely moving cluster can therefore move distances of the order of  $\frac{10}{\sqrt{n}} \mu\text{m}$ . This estimate is consistent with large fluctuations that we see from frame to frame captured within our movie. Sharply resolved images correspond to clusters that are temporarily bound to defects presumably arising either from lattice defects or height variations of our films.

## 4.5. Conclusions

While sharing the same topology, skyrmions embedded in a helical or a ferromagnetic environment have very different properties. Our studies highlight one aspect of this: attractive interactions in the helical background let skyrmions arrange in lines and clusters. These lines and clusters have characteristic shapes and orientations which we identified both in our magnetic simulations and electron microscopy experiments. From the viewpoint of application,

skyrmions in a helical background are potentially attractive since the helical stripes provide natural lanes along which skyrmions can be driven fast. However, one has to avoid the formation of zipper configuration which can, for example, be achieved in nanowires of suitable dimensions. The energy barrier for passing skyrmions between parallel lanes could be controlled, for example, with tailored light pulses or electric fields and will be explored in future experiments.

### Acknowledgments

We thank the Deutsche Telekom Stiftung (J.M.), the Bonn-Cologne Graduate School of Physics and Astronomy BCGS (J.M.), and the CRC 1238 (project C04) of the German Science Foundation (A. R., J.M.) for financial support. J.R. thanks the Swiss National Science Foundation (SNSF) for funding through the Ambizione Fellowship PZ00P2\_168035. Work at LUMES was supported by the National Center for Competence in Research Molecular Ultrafast Science and Technology (NCCR MUST), a research instrument of the SNSF. Work at LQM was supported by ERC project Controlled Quantum Effects and Spin Technology and SNSF (H.M.R.).

J. M., J. R., and P. H. contributed equally to this work.

## 4.6. Bibliography

- [1] I. E. Dzyaloshinskii, *Theory of Helicoidal Structures in Antiferromagnets. I. Nonmetals*, Zh. Eksp. Teo. Fiz. **46**, 1420 (1964).
- [2] A. N. Bogdanov and D. A. Yablonskii, *Thermodynamically stable “vortices” in magnetically ordered crystals. The mixed state of magnets*, Zh. Eksp. Teo. Fiz. **95**, 178-182 (1989).
- [3] A. N. Bogdanov and A. Hubert, *Thermodynamically stable magnetic vortex states in magnetic crystals*, J. Magn. Magn. Mater. **138**, 255-269 (1994).
- [4] O. Janson, I. Rousochatzakis, A. A. Tsirlin, M. Belesi, A. A. Leonov, U. K. Röbker, J. van den Brink, and H. Rosner, *The quantum nature of skyrmions and half-skyrmions in  $\text{Cu}_2\text{OSeO}_3$* , Nat. Commun. **5**, 5376 (2014).
- [5] T. Adams, A. Chacon, M. Wagner, A. Bauer, G. Brandl, B. Pedersen, H. Berger, P. Lemmens, and C. Pfleiderer, *Long-wavelength helimagnetic order and skyrmion lattice phase in  $\text{Cu}_2\text{OSeO}_3$* , Phys. Rev. Lett. **108**, 237204 (2012).
- [6] S. Seki, J.-H. Kim, D. S. Inosov, R. Georgii, B. Keimer, S. Ishiwata, and Y. Tokura, *Formation and rotation of skyrmion crystal in the chiral-lattice insulator  $\text{Cu}_2\text{OSeO}_3$* , Phys. Rev. B **85**, 220406 (2012).
- [7] J. Rajeswari, P. Huang, G. F. Mancini, Y. Murooka, T. Latychevskaia, D. McGrouther, M. Cantoni, E. Baldini, J. S. White, A. Magrez, T. Giamarchi, H. M. Rønnow, and F. Carbone, *Filming the formation and fluctuation of skyrmion domains by cryo-Lorentz transmission electron microscopy*, Proc. Natl. Acad. Sci. USA **112**, 14212-14217 (2015).
- [8] S. Seki, X. Z. Yu, S. Ishiwata, and Y. Tokura, *Observation of skyrmions in a multiferroic material*, Science **336**, 198-201 (2012).
- [9] N. Nagaosa and Y. Tokura, *Topological properties and dynamics of magnetic skyrmions*, Nat. Nano. **8**, 899-911 (2013).
- [10] M. C. Langner, S. Roy, S. K. Mishra, J. C. T. Lee, X. W. Shi, M. A. Hossain, Y.-D. Chuang, S. Seki, Y. Tokura, S. D. Kevan, and R. W. Schoenlein, *Coupled skyrmion sublattices in  $\text{Cu}_2\text{OSeO}_3$* , Phys. Rev. Lett. **112**, 167202 (2014).
- [11] S. L. Zhang, A. Bauer, H. Berger, C. Pfleiderer, G. van der Laan, and T. Hesjedal, *Imaging and manipulation of skyrmion lattice domains in  $\text{Cu}_2\text{OSeO}_3$* , Appl. Phys. Lett. **109**, 192406 (2016).

- [12] S. L. Zhang, A. Bauer, H. Berger, C. Pfleiderer, G. van der Laan, and T. Hesjedal, *Resonant elastic x-ray scattering from the skyrmion lattice in  $\text{Cu}_2\text{OSeO}_3$* , Phys. Rev. B **93**, 214420 (2016).
- [13] S. L. Zhang, A. Bauer, D. M. Burn, P. Milde, E. Neuber, L. M. Eng, H. Berger, C. Pfleiderer, G. van der Laan, and T. Hesjedal, *Multidomain skyrmion lattice state in  $\text{Cu}_2\text{OSeO}_3$* , Nano Lett. **16**, 3285-3291 (2016).
- [14] S. Mühlbauer, B. Binz, F. Jonietz, C. Pfleiderer, A. Rosch, A. Neubauer, R. Georgii, and P. Böni, *Skyrmion lattice in a chiral magnet*, Science **323**, 915-919 (2009).
- [15] P. Milde, D. Köhler, J. Seidel, L. M. Eng, A. Bauer, A. Chacon, J. Kindervater, S. Mühlbauer, C. Pfleiderer, S. Buhrandt, C. Schütte, and A. Rosch, *Unwinding of a skyrmion lattice by magnetic monopoles*, Science **340**, 1076 (2013).
- [16] J. Hagemester, N. Romming, K. von Bergmann, E. Y. Vedmedenko, and R. Wiesendanger, *Stability of single skyrmionic bits*, Nat. Commun. **6**, 8455 (2015).
- [17] J. Müller and A. Rosch, *Capturing of a magnetic skyrmion with a hole*, Phys. Rev. B **91**, 054410 (2015).
- [18] J. Iwasaki, M. Mochizuki, and N. Nagaosa, *Universal current-velocity relation of skyrmion motion in chiral magnets*, Nat. Commun. **4**, 1463 (2013).
- [19] F. Jonietz, S. Mühlbauer, C. Pfleiderer, A. Neubauer, W. Münzer, A. Bauer, T. Adams, R. Georgii, P. Böni, R. A. Duine, K. Everschor, M. Garst, and A. Rosch, *Spin transfer torques in  $\text{MnSi}$  at ultralow current densities*, Science **330**, 1648-1651 (2010).
- [20] X. Z. Yu, N. Kanazawa, W. Z. Zhang, T. Nagai, T. Hara, K. Kimoto, Y. Matsui, Y. Onose, and Y. Tokura, *Skyrmion flow near room temperature in an ultralow current density*, Nat. Commun. **3**, 988 (2012).
- [21] S.-Z. Lin, C. D. Batista, C. Reichhardt, and A. Saxena, *AC current generation in chiral magnetic insulators and skyrmion motion induced by the spin Seebeck effect*, Phys. Rev. Lett. **112**, 187203 (2014).
- [22] S. Seki, S. Ishiwata, and Y. Tokura, *Magnetoelectric nature of skyrmions in a chiral magnetic insulator  $\text{Cu}_2\text{OSeO}_3$* , Phys. Rev. B **86**, 060403 (2012).
- [23] J. S. White, I. Levatić, A. A. Omrani, N. Egetenmeyer, K. Prša, I. Živković, J. L. Gavilano, J. Kohlbrecher, M. Bartkowiak, H. Berger, and H. M. Rønnow, *Electric field control of the skyrmion lattice in  $\text{Cu}_2\text{OSeO}_3$* , J. Phys. Condens. Matter **24**, 432201 (2012).
- [24] J. S. White, K. Prša, P. Huang, A. A. Omrani, I. Živković, M. Bartkowiak, H. Berger, A. Magrez, J. L. Gavilano, G. Nagy, J. Zang, and H. M. Rønnow, *Electric-field-induced skyrmion distortion and giant lattice rotation in the magnetoelectric insulator  $\text{Cu}_2\text{OSeO}_3$* , Phys. Rev. Lett. **113**, 107203 (2014).
- [25] A. A. Omrani, J. S. White, K. Prša, I. Živković, H. Berger, A. Magrez, Y.-H. Liu, J. H. Han, and H. M. Rønnow, *Exploration of the helimagnetic and skyrmion lattice phase diagram in  $\text{Cu}_2\text{OSeO}_3$  using magnetoelectric susceptibility*, Phys. Rev. B **89**, 064406 (2014).
- [26] W. Koshibae and N. Nagaosa, *Creation of skyrmions and antiskyrmions by local heating*, Nat. Commun. **5**, 5148 (2014).
- [27] N. Ogawa, S. Seki, and Y. Tokura, *Ultrafast optical excitation of magnetic skyrmions*, Sci. Rep. **5**, 9552 (2015).
- [28] G. Berruto and F. Carbone, (to be published).
- [29] J. Sampaio, V. Cros, S. Rohart, A. Thiaville, and A. Fert, *Nucleation, stability and current-induced motion of isolated magnetic skyrmions in nanostructures*, Nat. Nano. **8**, 839-844 (2013).
- [30] S. Woo, K. Litzius, B. Krüger, M.-Y. Im, L. Caretta, K. Richter, M. Mann, A. Krone, R. M. Reeve, M. Weigand, P. Agrawal, I. Lemesh, M.-A. Mawass, P. Fischer, M. Kläui, and G. S. D. Beach, *Observation of room-temperature magnetic skyrmions and their current-driven dynamics in ultrathin metallic ferromagnets*, Nat. Mater. **15**, 501-506 (2016).

- 
- [31] X. Zhang, G. P. Zhao, H. Fangohr, J. P. Liu, W. X. Xia, J. Xia, and F. J. Morvan, *Skyrmion-skyrmion and skyrmion-edge repulsions in skyrmion-based racetrack memory*, Sci. Rep. **5**, 7643 (2015).
- [32] X. Zhang, J. Müller, J. Xia, M. Garst, X. Liu, and Y. Zhou, *Motion of skyrmions in nanowires driven by magnonic momentum-transfer forces*, New J. Phys. **19**, 065001 (2017).
- [33] A. Fert, V. Cros, and J. Sampaio, *Skyrmions on the track*, Nat. Nano. **8**, 152-156 (2013).
- [34] J. Müller, *Magnetic skyrmions on a two-lane racetrack*, New J. Phys. **19**, 025002 (2017).
- [35] M. Ezawa, *Compact merons and skyrmions in thin chiral magnetic films*, Phys. Rev. B **83**, 100408 (2011).
- [36] C. Schütte and A. Rosch, *Dynamics and energetics of emergent magnetic monopoles in chiral magnets*, Phys. Rev. B **90**, 174432 (2014).
- [37] J. Iwasaki, M. Mochizuki, and N. Nagaosa, *Current-induced skyrmion dynamics in constricted geometries*, Nat. Nanotech. **8**, 742-747 (2013).
- [38] J. Müller, A. Rosch, and M. Garst, *Edge instabilities and skyrmion creation in magnetic layers*, New J. Phys. **18**, 065006 (2016).
- [39] I. Kézsmárki, S. Bordács, P. Milde, E. Neuber, L. M. Eng, J. S. White, H. M. Rønnow, C. D. Dewhurst, M. Mochizuki, K. Yanai, H. Nakamura, D. Ehlers, V. Tsurkan, and A. Loidl, *Néel-type skyrmion lattice with confined orientation in the polar magnetic semiconductor  $GaV_4S_8$* , Nat. Mater. **14**, 1116-1122 (2016).
- [40] W. Koshibae and N. Nagaosa, *Theory of antiskyrmions in magnets*, Nat. Commun. **7**, 10542 (2016).
- [41] A. Bogdanov, *New localized solutions of the nonlinear field equations*, JEPT Lett. **62**, 247 (1995).
- [42] A. O. Leonov, T. L. Monchesky, J. C. Loudon, and A. N. Bogdanov, *Three-dimensional chiral skyrmions with attractive interparticle interactions*, *Phys. Condens. Matter* **28**, 35LT01 (2016).
- [43] A. O. Leonov, Y. Togawa, T. L. Monchesky, A. N. Bogdanov, J. Kishine, Y. Kousaka, M. Miyagawa, T. Koyama, J. Akimitsu, Ts. Koyama, K. Harada, S. Mori, D. McGrouther, R. Lamb, M. Krajenak, S. McVitie, R. L. Stamps, and K. Inoue, *Chiral surface twists and skyrmion stability in nanolayers of cubic helimagnets*, Phys. Rev. Lett. **117**, 087202 (2016).
- [44] J. C. Loudon, A. O. Leonov, A. N. Bogdanov, M. Ciomaga Hatnean, and G. Balakrishnan, *Direct observation of attractive skyrmions and skyrmion clusters in a cubic helimagnet  $Cu_2OSeO_3$* , Arxiv e-print (2017), arXiv:1704.06876.
- [45] L. Rózsa, A. Deák, E. Simon, R. Yanes, L. Udvardi, L. Szunyogh, and U. Nowak, *Skyrmions with attractive interactions in an ultrathin magnetic film*, Phys. Rev. Lett. **117**, 157205 (2016).
- [46] X. Zhao, C. Jin, C. Wang, H. Du, J. Zang, M. Tian, R. Che, and Y. Zhang, *Direct imaging of magnetic field-driven transitions of skyrmion cluster states in  $FeGe$  nanodisks*, Proc. Nat. Acad. Sci. USA **113**, 4918-4923 (2016).
- [47] See Supplemental Material at <http://link.aps.org/supplemental/10.1103/PhysRevLett.119.137201> for more detailed information.
- [48] A. A. Thiele, *Steady-state motion of magnetic domains*, Phys. Rev. Lett. **30**, 230-233 (1973).
- [49] Y. Onose, Y. Okamura, S. Seki, S. Ishiwata, and Y. Tokura, *Observation of Magnetic Excitations of Skyrmion Crystal in a Helimagnetic Insulator  $Cu_2OSeO_3$* , Phys. Rev. Lett. **109**, 037603 (2012).
- [50] B. Heinrich, C. Burrowes, E. Montoya, B. Kardasz, E. Girt, Y.-Y. Song, Y. Sun, and M. Wu, *Spin Pumping at the Magnetic Insulator (YIG)/Normal Metal (Au) Interfaces*, Phys. Rev. Lett. **107**, 066604 (2011).

## 4.7. Supplemental Material

### Abstract

We present some details on the micromagnetic simulations, the calculation of interaction potentials and diffusion constants. Furthermore, we give experimental details and show that skyrmions close to the phase transition to the ferromagnetic state do not display the characteristic cluster formation observed in the helical phase.

### 4.7.1. Micromagnetic Simulations

We consider a two-dimensional plane with the magnetization  $\mathbf{M}$  represented by a three-dimensional vector field. The free energy functional,  $F = \int d^2\mathbf{r}\mathcal{F}$ , includes exchange interaction  $A$ , Dzyaloshinskii-Moriya-interaction  $D$  and an external magnetic field  $B$ :

$$\mathcal{F} = A(\nabla\hat{n})^2 + D\hat{n} \cdot (\nabla \times \hat{n}) - BM\hat{n}_z, \quad (4.7.1)$$

where  $\hat{n} = \mathbf{M}/M$  is the normalized magnetization. Since the theory is continuous, we introduce dimensionless scales for the momentum  $Q$ , energy per layer  $E_0$  and magnetic field  $B_0$

$$Q = \frac{D}{2A}, \quad E_0 = 2A, \quad B_0 = \frac{2AQ^2}{M}. \quad (4.7.2)$$

For numerical implementation, we discretize the system, typically using 22 spins per pitch  $2\pi/Q$  of the helix. For the calculation of energy minima we prepare an initial magnetic texture and let it then relax by a fourth order Runge-Kutta integration of the equation

$$\partial_t \hat{n} = \mathbf{B}_{\text{eff}}^\perp \quad (4.7.3)$$

with  $\mathbf{B}_{\text{eff}}^\perp$  the component of the effective magnetic field  $\mathbf{B}_{\text{eff}} = -\frac{1}{M}\delta F/\delta\hat{n}$  perpendicular to the magnetization. This equation can be interpreted as the Landau-Lifshitz-Gilbert equation where the precession term is omitted. For the calculation of interaction potentials we fixed a couple of spins (one to nine) in the center of the monomers during the minimization and hence ensure that the distance is preserved during the minimization process. We have checked that the results are approximately independent of the number of fixed spins.

### Localization of topological charge

We compute the topological charge density  $w(\mathbf{r})$  from the relaxed monomer, anti-monomer and dimer configurations via the formula

$$w(\mathbf{r}) = \frac{1}{4\pi} \hat{n}(\mathbf{r}) \cdot (\partial_x \hat{n}(\mathbf{r}) \times \partial_y \hat{n}(\mathbf{r})) \quad (4.7.4)$$

and show the results in Fig. 4.7.4. What should be noticed here is that the charge distribution is indeed localized. Furthermore, upon integration we find that the total charge  $W = \int w(\mathbf{r}) d^2r$  is  $-1$  for the interstitial (a) and the H-shaped skyrmion (b),  $+1$  for the antiskyrmion (c) and  $-2$  for the skyrmion dimer (d).

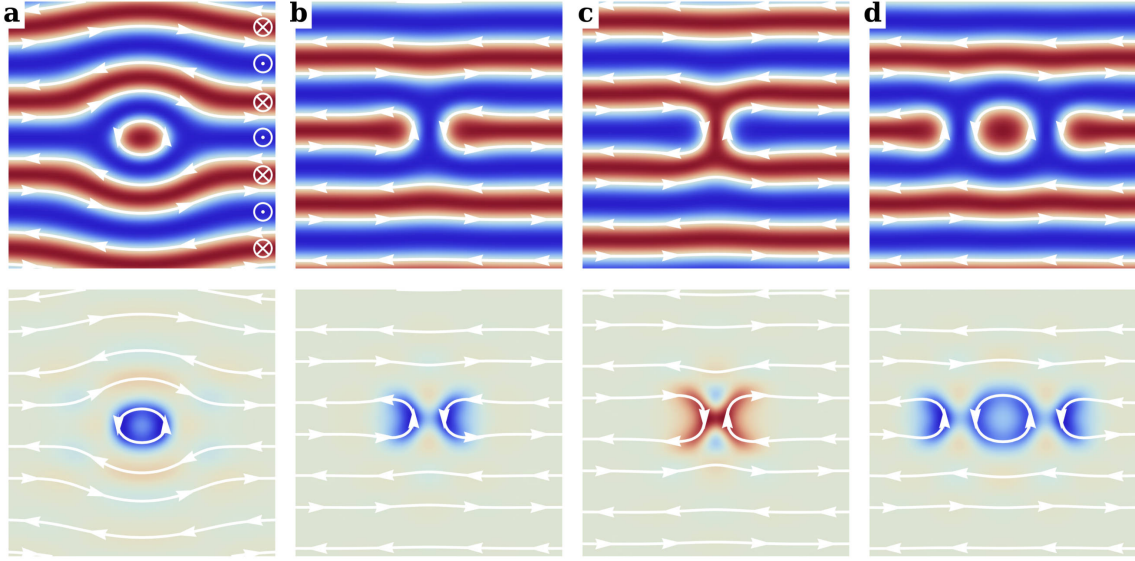


Figure 4.7.4.: Skyrmions in the helical phase ( $B = 0.2B_0$ ) as also shown in the main text (upper row). The lower row of figures shows the corresponding winding number densities, rescaled to arbitrary units. The colorcode denotes the charge density as positive (red) or negative (blue) as compared to the uncharged helical state (pale green).

### Dimer potentials and energetics of clusters

In the main text the monomer-monomer potentials are discussed. Figures 4.7.5 and 4.7.6 show the interaction potential of a dimer (i.e. a bound pair of monomers) with a monomer on the same lane (Fig. 4.7.5, red dashed) and on the neighboring lane (Fig. 4.7.6, blue dashed). We emphasize that these interactions can be reduced to the potentials of only monomer interaction by additionally plotting the interaction between monomers in the same setups (solid lines respectively). These two-particle interaction potentials are shifted on the x-axis such that they match the positions of the single monomer and the nearest other monomer of the full three-particle potentials. In the case of the dimer and the monomer being placed on neighboring lanes, Fig. 4.7.6, the monomer can be located between the two constituents of the dimer and thus feels both of them. Here the full three-particle potential can be accurately described by a superposition of two two-particle interaction potentials accordingly shifted (solid green).

The energy of a cluster of skyrmions can then be estimated by simply adding the energies at the interaction minima. For example, the energy of the 12-skyrmion cluster, Fig. 1(h) in the main text, is the sum of in total 8 monomer pairs on the same lane and 16 monomer pairs on neighboring lanes. This gives a total binding energy of  $-4.67E_0$  compared to  $-4.60E_0$  from the full relaxation.

### Diffusion

The dynamics of the magnetization are governed by the Landau-Lifshitz-Gilbert equation (LLG). In the presence of thermal fluctuations, these equations are made stochastic by adding a fluctuating term  $\mathbf{b}^{\text{th}}(\mathbf{r}, t)$  to the effective magnetic field  $\mathbf{B}_{\text{eff}} \rightarrow \mathbf{B}_{\text{eff}} + \mathbf{b}^{\text{th}}(\mathbf{r}, t)$ . This fluctuating field has to vanish on average

$$\langle \mathbf{b}_i^{\text{th}}(\mathbf{r}, t) \rangle = 0 \quad (4.7.5)$$

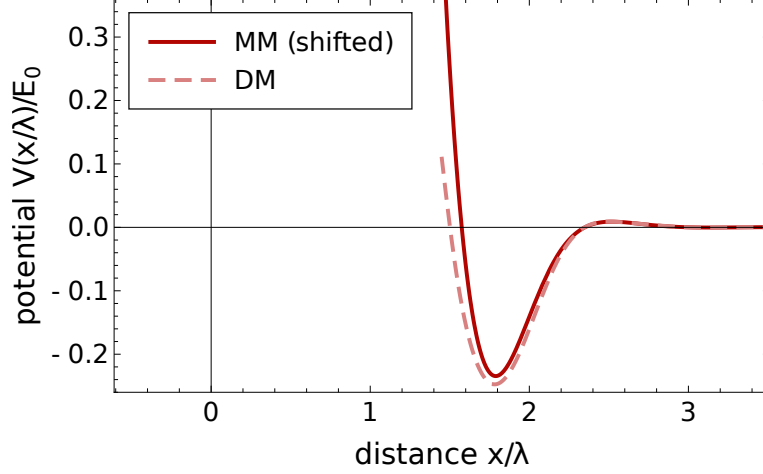


Figure 4.7.5.: Interaction potential of a dimer with a monomer (*DM*, dashed) and a monomer with a monomer (*MM*, solid) on the same helical lane. The *MM* potential is shifted such that the position of one monomer matches the position of the central monomer in the *DM* potential.

and is uncorrelated with a suitable normalization factor

$$\langle \mathbf{b}_i^{\text{th}}(\mathbf{r}, t) \mathbf{b}_j^{\text{th}}(\mathbf{r}', t') \rangle = 2\alpha \frac{k_B T}{\gamma M} \delta_{ij} \delta(r - r') \delta(t - t'), \quad (4.7.6)$$

where  $\alpha$  is the Gilbert damping,  $\gamma$  the gyromagnetic ratio and  $M$  the saturation magnetization. Application of the Thiele ansatz, where the magnetization is assumed a rigid object, yields the thermal stochastic force  $\mathbf{F}^{\text{th}}(t)$  on a skyrmion. Its average properties follow directly from the LLG after the Thiele procedure

$$\langle \mathbf{F}_i^{\text{th}}(t) \rangle = 0, \quad \langle \mathbf{F}_i^{\text{th}}(t) \mathbf{F}_j^{\text{th}}(t') \rangle = 2\alpha \mathcal{D}_{ij} k_B T \delta(t - t'), \quad (4.7.7)$$

where  $\mathcal{D}_{ij} = sd \int \left( \frac{d\hat{\mathbf{M}}}{dr_i} \cdot \frac{d\hat{\mathbf{M}}}{dr_j} \right) dr^2$  is the corresponding entry of the dissipation matrix, including the spin density  $s$  and the thickness  $d$  of the sample.  $\hat{\mathbf{M}} = \mathbf{M}/M$  is the normalized magnetization.

Via the Thiele equation, the thermal force  $\mathbf{F}^{\text{th}}(t)$  relates directly to the velocity  $\dot{\mathbf{R}}$  of the skyrmion. The resulting mean squared displacement  $\langle \Delta \mathbf{R}^2 \rangle_t$  for the free motion in two spatial dimensions follows to vanish linear in the damping  $\alpha$ ,

$$\langle \Delta \mathbf{R}^2 \rangle_t = 2 \frac{2\alpha \mathcal{D}}{(\alpha \mathcal{D})^2 + \mathcal{G}^2} k_B T t, \quad (4.7.8)$$

which can be understood as the strong circular motion of the skyrmion due to a dominant Magnus force if the damping is low. However, the motion of a skyrmion in the helical background is effectively confined to only one dimension. In this case, a low damping results in a fast velocity since the mean squared displacement in the helical lane after a time  $t$  follows as

$$\langle \Delta x^2 \rangle_t = 2 \frac{k_B T}{\alpha \mathcal{D}_{xx}} t = 2Dt \quad (4.7.9)$$

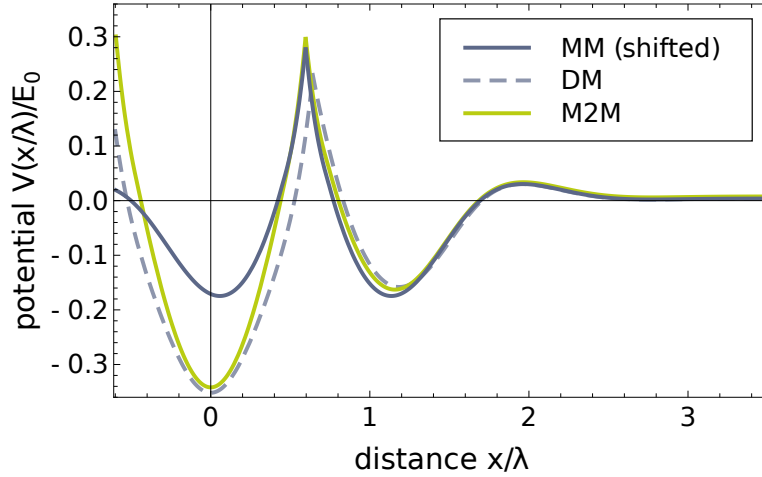


Figure 4.7.6.: Interaction potential of a dimer with a monomer (*DM*, dashed) and a monomer with a monomer (*MM*, solid blue) on the same helical lane. The *MM* potential is shifted such that the position of one monomer matches the position of one monomer of the dimer in the *DM* potential. The green curve (*M2M*) shows a simple two-particle approximation of the *DM* potential. It is a superposition of twice the *MM* potential, shifted to the positions of both the monomers in a dimer.

where we obtained the diffusion constant  $D = \frac{k_B T}{\alpha \mathcal{D}_{xx}}$ . Numerical evaluation of the dimensionless integral in the dissipation matrix coefficient yields  $\mathcal{D}_{xx} \approx 65sd$ . We used for the spin density  $s = 1\hbar/89 \text{ \AA}^3$ , the sample thickness  $d = 150\text{nm}$ , the temperature  $T = 13\text{K}$  and estimated a Gilbert damping of  $\alpha = 0.01$ . Consequently, we obtain an estimate for the diffusion constant of the order  $D = 10^{-9}\text{m}^2/\text{s}$ . Since the dissipation element  $\mathcal{D}_{xx}$  is linear in the number of skyrmions  $n$ , the diffusion constant scales as  $D \propto n^{-1}$ .

#### 4.7.2. Experimental details

A high-quality single crystal of  $\text{Cu}_2\text{OSeO}_3$  was grown by the chemical vapor transport method. The single crystal was aligned and cut into a cube so that the three main directions correspond to  $[1\bar{1}0]$ ,  $[111]$  and  $[\bar{1}\bar{1}2]$ , respectively. Then, choosing  $(1\bar{1}0)$  as the main surface, the cube was cut into slices of  $\approx 0.5 \text{ mm}$  thickness. The sample was thinned to about  $110 \text{ nm}$  by Focused Ion Beam (FIB) technique.

The magnetic structures of the sample were investigated using the FEI Titan Themis cryo-LTEM [1] after zero-field cooling. The microscope equipped with a field emission gun was operated at  $300 \text{ kV}$  in the Fresnel mode. The magnetic field was applied normal to the sample surface along the  $[1\bar{1}0]$  direction.

#### 4.7.3. Fluctuation of helical and skyrmion domains

Figure 4.7.7 presents four different frames from the movie indicating the coexistence as well as the fluctuation of helical and skyrmion domains. Magnified views of the highlighted red squares are shown in the bottom panels. For clarity, some of the helical regions are drawn in red to underline their movement as function of time.

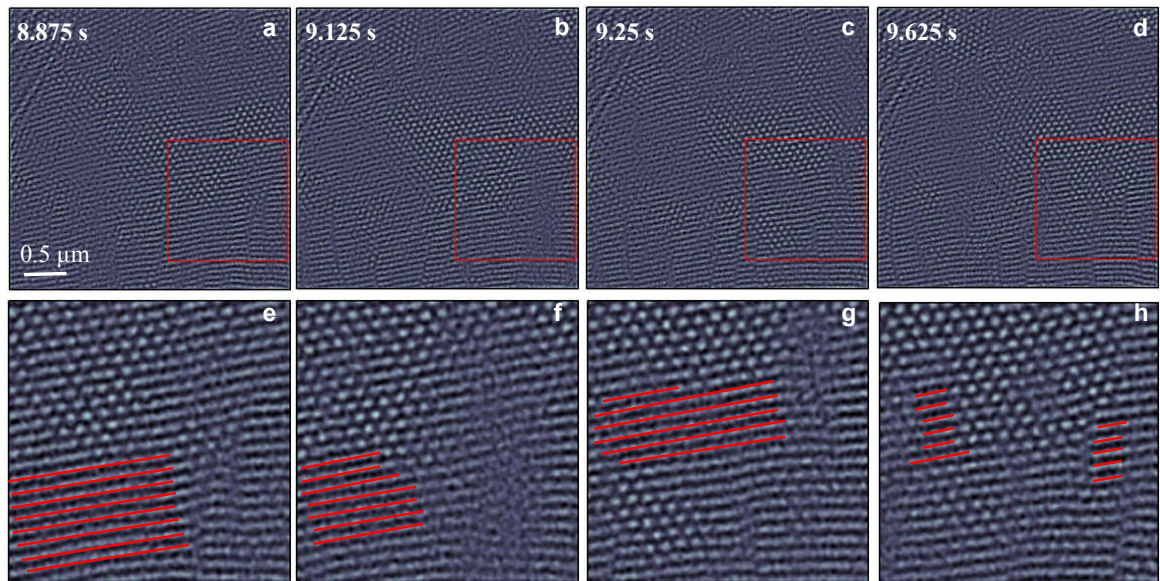


Figure 4.7.7.: Four different frames of a moving depicting the energetic fluctuations between the skyrmion and helical phases.

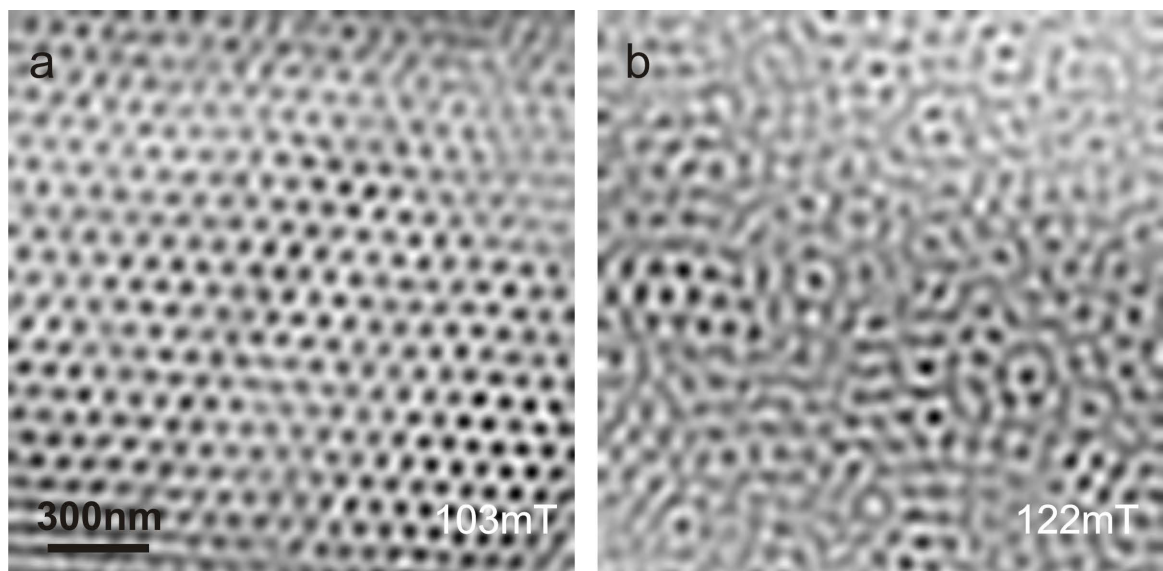


Figure 4.7.8.: Lorentz TEM images depicting the skyrmion to ferrimagnet phase transition under increasing external magnetic fields.

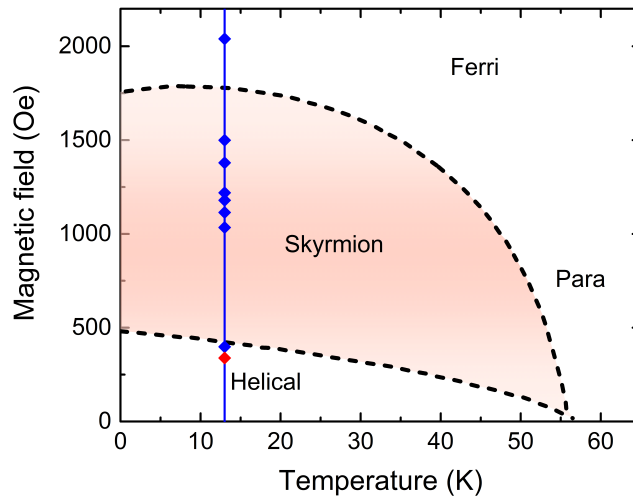


Figure 4.7.9.: Schematic phase diagram for a  $\approx 100\text{nm}$  thin film of  $\text{Cu}_2\text{OSeO}_3$ . The parameters of our measurements are marked by diamond shaped dots. The red dot indicates the frames of the main text. The schematic phase diagram is a sketch based on the data points from Ref. [2].

#### 4.7.4. Skyrmions in a ferromagnetic background

Figure 4.7.8 shows Lorentz micrographs upon increasing magnetic fields as the system passes from the skyrmion to the ferrimagnetic or conical phase. Since our method averages the signal over the sample thickness, we can not clearly distinguish between these two phases which occur at higher fields. As discussed in the main text, the interactions between skyrmions depend on the precise phase in which they are embedded. While skyrmions in the helical background form characteristic line defects, no such clusters can be found in Fig. 4.7.8b, where skyrmions are embedded in a polarized background.

#### 4.7.5. Phase diagram

Figure 4.7.9 shows a schematic phase diagram for a  $\approx 100\text{nm}$  thin film of  $\text{Cu}_2\text{OSeO}_3$ . The schematic phase diagram is a sketch based on the data points which we have taken from Ref. [2]. We have marked the positions in the phase diagram at which we record movies. The red diamond marks the point in phase space (13K, 33mT) for which the movies in the main text were recorded. The blue diamonds mark other experimental parameters for which we have performed our measurements, among which are also the frames for the decay into the polarized phase, shown in Fig. 4.7.8.

#### 4.7.6. Bibliography

- [1] CIME EPFL, <http://cime.epfl.ch/titan>.
- [2] S. Seki, X. Z. Yu, S. Ishiwata, and Y. Tokura, *Observation of skyrmions in a multiferroic material*, *Science* **336**, 198-201 (2012).



# 5. Entropy-limited topological protection of skyrmions

J. Wild<sup>1</sup>, T.N.G. Meier<sup>1</sup>, S. Pöllath<sup>1</sup>, M. Kronseder<sup>1</sup>, A. Bauer<sup>2</sup>, A. Chacon<sup>2</sup>, M. Halder<sup>2</sup>, M. Schowalter<sup>3</sup>, A. Rosenauer<sup>3</sup>, J. Zweck<sup>1</sup>, J. Müller<sup>4</sup>, A. Rosch<sup>4</sup>, C. Pfeiderer<sup>2</sup>, and C. H. Back<sup>1</sup>

*Entropy-limited topological protection of skyrmions*

Science Advances 3 (9), e1701704 (2017)

Doi: 10.1126/sciadv.1701704

Copyright: Creative Commons Attribution-NonCommercial (CC BY-NC 4.0)<sup>5</sup>

## Abstract

Magnetic skyrmions are topologically protected whirls that decay through singular magnetic configurations known as Bloch points. We have used Lorentz transmission electron microscopy to infer the energetics associated with the topological decay of magnetic skyrmions far from equilibrium in the chiral magnet  $\text{Fe}_{1-x}\text{Co}_x\text{Si}$ . We observed that the lifetime  $\tau$  of the skyrmions depends exponentially on temperature,  $\tau \sim \tau_0 e^{\Delta E/k_B T}$ . The prefactor  $\tau_0$  of this Arrhenius law changes by more than 30 orders of magnitude for small changes of magnetic field, reflecting a substantial reduction of the lifetime of skyrmions by entropic effects and, thus, an extreme case of enthalpy-entropy compensation. Such compensation effects, being well-known across many different scientific disciplines, affect topological transitions and, thus, topological protection on an unprecedented level.

## 5.1. Introduction

A question studied in many fields of the natural sciences concerns the lifetime of metastable states. Thermal activation across energy barriers governs (for example, chemical reactions) the lifetime of memory elements in computers and in hard disks and transport of ions and electrons in disordered media. Often, these processes are controlled by a characteristic energy, the activation energy. However, it has also been established that a large number of different pathways across an activation barrier leads to a large entropic correction, reducing the lifetime of metastable states and, thus, the importance of the energy barriers. This effect is known as enthalpy-entropy compensation in the context of chemistry or Meyer-Neldel rule in material sciences. Enthalpy-entropy compensation has, for example, been observed for catalytic reactions [1], transport in semiconductors [2, 3], biological processes [4], and in many other fields [5, 6].

---

<sup>1</sup>Institut für Experimentelle Physik, Universität Regensburg, D-93040 Regensburg, Germany

<sup>2</sup>Physik-Department, Technische Universität München, D-85748 Garching, Germany

<sup>3</sup>Institut für Festkörperphysik, Universität Bremen, Otto-Hahn-Allee 1, D-28359 Bremen, Germany

<sup>4</sup>Institut für Theoretische Physik, Universität zu Köln, D-50937 Köln, Germany

<sup>5</sup><https://creativecommons.org/licenses/by-nc/4.0/>

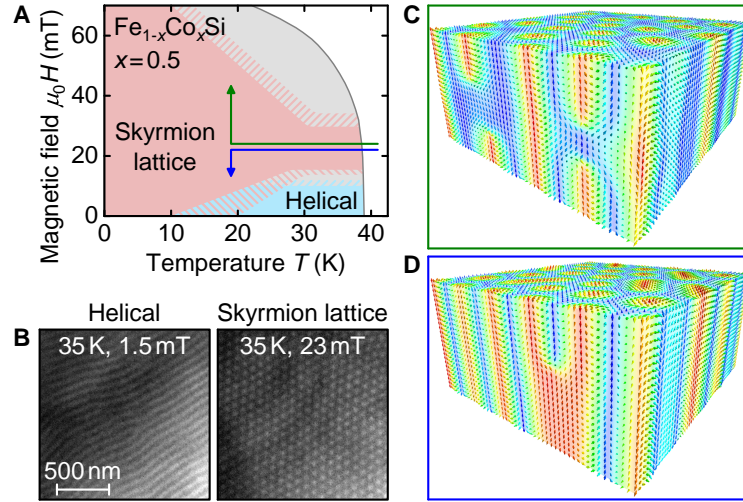


Figure 5.1.1.: Magnetic phases and skyrmion decay in  $\text{Fe}_{1-x}\text{Co}_x\text{Si}$ . (A) Magnetic phase diagram of  $\text{Fe}_{1-x}\text{Co}_x\text{Si}$  with  $x = 0.5$  obtained by first cooling the system at a fixed magnetic field,  $B \approx 23\text{mT}$ , and then raising or lowering the field at fixed temperature  $T$ . The decrease in the applied field triggers the decay into a helical configuration, whereas either a conical or ferromagnetic state is reached for an increase of the field. (B) Typical LTEM images of helical and skyrmion lattice order, respectively. (C) Schematic image of an early state of the decay of the skyrmion lattice toward a ferromagnetic state. The skyrmion splits by the formation of a pair of Bloch points located at the end of the skyrmion strings, which move toward the surface. (D) Decay of skyrmion lattice order toward the helical state. Neighboring skyrmions merge, and a Bloch point at the merging points moves toward the surface.

In recent years, differences of the topology of physical states have been widely portrayed as providing exceptionally high stability. Topology represents a branch of mathematics concerned with those properties of geometric configurations that are unaffected by smooth deformations. Famous examples for topologically nontrivial objects include superconducting vortices, certain magnetic textures, structural defects and surface states of topological materials. However, despite this abundance of topologically nontrivial configurations in nature, an unresolved key question concerns their stability when being part of an ensemble far from equilibrium.

Skyrmions in spin systems with chiral interactions are particularly suitable to clarify this issue, because a well-founded highly advanced theoretical understanding exists in excellent agreement with the experiment. Representing topologically nontrivial spin whirls, skyrmions were experimentally first identified in the B20 compounds  $\text{MnSi}$  and  $\text{Fe}_{1-x}\text{Co}_x\text{Si}$  [7, 8], followed more recently by a wide range of bulk compounds [9–11], surface- and interface-based systems [10, 12–14], as well as hetero- and nanostructures [15, 16]. With typical dimensions from a few up to several hundred nanometers, skyrmions in magnetic materials are accessible to a wide range of experimental techniques. Moreover, they are also of immediate interest for spintronics applications. At present, this concerns foremost memory elements [15, 17, 18], where lifetimes exceeding 10 years represent the technical requirement. In turn, the design of metastable states with long lifetimes is both mandatory and a major motivation for the study reported here.

## 5.2. Results

Here, we have chosen the B20 compound  $\text{Fe}_{1-x}\text{Co}_x\text{Si}$  with  $x = 0.5$ , which displays a well-understood bulk phase diagram that is generic for this class of materials [7, 8, 19, 20]. With decreasing temperature, a paramagnetic to helimagnetic transition occurs at  $T_c$ . A lattice of skyrmion lines forms in a small field and temperature window just below  $T_c$ , as first established by small-angle neutron scattering (SANS) [8]. Lorentz force transmission electron microscopy (LTEM) in  $\text{Fe}_{1-x}\text{Co}_x\text{Si}$  provided real-space images of the skyrmions [21]. Although the skyrmion phase in bulk materials is thermodynamically stable only in a small pocket of phase space, it was shown early on that the range of stability, albeit being hysteretic, increases markedly and extends down to zero temperature in ultrathin bulk samples [21–23]. A typical phase diagram obtained from our sample when cooling at a fixed magnetic field and followed by an increase or a decrease of the field at a fixed low temperature is shown in Fig. 5.1.1A. In the red shaded region, the skyrmion lattice is stable on experimentally relevant time scales but decays when the magnetic field is increased or decreased further.

Schematic depictions of typical spin configurations during the early stages of the decay into a ferromagnetic state under increasing field or into a helical state under decreasing field are shown in Fig. 5.1.1(C and D). The decay into the helical state was first addressed by means of magnetic force microscopy (MFM) of the surface of a bulk sample of  $\text{Fe}_{1-x}\text{Co}_x\text{Si}$  ( $x = 0.5$ ) [24]. Here, the decay was found to occur by a merging of skyrmions, implying the presence of a Bloch point that acts like a zipper between skyrmions, that is, a point of vanishing magnetization enabling the unwinding of the nontrivial topology (Fig. 5.1.1D). In comparison, the decay into the conical or ferromagnetic state is theoretically predicted to take place by a pinching-off through the creation of a pair of Bloch points, as shown in Fig. 5.1.1C, and the subsequent motion of the Bloch points toward the surface [23, 25].

Several studies had reported hysteretic and metastable skyrmion states. Early SANS studies on bulk samples of  $\text{Fe}_{1-x}\text{Co}_x\text{Si}$  revealed the possibility to super-cool the skyrmion lattice into a metastable state [8, 26]. Detailed magnetization and ac susceptibility measurements combined with SANS showed [27] that the super-cooled skyrmion lattice order for temperatures below  $\sim 10$  K may only be destroyed by means of an applied magnetic field exceeding the conical to ferromagnetic transition field, that is, at low temperatures, thermal activation is not sufficient to trigger a decay of the metastable skyrmion state. The observation of sizeable super-cooling effects in MnSi under pressure [28] or after violent quenches exceeding 400 K/min [29], and, in  $\text{Cu}_2\text{OSeO}_3$ , under electric field cooling [30], and the observation of slow relaxation at low temperatures in  $\text{GaV}_4\text{S}_8$  [31] underscore the generic existence of supercooling effects noticed first in  $\text{Fe}_{1-x}\text{Co}_x\text{Si}$ . Several studies also investigated skyrmion generation and destruction triggered by electric currents [16, 32, 33]. The energy barrier for skyrmion creation/annihilation in two dimensions was studied theoretically in the studies by Bessarab *et al.* and Hagemeyer *et al.* [34, 35] and was extended to three dimensions by Rybakov *et al.* and Schütte *et al.* [23, 25]. An elegant approach to explore the energetics requires time-resolved real-space imaging of large ensembles.

Here, we used time-resolved LTEM on thin bulk samples of  $\text{Fe}_{1-x}\text{Co}_x\text{Si}$ . On the one hand, this method provides the required spatial and temporal information, without driving the skyrmion decay. On the other hand, and as explained above,  $\text{Fe}_{1-x}\text{Co}_x\text{Si}$  represents an extremely well-understood and well-characterized material suitable to address these issues.

For our measurements, a sample with a thickness of  $d \approx 240$  nm was prepared using a focused

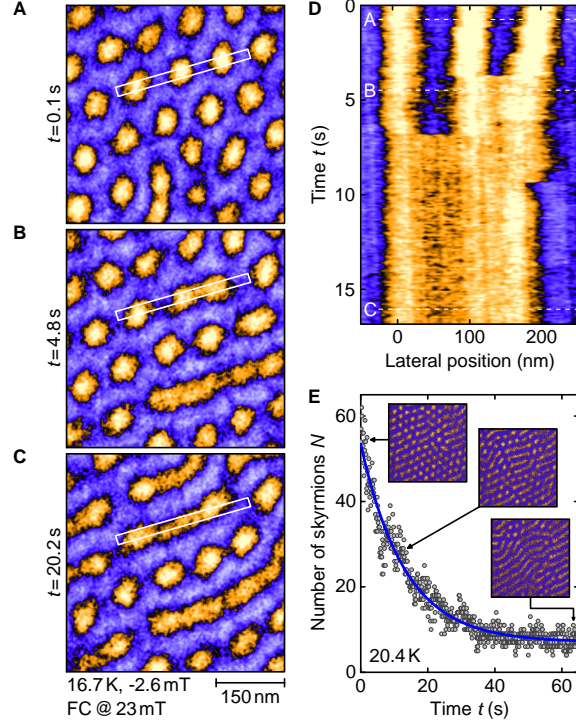


Figure 5.2.2.: Key characteristics of the decay of skyrmions into a helical order. The sample was field-cooled (FC) from above the helical transition temperature ( $T_c \approx 38\text{K}$ ) under an applied magnetic field  $B = 23\text{mT}$  down to  $T_m$ , where the field was reduced to  $B_m$  and data recorded as a function of time  $t$ . (A to C) Typical LTEM patterns at  $T_m = 16.7\text{K}$  after reaching  $B_m = -2.6\text{mT}$  for  $t = 0.1$ , 4.8, and 20.2s, respectively. (D) Evolution of the intensity across the white box marked in (A), (B), and (C) as a function of time (vertical axis). (E) Typical time dependence of the number of skyrmions  $N$  for  $T_m = 20.4\text{K}$  and  $B_m = -2.6\text{mT}$ . The blue curve represents an exponential fit.

ion beam (FIB) from the same optically float-zoned single crystal studied before [24, 26]. The single crystal was cut such that a  $\langle 100 \rangle$  axis was normal to the platelet. The magnetic field was applied along the same direction. As shown in Fig. 5.1.1B, for zero magnetic field and low temperatures, a well-defined helical order is observed with a modulation length  $\lambda \approx 90\text{nm}$ , in agreement with previous reports. Furthermore, under field cooling in an applied field of 23 mT, a well-defined hexagonal skyrmion lattice forms just below  $T_c$ . When reducing the temperature further, the same unchanged skyrmion lattice persists down to the lowest temperatures studied (12 K).

In our LTEM measurements, the evolution of the magnetic state was studied with a time resolution of  $\sim 100\text{ms}$ , where movies were recorded after field cooling and a subsequent field change. We first investigate the destruction of the skyrmion state when the magnetic field is decreased. Shown in Fig. 5.2.2 are typical data for a decay into the helical state observed after field cooling at 23 mT down to  $T_m = 16.7\text{K}$  and a reduction of the field to  $B_m = 2.6\text{mT}$ . As illustrated in Fig. 5.2.2(A to C) for patterns recorded at  $t = 0.1$ , 4.8, and 20.2 s after reaching  $B_m$ , respectively, the intensity pattern displays a merging of the skyrmions. This process corresponds accurately to the mechanism observed by means of MFM on the surface of bulk specimens cut from the same single crystal [24].

The merging of skyrmions is additionally illustrated in Fig. 5.2.2D, which displays the in-

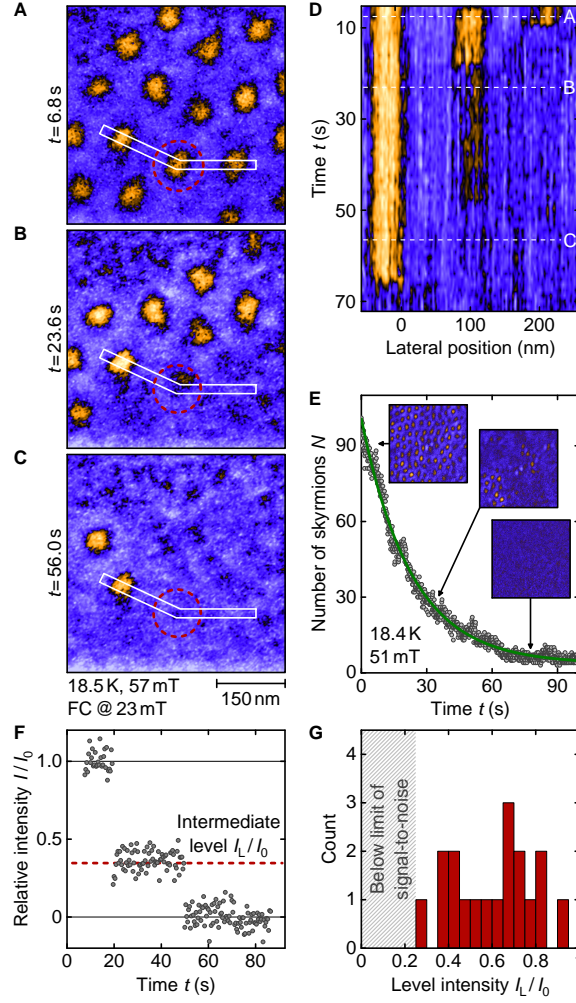


Figure 5.2.3.: Key characteristics of the decay of skyrmions for increasing magnetic fields. The sample was field-cooled (FC) from above the helical transition temperature ( $T_c \approx 38\text{K}$ ) under an applied magnetic field  $B = 23\text{mT}$  down to  $T_m$ , where the field was increased to  $B_m$  and the data were recorded as a function of time  $t$ . (A to C) Typical LTEM patterns at  $T_m = 18.5\text{K}$  after reaching  $B_m = 57\text{mT}$ , for  $t = 6.8, 23.6,$  and  $56.0$  s, respectively. (D) Evolution of the intensity across the white box marked in (A), (B), and (C) as a function time (vertical axis). (E) Typical time dependence of the number of skyrmions for  $T_m = 20.4\text{K}$  and  $B_m = 57\text{mT}$ , fitted by an exponential (green line). (F) Time dependence of the intensity within the red dashed circle in (A), (B), and (C). For a small number of skyrmions, a two-step decay via an intermediate state with lower intensity is observed. (G) Statistics of the intermediate-state intensities.

tensity across the white box in panels (A) to (C) as a function of time along the vertical axis. Details of the merging cannot be resolved for the frame rate of our experiments, that is, the motion of the monopoles across the 250-nm thickness of the sample is faster than 100 ms corresponding to a speed greater than  $2.5 \times 10^{-6}$  m/s. However, by using a bespoke algorithm, we could track the number of skyrmions  $N$  for a given area as a function of time as illustrated in Fig. 5.2.2E. As a main new result, we observe an exponential time dependence,  $N \approx N_0 \exp\left(-\frac{t}{\tau(B,T)}\right)$  (blue line), from which we extract the lifetime,  $\tau(B,T)$ , as a function

of field and temperature, analyzed further below. Note that  $N_0$  is, in general, smaller than the initial number of skyrmions, because some skyrmions have already decayed during the field sweep when only blurred images are recorded because of image drifts.

The destruction of the skyrmion state after field cooling, when an increase in magnetic field triggers a decay into a conical (or ferromagnetic) state, is summarized in Fig. 5.2.3. Data shown were recorded after field cooling at 23 mT down to  $T_m = 18.5$  K and an increase of the field to  $B_m = 57$  mT. As predicted by theory [23], the decay pattern is characterized by the disappearance of individual skyrmions, as opposed to the merging observed for a decay into the helical state. Figure 5.2.3D displays the intensity across the white box in panels (A) to (C) as a function of time along the vertical axis. Using the same algorithm to track the number of skyrmions again, an exponential time dependence is observed for the entire parameter range accessible, as shown in Fig. 5.2.3E. Both the qualitative decay mechanism and the specific time dependence analyzed below represent the main results of our study.

We note that for most of the decays, individual skyrmions vanish suddenly between two frames of our movies. However, for less than 10% of the skyrmions, the intensity does not vanish in a single step but exhibits a two-step process. An example is marked by the red dashed circle in Fig. 5.2.3 (A to C), corresponding to a diameter of  $\sim 100$  nm in Fig. 5.2.3D. The relative change of intensity in this region,  $I/I_0$ , as a function of time is shown in Fig. 5.2.3F. The observation of the intermediate level implies that part of the skyrmion survives as an intermediate, metastable skyrmion string with a length shorter than the thickness of the sample. At least one end of the skyrmion string is, therefore, inside the sample, and topology enforces the presence of a Bloch point at this location. In turn, the metastable state consists of at least one Bloch point and a skyrmion string that either connects one Bloch point (or two) to the surface or connects a pair of Bloch points which each other.

One of the most likely mechanisms causing the metastable intermediate state is trapping of the Bloch points by local defects. As an interesting alternative, the metastable state may be a so-called chiral bobber, predicted theoretically by Rybakov *et al.* [23]. The authors of this study pointed out that the surface energy of the skyrmion provides a repulsive potential for the Bloch point. Thus, a chiral bobber represents a Bloch point located immediately below the surface of the sample. To clarify the nature of the metastable states we observed, we analyzed the intensity of 18 of these inhibited decays (out of the 355 decays we investigated in detail). By plotting the number of inhibited decays as a function of relative intermediate intensity shown in Fig. 5.2.3G, we observe a very broad distribution. Taking these intensities as a measure of the length of the intermediate states, most of them are larger than expected theoretically for a single bobber located close to the surface. Hence, within our limited statistics, an interpretation in terms of Bloch points trapped by defects appears to be the most likely scenario.

### 5.3. Discussion

Taking together all of our data, the lifetime  $\tau(B, T)$  of skyrmions depends sensitively on the magnetic field and the temperature. Shown in Fig. 5.3.4A are typical decay times as a function of temperature for selected field values. The phase diagram shown in the background of that figure is identical to Fig. 5.1.1A. On a double-logarithmic scale, the decay times as a function of thermal energy display strong variations with magnetic field, where the decay into the conical and helical states is shown in Fig. 5.3.4 (B and C), respectively. As expected, the temperature dependence can be described approximately by an Arrhenius law,  $\tau(B, T) \approx \tau_0(B)e^{\Delta E(B)/k_B T}$ .

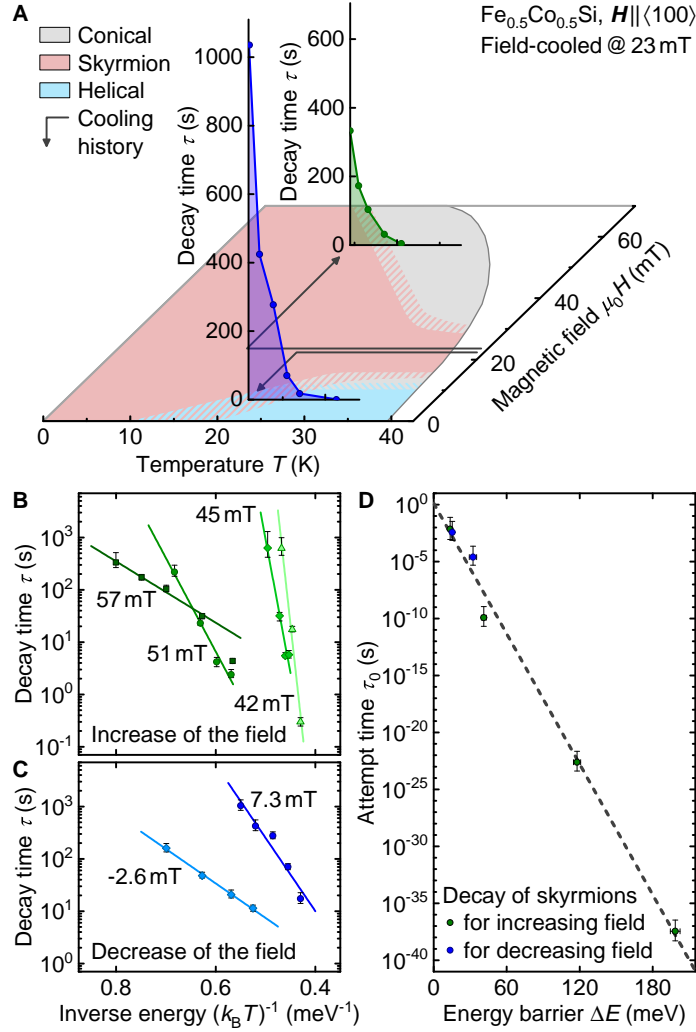


Figure 5.3.4.: Key characteristics of the decay rates of supercooled skyrmions in  $\text{Fe}_{1-x}\text{Co}_x\text{Si}$  ( $x = 0.5$ ). (A) Typical decay times  $\tau$  after field cooling at  $B = 23\text{mT}$ , followed by a decrease/increase to  $B_m$ . (B and C) Decay time  $\tau$  as a function of thermal energy for increasing and decreasing magnetic fields, respectively, and various values of  $B_m$ . (D) Attempt time  $\tau_0$  as a function of energy barrier  $\Delta E$  inferred from the exponential time dependence of the skyrmion decay. The variation of more than 30 orders of magnitude of  $\tau_0$  reflects the extreme enthalpy-entropy compensation.

However, the energy barriers vary strongly with the strength of the magnetic field, the largest being close to the stability regime of the skyrmion lattice. The energy barrier therefore drops for increasing field, for example, from  $\Delta E = (199 \pm 4)$  meV for  $B_m = 42.2$  mT down to  $\Delta E = (13 \pm 1)$  meV for  $B_m = 56.8$  mT. When the field is reduced and the skyrmions decay into the helical state, the activation energy  $\Delta E = (32 \pm 3)$  meV at  $B_m = 7.3$  mT close to the stability region is again larger than that further away, where we find  $(15 \pm 1)$  meV for  $B_m = -2.6$  mT.

This qualitative trend is consistent with existing theoretical predictions. Namely, in the study by Schütte and Rosch [25], stochastic micromagnetic simulations at finite temperatures were used to investigate the activation energy and magnetic field dependence for the decay of

a single skyrmion into the helical state. Similar to our experiments, a strong dependence on the magnetic field  $B$  was found: Notably, the decay rate increases rapidly when the field is lowered. Furthermore, Rybakov *et al.* [23] used a variational approach at  $T = 0$  to estimate activation barriers for a transition into a conical state. As in our experiments, theoretically predicted activation energies for this transition exceed those for the transition into the helical state. Using straightforward scaling arguments (see the Supplementary Materials) to extrapolate the calculated activation energies to the experimentally relevant parameter regime, we find, however, that the measured activation energies are about an order of magnitude smaller than the predicted ones. At present, we have no explanation for this substantial discrepancy; however, we speculate that it is connected with the large entropic effects discussed below, which become most pronounced for large activation barriers.

Surprisingly, measurements of the activation energies alone do not allow for the prediction of the lifetime of the metastable skyrmion state. Instead, we find that the prefactor  $\tau_0(B)$  – the so-called attempt time – of the Arrhenius dependence assumes extremely small values and shows an unusually strong sensitivity to magnetic fields. This is emphasized in Fig. 5.3.4D, which shows that  $\tau_0$ , as a function of the activation energy, changes from extremely low values, smaller than  $10^{-37}$  s, for the measurements at  $B_m = 42.2$  mT, where the largest activation energy was measured, to almost macroscopic time scales  $\sim 10^{-2}$  s at  $B_m = 57$  mT. These values should be contrasted with typical microscopic time scales  $\sim 10^{-9}$  s commonly accepted for estimates of attempt times in magnetic materials [36–38].

To account for this extreme variation, we revisit the Arrhenius law used for fitting the decay times. At finite temperature, thermodynamics and transition rates are governed by the free energy  $F(T, B) = E(T, B) - T \cdot S(T, B)$ . Thus, the Arrhenius-type decay law for a single energy barrier assumes the form  $\tau(B) = \tau_{00} \exp\left(\frac{\Delta F(T, B)}{k_B T}\right)$ , where  $\Delta F = F_b - F_0$  is the free-energy difference of the initial state,  $F_0$ , and a highly excited state,  $F_b$ , which defines the bottleneck of the skyrmion decay. Inserting the definition of the free energy one obtains

$$\tau(B) = \tau_{00} \exp\left(-\frac{\Delta S(B)}{k_B}\right) \exp\left(\frac{\Delta E(B)}{k_B T}\right). \quad (5.3.1)$$

In turn, the high-energy offset of the decay time, given by  $\tau_0 = \tau_{00} \exp\left(-\frac{\Delta S}{k_B}\right)$ , depends exponentially on the entropy difference,  $\Delta S$ , between the skyrmion state and the bottleneck state. A large positive value of  $\Delta S$  leads to an exponential reduction of  $\tau_0$  and strongly increases the transition rates. Physically, this is due to the exponentially large number  $N_p$  of microscopic pathways across the energy barrier,  $\Delta S = k_b \ln[N_p]$ , which increases the transition rate by the factor  $N_p$ . Similarly, a negative value of  $\Delta S$  takes into account a reduction of the transition rate, which arises when the number of microscopic realizations of the initial state with skyrmion is much larger than the number of states close to the bottleneck.

Similar entropic effects as discussed here occur in many different systems in biology, chemistry, and physics. Because the high-energy states typically have a larger entropy, these entropic effects tend to partially counterbalance the energetic effects. Therefore, this phenomenon is often referred to as the “compensation effect.” Phenomenologically, linear relationships of activation energy and entropy are known as the Meyer-Neldel rule in the context of solid-state physics [2, 5, 6]. In the limit where the activation energy is much larger than the typical microscopic energy scale  $E_m$ , they arise [5, 6] because the number of ways the activation barrier can be reached by microscopic processes varies exponentially in  $\frac{\Delta E}{E_m}$ ,  $N_p \sim \exp\left(\frac{\Delta E}{E_m}\right)$  and hence

$\Delta S \sim k_B \frac{\Delta E}{E_m}$ . The fit in Fig. 5.3.4D shows that  $\tau_0$  follows the Meyer-Neldel rule approximately and exhibits an exponential dependence on the activation energy  $\Delta E$ . From the fit, we obtain  $\frac{E_m}{k_B} \approx 27 \pm 3$  K, which is of the correct order of magnitude expected for our system where  $T_c \approx 38$  K. Remarkably, the approximate linear relation of  $\Delta S$  and  $\Delta E$  extends even in the regime where  $\tau_0$  is much larger than microscopic time scales, strongly suggesting a negative  $\Delta S$ .

Our study reveals unprecedentedly large compensation effects by more than 30 orders of magnitude for the decay of topologically non-trivial spin configurations, notably skyrmions, as part of an ensemble far from equilibrium. This may seem particularly relevant in view of the technological impact expected of topological protection. It concerns, for instance, specifically the long-term stability of magnetic memory devices inferred from measurements of activation energies. Whereas typical values of  $\tau_0 \sim 10^{-9}$  s are broadly accepted [36, 37], our results show that, especially for the large activation energies required for long-term stability, these estimates may overestimate the thermal stability of skyrmion-based memory devices by factors of the order of  $10^{20}$  and more. This illustrates that entropic effects will be very important for the technological exploitation of topologically nontrivial systems, such as memory technology based on skyrmions [39].

## 5.4. Materials and methods

### 5.4.1. Crystal growth and sample preparation

A large single crystal of  $\text{Fe}_{1-x}\text{Co}_x\text{Si}$  with  $x = 0.5$  was grown by means of the optical floating zone technique under ultrahigh vacuum conditions [26, 39, 40]. From the single-crystal ingot, we cut a bulk sample of  $200 \mu\text{m}$  thickness along a  $\langle 100 \rangle$  axis using x-ray Laue diffraction and a wire saw. This platelet was thinned by the FIB milling technique in plane-view configuration and subsequently polished by Ar ions at low voltages. The finished TEM lamella is shown in fig. S1A with dimensions of  $10 \times 10 \mu\text{m}$ . A TEM diffraction pattern in fig. S1B confirms the thinning of the specimen in the  $\langle 100 \rangle$  direction. The thickness of the specimen was determined by high-angle annular dark-field scanning TEM imaging. The measured signal was normalized to the incoming beam intensity extracted from a detector scan [41]. The normalized intensity was then compared with frozen phonon multislice simulations yielding the local specimen thickness. A thickness map is shown in fig. S1C. All measurements were performed in the marked area with a thickness of  $241 \pm 8$  nm.

It is interesting to note that the thickness of our sample exceeds the modulation length of the helical state by a factor of 2.7. In comparison to bulk samples cut from the same ingot, which show a helimagnetic transition temperature of  $T_c = 47$  K, the ordering temperature observed in the thin sample was  $T_c = 38$  K. This reduction corresponds very well with a similar effect observed in MnSi, which was attributed to an enhancement of fluctuations with a reduction of sample thickness. Moreover, in a study on MnSi, a skyrmion lattice was observed across the entire magnetic phase diagram [42], consistent with LTEM studies in FeGe, where an increase of the temperature and field range of the skyrmion lattice was observed with a reduction of sample thickness [21, 43].

### 5.4.2. Magnetic imaging

Magnetic images were taken with an FEI Tecnai F30 transmission electron microscope in Lorentz mode (LTEM), where the magnetic field normal to the sample surface was tuned by the objective lens current. A defocused image was projected onto a phosphorescence screen, which is filmed by a high-speed camera through a lead glass window. We cooled and controlled the temperature of the specimen with a Gatan liquid helium holder.

### Acknowledgements

We would like to thank M. Garst and T. Michely for the insightful discussions and S. Mayr for the support.

### Funding

We acknowledge financial support through DFG TRR 80 (project E1), CRC1238 (project C04), and ERC (European Research Council) AdG 291079 (TOPFIT). A.B., M.H., and A.C. acknowledge support through the TUM (Technische Universität München) graduate school, and J.M. acknowledges support by the Telekomstiftung and the Bonn-Cologne Graduate School of Physics and Astronomy.

### Author contributions

C.H.B. and C.P. initiated the study. A.B. grew the crystal. M.S. and A. Rosenauer fabricated the TEM lamella and performed the thickness calibration. J.W. and S.P. performed the TEM study under the supervision of J.Z. and C.H.B. T.N.G.M., S.P., A.B., J.M., A. Rosch, C.H.B., and C.P. analyzed the data. J.W., T.N.G.M., S.P., M.K., A.B., A.C., M.H., J.M., A. Rosch, C.P., and C.H.B. discussed the results. J.M. and A. Rosch provided the theoretical analysis. J.W., C.H.B., A. Rosch, and C.P. wrote the paper.

### Competing interests

The authors declare that they have no competing interests.

### Data and materials availability

All data needed to evaluate the conclusions in the paper are present in the paper and/or the Supplementary Materials. Additional data related to this paper may be requested from the authors.

## 5.5. Bibliography

- [1] F. H. Constable, *The mechanism of catalytic decomposition*, Proc. R. Soc. Lond., Ser. A **108**, 355-378 (1925).
- [2] W. Meyer and H. Neldel, *Concerning the relationship between the energy constant epsilon and the quantum constant alpha in the conduction-temperature formula in oxidising semi-conductors*, Phys. Z. **38**, 1014-1019 (1937)
- [3] T. Kamiya, K. Nomura, and H. Hosono, *Present status of amorphous In-Ga-Zn-O thin-film transistors*, Sci. Technol. Adv. Mater. **11**, 044305 (2010).

- 
- [4] A. Cooper, C. Johnson, J. Lakey, M. Nollmann, *Heat does not come in different colours: Entropy-enthalpy compensation, free energy windows, quantum confinement, pressure perturbation calorimetry, solvation and the multiple causes of heat capacity effects in biomolecular interactions*, Biophys. Chem. **93**, 215-230 (2001).
- [5] E. Peacock-López and H. Suhl, *Compensation effect in thermally activated processes*, Phys. Rev. B **26**, 3774-3782 (1982).
- [6] A. Yelon, B. Movaghar, and H. M. Branz, *Origin and consequences of the compensation (Meyer-Neldel) law*, Phys. Rev. B **46**, 12244-12250 (1992).
- [7] S. Mühlbauer, B. Binz, F. Jonietz, C. Pfleiderer, A. Rosch, A. Neubauer, R. Georgii, and P. Böni, *Skyrmion lattice in a chiral magnet*, Science **323**, 915-919 (2009).
- [8] W. Münzer, A. Neubauer, T. Adams, S. Mühlbauer, C. Franz, F. Jonietz, R. Georgii, P. Böni, B. Pedersen, M. Schmidt, A. Rosch, and C. Pfleiderer, *Skyrmion lattice in the doped semiconductor  $Fe_{1-x}Co_xSi$* , Phys. Rev. B **81**, 041203 (2010).
- [9] S. Seki, X. Z. Yu, S. Ishiwata, and Y. Tokura, *Observation of skyrmions in a multiferroic material*, Science **336**, 198-201 (2012).
- [10] N. Nagaosa and Y. Tokura, *Topological properties and dynamics of magnetic skyrmions*, Nat. Nano. **8**, 899-911 (2013).
- [11] Y. Tokunaga, X. Z. Yu, J. S. White, H. M. Rønnow, D. Morikawa, Y. Taguchi, and Y. Tokura, *A new class of chiral materials hosting magnetic skyrmions beyond room temperature*, Nat. Commun. **6**, 7638 (2015).
- [12] S. Heinze, K. von Bergmann, M. Menzel, J. Brede, A. Kubetzka, R. Wiesendanger, G. Bihlmayer, and S. Blügel, *Spontaneous atomic-scale magnetic skyrmion lattice in two dimensions*, Nat. Phys. **7**, 713-718 (2011).
- [13] O. Boulle, J. Vogel, H. Yang, S. Pizzini, D. de Souza Chaves, A. Locatelli, T. O. Mendes, A. Sala, L. D. Buda-Prejbeanu, O. Klein, M. Belmeguenai, Y. Roussigné, A. Stashkevich, S. M. Chérif, L. Aballe, M. Foerster, M. Chshiev, S. Auffret, I. M. Miron, and G. Gaudin, *Room-temperature chiral magnetic skyrmions in ultrathin magnetic nanostructures*, Nat. Nano. **11**, 449-454 (2016).
- [14] C. Moreau-Luchaire, C. Moutafis, N. Reyren, J. Sampaio, C. A. F. Vaz, N. Van Horne, K. Bouzehouane, K. Garcia, C. Deranlot, P. Warnicke, P. Wohlhüter, J.-M. George, M. Weigand, J. Raabe, V. Cros, and A. Fert, *Additive interfacial chiral interaction in multilayers for stabilization of small individual skyrmions at room temperature*, Nat. Nano. **11**, 444-448 (2016).
- [15] A. Fert, V. Cros, and J. Sampaio, *Skyrmions on the track*, Nat. Nanol. **8**, 152-156 (2013).
- [16] W. Jiang, P. Upadhyaya, W. Zhang, G. Yu, M. B. Jungfleisch, F. Y. Fradin, J. E. Pearson, Y. Tserkovnyak, K. L. Wang, O. Heinonen, S. G. E. te Velthuis, and A. Hoffmann, *Blowing magnetic skyrmion bubbles*, Science **349**, 283-286 (2015).
- [17] J. Müller, *Magnetic skyrmions on a two-lane racetrack*, New J. Phys. **19**, 025002 (2017).
- [18] P.-J. Hsu, A. Kubetzka, A. Finco, N. Romming, K. von Bergmann, R. Wiesendanger, *Electric-field-driven switching of individual magnetic skyrmions*, Nat. Nano. **12**, 123-126 (2017).
- [19] S. Buhrandt and L. Fritz, *Skyrmion lattice phase in three-dimensional chiral magnets from Monte Carlo simulations*, Phys. Rev. B **88**, 195137 (2013).
- [20] A. Bauer and C. Pfleiderer, *Generic aspects of skyrmion lattices in chiral magnets*, In: Seidel J. (eds) Topological Structures in Ferroic Materials. Springer Series in Materials Science , vol. 228 Springer, Cham (2016).
- [21] X. Z. Yu, Y. Onose, N. Kanazawa, J. H. Park, J. H. Han, Y. Matsui, N. Nagaosa, and Y. Tokura, *Real-space observation of a two-dimensional skyrmion crystal*, Nature **465**, 901-904 (2010).
- [22] F. N. Rybakov, A. B. Borisov, and A. N. Bogdanov, *Three-dimensional skyrmion states in thin films of cubic helimagnets*, Phys. Rev. B **87**, 094424 (2013).
- [23] F. N. Rybakov, A. B. Borisov, S. Blügel, and N. S. Kiselev, *New type of stable particlelike states in chiral magnets*, Phys. Rev. Lett. **115**, 117201 (2015).
-

- [24] P. Milde, D. Köhler, J. Seidel, L. M. Eng, A. Bauer, A. Chacon, J. Kindervater, S. Mühlbauer, C. Pfeiderer, S. Buhrandt, C. Schütte, and A. Rosch, *Unwinding of a skyrmion lattice by magnetic monopoles*, Science **340**, 1076-1080 (2013).
- [25] C. Schütte and A. Rosch, *Dynamics and energetics of emergent magnetic monopoles in chiral magnets*, Phys. Rev. B **90**, 174432 (2014).
- [26] A. Bauer, M. Garst, and C. Pfeiderer, *History dependence of the magnetic properties of single-crystal  $Fe_{1-x}Co_xSi$* , Phys. Rev. B **93**, 235144 (2016).
- [27] A. Bauer, *Investigation of Itinerant Antiferromagnets and Cubic Chiral Helimagnets*, Thesis, Technische Universität München (2014).
- [28] R. Ritz, M. Halder, C. Franz, A. Bauer, M. Wagner, R. Bamler, A. Rosch, and C. Pfeiderer, *Giant generic topological Hall resistivity of  $MnSi$  under pressure*, Phys. Rev. B **87**, 134424 (2013).
- [29] H. Oike, A. Kikkawa, N. Kanazawa, Y. Taguchi, M. Kawasaki, Y. Tokura, and F. Kagawa, *Interplay between topological and thermodynamic stability in a metastable magnetic skyrmion lattice*, Nat. Phys. **12**, 62-66 (2016).
- [30] Y. Okamura, F. Kagawa, S. Seki, and Y. Tokura, *Transition to and from the skyrmion lattice phase by electric fields in a magnetoelectric compound*, Nat. Commun. **7**, 12669 (2016).
- [31] Á. Butykai, S. Bordács, L. F. Kiss, B. G. Szigeti, V. Tsurkan, A. Loidl, and I. Kézsmárki, *Relaxation dynamics of modulated magnetic phases in skyrmion host  $GaV_4S_8$ : An ac magnetic susceptibility study*, Arxiv e-print (2017), arXiv:1703.10928.
- [32] N. Romming, C. Hanneken, M. Menzel, J. E. Bickel, B. Wolter, K. von Bergmann, A. Kubetzka, and R. Wiesendanger, *Writing and deleting single magnetic skyrmions*, Science **341**, 636-639 (2013).
- [33] S. Woo, K. Litzius, B. Krüger, M.-Y. Im, L. Caretta, K. Richter, M. Mann, A. Krone, R. M. Reeve, M. Weigand, P. Agrawal, I. Lemesh, M.-A. Mawass, P. Fischer, M. Kläui, and G. S. D. Beach, *Observation of room-temperature magnetic skyrmions and their current-driven dynamics in ultrathin metallic ferromagnets*, Nat. Mater. **15**, 501-506 (2016).
- [34] P. F. Bessarab, V. M. Uzdin, and H. JÅnsson, *Method for finding mechanism and activation energy of magnetic transitions, applied to skyrmion and antivortex annihilation*, Comput. Phys. Commun. **196**, 335-347 (2015).
- [35] J. Hagemester, N. Romming, K. von Bergmann, E. Y. Vedmedenko, and R. Wiesendanger, *Stability of single skyrmionic bits*, Nat. Commun. **6**, 8455 (2015).
- [36] D. Weller and A. Moser, *Thermal effect limits in ultrahigh-density magnetic recording*, IEEE Trans. Magn. **35**, 4423-4439 (1999).
- [37] E. Chen, D. Apalkov, Z. Diao, A. Driskill-Smith, D. Druist, D. Lottis, V. Nikitin, X. Tang, S. Watts, S. Wang, S. A. Wolf, A. W. Ghosh, J. W. Lu, S. J. Poon, M. Stan, W. H. Butler, S. Gupta, C. K. A. Mewes, T. Mewes, and P. B. Visscher, *Advances and future prospects of spin-transfer torque random access memory*, IEEE Trans. Magn. **46**, 1873-1878 (2010).
- [38] M. Lederman, S. Schultz, and M. Ozaki, *Measurement of the dynamics of the magnetization reversal in individual single domain ferromagnetic particles*, Phys. Rev. Lett. **73**, 1986-1989 (1994).
- [39] A. Neubauer, J. Bœuf, A. Bauer, B. Russ, H. v. Löhneysen, and C. Pfeiderer, *Ultra-high vacuum compatible image furnace*, Rev. Sci. Instrum. **82**, 013902 (2011).
- [40] A. Bauer, G. Benka, A. Regnat, C. Franz, and C. Pfeiderer, *Ultra-high vacuum compatible preparation chain for intermetallic compounds*, Rev. Sci. Instrum. **87**, 113902 (2016).
- [41] A. Rosenauer, K. Gries, K. Müller, A. Pretorius, M. Schowalter, A. Avramescu, K. Engl, and S. Lutgen, *Measurement of specimen thickness and composition in  $Al_xGa_{1-x}N/GaN$  using high-angle annular dark field images*, Ultramicroscopy **109**, 1171-1182 (2009).
- [42] A. Tonomura, X. Yu, K. Yanagisawa, T. Matsuda, Y. Onose, N. Kanazawa, H. S. Park, and Y. Tokura, *Real-space observation of skyrmion lattice in helimagnet  $MnSi$  thin samples*, Nano Lett. **12**, 1673-1677 (2012).

- 
- [43] X. Z. Yu, N. Kanazawa, Y. Onose, K. Kimoto, W. Z. Zhang, S. Ishiwata, Y. Matsui, and Y. Tokura, *Near room-temperature formation of a skyrmion crystal in thin-films of the helimagnet FeGe*, Nat. Mater. **10**, 106-109 (2011).
- [44] T. Schwarze, J. Waizner, M. Garst, A. Bauer, I. Stasinopoulos, H. Berger, C. Pfleiderer, and D. Grundler, *Universal helimagnon and skyrmion excitations in metallic, semiconducting and insulating chiral magnets*, Nat. Mater. **14**, 478-483 (2015).

## 5.6. Supplementary Materials

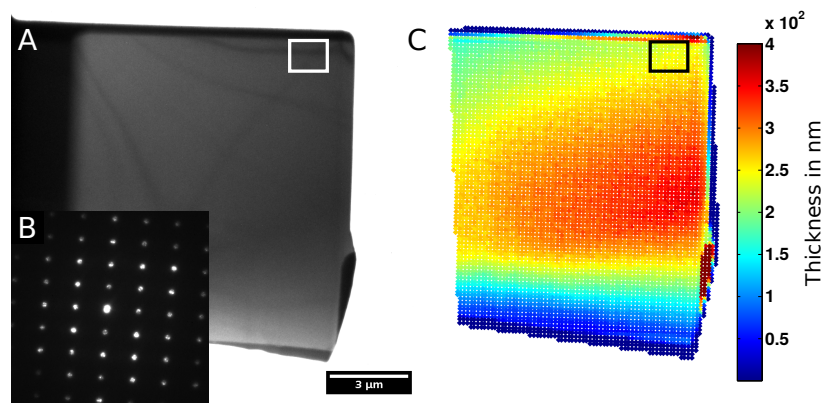


Figure 5.6.5.: Thickness determination of the FIB lamella. (A) shows the FIB prepared sample with a dimension  $10 \times 10 \mu\text{m}$  of A diffraction pattern in (B) confirms the thinning of the specimen in [100] direction. The thickness extracted from HAADF-STEM in (C) gives a thickness of  $241 \pm 8\text{nm}$  for the measurement position.

### 5.6.1. Image processing for the skyrmion decay measurements

Within this section the analysis of the LTEM-images for the skyrmion decay measurements is described. The image processing approach can be divided into the preprocessing and the extraction of physical quantities from the preprocessed images. For the two cases of the skyrmion decay to the helical phase and the decay to the conical phase two completely different image processing approaches were developed. Before describing these methods in detail first the preprocessing steps, which both methods have in common are explained.

#### Preprocessing

The raw LTEM-images not only contain information about the magnetic texture of the sample, but also nonmagnetic information for example due to crystal contrasts. The first step is hence to subtract the nonmagnetic background from the images. Since the nonmagnetic contrast is mostly present on much larger length scales than the helix pitch length or the size of a skyrmion, it can be removed from the images by subtracting a Gaussian filtered version of the image, where the sigma of the Gaussian kernel has to be chosen much larger than the skyrmion size. The signal-to-noise ratio of these images can be further enhanced by applying a Fourier-filter using a suitable bandpass-like filter mask to keep only objects with the lateral dimensions of a skyrmion.

#### Analysis of the skyrmion decay to the conical phase

In the case of the decay to the conical phase the skyrmions are counted in each frame of the video by an automated detection approach, which is illustrated in Fig. 5.6.6. The algorithm searches for local maxima of the intensity in each of the images. Each local maximum is considered as a candidate for a skyrmion and is further tested by computing a “local threshold” by comparing the image intensity at the possible skyrmion position with the intensity in a larger area around

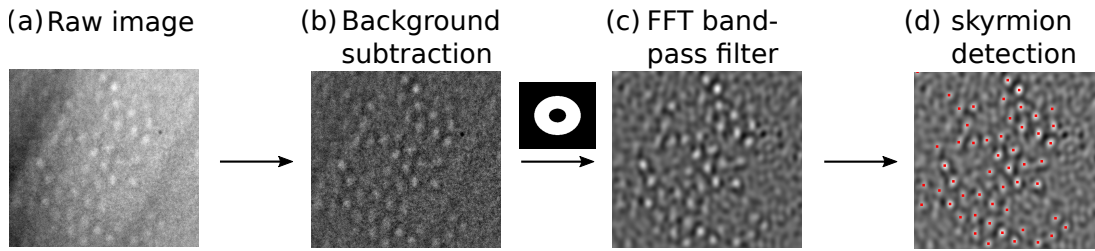


Figure 5.6.6.: Illustration of the evaluation of the skyrmion decay to the concical phase. (a) shows raw data, (b) the image after background subtraction and (c) a bandpass Fourier-filtered version, which is used for the local maximum detection in step (d) resulting in the skyrmion positions.

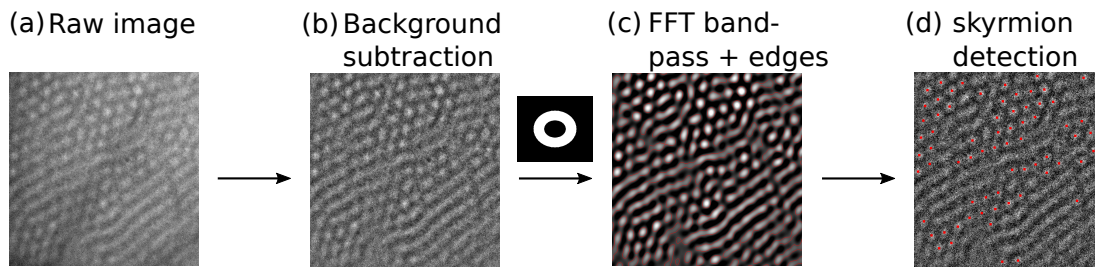


Figure 5.6.7.: Illustration of the evaluation of the skyrmion decay to the helical phase. (a) shows raw data, (b) the image after background subtraction, (c) a bandpass Fourier-filtered version with contours obtained by the LoG-edge detection algorithm. In (d) the skyrmion positions obtained from the contour image are visualized by red squares.

this position. If the skyrmion candidate exceeds a certain threshold value it will be counted as a skyrmion.

### Analysis of the decay to the helical phase - skyrmion number method

The decay of the skyrmions to the helical phase is investigated by two different methods. One of them relies on counting the skyrmion number versus time as the skyrmions merge into the stripes of the helical phase. The other approach is based on tracing the intensity of the two peaks of the helical phase in reciprocal space versus time and is described within the next subsection.

In contrast to the previous subsection the skyrmion counting approach cannot be based on finding local maxima of the intensity, since not only the skyrmions but also the stripes of the helical phase would contribute local maxima. Hence a different skyrmion detection approach was developed and is illustrated in Fig. 5.6.7. It relies on finding lines of equal intensity within the video frames by an edge detection algorithm using the Laplacian-of-Gaussian (LoG)-method. After processing with the edge detection skyrmions can be identified as circular contours with a certain enclosed area. The skyrmions are detected by identifying the connected components in the inverted contour image and subjecting each connected component to certain test criteria. The first criterium is that the area enclosed within the contour lies in a certain range, the second criterium is that the eccentricity of the contour has to be low enough (skyrmions are circular) and the final criterium is that the local threshold of the skyrmion compared to its environment is large enough.

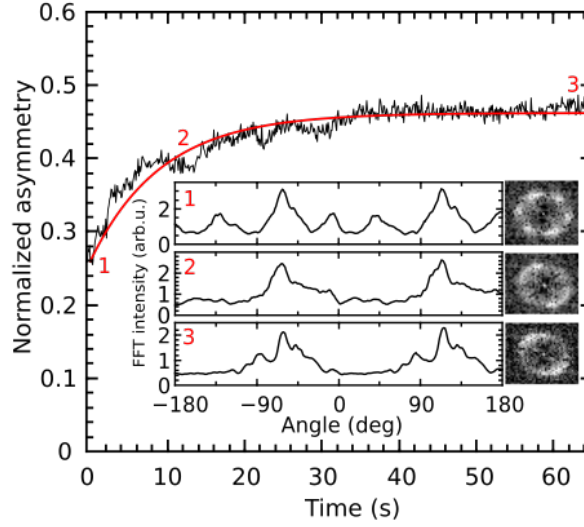


Figure 5.6.8.: Reduction of the skyrmion order deduced from the Fourier transform of the real-space data. Reduction of skyrmion order deduced from the Fourier transform of the real space data after the magnetic field has been reduced to  $B_{\text{ext}} = -2.6$  mT from an initial field value of  $B_{\text{ext}} = 23$  mT. The insets show radial averages at distinct times over the FT data shown at the right. The measurement temperature is  $T_m = 20.4$  K.

### Analysis of the decay to the helical phase - order method

The second method for the evaluation of the transition to the helical phase relies on an analysis of the video frames in reciprocal space. In the skyrmion phase the Fourier-transformed image shows six spots. During the transition intensity is transferred from the six spots into the two spots of the helical phase. By defining a ring-shaped mask and comparing the intensity (averaged absolute value of the FFT) of the helical spots with the intensity of the complement of these spots with respect to the ring-shaped mask, while normalizing to the overall intensity, an order parameter can be defined as follows

$$A_{\text{FFT}} = \frac{I_{\text{angle}} - I_{\text{compl}}}{I_{\text{angle}} + I_{\text{compl}}} . \quad (5.6.2)$$

This order parameter can be evaluated for each frame in the movies. Since during the transition to the helical phase intensity from the six spots of the skyrmion lattice is transferred into the two spots of the helical phase, the order parameter  $A_{\text{FFT}}$  will increase with time as shown in Fig. 5.6.8. Note that the decay time for skyrmion order is shorter than the decay time for the reduction of the number of skyrmions.

### 5.6.2. Evaluation of intermediate states

The evaluation of the intermediate state intensity levels which were observed during the skyrmion decay into the conical phase was done as follows. First, the temporal average intensity of the spatially static skyrmion, intermediate state and conical phase is calculated. Second, a linescan through the maximum intensity of the respective spin object is taken and fitted by a Gaussian function, which gives the skyrmion and intermediate state intensity  $I_{\text{Sk}}$  and  $I_i$ . The intensity

level of the conical background  $I_{\text{con}}$  is calculated by averaging within an area of the former skyrmion size. The levels shown in Fig. 5.2.3(F) of the main text are then calculated by  $\frac{I_L}{I_0} = \frac{I_i - I_{\text{con}}}{I_{\text{sk}} - I_{\text{con}}}$ . The temporal linescan in Fig. 5.2.3(G) of the main text is obtained by averaging the intensity in a small circular area of approximately half the skyrmion diameter around the skyrmion core position that is tracked in time.

### 5.6.3. Scaling analysis of activation energies

As the size of skyrmions is much larger than lattice constants, one can efficiently describe their properties in the continuum limit by a field theory. Such a description will, however, break down in the center of a Bloch point where the spin configuration is singular. Within a non-linear sigma model the energy of magnetic textures is computed from

$$E = \int d^3r A(\nabla\hat{n})^2 + D\hat{n} \cdot \nabla \times \hat{n} - \mu_0 H M \hat{n}_3 - \frac{\mu_0 M}{2} \mathbf{H}_D \hat{n} \quad (5.6.3)$$

where  $\mathbf{H}_D(r) = -\frac{M}{4\pi} \nabla \int d^3r' \frac{r-r'}{|r-r'|^3} \hat{n}(r')$  is the demagnetization field from dipole-dipole interactions. Skyrmion formation is governed by the length scale  $2\frac{A}{D}$ . Therefore, we rewrite the energy by expressing all distances in this lengthscale. In the resulting dimensionless units, we label coordinates by  $\mathbf{x}$  with  $\mathbf{r} = \frac{2A}{D}\mathbf{x}$  and the wavelength of the helical state is  $2\pi$ . The thickness  $d_s$  of the sample can be expressed by the dimensionless  $d = \frac{d_s D}{2A}$ . The energy functional then takes the form

$$E = \frac{4A^2}{D} \int d^3x \frac{1}{2} (\nabla\hat{n})^2 + \hat{n} \cdot \nabla \times \hat{n} - h\hat{n}_3 - \frac{\tau_D}{2} \hat{n} \cdot \mathbf{h}_D \quad (5.6.4)$$

with the dimensionless demagnetization field  $\mathbf{h}_D(x) = -\frac{1}{4\pi} \nabla \int d^3x' \frac{x-x'}{|x-x'|^3} \hat{n}(x')$ , controlled by two dimensionless parameters  $h$  and  $\tau_D$ , where  $h = \frac{2A\mu_0 M}{D^2} H$  is the dimensionless magnetic field measured in units such that the transition from the conical to ferromagnetic state takes place at  $h = 1$  and  $\tau_D = \frac{2A\mu_0 M^2}{D^2}$  is a dimensionless measure for the strength of the dipole-dipole interaction which typically takes values of order one [with, e.g.,  $\tau_D = 0.65$  for  $\text{Fe}_{0.8}\text{Co}_{0.2}\text{Si}$  [1]].

The activation energy  $\Delta E$  for the decay of the skyrmion is determined by a high-energy state containing a pair of Bloch points [2, 3]. The continuum description breaks down at the core of these singular spin configurations. This regime contributes the core energy  $E_c$  which depends on microscopic details. In a metal, for example, the details of the electronic band-structure will enter. Nevertheless, one can estimate that this energy is of the order of the exchange coupling  $J$ , which can be estimated from the spin-stiffness  $A$  using  $E_c \sim J \sim Aa$ , where  $a$  is the relevant microscopic length scale (e.g. distance of magnetic ions).

These arguments show that the activation energy can be written in the form

$$\Delta E = \frac{4A^2}{D} f(h, \tau_D, d) + O(Aa) = \frac{JN_s}{2\pi} f(h, \tau_D, d) + O(J) \quad (5.6.5)$$

where  $f$  is a dimensionless scaling function which depends on the dimensionless parameters  $h$ ,  $\tau_d$  and  $d$  and is independent of the cutoff parameter  $a$  in  $d = 3$ . For the second equality, we identified  $A = \frac{J}{2a}$  with the exchange coupling  $J$  of a classical Heisenberg model on a cubic lattice with lattice constant  $a$  and introduced  $N_s = \frac{4\pi A}{Da}$ , the number of spins per pitch of the helix. Importantly, for  $\text{Fe}_{0.5}\text{Co}_{0.5}\text{Si}$ , where the pitch of the helix is  $\lambda \sim 90$  nm, the universal

first term arising from the continuum model, is expected to exceed the non-universal second term by a large factor of order  $10^2$  for temperatures  $T \ll T_c$  where the above analysis applies.

Previous theoretical results computed  $\Delta E$  for  $N_s \sim 10$  and  $\tau_D = 0$  [2,3]. Assuming that the numerical results were dominated by the universal contribution, we can estimate  $f(0, 0, 31) \approx 3.6$  [2] and  $f(0.8, 0, 12) \approx f(0.8, 0, 18) \approx 13$  [3] for the decay into the helical and conical state, respectively. Using  $J \sim k_B T_c$  and  $N_s \approx 300$  for an order-of-magnitude estimate, we obtain  $\frac{4A^2}{D} \sim \frac{JN_s}{2\pi} \sim 150$  meV. Using this value, we conclude that the predicted activation energies are about an order of magnitude larger than the measured ones.

#### 5.6.4. Bibliography

- [1] T. Schwarze, J. Waizner, M. Garst, A. Bauer, I. Stasinopoulos, H. Berger, C. Pfleiderer, and D. Grundler, *Universal helimagnon and skyrmion excitations in metallic, semiconducting and insulating chiral magnets*, Nat. Mater. **14**, 478-483 (2015).
- [2] C. Schütte and A. Rosch, *Dynamics and energetics of emergent magnetic monopoles in chiral magnets*, Phys. Rev. B **90**, 174432 (2014).
- [3] F. N. Rybakov, A. B. Borisov, S. Blügel, and N. S. Kiselev, *New type of stable particlelike states in chiral magnets*, Phys. Rev. Lett. **115**, 117201 (2015).

## 6. Edge instabilities and skyrmion creation in magnetic layers

Jan Müller<sup>1</sup>, Achim Rosch<sup>1</sup>, and Markus Garst<sup>1</sup>

*Edge instabilities and skyrmion creation in magnetic layers*

New Journal of Physics 18, 065006 (2016)

Doi: 10.1088/1367-2630/18/6/065006

Copyright: Creative Commons Attribution 3.0 Unported (CC-BY)<sup>2</sup>

### Abstract

We study both analytically and numerically the edge of two-dimensional ferromagnets with Dzyaloshinskii-Moriya (DM) interactions, considering both chiral magnets and magnets with interface-induced DM interactions. We show that in the field-polarized (FP) ferromagnetic phase magnon states exist which are bound to the edge, and we calculate their spectra within a continuum field theory. Upon lowering an external magnetic field, these bound magnons condense at a finite momentum and the edge becomes locally unstable. Micromagnetic simulations demonstrate that this edge instability triggers the creation of a helical phase which penetrates the FP state within the bulk. A subsequent increase of the magnetic field allows to create skyrmions close to the edge in a controlled manner.

### 6.1. Introduction

The presence of the Dzyaloshinskii-Moriya (DM) interaction in ferromagnets favors a spatial twist of the magnetization leading to modulated magnetic textures like helices and skyrmion lattices, i.e., closely packed arrangements of single skyrmions. Skyrmions are spatial configurations of the magnetization with a finite topological winding number. They are not only found in the thermodynamic ground state but single skyrmions also arise as topologically protected excitations of the field-polarized (FP) state. Skyrmions couple very efficiently to spin currents so that ultralow current densities are already sufficient to drive skyrmion configurations [1, 2]. Both properties, their topological protection as well as their mobility, identify skyrmions as promising candidates for elementary units of future spintronic devices, see the reviews of [3–5].

A prerequisite for a skyrmion technology [6] is, however, the stabilization of magnetic skyrmion configurations at ambient conditions as well as their controlled writing and deleting. The existence of skyrmions far below room temperature has been experimentally demonstrated some years ago in the chiral magnets with space group  $P2_13$  like MnSi [7, 8], FeGe [9] or Cu<sub>2</sub>OSeO<sub>3</sub> [10, 11] as well as in magnetic mono- and bilayers [12, 13]. Recently, various groups have reported the observation of skyrmion configurations at ambient temperatures. Co-Zn-Mn

---

<sup>1</sup>Institut für Theoretische Physik, Universität zu Köln, D-50937 Cologne, Germany

<sup>2</sup><https://creativecommons.org/licenses/by/3.0/>

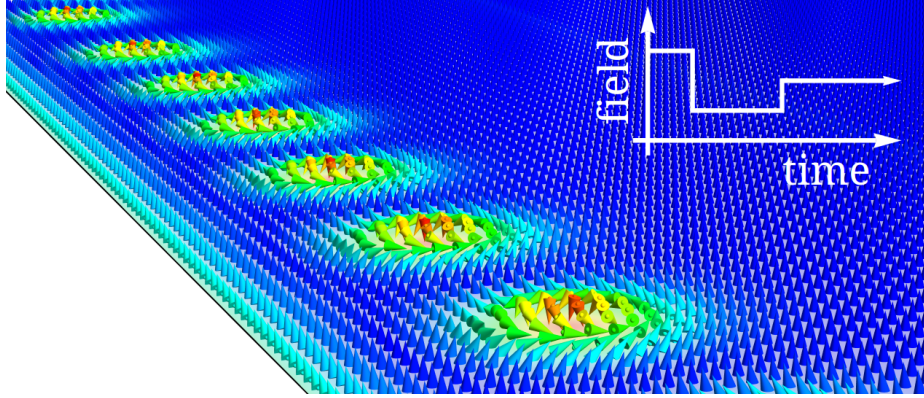


Figure 6.1.1.: Chain of skyrmions at the edge of a two-dimensional chiral magnet that were created with the help of the magnetic field protocol shown in the inset exploiting the local edge instability of the field-polarized state. These results were obtained with micromagnetic simulations of the Landau-Lifshitz-Gilbert equation. The color code reflects the  $z$ -component of the magnetization.

alloys with the chiral space group  $P4_132$  were shown to possess the typical phase diagram of other chiral magnets but with a skyrmion lattice phase stabilized at room temperature [14]. In addition, certain magnetic multilayers comprising magnetic Co and Fe atoms also show stable skyrmion configurations at room temperatures [15–17]. In all these systems, the DM interaction arises due to a lack of inversion symmetry. The atomic crystal of chiral magnets explicitly breaks inversion symmetry so that the DM interaction is even present in bulk samples. In magnetic multilayers, on the other hand, the DM interaction is induced by the interface between a magnetic layer and a substrate containing heavy elements.

As skyrmion configurations are topologically protected, their creation or annihilation usually requires the climb of a topological energy barrier in some way or another. It has been theoretically discussed that magnetic skyrmions can be nucleated by the local injection of a spin-polarized current [18], local heating [19,20], local application of a magnetic [20] or electric field [21], and by thermal fluctuations [22]. Experimentally, it has been already demonstrated that skyrmions can be created in magnetic multilayers with the help of local currents from an STM tip [23]. Magnetic skyrmions also materialize when driving stripe domains through a geometric constriction with the help of a spin-current [16,24]. It was also shown that skyrmion crystals (SkXs) can be unwound with the help of Bloch points [25]. Such Bloch points correspond to magnetic monopoles in the emergent electrodynamics [2,26] that arises when itinerant electrons locally adapt their magnetic moment to the skyrmion configurations [3,5]. Climbing the topological energy barrier and the concomitant singular Bloch point configuration of the magnetization can be avoided however by feeding in skyrmions from the edge of the sample. In fact, recent experiments on FeGe nanostripes have beautifully demonstrated already the edge-mediated nucleation of skyrmions [27]. In the present work we provide a theoretical explanation of this phenomenon. In addition, we demonstrate that with the help of a certain magnetic field protocol skyrmions can be created in a controlled manner at the edge of a magnetic monolayer by exploiting a local edge instability of the FP state, see Fig. 6.1.1.

For this purpose, we investigate the edge of a single magnetic layer with DM interaction that is polarized by a perpendicular magnetic field. The boundary conditions arising from the DM interaction result in a twist of the magnetization close to the edge which was discussed independently by Wilson *et al.* [28] and Rohart and Thiaville *et al.* [29]. This surface twist

was experimentally investigated in Refs. [27, 30], and it also plays an important role in the stabilization of skyrmion configurations in thin films of finite thickness [31–33]. Here, we focus on the magnon excitations of the FP layer, and we demonstrate that the surface twist result in spin-wave excitations that are bound to the edge of the magnetic layer. Within a continuum field theory, we determine analytically the effective Hamiltonian of these bound magnon modes and evaluate their spectrum for various values of the effective magnetic field and the magnetic anisotropy. For vanishing  $\vec{H} = 0$ , we reproduce the results of a recent numerical study of these edge excitations [34]. Moreover, for finite  $\vec{H}$  and intermediate values of the magnetic anisotropy the edge magnons become locally unstable and condense at a finite momentum. It is this local instability that facilitates the skyrmion creation.

The outline of the paper is as follows. In section 6.2 we determine the magnetization at the edge of a single layer, we derive the magnon Hamiltonian and discuss its eigenmodes that are bound to the edge of the magnetic layer. We summarize the instabilities of the FP state in section 6.2.5 with a particular focus on the local instability triggered by the bound states that become unstable at a finite transversal momentum. In section 6.3 we demonstrate with the help of micromagnetic simulations that this latter instability triggers the formation of a helical phase, and, in addition, how this instability can be used to create skyrmions. We conclude in section 6.4 with a short discussion.

## 6.2. Magnons at the edge of a chiral magnet

### 6.2.1. The free energy functional

For our study, we consider the one-dimensional edge of a two-dimensional magnetic layer. In the following, when we speak about the bulk of the system we refer in fact to the interior of this two-dimensional layer. For sufficiently low temperatures, one can neglect (thermal) amplitude fluctuations of the spins and the local direction of the magnetization can be described by the unit vector  $\hat{n}$ . All modes discussed in the following including the boundary states at the edge are characterized by length scales much larger than the lattice spacing, so that a description in terms of a continuum model is applicable.

The free energy functional of the magnetic layer,  $F = \int d^2\vec{r}\mathcal{F}$ , reads

$$\mathcal{F} = A(\partial_\alpha\hat{n}_i)^2 - K\hat{n}_3^2 - \mu_0HM\hat{n}_3 + \mathcal{F}_{DM}, \quad (6.2.1)$$

with  $\alpha = x, y$  and  $i = 1, 2, 3$ ,  $A$  is the stiffness, and  $K$  is the magnetic anisotropy with an easy-axis and easy-plane anisotropy for  $K > 0$  and  $K < 0$ , respectively. Note that for a two-dimensional layer the dipolar interactions are effectively accounted for by a renormalized anisotropy  $K$  [35]. The third term is the Zeemann energy with an external field  $\vec{H}$  applied perpendicular to the plane,  $\vec{H} = H\hat{z}$  with  $H > 0$ , and the magnitude of the local magnetization  $M$  (integrated over the  $z$  direction). There are two different types of Dzyaloshinskii-Moriya (DM) interactions  $\mathcal{F}_{DM}$ . For chiral magnets like MnSi or FeGe where the inversion symmetry is broken by the atomic crystal the DM interaction reads [36]

$$\mathcal{F}_{DM}^{chiral} = D\epsilon_{\alpha j}\hat{n}_i\partial_\alpha\hat{n}_j, \quad (6.2.2)$$

where  $\epsilon_{\alpha j}$  is the Levi-Civita symbol, while for interface-induced DM interactions relevant, e.g.,

for Co films grown on heavy-element layers (e.g. Pt or Ir), we have [37, 38]

$$\mathcal{F}_{DM}^{interface} = D (\hat{n}_\alpha \partial_\alpha \hat{n}_3 - \hat{n}_3 \partial_\alpha \hat{n}_\alpha) \quad (6.2.3)$$

with  $\alpha = x, y$  and  $i, j = 1, 2, 3$ . It has been pointed out in Ref. [39] that for two-dimensional systems both types of DM interactions are actually equivalent because they can be transformed into each other by rotating  $\hat{n}$  by  $\pi/2$  around the  $z$ -axis, i.e., by  $\hat{n}_x \rightarrow \hat{n}_y, \hat{n}_y \rightarrow -\hat{n}_x$ . We will use in the main part of this work the formulae appropriate for  $\mathcal{F}_{DM}^{chiral}$  and assume  $D > 0$ . Our results are straightforwardly generalized to interface-induced DM interactions with the help of the above symmetry.

The dynamics of the magnetization is governed by the equation of motion

$$\partial_t \hat{n} = -\gamma \hat{n} \times \vec{B}_{eff} \quad (6.2.4)$$

with the gyromagnetic ratio  $\gamma = g\mu_B/\hbar > 0$  and the effective magnetic field obtained by the functional derivative  $\vec{B}_{eff} = -\frac{1}{M} \delta F / \delta \hat{n}$  where  $F = \int d^2\vec{r} \mathcal{F}$ . For our micromagnetic simulations, we furthermore add Gilbert damping to these equations, see Ref. [40]. The typical momentum, time and energy scales are given by

$$Q = \frac{D}{2A}, \quad t_{DM} = \frac{\hbar M}{g\mu_B 2AQ^2}, \quad \varepsilon_{DM} = \frac{\hbar}{t_{DM}}. \quad (6.2.5)$$

In the main part of the paper, we will measure length, time and energy in dimensionless units by denoting the variables with a tilde, e.g.

$$\tilde{x} = xQ, \quad \tilde{y} = yQ, \quad \tilde{t} = t/t_{DM}, \quad \tilde{\varepsilon} = \varepsilon/\varepsilon_{DM}. \quad (6.2.6)$$

Moreover, it is convenient to introduce the dimensionless magnetic field  $h$  and the dimensionless anisotropy  $\kappa$ ,

$$h = \frac{\mu_0 HM}{2AQ^2}, \quad \kappa = \frac{K}{AQ^2}. \quad (6.2.7)$$

As we are interested in the properties of the edge of the layered sample, we have to supplement the equations of motion (6.2.4) by a boundary condition. We assume the edge parallel to the  $x$ -axis. By varying the free energy  $F = \int_{-\infty}^{\infty} dx \int_0^{\infty} dy \mathcal{F}$ , one obtains for chiral magnets described by Eq. (6.2.2) the boundary condition [30]

$$\partial_y \hat{n} - Q \hat{y} \times \hat{n} = 0 \quad \text{at } y = 0 \quad (6.2.8)$$

while for interface-DM interactions (6.2.3) one finds the boundary condition [29]

$$\partial_y \hat{n} + Q \hat{x} \times \hat{n} = 0 \quad \text{at } y = 0. \quad (6.2.9)$$

A subtle question is whether the continuum approach advocated above is valid for real materials. In general, the chemistry and therefore the exchange couplings, the anisotropies, and DM interactions at the edge will differ from the ones within the layer. These changes do, however, affect our results only weakly if (i) the modification of the chemical properties is limited to distances of a few lattice constants  $a$  away from the edge and (ii) spin-orbit coupling effects are weak. The latter condition implies that the typical length scale on which the magnetization

varies is much larger than the lattice constant  $a$  and, furthermore, that anisotropy terms remain small compared to exchange interactions even at the surface. Technically, one can check for the importance of surface modification by adding surface, i.e., edge terms to the continuum Lagrange density, e.g., of the form  $K_s \delta(y) \hat{n}_3^2$ ,  $A_s \delta(y) (\partial_y \hat{n}_i)^2$ , or  $D_s \delta(y) \hat{n}_1 \partial_x \hat{n}_2$  with coupling constants  $K_s$ ,  $A_s$ ,  $D_s$ . The  $\delta$ -function takes into account that only the edge is affected. The importance of such terms can be evaluated by doing power-counting in the strength of spin orbit coupling  $\lambda_{SO}$  where we assume that  $A \sim A_s \sim \lambda_{SO}^0$ ,  $D \sim D_s \sim \lambda_{SO}$ , and  $K \sim K_s \sim \lambda_{SO}^2$  such that the dimensionless parameters  $h$  and  $\kappa$  are of order 1. Under this condition all length scales are proportional to  $1/\lambda_{SO}$ . As  $\delta(y) = \lambda_{SO} \delta(y \lambda_{SO})$  all extra terms discussed above are suppressed by the small factor  $\lambda_{SO}$  compared to the bulk contributions. This argument does nominally not hold for the surface term  $\delta(y) \hat{n} \partial_y \hat{n}$  which by powercounting is as important as the bulk contributions but this term is identical to zero as  $\partial_y \hat{n}^2 = 0$ . For a discussion of surface terms for a three-dimensional magnet see Meynell *et al.* [30].

### 6.2.2. The magnetization at the edge of the layer

We first consider the static magnetization close to the edge assuming that the magnetic layer is in a polarized state with  $\hat{n} = \hat{H} = \hat{z}$  within the bulk of the layer. Close to the edge of the two-dimensional chiral magnet, the magnetization has to twist due to the boundary conditions (6.2.8) or (6.2.9). An analytic solution for this twist has already been derived by Meynell *et al.* [30] for a system without magnetic anisotropy  $K = 0$ . Below, we generalize their result including a finite  $K$ . In order to simplify notations we use the rescaled coordinates of Eq. (6.2.6).

The translational invariance along the edge ensures that  $\hat{n}$  is only a function of  $\tilde{y}$ , i.e., the distance from the edge. We consider a chiral magnet described by Eqs. (6.2.2) and (6.2.8) where the magnetization twists perpendicular to the propagation direction similar to a Bloch-type domain wall. Hence we choose

$$\hat{n}_0^T = (\sin(\theta(\tilde{y})), 0, \cos(\theta(\tilde{y}))) \quad (6.2.10)$$

as an ansatz for the magnetization. The equation of motion (6.2.4) in the static limit and the boundary condition of Eq. (6.2.8), respectively, then reduce to

$$\theta''(\tilde{y}) = h \sin(\theta(\tilde{y})) + \frac{\kappa}{2} \sin(2\theta(\tilde{y})), \quad (6.2.11)$$

$$\theta'(\tilde{y})|_{\tilde{y}=0} = 1. \quad (6.2.12)$$

Moreover,  $\theta(\tilde{y}), \theta'(\tilde{y}) \rightarrow 0$  for  $\tilde{y} \rightarrow \infty$  as we assume the magnetization  $\hat{n} = \hat{z}$  to be aligned with the field within the bulk of the layer.

#### Kink soliton of the double sine-Gordon model

The equation of motion Eq. (6.2.11) is just the Euler-Lagrange equation of the double sine-Gordon model [41, 42]. It turns out that the magnetization at the edge can be obtained by placing a kink soliton of this model close to the edge. The analytical expression for this kink soliton is known in closed form [41, 42] and we shortly discuss its derivation in the following. As the derivative at the edge is positive,  $\theta'(0) > 0$ , we will look for a kink that interpolates  $\theta$  from  $-2\pi$  to 0 for increasing  $\tilde{y}$ . The first integral of the equation of motion is obtained in

a standard fashion by multiplying Eq. (6.2.11) with  $\theta'$ , integrating and using the boundary conditions within the bulk of the layer,  $\theta(\infty) = \theta'(\infty) = 0$ ,

$$\frac{\theta'^2}{2} + h \cos \theta + \frac{\kappa}{2} \cos^2 \theta = h + \frac{\kappa}{2}. \quad (6.2.13)$$

The kink is obtained by solving Eq. (6.2.13) for  $\theta'(\tilde{y}) > 0$ . Integrating Eq. (6.2.13) by separation of variables yields the kink soliton

$$\theta(\tilde{y}) = -\pi + 2 \arctan \left( \sqrt{\frac{h}{h+\kappa}} \sinh(\sqrt{h+\kappa}(\tilde{y} - \tilde{y}_0)) \right) \quad (6.2.14)$$

where  $\tilde{y}_0$  is an integration constant that specifies the position of the kink. For later convenience, we will also discuss the energy of the kink when it is placed deeply within the bulk,  $\tilde{y}_0 \rightarrow \infty$ . The kink energy per length  $L_x$  is obtained by integrating  $E_{kink}/L_x = \int dy(\mathcal{F}_{kink} - \mathcal{F}_{FP})$  where  $\mathcal{F}_{kink}$  is the free energy density evaluated for the kink, and we have subtracted the energy density of the FP state,  $\mathcal{F}_{FP}$ ,

$$\frac{E_{kink}}{2AQ L_x} = -2\pi + 4\sqrt{h+\kappa} + \frac{4h \operatorname{arctanh} \sqrt{\frac{\kappa}{h+\kappa}}}{\sqrt{\kappa}}. \quad (6.2.15)$$

There exists a critical magnetic field  $h_{kink}^{cr}$  for which the kink energy vanishes,

$$E_{kink}|_{h_{kink}^{cr}} = 0. \quad (6.2.16)$$

This critical field is defined within the range  $-1 < \kappa < \pi^2/4$  where it monotonically decreases from  $h_{kink}^{cr} = 1$  to zero. For  $\kappa = 0$  one recovers  $h_{kink}^{cr} = \pi^2/16$  (Ref. [38]). Whereas for larger fields the kink is an excitation of the FP state, the commensurate-incommensurate transition can take place at  $h_{kink}^{cr}$ , and kinks become energetically preferred resulting in a soliton lattice. However, as the kink is a topological excitation it does not correspond to a local but rather a global instability of the FP state for  $h \leq h_{kink}^{cr}$ .

## Edge magnetization

The full magnetization profile is now easily obtained by placing the kink Eq. (6.2.14) close to the edge so that the boundary condition,  $\theta'(0) = 1$ , is fulfilled. This is achieved with the integration constant

$$\tilde{y}_0 = -\frac{1}{\sqrt{\kappa+h}} \operatorname{arccosh} \left( \frac{h+\kappa + \sqrt{(h+\kappa)^2 - \kappa}}{\sqrt{h}} \right). \quad (6.2.17)$$

The center of the kink is positioned outside the sample  $\tilde{y}_0 < 0$ . Note that there is also a solution of the boundary condition with a positive  $\tilde{y}_0$  but it yields a state with larger energy. The result of Eq. (6.2.14) together with Eq. (6.2.17) determines the magnetization close to the edge of the FP magnetic layer.

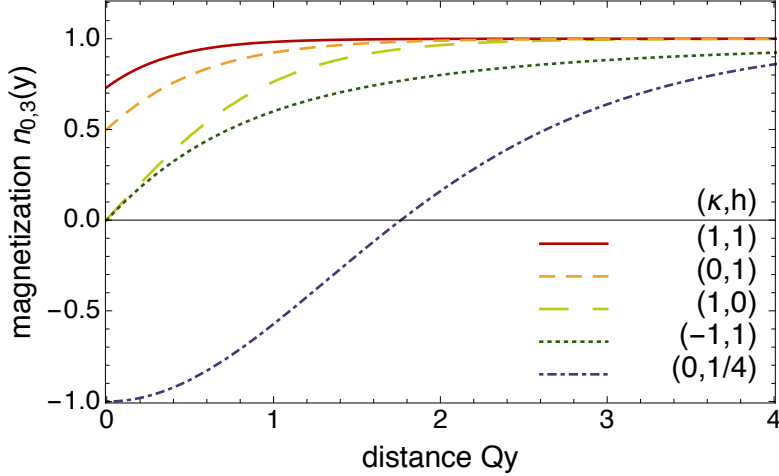


Figure 6.2.2.: Profile of the  $z$ -component of the normalized magnetization  $\hat{n}_{0,3} = \cos\theta(\tilde{y})$ , see Eq. (6.2.14), as a function of the dimensionless distance to the edge  $\tilde{y} = Qy$  for various values of the dimensionless field  $h$  and anisotropy  $\kappa$ . Note that the profile for the values  $(\kappa, h) = (0, 1/4)$  is unstable, see discussion in sec. 6.2.5.

In the limit of vanishing anisotropy,  $\kappa = 0$ , we recover the results of Ref. [30],

$$\theta(\tilde{y})|_{\kappa=0} = -4 \arctan \left( e^{-\sqrt{h}(\tilde{y}-\tilde{y}_0)} \right), \quad (6.2.18)$$

$$\tilde{y}_0|_{\kappa=0} = -\frac{1}{\sqrt{h}} \ln \tan \left( \frac{1}{2} \arcsin \frac{1}{2\sqrt{h}} \right). \quad (6.2.19)$$

We checked the result for various combinations of  $h$  and  $\kappa$  also numerically by simulating the damped Landau-Lifshitz-Gilbert equation and find that numerics are in excellent agreement with the analytic expression. In Fig. 6.2.2 we show the analytic result for the  $z$ -component of the magnetization in the proximity of the edge.

### 6.2.3. Effective magnon Hamiltonian

Having established the profile of the magnetization, we now consider the fluctuations around the saddle-point solution defined by Eqs. (6.2.10), (6.2.14) and (6.2.17) following the approach of Ref. [43]. We introduce a local basis

$$\hat{e}_1^T = \hat{y}^T = (0, 1, 0) \quad (6.2.20)$$

$$\hat{e}_2^T = -\partial_\theta \hat{n}_0^T = (-\cos\theta, 0, \sin\theta) \quad (6.2.21)$$

$$\hat{e}_3^T = \hat{n}_0^T = (\sin\theta, 0, \cos\theta) \quad (6.2.22)$$

with the angle  $\theta = \theta(\tilde{y})$  given by Eq. (6.2.14). We use the following parametrization of the field  $\hat{n}$ ,

$$\hat{n} = \hat{e}_3 \sqrt{1 - 2|\psi|^2} + \hat{e}_+ \psi + \hat{e}_- \psi^* \quad (6.2.23)$$

with  $\hat{e}_\pm = \frac{1}{\sqrt{2}}(\hat{e}_1 \pm i\hat{e}_2)$ . A change of phase of the complex magnon wavefunction  $\psi = \psi(\tilde{x}, \tilde{y}, \tilde{t})$  naturally encodes the precession of the magnetization.

Expanding the Landau-Lifshitz equation (6.2.4) up to linear order in the wavefunction  $\psi$  and  $\psi^*$ , we obtain the wave equation

$$i\tau^z \partial_{\tilde{t}} \vec{\psi} = H \vec{\psi} \quad (6.2.24)$$

for the two-component spinor  $\vec{\psi} = \begin{pmatrix} \psi \\ \psi^* \end{pmatrix}$ ,  $\tau^i$  are Pauli-matrices, and  $H$  is an effective Bogoliubov-deGennes Hamiltonian.

It can be split into the bulk contribution  $H_0$  and the edge potential  $V = V(\tilde{y})$  that vanishes  $V \rightarrow 0$  for  $\tilde{y} \rightarrow \infty$ ,

$$H = H_0 + V. \quad (6.2.25)$$

After performing a Fourier transformation of the spinor wavefunction,  $\vec{\psi}(\tilde{q}_x, \tilde{y}, \tilde{t}) = \int d\tilde{x} e^{-i\tilde{q}_x \tilde{x}} \vec{\psi}(\tilde{x}, \tilde{y}, \tilde{t})$ , for the  $\tilde{x}$  direction along which the problem is translationally invariant, we obtain

$$H_0 = -\partial_{\tilde{y}}^2 + \tilde{q}_x^2 + \Delta_b, \quad (6.2.26)$$

where  $\tilde{q}_x$  is the dimensionless wavevector along  $\tilde{x}$ . The magnon gap within the bulk of the layer is given by

$$\Delta_b = h + \kappa. \quad (6.2.27)$$

For  $\Delta_b < 0$ , the FP state within the bulk is locally unstable with respect to a tilt of the magnetization away from the field axis. The potential reads

$$\begin{aligned} V(\tilde{q}_x, \tilde{y}) = & \mathbf{1} \left( -\theta'^2(\tilde{y}) + \theta'(\tilde{y}) - \kappa \sin^2(\theta(\tilde{y})) \right) \\ & + \tau^z 2\tilde{q}_x \sin(\theta(\tilde{y})) \\ & + \tau^x \left( -\frac{1}{2}\theta'^2(\tilde{y}) + \theta'(\tilde{y}) + \frac{\kappa}{2} \sin^2(\theta(\tilde{y})) \right) \end{aligned}$$

with the angle  $\theta(\tilde{y})$  given in Eq. (6.2.14). We have used the first integral (6.2.13) to simplify the potential and, in particular, to eliminate the explicit dependence on dimensionless magnetic field  $h$ . Moreover, an explicit calculation shows that the boundary conditions for the spinor is simply given by

$$\partial_{\tilde{y}} \vec{\psi} \Big|_{\tilde{y}=0} = 0. \quad (6.2.28)$$

The bosonic Bogoliubov-de Gennes Hamiltonian  $H$ , Eq. (6.2.25), possesses scattering states that extend into the bulk of the layer as well as magnon states that are bound to the edge by the potential  $V$ . In the following, we will concentrate on these magnon edge modes.

#### 6.2.4. Bound magnon edge modes

We will look for eigenstates  $\vec{\phi} = \vec{\phi}_{\tilde{\varepsilon}, \tilde{q}}(\tilde{y})$  that are localized at the edge of the chiral magnet, which requires the dimensionless energy  $\tilde{\varepsilon}$  to have values within the range,  $0 \leq \tilde{\varepsilon} < \Delta_b + \tilde{q}_x^2$ . The localized eigenstates obey the stationary wave equation [43]

$$H \vec{\phi} = \tilde{\varepsilon} \tau^z \vec{\phi}, \quad (6.2.29)$$

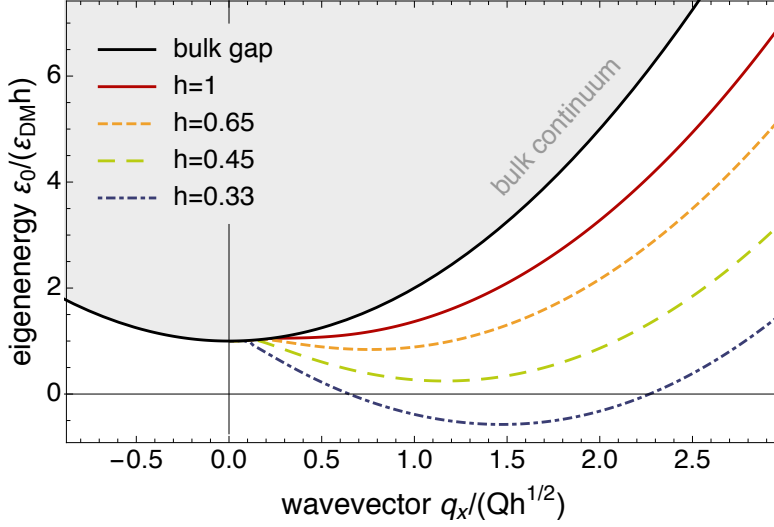


Figure 6.2.3.: Dispersions  $\varepsilon_0(q_x)/\varepsilon_{DM} = \tilde{\varepsilon}_0(\tilde{q}_x)$  with  $\tilde{q}_x = q_x/Q$  of the magnon edge modes with lowest energy,  $n = 0$ , as a function of momentum  $q_x$  along the edge for fields  $h = 1, 0.65, 0.45, 0.33$  and anisotropy  $\kappa = 0$ . The grey shaded area is the bulk continuum that terminates at the solid black line.

with the normalization condition

$$\int_0^\infty \vec{\phi}^\dagger \tau^z \vec{\phi} dy = 1. \quad (6.2.30)$$

From the spinor-wavefunction  $\vec{\phi}^T = (\phi_1, \phi_2)$  then follows the corresponding time-dependent magnon wavefunction in the parametrization of Eq. (6.2.23), that is  $\psi(t) = \phi_1 e^{-i\epsilon t/\hbar} + \phi_2^* e^{i\epsilon t/\hbar}$  with  $\epsilon = \tilde{\varepsilon}\varepsilon_{DM}$  where  $\varepsilon_{DM}$  was defined in Eq. (6.2.5).

We numerically search for bound state solutions using the shooting method. Starting from the boundary condition at the edge  $\vec{\phi}^T(0) = c_1(\cos \alpha, \sin \alpha)$  and  $\vec{\phi}'(0) = 0$  where  $c_1$  is an arbitrary constant that will be fixed afterwards by the normalization condition (6.2.30), we vary the energy  $\tilde{\varepsilon}$  and the parameter  $\alpha$  until we find a solution of Eq. (6.2.29) that is bound to the edge so that it decays for  $\tilde{y} \rightarrow \infty$ . The asymptotic decay of the localized wavefunction directly follows from  $H_0$  of Eq. (6.2.26),

$$\vec{\phi}(\tilde{y}) \sim \begin{pmatrix} c_2 e^{-\sqrt{\Delta_b + \tilde{q}_x^2 - \tilde{\varepsilon}} \tilde{y}} \\ c_3 e^{-\sqrt{\Delta_b + \tilde{q}_x^2 + \tilde{\varepsilon}} \tilde{y}} \end{pmatrix}, \quad \text{for } \tilde{y} \rightarrow \infty \quad (6.2.31)$$

with constants  $c_2$  and  $c_3$ . The problem (6.2.29) corresponds to an effective one-dimensional wave equation, and its bound states can be labelled by a discrete quantum number  $n = 0, 1, 2, \dots$  that count the nodes of the wavefunction. Moreover, the solutions for given momenta along the edge  $q_x$  define dispersing eigenenergies  $\varepsilon_n(q_x) = \varepsilon_{DM} \tilde{\varepsilon}_n(\tilde{q}_x)$  with  $\tilde{q}_x = q_x/Q$  for the magnon bound states that are discussed in the following.

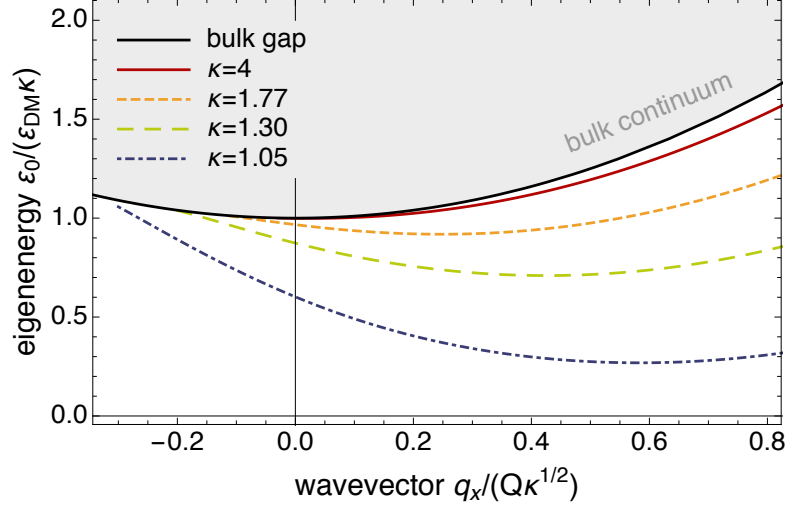


Figure 6.2.4.: Dispersions  $\varepsilon_0(q_x)/\varepsilon_{DM} = \tilde{\varepsilon}_0(\tilde{q}_x)$  with  $\tilde{q}_x = q_x/Q$  of the magnon edge modes with lowest energy,  $n = 0$ , as a function of momentum  $q_x$  along the edge for anisotropies  $\kappa = 1.05, 1.30, 1.77, 4.00$  and field  $h = 0$ . The grey shaded area is the bulk continuum that terminates at the solid black line.

### Lowest-energy magnon edge modes

The dispersion of magnon edge modes with lowest energy  $\varepsilon_0(q_x)$ , i.e., quantum number  $n = 0$  and momentum  $q_x$  along the edge are shown for various values of the dimensionless magnetic field  $h$  and  $\kappa = 0$  in Fig. 6.2.3 as well as for various values of the dimensionless magnetic anisotropy  $\kappa$  and  $h = 0$  in Fig. 6.2.4. We have rescaled the energy by the dimensionless bulk gap  $\Delta_b = h + \kappa$  and the momenta by  $\sqrt{\Delta_b}$  such that the bottom of the bulk continuum,  $\Delta_b + \tilde{q}_x^2$ , is given by a single black line for all parameters. Our results are in agreement with the numerical study by Garcia-Sanchez *et al.* in Ref. [34].

Generally, we always find a range of momenta  $q_x$  where magnon modes exist that are bound to the edge. Interestingly, the spectrum is chiral, i.e., it is not symmetric around  $q_x = 0$  as the presence of the magnetic field breaks all  $q_x \rightarrow -q_x$  symmetries at the boundary. Especially for larger magnetic fields  $h$  the group velocity  $\partial\varepsilon_0(q_x)/\partial q_x$  is mostly positive, which implies that magnons travel along the edge in a preferred direction [34], for example, after they have been excited locally by a laser pulse. Note that the modes with the reversed dispersion  $\varepsilon_n(q_x) \rightarrow \varepsilon_n(-q_x)$  are found at opposite edges of the layer. Theoretically speaking, the dispersion could be reversed at the same edge by reversing the sign of the gyromagnetic ratio  $\gamma \rightarrow -\gamma$ , e.g., by considering holes instead of particles. However, reversing the sign of the DM interaction,  $D \rightarrow -D$ , modifies the edge magnetization but eventually leaves the dispersion  $\varepsilon_n(q_x)$  invariant in contrast to the claim of Ref. [34]. This also applies for interfacial DM interaction. While for  $\kappa = 0$  (Fig. 6.2.3) bound states exist only for  $q_x > 0$ , one obtains edge magnons at  $q_x = 0$  for  $h = 0$  and  $\kappa > 1.005$ . In the latter case an homogeneously oscillating magnetic field can be used to excite a left-moving edge mode. In the presence of disorder at the edge, i.e., when the momentum  $q_x$  parallel to the edge is not conserved, also right-moving modes can be excited by such an ac field.

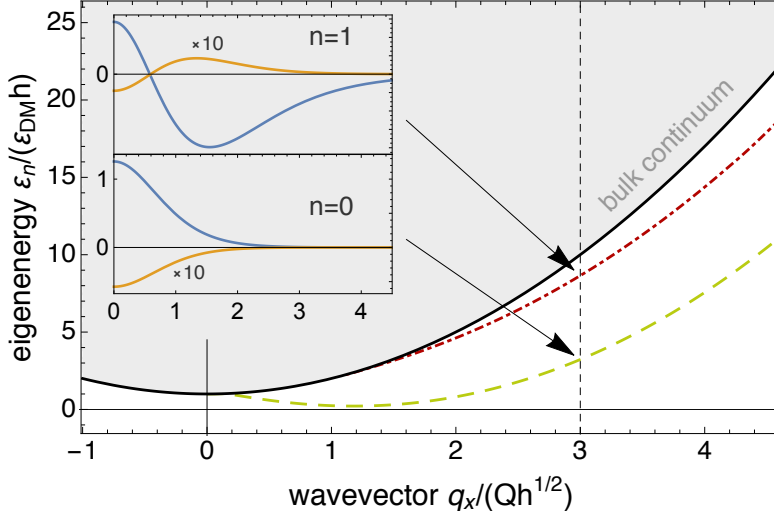


Figure 6.2.5.: Dispersions  $\varepsilon_n(q_x)$  of the magnon edge mode without and a single node,  $n = 0$  and  $n = 1$ , respectively, for  $h = 0.44$  and  $\kappa = 0$ . The inset shows the first (blue) and second (orange) component of the eigenfunction  $\vec{\phi}$  at  $q_x = 3Q$ , where the latter is multiplied by a factor 10 to make it visible. The grey shaded area is the bulk continuum that terminates at the solid black line.

With lower magnetic fields the minimum of the spectrum,

$$\Delta_e(h, \kappa) = \min \tilde{\varepsilon}_0(\tilde{q}_x) \quad (6.2.32)$$

is shifted down to lower energies and to larger wave vectors. At a critical dimensionless magnetic field  $h_c = 0.4067$  at  $\kappa = 0$  the minimum of the spectrum goes to zero energy,  $\Delta_e = 0$ , at a finite momentum  $q_x$ . The system therefore experiences a local instability at the edge which we discuss in further detail in Sec. 6.2.5. Similarly, we find such a local edge instability for  $\kappa_c = 1.005$  and  $h = 0$ .

### Higher-order magnon edge modes

For larger values of  $q_x$ , the gap between the lowest bound magnon mode  $\varepsilon_0(q_x)$  and the bulk continuum increases approximately linear. This dependence can also be estimated from the potential, Eq. (6.2.28), which grows linear in  $q_x$  for large  $q_x$ . As the potential becomes deeper, higher-order bound states,  $\varepsilon_n(q_x)$  with  $n > 0$ , arise at the edge which are characterized by one (or more) nodes in their wave function. The spectrum of the bound states with zero and one node is shown in Fig. 6.2.5 for the magnetic field  $h = 0.44$ .

### 6.2.5. Phase diagram and instabilities of the metastable FP state

In the following we discuss the phase diagram of the magnetic layer as a function of magnetic field  $h$  and magnetic anisotropy  $\kappa$ , see Fig. 6.2.6. First, we review the thermodynamically stable phases, and, afterwards, we focus on the metastable FP phase and its global and local bulk and local edge instabilities.

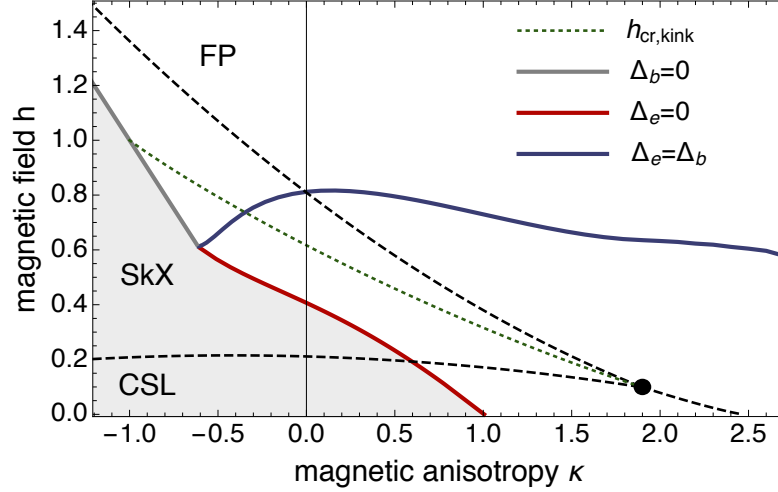


Figure 6.2.6.: Overview of the local and global stability of the field-polarized state (FP). The black dashed lines are reproduced from Ref. [44] and denote thermodynamic phase transitions between the FP state, the skyrmion crystal (SkX) and the chiral soliton lattice (CSL). Within the white regime the FP state remains metastable, but it is locally unstable within the grey shaded regime. The green dotted line indicates a global instability  $h_{cr,kink}^{cr}$  where the energy of the kink soliton vanishes, see Eq. (6.2.16). On the grey solid line  $h = -\kappa$  the magnon gap  $\Delta_b$  vanishes within the bulk while the edge gap  $\Delta_e$  is zero on the red solid line. On the blue solid line the magnon gap within the bulk and at the edge are equal,  $\Delta_e = \Delta_b$ .

### Thermodynamic phase diagram

The bulk thermodynamic phase diagram of a magnetic layer in the presence of a perpendicular magnetic field has been studied in Refs. [39, 44–46]. For a two-dimensional chiral magnet, there exist three stable thermodynamic phases for values of  $\kappa$  that are of interest here: the FP state, the SkX, and the chiral soliton lattice (CSL), i.e., a helix that in general possesses higher harmonics [47]. The black dashed lines in Fig. 6.2.6 show the phase boundaries that were given by Wilson *et al.* [44]. (We have slightly extrapolated the phase transition lines of Ref. [44] to more negative values of  $\kappa$ .) There exists a triple point (black dot) at  $(\kappa, h) \approx (1.9, 0.1)$  where the three phases meet [44].

### Global, local bulk and local edge instabilities of the metastable FP state

Importantly, the transition between the FP state and the SkX corresponds to a global instability as the two states belong to different topological sectors. If the magnetic field is reduced adiabatically at low enough temperatures to a value within the SkX regime, there is the possibility that the magnetic layer remains in a metastable FP state. As the field is reduced further, another global instability of the metastable FP state is encountered at  $h_{cr,kink}^{cr}$  within the range  $-1 < \kappa < 1.9$  that is shown as the dashed green line in Fig. 6.2.6. Here the energy of a kink soliton vanishes, see Eq. (6.2.16), triggering the formation of a chiral soliton lattice. The phase boundary between FP and CSL state within the range  $1.9 < \kappa < \pi^2/4$  is also defined by  $h_{cr,kink}^{cr}$ .

The FP state is stable or metastable in the whole white regime of Fig. 6.2.6. It becomes locally unstable however when one of its magnon excitations reaches zero energy upon decreasing the magnetic field  $h$ . This instability can occur either in the bulk or at the edge. For  $\kappa < -0.61$ ,

first the bulk becomes locally unstable at  $h = -\kappa$  (grey solid line) where the bulk gap vanishes,  $\Delta_b = 0$ , see Eq. (6.2.27). For  $-0.61 < \kappa < 1.005$ , on the other hand, the gap of the magnon edge modes vanishes first,  $\Delta_e = 0$ , see Eq. (6.2.32), at the red solid line. This edge instability occurs at a finite transversal momentum  $q_x$ , see Fig. 6.2.3 and Fig. 6.2.4.

Finally, the blue solid line in Fig. 6.2.6 indicates where the bulk and edge gap have equal size. Below that line the gap  $\Delta_e$  of the edge magnons is smaller than the gap  $\Delta_b$  of the bulk magnons, and the spin wave excitation with lowest energies are located at the edge of the sample. Within this regime, for frequencies  $\Delta_e \leq \hbar\tilde{\omega} < \Delta_b$  only edge magnons of the stable or metastable FP state are thus excited.

### 6.3. Edge instability and creation of skyrmions

In the following we demonstrate that the local edge instability of the metastable FP state at the red line in Fig. 6.2.6 triggers the formation of a helical state (CLS) although in some region of the phase diagram the SkX is in fact thermodynamically more stable. Moreover, we show that this edge instability can be exploited to create skyrmions in a controlled manner. In order to investigate the evolution of the magnetic state in the regime where the FP state is locally unstable, we have performed micromagnetic simulations using the Landau-Lifshitz-Gilbert (LLG) equation at  $T = 0$ , for details see Ref. [40]. Typically we use  $\alpha = 0.1$  or  $0.4$  as a damping constant in our simulations. We simulated a two-dimensional stripe with open boundary conditions in one and periodic boundary conditions in the perpendicular direction.

We focus on the range of magnetic anisotropies where the edge magnons locally destabilize the FP state, i.e.,  $-0.61 < \kappa < 1.005$  for the two-dimensional system, see Fig. 6.2.6. The following protocol for the time-dependent magnetic field allows for a controlled creation of a skyrmion chain close to the edge

$$h(t) = \begin{cases} h_i & \text{for } t < 0 \\ h_0 & \text{for } 0 < t < t_f \\ h_f & \text{for } t_f < t. \end{cases} \quad (6.3.33)$$

The initial field value  $h_i$  is located above the upper black dashed line in Fig. 6.2.6 so that we start with a magnetization which is FP. At  $t = 0$  the field is reduced  $h_0 < h_i$  below the red line in Fig. 6.2.6 so that  $\Delta_e < 0$ . Finally, at time  $t_f$  we increase the field again to a value,  $h_f > h_{\text{kin}k}^{\text{cr}}$ , that is located above the green dashed line in Fig. 6.2.6. The result of the micromagnetic simulation for such a protocol at  $\kappa = 0$  is shown in Fig. 6.3.7.

Initially, the magnetization is fully polarized except close to the lower edge of Fig. 6.3.7(a) that shows the surface twist of Eq. (6.2.14). As the field is lowered for  $t > 0$ , the edge magnon becomes soft at a finite transversal momentum  $q_x$  and destabilizes the magnetization whose time evolution is shown in Fig. 6.3.7(b)-(d). To trigger the edge instability in the numerics, we explicitly broke translation symmetry by introducing a tiny perturbation by canting one spin at the right-hand side of the boundary by 1%. First, a periodic modulation of the edge spins grows in amplitude – the edge magnon with negative energy becomes macroscopically occupied at finite momentum  $q_x$ . This state evolves smoothly into a helical state which penetrates into the FP state of the bulk. The interface between the helical and polarized phase is thereby described by a chain of merons, i.e., half-skyrmions with winding number  $1/2$ . As a function of time, the interface moves further and further into the FP state of the bulk. For this simulation the intermediate field value  $h_0$  of Eq. (6.3.33) was chosen to be located within the regime

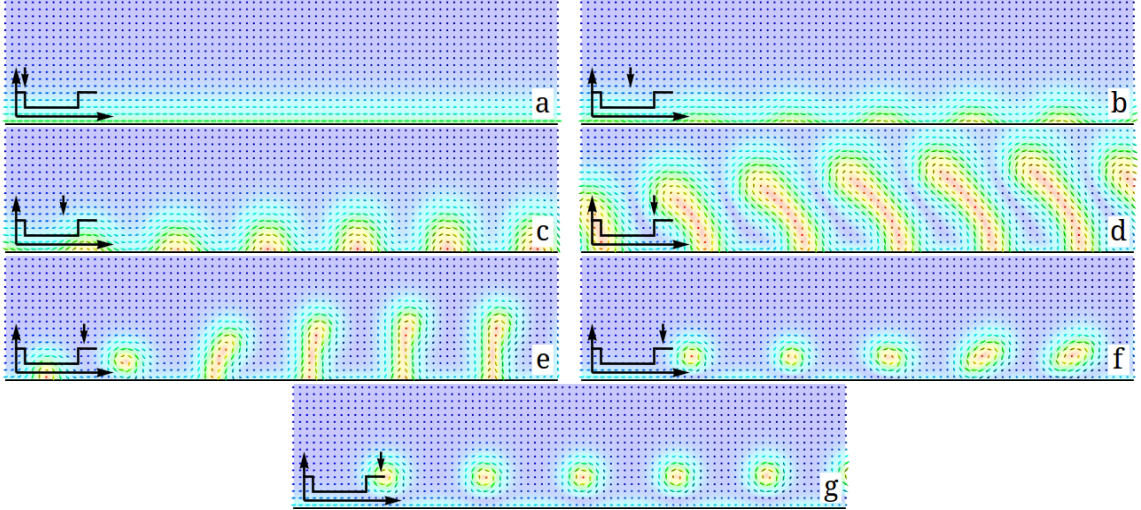


Figure 6.3.7.: Creation of a chain of skyrmions using the local edge instability of the field-polarized state. The panels show snapshots at various times obtained by LLG simulations of the field-protocol in Eq. (6.3.33) as sketched in the inset with Gilbert damping  $\alpha = 0.4$ ,  $\kappa = 0$ ,  $h_i = 1$ ,  $h_0 = 0.39$ ,  $h_f = 1$ , and  $\tilde{t}_f = 40.5$ . (a)-(d) Triggered by the edge instability, a chain of merons forms that penetrates into the field-polarized state of the bulk. (e)-(g) The merons are pushed back towards the edge and their local dynamics close to the edge results in the formation of a chain of skyrmions. Steps (e)-(g) have been observed experimentally in Ref. [27]. The color code denotes the  $z$ -component of the magnetization.

where the SkX is thermodynamically stable. Nevertheless, the local edge instability prompts the formation of a helical state which is metastable in this case.

In a second step, the magnetic field is again increased to a value  $h_f$  at  $t = t_f$ , and, as a consequence, the helical phase is pushed back towards the edge. For this to happen, it is required that  $h_f > h_{kink}^{cr}$  so that the FP state is energetically favored compared to the CSL state and can exert a positive pressure on the interface. For the simulation in Fig. 6.3.7(e)-(g), we have chosen  $h_f = h_i$ . Remarkably, the initial state is however not recovered. An interesting local dynamics governs the fate of the helical fingers as they are pushed towards the edge. When the merons, i.e., the half-skyrmions approach the boundary, each of them pulls a second meron out of the edge. Both combine to a skyrmion which gets repelled from the edge by the surface twist of the magnetization. As a result, one obtains a chain of equally spaced skyrmions. Note that  $h_f = h_i$  is here located within the regime where the FP phase is thermodynamically stable. The interaction of the receding meron with the spin configuration at the edge thus results in a final state, Fig. 6.3.7(g), that possesses a larger energy than the initial FP state of Fig. 6.3.7(a). The spin configuration at the boundary with its surface twist apparently acts as a repulsive potential for the merons hindering them to leave the sample so that the FP thermodynamic groundstate becomes dynamically inaccessible. The system is thus trapped in a metastable state containing a chain of skyrmions.

The advantage of the protocol (6.3.33) is that it is extremely robust. The final state is, for example, completely independent of the time  $t_f$  for which the magnetic field is lowered. The precise field values and the size of the damping term is also not important. Another important aspect of this protocol is that during the process, the magnetic configuration is always smooth and singular intermediate spin configurations, i.e., Bloch points are not needed. This is in

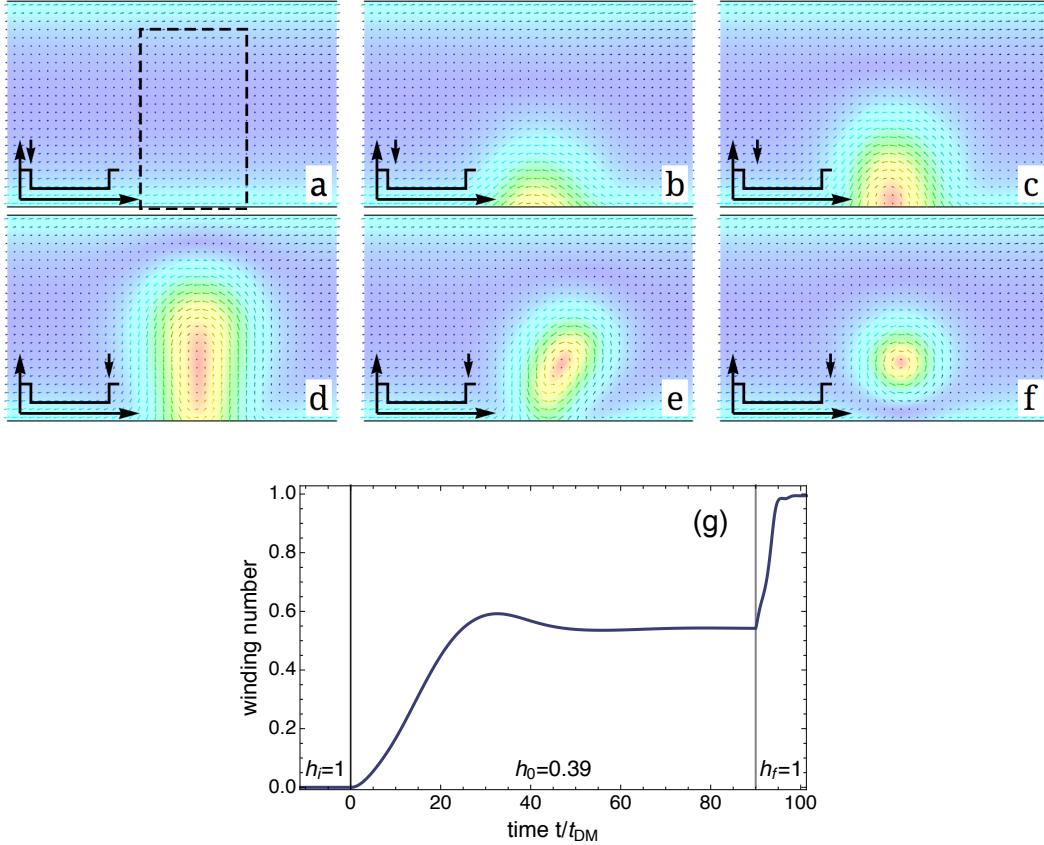


Figure 6.3.8.: Creation of a single skyrmion using the edge instability. We use a similar protocol as in Fig. 6.3.7 with  $\alpha = 0.4$ ,  $\kappa = 0$ ,  $h_i = 1$ ,  $h_0 = 0.39$ ,  $h_f = 1$  and  $\tilde{t}_f = 90$  but this time the magnetic field is only reduced in the finite region marked by the dashed rectangle in panel (a). We have chosen the extent of this region along the edge to be half of the wavelength,  $\lambda_x/2 = \pi/q_x$ , at which the edge magnon softens. The color code in panel (a)-(f) denotes the  $z$ -component of the magnetization. Panel (g) shows the time evolution of the winding number.

contrast to processes where skyrmions are created within the bulk [21, 25].

The second part of our protocol, the creation of a chain of skyrmions by pushing the helical state towards the edge with the help of a magnetic field has been realized recently for FeGe nanostrips in a beautiful experiment by Du *et al.* in Ref. [27]. In this experiment, the system was first prepared in a helical state. After an increase of the magnetic field, helices ultimately reconstruct yielding skyrmions. For nanostrips with a small width, the skyrmions recombined in the center of the strip while for larger width precisely the same process was observed that we discuss above.

The same protocol can also be used to create a single skyrmion by reducing the magnetic field however only within a confined region close to the edge as indicated by the dashed box in Fig. 6.3.8(a). Experimentally, one can use, e.g., a magnetic tip to change locally the magnetic field. Previous micromagnetic simulation by Koshibae *et al.* [20] have already demonstrated that pulses of magnetic field in a small area can trigger the creation of a skyrmion close to the edge. Here, we identify the edge magnon instability as the underlying principle of this phenomenon. As the field is locally reduced below the edge magnon instability, a meron is

protruding into the system as shown in Fig. 6.3.8(b)-(d). As the magnetic field is increased again a single skyrmion forms, see Fig. 6.3.8(e) and (f). In panel (g) we show the time evolution of the total skyrmion winding number. As the field is decreased at time  $t = 0$ , the winding number increases and saturates to a value close to  $1/2$  reflecting the presence of a single meron. As the field is increased again at  $t_f = 90t_{DM}$ , the winding number increases assuming a value close to one when the skyrmion formation is completed.

## 6.4. Discussion

The Dzyaloshinskii-Moriya (DM) interaction imposes boundary conditions on the magnetization [28, 29] which results in a reconstruction of the magnetization profile close to surfaces. For the FP state this just translates to a twist of the magnetization along or perpendicular to the surface normal depending on the type of DM interaction. We have demonstrated that this surface twist can act as an attractive potential on the spin wave excitations leading to magnon modes that are bound to the edge of the sample. The energy of these edge modes as a function of momentum transverse to the edge has been calculated and is shown in Figs. 6.2.3 and 6.2.4. These bound magnons become soft at a finite momentum thus locally destabilizing the metastable FP phase, and this edge instability triggers the formation of a helical state as shown in Fig. 6.3.7. We have shown by micromagnetic simulations that the process of helix formation via the edge instability is dynamically irreversible allowing for the creation of skyrmions close to the edge.

In the present work, we confined ourselves to a two-dimensional monolayer where the edge instability corresponds to a local instability of the FP state. We now shortly comment on the modifications expected for a magnetic film of finite thickness. In this latter case, the FP state becomes locally unstable upon decreasing the magnetic field with respect to the formation of a conical phase [44, 45]. Importantly, this instability occurs before the local edge instability discussed in this paper so that our results cannot be directly applied to thin films. However, the conical phase should also exhibit its own edge instability whose analytical description is however more involved due to the coupling of the helical modulation and the surface twist. Nevertheless, we expect the edge instability of the conical phase to possess a similar character also allowing for the creation of skyrmions as discussed above. We thus believe that our results basically explain the mechanism of the edge-mediated nucleation of skyrmions experimentally observed by Du *et al.* [27] in thin films of FeGe.

Whereas we focused here on the properties of the FP state, the surface reconstruction is also expected [31–33] for the other thermodynamically stable phases, i.e., the SkX and the helix. It is an interesting open question how it influences the spin wave spectrum and whether or not bound magnon edge modes also exist in these other phases. At least for the SkX phase, magnon edge modes are indeed expected but for a very different reason. Magnons experience an emergent orbital magnetic field when they scatter off a topological skyrmion configuration [3, 43, 48]. In a magnetic SkX this should give rise to a topological magnon band structure characterized by finite Chern numbers and the concomitant topological edge modes [49].

## Acknowledgements

J.M. acknowledges helpful discussions with V. Cros and J.-V. Kim as well as support from the Deutsche Telekom Stiftung and BCGS.

## 6.5. Bibliography

- [1] F. Jonietz, S. Mühlbauer, C. Pfleiderer, A. Neubauer, W. Münzer, A. Bauer, T. Adams, R. Georgii, P. Böni, R. A. Duine, K. Everschor, M. Garst, and A. Rosch, *Spin transfer torques in MnSi at ultralow current densities*, Science **330**, 1648-1651 (2010).
- [2] T. Schulz, R. Ritz, A. Bauer, M. Halder, M. Wagner, C. Franz, C. Pfleiderer, K. Everschor, M. Garst, and A. Rosch, *Emergent electrodynamics of skyrmions in a chiral magnet*, Nat. Phys. **8**, 301-304 (2013).
- [3] N. Nagaosa and Y. Tokura, *Topological properties and dynamics of magnetic skyrmions*, Nat. Nano. **8**, 899-911 (2013).
- [4] A. Fert, V. Cros, and J. Sampaio, *Skyrmions on the track*, Nat. Nanol. **8**, 152-156 (2013).
- [5] J. Seidel (eds), *Topological Structures in Ferroic Materials*, Springer Series in Materials Science , vol. 228 Springer, Cham (2016)
- [6] R. Tomasello, E. Martinez, R. Zivieri, L. Torres, M. Carpentieri, and G. Finocchio, *A strategy for the design of skyrmion racetrack memories*, Sci. Rep. **4**, 6784 EP (2014).
- [7] S. Mühlbauer, B. Binz, F. Jonietz, C. Pfleiderer, A. Rosch, A. Neubauer, R. Georgii, and P. Böni, *Skyrmion lattice in a chiral magnet*, Science **323**, 915-919 (2009).
- [8] T. Adams, S. Mühlbauer, C. Pfleiderer, F. Jonietz, A. Bauer, A. Neubauer, R. Georgii, P. Böni, U. Keiderling, K. Everschor, M. Garst, and A. Rosch, *Long-range crystalline nature of the skyrmion lattice in MnSi*, Phys. Rev. Lett. **107**, 217206 (2011).
- [9] X. Z. Yu, N. Kanazawa, Y. Onose, K. Kimoto, W. Z. Zhang, S. Ishiwata, Y. Matsui, and Y. Tokura, *Near room-temperature formation of a skyrmion lattice in thin-films of the helimagnet FeGe*, Nat. Mater. **10**, 106-109 (2011).
- [10] T. Adams, A. Chacon, M. Wagner, A. Bauer, G. Brandl, B. Pedersen, H. Berger, P. Lemmens, and C. Pfleiderer, *Long-wavelength helimagnetic order and skyrmion lattice phase in Cu<sub>2</sub>OSeO<sub>3</sub>*, Phys. Rev. Lett. **108**, 237204 (2012).
- [11] S. Seki, X. Z. Yu, S. Ishiwata, and Y. Tokura, *Observation of skyrmions in a multiferroic material*, Science **336**, 198-201 (2012).
- [12] S. Heinze, K. von Bergmann, M. Menzel, J. Brede, A. Kubetzka, R. Wiesendanger, G. Bihlmayer, and S. Blügel, *Spontaneous atomic-scale magnetic skyrmion lattice in two dimensions*, Nat. Phys. **7**, 713-718 (2011).
- [13] K. von Bergmann, A. Kubetzka, O. Pietzsch, and R. Wiesendanger, *Interface-induced chiral domain walls, spin spirals and skyrmions revealed by spin-polarized scanning tunneling microscopy*, J. Phys. Condens. Matter **26**, 394002 (2014).
- [14] Y. Tokunaga, X. Z. Yu, J. S. White, H. M. Rønnow, D. Morikawa, Y. Taguchi, and Y. Tokura, *A new class of chiral materials hosting magnetic skyrmions beyond room temperature*, Nat. Commun. **6**, 7638 (2015).
- [15] S. Woo, K. Litzius, B. Krüger, M.-Y. Im, L. Caretta, K. Richter, M. Mann, A. Krone, R. M. Reeve, M. Weigand, P. Agrawal, I. Lemesh, M.-A. Mawass, P. Fischer, M. Kläui, and G. S. D. Beach, *Observation of room-temperature magnetic skyrmions and their current-driven dynamics in ultrathin metallic ferromagnets*, Nat. Mater. **15**, 501-506 (2016).
- [16] W. Jiang, P. Upadhyaya, W. Zhang, G. Yu, M. B. Jungfleisch, F. Y. Fradin, J. E. Pearson, Y. Tserkovnyak, K. L. Wang, O. Heinonen, S. G. E. te Velthuis, and A. Hoffmann, *Blowing magnetic skyrmion bubbles*, Science **349**, 283-286 (2015).
- [17] C. Moreau-Luchaire, C. Moutafis, N. Reyren, J. Sampaio, C. A. F. Vaz, N. Van Horne, K. Bouzehouane, K. Garcia, C. Deranlot, P. Warnicke, P. Wohlhüter, J.-M. George, M. Weigand, J. Raabe, V. Cros, and A. Fert, *Additive interfacial chiral interaction in multilayers for stabilization of small individual skyrmions at room temperature*, Nat. Nano. **11**, 444-448 (2016).
- [18] J. Sampaio, V. Cros, S. Rohart, A. Thiaville, and A. Fert, *Nucleation, stability and current-induced motion of isolated magnetic skyrmions in nanostructures*, Nat. Nano. **8**, 839-844 (2013).

- [19] W. Koshibae and N. Nagaosa, *Creation of skyrmions and antiskyrmions by local heating*, Nat. Commun. **5**, 5148 (2014).
- [20] W. Koshibae, Y. Kaneko, J. Iwasaki, M. Kawasaki, Y. Tokura, and N. Nagaosa, *Memory functions of magnetic skyrmions*, Jpn. J. Appl. Phys. **54**, 053001 (2015).
- [21] M. Mochizuki and Y. Watanabe, *Writing a skyrmion on multiferroic materials*, Appl. Phys. Lett. **107**, 0824091 (2015).
- [22] J. Hagemeyer, N. Romming, K. von Bergmann, E. Y. Vedmedenko, and R. Wiesendanger, *Stability of single skyrmionic bits*, Nat. Commun. **6**, 8455 (2015).
- [23] N. Romming, C. Hanneken, M. Menzel, J. E. Bickel, B. Wolter, K. von Bergmann, A. Kubetzka, and R. Wiesendanger, *Writing and deleting single magnetic skyrmions*, Science **341**, 636-639 (2013).
- [24] Y. Zhou and M. Ezawa, *A reversible conversion between a skyrmion and a domain-wall pair in a junction geometry*, Nat. Commun. **5**, 4652 (2014).
- [25] P. Milde, D. Köhler, J. Seidel, L. M. Eng, A. Bauer, A. Chacon, J. Kindervater, S. Mühlbauer, C. Pfleiderer, S. Buhrandt, C. Schütte, and A. Rosch, *Unwinding of a skyrmion lattice by magnetic monopoles*, Science **340**, 1076 (2013).
- [26] A. Neubauer, C. Pfleiderer, B. Binz, A. Rosch, R. Ritz, P. G. Niklowitz, and P. Böni, *Topological Hall Effect in the A Phase of MnSi*, Phys. Rev. Lett. **102**, 186602 (2009).
- [27] H. Du, R. Che, L. Kong, X. Zhao, C. Jin, C. Wang, J. Yang, W. Ning, R. Li, C. Jin, X. Chen, J. Zang, Y. Zhang, and M. Tian, *Edge-mediated skyrmion chain and its collective dynamics in a confined geometry*, Nat. Commun. **6**, 8504 (2015).
- [28] M. N. Wilson, E. A. Karhu, D. P. Lake, A. S. Quigley, S. Meynell, A. N. Bogdanov, H. Fritzsche, U. K. Rößler, and T. L. Monchesky, *Discrete helicoidal states in chiral magnetic thin films*, Phys. Rev. B **88**, 214420 (2013).
- [29] S. Rohart and A. Thiaville, *Skyrmion confinement in ultrathin film nanostructures in the presence of Dzyaloshinskii-Moriya interaction*, Phys. Rev. B **88**, 184422 (2013).
- [30] S. A. Meynell, M. N. Wilson, H. Fritzsche, A. N. Bogdanov, and T. L. Monchesky, *Surface twist instabilities and skyrmion states in chiral ferromagnets*, Phys. Rev. B **90**, 014406 (2014).
- [31] F. N. Rybakov, A. B. Borisov, and A. N. Bogdanov, *Three-dimensional skyrmion states in thin films of cubic helimagnets*, Phys. Rev. B **87**, 094424 (2013).
- [32] F. N. Rybakov, A. B. Borisov, S. Blügel, and N. S. Kiselev, *New type of stable particlelike states in chiral magnets*, Phys. Rev. Lett. **115**, 117201 (2015).
- [33] F. N. Rybakov, A. B. Borisov, S. Blügel, and N. S. Kiselev, *New spiral state and skyrmion lattice in 3D model of chiral magnets*, New J. Phys. **18**, 045002 (2016).
- [34] Felipe Garcia-Sanchez, Pablo Borys, Arne Vansteenkiste, Joo-Von Kim, and Robert L. Stamps, *Nonreciprocal spin-wave channeling along textures driven by the Dzyaloshinskii-Moriya interaction*, Phys. Rev. B **89**, 224408 (2014).
- [35] A. Hubert and R. Schäfer, *Magnetic Domains: The Analysis of Magnetic Microstructures*, Springer-Verlag Berlin Heidelberg, (1998).
- [36] P. Bak and M. H. Jensen, *Theory of helical magnetic structures and phase transitions in MnSi and FeGe*, J. Phys. C **13**, L881 (1980).
- [37] A. N. Bogdanov and D. A. Yablonskii, *Thermodynamically stable "vortices" in magnetically ordered crystals. The mixed state of magnets*, Zh. Eksp. Teo. Fiz. **95**, 178-182 (1989).
- [38] A. N. Bogdanov and A. Hubert, *Thermodynamically stable magnetic vortex states in magnetic crystals*, J. Magn. Mater. **138**, 255-269 (1994).
- [39] U. Güngördü, R. Nepal, O. A. Tretiakov, K. Belashchenko, and A. A. Kovalev, *Stability of skyrmion lattices and symmetries of quasi-two-dimensional chiral magnets*, Phys. Rev. B **93**, 064428 (2016).
- [40] J. Müller and A. Rosch, *Capturing of a magnetic skyrmion with a hole*, Phys. Rev. B **91**, 054410 (2015).

- 
- [41] C. A. Condat, R. A. Guyer, and M. D. Miller, *Double sine-Gordon chain*, Phys. Rev. B **27**, 474 (1983).
- [42] D. K. Campbell, M. Peyrard, and P. Sodano, *Kink-antikink interactions in the double sine-Gordon equation*, Physica D **19**, 165-205 (1986).
- [43] C. Schütte and M. Garst, *Magnon-skyrmion scattering in chiral magnets*, Phys. Rev. B **90**, 094423 (2014).
- [44] M. N. Wilson, A. B. Butenko, A. N. Bogdanov, and T. L. Monchesky, *Chiral skyrmions in cubic helimagnet films: The role of uniaxial anisotropy*, Phys. Rev. B **89**, 094411 (2014).
- [45] S. Banerjee, J. Rowland, O. Erten, and M. Randeria, *Enhanced Stability of Skyrmions in Two-Dimensional Chiral Magnets with Rashba Spin-Orbit Coupling*, Phys. Rev. X **4**, 031045 (2014).
- [46] R. Keesman, A. O. Leonov, P. van Dieten, S. Buhrandt, G. T. Barkema, L. Fritz, and R. A. Duine, *Degeneracies and fluctuations of Néel skyrmions in confined geometries*, Phys. Rev. B **92**, 134405 (2015).
- [47] Y. Togawa, T. Koyama, K. Takayanagi, S. Mori, Y. Kousaka, J. Akimitsu, S. Nishihara, K. Inoue, A. S. Ovchinnikov, and J. Kishine, *Chiral magnetic soliton lattice on a chiral helimagnet*, Phys. Rev. Lett. **108**, 107202 (2012).
- [48] S. Schroeter and M. Garst, *Scattering of high-energy magnons off a magnetic skyrmion*, Low Temp. Phys. **41**, 817-825 (2015).
- [49] A. Roldán-Molina, A. S. Nunez, and J. Fernández-Rossier, *Topological spin waves in the atomic-scale magnetic skyrmion lattice*, New J. Phys. **18**, 045015 (2016).



# 7. Magnetic Skyrmions on a Two-Lane Racetrack

Jan Müller<sup>1</sup>

*Magnetic Skyrmions on a Two-Lane Racetrack*

New Journal of Physics 19, 025002 (2017)

Doi: 10.1088/1367-2630/aa5b55

Copyright: Creative Commons Attribution 3.0 Unported (CC-BY)<sup>2</sup>

## Abstract

Magnetic skyrmions are particle-like textures in the magnetization, characterized by a topological winding number. Nanometer-scale skyrmions have been observed at room temperature in magnetic multilayer structures. The combination of small size, topological quantization, and their efficient electric manipulation makes them interesting candidates for information carriers in high-performance memory devices. A skyrmion racetrack memory has been suggested where information is encoded in the distance between skyrmions moving in a one-dimensional nanostrip. Here, I propose an alternative design where skyrmions move in two (or more) parallel lanes and the information is stored in the lane number of each skyrmion. Such a multilane track can be constructed by controlling the height profile of the nanostrip. Repulsive skyrmion-skyrmion interactions in narrow nanostrips guarantee that skyrmions on different lanes cannot pass each other. Current pulses can be used to induce a lane change. Combining these elements provides a robust, efficient design of skyrmion-based storage devices.

## 7.1. Introduction

Magnetic storage devices today predominantly use the orientation of magnetic domains to encode huge amounts of information [1]. The information density is limited by the size of the domains, which not only have to be thermally stable, but should also support features as easy and non-mechanically controlled writing and reading of information. Magnetic skyrmions are particle-like textures in the magnetization [2–4] of nanometer size, which can be controlled by ultra-low electronic [5–7] or magnonic [8, 9] current densities. Due to these properties, they are often treated as promising candidates for information carriers in high-density, non-volatile, solid state storage devices [10, 11].

Since the experimental discovery of the skyrmion lattice in the chiral magnet MnSi at low temperatures [2], skyrmion lattices and also single skyrmions have been observed in many different systems. The energetic stability of skyrmions can be explained by Dzyaloshinskii-Moriya interaction (DMI), a spin-orbit coupling effect which arises either from broken inversion

---

<sup>1</sup>Institut für Theoretische Physik, Universität zu Köln, D-50937 Cologne, Germany

<sup>2</sup><https://creativecommons.org/licenses/by/3.0/>

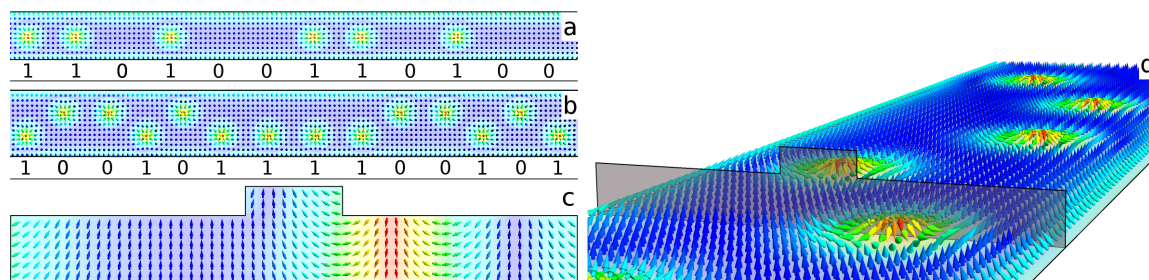


Figure 7.1.1.: Skyrmion racetrack models. The color code denotes the  $z$ -component of the magnetization. Only a subset of the simulated spins is shown. (a) One-lane skyrmion racetrack as proposed by Fert et al [11]: The information is encoded in the skyrmion distance. (b) Two-lane skyrmion racetrack (top view of bottom layer): Here the information is encoded in the lane index of each skyrmion. (c) Magnetization in the gray shaded profile of (d). (d) Magnetization in the bottom layer and profile (gray area) of the two-lane racetrack. The two lanes are separated by a region of increased height.

symmetry within the unit cell [12–14] (bulk DMI) or inversion broken by an interface [15] (interfacial DMI). In the latter case the thermal stability of skyrmions could be enhanced by a chiral stacking of thin films [16], so that skyrmions have recently been stabilized at room temperature in these multilayer systems [17].

Experimentally, a wide range of techniques is now used to image single skyrmions, e.g. Lorentz transmission electron microscopy [3], magnetic force microscopy [18], spin-polarized scanning tunnelling microscopy [4] or also X-ray based techniques, e.g. magnetic transmission soft X-ray microscopy [19]. For applications in memory devices it is important that single skyrmions can also be detected purely electronically exploiting their non-coplanar magnetoresistance [20] or the topological Hall effect [21].

On the road towards applications, controlled writing and deleting of single skyrmions has been shown to work in experiments using current injection [22]. The creation of chains of skyrmions at the edge of a sample has also been demonstrated experimentally [23]. Other processes for the creation of single skyrmions near the edge have been proposed theoretically [24, 25]. Also the driving of a chain of skyrmions by electric current in a nanowire was shown in experiments [19].

A prominent model for such a skyrmion-based storage device is the skyrmion racetrack [11], a nanostrip with a one-dimensional distribution of skyrmions, Fig. 7.1.1a. The information in this device is encoded in the distance between the individual skyrmions. By applying an electric current along the track, the train of skyrmions is pushed along the nanowire towards fixed read and write elements of the memory. Since the drift velocity of the skyrmions is increased by the Magnus force when they are pushed against the edges of the track, the translation can be designed more efficient by using perpendicular driving forces, e.g. by the spin Hall effect [26]. This way, a non-volatile, non-mechanic, and high-density magnetic memory device is created [11].

As the information in this device is encoded in the distance between skyrmions, this distance needs to be preserved on the operational time scales. Here the model has to fight problems: Thermal diffusion [27] and, more importantly, the noise created when operating the memory devices at high frequencies in a disordered environment will lead to a redistribution of the skyrmion distances. Furthermore the interaction of skyrmions is repulsive [28]. These problems can however be solved, if the continuous translational invariance along the track is reduced to

a discrete one. Devices based on the racetrack have been proposed, that for example use a regular arrangement of notches [29] or electric potentials [30, 31] to divide the track into a sequence of parking lots for skyrmions. Such obstacles can, however, hinder the motion of the skyrmions towards read or write elements. Due to the complex pulsed motion of the skyrmions also disorder effects may become more important [32, 33].

In this paper, I present a new ansatz for the application of skyrmions as information carriers in racetrack layout devices, which combines digital encoding of information with the benefits of continuous driving. We prepare a racetrack with not one but two lanes on the same strip, Fig. 7.1.1b, which are separated by a high enough energy barrier such that skyrmions do not change the lane by thermal activation. The barrier can have various origins, but in this paper we focus on an additional nanostrip on top of the racetrack. This creates a repulsive potential, Fig. 7.1.1d, complementary to the idea in Ref. [34] where an attractive potential is created from a scratch on the racetrack. In other skyrmion systems, however, the separation into lanes can even occur naturally [35, 36]. The two lanes are chosen to be sufficiently close that skyrmions on different lanes repulsively interact and therefore can not pass each other. The main difference to the original skyrmion racetrack concept is the encryption of information: It is encoded in the index of the occupied lane and not in the distance between skyrmions [11]. The information in this model is therefore unaffected by the exact distance between skyrmions. When applying an electric current to this densely packed sequence of skyrmions, they can still move along the track with all the speed-up benefits of the original skyrmion racetrack [26]. A writing element is installed on a fixed position, where it induces a lane change, for example by applying a strong electric current pulse. With the redefinition of the logic bit, thermal diffusion does not play a role anymore as long as the potentials are large enough. Also perturbations by disorder only become relevant if they are of the order of the artificial potentials between skyrmions and the nanostructure or other skyrmions, respectively.

## 7.2. Potentials and landscapes

The operation of a two-lane racetrack builds on (i) a potential which keeps the skyrmions on the lanes, (ii) the skyrmion-skyrmion repulsion both for skyrmions on the same and on different lanes and (iii) a mechanism to let a skyrmion change lanes. We calculate the racetrack and interaction potentials based on a micromagnetic model which considers the exchange coupling  $A$  of spins, interfacial DM interactions  $D$  and an external magnetic field  $H$ , see methods 7.5. I have checked that a realistic anisotropy does not change the main results qualitatively and thus neglect anisotropies and also dipolar interactions for simplicity. Within our setup, all results depend only on a small number of dimensionless parameters, see methods 7.5. Most importantly, all length scales are measured in units of  $1/Q = 2A/D$ , which ranges from 1-100 nm for different types of skyrmion realizations [17, 19, 33]. The field  $H = 0.75h_D$  is chosen such that it stabilizes single skyrmions and they do not decay into bimerons [37].

The effective skyrmion potential can be designed by changing the height and width of the track and the barrier. For fixed widths, we find that for a wide range of parameters, the dependence on the height of the track and the barrier can to high accuracy be obtained from a simple linear relation

$$V(y) = h_{\text{track}}v^{\text{track}}(y) + h_{\text{barrier}}v^{\text{barrier}}(y). \quad (7.2.1)$$

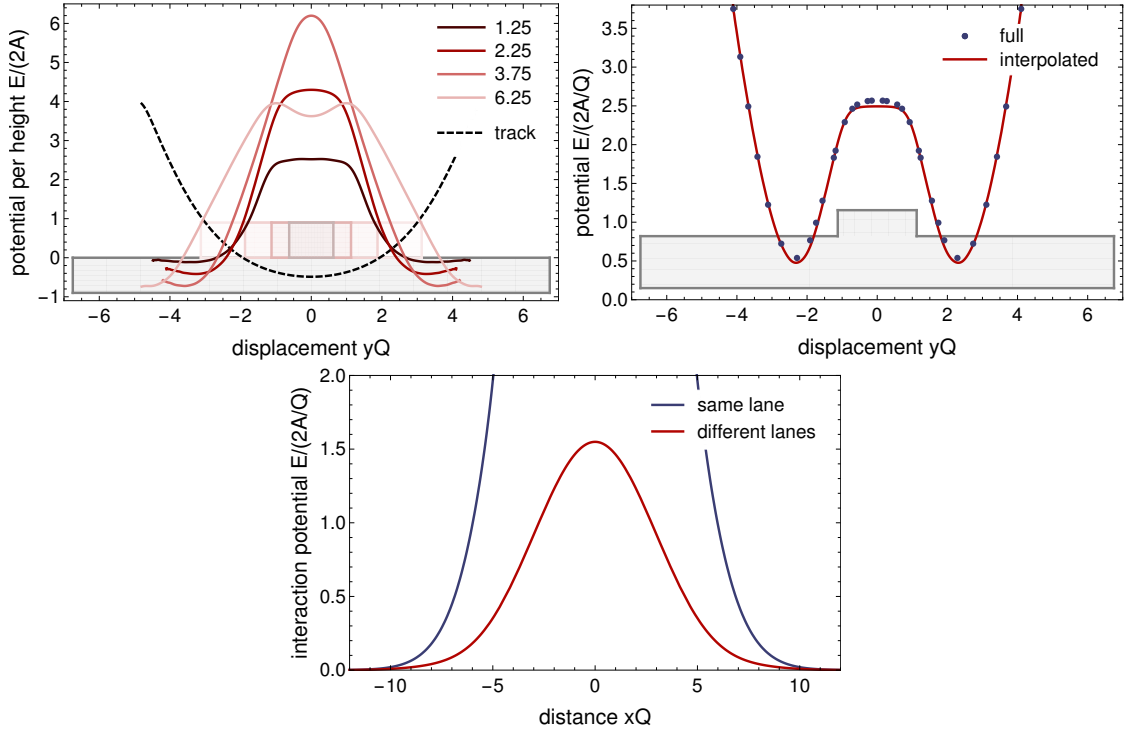


Figure 7.2.2.: Skymion potentials in a nanostructured racetrack. The effective potential of the skymion in the nanostructure can be obtained by adding potentials for the bottom layers and the barrier in the center scaled by their respective heights. All figures show results for a magnetic field  $H = 0.75h_D$ . Top-left panel: Potential per height for the bottom layers (dashed line) and various central barriers (solid lines). Bottom layer width is  $13.75/Q$  (gray shaded area); presented barrier widths are  $1.25/Q$ ,  $2.25/Q$ ,  $3.75/Q$ , and  $6.25/Q$  (colored shaded areas). Top-right panel: Comparison of the full skymion potential (dots) to the interpolated potential (line) for a nanostructure with bottom height  $1.50/Q$ , barrier height  $0.75/Q$ , barrier width  $2.25/Q$  (gray shaded area). Lower panel: Interaction potential of two skymions on the same lane (blue) and distinct lanes (red) as a function of distance along the track.

The simple additivity reflects that deformations of the magnetic texture along the track normal are small and it may be useful to design track potentials in experimental systems. Qualitatively the shape of the potentials can be understood from the fact that skymions are repelled by edges [28]. Therefore not only the track potential raises towards the edge of the track but also the barrier itself is repulsive, see Fig. 7.2.2a. The magnetic texture is continued from the bottom layers into the nanostructured upper layers, where effectively the skymion is in close proximity to an edge. We find the largest potential barriers if the strip and the skymion are of comparable width, compare Fig. 7.2.2a. If the strip is very broad, the skymion in the center of the track is again relatively far away from the edges in the barrier structure. The exact shape of the potential, however, strongly depends on the width of the strip.

In the following, we will focus on a particular example of a two-lane racetrack. We consider a track with a width of  $13.75/Q$  and a height of  $1.50/Q$ . The additional nanostructure on top is  $2.25/Q$  in width and  $0.75/Q$  in height, see Fig. 7.1.1c. From the scaling argument, Eq. 7.2.1, an estimation of the potential yields a double-well shape with two degenerate minima. As a check, we calculated the full potential of this geometry and find that the results are in very

good agreement, see Fig. 7.2.2b.

Finally, we also calculated the potential of two interacting skyrmions where we have to distinguish the two cases where skyrmions move in the same or in different lanes, see methods 7.5. In both cases the interactions are always repulsive, see Fig. 7.2.2c, and scale linearly in the height of the structure. Note that for the chosen parameters the repulsive interaction of skyrmions in different lanes is sizable and comparable to the height of the barrier between the lanes.

### 7.3. Operation of a two-lane racetrack

The above analysis of the separating potential provides a toolbox to engineer the barrier in a way that the order of the skyrmions is conserved with the help of repulsive potentials. For the operation of the two-lane racetrack as a memory device, a read and write protocol is needed.

The thermodynamic ground state of the two-lane racetrack is the polarized phase for parameters discussed above. Due to their topology, metastable skyrmions are, however, even at room temperatures very stable [19]. To initialize the track, i.e. fill it with skyrmions, I suggest to simply lower the magnetic field for a short period, see Fig. 7.3.3 and Supplementary Movie 1. As discussed in Ref. [25], this triggers an edge instability where magnons with finite momentum condense at both edges. The polarized phase then becomes unstable and a chain of merons invades from the edges. Technically, one has to add a small noise term or an edge inhomogeneity to trigger the magnon condensation. In an experimental realization this is done by defects and thermal fluctuations. By afterwards increasing the field above the critical field to its original value, each meron either pulls a second meron from the edge to form a skyrmion, or is pushed back into the edge and vanishes. Thereby the system automatically generates a finite density of skyrmions. We find that the average distance between skyrmions, here approximately  $8/Q$ , is equal to the wavelength of the edge instability. The initialized configuration, however, is random. Lowering the external field on only one lane generates a homogeneous initialization but is technically more difficult.

For a large operational speed and maximal durability, the read and write elements should be non-mechanic. I suggest to install them both in a combined operational unit as a write operation requires reading the state first. Reading information can be realized in various ways. One option is to use a tunnel contact on top or below each lane which exploits the non-collinear magnetoresistance of a skyrmion [20]. Alternatively, one could also use the topological Hall effect [21] to detect skyrmions.

Once a skyrmion is detected, one can decide if it has to switch lanes or already represents the desired information. The lane change, in general, can be induced by a variety of forces. While in insulating materials magnonic currents provide an extremely efficient method to control skyrmion motion in nanostructures [38], we restrict our considerations to only electric currents. The here considered write element consist of a pair of nanocontacts attached to both edges of the track, such that an applied electric current pulse flows predominantly through a narrow stripe as depicted in Fig. 7.3.4. The stripe has to be narrow such that only one skyrmion is affected by the current pulse. For our calculations, we choose a stripe with a width of  $5/Q$ . The minimal current density required to induce a lane change can be roughly estimated from the separating potential barrier  $V(y)$  in a Thiele approach [39]. The simplified Thiele equation, the equation of motion for the skyrmion coordinate  $\mathbf{R}$ , see methods 7.5, reads:

$$-\frac{1}{h_{\text{track}}}\frac{dV}{d\mathbf{R}} = \mathbf{G} \times (\dot{\mathbf{R}} - \mathbf{v}_s) + \mathcal{D}(\alpha\dot{\mathbf{R}} - \beta\mathbf{v}_s). \quad (7.3.2)$$

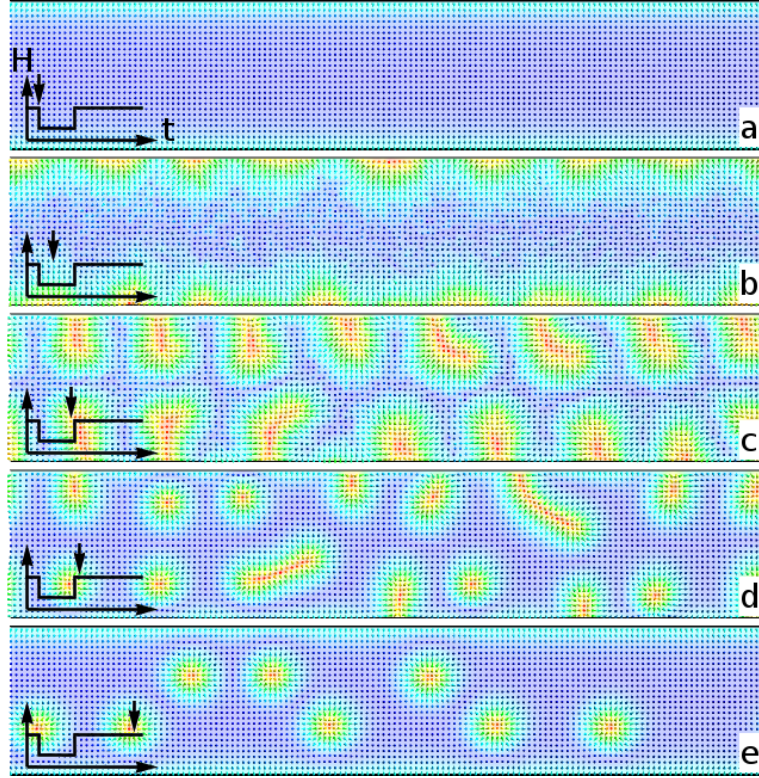


Figure 7.3.3.: Creation of skyrmions. Topview on the bottom layer at times  $t/t_D = 0, 30, 60, 80, 200$ . We start from the polarized ground state with an external magnetic field  $H = 0.75 h_D$  (a). The field is suddenly reduced to  $H = 0.3 h_D$  (b) (plus small fluctuations) which triggers the edge instability: Magnons condense at the edges (b) and merons enter (c). Upon suddenly increasing the field again to  $H = 0.75 h_D$ , the merons either leave the system or pull a second meron from the edge to turn into a skyrmion (d). The skyrmions redistribute over the two-lane track (e).

A suitable current density for a lane change  $v_s$  requires that during the lane change, the transversal shift of the skyrmion is smaller than the width of the current carrying region. Solving the Thiele equation numerically for various  $v_s$ , which can easily be done, we find that these requirements are fulfilled for  $v_s \geq 0.1 v_D$ . Comparing the simplified Thiele estimate to the full micromagnetic simulation, we find that they are in very good agreement, see Fig. 7.3.4, and the current density is indeed suitable for a writing process. The excellent agreement indicates that all skyrmion dynamics are entirely governed within the Thiele approach and its effective potentials. In the simulation, we applied the current pulse significantly longer than necessary for a lane change, to explore the skyrmion motion beyond the limits of our simple Thiele approach. Instead of leaving the track, the skyrmion pushes its neighbor (which is artificially fixed in the Thiele ansatz) and all following skyrmion in the train to the side, while the order is still preserved. Consequently, for a writing process a pulse time of  $\Delta t = 50 - 75 t_D$  is sufficient, see Figs. 7.3.4(a-d), but the writing operation is very robust against disturbance in the process timing.

Since the write and read elements are fixed in position, the skyrmions have to be moved. The current-driven motion of skyrmions in a nanostructure has been nicely discussed in Refs. [40] and [26]. As previously pointed out by the authors, one can obtain much higher velocities

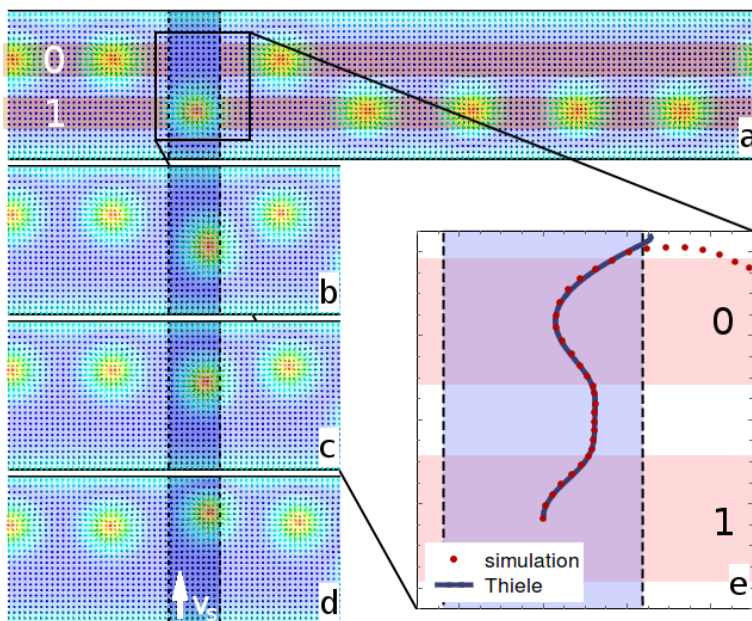


Figure 7.3.4.: Writing information. An electric current  $j$  flows in the blue shaded area ( $\mathbf{v}_s = 0.1v_D \hat{e}_y$ ). Initial state (a) and snapshots (b-d) in time steps  $\Delta t = 25 t_D$ : Lane change of a skyrmion under applied current. Comparison (e) of the skyrmion trajectories obtained from a simplified Thiele model (blue) and the micromagnetic simulation (red).

for skyrmions moving in racetracks compared to freely moving skyrmions. Alternatively, the skyrmions can be driven highly efficient by a magnonic current [9, 38]. Using one of these methods, the bit sequence is driven along the two lanes, see also Supplementary Movie 2.

## 7.4. Summary

I propose a new approach towards skyrmion-based storage devices. The two-lane skyrmion racetrack uses the displacement of skyrmions in a racetrack relative to the center of the track to encode information. Therefore, in contrast to previous models, there is no need to ensure a constant distance between single skyrmions. I provide methods to calculate the potential barrier between different lanes as well as the interaction between skyrmions in the lanes. In this paper I show that these potentials can be used to efficiently design such a two-lane racetrack and to determine current pulses to write information. With these informations I explain how to operate a particular example of a two-lane racetrack by electric current pulses and confirm the results by micromagnetic simulations. Despite that the model we used throughout this work does not take into account uniaxial anisotropy or dipolar interactions, which may be of interest for realistic systems, the idea presented here is universal. The idea of a two-lane racetrack combines the powerful idea of a skyrmion racetrack with the promising properties of the skyrmion lattices, i.e. low depinning current thresholds and highest information carrier densities whilst the information is protected against perturbations. I believe that designs based on the two-lane skyrmion racetrack are promising candidates for a future skyrmion-based information technology.

## 7.5. Methods

### 7.5.1. Model and units

The starting point of our analysis is a non-linear sigma model in which the magnetization is described by the normalized vector field  $\hat{n}^T = (\hat{n}_x, \hat{n}_y, \hat{n}_z)$  with  $\|\hat{n}\| = 1$ . The free energy functional,  $F = \int d^3\vec{r}\mathcal{F}$ , with the minimal set of interactions that we choose in this work, contains only the ferromagnetic exchange interaction  $A$ , interfacial Dzyaloshinskii-Moriya interaction  $D$  and an external magnetic field  $H$ :

$$\mathcal{F} = A(\partial_\alpha \hat{n}_\beta)^2 + D(\hat{n}_\gamma \partial_\gamma \hat{n}_z - \hat{n}_z \partial_\gamma \hat{n}_\gamma) - \mu_0 H M \hat{n}_z, \quad (7.5.3)$$

with  $\alpha, \beta = x, y, z$ ,  $\gamma = x, y$  and  $M$  the saturation magnetization. The scales for momentum, total energy, and magnetic field are chosen in accordance with previous works

$$Q = \frac{D}{2A}, \quad E_D = \frac{2A}{Q}, \quad h_D = \frac{2AQ^2}{\mu_0 M} \quad (7.5.4)$$

and are used throughout the work. From the LLG equation

$$\begin{aligned} [\partial_t + (\mathbf{v}_s \cdot \nabla)] \hat{n} = & - \gamma \hat{n} \times \mathbf{B}_{\text{eff}} \\ & + \alpha \hat{n} \times \left[ \partial_t \hat{n} + \frac{\beta}{\alpha} (\mathbf{v}_s \cdot \nabla) \hat{n} \right], \end{aligned} \quad (7.5.5)$$

with the effective magnetic field  $\vec{B}_{\text{eff}} = -\frac{1}{M} \delta F / \delta \hat{n}$  we deduce the dependence of the drift velocity of the spin currents  $\mathbf{v}_s$  and the time  $t$  on the spin density  $s = \frac{M}{\gamma}$ :

$$t_D = \frac{s}{2AQ^2}, \quad v_D = \frac{2AQ}{s}. \quad (7.5.6)$$

Note that  $s$  is the spin per unit cell of the atomic lattice, i.e. independent of  $Q$ .

With realistic values [16] for the exchange coupling  $A = 10 \text{ pJ m}^{-1}$ , interfacial DMI  $D = 1.9 \text{ mJ m}^{-2}$  and a saturation magnetization of  $M = 956 \text{ kA/m}$ , the corresponding magnetic field that we apply in our simulations is  $\mu_0 H = 0.75 \frac{2AQ^2}{M} = 0.14 \text{ T}$ . Note that in systems with uniaxial anisotropy skyrmions of similar size can be realized with considerably smaller (or even vanishing) external magnetic field. Here, the unit of length corresponds to approximately  $1/Q = 10.5 \text{ nm}$ . Hence our simulated racetrack has a width of  $13.75/Q = 145 \text{ nm}$  and a height of  $1.5/Q = 16 \text{ nm}$ , while the strip is of  $2.25/Q = 24 \text{ nm}$  width and  $0.75/Q = 8 \text{ nm}$  height. With the unit of energy  $E_D = 2A/Q = 2.1 \times 10^{-19} \text{ J}$  we obtain an activation energy for the barrier between the lanes of about  $2E_D/k_B = 30,000 \text{ K}$  implying thermal stability at room temperature. Finally, with the unit of time  $t_D = \frac{s}{2AQ^2} = 0.03 \text{ ns}$  (assuming  $g = 2$ ) the writing process with minimal current (of the order of  $10^{10} \text{ A/m}^2$ ) as described in the main text takes only  $1.5 - 2.2 \text{ ns}$ .

### 7.5.2. Micromagnetic simulations

For simulations of the continuous model, we discretize the magnetization  $\hat{n}$  to Heisenberg spins on a cubic lattice. We approximate the derivatives in Eqs. 7.5.3 and 7.5.5 by finite differences. The lattice constant is  $a = 0.25/Q$  throughout the paper in all three spatial directions. It is

small enough that the results are independent of the discretization length. We have written a code which integrates the discretized LLG equation over time with a fourth order Runge-Kutta-method. The boundary conditions are such that the wire is periodic in the extended direction and open in the other directions. The initial states in Sec. 7.2 are polarized along the direction of the magnetic field. For the energies as a function of the skyrmion position, we manually inserted a single skyrmion and for the skyrmion interaction two skyrmions, respectively. The initial state in Sec. 7.3 is polarized and skyrmions are created automatically as a result of the system dynamics. In the creation process, we added a small random fluctuating field to  $\mathbf{B}_{\text{eff}}$ , see Eq. 7.5.5.

### 7.5.3. Calculation of the potentials

We calculated the skyrmion potential  $V(y)$  numerically as the energy difference between a skyrmion at a given displacement from the center of the track  $y$  and the polarized state without skyrmions:

$$V(y) = E_{\text{skyrmion}}(y) - E_{\text{polarized}} \quad (7.5.7)$$

The position of a skyrmion is here defined as the coordinate in the bottom layer, where the magnetization points antiparallel to the external field  $H$ . Previous works fixed this center of the skyrmion to evaluate the potential at various positions [32, 41]. In this setup, however, the forces from the nanostructures are large compared to the artificial pinning forces. Therefore we can not fix the skyrmion coordinate. We resolve this problem by a dynamical evaluation of the potential, i.e. we record the energy while running a simulation of the Landau-Lifshitz-Gilbert equation in which the skyrmion moves adiabatically, i.e. slow enough that no internal modes are excited. In order to guide the skyrmion to different positions, we apply a sufficiently large current density, here  $v_s = 0.032v_D$  and  $\alpha = \beta = 0.1$  for the potential of the track. For these potentials of the skyrmion-skyrmion interaction, we define an inhomogeneous current density ( $v_s = 0.128v_D$ ) which either drives the skyrmions into a collision if they start on the same lane or drives them in different directions if they start on different lanes, such that they pass each other. Note that when running on different lanes, the magnus force breaks the mirror symmetry of the motion, i.e. it makes a difference if the skyrmions run on the right or the left lane. For skyrmions on the same lane, the magnus force can induce a lane change if the damping is low ( $\alpha \lesssim 1$ ). As we are interested in the low energy limit, we suppress these effects by a relatively large damping  $\alpha = \beta = 2$ .

### 7.5.4. Thiele analysis

In the Thiele analysis one assumes that the dynamics of the magnetic texture reduces to an effective particle coordinate  $\mathbf{R}(t)$  in the two-dimensional plane,  $\hat{n}(\mathbf{r} - \mathbf{R}(t))$ . This assumption is clearly violated in the system, but as the skyrmion centers are to good approximation local and rigid objects, it still holds to large extents. Along the track normal, we further assume that the magnetic texture is mainly constant, hence  $\mathbf{R}(t)$  is equal in all layers of total height  $h_{\text{track}}$ . Thus the system is effectively two-dimensional. The Thiele equation is then recovered by first multiplying the LLG equation from the left with  $\hat{n} \times$  and then projecting it down onto the translational mode by multiplying the equation with  $\frac{d\hat{n}}{dR_i}$  and integrating over space  $\int d^3r$ . Finally, this results in the equation of motion for the skyrmion coordinate  $\mathbf{R}(t)$  in the

two-dimensional track plane  $(x, y)$ :

$$-\frac{1}{h_{\text{track}}}\frac{dV}{d\mathbf{R}} = \mathbf{G} \times (\dot{\mathbf{R}} - \mathbf{v}_s) + \mathcal{D}(\alpha\dot{\mathbf{R}} - \beta\mathbf{v}_s) \quad (7.5.8)$$

where only the potential  $V(\mathbf{R})$  is obtained from a full three-dimensional calculation. We approximated the values for  $\mathbf{G}$  and  $\mathcal{D}$  with the values for a single skyrmion in an infinite extended polarized background in two dimensions. For the analysis of a lane change, we assume a constant current density in the whole system. However we note that the Thiele ansatz then only holds as long as the skyrmion is at sufficient distance ( $\gtrsim 1/Q$ ) to the edges of the area where the current density is actually applied.

### Acknowledgements

I thank A. Rosch, V. Cros, A. Fert, and M. Kläui for the stimulating discussions, and Deutsche Telekom Stiftung and the Bonn-Cologne Graduate School of Physics and Astronomy BCGS for financial support. I furthermore thank the Regional Computing Center of the University of Cologne (RRZK) for providing computing time on the DFG-funded High Performance Computing (HPC) system CHEOPS as well as support. I also gratefully acknowledge support by the DFG within the CRC 1238 (project C04).

### Author contributions

J.M. performed the numerical calculations, analyzed the data and wrote the manuscript.

### Competing financial interests

J.M. has a German patent application related to this work, number 10 2016 200 161.2, 'Logischer Speicher mit einer Vielzahl von magnetischen Skyrmionen'.

## 7.6. Bibliography

- [1] C. Chappert, A. Fert, and F. N. Van Dau, *The emergence of spin electronics in data storage*, Nat. Mater. **6**, 813-823 (2007).
- [2] S. Mühlbauer, B. Binz, F. Jonietz, C. Pfleiderer, A. Rosch, A. Neubauer, R. Georgii, and P. Böni, *Skyrmion lattice in a chiral magnet*, Science **323**, 915-919 (2009).
- [3] X. Z. Yu, Y. Onose, N. Kanazawa, J. H. Park, J. H. Han, Y. Matsui, N. Nagaosa, and Y. Tokura, *Real-space observation of a two-dimensional skyrmion crystal*, Nature **465**, 901-904 (2010).
- [4] S. Heinze, K. von Bergmann, M. Menzel, J. Brede, A. Kubetzka, R. Wiesendanger, G. Bihlmayer, and S. Blügel, *Spontaneous atomic-scale magnetic skyrmion lattice in two dimensions*, Nat. Phys. **7**, 713-718 (2011).
- [5] F. Jonietz, S. Mühlbauer, C. Pfleiderer, A. Neubauer, W. Münzer, A. Bauer, T. Adams, R. Georgii, P. Böni, R. A. Duine, K. Everschor, M. Garst, and A. Rosch, *Spin transfer torques in MnSi at ultralow current densities*, Science **330**, 1648-1651 (2010).
- [6] X. Z. Yu, N. Kanazawa, W. Z. Zhang, T. Nagai, T. Hara, K. Kimoto, Y. Matsui, Y. Onose, and Y. Tokura, *Skyrmion flow near room temperature in an ultralow current density*, Nat. Commun. **3**, 988 (2012).
- [7] J. Iwasaki, M. Mochizuki, and N. Nagaosa, *Universal current-velocity relation of skyrmion motion in chiral magnets*, Nat. Commun. **4**, 1463 (2013).

- 
- [8] K. Everschor, M. Garst, B. Binz, F. Jonietz, S. Mühlbauer, C. Pfleiderer, and A. Rosch, *Rotating skyrmion lattices by spin torques and field or temperature gradients*, Phys. Rev. B **86**, 054432 (2012).
- [9] C. Schütte and M. Garst, *Magnon-skyrmion scattering in chiral magnets*, Phys. Rev. B **90**, 094423 (2014).
- [10] N. S. Kiselev, A. N. Bogdanov, R. Schäfer, and U. K. Rößler, *Chiral skyrmions in thin magnetic films: new objects for magnetic storage technologies?*, J. Phys. D **44**, 392001 (2011).
- [11] A. Fert, V. Cros, and J. Sampaio, *Skyrmions on the track*, Nat. Nano. **8**, 152-156 (2013).
- [12] A. N. Bogdanov and A. Hubert, *Thermodynamically stable magnetic vortex states in magnetic crystals*, J. Magn. Magn. Mater. **138**, 255-269 (1994).
- [13] U. K. Rößler, A. N. Bogdanov, and C. Pfleiderer, *Spontaneous skyrmion ground states in magnetic metals*, Nature **442**, 797-801 (2006).
- [14] J.-H. Han, J. Zang, Z. Yang, J.-H. Park, and N. Nagaosa, *Skyrmion lattice in a two-dimensional chiral magnet*, Phys. Rev. B **82**, 094429 (2010).
- [15] A. Crépieux and C. Lacroix, *Dzyaloshinskii-Moriya interactions induced by symmetry breaking at a surface*, J. Magn. Magn. Mater. **182**, 341-349 (1998).
- [16] H. Yang, O. Boulle, V. Cros, A. Fert, and M. Chshiev, *Controlling Dzyaloshinskii-Moriya interaction via chirality dependent layer stacking, insulator capping and electric field*, Arxiv e-print (2016), arXiv:1603.01847.
- [17] C. Moreau-Luchaire, C. Moutafis, N. Reyren, J. Sampaio, C. A. F. Vaz, N. Van Horne, K. Bouzehouane, K. Garcia, C. Deranlot, P. Warnicke, P. Wohlhüter, J.-M. George, M. Weigand, J. Raabe, V. Cros, and A. Fert, *Additive interfacial chiral interaction in multilayers for stabilization of small individual skyrmions at room temperature*, Nat. Nano. **11**, 444-448 (2016).
- [18] P. Milde, D. Köhler, J. Seidel, L. M. Eng, A. Bauer, A. Chacon, J. Kindervater, S. Mühlbauer, C. Pfleiderer, S. Buhrandt, C. Schütte, and A. Rosch, *Unwinding of a skyrmion lattice by magnetic monopoles*, Science **340**, 1076 (2013).
- [19] S. Woo, K. Litzius, B. Krüger, M.-Y. Im, L. Caretta, K. Richter, M. Mann, A. Krone, R. M. Reeve, M. Weigand, P. Agrawal, I. Lemesch, M.-A. Mawass, P. Fischer, M. Kläui, and G. S. D. Beach, *Observation of room-temperature magnetic skyrmions and their current-driven dynamics in ultrathin metallic ferromagnets*, Nat. Mater. **15**, 501-506 (2016).
- [20] C. Hanneken, F. Otte, A. Kubetzka, B. Dupé, N. Romming, K. von Bergmann, R. Wiesendanger, and S. Heinze, *Electrical detection of magnetic skyrmions by tunnelling non-collinear magnetoresistance*, Nat. Nano. **10**, 1039-1042 (2015).
- [21] A. Neubauer, C. Pfleiderer, B. Binz, A. Rosch, R. Ritz, P. G. Niklowitz, and P. Böni, *Topological Hall Effect in the A Phase of MnSi*, Phys. Rev. Lett. **102**, 186602 (2009).
- [22] N. Romming, C. Hanneken, M. Menzel, J. E. Bickel, B. Wolter, K. von Bergmann, A. Kubetzka, and R. Wiesendanger, *Writing and deleting single magnetic skyrmions*, Science **341**, 636-639 (2013).
- [23] H. Du, R. Che, L. Kong, X. Zhao, C. Jin, C. Wang, J. Yang, W. Ning, R. Li, C. Jin, X. Chen, J. Zang, Y. Zhang, and M. Tian, *Edge-mediated skyrmion chain and its collective dynamics in a confined geometry*, Nat. Commun. **6**, 8504 (2015).
- [24] W. Koshibae, Y. Kaneko, J. Iwasaki, M. Kawasaki, Y. Tokura, and N. Nagaosa, *Memory functions of magnetic skyrmions*, Jpn. J. Appl. Phys. **54**, 053001 (2015).
- [25] J. Müller, A. Rosch, and M. Garst, *Edge instabilities and skyrmion creation in magnetic layers*, New J. Phys. **18**, 065006 (2016).
- [26] J. Sampaio, V. Cros, S. Rohart, A. Thiaville, and A. Fert, *Nucleation, stability and current-induced motion of isolated magnetic skyrmions in nanostructures*, Nat. Nano. **8**, 839-844 (2013).
- [27] C. Schütte, J. Iwasaki, A. Rosch, and N. Nagaosa, *Inertia, diffusion, and dynamics of a driven skyrmion*, Phys. Rev. B **90**, 174434 (2014).
-

- [28] X. Zhang, G. P. Zhao, H. Fangohr, J. P. Liu, W. X. Xia, J. Xia, and F. J. Morvan, *Skyrmion-skyrmion and skyrmion-edge repulsions in skyrmion-based racetrack memory*, Sci. Rep. **5**, 7643 (2015).
- [29] H. T. Fook, W. L. Gan, and W. S. Lew, *Gateable Skyrmion Transport via Field-induced Potential Barrier Modulation*, Sci. Rep. **6**, 21099 (2016).
- [30] W. Kang, Y. Huang, C. Zheng, W. Lv, N. Lei, Y. Zhang, X. Zhang, Y. Zhou, and W. Zhao, *Voltage Controlled Magnetic Skyrmion Motion for Racetrack Memory*, Sci. Rep. **6**, 23164 (2016).
- [31] W. Kang, C. Zheng, Y. Huang, X. Zhang, Y. Zhou, W. Lv, and W. Zhao, *Complementary Skyrmion Racetrack Memory With Voltage Manipulation*, IEEE El. Dev. Lett. **37**, 924-927 (2016).
- [32] J. Müller and A. Rosch, *Capturing of a magnetic skyrmion with a hole*, Phys. Rev. B **91**, 054410 (2015).
- [33] C. Hanneken, A. Kubetzka, K. von Bergmann, and R. Wiesendanger, *Pinning and movement of individual nanoscale magnetic skyrmions via defects*, New J. Phys. **18**, 055009 (2016).
- [34] I. Purnama, W. L. Gan, D. W. Wong, and W. S. Lew, *Guided current-induced skyrmion motion in 1D potential well*, Sci. Rep. **5**, 10620 (2015).
- [35] A. O. Leonov, J. C. Loudon, and A. N. Bogdanov, *Spintronics via non-axisymmetric chiral skyrmions*, Appl. Phys. Lett. **109**, 172404 (2016).
- [36] A. O. Leonov and M. Mostovoy, *Edge states and skyrmion dynamics in nanostripes of frustrated magnets*, Arxiv e-print (2016), arXiv:1605.08645.
- [37] M. Ezawa, *Compact merons and skyrmions in thin chiral magnetic films*, Phys. Rev. B **83**, 100408 (2011).
- [38] X. Zhang, M. Ezawa, D. Xiao, G. P. Zhao, Y. Liu, and Y. Zhou, *All-magnetic control of skyrmions in nanowires by a spin wave*, Nanotechnology **26**, 225701 (2015).
- [39] A. A. Thiele, *Steady-state motion of magnetic domains*, Phys. Rev. Lett. **30**, 230-233 (1973).
- [40] J. Iwasaki, M. Mochizuki, and N. Nagaosa, *Current-induced skyrmion dynamics in constricted geometries*, Nat. Nanotech. **8**, 742-747 (2013).
- [41] S.-Z. Lin, C. Reichhardt, C. D. Batista, and A. Saxena, *Particle model for skyrmions in metallic chiral magnets: Dynamics, pinning, and creep*, Phys. Rev. B **87**, 214419 (2013).

## 8. Shape-dependence of the barrier for skyrmions on a two-lane racetrack

Jan Müller<sup>1</sup>

*Shape-dependence of the barrier for skyrmions on a two-lane racetrack*

Spintronics IX, edited by Henri-Jean Drouhin, Jean-Eric Wegrowe, Manijeh Razeghi, Proc. of SPIE Vol. 9931, 993136, (2016)

Copyright 2016 Society of Photo-Optical Instrumentation Engineers. One print or electronic copy may be made for personal use only. Systematic reproduction and distribution, duplication of any material in this paper for a fee or for commercial purposes, or modification of the content of the paper are prohibited.

Online abstract: <http://dx.doi.org/10.1117/12.2237624>

### Abstract

Single magnetic skyrmions are localized whirls in the magnetization with an integer winding number. They have been observed on nano-meter scales up to room temperature in multilayer structures. Due to their small size, topological winding number, and their ability to be manipulated by extremely tiny forces, they are often called interesting candidates for future memory devices. The two-lane racetrack has to exhibit two lanes that are separated by an energy barrier. The information is then encoded in the position of a skyrmion which is located in one of these close-by lanes. The artificial barrier between the lanes can be created by an additional nanostrip on top of the track. Here we study the dependence of the potential barrier on the shape of the additional nanostrip, calculating the potentials for a rectangular, triangular, and parabolic cross section, as well as interpolations between the first two. We find that a narrow barrier is always repulsive and that the height of the potential strongly depends on the shape of the nanostrip, whereas the shape of the potential is more universal. We finally show that the shape-dependence is redundant for possible applications.

### 8.1. Introduction

The ever growing demand for more storage capacity on steadily shrinking scales in electronic devices requires information carrying units at minimal size. But even on the smallest scales, the information in these units needs to be controllably read and written, while at the same time it has to be stable against thermal fluctuations. Particle-like whirls with integer topological winding number in the magnetization, so-called *skyrmions* [1–3], were observed on scales down to nanometers and can be created and destroyed on demand [4]. Their efficient coupling to electronic [5–7] or magnonic [8, 9] currents makes ultra-low current densities sufficient to manipulate the motion of skyrmions. Therefore they are often discussed as possible candidates for

---

<sup>1</sup>Institut für Theoretische Physik, Universität zu Köln, D-50937 Cologne, Germany

information carriers in future high-density, non-volatile memory devices [10], and in particular due to their high mobility in racetrack layouts [11, 12].

Chiral skyrmions have been predicted theoretically in chiral magnets [13, 14] and were experimentally discovered as the skyrmion lattice phase in the chiral magnet MnSi [1]. They are stabilized by Dzyaloshinskii-Moriya interaction (DMI) which favors a twisting in the magnetization and arises due to spin-orbit coupling combined with broken inversion symmetry. The broken inversion symmetry, however, does not necessarily arise from the broken inversion inside the unit cell as in MnSi. Also interfaces (or surfaces) break inversion symmetry and contribute to an interfacial DMI [15] (iDMI). A system with iDMI can be constructed in multilayer systems, where the thermal stability of skyrmion is enhanced by chiral stacking of the multilayers [16] which lead to the stabilization of single skyrmions at room temperature [17]. Since then, even the driving of skyrmions by an electric current in a racetrack was shown in experiments [18] and for detecting a skyrmion in a future device, their non-coplanar magnetoresistance [19] is a delightful candidate.

As an orthogonal ansatz to the skyrmion racetrack [11], which is a nanowire with a sequence of skyrmions in fixed distances, the two-lane skyrmion racetrack [12] was proposed. Here the information is not encoded in the distance between skyrmions but by the lane on which the skyrmion moves. The two lanes are separated by an energy barrier that is large enough to suppress thermally activated switching of lanes. In micromagnetic simulations the energy barrier was achieved by an additional strip on top of the racetrack, see Fig. 8.1.1, which creates a repulsive potential for skyrmions. To preserve the order of skyrmions, the two lanes are close enough such that the repulsive interaction between skyrmions on different lanes prevents them from overtaking each other.

A challenging task for the construction of a two-lane racetrack seems to be the preparation of the nanostrip, since the originally proposed geometry demands sharp edges and flat surfaces which in practice is hard to prepare. Hence the aim of this paper is to analyze how the energy barrier depends on the shape of the physical barrier and in particular if this concept is robust against deviations from the actual shape.

## 8.2. The Model

We consider a magnetic multilayer system with interfacial Dzyaloshinskii-Moriya interaction (iDMI) which arises from the broken inversion symmetry at the interfaces of the stacked layers. The dominant interaction in the system is the ferromagnetic exchange  $A$ , followed by the much weaker iDMI  $D$ . Since the latter interaction prefers the magnetic moments in the system to be pairwise orthogonal, the uniform texture that is preferred by the ferromagnetic exchange

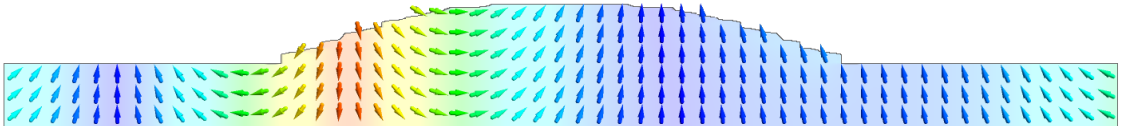


Figure 8.1.1.: Example of the magnetization (arrows) in a two-lane racetrack with a non-rectangular nanostrip on top. Side view on a cut ( $y$ - $z$ -plane) through the two-lane racetrack. The color encodes the  $z$ -component of the magnetization. Result from micromagnetic simulation, see Sec. 8.2. The arrows picture the magnetization on a subset of simulated lattice sites.

as a compromise winds into smoothly twisting spirals. The wavelength of these spirals,  $\lambda = 1/Q = 2A/D$ , defines the length scale on which the magnetization changes. It ranges from 1-100 nm for different systems with skyrmions [17, 18, 20]. Since typically this magnetic length  $\lambda$  is much larger than the length scale of the underlying atomic lattice  $a$ ,  $\lambda \gg a$ , we can apply a continuous theory in which the magnetization is represented by a continuous vector field  $\mathbf{M}(\mathbf{r})$  with  $\|\mathbf{M}\| = M$ . Furthermore, including an external magnetic field  $\mu_0 H$  and uniaxial anisotropy  $K$ , the free energy functional,  $F = \int d^3\vec{r} \mathcal{F}$ , reads

$$\mathcal{F} = A(\partial_\alpha \hat{n}_\beta)^2 + D(\hat{n}_i \partial_i \hat{n}_z - \hat{n}_z \partial_i \hat{n}_i) - \mu_0 H M \hat{n}_z - K \hat{n}_z^2, \quad (8.2.1)$$

with the normalized magnetization  $\hat{n} = \mathbf{M}/M$  and summation indices  $\alpha, \beta = x, y, z$  and  $i = x, y$ . In the following we will neglect the anisotropy term,  $K = 0$ , since it does not change our results qualitatively and apply a magnetic field to stabilize the polarized phase and single skyrmions therein. The dynamics of the system (including an applied spin current with drift velocity  $\mathbf{v}_s$ ) are governed by the Landau-Lifshitz-Gilbert (LLG) equation

$$[\partial_t + (\mathbf{v}_s \cdot \nabla)] \hat{n} = -\gamma \hat{n} \times \mathbf{B}_{\text{eff}} + \alpha \hat{n} \times \left[ \partial_t \hat{n} + \frac{\beta}{\alpha} (\mathbf{v}_s \cdot \nabla) \hat{n} \right], \quad (8.2.2)$$

with the effective magnetic field  $\vec{B}_{\text{eff}} = -\frac{1}{M} \delta F / \delta \hat{n}$  and the spin density  $s = \frac{M}{\gamma}$ . The phenomenologic adiabatic and non-adiabatic damping coefficients  $\alpha$  and  $\beta$  are chosen equally  $\alpha = \beta = 0.1$  throughout this paper. Since the continuous field theory can be rescaled, the units we use in the following are in accordance with previous works the dimensionless momentum  $Q = \frac{D}{2A}$ , total energy  $E_D = \frac{2A}{Q}$ , magnetic field  $h_D = \frac{2AQ^2}{\mu_0 M}$ , time  $t_D = \frac{s}{2AQ^2}$ , and velocity  $v_D = \frac{2AQ}{s}$ . In the whole paper, the magnetic field is set to  $h = 0.75h_D$ .

For the evaluation of the different potentials that are discussed in this work we use the same methods as in Ref. [12]. However, in order to be able to resolve the nanostrip sufficiently detailed for an analysis of the shape-dependence, we choose the numeric lattice discretization equal in the plane of the track,  $a_x = a_y = 0.25/Q$ , and finer in the z-direction perpendicular to the track,  $a_z = 0.05/Q$ . With these discretizations we simulate a single skyrmion in a two-lane racetrack with unpatterned bottom layers of width  $13.75/Q$  and height  $0.75/Q$  and on top of that *rectangular*, *triangular*, or *parabolic* barriers of height  $0.75/Q$  and various widths, see Fig. 8.2.2 left. Generally, the geometry has more tunable parameters, but it has been shown in Ref. [12] that this width of the bottom layers works well for a two-lane racetrack. The heights of the bottom and top part of the nanostructure could be varied in the simulations, but it has furthermore been shown that the potential obeys a scaling law, see Fig. 8.2.2 right. Due to the extreme robustness of the magnetic structure against deformations along the z-direction, the total potential can be expressed as a superposition of the potential from the bottom layers and the top layers, each scaled with their respective heights:

$$V(y) = h_{\text{track}} v^{\text{track}}(y) + h_{\text{barrier}} v^{\text{barrier}}(y). \quad (8.2.3)$$

Since we want to analyze the impact of the shape of the top structure on the potential, we will in the following exclusively focus on the potential per height of this upper layers,  $v^{\text{barrier}}(y)$ .

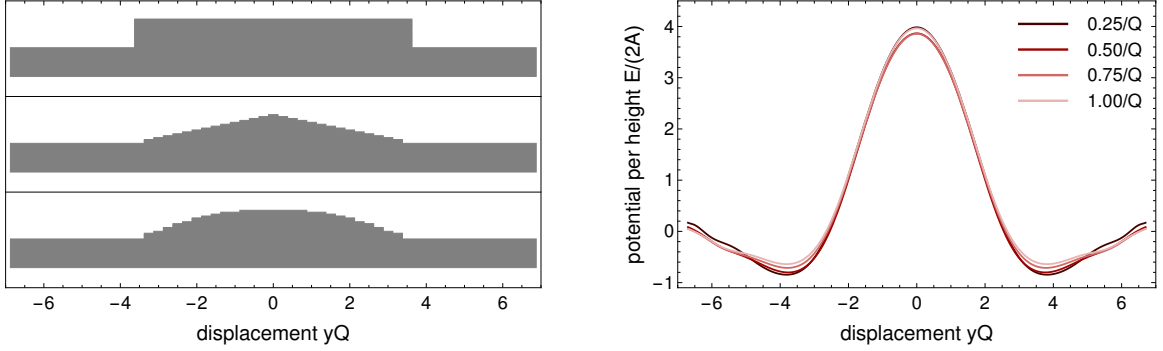


Figure 8.2.2.: Left: The shapes of the nanostructures on top of the racetrack (*rectangular*, *triangular*, and *parabolic*) that are considered in this paper, here all shown at width  $7.25/Q$ . Right: Linear scaling of the potentials with the height of the structure. Plot shows the potential per height calculated for the triangular barrier with width  $6.25/Q$  and various heights as shown in the inset.

## 8.3. Barriers and potentials

### 8.3.1. Comparison of the different barriers

The potentials per height,  $v^{\text{barrier}}(y)$ , for all three considered shapes of nanostrips (rectangular, triangular, parabolic) are shown in the first three plots in Fig. 8.3.3 for the whole range of possible widths, i.e. ranging from a narrow peak with a width of only three numeric discretization lengths (black curves) to a broad shape which covers the whole racetrack underneath (very light curves). The potential per height of the bottom layers of the track,  $v^{\text{track}}(y)$ , is not shown explicitly but is approximately given by the potential of the broadest rectangular strip.

The exact dependence of the potential on the geometry of the strip is for all three cases very complex. For low widths, which were considered the important regime for a two-lane potential, a repulsive peak grows with the width in the center of the track, independent of the shape of the nanostrip. The height of the peak, however, differs for the various cases, see Fig. 8.3.3 bottom right, up to a factor two: In the narrow peak is not much room for the magnetization to develop structures that adapt to the shape. This effect can more likely be explained by the fact that the volume of the triangular nanostrip is twice as low as in the rectangular case. Consequently, for a two-lane racetrack any of the different shapes can in principle be considered as suitable for producing the desired energy barrier, if the heights are scaled properly.

If the nanostrip is about half the width of the total racetrack, the different shapes start to develop a more characteristic potential per height,  $v^{\text{barrier}}(y)$ , see Fig. 8.3.3 bottom right. In the case of the rectangular nanostrip, the repulsive peak in the center decays into two peaks which with growing width move apart to the edges of the racetrack. The result is a local minimum in the center of the track which grows in both, depth and width. In the limit where the width of the nanostrip is equal to the width of the racetrack the potential minimum in the center is the reason why skyrmions in a racetrack are repelled from the edges and it becomes even the global minimum, i.e. the racetrack prefers to have skyrmions for this choice of magnetic field [12],  $h = 0.75h_D$ .

Differently, the center of the triangular geometry, where the only edge in the continuous limit is located, remains repulsive for all widths and the peak in the center is always sharper than the

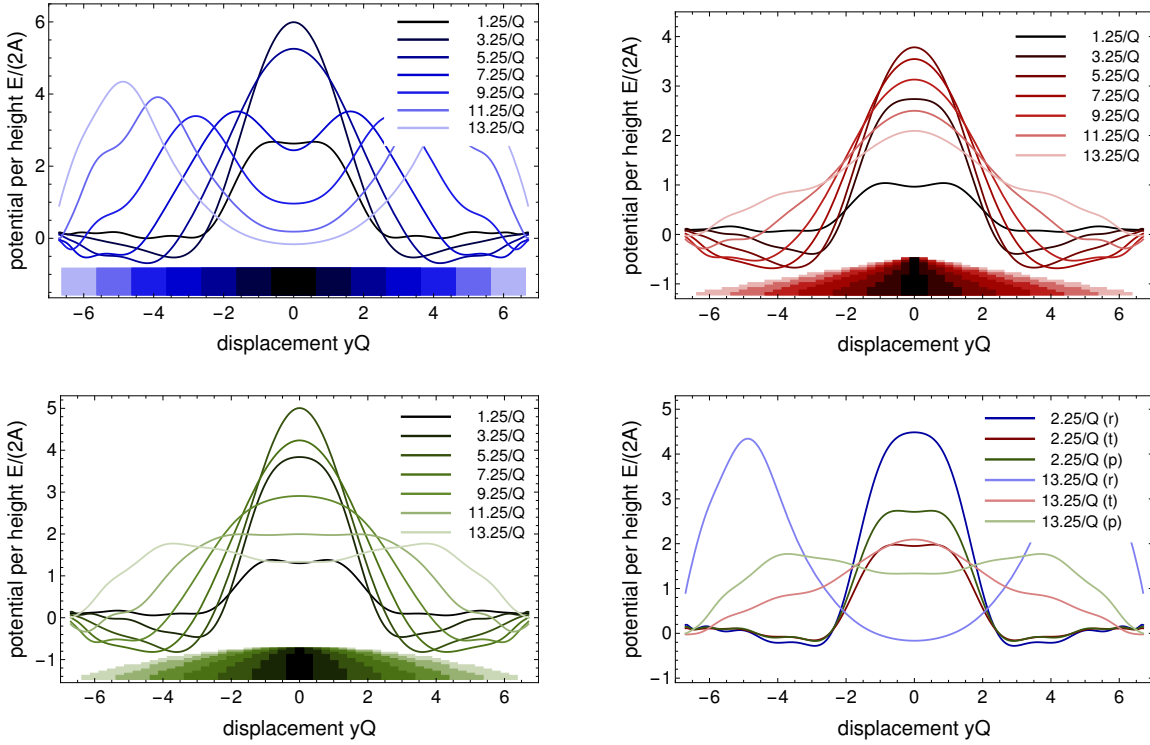


Figure 8.3.3.: Potentials per height for different shapes of nanostrips on the racetrack. The color (blue, red, green) denotes the shape (rectangular, triangular, parabolic). The brightness (dark to light) corresponds to the width of the strip (narrow to broad) as more precisely given in the insets. The solid blocks on the bottom of the first three figures show, as a guide to the eye, the corresponding cross section of the strip.

minimum of the potential of the bottom layers of the track. For the construction of a two-lane racetrack this means in particular that triangular nanostrips of any width can in total produce a two-lane potential if the thickness of underlying bottom layers is chosen accordingly.

The parabolic shaped nanostrip with its flat center and curved edges acts as a compromise between the flat rectangular shape and the triangular with its constant gradient in height. For larger widths the peak in the center decays just as in the triangular case without the formation of a minimum (except for the limit of same width as the racetrack), but in contrast to the sharp peak of the triangular case it becomes much broader, comparable to the two disconnecting peaks of the rectangular setup. Since the repulsive peak is extremely flat around the center, the parabolic nanostrip can only up to limited width be able to yield a two-lane potential. Interestingly, in the limit of equal width with the racetrack, the parabolic nanostrip exhibits a minimum in the center and therefore keeps skyrmions naturally on the (single-lane) racetrack. The fact that this minimum is only very flat, on the other hand, is an indicator that a normal racetrack with an approximately parabolic cross section can hardly keep the skyrmions on the track. In conclusion we find for the cross section of the unpatterned racetrack layers in the bottom half as for the nanostrip on top that the sharper the edges are, the stronger is the repulsion.

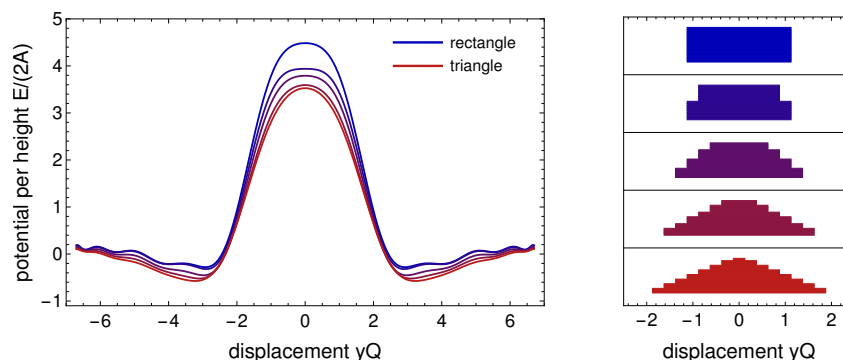


Figure 8.3.4.: Left: Potentials per height for different shapes of nanostrips on the racetrack. The color (blue to red) denotes the shape (rectangular to triangular) and corresponds to the shapes shown in the figure on the right. Right: Cross sections of the different nanostrips used for the potentials in the figure on the left.

### 8.3.2. Smeared out edges

For the realization of a two-lane racetrack, a sharp repulsive potential peak is needed and can, according to the previous section, be constructed from a nanostrip of any shape if it is narrow enough. In the following we therefore discuss shortly the effect of an imperfect preparation method, which is supposed to prepare the rectangular nanostrip discussed in Ref. [12] ( $2.25/Q$  width,  $0.75/Q$  height) but does not resolve the edges sharply such that they smear out. In our simulations, we smear out the original shape by replacing the sharp edges by edges with a linear slope. Upon increasing the slope, the rectangle is smoothly (within the limits of the numerical discretization) transformed into a trapezoid and finally a triangle of doubled width, see Fig. 8.3.4 right. The respective potentials are shown on the left hand side of Fig. 8.3.4. The results are consistent with the above claim, namely that the potential for narrow nanostrips is only slightly affected by the exact shape whereas the amplitude depends to good approximation linearly on the volume of the nanostrip. Hence the potentials are for all shapes qualitatively similar and differ only slightly in height, which can be explained with slightly lower volumes for the more triangular shapes due to numerical discretization. In conclusion we find that the actual shape of the nanostrip is of minor importance if the volume of the nanostrip is conserved.

## 8.4. Summary

The two-lane skyrmion racetrack, with its new concept of encoding information in a sequence of repulsive skyrmions on different lanes of a racetrack, is a promising new approach towards skyrmion-based storage devices. The two lanes can be created by a repulsive potential in the center of a racetrack. One can achieve such a potential by an additional nanostrip on top of the racetrack. We show that the repulsive potential generally depends on the shape of this nanostrip, especially if the nanostrip is wide. However, various shapes fulfill the requirements for the potential barrier if they are sufficiently narrow. We show that for a particular example, that has been proposed as being suitable for practical purposes, the exact shape of this nanostrip is only of minor importance. We therefore believe that the separation of lanes by a nanostrip is a robust method since it is mostly unaffected by small deformations of the strip.

## Acknowledgments

This work was supported by Deutsche Telekom Stiftung and the Bonn-Cologne Graduate School of Physics and Astronomy BCGS. We furthermore thank the Regional Computing Center of the University of Cologne (RRZK) for providing computing time on the DFG-funded High Performance Computing (HPC) system CHEOPS as well as support.

## 8.5. Bibliography

- [1] S. Mühlbauer, B. Binz, F. Jonietz, C. Pfleiderer, A. Rosch, A. Neubauer, R. Georgii, and P. Böni, *Skyrmion lattice in a chiral magnet*, Science **323**, 915-919 (2009).
- [2] X. Z. Yu, Y. Onose, N. Kanazawa, J. H. Park, J. H. Han, Y. Matsui, N. Nagaosa, and Y. Tokura, *Real-space observation of a two-dimensional skyrmion crystal*, Nature **465**, 901-904 (2010).
- [3] S. Heinze, K. von Bergmann, M. Menzel, J. Brede, A. Kubetzka, R. Wiesendanger, G. Bihlmayer, and S. Blügel, *Spontaneous atomic-scale magnetic skyrmion lattice in two dimensions*, Nat. Phys. **7**, 713-718 (2011).
- [4] N. Romming, C. Hanneken, M. Menzel, J. E. Bickel, B. Wolter, K. von Bergmann, A. Kubetzka, and R. Wiesendanger, *Writing and deleting single magnetic skyrmions*, Science **341**, 636-639 (2013).
- [5] F. Jonietz, S. Mühlbauer, C. Pfleiderer, A. Neubauer, W. Münzer, A. Bauer, T. Adams, R. Georgii, P. Böni, R. A. Duine, K. Everschor, M. Garst, and A. Rosch, *Spin transfer torques in MnSi at ultralow current densities*, Science **330**, 1648-1651 (2010).
- [6] X. Z. Yu, N. Kanazawa, W. Z. Zhang, T. Nagai, T. Hara, K. Kimoto, Y. Matsui, Y. Onose, and Y. Tokura, *Skyrmion flow near room temperature in an ultralow current density*, Nat. Commun. **3**, 988 (2012).
- [7] J. Iwasaki, M. Mochizuki, and N. Nagaosa, *Universal current-velocity relation of skyrmion motion in chiral magnets*, Nat. Commun. **4**, 1463 (2013).
- [8] K. Everschor, M. Garst, B. Binz, F. Jonietz, S. Mühlbauer, C. Pfleiderer, and A. Rosch, *Rotating skyrmion lattices by spin torques and field or temperature gradients*, Phys. Rev. B **86**, 054432 (2012).
- [9] C. Schütte and M. Garst, *Magnon-skyrmion scattering in chiral magnets*, Phys. Rev. B **90**, 094423 (2014).
- [10] N. S. Kiselev, A. N. Bogdanov, R. Schäfer, and U. K. Röfller, *Chiral skyrmions in thin magnetic films: new objects for magnetic storage technologies?*, J. Phys. D **44**, 392001 (2011).
- [11] A. Fert, V. Cros, and J. Sampaio, *Skyrmions on the track*, Nat. Nano. **8**, 152-156 (2013).
- [12] J. Müller, *Magnetic skyrmions on a two-lane racetrack*, New J. Phys. **19**, 025002 (2017).
- [13] A. N. Bogdanov and A. Hubert, *Thermodynamically stable magnetic vortex states in magnetic crystals*, J. Magn. Magn. Mater. **138**, 255-269 (1994).
- [14] U. K. Röfller, A. N. Bogdanov, and C. Pfleiderer, *Spontaneous skyrmion ground states in magnetic metals*, Nature **442**, 797-801 (2006).
- [15] A. Crépieux and C. Lacroix, *Dzyaloshinskii-Moriya interactions induced by symmetry breaking at a surface*, J. Magn. Magn. Mater. **182**, 341-349 (1998).
- [16] H. Yang, O. Boulle, V. Cros, A. Fert, and M. Chshiev, *Controlling Dzyaloshinskii-Moriya interaction via chirality dependent layer stacking, insulator capping and electric field*, Arxiv e-print (2016), arXiv:1603.01847.
- [17] C. Moreau-Luchaire, C. Moutafis, N. Reyren, J. Sampaio, C. A. F. Vaz, N. Van Horne, K. Bouzehouane, K. Garcia, C. Deranlot, P. Warnicke, P. Wohlhüter, J.-M. George, M. Weigand, J. Raabe, V. Cros, and A. Fert, *Additive interfacial chiral interaction in multilayers for stabilization of small individual skyrmions at room temperature*, Nat. Nano. **11**, 444-448 (2016).

- [18] S. Woo, K. Litzius, B. Krüger, M.-Y. Im, L. Caretta, K. Richter, M. Mann, A. Krone, R. M. Reeve, M. Weigand, P. Agrawal, I. Limesh, M.-A. Mawass, P. Fischer, M. Kläui, and G. S. D. Beach, *Observation of room-temperature magnetic skyrmions and their current-driven dynamics in ultrathin metallic ferromagnets*, Nat. Mater. **15**, 501-506 (2016).
- [19] C. Hanneken, F. Otte, A. Kubetzka, B. Dupé, N. Romming, K. von Bergmann, R. Wiesendanger, and S. Heinze, *Electrical detection of magnetic skyrmions by tunnelling non-collinear magnetoresistance*, Nat. Nano. **10**, 1039-1042 (2015).
- [20] C. Hanneken, A. Kubetzka, K. von Bergmann, and R. Wiesendanger, *Pinning and movement of individual nanoscale magnetic skyrmions via defects*, New J. Phys. **18**, 055009 (2016).

## 9. Motion of skyrmions in nanowires driven by magnonic momentum-transfer forces

Xichao Zhang<sup>1,2,6</sup>, Jan Müller<sup>3,6</sup>, Jing Xia<sup>1</sup>, Markus Garst<sup>4</sup>, Xiaoxi Liu<sup>5</sup>, and Yan Zhou<sup>1</sup>

*Motion of skyrmions in nanowires driven by magnonic momentum-transfer forces*

New Journal of Physics 19, 065001 (2017)

Doi: 10.1088/1367-2630/aa6b70

Copyright: Creative Commons Attribution 3.0 Unported (CC-BY)<sup>7</sup>

### Abstract

We study the motion of magnetic skyrmions in a nanowire induced by a spin-wave current  $J$  flowing out of a driving layer close to the edge of the wire. By applying micromagnetic simulation and an analysis of the effective Thiele equation, we find that the skyrmion trajectory is governed by an interplay of both forces due to the magnon current and the wire boundary. The skyrmion is attracted to the driving layer and is accelerated by the repulsive force due to the wire boundary. We consider both cases of longitudinal and transverse driving to the nanowire, but a steady-state motion of the skyrmion is only obtained for a transverse magnon current. For the latter case, we find in the limit of low current densities  $J$  the velocity-current relation  $v \sim J/\alpha$  where  $v$  is the skyrmion velocity and  $\alpha$  is the Gilbert damping. For large  $J$ , in case of strong driving, the skyrmion is pushed into the driving layer, resulting in a drop in skyrmion velocity and, eventually, the destruction of the skyrmion.

### 9.1. Introduction

Magnetic skyrmions are topological, protected textures of magnetization [1–3] that have been observed experimentally in various magnetic materials, in bulk systems, thin magnetic films, and magnetic multilayers [4–18]. As a topological object, the skyrmion is stable and possesses a peculiar particle-like nature, which makes it suitable for application as an information carrier. Indeed, a number of theoretical and numerical works have demonstrated that magnetic skyrmions could be essential components for future magnetic and spintronic devices for data storage and computation [19–38].

The position of an isolated magnetic skyrmion can be manipulated by an external driving force. A spin-polarized electric current has been reported to be an effective driving force

---

<sup>1</sup>School of Science and Engineering, The Chinese University of Hong Kong, Shenzhen 518172, China

<sup>2</sup>School of Electronic Science and Engineering, Nanjing University, Nanjing 210093, China

<sup>3</sup>Institut für Theoretische Physik, Universität zu Köln, D-50937 Cologne, Germany

<sup>4</sup>Institut für Theoretische Physik, Universität zu Köln, D-50937 Cologne, Germany

<sup>5</sup>Department of Information Engineering, Shinshu University, 4-17-1 Wakasato, Nagano 380-8553, Japan

<sup>6</sup>These authors contributed equally to this work.

<sup>7</sup><https://creativecommons.org/licenses/by/3.0/>

for the motion of magnetic skyrmions in confined geometries [14, 21, 22, 39–41]. In addition, the scattering of a propagating spin wave has been demonstrated to generate a momentum transfer, resulting in a skyrmion or domain wall motion [42–50]. In the absence of boundaries, the skyrmion will be driven towards the magnon source, i.e., the skyrmion velocity possesses a component antiparallel to the magnon current [42–45]. In confined geometries, the boundary acts as a potential barrier and its repulsive force can also result in an effective motion parallel to the magnon current [46, 47].

In this paper, we study in detail the motion and dynamics of an isolated magnetic skyrmion in a magnetic nanowire driven by spin waves travelling longitudinally or transversely to the wire. As the magnon current decays on a length scale set by Gilbert damping, the longitudinal driving is only viable for short wires. For transverse driving, a steady-state skyrmion motion is obtained with a characteristic velocity-current relation. We find that it is determined by an interplay of the magnonic driving and the repulsive potential arising from the edge of the wire. For large magnon currents, however, the skyrmion is pushed into the driving layer, which generates spin waves, leading to a breakdown of the skyrmion velocity. Our results provide a guide for future experimental studies on skyrmion motion in confined geometries driven by magnonic momentum-transfer forces.

## 9.2. Results

We consider a magnetic wire with a surface-induced Dzyaloshinskii-Moriya interaction (DMI) that stabilizes magnetic skyrmions; see the appendix, Sec. 9.4, for details. We investigate the motion of an isolated magnetic skyrmion which is driven by spin waves propagating longitudinally and transversely to the wire. We first discuss the resulting skyrmion trajectories and then turn to a discussion of the relation between the driving current and the skyrmion velocity in the steady state.

### 9.2.1. Skyrmion trajectories for longitudinal and transverse driving by spin waves

We first present results for the skyrmion trajectories obtained with the help of micromagnetic simulations. As shown in Figs. 9.2.1 and 9.2.2, we consider a nanowire consisting of a magnetic layer with length  $l = 400$  nm in the  $x$ -direction and various different widths  $w = 400, 200, 100,$  and  $50$  nm in the  $y$ -direction, corresponding to panels (a)-(d), respectively. The thickness of the magnetic layer in the  $z$ -direction is fixed at  $1$  nm. The initial magnetization profile of the magnetic layer corresponds to a magnetization pointing along the  $+z$ -direction except at the center of the sample, where the skyrmion is initially located, and at the sample edges, where the magnetization is tilted due to the Dzyaloshinskii-Moriya interaction.

Two setups with longitudinal and transverse driving are considered, Figs. 9.2.1 and 9.2.2, respectively. The driving is generated by a locally applied oscillating magnetic field, that is, a radio frequency (RF) field. It is applied only within a narrow strip of width  $15$  nm that is either located on the left-hand side of the sample for longitudinal driving or at the top of the nanowire for transversal driving. We consider an RF field  $\mathbf{H} = H_a \sin(2\pi ft)\hat{s}$  with amplitude  $H_a = 1000$  mT and frequency  $f = 200$  GHz. It possesses a longitudinal polarization with  $\hat{s} = \hat{y}$  for Fig. 9.2.1 and  $\hat{s} = \hat{x}$  for Fig. 9.2.2. More details on the simulation and material parameters are given in the Appendix, Sec. 9.4.

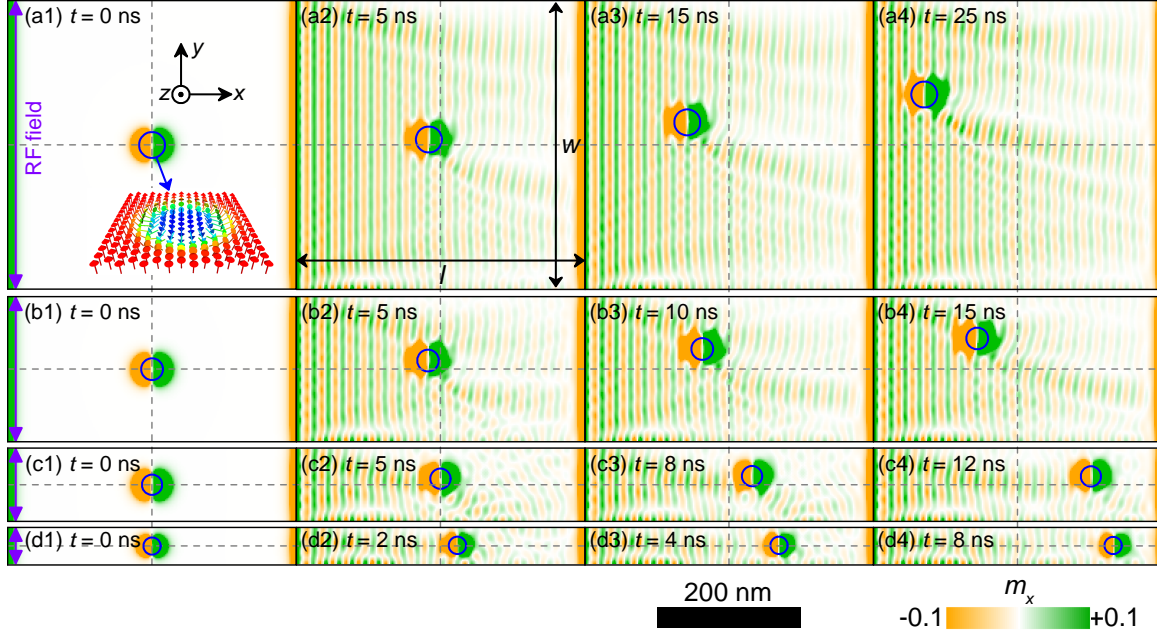


Figure 9.2.1.: Snapshots of a skyrmion driven by magnons parallel to the nanostrip of length  $l = 400$  nm. (a1)-(a4): the width  $w = 400$  nm of the strip is equal to the length; (b1)-(b4):  $w = 200$  nm; (c1)-(c4):  $w = 100$  nm; (d1)-(d4):  $w = 50$  nm; time steps of the snapshots are indicated. An RF field with an amplitude of  $H_a = 1000$  mT and a frequency of  $f = 200$  GHz is applied at the left edge of all samples, producing magnons traveling towards the right edge. The Gilbert damping  $\alpha = 0.02$ . The inset of (a1) shows the structure of the Néel-type skyrmion in our simulation, which is indicated by blue circles in all snapshots. The color scale shows the in-plane component of the magnetization  $m_x$ , which is rescaled to  $[-0.1, +0.1]$  in order to show the magnon profile more clearly. A length scale is also provided.

We first discuss the situation of *longitudinal driving*. Figure 9.2.1(a1) shows the case of a square-shaped thin film where  $l = w = 400$  nm at time  $t = 0$ . The panels (a2)-(a4) show snapshots at later times after the driving field has been switched on. The RF field at the left edge produces spin waves traveling towards the right, along the length direction of the sample. Since the magnetic skyrmion is far away from the sample edges, we observe a nearly pure skew scattering between the propagating spin wave and the magnetic skyrmion, which is in good agreement with that reported in Ref. [44]. Indeed, the spin wave-skyrmion scattering leads to a backwards motion of the magnetic skyrmion. Notice that the magnetic skyrmion basically moves against the propagation direction of the spin wave, and reaches the left edge in a finite time. In addition, the skyrmion gets slightly dragged towards the upper edge.

The width in Figs. 9.2.1(a) is sufficiently large so that the skyrmion reaches the magnon source before it touches the upper edge of the wire. The situation changes when the track is narrower. In Figs. 9.2.1(b) the width is  $w = 200$  nm and the skyrmion has still not reached the upper edge at a time  $t = 15$  ns. However, for even narrower wires with  $w = 100$  nm and  $w = 50$  nm, see Figs. 9.2.1(c) and 9.2.1(d), it reaches the edge after a short time. Close to the edge, the skyrmion changes the direction of its motion. Instead of approaching the driving layer, it moves along the edge away from it. This evading motion along the edge is also much faster than the attractive motion towards the magnon source.

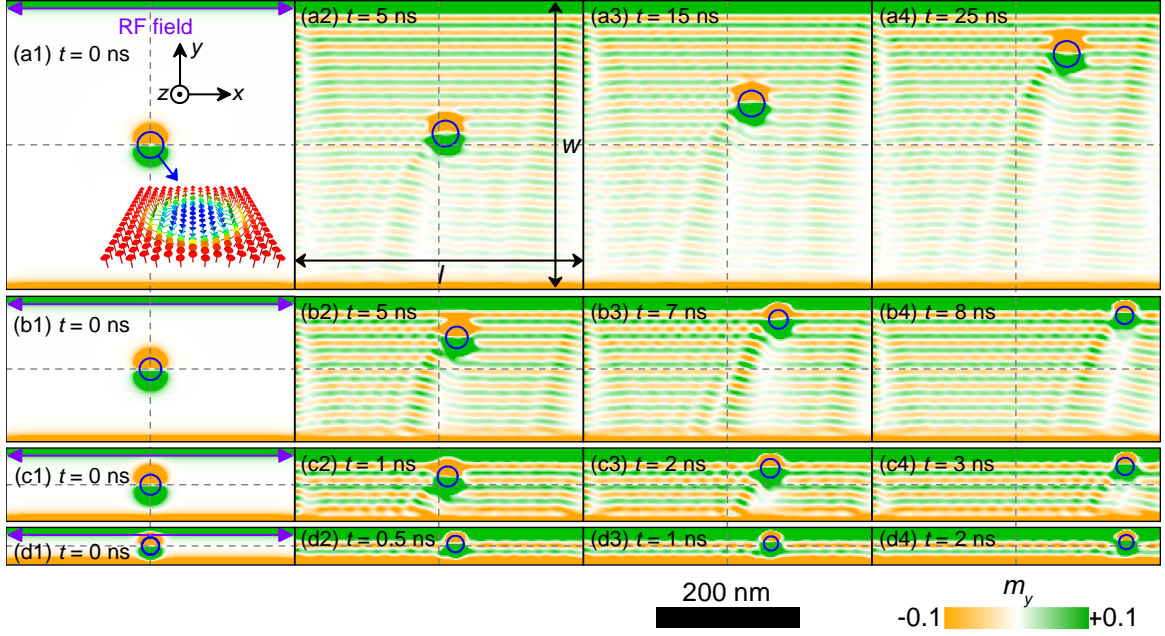


Figure 9.2.2.: Snapshots of a skyrmion driven by magnons transverse to the nanostrip of length  $l = 400$  nm. (a1)-(a4): the width  $w = 400$  nm of the strip is equal to the length; (b1)-(b4):  $w = 200$  nm; (c1)-(c4):  $w = 100$  nm; (d1)-(d4):  $w = 50$  nm; time steps of the snapshots are indicated. An RF field with an amplitude of  $H_a = 1000$  mT and a frequency of  $f = 200$  GHz is applied at the lower edge of all samples, producing magnons traveling towards the upper edge. The Gilbert damping  $\alpha = 0.02$ . The inset of (a1) shows the structure of the Néel-type skyrmion in our simulation, which is indicated by blue circles in all snapshots. The color scale shows the in-plane component of the magnetization  $m_y$ , which is rescaled to  $[-0.1, +0.1]$  in order to show the magnon profile more clearly. A length scale is also provided.

For the *transverse driving* we observe similar effects. The RF field is applied on the upper edge of the nanowire, see Fig. 9.2.2, in the same wire geometries as for the parallel driving. Due to the oscillating magnetic field, magnons are excited and propagate downwards along the  $-y$ -direction. The interaction with magnons pushes the skyrmion towards the upper edge of the wire with a slight side-shift to the right-hand side. This can be particularly clearly seen for the wide wire in Fig. 9.2.2(a). This setup is, however, too wide to observe the effects from the sample edge within the simulated time span. In contrast to the longitudinal driving mechanism, the skyrmion is now driven faster towards the upper edge, which becomes apparent for the narrower wires shown in Figs. 9.2.1(b)-(d). When the skyrmion arrives at the edge, it speeds up dramatically and moves along the upper edge towards the right-hand side. It reaches the end of the wire in a much shorter time than for longitudinal driving.

### 9.2.2. Thiele approximation

The skyrmion trajectories observed by our micromagnetic simulation can be understood in the framework of an effective Thiele equation of motion for the skyrmion [51]. Within this description, the skyrmion coordinate  $\mathbf{R}$  is governed by the equation:

$$\mathbf{G} \times \dot{\mathbf{R}} + \alpha \mathcal{D} \cdot \dot{\mathbf{R}} = \mathbf{F}(\mathbf{R}) \quad (9.2.1)$$

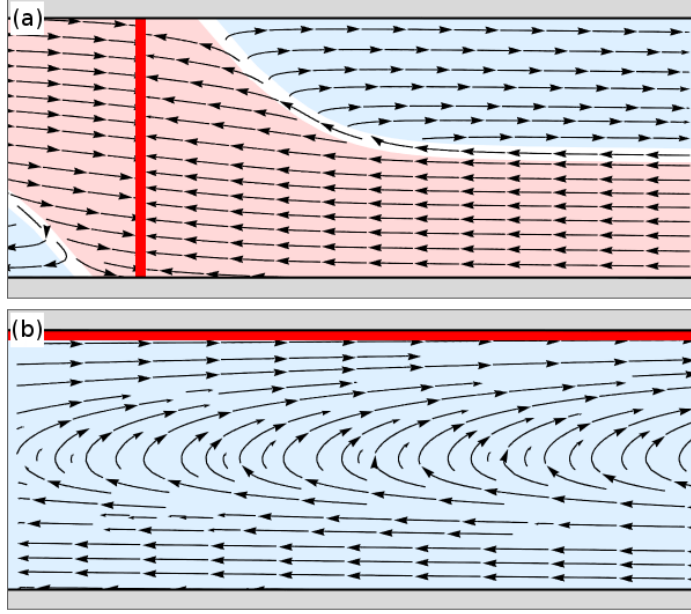


Figure 9.2.3.: Trajectories (black arrows) of a magnetic skyrmion derived within the Thiele approximation. The skyrmion is driven by magnons from a source (red line) and flowing longitudinal (a) and transverse (b) to the nanotrack (gray boundaries). Skyrmions in one of the colored areas either run free along the track (blue) or get captured by the magnon source (red). Areas with different scenarios are divided by a separatrix (white). Parameters are  $D/|G| = 1$ ,  $\alpha = 0.01$ ,  $\sigma_{\parallel}/L_{\text{edge}} = 0.1$ ,  $\sigma_{\perp}/L_{\text{edge}} = 0.1$ ,  $w/L_{\text{mag}} = 5$  for both plots and  $L_{\text{mag}}/L_{\text{edge}} = 1$  and  $Jq/V_{\text{edge}} = 3$  for the parallel driving (a) and  $L_{\text{mag}}/L_{\text{edge}} = 3$  and  $Jq/V_{\text{edge}} = 0.01$  for the transverse driving (b).

where  $\mathbf{G} = G\hat{z}$  is the gyrocoupling vector with  $G < 0$ , which is related to the topological winding number of the skyrmion,  $\alpha$  is the Gilbert damping, and  $\mathcal{D}$  the dissipative tensor which can be approximated to be diagonal,  $\mathcal{D}_{ij} = \mathcal{D}\delta_{ij}$ . The force on the right-hand side is attributed to the magnon driving and the edge of the sample,  $\mathbf{F} = \mathbf{F}_{\text{edge}} + \mathbf{F}_{\text{mag}}$ .

Close to the edge, the Dzyaloshinskii-Moriya interaction leads to a twist of the magnetization [52] which acts as a repulsive potential for the skyrmion [22,26]. To a good approximation, this potential falls off exponentially with the distance to the edge [53]. We thus describe the repulsive force by the edges of a nanostrip of width  $w$  by a superposition of edges at positions  $y_1 = 0$  and  $y_2 = w$ :

$$\mathbf{F}_{\text{edge}}(\mathbf{R}) = -V_{\text{edge}} \nabla \left( e^{-\frac{y}{L_{\text{edge}}}} + e^{\frac{y-w}{L_{\text{edge}}}} \right) \quad (9.2.2)$$

where  $V_{\text{edge}} > 0$  parametrizes the strength of the potential and  $L_{\text{edge}}$  the penetration depth of the magnetization twist.

The momentum transfer from the magnon current to the skyrmion also results in a force,

$$\mathbf{F}_{\text{mag}}(\mathbf{R}) = J e^{-\frac{\mathbf{r} \cdot \hat{q}}{L_{\text{mag}}}} q \left( \sigma_{\parallel} \hat{q} + \sigma_{\perp} (\hat{z} \times \hat{q}) \right), \quad (9.2.3)$$

where  $J > 0$  is the two-dimensional magnon-current density, and  $\vec{q}$  is the wavevector of the spin wave with  $q = |\vec{q}|$  and  $\hat{q} = \vec{q}/q$ . It was shown in Refs. [42] that the force is determined by the two-dimensional transport scattering cross section of the skyrmion,  $\sigma_{\parallel}$  and  $\sigma_{\perp}$ , longitudinal and transverse to the flow direction  $\hat{q}$  of the magnon current. In general, they depend in a

non-trivial manner on the magnon frequency. In the high-frequency limit or, equivalently, for large magnon wavevectors  $q$  [45], the transversal transport scattering cross section is universal  $\sigma_{\perp} \approx 4\pi/q$  and  $\sigma_{\parallel} \sim 1/q^2$  so that  $\sigma_{\perp} > \sigma_{\parallel} > 0$ . We also accounted for the decay of the magnon current on a length scale set by the Gilbert damping,  $1/L_{\text{mag}} \approx \alpha\sqrt{\frac{m}{2\hbar}}2\pi f$  where  $m$  is the magnon mass and  $f$  is the frequency of the wave.

The solution of the Thiele equation is plotted in Fig. 9.2.3 for some set of parameters. For longitudinal driving in panel (a), the wire can be divided into two different areas. The skyrmion trajectories belonging to the red shaded area, on the one hand, will end up at the driving layer (red line). When the skyrmion starts within the blue shaded area, on the other hand, it will be driven away from the driving layer. The interplay between the magnon and edge forces dominates the motion. As the magnon current decays exponentially on the length scale  $L_{\text{mag}}$  with increasing distance to the driving layer, the magnon force that keeps the skyrmion close to the edge also decays so that eventually the skyrmion slowly approaches the center of the wire. The red and blue shaded areas are separated by a critical skyrmion trajectory (white line). In any case, the longitudinal driving setup will not produce a steady state.

In case of transverse driving in Fig. 9.2.3(b), a skyrmion initially positioned at the center of the wire gets attracted towards the driving layer at the top of the wire. At the same time, it gets repelled by the edge twist of the magnetization and if the driving is not too strong the skyrmion reaches a steady state with  $v_{ys} = 0$  and a constant velocity,  $v_{xs}$ , along the edge. Within the Thiele approximation, this saturated velocity is given by:

$$v_{xs} = \frac{J}{\alpha D} e^{y/L_{\text{mag}}} q \sigma_{\perp} \approx \frac{4\pi J}{\alpha D} . \quad (9.2.4)$$

It depends on the steady state distance to the edge,  $y$ , which is in turn governed by the driving amplitude  $J$ . The last equation applies in the high-frequency limit  $\sigma_{\perp} \approx 4\pi/q$  and, in addition,  $y/L_{\text{mag}} \ll 1$ . In the limit of a small driving amplitude  $H_a$ , the current  $J$  will obey Fermi's Golden rule  $J \propto |H_a|^2$ . In this case, the saturated velocity will scale as  $v_{xs} \propto |H_a|^2/\alpha$ .

### 9.2.3. Damping dependence of the skyrmion motion

In order to study the dependence of the skyrmion motion on the Gilbert damping parameter  $\alpha$ , we performed further simulations with a long and narrow wire with  $w = 60$  nm and  $l = 1000$  nm for various values of  $\alpha$  in the range from 0.01 to 0.05. We consider two amplitudes for the excitation field  $H_a = 300$  mT and  $H_a = 1000$  mT with a frequency  $f = 180$  GHz. The results are shown in Fig. 9.2.4. All setups share the common property that the skyrmion moves faster and also further if the damping is lower. The exact dependence on the damping is, however, very different for longitudinal and transverse driving.

For longitudinal driving in Fig. 9.2.4(a), the skyrmion starts within the blue shaded area of Fig. 9.2.3(a) so that its motion is eventually along the edge of the wire. The distance travelled after a time of 7 ns for a driving amplitude  $H_a = 1000$  mT decreases approximately exponentially with increasing  $\alpha$ . While for the lowest simulated damping,  $\alpha = 0.01$ , the skyrmion travels 514 nm, it travels only half as far (254 nm) if the damping is doubled to  $\alpha = 0.02$ . If we increase the damping further by another  $\Delta\alpha = 0.01$ , the travelled distance again decreases by a factor 2 to only 139 nm. At even larger damping,  $\alpha = 0.04$ , the skyrmion moves 81 nm. The corresponding components of the velocity along the track,  $v_x(t)$ , are shown in Fig. 9.2.4(b). The period of acceleration lasts approximately 5 ns for low damping,  $\alpha = 0.01$ ,

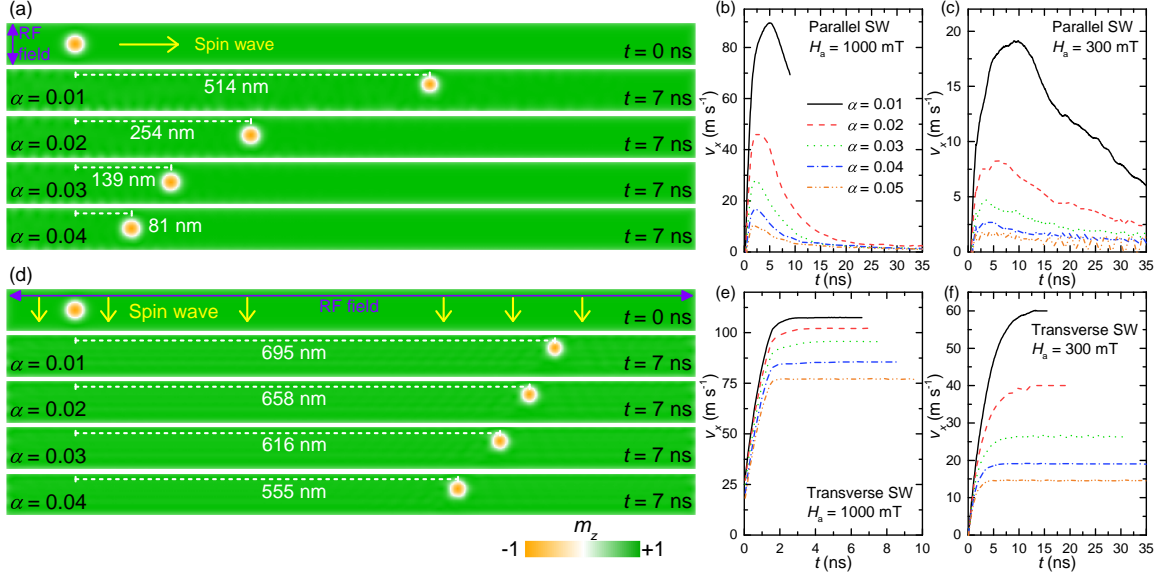


Figure 9.2.4.: Travelled distance and velocity of a single skyrmion in a nanowire ( $1000 \text{ nm} \times 60 \text{ nm} \times 1 \text{ nm}$ ). Snapshots of the system after 7 ns are shown for longitudinal (a) and transverse (d) driving with different damping coefficients  $\alpha$ . Magnons are excited by an RF field as indicated with  $H_a = 1000 \text{ mT}$  and  $f = 180 \text{ GHz}$ . The color scale represents the out-of-plane component of the magnetization  $m_z$ . In panel (b), (c) and (e),(f), the velocity parallel to the wire as a function of time,  $v_x(t)$ , is shown for longitudinal and transverse driving for two different driving amplitudes  $H_a = 1000 \text{ mT}$  and  $H_a = 300 \text{ mT}$  and for various damping coefficients  $\alpha$  as given in the inset of (b). The curves are only plotted in the regime where the skyrmion is sufficiently far from the end of the wire.

and becomes shorter with increasing damping. After the peak velocity is reached, the skyrmion decelerates again. This peak velocity can be up to  $\sim 90 \text{ m s}^{-1}$  for  $\alpha = 0.01$ , while it is only  $\sim 45 \text{ m s}^{-1}$  for  $\alpha = 0.02$  and  $\sim 25 \text{ m s}^{-1}$  for  $\alpha = 0.03$ . If we lower the RF field amplitude down to  $H_a = 300 \text{ mT}$ , see Fig. 9.2.4(c), the overall shape of the velocity curves stays the same but the time axis rescales with a factor  $\sim 2$  while the value of the velocity rescales by  $\sim 0.2$ . The highest velocity, at  $\alpha = 0.01$ , is now only  $\sim 20 \text{ m s}^{-1}$  and already  $< 5 \text{ m s}^{-1}$  for  $\alpha = 0.03$ . For  $\alpha > 0.03$  the motion is almost immediately damped out.

For transverse driving in Fig. 9.2.4(d), the skyrmion moves much faster and further as compared to longitudinal driving. For low damping  $\alpha = 0.01$ , the skyrmion travels 695 nm to be compared with 514 nm for longitudinal driving. For large damping  $\alpha = 0.04$  the skyrmion still travels 555 nm. A closer look at the corresponding velocity, see Fig. 9.2.4(e), reveals that after an acceleration time of  $\sim 2 \text{ ns}$  the skyrmion velocity reaches a steady state. For all simulated damping constants,  $\alpha \in [0.01, 0.05]$ , the saturated velocities,  $v_{x,s}$ , are in the regime of 75 up to  $110 \text{ m s}^{-1}$  for  $H_a = 1000 \text{ mT}$ , which is only comparable to the peak velocity at lowest damping for longitudinal driving. The dependence of  $v_{x,s}$  on the Gilbert damping becomes much more pronounced for smaller driving amplitude  $H_a = 300 \text{ mT}$ , as shown in Fig. 9.2.4(f).

#### 9.2.4. Steady-state motion for transverse driving

For transverse driving, the skyrmion motion can assume a steady state with a constant, saturated velocity. In order to compare with the expression in Eq. (9.2.4) predicted by the Thiele

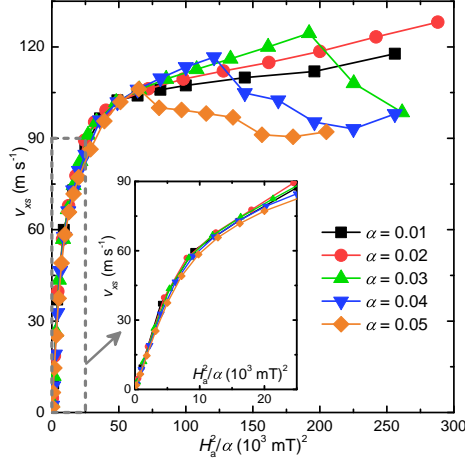


Figure 9.2.5.: Saturation velocity  $v_{xs}$  of a skyrmion in a nanostrip as a function of the scaling variable  $H_a^2/\alpha$  where  $H_a$  is the driving amplitude and  $\alpha$  is the Gilbert damping. Results from micromagnetic simulations for transverse driving. The stimulating field  $H_a$  ranges from 0 to 3200 mT and the frequency is fixed to  $f = 180$  GHz. Dimensions of the strip are  $1000 \text{ nm} \times 60 \text{ nm} \times 1 \text{ nm}$ . The saturation velocity  $v_{xs}$  is measured when the skyrmion velocity is converged. The inset shows a close-up for low driving where the data approximately collapses onto one single curve.

approximation, we obtained the saturated velocity for transverse driving with the help of micromagnetic simulations using damping coefficients  $\alpha = 0.01$  up to  $0.05$  and driving amplitudes within the range from 0 to 3200 mT at a fixed frequency of 180 GHz. The results are shown in Fig. 9.2.5 as a function of the scaling variable  $H_a^2/\alpha$ .

For small values of  $H_a^2/\alpha < 10 \times (10^3 \text{ mT})^2$ , the data collapses onto a universal straight line, corroborating the prediction from the Thiele approximation, Eq. (9.2.4), using Fermi's Golden rule  $J \propto |H_a|^2$ . For larger values, the data still follow approximately a common curve but the steep increase of  $v_{xs}$  flattens out. Close to the value  $H_a^2/\alpha \approx 70 \times (10^3 \text{ mT})^2$ , the saturated velocity  $v_{xs}$  with damping  $\alpha = 0.05$  shows a cusp and abruptly decreases. Subsequently, at higher values of  $H_a^2/\alpha$  the velocities for smaller damping parameters also exhibit a sudden breakdown.

In order to elucidate this sudden decrease of the saturated velocity, we show in Fig. 9.2.6(a) the saturated velocity  $v_{xs}$  versus the driving amplitude  $H_a$  at a fixed damping  $\alpha = 0.04$ . Depending on the strength of  $H_a$ , we can distinguish four different scenarios A to D. Snapshots of the skyrmion corresponding to these scenarios are shown in panel (b). The shaded area at the top corresponds to the strip where the oscillating driving field is applied. The scenarios are characterized as follows.

Scenario A (green region) corresponds to lowest driving fields. In the range from  $H_a = 0$  up to 1200 mT, the saturated velocity  $v_{xs}$  first increases with  $H_a^2/\alpha$  as predicted from the Thiele approximation and then turns to a less steep increase. In this regime, the skyrmion smoothly moves along the nanotrack, and does not suffer any significant deformations. Moreover, only a minor fraction of the skyrmion area has entered the region where the oscillating RF field is applied, see Fig. 9.2.6(b-A).

Scenario B (blue region) is the intermediate regime between  $H_a = 1200$  and 2200 mT. Here, the saturated velocity still increases with the amplitude of the stimulating RF field but the increase is less steep than in scenario A. This is related to a power loss from the emission of

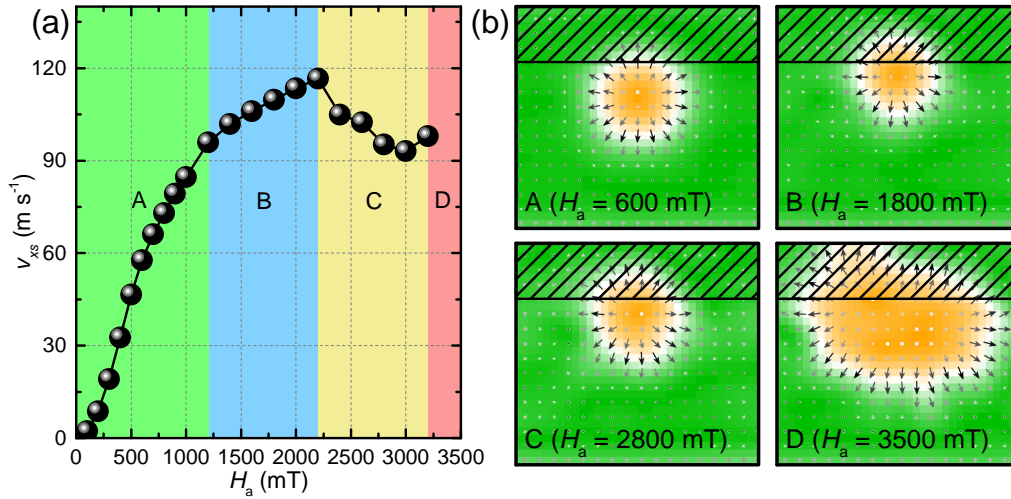


Figure 9.2.6.: (a) Saturation velocity  $v_{xs}$  of a skyrmion driven by a transverse magnon current in a nanostrip as a function of the stimulating field amplitude  $H_a$ . Results are from micromagnetic simulations. Four different scenarios are marked with a letter and background color. “A”, green: the skyrmion moves rigidly along the edge of the nanotrack. “B”, blue: the skyrmion moves along the nanotrack and simultaneously emits spin waves. “C”, yellow: the skyrmion moves along the nanotrack, emits spin waves, and periodically expands/shrinks in size, i.e., its *breathing mode* is excited. “D”, red: the skyrmion is driven into the edge and gets destroyed when touching it. The frequency of the RF field is  $f = 180$  GHz and the damping coefficient is  $\alpha = 0.04$ . Dimensions of the strip are  $1000 \text{ nm} \times 60 \text{ nm} \times 1 \text{ nm}$ . (b) Snapshots of the magnetization in the four regimes described in (a). The RF field is applied at the upper edge with a width of  $15 \text{ nm}$ , which is indicated by the shadowed area. The color scale shows the component of the magnetization  $m_z$ , perpendicular to the film. Black arrows indicate the in-plane components.

additional spin waves by the skyrmion, which can be discerned in our simulations.

Scenario C (yellow region) is obtained in the range from  $H_a = 2200$  up to  $3200 \text{ mT}$  which is the highest accessible driving amplitude. In this regime the saturated velocity suddenly drops to a lower value. We can associate this sudden drop with the excitation of the internal breathing mode of the skyrmion. As can be seen in Fig. 9.2.6(b-C), a sizeable fraction of the skyrmion is located within the area of the applied RF field, which facilitates the excitation of internal modes.

Scenario D (red region) is the regime where the drive is so strong that the skyrmion will be destroyed shortly after the RF field is applied. In this limit,  $H_a > 3200 \text{ mT}$ , the skyrmion is driven so hard towards the edge that it is eventually pushed over the edge barrier. The topologically non-trivial skyrmion then unwinds and disappears. A snapshot of the destruction process is shown in Fig. 9.2.6(b-D).

It is worth mentioning that, for the purpose of avoiding the reflection of spin waves on the sample edges, absorbing boundary conditions (ABCs) are implemented in all simulations discussed above. However, in real-world experiments with nanoscale samples, the sample edges might indeed reflect spin waves. Hence, for comparison, we also performed simulations with open boundary conditions (OBCs) for the representative case of a  $1000 \text{ nm} \times 60 \text{ nm} \times 1 \text{ nm}$  nanotrack, where the skyrmion is driven by a transverse magnon current. As shown in Fig. 9.2.7(a), the nanotrack with ABCs has an exponentially increasing damping coefficient at

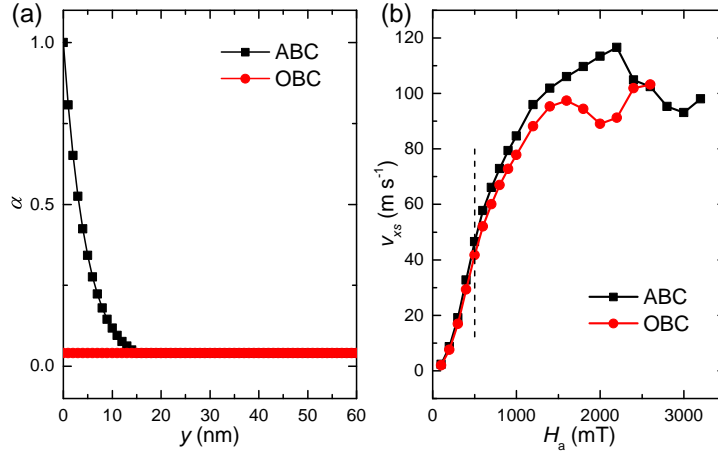


Figure 9.2.7.: (a) Damping coefficient as a function of  $y$  coordinate for the absorbing boundary conditions (ABCs) and open boundary conditions (OBCs). (b) The saturation velocity  $v_{xs}$  of a skyrmion driven by a transverse magnon current in a nanostrip as a function of the stimulating field amplitude  $H_a$  for the models with ABCs and OBCs. The results for these two cases start to differ above  $H = 500 \text{ mT}$  (vertical dashed line).

the edges, while the nanotrack with OBCs has a uniform damping coefficient. Fig. 9.2.7(b) shows the saturation velocity  $v_{xs}$  of a skyrmion driven by a transverse magnon current as a function of the stimulating field amplitude  $H_a$  for the models with ABCs and OBCs. The comparison shows that, when the stimulating field is relatively small ( $H_a < 500 \text{ mT}$ ), the results obtained for the model with OBCs are in good agreement with those obtained for the model with ABCs. The reason is that the reflection of magnons is negligible if the exciting field is sufficiently small. Also the skyrmion barely enters the region of increased damping at the edge. However, when the stimulating field is relatively large ( $H_a > 500 \text{ mT}$ ), the results for  $v_{xs}$  obtained for the model with OBCs differ quantitatively from those obtained for the model with ABCs, and the difference increases with increasing  $H_a$ . Nevertheless, it can be seen that qualitatively the four different scenarios can also be identified for the model with OBCs, which are now shifted to lower field values  $H_a$ .

### 9.3. Summary

We studied in depth the motion of an isolated magnetic skyrmion in a nanotrack driven by a magnonic momentum-transfer force provided by a spin wave. We considered two setups where spin waves are excited either longitudinal or transverse to the nanotrack. We find that the longitudinal driving is less efficient partly due to the damping of the spin waves.

For transverse driving, the skyrmion motion attains a steady-state with constant velocity along the track. We analyzed the saturated velocity,  $v_{xs}$ , as a function of the Gilbert damping  $\alpha$  and the driving amplitude  $H_a$  of the magnetic field that generates the spin waves. It obeys for low driving the scaling relation  $v_{xs} \propto J/\alpha \propto |H_a|^2/\alpha$  where the magnon current amplitude  $J \propto |H_a|^2$ . The enhancement of the skyrmion velocity by the factor  $1/\alpha$  is comparable to previous results obtained for the skyrmion motion in confined geometries but driven by electronic spin currents [22, 53].

For large transverse driving, the skyrmion is pushed into the driving layer and additional

magnon modes and even the internal breathing mode of the skyrmion become excited. This limits a further increase of the skyrmion velocity and, finally, results in the destruction of the skyrmion.

Our study demonstrates that the position of a skyrmion can be efficiently manipulated by the magnonic momentum-transfer force, and it elucidates the principle of a magnon-driven skyrmion motion which might be of interest for practical applications.

### Acknowledgments

XZ was supported by JSPS RONPAKU (Dissertation PhD) Program. JM thanks Deutsche Telekom Stiftung, Bonn-Cologne Graduate School of Physics and Astronomy BCGS and the German funding program CRC 1238 for financial support. MG was supported by the SFB 1143 (Correlated Magnetism: from Frustration to Topology). YZ acknowledges the support by the National Natural Science Foundation of China (Project No. 11574137) and Shenzhen Fundamental Research Fund under Grant No. JCYJ20160331164412545.

## 9.4. Appendix. Micromagnetic modeling

We performed three-dimensional (3D) micromagnetic simulations by using the 1.2a5 release of the Object Oriented MicroMagnetic Framework (OOMMF) software developed at the National Institute of Standards and Technology (NIST) [54]. The simulations are handled by the OOMMF extensible solver (OXS) objects of the standard OOMMF distribution with the OXS extension module for simulating the interface-induced Dzyaloshinskii-Moriya interaction (DMI) [52]. The magnetization dynamics are controlled by the Landau-Lifshitz-Gilbert (LLG) equation [54–56] given as:

$$\frac{d\mathbf{M}}{dt} = -\gamma_0 \mathbf{M} \times \mathbf{H}_{\text{eff}} + \frac{\alpha}{M_S} \left( \mathbf{M} \times \frac{d\mathbf{M}}{dt} \right), \quad (9.4.5)$$

where  $\mathbf{M}$  is the magnetization,  $\mathbf{H}_{\text{eff}} = -\mu_0^{-1} \frac{\partial E}{\partial \mathbf{M}}$  is the effective field,  $t$  is the time,  $\gamma_0$  is the gyromagnetic ratio,  $\alpha$  is the Gilbert damping coefficient, and  $M_S = |\mathbf{M}|$  is the saturation magnetization. The average energy density  $E$  of the system contains the exchange energy, the anisotropy energy, the applied field (Zeeman) energy, the magnetostatic (demagnetization) energy, and the DMI energy terms, which is expressed as follows:

$$E = A \left[ \nabla \left( \frac{\mathbf{M}}{M_S} \right) \right]^2 - K \frac{(\mathbf{n} \cdot \mathbf{M})^2}{M_S^2} - \mu_0 \mathbf{M} \cdot \mathbf{H} - \frac{\mu_0}{2} \mathbf{M} \cdot \mathbf{H}_d(\mathbf{M}) + \frac{D}{M_S^2} \left( M_z \frac{\partial M_x}{\partial x} + M_z \frac{\partial M_y}{\partial y} - M_x \frac{\partial M_z}{\partial x} - M_y \frac{\partial M_z}{\partial y} \right), \quad (9.4.6)$$

where  $A$  and  $K$  are the exchange and anisotropy energy constants, respectively.  $\mathbf{H}$  and  $\mathbf{H}_d(\mathbf{M})$  are the applied field and the magnetostatic self-interaction field. The  $M_x$ ,  $M_y$  and  $M_z$  are the components of the magnetization  $\mathbf{M}$ . The five terms at the right-hand side of Eq. 9.4.6 correspond to the exchange energy, the anisotropy energy, the applied field (Zeeman) energy, the magnetostatic (demagnetization) energy, and the DMI energy, respectively. The material parameters used by the simulation program are adopted from Refs. [21, 25–29, 34, 46]: the Gilbert damping coefficient  $\alpha = 0.01 \sim 0.05$ , the gyromagnetic ratio  $\gamma = -2.211 \times 10^5$  m

$\text{A}^{-1} \text{s}^{-1}$ , the saturation magnetization  $M_S = 580 \text{ kA m}^{-1}$ , the exchange stiffness  $J = 15 \text{ pJ m}^{-1}$ , the interface-induced DMI constant  $D = 3.5 \text{ mJ m}^{-2}$ , and the perpendicular magnetic anisotropy (PMA) constant  $K = 0.8 \text{ MJ m}^{-3}$ , unless otherwise specified. The simulated models are discretized into tetragonal cells with the optimum cell size of  $2 \text{ nm} \times 2 \text{ nm} \times 1 \text{ nm}$ , which offers a good trade-off between the computational accuracy and efficiency. Absorbing boundary conditions are implemented in all simulations (except the simulations given in Fig. 9.2.7) in order to avoid the reflection of spin waves on the sample edges.

## 9.5. Bibliography

- [1] U. K. Rößler, A. N. Bogdanov, and C. Pfleiderer, *Spontaneous skyrmion ground states in magnetic metals*, Nature **442**, 797-801 (2006).
- [2] N. Nagaosa and Y. Tokura, *Topological properties and dynamics of magnetic skyrmions*, Nat. Nano. **8**, 899-911 (2013).
- [3] S. Seki and M. Mochizuki, *Skyrmions in Magnetic Materials*, Springer International Publishing, (2016).
- [4] S. Mühlbauer, B. Binz, F. Jonietz, C. Pfleiderer, A. Rosch, A. Neubauer, R. Georgii, and P. Böni, *Skyrmion lattice in a chiral magnet*, Science **323**, 915-919 (2009).
- [5] X. Z. Yu, Y. Onose, N. Kanazawa, J. H. Park, J. H. Han, Y. Matsui, N. Nagaosa, and Y. Tokura, *Real-space observation of a two-dimensional skyrmion crystal*, Nature **465**, 901-904 (2010).
- [6] S. Heinze, K. von Bergmann, M. Menzel, J. Brede, A. Kubetzka, R. Wiesendanger, G. Bihlmayer, and S. Blügel, *Spontaneous atomic-scale magnetic skyrmion lattice in two dimensions*, Nat. Phys. **7**, 713-718 (2011).
- [7] T. Schulz, R. Ritz, A. Bauer, M. Halder, M. Wagner, C. Franz, C. Pfleiderer, K. Everschor, M. Garst, and A. Rosch, *Emergent electrodynamics of skyrmions in a chiral magnet*, Nat. Phys. **8**, 301-304 (2013).
- [8] N. Romming, C. Hanneken, M. Menzel, J. E. Bickel, B. Wolter, K. von Bergmann, A. Kubetzka, and R. Wiesendanger, *Writing and deleting single magnetic skyrmions*, Science **341**, 636-639 (2013).
- [9] M. Finazzi, M. Savoini, A. R. Khorsand, A. Tsukamoto, A. Itoh, L. Duó, A. Kirilyuk, T. Rasing, and M. Ezawa, *Laser-induced magnetic nanostructures with tunable topological properties*, Phys. Rev. Lett. **110**, 177205 (2013).
- [10] I. Kézsmárki, S. Bordács, P. Milde, E. Neuber, L. M. Eng, J. S. White, H. M. Rønnow, C. D. Dewhurst, M. Mochizuki, K. Yanai, H. Nakamura, D. Ehlers, V. Tsurkan, and A. Loidl, *Néel-type skyrmion lattice with confined orientation in the polar magnetic semiconductor  $\text{GaV}_4\text{S}_8$* , Nat. Mater. **14**, 1116-1122 (2016).
- [11] T. Schwarze, J. Waizner, M. Garst, A. Bauer, I. Stasinopoulos, H. Berger, C. Pfleiderer, and D. Grundler, *Universal helimagnon and skyrmion excitations in metallic, semiconducting and insulating chiral magnets*, Nat. Mater. **14**, 478-483 (2015).
- [12] H. Du, R. Che, L. Kong, X. Zhao, C. Jin, C. Wang, J. Yang, W. Ning, R. Li, C. Jin, X. Chen, J. Zang, Y. Zhang, and M. Tian, *Edge-mediated skyrmion chain and its collective dynamics in a confined geometry*, Nat. Commun. **6**, 8504 (2015).
- [13] Y. Nii, T. Nakajima, A. Kikkawa, Y. Yamasaki, K. Ohishi, J. Suzuki, Y. Taguchi, T. Arima, Y. Tokura, and Y. Iwasa, *Uniaxial stress control of skyrmion phase*, Nat. Commun. **6**, 8539 (2015).
- [14] W. Jiang, P. Upadhyaya, W. Zhang, G. Yu, M. B. Jungfleisch, F. Y. Fradin, J. E. Pearson, Y. Tserkovnyak, K. L. Wang, O. Heinonen, S. G. E. te Velthuis, and A. Hoffmann, *Blowing magnetic skyrmion bubbles*, Science **349**, 283-286 (2015).

- [15] O. Boulle, J. Vogel, H. Yang, S. Pizzini, D. de Souza Chaves, A. Locatelli, T. O. Mentès, A. Sala, L. D. Buda-Prejbeanu, O. Klein, M. Belmeguenai, Y. Roussigné, A. Stashkevich, S. M. Chérif, L. Aballe, M. Foerster, M. Chshiev, S. Auffret, I. M. Miron, and G. Gaudin, *Room-temperature chiral magnetic skyrmions in ultrathin magnetic nanostructures*, Nat. Nano. **11**, 449-454 (2016).
- [16] W. Jiang, X. Zhang, G. Yu, W. Zhang, X. Wang, B. Jungfleisch, J. E. Pearson, X. Cheng, O. Heinonen, W. Kang, Y. Zhou, A. Hoffmann, and S. G. E. te Velthuis, *Direct observation of the skyrmion Hall effect*, Nat. Phys. **13**, 162-169 (2017).
- [17] W. Jiang, W. Zhang, G. Yu, B. Jungfleisch, P. Upadhyaya, H. Somaïly, J. E. Pearson, Y. Tserkovnyak, K. L. Wang, O. Heinonen, S. G. E. te Velthuis, and A. Hoffmann, *Mobile Néel skyrmions at room temperature: status and future*, AIP Adv. **6**, 055602 (2016).
- [18] S. Woo, K. Litzius, B. Krüger, M.-Y. Im, L. Caretta, K. Richter, M. Mann, A. Krone, R. M. Reeve, M. Weigand, P. Agrawal, I. Lemesch, M.-A. Mawass, P. Fischer, M. Kläui, and G. S. D. Beach, *Observation of room-temperature magnetic skyrmions and their current-driven dynamics in ultrathin metallic ferromagnets*, Nat. Mater. **15**, 501-506 (2016).
- [19] A. Fert, V. Cros, and J. Sampaio, *Skyrmions on the track*, Nat. Nanol. **8**, 152-156 (2013).
- [20] J. Müller, *Magnetic skyrmions on a two-lane racetrack*, New J. Phys. **19**, 025002 (2017).
- [21] J. Sampaio, V. Cros, S. Rohart, A. Thiaville, and A. Fert, *Nucleation, stability and current-induced motion of isolated magnetic skyrmions in nanostructures*, Nat. Nano. **8**, 839-844 (2013).
- [22] J. Iwasaki, M. Mochizuki, and N. Nagaosa, *Current-induced skyrmion dynamics in constricted geometries*, Nat. Nanotech. **8**, 742-747 (2013).
- [23] L. Sun, R. X. Cao, B. F. Miao, Z. Feng, B. You, D. Wu, W. Zhang, An Hu, and H. F. Ding, *Creating an artificial two-dimensional skyrmion crystal by nanopatterning*, Phys. Rev. Lett. **110**, 167201 (2013).
- [24] R. Tomasello, E. Martinez, R. Zivieri, L. Torres, M. Carpentieri, and G. Finocchio, *A strategy for the design of skyrmion racetrack memories*, Sci. Rep. **4**, 6784 (2014).
- [25] Y. Zhou and M. Ezawa, *A reversible conversion between a skyrmion and a domain-wall pair in a junction geometry*, Nat. Commun. **5**, 4652 (2014).
- [26] X. Zhang, G. P. Zhao, H. Fangohr, J. P. Liu, W. X. Xia, J. Xia, and F. J. Morvan, *Skyrmion-skyrmion and skyrmion-edge repulsions in skyrmion-based racetrack memory*, Sci. Rep. **5**, 7643 (2015).
- [27] X. Zhang, M. Ezawa, and Y. Zhou, *Magnetic skyrmion logic gates: conversion, duplication and merging of skyrmions*, Sci. Rep. **5**, 9400 (2015).
- [28] X. Zhang, Y. Zhou, M. Ezawa, G. P. Zhao, and W. Zhao, *Magnetic skyrmion transistor: skyrmion motion in a voltage-gated nanotrack*, Sci. Rep. **5**, 11369 (2015).
- [29] Y. Zhou, E. Iacocca, A. A. Awad, R. K. Dumas, F. C. Zhang, H. B. Braun, and J. Åkerman, *Dynamically stabilized magnetic skyrmions*, Nat. Commun. **6**, 8193 (2015).
- [30] F. Ma, Y. Zhou, H. B. Braun, and W. S. Lew, *Skyrmion-Based Dynamic Magnonic Crystal*, Nano Lett. **15**, 4029-4036 (2015).
- [31] M. Beg, R. Carey, W. Wang, D. Cortés-Ortuño, M. Vousden, M.-A. Bisotti, M. Albert, D. Chernyshenko, O. Hovorka, R. L. Stamps, and H. Fangohr, *Ground state search, hysteretic behaviour, and reversal mechanism of skyrmionic textures in confined helimagnetic nanostructures*, Sci. Rep. **5**, 17137 (2015).
- [32] P. Upadhyaya, G. Yu, P. K. Amiri, and K. L. Wang, *Electric-field guiding of magnetic skyrmions*, Phys. Rev. B **92**, 134411 (2015).
- [33] W. Koshibae, Y. Kaneko, J. Iwasaki, M. Kawasaki, Y. Tokura, and N. Nagaosa, *Memory functions of magnetic skyrmions*, Japan. J. Appl. Phys. **54**, 053001 (2015).
- [34] X. Zhang, Y. Zhou, and M. Ezawa, *Magnetic bilayer-skyrmions without skyrmion hall effect*, Nat. Commun. **7**, 10293 (2016).

- [35] H. Y. Yuan and X. R. Wang, *Skyrmion creation and manipulation by nano-second current pulses*, Sci. Rep. **6**, 22638 (2016).
- [36] S. Zhang, J. Wang, Q. Zheng, Q. Zhu, X. Liu, S. Chen, C. Jin, Q. Liu, C. Jia, and D. Xue, *Current-induced magnetic skyrmions oscillator*, New J. Phys. **17**, 023061 (2015).
- [37] M. Beg, M. Albert, M.-A. Bisotti, D. Cortés-Ortuño, W. Wang, R. Carey, M. Vousden, O. Hovorka, C. Ciccarelli, C. S. Spencer, C. H. Marrows, and H. Fangohr, *Dynamics of skyrmionic states in confined helimagnetic nanostructures*, Phys. Rev. B **95**, 014433 (2017).
- [38] D. Bazeia, J. G. G. S. Ramos, and E. I. B. Rodrigues, *Topological strength of magnetic skyrmions*, J. Magn. Magn. Mater. **423**, 411-420 (2017).
- [39] S.-Z. Lin, C. Reichhardt, C. D. Batista, and A. Saxena, *Dynamics of skyrmions in chiral magnets: Dynamic phase transitions and equation of motion*, J. Appl. Phys. **115**, 17D109 (2014).
- [40] C. Reichhardt and C. J. Olsen Reichhardt, *Shapiro steps for skyrmion motion on a washboard potential with longitudinal and transverse ac drives*, Phys. Rev. B **92**, 224432 (2015).
- [41] G. Yu, P. Upadhyaya, Q. Shao, H. Wu, G. Yin, X. Li, C. He, W. Jiang, X. Han, P. K. Amiri, and K. L. Wang, *Room-temperature skyrmion shift device for memory application*, Nano Lett. **17**, 261-268 (2017).
- [42] C. Schütte and M. Garst, *Magnon-skyrmion scattering in chiral magnets*, Phys. Rev. B **90**, 094423 (2014).
- [43] C. Schütte, J. Iwasaki, A. Rosch, and N. Nagaosa, *Inertia, diffusion, and dynamics of a driven skyrmion*, Phys. Rev. B **90**, 174434 (2014).
- [44] J. Iwasaki, A. J. Beekman, and N. Nagaosa, *Theory of magnon-skyrmion scattering in chiral magnets*, Phys. Rev. B **89**, 064412 (2014).
- [45] S. Schroeter and M. Garst, *Scattering of high-energy magnons off a magnetic skyrmion*, Low Temp. Phys. **41**, 817-825 (2015).
- [46] X. Zhang, M. Ezawa, D. Xiao, G. P. Zhao, Y. Liu, and Y. Zhou, *All-magnetic control of skyrmions in nanowires by a spin wave*, Nanotechnology **26**, 225701 (2015).
- [47] J. Kim and S. K. Kim, *Origin of robust interaction of spin waves with a single skyrmion in perpendicularly magnetized nanostripes*, Arxiv e-print (2015), arXiv:1508.05682.
- [48] W. Jiang, P. Upadhyaya, Y. Fan, J. Zhao, M. Wang, L.-T. Chang, M. Lang, K. L. Wong, M. Lewis, Y.-T. Lin, J. Tang, S. Cherepov, X. Zhou, Y. Tserkovnyak, R. N. Schwartz, and K. L. Wang, *Direct imaging of thermally driven domain wall motion in magnetic insulators*, Phys. Rev. Lett. **110**, 177202 (2013).
- [49] P. Yan, X. S. Wang, and X. R. Wang, *All-magnonic spin-transfer torque and domain wall propagation*, Phys. Rev. Lett. **107**, 177207 (2011).
- [50] X. S. Wang, P. Yan, Y. H. Shen, G. E. W. Bauer, and X. R. Wang, *Domain wall propagation through spin wave emission*, Phys. Rev. Lett. **109**, 167209 (2012).
- [51] A. A. Thiele, *Steady-state motion of magnetic domains*, Phys. Rev. Lett. **30**, 230-233 (1973).
- [52] S. Rohart and A. Thiaville, *Skyrmion confinement in ultrathin film nanostructures in the presence of Dzyaloshinskii-Moriya interaction*, Phys. Rev. B **88**, 184422 (2013).
- [53] C. Navau, N. Del-Valle, and A. Sanchez, *Analytical trajectories of skyrmions in confined geometries: Skyrmionic racetracks and nano-oscillators*, Phys. Rev. B **94**, 184104 (2016).
- [54] M. J. Donahue and D. G. Porter, *OOMMF user guide, version 1.0*, Interagency Report , NISTIR 6376 (1999) Available at <http://math.nist.gov/oommf/>
- [55] T. L. Gilbert, *A Lagrangian Formulation of the Gyromagnetic Equation of the Magnetization Field*, Phys. Rev. **100**, 1243 (1955)
- [56] L. Landau and E. Lifshitz, *On the theory of the dispersion of magnetic permeability in ferromagnetic bodies*, Phys. Z. Sowjet. **8**, 153-169 (1935)

Part III.  
Further Work



## 10. Theoretical models and methods

The aim of the following chapter is to introduce the micromagnetic model which is used throughout this thesis in order to describe magnetism on scales much larger than the atomic lattice constants. In addition, the most frequently used methods are explained in more detail than the previous sections permitted. The more detailed methods that are specifically tailored for certain problems are later introduced when they are needed.

### 10.1. Atomistic Heisenberg model

When describing the magnetization in a solid, the complexity of a full quantum mechanical treatment outreaches the computational capabilities already if more than a few atoms are involved. In order to describe magnetic phenomena and phases on large scales, simplifications are needed. This paragraph follows the presentation in Ref. [221].

The celebrated atomistic Heisenberg model provides an efficient approximation by describing magnetism in terms of classical spins, i.e., simple vectors  $\mathbf{s}_i$  with  $|\mathbf{s}_i| = 1$ . These classical spins are each located on an atomic lattice site  $i$ . The former electronic wave functions of the quantum mechanical description enter the model as effective interactions between the spins  $\{\mathbf{s}_i\}$  and can in principle be calculated from ab initio methods by integrating out the overlap between the wave functions that are localized on the respective lattice sites  $\{i\}$ . Consequently, the more that the wave functions are localized, the smaller are the overlaps and thus the less interactions become relevant for the effective description. This means that insulators only couple spins on short distances whereas a metal with its delocalized electrons requires long-ranged interactions.

The hypothetical zoo of interactions such as simple on-site anisotropies, two-spin interactions that can couple spins on arbitrary distances, and exotic multi-spin interactions, is in practice only composed of the following energy terms:

$$\mathcal{H} = \mathcal{H}_{\text{ex}} + \mathcal{H}_{\text{dmi}} + \mathcal{H}_z + \mathcal{H}_{\text{ani}} + \mathcal{H}_{\text{dipole}}. \quad (10.1.1)$$

The individual constituents are known as the exchange energy  $\mathcal{H}_{\text{ex}}$ , the Dzyaloshinskii-Moriya interaction (DMI)  $\mathcal{H}_{\text{dmi}}$ , the Zeeman energy  $\mathcal{H}_z$ , the anisotropy  $\mathcal{H}_{\text{ani}}$ , and the dipolar interaction  $\mathcal{H}_{\text{dipole}}$ .

The first two energy terms describe an interaction of two spins and are commonly written in the form

$$\mathcal{H}_{\text{ex}} = - \sum_{\langle i < j \rangle} J_{ij} \mathbf{s}_i \cdot \mathbf{s}_j \quad \text{and} \quad \mathcal{H}_{\text{dmi}} = - \sum_{\langle i < j \rangle} \mathbf{D}_{ij} \cdot (\mathbf{s}_i \times \mathbf{s}_j) \quad (10.1.2)$$

where the sum  $\sum_{\langle i < j \rangle}$  technically includes interactions between all possible pairs of spins in the system. However, the interaction constants  $J_{ij}$  and  $\mathbf{D}_{ij} = (D_{ij}^x, D_{ij}^y, D_{ij}^z)^T$  are usually non-zero only for small distances between  $i$  and  $j$ . A more general form of writing these interactions exploits that both are quadratic in the spin, thus one can contract them to a combined energy

term:

$$\mathcal{H}_{\text{ex+dmi}} = - \sum_{\langle i < j \rangle} \mathbf{s}_i \mathcal{J}_{ij} \mathbf{s}_j \quad \text{with} \quad \mathcal{J}_{ij} = \begin{pmatrix} J_{ij} & D_{ij}^z & -D_{ij}^y \\ -D_{ij}^z & J_{ij} & D_{ij}^x \\ D_{ij}^y & -D_{ij}^x & J_{ij} \end{pmatrix} \quad (10.1.3)$$

which is the reason why the exchange energy  $\mathcal{H}_{\text{ex}}$  is also referred to as *symmetric exchange* while the DMI energy  $\mathcal{H}_{\text{dmi}}$  is the *asymmetric exchange*. Within this formulation, also the overlap integral of the Wannier functions that are localized on site  $i$ ,  $\varphi_i(\mathbf{r})$ , and site  $j$ ,  $\varphi_j(\mathbf{r})$ , could (at least in principle) be expressed simultaneously for both interactions as

$$\mathcal{J}_{ij}^{\alpha\beta} = \iint \bar{\varphi}_i^\alpha(\mathbf{r}_1) \bar{\varphi}_j^\beta(\mathbf{r}_2) \mathcal{H}(\mathbf{r}_1, \mathbf{r}_2) \varphi_i^\alpha(\mathbf{r}_2) \varphi_j^\beta(\mathbf{r}_1) \, d\mathbf{r}_1 d\mathbf{r}_2 \quad (10.1.4)$$

where the spin-components  $\alpha, \beta = x, y, z$  are explicitly included. Note also that the overlap elements  $\mathcal{J}_{ij}^{\alpha\beta}$  are non-zero for  $\alpha \neq \beta$  only if the full quantum mechanical Hamiltonian  $\mathcal{H}(\mathbf{r}_1, \mathbf{r}_2)$  includes spin-orbit coupling.

The next two terms in the atomistic energy, Eq. 10.1.1, are on-site energy contributions. The first comes from the Zeeman coupling to the external magnetic field  $\mathbf{B}_{\text{ext}}$

$$\mathcal{H}_z = -\mu_s \sum_i \mathbf{B}_{\text{ext}} \cdot \mathbf{s}_i \quad (10.1.5)$$

where the magnetization of the normalized classical spin  $\mathbf{s}_i$  is encoded in the prefactor  $\mu_s$ . The anisotropy contribution is dependent on the considered lattice which couples to the spin via spin-orbit coupling. For a cubic magnet with an additional uniaxial anisotropy in the direction  $\hat{\nu}$ , this term reads

$$\mathcal{H}_{\text{ani}} = - \sum_i K_u (\hat{\nu} \cdot \mathbf{s}_i)^2 + K_c (\mathbf{s}_{i,x}^4 + \mathbf{s}_{i,y}^4 + \mathbf{s}_{i,z}^4) \quad (10.1.6)$$

with the uniaxial anisotropy  $K_u$  which can either yield an easy-plane ( $K_u < 0$ ) or easy-axis anisotropy ( $K_u > 0$ ) and with the cubic anisotropy  $K_c$  which for  $K_c < 0$  prefers the spins aligned with the diagonals of the cubic lattice. Higher order terms or other lattice symmetries can also be considered but lattice anisotropies are not subject of this thesis.

The last term that was included in Eq. 10.1.1 is the dipolar interaction (also *magnetostatic interaction*) of the spins which is the only term with an explicit long-range interaction

$$\mathcal{H}_{\text{dipole}} = -\frac{\mu_s^2 \mu_0}{4\pi a^3} \sum_{i < j} -\frac{3(\hat{\mathbf{r}}_{ij} \cdot \mathbf{s}_i)(\hat{\mathbf{r}}_{ij} \cdot \mathbf{s}_j) - \mathbf{s}_i \cdot \mathbf{s}_j}{|\mathbf{r}_{ij}|^3} \quad (10.1.7)$$

with the vector  $\mathbf{r}_{ij}$ ,  $\hat{\mathbf{r}}_{ij} = \mathbf{r}_{ij}/|\mathbf{r}_{ij}|$ , that connects the sites  $i$  and  $j$ , the magnetic moment per spin  $\mu_s$ , and the volume of a unit cell  $a^3$ . In some cases, this terms leads only to a renormalized anisotropy  $K_u$  [222] but if considered in full detail, the long-range character makes computations far more costly. In the following discussions, we will either assume that this contribution is not relevant for the observed effects or is included as an approximation in the anisotropy.

## 10.2. Micromagnetic model

The micromagnetic model is the one which is used throughout this work. It assumes magnetization as a continuous function in space and time. Nevertheless, for most numerical purposes it is afterwards discretized, see Sec. 10.5.

### 10.2.1. Derivation from symmetry considerations

Consider the magnetization  $\mathbf{M}(\mathbf{r})$  a classical function that varies smoothly over large distances  $\lambda \gg a$ , where  $a$  is the atomic lattice constant. Then, we can follow the idea of Landau and Lifshitz and write a phenomenological free energy functional  $F[\mathbf{M}] = \int \mathcal{F}[\mathbf{M}] d\mathbf{r}^3$  as an expansion in terms of slowly varying textures in space. We hence sum over all possible polynomials  $f_{QR}(\nabla, \mathbf{M})$  composed of  $Q$  powers of derivatives  $\partial_i$  and  $R$  powers of components of the magnetization  $\mathbf{M}_j$ , each with an independent prefactor [223]. By considering the symmetries of the underlying system, we can then reduce the number of prefactors.

Most materials considered here have a B20 crystal structure (P2<sub>1</sub>3 space group), which obeys a threefold rotation axis  $\langle 111 \rangle$  and the twofold screw axis  $\langle 100 \rangle$ . If considering these symmetry requirements, the remaining terms up to  $Q = 2$  and  $R = 4$  can be found e.g. in Bak and Jensen, Ref. [11], as

$$\begin{aligned} \mathcal{F}[\mathbf{M}] = & r_0 \mathbf{M}^2 + U(\mathbf{M}^2)^2 + D \mathbf{M} \cdot (\nabla \times \mathbf{M}) - \mathbf{H} \cdot \mathbf{M} \\ & + \frac{J}{2} [(\partial_i M_j)^2] + \frac{J'}{2} [(\delta_{ij} \partial_i M_j)^2] + U'(M_x^4 + M_y^4 + M_z^4) \end{aligned} \quad (10.2.8)$$

where  $i, j \in \{x, y, z\}$  are summed over and with the parameters and their physical interpretations as there are the Dzyaloshinskii-Moriya interaction  $D$ , the magnetic stiffness (ferromagnetic exchange)  $J$ , the anisotropic stiffness  $J'$ , the cubic anisotropies  $U'$ , and the Zeeman coupling to the magnetic field  $\mathbf{H}$ . The Ginzburg-Landau parameters  $r_0$  and  $U$  handle the absolute value of the magnetization with  $r_0$  the reduced temperature, such that the magnetization is large at low temperatures and vanishes,  $|\mathbf{M}| = 0$ , at the phase transition to the paramagnetic phase.

Note that the higher order dependence on  $M_i$  in the cubic anisotropy  $U'$  makes this term less relevant if the temperature is elevated. On lower temperatures, however, this term becomes more important and has recently been identified to even stabilize a long overlooked skyrmion phase [224]. The pinning of the helical phase at lower magnetic fields can be described by the anisotropic stiffness  $J'$  [11] and persists to high temperatures. Notwithstanding, it turns out that this term is not necessary to describe the formation of a skyrmion lattice but it might have an impact on the orientation of a such. Note also that long-ranged interactions, in particular dipolar interactions, are not included at this stage.

### 10.2.2. The isotropic bulk chiral magnet

In this thesis we always assume that we act in regimes where effects due to anisotropies are negligible. This is well justified since spin-orbit-coupling is usually a small number and anisotropies are at least fourth order in the spin-orbit-coupling as compared to the Dzyaloshinskii-Moriya-term which is only second order. Therefore we introduce a simplification by ignoring the anisotropic effects,  $J' = U' = 0$ . Furthermore, the actual amplitude of the magnetization is fixed by the Ginzburg-Landau parameters. We consequently remove these degrees of freedom,  $r_0 = U = 0$ , at the price of assuming a magnetization with constant amplitude throughout the

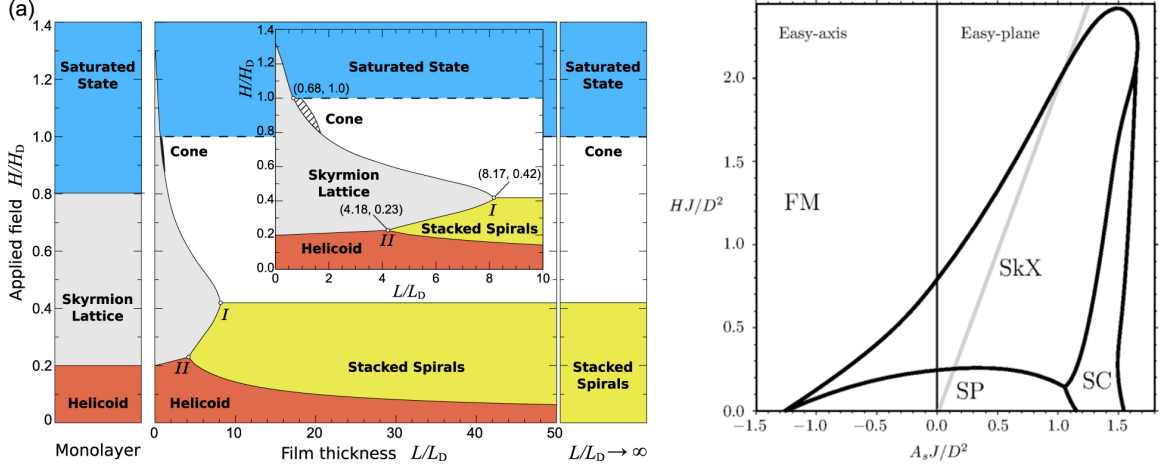


Figure 10.2.1.: Phase diagrams of the micromagnetic models for the isotropic bulk chiral magnet (left, taken from Ref. [111]) and the isotropic two-dimensional magnet (right, taken from Ref. [108]). The left phase diagram includes also thin films of the bulk chiral magnet. Note that the right phase diagram is valid for both types of DMI, see Eq. 10.2.10 and Eq. 10.2.11. The axes are labeled in rescaled units, see Sec. 10.4.

system,  $|\mathbf{M}(\mathbf{r})| = M_s$ . The normalized magnetization is then denoted as  $\hat{n} = \mathbf{M}/M_s$ . The free energy of an isotropic chiral magnet in this model then simply reads

$$F[\hat{n}] = \int \frac{J}{2} (\nabla \hat{n})^2 + D \hat{n} \cdot (\nabla \times \hat{n}) - \mu_0 M_s \mathbf{H} \cdot \hat{n} \, d\mathbf{r}^3 \quad (10.2.9)$$

with only the exchange stiffness  $J$ , DMI  $D$ , and Zeeman coupling  $\mathbf{H}$  left. Sometimes the substitution  $A = J/2$  is used. The ground-state phase diagram for this model as a function of thickness is shown in the left panel of Fig. 10.2.1. Due to the normalization of the magnetization this simplification is also known as the *non-linear sigma model*.

### 10.2.3. The isotropic two-dimensional magnet

When reducing the isotropic model from  $d = 3$  to  $d = 2$  spatial dimensions,  $\hat{\nu}$  denotes the direction perpendicular to the two-dimensional plane. While the model is still assumed isotropic in the plane, it has explicitly become anisotropic in the  $\hat{\nu}$ -direction. A polynomial expansion of the free energy can hence include the anisotropy term  $-K(\hat{\nu} \cdot \hat{n})^2$  where we distinguish between anisotropies with an *easy-axis* ( $K > 0$ ) or an *easy-plane* ( $K < 0$ ). In the following chapters, the normal of the plane is chosen as  $\hat{\nu} = \hat{z}$ , hence  $-K(\hat{z} \cdot \hat{n})^2 = -K\hat{n}_z^2$ ,

$$F[\hat{n}] = \int \frac{J}{2} (\nabla \hat{n})^2 + D \hat{n} \cdot (\nabla \times \hat{n}) - \mu_0 M_s \mathbf{H} \cdot \hat{n} - K \hat{n}_z^2 \, d\mathbf{r}^2 \quad (10.2.10)$$

This energy functional describes the monolayer of a chiral magnet, accordingly, it includes the bulk-type DMI and will stabilize Bloch-type helices and skyrmions. Furthermore, if the monolayer is an approximation to a thin film of thickness  $t$ , then the dipolar interaction, Eq. 10.1.7, can be approximated as an effective contribution to the uni-axial anisotropy,  $K \rightarrow K - \mu_0 M_s^2 t/2$ , with  $t$  the thickness of the thin film [222]. If, however, we consider thin films or multilayer systems which are inversion symmetric in the plane but break mirror symmetry

along the normal  $\hat{\nu}$  by a chiral stacking of layers or a surface, interfacial DMI replaces its bulk counterpart and stabilizes spirals and Néel-type skyrmions. We can deduce the interfacial DMI directly from the bulk DMI by replacing  $\nabla \rightarrow \hat{z} \times \nabla$ , as a result

$$F[\hat{n}] = \int \frac{J}{2} (\nabla \hat{n})^2 + D \hat{n} \cdot ((\hat{z} \times \nabla) \times \hat{n}) - \mu_0 M_s \mathbf{H} \cdot \hat{n} - K \hat{n}_z^2 \, d\mathbf{r}^2 \quad . \quad (10.2.11)$$

The common phase diagram for both these models is shown in the right panel of Fig. 10.2.1.

Note that we have only discussed the isotropic scenario. Apart from the anisotropic terms discussed in the context of B20 symmetries, systems with less symmetries might explicitly break rotation symmetries and hence allow for direction-dependent exchange constants. It might then turn out useful to do a more general replacement as before, where based on Eq. 10.2.10 we can make the replacement  $D\nabla \rightarrow \mathbb{D}\nabla$  where  $\mathbb{D}$  now is a matrix. Materials can be classified according to the rank  $r$  of  $\mathbb{D}$  [201]. Interestingly, it directly turns out that skyrmions are stabilized if  $\det(P(\mathbb{D})) = 1$  whereas anti-skyrmions are stabilized if  $\det(P(\mathbb{D})) = -1$  [201], where  $P$  is the projection of  $\mathbb{D}$  onto the plane in which the objects should appear. Finally, skyrmions and anti-skyrmions coexist with equal energy if  $\det(P(\mathbb{D})) = 0$ , e.g. in mono-axial chiral magnets. Note that in these scenarios also the exchange  $J$  can be anisotropic beyond the terms discussed in Eq. 10.2.8.

#### 10.2.4. Connection to atomistic model

The micromagnetic model can alternatively be derived from the atomistic model. Here, the basic requirement is that the interactions between the Heisenberg spins  $\{\hat{s}_i\}$  of the atomistic model are such that variations in the magnetic texture occur on large length scales compared to the lattice spacings. Then the spin texture can be approximated by a continuous magnetization  $\hat{n}(\mathbf{r})$  which takes the values  $\{\hat{s}_i\}$  on the respective lattice sites  $\mathbf{r} = \mathbf{r}_i$ . As an example, consider now the Heisenberg coupling  $J_{ij} \hat{s}_i \cdot \hat{s}_j$  between spins at sites  $i$  and  $j$ . Let the spatial distance between these sites be given in terms of the distance  $a_{ij}$  and the unit vector  $\hat{\nu}$  pointing from  $i$  to  $j$ . Then we can derive the corresponding exchange stiffness in the micromagnetic model as follows:

$$\begin{aligned} 2J_{ij} \hat{s}_i \cdot \hat{s}_j &= -J_{ij} (\hat{s}_i - \hat{s}_j)^2 + J_{ij} (\hat{s}_i^2 + \hat{s}_j^2) \\ &\quad \text{use that the } \{\hat{s}_i\} \text{ are Heisenberg spins, i.e. } \hat{s}_i^2 = 1 \\ &= -J_{ij} a_{ij}^2 \left( \frac{\hat{s}_i - \hat{s}_j}{a_{ij}} \right)^2 + \text{const} \\ &\quad \text{use that } \hat{s}_i = \hat{n}(\mathbf{r}_i) \text{ on the lattice sites } \mathbf{r}_i \\ &= -J_{ij} a_{ij}^2 \left( \frac{\hat{n}(\mathbf{r}_i) - \hat{n}(\mathbf{r}_j)}{a_{ij}} \right)^2 + \text{const} \\ &\quad \text{use that } \hat{n}(\mathbf{r}) \text{ is smooth, thus } \partial_\nu \hat{n}(\mathbf{r}_i) \approx a_{ij}^{-1} [\hat{n}(\mathbf{r}_j) - \hat{n}(\mathbf{r}_i)] \\ &\quad \text{use further that } \partial_\nu \hat{n}(\mathbf{r}_i) = \partial_\nu \hat{n}(\mathbf{r}) \text{ by translational symmetry} \\ &\approx -J_{ij} a_{ij}^2 [\partial_\nu \hat{n}(\mathbf{r})]^2 + \text{const} \end{aligned} \quad (10.2.12)$$

In order to finally obtain the exchange constant for the micromagnetic model, the symmetries of the atomic lattice have to be taken into account. Assuming a simple cubic lattice with only

nearest neighbor interaction  $J_1$  and lattice spacing  $a$ , we obtain the mapping

$$\sum_{\langle ij \rangle} J_1 \hat{s}_i \cdot \hat{s}_j = \sum_{i, \hat{\nu}} \frac{J_1}{2} \hat{s}_i \cdot \hat{s}_{i+\hat{\nu}} \approx E_0 - \sum_i a^3 \frac{J_1}{2a} [\nabla \hat{n}(\mathbf{r})]^2 \approx E_0 - \int \frac{J}{2} [\nabla \hat{n}(\mathbf{r})]^2 d\mathbf{r}^3 \quad (10.2.13)$$

where the second sum includes only the nearest neighbors,  $\hat{\nu} = \pm\hat{x}, \pm\hat{y}, \pm\hat{z}$ , and the micromagnetic exchange constant evaluates to  $J = aJ_1$ . In general, however, the stiffness is a function of all hierarchies of neighbors,  $J = J(J_1, J_2, \dots)$ . An advantage of this mapping is that the micromagnetic model is independent of the atomic lattice. Consequently, the distance between lattice sites for a numerical implementation of the micromagnetic model may exceed the distance of the underlying atomistic model by far which can be exploited for more efficient numerical calculations, see e.g. Ref. [225]. Note that if the atomistic exchange interaction is frustrated, higher order derivatives in the free energy functional become important [120, 122].

## 10.3. Dynamics of magnetization

### 10.3.1. The Landau-Lifshitz-Gilbert equation

Already back in 1935, Landau and Lifshitz proposed a phenomenological equation of motion for the magnetization [226], which is therefore called the *Landau-Lifshitz equation*. To derive the equation phenomenologically, it is handy to start from the equation of motion for a single magnetic moment  $\mathbf{M}$  in an external magnetic field  $\mathbf{B}_{\text{ext}}$ . If the magnetic moment is not aligned with the field, it will precess around the field with a frequency set by the gyromagnetic ratio  $\gamma$ . We introduce again the normalized magnetic moment  $\hat{n} = \mathbf{M}/M_s$  and write the equation of motion:

$$\partial_t \hat{n} = -\gamma \hat{n} \times \mathbf{B}_{\text{ext}}. \quad (10.3.14)$$

In a solid, however, the magnetic moment interacts with its environment via phonons or magnons which causes dissipation of energy and angular momentum. Henceforth, in a real world setup, we have to add dissipation to this equation of motion. In addition to the precession, a term is required that aligns the moment in the direction of the effective field. This can be achieved by an additional term in the time-evolution which stands perpendicular on the precession, pointing towards the now *effective field*  $\mathbf{B}_{\text{eff}}$  which differs from the external field since it also takes interactions between the moments into account. The Landau-Lifshitz equation (LL) then reads

$$\partial_t \hat{n} = -\gamma \hat{n} \times \mathbf{B}_{\text{eff}} - \gamma \lambda \hat{n} \times \hat{n} \times \mathbf{B}_{\text{eff}} \quad (10.3.15)$$

with the dimensionless damping parameter  $\lambda$ . It turns out that for large damping, however, this simple equation leads to unphysical results since the damping contribution then accelerates the overall motion. A way out of this dilemma was proposed by Gilbert [227, 228] who reformulated the LL equation such that it is also consistent for larger damping<sup>1</sup>. The resulting equation is known as the *Landau-Lifshitz-Gilbert equation* (LLG) and reads

$$\partial_t \hat{n} = -\gamma_G \hat{n} \times \mathbf{B}_{\text{eff}} + \alpha \hat{n} \times \partial_t \hat{n} \quad (10.3.16)$$

---

<sup>1</sup>Note that the original work from 1955 by Gilbert, Ref. [227], is only published as an abstract. The full report has been classified as “*Armor Research Foundation Project No. A059, Supplementary Report, May 1, 1956*” and has never been published. In 2004, however, Gilbert summarized the original content in Ref. [228].

with the dimensionless damping parameter  $\alpha$  and the gyromagnetic ratio  $\gamma_G$  in the Gilbert formulation. Note that the LL equation 10.3.15 and the LLG equation 10.3.16 are related via  $\lambda = \alpha$  and  $\gamma = \gamma_G/(1 + \alpha^2)$ . Finally, we identify the effective magnetic field  $\mathbf{B}_{\text{eff}}$  with a variation of the free energy functional  $F[\hat{n}]$ , namely such that  $\mathbf{B}_{\text{eff}}$  points in the direction which minimizes  $F[\hat{n}]$  locally:

$$\mathbf{B}_{\text{eff}}(\mathbf{r}) = -\frac{\delta}{M_s \delta \hat{n}(\mathbf{r})} F[\hat{n}]. \quad (10.3.17)$$

If we consider, for example, an isotropic bulk chiral magnet as described by the energy functional given in Eq. 10.2.9, then we recover the following expression for the effective magnetic field

$$\begin{aligned} -M_s \mathbf{B}_{\text{eff}} &= \frac{\delta}{\delta \hat{n}} F[\hat{n}] = \left( \partial_{(\hat{n}_i)} - \partial_j \partial_{(\partial_j \hat{n}_i)} \right) \mathcal{F}[\hat{n}] \\ &= \left( \partial_{(\hat{n}_i)} - \partial_j \partial_{(\partial_j \hat{n}_i)} \right) \left( \frac{J}{2} (\partial_k \hat{n}_l)^2 + D \varepsilon_{klm} \hat{n}_k \partial_l \hat{n}_m - \mu_0 M_s \mathbf{H}_k \hat{n}_k \right) \\ &= D \varepsilon_{ilm} \partial_l \hat{n}_m - \mu_0 M_s \mathbf{H}_i - \left( J \partial_j^2 \hat{n}_i + D \varepsilon_{kji} \partial_j \hat{n}_k \right) \\ &= -J \Delta \hat{n} + 2D \nabla \times \hat{n} - \mu_0 M_s \mathbf{H} \end{aligned} \quad (10.3.18)$$

where we used the abbreviation  $\partial_{(\hat{n}_i)} = \partial/(\partial \hat{n}_i)$  and implicit summations over indices that occur twice.  $\Delta = \nabla^2$  is the Laplace operator. Note that in a non-interacting model, the effective field is precisely given by the external field.

For simulations of the dynamics at finite temperature, a term  $\mathbf{b}_{\text{fl}}$  which fluctuates in space and time is added to the effective field,  $\mathbf{B}_{\text{eff}} \rightarrow \mathbf{B}_{\text{eff}} + \mathbf{b}_{\text{fl}}$ . On average, the fluctuating field has to vanish,  $\langle \mathbf{b}_{\text{fl}}(\mathbf{r}, t) \rangle = 0$ , but in order to fulfill the fluctuation-dissipation theorem, the variance has to follow

$$\langle \mathbf{b}_{\text{fl}}^i(\mathbf{r}, t) \mathbf{b}_{\text{fl}}^j(\mathbf{r}', t') \rangle = 2\alpha \frac{k_B T}{\gamma_G M_s} \delta_{ij} \delta(\mathbf{r} - \mathbf{r}') \delta(t - t') \quad (10.3.19)$$

where  $i$  and  $j$  are the vector-components of the field. However, all simulations that are presented in the following are done at  $T = 0$  without thermal fluctuations, except for those where a small fluctuating field is used to break the translational symmetries of the system. Thus, for a more detailed investigation of this topic see Ref. [229].

### 10.3.2. Spin-torques for the manipulation of magnetic textures

The interaction of spin-polarized currents and the magnetic texture is modeled by adding more torques to the LLG equation. Overall, there are four types of spin-torques that are commonly studied in the context of spintronics, see e.g. Ref. [146].

The first two stem from the adiabatic and non-adiabatic spin-transfer-torque, i.e. the torque that the texture experiences when the spin-current aligns locally to the magnetic structure: If the magnetic texture varies in space, the polarization of the spin-current has to align which means that a torque acts on the spins. Since torque is conserved, however, the same torque also acts on the magnetization:

$$\tau_{\text{adiab.}} = -(\mathbf{v}_s \cdot \nabla) \hat{n} \quad (10.3.20)$$

$$\tau_{\text{non-adiab.}} = \beta \hat{n} \times ((\mathbf{v}_s \cdot \nabla) \hat{n}). \quad (10.3.21)$$

Here  $\mathbf{v}_s$  is the spin-polarized current, which is directly proportional to the applied electric current density  $\mathbf{j} = nev$ . The adiabatic and the non-adiabatic spin-transfer-torques are often

directly included as corrections to the time derivatives  $\partial_t$  in the LLG equation

$$(\partial_t + (\mathbf{v}_s \cdot \nabla))\hat{n} = -\gamma_G \hat{n} \times \mathbf{B}_{\text{eff}} + \alpha \hat{n} \times (\partial_t + \frac{\beta}{\alpha}(\mathbf{v}_s \cdot \nabla))\hat{n} \quad (10.3.22)$$

where it then becomes more obvious that the case  $\alpha = \beta$  is Galilei invariant, i.e. the influences of the torques vanish under a transformation into a comoving frame of reference  $\partial_t \rightarrow \partial_t - (\mathbf{v}_s \cdot \nabla)$ . While here the terms appear phenomenologically, rigorous derivations of the LLG equation have been found by various methods, including Keldysh formalism [230], variational principle [231], or imaginary time methods [232] which even allow to calculate estimates for the damping coefficients  $\alpha$  and  $\beta$ . For an overview, see also Ref. [223], where also higher order damping terms are derived.

In the context of spin-orbitronics, often thin films are considered which are placed on top of a material with good conducting properties, see Ref. [233] for a detailed review or Ref. [234] for a popular review on spin-orbit-torques. In these setups the current in the conducting layer experiences a spin Hall effect [235] which leads to a separation of spin currents with opposite polarization. The separation induces a polarized spin-current [236,237] into the magnetic layer. The polarization properties are governed by the Rashba [238] or Dresselhaus [239] effect. In addition, the inverse spin galvanic effect leads to an accumulation of spin at the interface to the magnet which yields an additional torque on the magnetic moments. Using the notation from Ref. [146], the resulting torques can be written as

$$\tau_{\text{IP}} = \frac{u}{t} \hat{n} \times (\hat{p} \times \hat{n}) \quad (10.3.23)$$

$$\tau_{\text{OOP}} = -\xi \frac{u}{t} \hat{n} \times \hat{p} \quad (10.3.24)$$

with the current density  $u$ , the film thickness  $t$ , the ratio between the out-of-plane torque and the in-plane torque  $\xi$ , and the polarization of the spin current  $\hat{p}$ , which is perpendicular to both the direction of the current and the normal of the thin film if generated by spin Hall effect. This concept which is known to work for domain walls [240], has been proposed to also be promising for skyrmions [146] but in the following we restrict the analysis to only the spin-transfer-torques in Eqs. 10.3.20,10.3.21.

### 10.3.3. The Thiele equation of motion

The *Thiele equation* is named after A. A. Thiele who was the first to suggest that the spatial degree of freedom of the LLG equation 10.3.22 could be projected onto the translational motion of a collective coordinate  $\mathbf{R}(t) \in \mathbb{R}^2$  [241,242]. This idea has been widely used in the context of skyrmions, where in effectively two-dimensional systems each skyrmion is described by the dynamics of a coordinate which evolves according to the Thiele equation [45, 141–145, 150].

We follow the derivation in Ref. [150]. For simplicity, we first multiply the LLG equation from the left with  $\hat{n} \times$  and rearrange the terms:

$$\gamma_G \mathbf{B}_{\text{eff}} = -\frac{\gamma_G}{M_s} \frac{\delta}{\delta \hat{n}} F[\hat{n}] = \hat{n} \times (\partial_t + (\mathbf{v}_s \cdot \nabla))\hat{n} + \alpha (\partial_t + \frac{\beta}{\alpha}(\mathbf{v}_s \cdot \nabla))\hat{n} \quad (10.3.25)$$

where we used that  $\hat{n}$  is normalized, hence  $\partial_i \hat{n} \perp \hat{n}$ ,  $i = x, y, z, t$ , and also  $\mathbf{B}_{\text{eff}} \perp \hat{n}$ , since we can always add a constant term  $\propto \hat{n}^2$  to the free energy functional which then eliminates any component of  $\mathbf{B}_{\text{eff}}$  parallel to  $\hat{n}$ , thus  $\hat{n} \times \hat{n} \times \mathbf{B}_{\text{eff}} = -\mathbf{B}_{\text{eff}}$ . Now the crucial assumption is made

that the collective coordinate  $\mathbf{R}(t)$  captures all the time-dependence of the magnetization, thus  $\hat{n}(\mathbf{r}, t) = \hat{n}(\mathbf{r} - \mathbf{R}(t))$ . This implies that excitations of internal modes of the texture should be negligible. The projection  $\mathcal{P}(\mathbf{p}, \frac{d\hat{n}}{dR_i})$  of a function  $\mathbf{p}$  onto a translation of  $\hat{n}$  in the direction  $R_i$  is achieved by the scalar product, i.e.  $\mathcal{P}(\mathbf{p}, \frac{d\hat{n}}{dR_i}) = \langle \frac{d\hat{n}}{dR_i}, \mathbf{p} \rangle = \int \frac{d\hat{n}}{dR_i} \cdot \mathbf{p} d\mathbf{r}^2$ . Note that due to the dependence of the magnetization on  $\mathbf{R}$  we can write

$$\frac{d\hat{n}}{dR_i} = -\frac{d\hat{n}}{dr_i} \quad \text{and} \quad \frac{d\hat{n}}{dt} = \frac{d\mathbf{R}_i}{dt} \frac{d\hat{n}}{dR_i} = -\dot{\mathbf{R}}_i \frac{d\hat{n}}{dr_i} \quad \text{and} \quad (\mathbf{v}_s \cdot \nabla)\hat{n} = \mathbf{v}_{s,i} \frac{d\hat{n}}{dr_i} \quad (10.3.26)$$

where in particular the latter two equations appear as scalar products of the same form. Now the right hand side of Eq. 10.3.25 becomes after the projection

$$\begin{aligned} & \mathcal{P} \left( \hat{n} \times (\partial_t + (\mathbf{v}_s \cdot \nabla))\hat{n} + \alpha (\partial_t + \frac{\beta}{\alpha} (\mathbf{v}_s \cdot \nabla))\hat{n}, \frac{d\hat{n}}{dR_i} \right) \\ &= \int (\dot{\mathbf{R}}_m - \mathbf{v}_{s,m}) \varepsilon_{jkl} \hat{n}_k \frac{d\hat{n}_l}{dr_m} \frac{d\hat{n}_j}{dr_i} + (\alpha \dot{\mathbf{R}}_k - \beta \mathbf{v}_{s,k}) \frac{d\hat{n}_j}{dr_k} \frac{d\hat{n}_j}{dr_i} d\mathbf{r}^2 \\ &= \mathbf{G} \times (\dot{\mathbf{R}} - \mathbf{v}_s) + \mathcal{D}(\alpha \dot{\mathbf{R}} - \beta \mathbf{v}_s) \end{aligned} \quad (10.3.27)$$

with the gyrocoupling vector  $\mathbf{G}$  and the dissipation matrix  $\mathcal{D}$  defined as

$$\mathbf{G} = \hat{z} \int \hat{n} \cdot \left( \frac{d\hat{n}}{dx} \times \frac{d\hat{n}}{dy} \right) d\mathbf{r}^2 = 4\pi \mathcal{W}(\hat{n}) \hat{z} \quad \text{and} \quad \mathcal{D}_{ij} = \int \left( \frac{d\hat{n}}{dx_i} \cdot \frac{d\hat{n}}{dx_j} \right) d\mathbf{r}^2 \quad (10.3.28)$$

where  $\mathcal{W}(\hat{n}) \in \mathbb{Z}$  is the topological winding number as defined in Eq. 1.2.6. The projection of the left hand side of the equation sums over all forces acting on the object described by the collective coordinate. Formally, the functional derivative cancels with the integral and thus

$$-\frac{\gamma_G}{M_s} \frac{dV}{d\mathbf{R}} = \mathbf{G} \times (\dot{\mathbf{R}} - \mathbf{v}_s) + \mathcal{D}(\alpha \dot{\mathbf{R}} - \beta \mathbf{v}_s) \quad (10.3.29)$$

where we introduced the potential energy  $V$  which is defined as the local free energy minimum for a given position  $\mathbf{R}$ , i.e.  $V(\mathbf{R}) = \min_{\hat{n}} F[\hat{n}]$ .

For a rigid and rotation symmetric skyrmion, the dissipation tensor reduces to just a scalar number  $D$ ,  $\mathcal{D} = D\mathbf{1}$ . In a pure and infinitely extended system, i.e.  $V(\mathbf{r} = 0)$ , the direction of motion due to driving by a spin-polarized current  $\mathbf{v}_s$  then is given as

$$\dot{\mathbf{R}} = \frac{1}{\mathbf{G}^2 + \alpha^2 D^2} ((\alpha - \beta) D \mathbf{G} \times \mathbf{v}_s + (|\mathbf{G}|^2 + \alpha \beta D^2) \mathbf{v}_s) \quad (10.3.30)$$

upon inverting Eq. 10.3.29. The more general scenario,  $\mathcal{D} \neq D\mathbf{1}$ , is discussed in Sec. 13.

## 10.4. System of reduced units

The continuous models that we consider, see Eqs. 10.2.9, 10.2.10, 10.2.11, obey scaling relations that make the theoretical results universal for a whole manifold of micromagnetic parameters. The precise choice of reduced units can differ and may as a result dependent on the problem, see for example Ref. [183] and Ref. [150]. In the following, we will derive the two systems of units that are used throughout the following sections, dependent on the dimensionality  $d$  of the system.

This scaling behavior can easily be shown by rescaling all spatial lengths in the  $d$ -dimensional generalization of the minimal model given in Eq. 10.2.9 by a factor  $1/\xi$ , where for now  $\xi$  is some arbitrary number which will later be fixed. If we hence replace  $r \rightarrow \tilde{r} = r/\xi$  and accordingly  $\nabla \rightarrow \tilde{\nabla} = \nabla\xi$  and for consistency also  $\hat{n}(r) \rightarrow \tilde{n}(\tilde{r}) = \hat{n}(r/\xi)$  the equation for the free energy of the isotropic bulk model reads

$$F[\tilde{n}] = \int \frac{J}{2} \xi^{d-2} (\tilde{\nabla} \tilde{n})^2 + D \xi^{d-1} \tilde{n} \cdot (\tilde{\nabla} \times \tilde{n}) - \mu_0 M_s \xi^d \mathbf{H} \cdot \tilde{n} \, d\tilde{\mathbf{r}}^d. \quad (10.4.31)$$

We could now, in principle, solve the problem for a given set of parameters  $(J, D, \mathbf{H})$  and find that for any other set of parameters which related to the previous as  $(J\xi^{d-2}, D\xi^{d-2}, \mathbf{H}\xi^d)$  the same results apply, apart from a scaling factor  $\xi$  for the spatial extent of the texture. Furthermore, we can exploit that rescaling the energy by a constant factor does not change the physics but only the scales on which effects can be observed. Dividing both sides of the equation by  $J\xi^{d-2}$  yields

$$F[\tilde{n}] \frac{\xi^{2-d}}{J} = \int \frac{1}{2} (\tilde{\nabla} \tilde{n})^2 + \frac{D}{J} \xi \tilde{n} \cdot (\tilde{\nabla} \times \tilde{n}) - \frac{\mu_0 M_s}{J} \xi^2 \mathbf{H} \cdot \tilde{n} \, d\tilde{\mathbf{r}}^d. \quad (10.4.32)$$

Now we can make a choice for the parameter  $\xi$  which reduces the number of prefactors of the different expressions to a minimum. The convention in the following will be  $\xi = J/D = 1/Q$ . We can then introduce the dimensionless free energy  $\tilde{F} = F/F_D$  and the dimensionless magnetic field  $\tilde{\mathbf{H}} = \mathbf{H}/H_D$ , where the units  $F_D$  and  $H_D$  absorb all prefactors:

$$\tilde{F}[\tilde{n}] = \int \frac{1}{2} (\tilde{\nabla} \tilde{n})^2 + \tilde{n} \cdot (\tilde{\nabla} \times \tilde{n}) - \tilde{\mathbf{H}} \cdot \tilde{n} \, d\tilde{\mathbf{r}}^d \quad (10.4.33)$$

where the scales are made dimensionless by using the characteristic units of the inverse length  $Q = \xi^{-1}$ , the free energy  $F_D$ , the magnetic field  $H_D$ , and for completeness also the uniaxial anisotropy  $K_D$

$$Q = \frac{D}{J}, \quad F_D = JQ^{2-d}, \quad H_D = \frac{D^2}{\mu_0 M_s J}, \quad K_D = \frac{D^2}{J}. \quad (10.4.34)$$

The model in Eq. 10.4.33 is now described by only one parameter,  $\tilde{\mathbf{H}} = \mu_0 M_s J \mathbf{H} / D^2$  instead of the three initial parameters, which is an essential reduction of complexity. The length of a helical period  $\lambda_D = 2\pi/Q$  is sometimes used as an alternative to the inverse length  $Q$ . Note that the scaling behavior of the interfacial DM energy is identical to the bulk DMI, therefore, the same scaling applies.

This choice of reduced units has also consequences for the scaling properties of the time-dependence. When we rescale the free energy by  $F_D$ , this implies a rescaling of the effective magnetic field  $\mathbf{B}_{\text{eff}}$  which enters the LLG equation and thus the time-evolution. Note that the scaling of the spatial components rescales the functional derivative similar to  $\nabla^d$  by a factor  $Q^d$ :

$$-\gamma_G \mathbf{B}_{\text{eff}} = \frac{1}{M_s} \frac{\delta}{\delta \hat{n}} F[\hat{n}] = \frac{\gamma_G}{M_s} \left( Q^d \frac{\delta}{\delta \tilde{n}} \right) \left( JQ^{2-d} \tilde{F}[\tilde{n}] \right) = \frac{\gamma_G JQ^2}{M_s} \frac{\delta}{\delta \tilde{n}} \tilde{F}[\tilde{n}]. \quad (10.4.35)$$

Since we only consider the scaling properties of the LLG equation and the damping parameters

are already dimensionless, these terms can be safely ignored,  $\alpha = \beta = 0$ . We then recover for the time  $t$  and the current density  $\mathbf{v}_s$  the scaling relations by inserting the rescaled effective field into Eq. 10.3.25

$$-\frac{\gamma_G J Q^2}{M_s} \frac{\delta}{\delta \tilde{n}} \tilde{F}[\tilde{n}] = \gamma_G \mathbf{B}_{\text{eff}} = \tilde{n} \times \left( \frac{d}{dt} + (\mathbf{v}_s \cdot \nabla) \right) \tilde{n} = \tilde{n} \times \left( \frac{1}{t_D} \frac{d}{d\tilde{t}} + (Q v_D \tilde{\mathbf{v}}_s \cdot \tilde{\nabla}) \right) \tilde{n}. \quad (10.4.36)$$

From this equation now follows the characteristic time  $t_D$  and velocity  $v_D$

$$t_D = \frac{s}{J Q^2}, \quad v_D = \frac{1}{Q t_D} = \frac{J Q}{s}, \quad s = \frac{M_s}{\gamma_G} \quad (10.4.37)$$

where  $s$  is the spin density, e.g.  $s = \hbar/(2a_0^d)$  for a single spin 1/2 in a unit cell of a cubic lattice with length  $a_0$ . In the following sections, the rescaled units will often be used as the starting point and the extra tilde will be omitted for readability.

## 10.5. Micromagnetic simulations

For the analysis of the problems that are presented in the following sections, special analytical and numerical methods are introduced which are suited specifically for each problem. This introductory part, therefore, only captures the main method that is used throughout all chapters, the *micromagnetic simulations*. Here, the micromagnetic simulations serve as a tool with two major tasks: (i) to analyze time-dependent problems by solving the micromagnetic equations of motion, see Sec. 10.3, and (ii) to minimize magnetic textures in order to study thermodynamic ground states and calculate phase diagrams.

### 10.5.1. A simple discretization of space and time

The models for the continuous magnetization, see Eqs. 10.2.9, 10.2.10, 10.2.11, can be treated numerically via a discretization of the continuous function  $\hat{n}(\mathbf{r})$  onto a lattice  $\{\mathbf{r}_i\}$ , see Fig. 10.5.2. While the lattice may in general be arbitrary, we here consider a square lattice (cubic lattice for three-dimensional calculations) with the lattice constant  $a$ , whereas other works might use a triangular lattice for the implementation. However, since here our aim is to describe properties of the isotropic model, the lattice constant  $a$  has to be chosen sufficiently small compared to variations of the magnetization,  $a \ll \lambda_D$ , such that anisotropic effects due to the lattice symmetries become negligible.

For our simple cubic lattice which is spanned by the unit vectors  $\hat{e}_i$ ,  $i = x, y, z$ , the spatial derivatives are discretized by differences of nearest neighbors:

$$\partial_i \hat{n}(\mathbf{r}) = \frac{1}{2a} (\hat{n}(\mathbf{r} + a\hat{e}_i) - \hat{n}(\mathbf{r} - a\hat{e}_i)) + \mathcal{O}(a^2) \quad (10.5.38)$$

$$\partial_i^2 \hat{n}(\mathbf{r}) = \frac{1}{a^2} (\hat{n}(\mathbf{r} + a\hat{e}_i) - 2\hat{n}(\mathbf{r}) + \hat{n}(\mathbf{r} - a\hat{e}_i)) + \mathcal{O}(a^2) \quad (10.5.39)$$

where the numerical error scales with  $\mathcal{O}(a^2)$ . Hereafter, the approximation becomes better for smaller values of  $a \ll \lambda_D$ . This symmetric discretization is used throughout for all spatial derivatives in both the effective magnetic fields  $\mathbf{B}_{\text{eff}}$  and when computing the total energy of a configuration. Note that this discretization of the micromagnetic model is effectively an

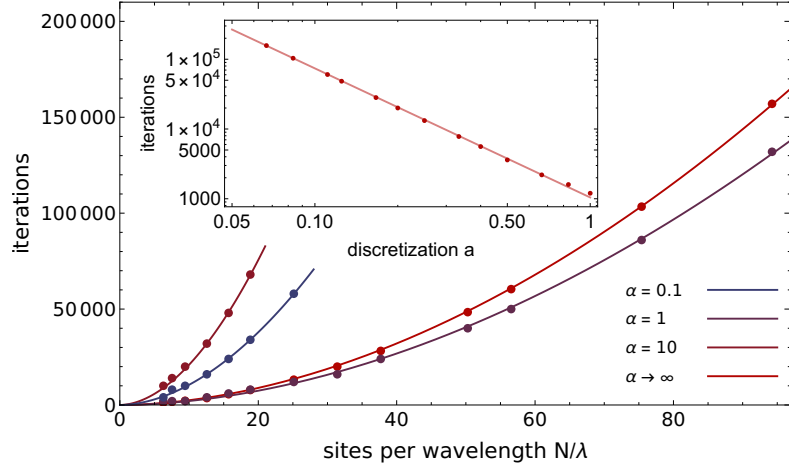


Figure 10.5.2.: The methods for minimization of energy were applied to a single skyrmion in a polarized background with  $\tilde{K} = 0$  and  $\tilde{\mathbf{H}} = \hat{z}$  on a  $10/Q \times 10/Q$  two-dimensional plane with periodic boundary conditions. The plot shows the number of iterations that were needed to reach convergence as a function of the number of lattice sites per helical wavelength  $\lambda = 2\pi/Q$  (dots). The color encodes the value for the Gilbert damping  $\alpha$ . The width of time-steps is constant  $\delta t = 0.05$  and not optimized. The lines are polynomial fits  $\propto a^{-1.85}$ . The number of iterations is thus approximately linear in the total number of spins  $N_{\text{total}} = 100 a^{-2}$ . Note that, however, the computation time per iteration also grows approximately linear in  $N_{\text{total}}$ .

atomistic model with only nearest neighbor interactions.

Concerning the time-evolution, the LLG equation, Eq. 10.3.22, is rewritten in a LL form which is more suitable for the numerical integration and reads in dimensionless units

$$\partial_t \hat{n} = \frac{1}{1 + \alpha^2} \left( -\hat{n} \times \mathbf{B}_{\text{eff}} - \alpha \hat{n} \times \hat{n} \times \mathbf{B}_{\text{eff}} - (1 + \alpha\beta)(\mathbf{v}_s \cdot \nabla) \hat{n} - (\alpha - \beta) \hat{n} \times (\mathbf{v}_s \cdot \nabla) \hat{n} \right). \quad (10.5.40)$$

This linear differential equation can be integrated over time with a standard fourth order Runge-Kutta method [243].

### 10.5.2. Infinite damping for energy minimization

The calculation of phase diagrams and interaction potentials requires a method which calculates the energy of a (local) energy minimum with respect to certain boundary conditions, e.g. a particular winding number density or a fixed distance between two skyrmions.

A simple method which is used throughout this thesis exploits the dissipative dynamics of the LLG equation 10.3.16 or 10.5.40 with  $\mathbf{v}_s = 0$ , which are governed by the Gilbert damping coefficient  $\alpha$ : While an initial texture is iterated for finite  $\alpha > 0$ , it dissipates energy and therefore will decay into a local minimum. The final state, however, depends on both the initial configuration and also the damping  $\alpha$  since fluctuations in the energy density might help the system to overcome energy barriers and even lead to changes in the winding number. In Sec. 3 the value for  $\alpha$  was fine-tuned to a fast relaxation while remaining in the same subspace of textures as the initial configuration.

An even simpler method can be deduced by exploiting the dissipative part of the LLG dynamics to the fullest. The idea here is that the nearest local minimum is, by definition, a

steady state, i.e.  $\partial_t \hat{n} = 0$ . The full magnetization dynamics, as provided by the LLG equation, therefore are not required to reach this state but only the dissipative part is. Thus, omitting the gyrational part of the LLG dynamics, which is equivalent to taking the limit  $\alpha \rightarrow \infty$ , results in a more direct descent in the energy landscape. After rescaling time by the remaining factor  $\alpha/(1 + \alpha^2)$ , the resulting dynamics are simply

$$\partial_t \hat{n}(\mathbf{r}) = \hat{n} \times \hat{n} \times \mathbf{B}_{\text{eff}}(\mathbf{r}) = \mathbf{B}_{\text{eff}}^\perp(\mathbf{r}) \quad (10.5.41)$$

where only the component of  $\mathbf{B}_{\text{eff}}$  perpendicular to  $\hat{n}$  is required. With this method we have a fast and also robust method for the minimization of energy at hand.

A straightforward comparison of the convergence properties of the two methods,  $\alpha = 0.1, 1, 10$  and  $\alpha \rightarrow \infty$ , is shown in Fig. 10.5.2. The plot shows the number of iterations of the entire LLG equation 10.5.40 which is needed in order to reach the convergence criterion (here  $\max_i |\partial_t \hat{n}(\mathbf{r}_i)| < 10^{-10}$ ). It turns out that in all cases the number of iterations grows almost linearly in the number of lattice sites. Note that the number of operations per iteration grows also linear in the number of sites since in each iteration the effective field  $\mathbf{B}_{\text{eff}}$  is calculated for every lattice site individually. The plot shows that for the particular setup – a single skyrmion in a polarized background – a damping coefficient  $\alpha = 1$  requires the least iterations. Yet the method with  $\alpha \rightarrow \infty$  is used mostly throughout this work, since it also offers a fast decay which is more universal.

### 10.5.3. Higher order discretization: Better accuracy, less runtime.

The symmetric discretization of derivatives as defined in Sec. 10.5.1 is a common technique that is widely spread and gives accurate results if the distance between lattice sites  $a$  is small. Consequently, if a high numerical accuracy is needed, the number of lattice sites becomes large and the computation soon very expensive. If additionally the system is large, as for example in Sec. 3, then the limits of computability are soon reached.

But not only calculations which need high accuracy suffer from the bad scaling properties of the simple discretization as has been pointed out in Ref. [96] by Buhrandt and Fritz. There, the anisotropy due to the discretization on the cubic lattice leads to a strong pinning of the helical phase and spoils the results. The authors propose a way out of the anisotropy problem by introducing next nearest neighbor interactions in their atomistic Heisenberg model which cancel the leading order anisotropic contributions.

Transferring this idea to the isotropic continuous models that we consider here, this idea corresponds to discretizing the derivatives to higher order than  $\mathcal{O}(a^2)$ . Let us consider a symmetric discretization of the derivatives by taking  $N$  spins on each side into account. Then most generally we can write

$$\partial_i \hat{n}(\mathbf{r}) = \frac{1}{a} \left( \sum_{m=-N}^N g_{m,1} \hat{n}(\mathbf{r} + ma\hat{e}_i) \right) + \mathcal{O}(a^{2N}) \quad (10.5.42)$$

$$\partial_i^2 \hat{n}(\mathbf{r}) = \frac{1}{a^2} \left( \sum_{m=-N}^N g_{m,2} \hat{n}(\mathbf{r} + ma\hat{e}_i) \right) + \mathcal{O}(a^{2N}) \quad (10.5.43)$$

where the values for the prefactors  $g_{m,i}$  have to be chosen accordingly. A list of the values  $g_{m,i}$  is provided in the Appendix, Sec. 14. Figure 10.5.3 shows the numerical error for  $N = 1, 2, 3, 4$

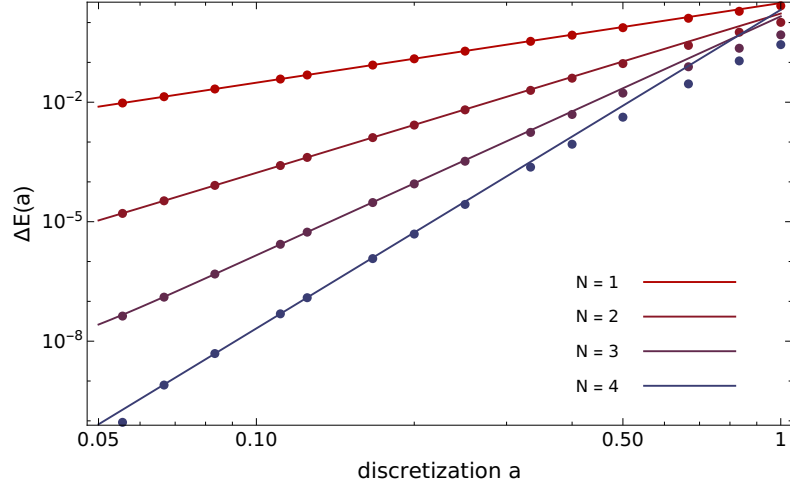


Figure 10.5.3.: The methods for minimization of energy were applied to a single skyrmion in a polarized background with  $\tilde{K} = 0$  and  $\tilde{\mathbf{H}} = \hat{z}$  on a  $10/Q \times 10/Q$  two-dimensional plane with periodic boundary conditions. The plot shows the difference between the numerically computed energy and the energy of the continuous model (dots) as a function of the numerical discretization  $a$ . The latter is determined from an extrapolation of the numerical data. The color encodes the number of neighbors  $N$  per side that was used to discretize the derivatives to a numerical error  $\mathcal{O}(a^{2N})$ . The lines are a fit  $E_{\text{fit}}(a) \propto a^{2N}$ . Note that the output file for the calculated energy only supports 10 digits after the decimal point, which is the reason why the data point for  $N = 4$  with the smallest discretization is not on the fit.

as a function of the discretization  $a$ . The system that was used to determine the energies is a single skyrmion in a ferromagnetic background with  $\tilde{K} = 0$  and  $\tilde{\mathbf{H}} = \hat{z}$  on a  $10/Q \times 10/Q$  two-dimensional plane with periodic boundary conditions. The plot confirms the scaling of the numerical error  $\varepsilon(a) \sim \mathcal{O}(a^{2N})$  and shows two important results:

(i) By taking higher order neighboring spins into account, significantly higher accuracies can be achieved with a reasonable discretization and (ii) the same accuracy is obtained with significantly less lattice sites which corresponds to an enormous speed-up.

Note that the latter is not only due to the smaller number of spins that have to be updated at each iteration but also due to the scaling of the convergence of the method, see Fig. 10.5.2. Let us, for example, compare the calculation with  $N = 1$  at  $a = 0.05$  to the implementation with  $N = 4$  and  $a = 0.5$ . The accuracy of both methods is almost equal while the total number of spins was reduced by a factor  $(a_4/a_1)^2 = 100$ . Now this has to be weighted with the increased computational effort per spin, which is almost 4, thus the net speed-up per iteration is 25. The convergence, however, requires less iterations which leads here to an additional factor that is of the order  $10^2$ . This leads to a total speed-up of the order  $10^3$  which was indeed observed during the calculation.

The discretizations were improved by only taking spins along the main axes of the lattice into account. This may lead to large anisotropic effects, since the total area that contributes becomes highly anisotropic whereas the functional itself is symmetric. An increased anisotropy is indeed observed when regarding the *relative* anisotropy. Fig. 10.5.4 shows a comparison of the anisotropies that arise when using  $N = 1$  neighbor (red curves) and  $N = 4$  neighbors (blue curves) for the discretization of a helix. As discussed in Ref. [96], the diagonal  $[1, 1]$ -direction is favored by the anisotropies of the square lattice. The least favorable directions are the main axes. The plots show that with finer discretization,  $a = \lambda/6, \lambda/12, \lambda/25, \lambda/42$ , the results

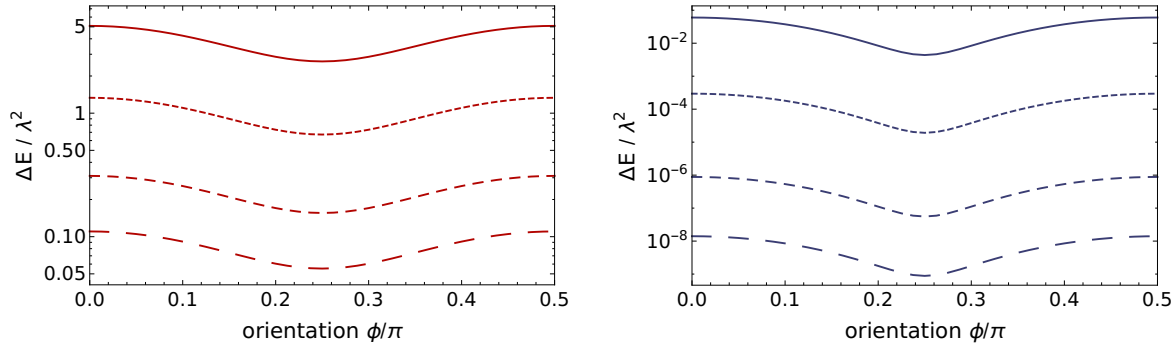


Figure 10.5.4.: Visualization of the anisotropy due to the lattice discretization. The exact helix solution without any anisotropy or external field,  $\lambda = 2\pi$ , was initialized on a square of size  $\lambda \times \lambda$  for discretizations  $a = \lambda/6, \lambda/12, \lambda/25, \lambda/42$  as indicated by the increasing dashing. Finally, the energy of this texture is calculated for different orientations  $\phi$  of the helix, where  $\phi = 0$  corresponds to a helix with a  $q$ -vector aligned to the  $x$ -axis. The plots show the energy difference  $\Delta E/\lambda^2$  to the analytic solution as a function of the orientation  $\phi$  of the helix, where  $N = 1$  neighbor (left) and  $N = 4$  neighbors (right) are taken into account for the discretization of the derivatives.

become more accurate and the absolute anisotropies smaller. The log-scale, however, reveals that the relative anisotropy, which is the ratio between the minimal and the maximal energy, remains approximately constant. While the factor is  $\Delta E_{\max}/\Delta E_{\min} = 2$  for  $N = 1$  it becomes as high as  $\Delta E_{\max}/\Delta E_{\min} = 16$  for  $N = 4$ . The higher order discretization as introduced here should thus be treated with care if relative anisotropies play a role. Also the higher order interpolation should be questioned when thermal fluctuations enter the model.

To summarize, higher order discretized derivatives are, however, an efficient tool to increase the accuracy of  $T = 0$  calculations and to decrease the runtime and the impact of (absolute) anisotropies.

#### 10.5.4. The implementation of boundary conditions at the surface

The physics at the surface of a solid can be very complex. The surface can suffer from roughness which is due to the growth process but also the contamination with dirt can change surface properties. Even the clean system still offers a lot of triggers: The missing neighbors for the atoms at the surface and therefore the missing pressure can lead to atomic reconstructions at the surface. Also the electronic wave functions adapt, e.g. by orbitals sticking out of the surface. Consequently, the overlap integrals in the proximity of a surface will vary which changes the atomistic interaction constants locally. Finally, also the physics of the bulk influence the edge as discussed in Sec. 6. The following lines focus on the implementation of boundary conditions as they arise from the bulk physics.

##### The poor man's solution

With a discretization as sketched in Fig. 10.5.5, the boundary conditions only enter when calculating a derivative so close to the edge, that at least one of the required spins is outside the lattice. The probably simplest ansatz for the implementation of open boundary conditions is to take the vacuum outside the solid literally and return

$$\hat{n}(x < 0, y) = 0 \quad (10.5.44)$$

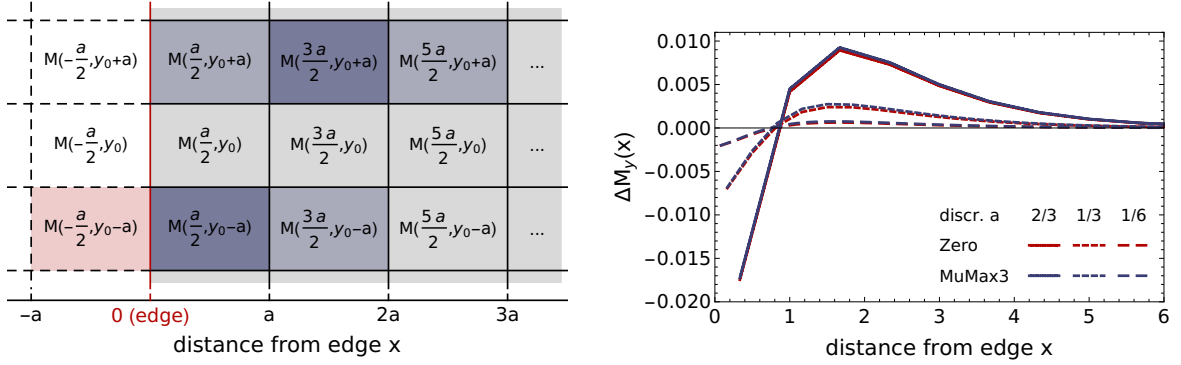


Figure 10.5.5.: Left: Schematic representation of the numerical discretization (black lines) of a sample (gray) with an edge (red line) to vacuum (white). The value of the discrete magnetization relates to the value in the center of a cell. A discretized derivative at a certain site (plain blue) requires the values of neighboring sites (pale blue). At the edge, sites are missing for this concept (pale red). Right: In a system with DMI, the magnetization twists close to the edge of the system, see Sec. 6. An edge is considered at  $x = 0$  with  $\vec{K} = 0$ ,  $\vec{H} = 1$ , and a polarized magnetization in  $z$ -direction at large distance. The analytic solution is given in Eq. 6.2.14. The plot shows the difference between the analytic solution and the solutions obtained by setting  $M(-a/2) = 0$  (red) and the implementation in MuMax3 (blue), respectively. Different numerical discretizations  $a = 2/3, 1/3, 1/6$  are indicated by the dasheding.

for all spins outside the solid. As a result, the correct behavior close to the edge is recovered as can be seen in Fig. 10.5.5 where this approach is referred to as the *zero* method (red). Here, the system is in the bulk polarized in the  $z$ -direction and twists due to DMI close to the edge. The exact solution for the magnetization profile is given in Eq. 6.2.14. The profile is also calculated using the above boundary conditions with only nearest neighbor interaction on the square lattice. The figure shows the deviation of the  $y$ -component of the magnetization between the exact solution and the numerical result. The numerical approximation becomes better for smaller discretization.

More elaborate implementations try to capture the full differential equation for the boundary condition, which can be deduced by using variational calculus as done for Eq. 6.2.8 and Eq. 6.2.9. In a general direction  $\hat{v}$ , these boundary conditions for the not rescaled system read

$$\partial_{\hat{v}} \hat{n} = \frac{D^B}{J} \hat{v} \times \hat{n} + \frac{D^N}{J} (\hat{z} \times \hat{v}) \times \hat{n} \quad (10.5.45)$$

where  $D^B$  is the Bloch-type DMI from systems Eq. 10.2.9 and Eq. 10.2.10 and  $D^N$  is the Néel-type DMI of the layered system Eq. 10.2.11. A widespread code which uses these boundary conditions is *MuMax3* [244]. The implementation in MuMax3 uses the boundary condition, Eq. 10.5.45. As an approximation, the right-hand-side is evaluated for the spin at  $x = a/2$  since there is no spin at  $x = 0$  by construction. The left-hand-side is then used to extrapolate the magnetization and to provide a return value for the virtual spin on the outside. In comparison to the simple method, Eq. 10.5.44, the more elaborate implementation in MuMax3 [245] does not clearly benefit from the use of the boundary conditions, see Fig. 10.5.5.

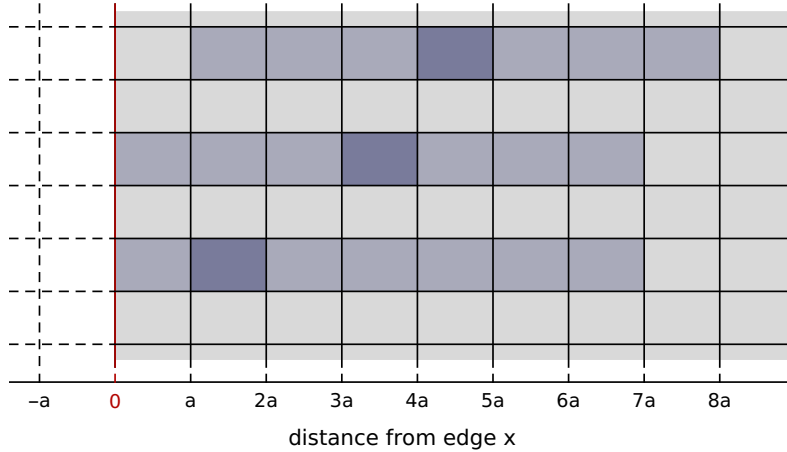


Figure 10.5.6.: Schematic representation of the numerical discretization (black lines) of a sample (gray) with an edge (red line) to vacuum (white). A discretized derivative at a certain site (plain blue) here requires the values of a total of 6 neighboring sites (pale blue). Too close to the edge, the discretization is asymmetric (lower panels) while it is symmetric if a sufficient number of sites in the bulk exist (upper two panels).

### The concept of asymmetric derivatives

We now follow the idea of Sec. 10.5.3 and cut the strings to the atomistic model by introducing artificial interactions in order to increase the numerical accuracy. This allows us to let loose the constraint of symmetric discretizations: When derivatives close to the edge are computed and a spin is missing, then the discretization can be shifted, see Fig. 10.5.6, in a way that only the physical sites inside the system contribute:

$$\partial_i \hat{n}(\mathbf{r}) = \frac{1}{a} \left( \sum_{m=-N_0}^{2N-N_0} g_{m,1}^{N_0} \hat{n}(\mathbf{r} + ma\hat{e}_i) \right) + \mathcal{O}(a^{2N}), \quad 0 \leq N_0 \leq N \quad (10.5.46)$$

$$\partial_i^2 \hat{n}(\mathbf{r}) = \frac{1}{a^2} \left( \sum_{m=-N_0}^{2N-N_0} g_{m,2}^{N_0} \hat{n}(\mathbf{r} + ma\hat{e}_i) \right) + \mathcal{O}(a^{2N}), \quad 0 \leq N_0 \leq N \quad (10.5.47)$$

where the prefactors  $g_{m,i}^{N_0}$  have to be chosen accordingly. A list of the values  $g_{m,i}^{N_0}$  is provided in the Appendix, Sec. 14.

On the one hand, this discretization scheme has got the advantage that it does not demand for the virtual spins outside the sample. On the other hand, there is no information about the boundary transferred at all. Consequently, these boundary conditions *can not* lead to the correct behavior of the model with open boundary conditions. It is, however, very handy to compute the energy in a system with an artificial boundary condition that is neither open nor periodic but for example a fixed texture, see Sec. 11.

### Asymmetric derivatives for high-accuracy boundary conditions

The concept of asymmetric discretizations can also be extended in order to describe open boundary conditions. A simple approach shifts the discretization such that exactly one site

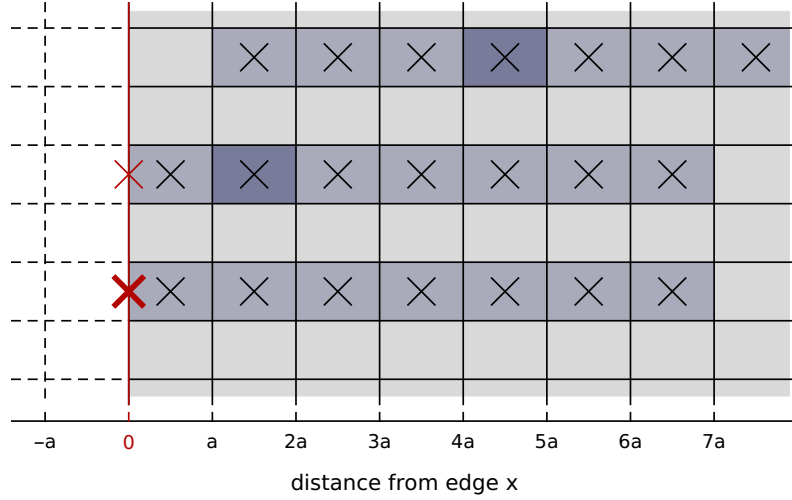


Figure 10.5.7.: Schematic representation of the numerical discretization (black lines) of a sample (gray) with an edge (red line) to vacuum (white). A discretized derivative at a certain site (plain blue) requires the values (crosses) of neighboring sites (pale blue). At the edge, the values of the sites (crosses) are complemented by the boundary condition (red cross). Also, the derivative of the virtual spin exactly on the edge (bold red cross) can be computed (lower panels).

outside the system is taken into account and treated as in the above methods for open boundary conditions. The more elaborate method which we discuss in the following, takes the analytic boundary condition, Eq. 10.5.45, into account.

We notice two important facts for the following derivation: (i) the boundary condition does not relate to the last numerical spin in the sample but instead to a virtual spin  $\hat{n}^B = \hat{n}(x=0)$  which is exactly at the edge. (ii) Discretizations do not necessarily rely on an equally spaced grid.

Combining those two arguments, we are able to write a discretized derivative for  $\hat{n}^B$ . We introduce the index notation  $\hat{n}^m = \hat{n}((m+1/2)a\hat{e}_x)$  for simplicity, where the site with index  $m=0$  is the first numerical lattice site in the sample. For an edge at  $x=0$  as depicted in Fig. 10.5.7 follows:

$$\partial_x \hat{n}^B = \frac{1}{a} \left( f_B^B \hat{n}^B + \sum_{m=0}^{2N} f_m^B \hat{n}^m \right) + \mathcal{O}(a^{2N+1}). \quad (10.5.48)$$

With this expression at hand, we can rewrite the boundary condition, Eq. 10.5.45, as a matrix equation

$$\partial_x \hat{n} = \frac{D^B}{J} \hat{x} \times \hat{n} + \frac{D^N}{J} (\hat{z} \times \hat{x}) \times \hat{n} = \frac{1}{J} \begin{pmatrix} 0 & 0 & D^N \\ 0 & 0 & -D^B \\ -D^N & D^B & 0 \end{pmatrix} \hat{n} = \mathcal{M}_B^x \hat{n} \quad (10.5.49)$$

where we can insert the discretized approximation from Eq. 10.5.48:

$$(a\mathcal{M}^x - f_B^B \mathbf{1}) \hat{n}^B = \sum_{m=0}^{2N} f_m^B \hat{n}^m + \mathcal{O}(a^{2N+2}). \quad (10.5.50)$$

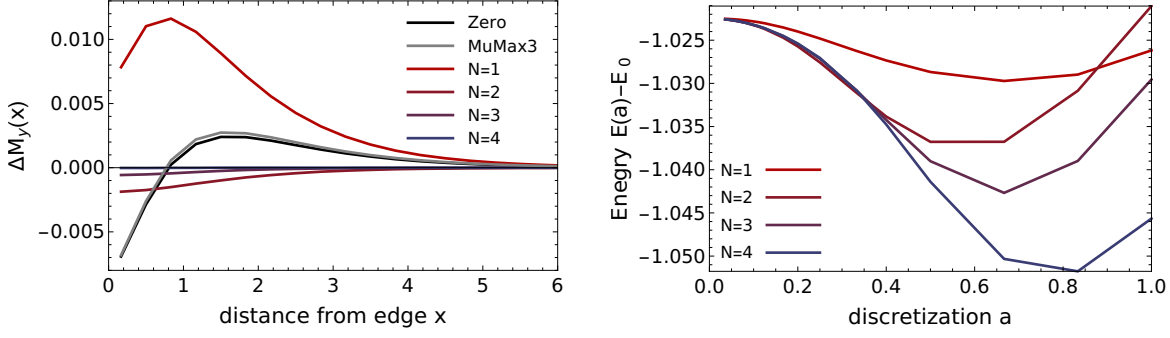


Figure 10.5.8.: Left: Result of a simulation of a polarized state in a large system with an edge at  $x = 0$ . Due to DMI, the magnetization twists close to the edge. The difference in the  $y$ -component of the magnetization between the analytic solution of the half-infinite system and the numerical result is plotted. The color encodes the method which was used. The numerical discretization is  $a = 1/3$ . Note that the blue line ( $N = 4$ ) is hardly visible on top of the  $x$ -axis. Right: The polarized state with edge-twists on an effectively one-dimensional system of length  $L = 10/Q$  was calculated using various discretization neighbors as indicated by the color. The energy difference between the numerically obtained solution with a twist and the analytic solution without a twist is plotted as a function of the discretization  $a$ .

Note that the matrix on the left-hand-side is invertible and furthermore constant, thus only needs to be inverted once. As an approximation for the virtual spin on the edge  $\hat{n}_B$  we obtain

$$\hat{n}^B \approx \sum_{m=0}^{2N} f_m^B (a\mathcal{M}_B^x - f_B^B \mathbb{1})^{-1} \hat{n}^m. \quad (10.5.51)$$

This expression can now be used again in an asymmetric discretization of a derivative in the proximity of the edge, which takes the virtual spin as a site into account. For the site  $k$ , the  $i$ -th derivative reads

$$\partial_x^i \hat{n}^k = \frac{1}{a^i} \left( f_{B,i}^k \hat{n}^B + \sum_{m=0}^{2N} f_{m,i}^k \hat{n}^m \right) + \mathcal{O}(a^{2N+1}), \quad i = 1, 2 \quad (10.5.52)$$

where the prefactors  $f_{B,i}^k$  have to be chosen accordingly and individually for every site  $k$ . A list of the values  $f_{B,i}^k$  is provided in the Appendix, Sec. 14. Now the expression for  $\hat{n}^B$ , Eq. 10.5.51, can be used to relate these derivatives to only real spins. The final expressions for the discretization of derivatives then reads

$$\partial_x^i \hat{n}^k = \frac{1}{a^i} \sum_{m=0}^{2N} \left( f_{m,i}^k \mathbb{1} + f_{B,i}^k f_m^B (a\mathcal{M}_B^x - f_B^B \mathbb{1})^{-1} \right) \hat{n}^m, \quad 0 \leq k \leq N \quad (10.5.53)$$

$$\partial_x^i \hat{n}^k = \frac{1}{a^i} \sum_{m=k-N}^{k+N} g_{m,i} \hat{n}^m, \quad k > N. \quad (10.5.54)$$

For the verification of this method, we consider an effectively one-dimensional system which is implemented as a chain of spins with the boundary conditions Eq. 10.5.53 on both ends. The symmetric discretization Eq. 10.5.54 is applied in the interior of the chain. We first reconsider

the comparison of textures obtained by the zero-return method and MuMax3 in Fig. 10.5.5 and add the results from the new method for  $N = 1, 2, 3, 4$ , see left panel of Fig. 10.5.8. As expected, the results become more accurate with more sites taken into account for the discretization until the difference is below the resolution of the output file.

As a further comparison, we compute the energy of a system with finite width for various discretizations, see right panel of Fig. 10.5.8. Here, the superior accuracy that is achieved with more sites,  $N > 1$ , is not visible. While the computation of the texture relies only on the local derivatives, the energy requires an integration over space. The simple method that we use here sums over the unweighted energy densities of all sites. Therefore, it has only an  $\mathcal{O}(a^2)$  scaling of the numerical error which turns important if an edge is present. The relatively poor scaling could thereafter be improved with a more advanced summation method.

# 11. Surface reconstructions in the helical phase

## 11.1. Motivation

The helical phase, see Sec. 1.3.1, is already long-known as a ground state in cubic chiral magnets [11–14]. Without magnetic fields applied, the propagation vector  $\mathbf{q}$  of the helix in MnSi and FeGe is pinned in the  $\langle 111 \rangle$ -direction by cubic anisotropies [11]. Therefore, when considering an arbitrary surface of a cubic chiral magnet, the helical phase that is seen on the surface should be a projection of the bulk periodicity, compare left panel of Fig. 11.1.1.

However, this expectation is confuted by the MFM-measurements in Sec. 3. There, the  $(100)$ -surface of a bulk FeGe crystal was measured and the helical periodicity was found to be the same as in the bulk where the helix is pinned by anisotropies. This mismatch can only be explained with defects in the helical phase. For a better understanding, the situation is sketched in the right panel of Fig. 11.1.1. Note that this is only a highly symmetric example, since the helical phases in the bulk and near the surface are both translation invariant in the same direction, here  $\langle 0-11 \rangle$ . In principle, both could be rotated independently by an arbitrary angle around the  $\langle 100 \rangle$ -axis.

As discussed in Sec. 10.5.4, the situation on the surface of a crystal may be very complex. Nevertheless, the simple micromagnetic model for the bulk system, see Sec. 10.2.2, already favors the helical phase parallel to the surface over a helix which is perpendicular: While the helix parallel to the surface is translation invariant along the normal of the surface, the helix perpendicular to the surface twists steadily into the edge and thereby precisely fulfills the boundary condition. However, the fact that the boundary condition is fulfilled by construction

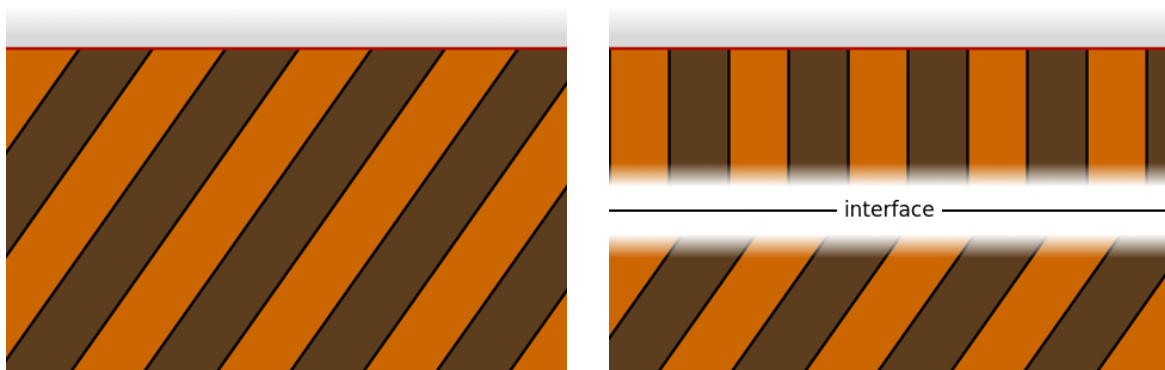


Figure 11.1.1.: Sketch of the helical phase (brown-orange stripes) near the surface (red line, gray background). The sketch displays only one  $(0-11)$  plane cut through the 3d bulk crystal. The helix in the bulk (bottom end of the panel) is oriented along the  $\langle 111 \rangle$ -direction and the surface is  $(100)$ . Left: A simple continuation of the helix to the surface leads to a projected period. Right: An interface makes a reorientation of the helix parallel to the surface possible,  $\mathbf{q} \parallel \langle 011 \rangle$ .

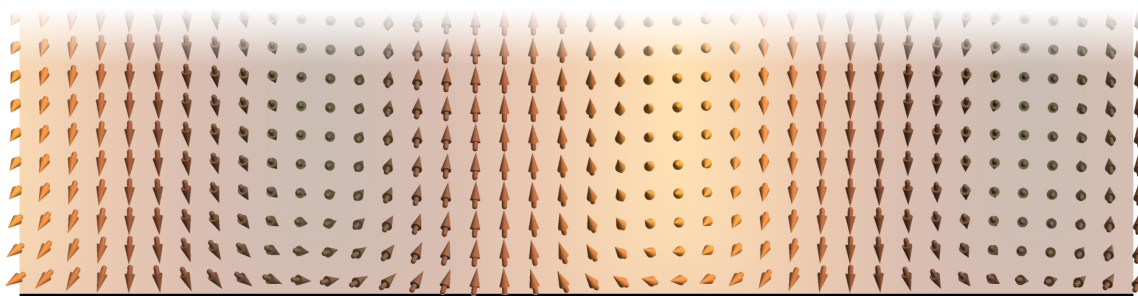


Figure 11.2.2.: The extra twist of the magnetic texture (arrows) close to a surface (black line). The figure shows the result of a micromagnetic minimization of a helix with  $\mathbf{q} \perp \hat{\nu}$  fixed on the upper end and an open boundary condition on the lower end. Note that only the first 10 spins at the edge are shown out of the 100 spins that were simulated. The numerical implementation contains only a single period which has been repeated here for better demonstration. The color code denotes the magnetization component into the sheet.

should not be confused with the statement that this implies an energetically favorable state: An additional twist close to the surface lowers the energy.

The same argument has already been used to explain the large skyrmion phase in thin films: While the conical phase matches the boundary conditions without further deformation, the skyrmion lattice has to adapt and therefore gains energy over the conical phase. The same argument also applies to the helical phase: it does not match the boundary conditions and therefore gains energy by adapting to the surface. The gain of energy is, however, of the same order as for the skyrmion lattice. Consequently, the phase boundary between the skyrmion lattice phase and the conical phase shifts as a function of film thickness whereas the transition to the helical phase is almost not influenced, see Ref. [111] or Fig. 10.2.1. The authors also find a reconstruction effect in the conical phase which breaks the translation symmetry at the surface in order to benefit from the additional modulation.

The question in this chapter is whether the energy gain of a reorientated helix also compensates the costs of an interface with defects.

## 11.2. A convenient twist at the surface

The simple argument drawn from the boundary condition of the micromagnetic model already explains that a helical phase with an orientation  $\mathbf{q}$  parallel to the normal of the surface  $\hat{\nu}$  is energetically more favorable than its opponent with  $\mathbf{q} \parallel \hat{\nu}$ . The extra twisting is depicted in Fig. 11.2.2 where this configuration was simulated.

In order to quantify the qualitative argument, we calculate the energy of a helical phase in a system with an edge numerically: We plan to initialize a helical phase that ideally extends over  $\lambda_a = 25$  lattice sites. The ideal discretization is then  $a = 2\pi/\lambda_a = 0.2513\dots$ . However, when changing the angle  $\phi$ , the discretization needs to adapt since the projected wavelength changes smoothly whereas the number of lattice sites can only be integer. We thus initialize the helix on a rectangular lattice with  $N_x(\phi) \times 100$  sites and a discretization  $a(\phi)$  with

$$N_x(\phi) = \text{round} \left( \frac{\lambda_a}{\sin(\phi)} \right), \quad a(\phi) = \frac{2\pi}{N_x(\phi) \sin(\phi)} \quad (11.2.1)$$

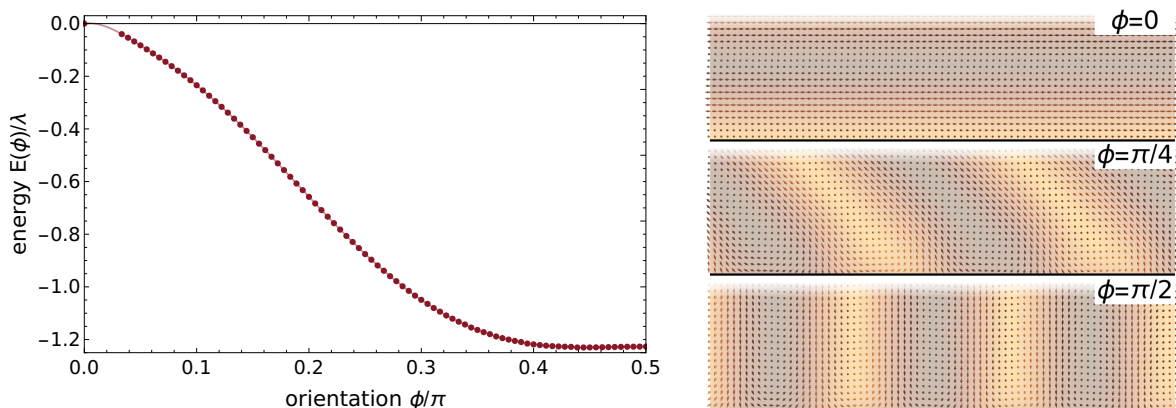


Figure 11.2.3.: Left: The energy gain  $E(\phi)/\lambda$  of the helical phase at the edge of the system is plotted as a function of the angle  $\phi$  between the orientation  $\mathbf{q}$  of the helix and the normal  $\hat{\nu}$  of the surface,  $\phi = \angle(\mathbf{q}, \hat{\nu})$ . The dots are the bare data and the line is guide to the eye. Right: The magnetization textures as obtained by minimizing the energy for  $\phi = 0, \pi/4, \pi/2$ . The surface is implemented on the lower edge and indicated by a black line. The upper edge is fixed to a helix with the desired angle  $\phi$ . Note that along the  $y$ -axis only the first 20 sites out of an implementation with 100 sites is shown here. The numerical implementation contains only a single period which has been repeated here for better visibility. The color code denotes the spin component into the sheet.

where here we used  $\lambda_a = 25$  lattice sites. The choice of  $a(\phi)$  leads to very small deviations from the ideal  $a = 2\pi/\lambda$ . This is important as we are only close to the continuous limit and hence the discretization influences the result. With very small deviations from the ideal  $a = 2\pi/\lambda$ , the error from using different discretizations is small.

For this initialization we minimize the energy using the higher order discretized derivatives with  $N = 4$  neighbors on each side, see Sec. 10.5.3. The semi-infinite setup is modeled with an open boundary condition on the lower edge, see Sec. 10.5.4, whereas the opposite edge is fixed to the desired bulk orientation of the helix by manually fixing the last  $N = 4$  rows of spins. Note that for  $\phi \rightarrow 0$ , the projected wavelength  $N_x(\phi)$  diverges, therefore we have to choose a cut-off for the angle. For  $\frac{\pi}{30} \leq \phi \leq \frac{\pi}{2}$  the maximal extension along the periodic direction is  $N_x(\frac{\pi}{30}) = 239$ . The special case  $\phi = 0$  is again translation invariant along this axis and hence reduces to  $N_x(0) = 1$ .

The model used here is a two-dimensional version of the isotropic bulk model for a chiral magnet, see Sec. 10.2.2. Since we omitted the magnetic field, the model in reduced units, see Sec. 10.4, has no parameters left but the angle of the helix to the surface. After minimization, the energy gain  $E(\phi)/\lambda$  per helical wavelength  $\lambda = 2\pi/Q$  along the surface is computed with respect to the analytic solution of the helix without a surface. The result is plotted in Fig. 11.2.3 where also parts of the optimal textures for  $\phi = 0, \pi/4, \pi/2$  are shown.

The numerical calculation reveals that within the micromagnetic model, the energy gain per length  $\lambda$  of the surface exhibits a broad plateau of the order  $E(\phi > 0.4\pi)/\lambda \approx -1.2E_D/\lambda$  while the helix with  $\mathbf{q} \parallel \hat{\nu}$  does not profit at all from the edge,  $E(0)/\lambda = 0$ . Assuming that anisotropies favor a helical orientation with  $\mathbf{q} \parallel \hat{\nu}$  in the bulk, the system could effort up to  $1.2E_D/\lambda$  for a domain wall that separates the bulk phase from another phase close to the surface with e.g.  $\mathbf{q} \perp \hat{\nu}$ .

In contrast, in the motivation, Fig. 11.1.1, the bulk phase is oriented with  $\mathbf{q} \parallel \langle 111 \rangle$  which yields an angle  $\phi = \arccos(1/\sqrt{3}) \approx 0.3\pi$  and thus an energy difference of only  $\Delta E/\lambda \approx$

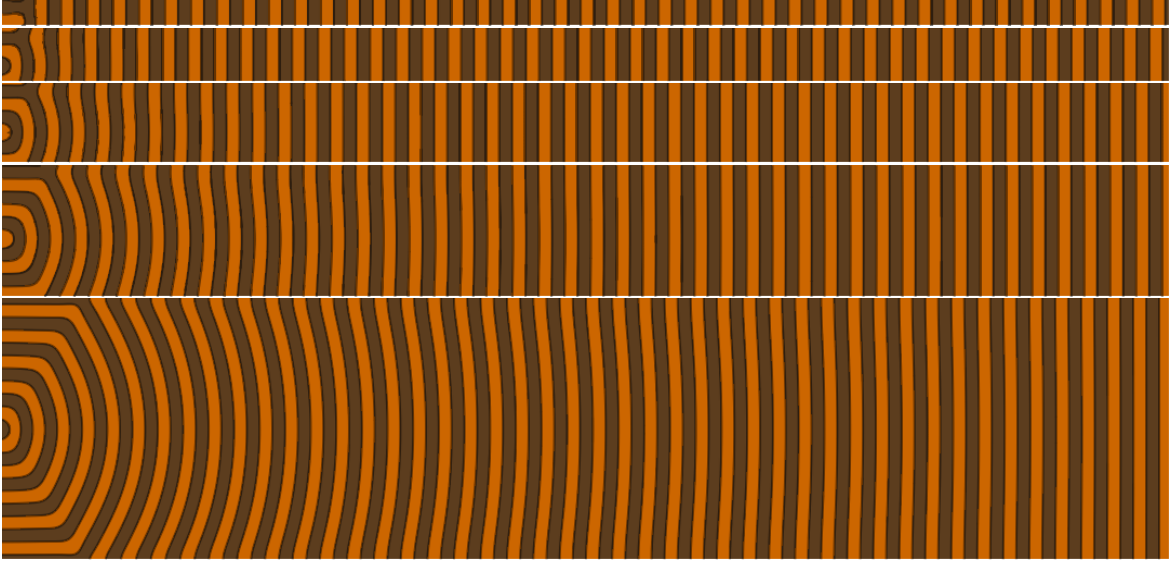


Figure 11.3.4.: Surface reconstruction in the helical phase. The magnetic texture is plotted after minimizing the energy of a system with two orthogonal helical phases,  $\mathbf{q}_{\text{left}} \perp \mathbf{q}_{\text{right}} \parallel \hat{\nu}$ , and a type-II domain wall connecting them. The left edge has open boundary conditions imposed while the right edge fixes a helical phase with a variable phase shift. From the upper to the lower panel, the distances  $D$  between  $+\pi$  and  $-\pi$  disclinations are  $D = 1\frac{\lambda}{2}, 2\frac{\lambda}{2}, 3\frac{\lambda}{2}, 5\frac{\lambda}{2}, 10\frac{\lambda}{2}$ . The color code denotes the sign of the in-sheet component of the magnetization.

$$0.2E_D/\lambda.$$

### 11.3. Reconstruction for the $90^\circ$ scenario

In the previous section the energy gain due to surface alignment was calculated. If an interface is found now that costs less energy than what is gained, a surface reconstruction can appear even within the micromagnetic model and can purely be driven by the bulk interactions.

Besides the limitations on the energy costs, the interface should also be periodic along the surface. Interestingly, for the scenario with  $\mathbf{q} \parallel \hat{\nu}$  in the bulk and  $\mathbf{q} \perp \hat{\nu}$  on the surface, we recover exactly the geometrical constraints matching the requirements of the  $90^\circ$  type-II domain wall in Sec. 3.

We choose this particular setup to prove that a surface reconstruction can indeed be energetically beneficial. Therefore, we prepare the helical phases on both sides of the interface accordingly, see Fig. 11.3.4. From the simulations that were performed for the domain walls in Sec. 3, we have learned that the healing length on the bulk side covers many wavelengths such that even the calculations with more than  $20\lambda$  on this side suffered from the cut-off. Furthermore, we face the problem that the anisotropy due to the discretization  $a = \lambda/42$  is not negligible as shown in Fig. 10.5.4, although the lattice with up to  $378 \times 1344$  sites is at the limits of what is computationally possible. We therefore switch to a numerical realization with an  $\mathcal{O}(a^8)$ -discretization with  $N = 4$  neighbors that are used to compute derivatives, see Sec. 10.5.3. With reference to the discretization error that we dealt with in Sec. 3, we choose  $a = \lambda/12$  which should yield smaller errors, compare Fig. 10.5.4, on much smaller lattices. The smaller lattices we can now use to extend the relaxation zone for the bulk phase, such that the

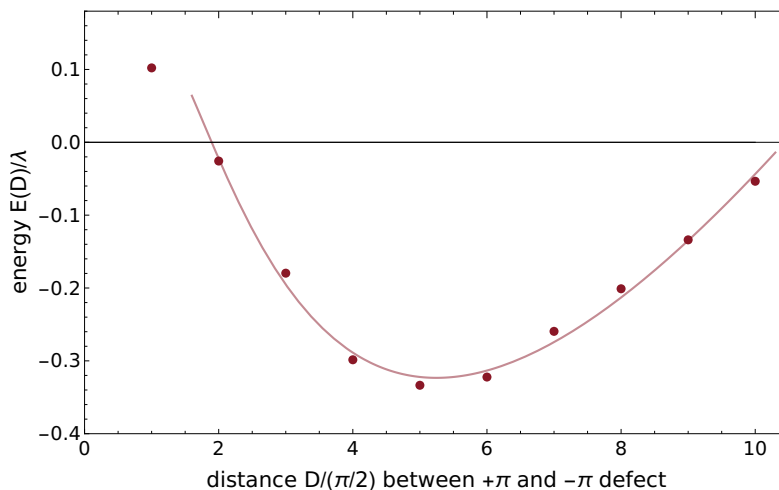


Figure 11.3.5.: Energy  $E(D)/\lambda$  per length  $\lambda$  along the surface of the helical phase with surface reconstruction due to a type-II domain wall, compare Fig. 11.3.4, as a function of the distance  $D$  between  $\pm\pi$  disclinations in the domain wall. The energy per length of the helix with  $\mathbf{q}_{\text{right}} \parallel \hat{\nu}$  is subtracted, hence, a negative energy value suggests that the domain wall pays out energetically. The dots are the bare data, the line is a fit. The upturn of the energy for larger values of  $D$  is due to numerical anisotropies.

entire length of the system is now  $540a = 45\lambda$ .

Finally, we want the interface to be mobile such that it can adjust the distance to the surface. The helical phase to the left of the domain wall is translation invariant along this direction, therefore, the domain wall can move there freely. On the bulk side, however, the distance of the domain wall is determined by the phase shift of the helix. We can lift this constraint in the numerical simulation by imposing also open boundary conditions on the right side: The phase of the perfectly flat helix with  $\mathbf{q} \parallel \hat{\nu}$  is not influenced by the boundary condition and can adjust dynamically.

Unfortunately, the helix on this side is not perfectly flat due to the healing deformations from the interface. This can nevertheless be resolved by manually averaging the outermost layers. This trick makes the edge on this side transparent for phase shifts of the helical phase and therefore provides the degree of freedom that is needed to move the interface in the direction  $\hat{\nu}$ .

The resulting magnetic textures are shown in Fig. 11.3.4 for type-II domain walls with 1, 2, 3, 5, and 10 rings around the  $+\pi$  disclination, respectively. One direct observation is that, even though the model is isotropic and no anisotropy favors the bulk phase, the domain wall still attaches to the edge directly. The case with  $D = \frac{\lambda}{2}$  is an exception where the domain wall is slightly more separated from the edge as in the other cases. The energies  $E(D)/\lambda$  per length  $\lambda$  along the surface are plotted in Fig. 11.3.5. The plot shows that the energies are indeed negative for domain walls with  $D > \lambda/2$ .

This result suggests that, indeed, a domain wall underneath the surface of the crystal is energetically favored by the immense energy gain of the reoriented state at the surface. Nevertheless, the result should be treated with care since the upturn of the energy for domain walls with higher  $D$  is counter-intuitive: The naive expectation from Sec. 3 would yield a  $\ln[D]/D$  decay of the energy.

A possible explanation is based on the fact that the relative anisotropy for the newly applied

$\mathcal{O}(a^8)$ -method is much larger than for the established  $\mathcal{O}(a^2)$ -method. The direct impact of this argument is affirmed by the observation that the arcs of the domain walls in the present case are flatter than the arcs in Sec. 3. The anisotropies contribute to the total energy per period proportional to the area, i.e.  $E_{\text{ani}} \sim e_{\text{ani}} D^2$  and  $E_{\text{ani}}(D)/\lambda \propto e_{\text{ani}} D$ . A fit that takes this correction into account is added to the data in Fig. 11.3.5. However, the validity of this argument should be checked with simulations on finer numerical meshes.

## 12. Tilted fields

### 12.1. Motivation

In the following, for simplicity, we will only discuss the micromagnetic models without uniaxial anisotropies,  $K = 0$ , and define the canted field as

$$\mathbf{H}(\phi) = H \begin{pmatrix} \sin(\phi) \\ 0 \\ \cos(\phi) \end{pmatrix} \quad (12.1.1)$$

where the angle  $\phi$  defines the tilt of the external field away from the normal  $\hat{z}$ .

The tilt angle of the external magnetic field is an interesting parameter since the phases of the micromagnetic models gain energy from modulations in different directions with respect to the magnetic field: On the one hand, for example, the skyrmion lattice extends in two spatial dimensions perpendicular to the magnetic field, while on the other hand, the conical phase is translation invariant in precisely these directions but instead modulates along the magnetic field direction. While the phases in the isotropic bulk chiral magnet can simply orient according to the field, new effects arise if the energy functional or the setup are anisotropic. The latter can, in particular, be achieved with dimensional confinement, i.e. by considering one-dimensional or two-dimensional systems, or by considering thin films with their surfaces. The tilt angle of the field then provides a tuning knob for stabilizing different phases.

Furthermore, a canted field breaks the rotation symmetry in extended samples and can therefore lead to new phases and phenomena. One example is shown in Fig. 12.1.1 where a chain of skyrmions is stabilized by an inclined field. Here, the interaction between skyrmions

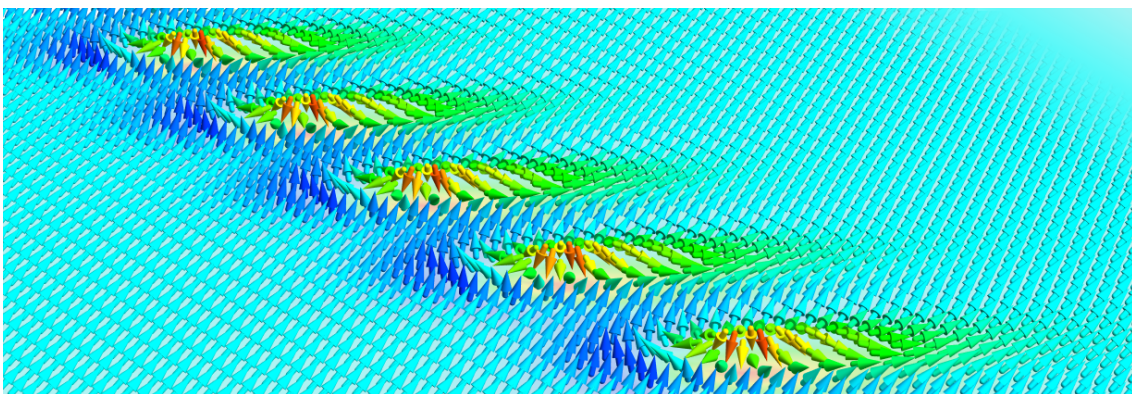


Figure 12.1.1.: Chain of Neel-type skyrmions as obtained from micromagnetic simulations for a magnetic field  $H = 0.75H_D$  at a tilting angle of  $45^\circ$  relative to the plane normal. The chain builds up in the direction perpendicular to the projection of the field. The cyan background polarization is parallel to the external field. The color code denotes the out-of-plane component of the magnetization.

is anisotropic and exhibits minima in one direction whereas it is repulsive in the perpendicular direction. This is in contrast to the situation with a perpendicular field where skyrmions are rotation symmetric and so is their repulsive interaction. Therefore the question arises, to which extent the already measured or predicted phenomena are stable, given that a perfect alignment of the field is not provided.

Note that in the following we will mostly discuss the models with Bloch-type Dzyaloshinskii-Moriya interaction (DMI). The idea in Sec. 6, that for one and two spatial dimensions the models with Bloch-type DMI can be translated into a model with Néel-type DMI by rotating the magnetization by  $90^\circ$  around the  $\hat{z}$ -axis, can still be applied here:

$$F_{\text{Bloch}}[\hat{n}, \mathbf{H}] = F_{\text{Néel}} \left[ \mathcal{R}_{\hat{z}} \left( \frac{\pi}{2} \right) \hat{n}, \mathcal{R}_{\hat{z}} \left( -\frac{\pi}{2} \right) \mathbf{H} \right]. \quad (12.1.2)$$

This means that for extended samples without edges the effects in both models are the same up to a rotation  $\mathcal{R}_{\hat{z}}(-\frac{\pi}{2})$  of the field. As a particular example, the chain of Néel skyrmion in Fig. 12.1.1 which extends perpendicular to the in-plane component of the field, would align parallel to the in-plane component if Bloch DMI was considered instead.

The following results have mostly been computed and discussed together with C. Faber and are also summarized in his Bachelor thesis [246]. In the meantime, a significant part of the following sections has already been published in Refs. [19, 20, 171, 247].

## 12.2. Computing phase diagrams: The simplex minimization

In order to calculate phase diagrams, we employ in the following the energy minimization as described in Sec. 10.5.2 with the  $\mathcal{O}(a^8)$  discretization scheme from Sec. 10.5.3 and compute the energy of a set of various initial states.

Here, however, we are not interested in the local energy minimum of a system with given dimensions but in the state with the lowest energy density on an infinite support. This is in contrast to the previous considerations because now the volume of the simulated cell needs to be optimized in addition to the magnetic texture, e.g., the wavelength of the helix needs to adjust at higher magnetic fields. In principle, this can be achieved by minimizing the same initial configurations on meshes with different discretization. Taking into account that possibly also different ratios  $N_i/N_j$ ,  $\{i, j\} \in \{x, y, z\}$  of the simulated cell need to be included, this straightforward method can soon get very costly.

The *simplex minimization* turns out to be a complementary method which works much more efficiently and is very easy to implement: Assume that we want to minimize the energy density of a state which requires optimization in  $d$  directions. Then we can regard the discretization  $a_i$  in every direction as independent and the set of discretizations  $\{a_x, a_y, a_z\}$  lives only on the  $d$ -dimensional manifold. We construct a  $d$ -dimensional tetrahedron, spanned between  $d + 1$  equidistant points on the  $d$ -dimensional manifold. The energy density on the  $d + 1$  points is calculated and after comparing, the tetrahedron is flipped over the edge which is opposite to the point with the highest energy density.

An iteration now consists of calculating the energy density for the new point, comparing it to the old points and flipping the tetrahedron again. Upon iteration of this procedure, the tetrahedron rolls downhill in energy density space with only a small computational effort. This procedure might sound time-consuming since it is only serial while the previous method allowed for a parallel evaluation of all discretizations and aspect ratios. However, the final texture of

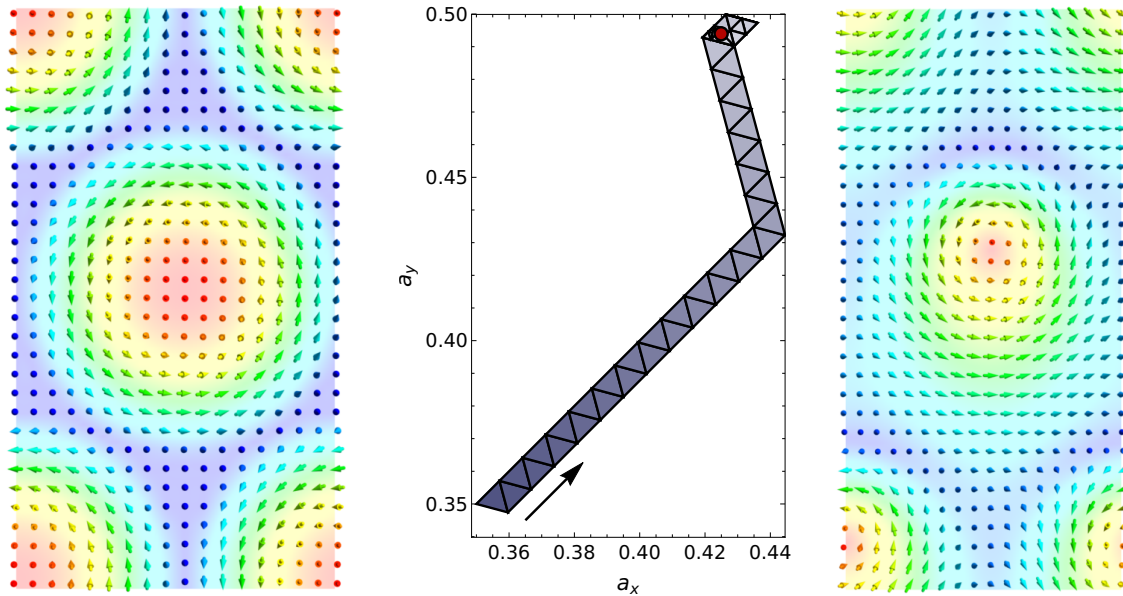


Figure 12.2.2.: Numerical optimization of the energy density of the Bloch-type skyrmion lattice at  $H = 0.6H_D$  and a tilt angle of  $\phi = 45^\circ$ . Left: Topview on the initial configuration with two skyrmions on an  $18 \times 31$  sites square lattice with spacing  $a = 0.35$ . The color code denotes the component of the magnetization into the sheet. The *triangular* skyrmion lattice can be represented as a *rectangular* lattice with two skyrmions per unit cell. Center: Simplex minimization of the energy density in the two-dimensional parameter space spanned by the independent discretizations  $a_x$  and  $a_y$ . The simplex iteration starts in the bottom left corner on the darkest triangle which then flips in every iteration. The color scale encodes the number of the iteration. In the top right corner the triangles refine until convergence at  $(a_x, a_y) = (0.424926, 0.493946)$ , indicated by the red dot. Right: Topview on the optimized skyrmion lattice where the field is inclined by  $\phi = 45^\circ$ , pointing to the right on the horizontal axis. The image has been rescaled to fit the height of the left image. Note that the aspect ratio has changed during the optimization of the discretizations.

the previous iterations can be used here as the new starting point which for small tetrahedrons is already very close to the final state and thus only needs little optimization. Finally, the tetrahedron gets stuck at the minimum if it is flipped over the same edge as in the previous iteration. Then, the size of the tetrahedron is reduced and the procedure continues until the tetrahedron gets stuck again. This can be continued until the desired accuracy is reached.

As an example, let us consider the simplex minimization for the skyrmion lattice in a monolayer. Using a square lattice of  $N_x \times N_y$  sites with periodic boundary conditions, the *triangular* skyrmion lattice can be initialized as a *rectangular* lattice with two skyrmions per unit cell, see left panel of Fig. 12.2.2. Since the triangular lattice will be distorted by the tilted magnetic field, the discretizations in both directions,  $a_x$  and  $a_y$ , need to be optimized.

The tetrahedron in this two-dimensional discretization space is a triangle. We choose the first corner on  $(a_x, a_y) = (0.35, 0.35)$ , minimize the energy, and then use the final texture as the input for the next two points of the triangle. It turns out that the first point has the largest energy density and is thus rejected. The next point for the iteration is chosen by flipping the triangle over the edge opposite to the just rejected point, see the central panel of Fig. 12.2.2. At some point, the triangle flips over the same edge in successive iterations and therefore the length of its edges is cut by two. This procedure continues until the length  $l$  of the edge is

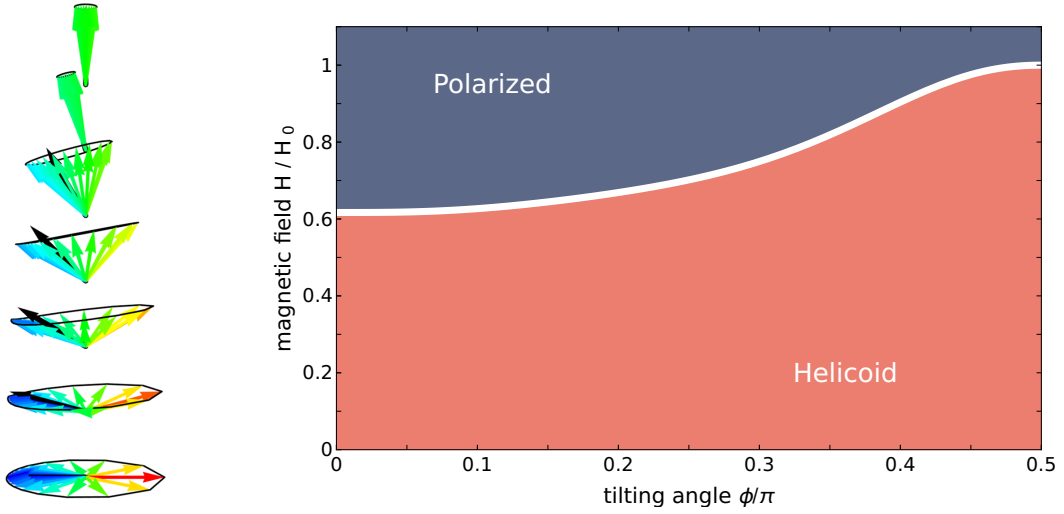


Figure 12.3.3.: Left: Visualization of the helicoid texture closely below the phase transition. The black arrow indicates the magnetic field which ranges from  $\phi = 0$  (bottom) to  $\phi = \pi/2$  (top) in equidistant steps. The color code denotes the component of the magnetization in the direction of  $\mathbf{H}(\phi = 0)$ . Right: Phase diagram for the one-dimensional chiral magnet as a function of magnetic field strength  $H$  and tilt angle of the field  $\phi$ . The phase diagram only exhibits the polarized phase and a one-dimensional modulated phase which we refer to as the *helicoid* phase.

below the critical value, here  $l < 10^{-4}$ . The final state with  $(a_x, a_y) = (0.424926, 0.493946)$  is shown in the right panel of Fig. 12.2.2.

### 12.3. One-dimensional systems

The one-dimensional systems are in a sense simple toy models since the spatial modulations can only occur along one direction, here  $\hat{x}$ . This makes a skyrmion phase already impossible by construction. These systems shall therefore serve as a starting point for the following studies. But already the simple one-dimensional system provides a nice example for the interesting phenomena that can be triggered with canted fields.

Let us first review the extreme values for the angle  $\phi$ . The field applied in a perpendicular direction,  $\phi = 0$  i.e.  $\mathbf{H} \parallel \hat{z}$ , is discussed in Sec. 6. Here, the micromagnetic model exhibits a helical phase at zero applied field and upon increasing the field, the wavelength also increases as the regions of the helix parallel to the field expand: The phase of the helix becomes a non-linear function of space. Finally, at higher fields  $H$  the wavelength diverges close to the critical field  $H_c = \frac{\pi^2}{16} H_D$ , at which not even a single soliton, i.e. a  $360^\circ$  turn, in the entire infinite chain is energetically favored. This commensurable-incommensurable transition turns the helical phase into a polarized phase. Interestingly, it has indeed been observed experimentally in the monoaxial chiral magnet  $\text{Cr}_{1/3}\text{NbS}_2$  [17] which serves as a quasi one-dimensional system.

In the other extreme scenario,  $\phi = 90^\circ$  i.e.  $\mathbf{H} \parallel \hat{x}$ , the helical phase only persists at  $H = 0$ . Any finite field  $H > 0$  breaks the  $\pi$ -rotation symmetry and helix becomes conical which is still symmetric under a combined  $\pi$ -rotation and time reversal. The angle of the cone steadily shrinks with increasing field  $H$  until it closes at the critical field  $H = 1$  which sets the second order phase transition to the polarized phase.

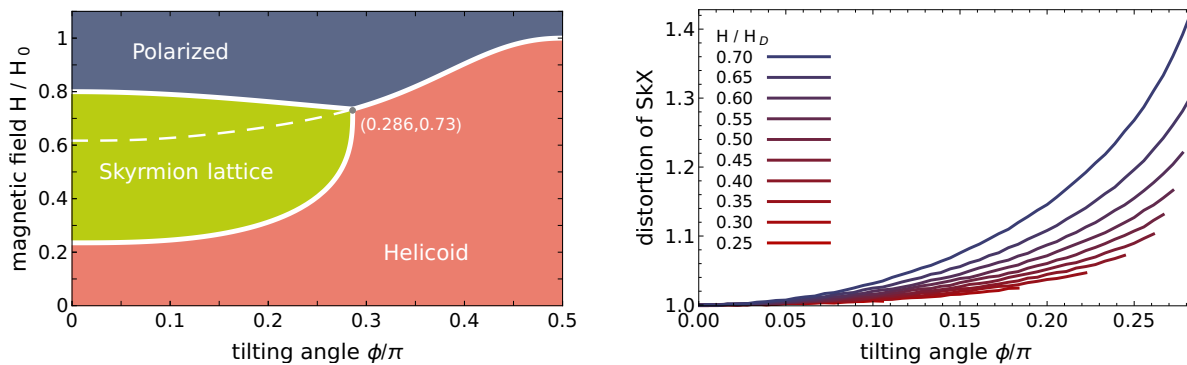


Figure 12.4.4.: Left: Phase diagram for the two-dimensional micromagnetic models, see Sec. 10.2.3. The polarized phase and the one-dimensionally modulated helicoid phase are supplemented by the skyrmion lattice phase. The boundaries are indicated by solid white lines. The former phase transition from the polarized to the helicoid phase is indicated by a dashed line. The triple point is indicated at  $(\phi, H) \approx (0.286\pi, 0.73H_D)$ . Right: Distortion of the skyrmion lattice phase (SkX) as a function of the tilt angle  $\phi$  for various magnetic fields  $H/H_D$  as indicated by the color scale. The lines are bare data points at every  $\Delta\phi = 0.01\pi$  which have been connected for better visibility.

Any tilted field, however, breaks the combined  $\pi$ -rotation and time reversal symmetry of the helical and conical phase, thus, we refer to it in general as the *helicoid phase*, compare also left panel of Fig. 12.3.3. We can use a simple helix as the initial texture and run the simplex minimization as described above in Sec. 12.2. The resulting phase diagram is shown in Fig. 12.3.3. A detailed study that also includes finite temperature calculations has been published recently by Laliena *et al.*, see Refs. [19, 20].

## 12.4. Two-dimensional systems

### 12.4.1. Phase diagram

Using the simplex minimization from Sec. 12.2, the energy density of the skyrmion lattice phase can be calculated. This energy density is then compared to the energy densities that we have already computed in the one-dimensional system, Sec. 12.3. In principle, the one-dimensional modulated helicoid phase could now as well build up modulations in the added direction. Numerical checks suggest that this is, however, not the case.

The resulting phase diagram is shown in Fig. 12.4.4. As mentioned above, the skyrmion lattice is usually found translation invariant in the direction of the applied field while the magnetization is modulated in the plane normal to the field. The optimal geometry for the skyrmion lattice is thus expected to be the perpendicularly applied field,  $\phi = 0$ . This expectation is in agreement with the results of the numerical minimization: The skyrmion lattice phase extends over the largest regime if the field is perpendicular to the two-dimensional plane. Interestingly, the situation remains almost unchanged for a broad range of angles  $\phi \lesssim \pi/10$ . Only then the skyrmion lattice slowly pays tribute to the better aligned helicoid phase until  $\phi > \pi/2$  when the skyrmion pocket shrinks fastly. The phase boundary to the polarized phase, in turn, remains almost constant. Within the accuracy of our calculations, the triple point where all three phases touch in the phase diagram is at  $(\phi, H) \approx (0.286\pi, 0.73H_D)$ , see Fig. 12.4.4.

As already shown in Fig. 12.2.2, the skyrmion lattice deforms under an inclined field: The

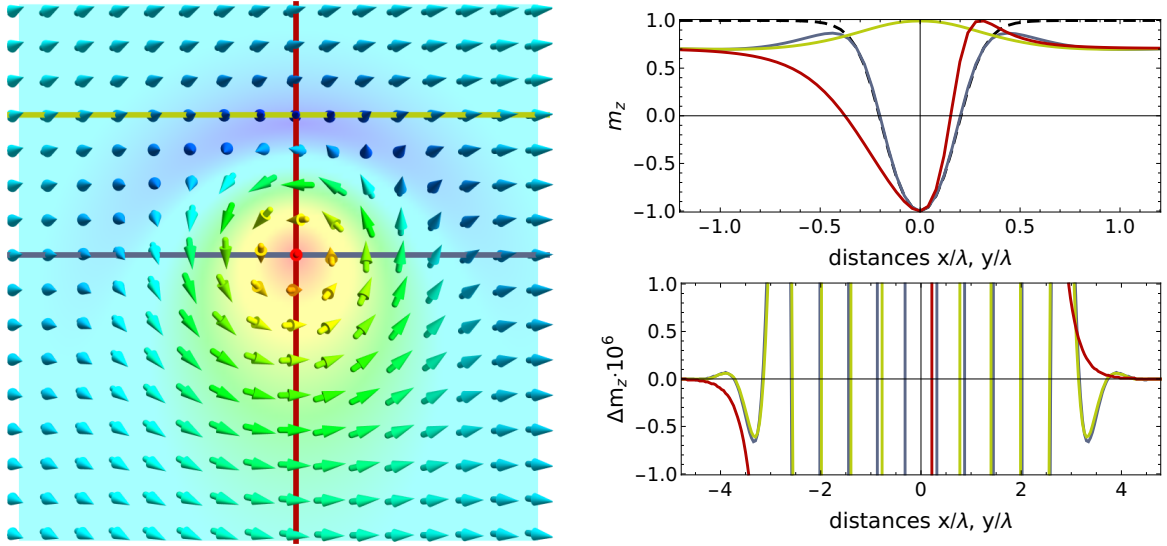


Figure 12.4.5.: The isolated skyrmion in a canted polarized background. Left: Magnetization texture as obtained on from minimizing a single skyrmion in a polarized background with  $H = 0.75H_D$  and  $\phi = 45^\circ$  tilted into the positive  $x$ -axis. The minimization is performed on a square lattice which is large enough that it can be considered infinite. The color code denotes the component of the magnetization into the sheet. The additional solid lines are markers for the plots on the right panels. Right: The  $z$ -component of the magnetization along the solid lines of the corresponding color in the left panel. Upper panel: The full magnetization  $m_z \in [-1, 1]$  is plotted as a function of distance. The skyrmion is symmetric with respect to the vertical red line through the center. For comparison, the profile for  $\phi = 0$  is plotted additionally (black dashed line). Lower panel: Difference between the local magnetization  $m_z(\mathbf{r})$  and the saturation value at large distance  $m_z(\infty) = 1/\sqrt{2}$ , magnified by a factor  $10^6$ . The magnetization oscillates along the horizontal direction (blue, green) even at very large distances of multiples of the helical wavelength  $\lambda$ . On the vertical axis (red) the profile decays without oscillations.

regions of the skyrmion lattice where the magnetization points in the direction of the in-plane projected magnetic field expand which breaks the six-fold rotation symmetry of the lattice and leads to distorted skyrmions. The distortion of the skyrmion lattice can be quantified by the aspect ratio of the lattice, normalized to the value for the perfect triangular lattice at  $\phi = 0$ . The results are shown in the right panel of Fig. 12.4.4. It turns out that not only the tilt angle of the external field but also the field strength itself contribute strongly to the distortion of the lattice. The largest distortion is therefore found in the proximity of the triple point.

A detailed study that also includes the effects of uniaxial anisotropy has been published recently by Leonov and Kézsmárki, see Ref. [171].

### 12.4.2. Skyrmion interactions

Single skyrmions can exist as metastable and localized solutions in perpendicular polarized backgrounds, see Secs. 6,7,8,9, and also in modulated phases, see Sec. 4, where they can be embedded, as long as the phase which provides the background remains stable itself.

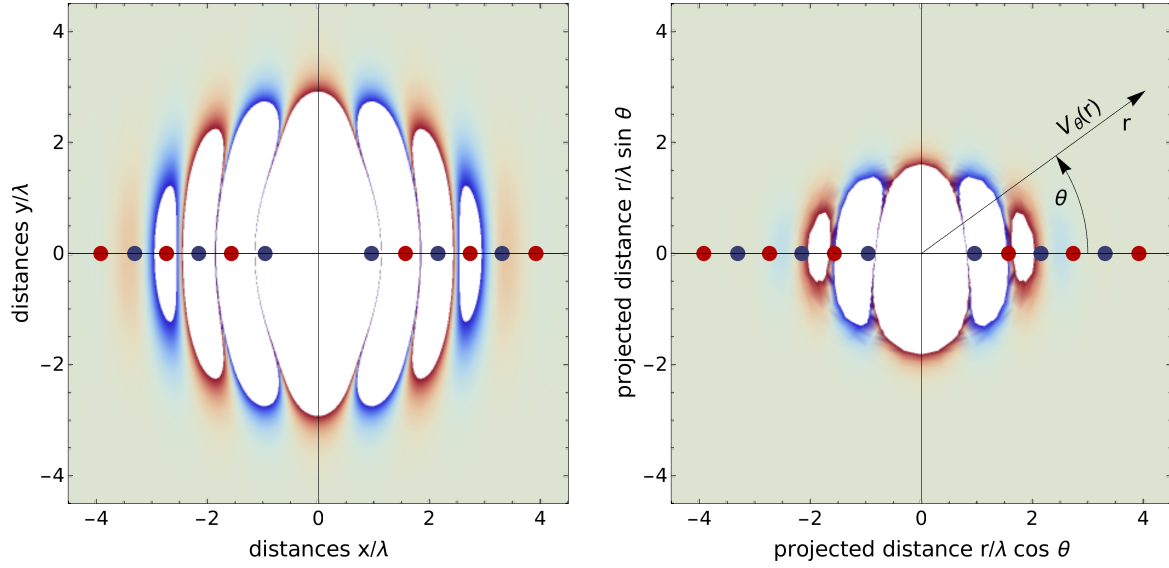


Figure 12.4.6.: Potentials for the skyrmion in Fig. 12.4.5 for the interaction with another skyrmion of the same kind (left panel) or an edge of the system (right panel). In the right panel, the radial distance  $r$  represents the distance between the edge and the center of the skyrmion ( $\hat{n}(\mathbf{r}) = -\hat{z}$ ) for a given angle  $\theta = \angle(\hat{\nu}, B_{\text{in}})$  between the normal  $\hat{\nu}$  of the edge and the inplane projection  $B_{\text{in}}$  of the tilted magnetic field. The fixed angle  $\theta$  is encoded in the angular component of the plot. The color code of the continuous map encodes the strength of the interaction potential  $V(x, y)$  which is only plotted in the range from  $V_{\text{min}} = -0.01E_D$  (blue, attractive) to  $V_{\text{max}} = +0.01E_D$  (red, repulsive). In the white regions the potential is outside the range. In addition, the minima (blue dots) and maxima (red dots) of the oscillatory decay of the skyrmion profile along the green axis in Fig. 12.4.5 are shown.

### Isolated skyrmions in tilted polarized backgrounds

When calculating the profile of an isolated skyrmion in a canted polarized background numerically for  $H = 0.75H_D$  and  $\phi = 45^\circ$ , see Fig. 12.4.5, it turns out that the skyrmion profile shows a monotonous decay along the symmetry axis (which for Bloch-type DMI is the axis perpendicular to the in-plane component of the field), whereas the profile along the perpendicular axis oscillates periodically around the value of the polarized background, see right panels of Fig. 12.4.5. Note that, however, the decay length for both axes is equal. The different decay behaviors along the two axes are not only useful to visualize the asymmetric character, but the length scale of the oscillations also determines the oscillatory character of the skyrmion interactions that are discussed in the following.

### Skyrmion-skyrmion potentials and skyrmion chains

The interaction potential between two individual skyrmions at  $H = 0.75H_D$  and  $\phi = 45^\circ$  is calculated by the standard method which is, for example, also used in Sec. 7: Two skyrmions are initialized at various distances  $\mathbf{r}$  on a very large lattice such that their interaction via the (periodic) boundary conditions is negligible. The lattice sites of the numerical lattice where  $\hat{n}(\mathbf{r}) = \hat{z}$  are artificially fixed during the subsequent minimization of energy, see Sec. 10.5.2. Here, we use the  $\mathcal{O}(a^8)$  discretization method, see Sec. 10.5.3. The results are shown in the left panel of Fig. 12.4.6.

Note that one only needs to calculate the potential in one quarter of the map and receives

the full map by symmetry. While at small distances  $|\mathbf{r}| < \lambda$  the potential is always repulsive, it inherits the oscillatory character of the skyrmion profiles along the one axis, while it shows a monotonous decay in the perpendicular direction. This stands in contrast to the results in systems with a perpendicular magnetic field and background, where the interaction is repulsive [169]. However, for a system where the background polarization is tilted due to a strong easy-plane anisotropy, a similar behavior has been reported [170].

Plotting the extremal points of the skyrmion profile together with the potential visualizes that the oscillatory potential stems from an interlocking of the oscillatory profiles. As a result, two nearby skyrmions can form a dimer with a pairing energy given by the potential minimum, i.e. here  $E_{\text{dimer}} \approx -0.47E_D$ . The lowest energy state for a fixed number of skyrmions is then a chain as displayed in Fig. 12.1.1. We have furthermore checked that these chains of skyrmions also show a short-range attractive interaction that binds two chains like a zipper, i.e. with a parallel offset of half a skyrmion width.

### Skyrmion-edge potentials

When calculating the potential for the interaction between a skyrmion and the edge of the system, we face the problem that the two objects are not identical and the setup offers less symmetries. In particular, in contrast to the previous skyrmion-skyrmion interaction this means that the potential in the  $y$ -direction depends on the definition of the skyrmion coordinate. Here, we define the position  $\mathbf{r}$  with  $\hat{n}(\mathbf{r}) = -\hat{z}$  as the skyrmion coordinate. While the skyrmion-skyrmion potential is a function of two spatial coordinates, the distance to the edge is only scalar.

However, the relative orientation between the normal  $\hat{\nu}$  of the edge and the in-plane component  $\hat{x}$  of the magnetic field remain as a degree of freedom, characterized by an angle  $\theta$ . The resulting interaction potential between a skyrmion and an edge for  $H = 0.75H_D$  and  $\phi = 45^\circ$  is shown in the right panel of Fig. 12.4.6 in the same manner as the skyrmion-skyrmion interaction. Note that in this plot, the radial coordinate  $r$  encodes the distance between the skyrmion and the edge for a fixed angle  $\theta$  which is encoded in the angular coordinate.

Remarkably, the interaction is purely repulsive and not symmetric for  $\hat{\nu} \perp \hat{x}$  whereas it oscillates symmetrically for  $\hat{\nu} \parallel \hat{x}$ , where  $\hat{x}$  is the direction in which the magnetic field is tilted. This behavior matches the expectations based on the skyrmion profile, see Fig. 12.4.5, which is symmetric and oscillating along  $\hat{x}$  and asymmetric and monotonous along  $\hat{y}$ . This result is again different from the purely repulsive interaction in systems with a perpendicular polarized background [169]. As a consequence, skyrmions in systems with a canted background phase can bind to the edge, similar to skyrmions in a conical background [173]. The binding energy is given by the minimum of the potential, here  $E_{\text{bind}} \approx -0.21E_D$ .

Summarizing, the interaction between a skyrmion and an edge shows the exact same features as the interaction between two skyrmions, i.e. the repulsive behavior along the one axis and the oscillating potential in the perpendicular direction which are features that are inherited from the profile of the isolated skyrmion.

## 12.5. Thin films of chiral magnets

When considering thin films of chiral magnets, the additional dimension offers a new direction for modulations and in particular the conical phase can be realized also in perpendicular fields.

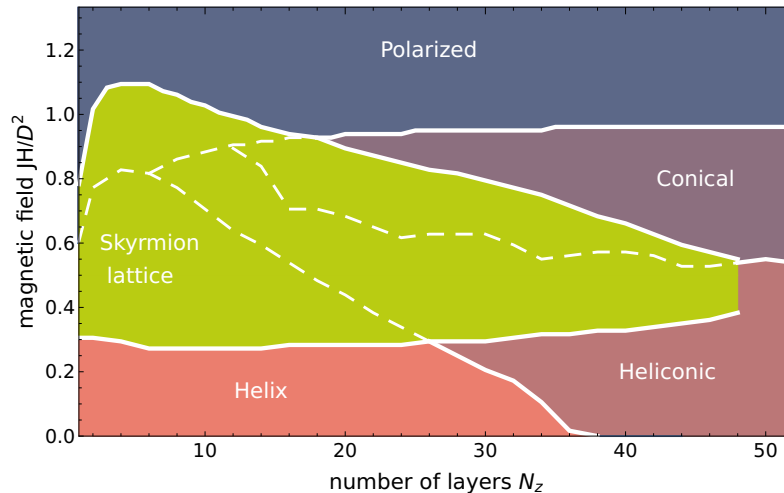


Figure 12.5.7.: Phase diagram for thin films of a chiral magnet (atomistic model) as a function of a perpendicular magnetic field  $\mathbf{H} = H\hat{z}$  and the number  $N_z$  of stacked layers. In the atomistic model, the DMI strength is fixed to  $D = 0.3J$  and the lattice constant is  $a = 1$ . The five distinct phases (as indicated) are explained in the main text. The phase boundaries as calculated are the solid white lines. The dashed lines hint at the phase diagram under the constraint that the skyrmion lattice phase is absent. Note that the skyrmion lattice phase (green) is not bounded by a white line at large  $N_z$  due to a lack of data. Beyond this point, we could not determine the phase boundaries.

In turn, the open surfaces allow for new twists in the magnetization from which the skyrmion lattice and the helical phase can benefit.

### 12.5.1. A first atomistic approach

For most of the considerations in this entire work, it does not make a big difference if the continuous micromagnetic model is considered or, instead, an atomistic model with a small lattice constant  $a \ll 1$ . Here, however, when discussing thin films, it makes indeed a difference if the thickness  $d$  is interpreted in terms of stacked atomistic layers,  $d = N_z a$ ,  $N_z \in \mathbb{N}$ , or if the thickness can be scaled to arbitrarily thin films within the continuous model. In particular, the scenario  $N_z = 1$  restores the two-dimensional monolayer at a finite discretization whereas the limit  $d \rightarrow 0$  of the continuous model still inherits the surface effects.

In an earlier attempt, we calculated the phase diagram as a function of field  $\mathbf{H} = H\hat{z}$  and number of layers  $N_z$  in the atomistic model, see Fig. 12.5.7. In this model, we used a DMI  $D = 0.3J$  and lattice constant  $a = 1$ . Due to the lattice anisotropy, the helical phase prefers a pinning with  $\mathbf{q} \parallel \langle 111 \rangle$ . Since this direction is confined by surfaces with  $\hat{\nu} = \hat{z}$ , the helix orients as  $\mathbf{q} \parallel \langle 110 \rangle$ . For larger thicknesses, however, the bulk pinning becomes important and in an regime between the helical phase and the conical phase, an intermediate phase forms, that interpolates between the phases.

Unfortunately, minimizing the energy density in an atomistic model is complicated since the spacing  $a$  is equal for all directions. This means that the number of lattice sites needs to be varied in order to optimize the periodicity. Note that we had to restrict calculations to only one magnetic unit cell which leads to errors since in general the periodicity of the magnetization is not commensurate with the discrete lattice. Furthermore, we did not manage to control the minimization of the skyrmion lattice phase since the computational effort for minimizing many

sets of three-dimensional configurations was too high.

Taking into account that the skyrmion lattice deforms under tilted fields, i.e. the ratio of the lattice becomes an additional dimension where optimization is required, we did not further investigate the atomistic scenario.

### 12.5.2. The continuous thin film

In practice, the differences between the continuous model and the atomistic model only become relevant when the thickness of the film becomes of the order of the lattice constant of the latter model,  $d \sim a$ . While the atomistic model reduces to a discrete monolayer, the continuous model can in principle scale to arbitrarily low thicknesses  $d > 0$  and does not restore the two-dimensional model.

A handwavy argument for the different limits is obtained by keeping the boundary condition  $\partial_z \hat{n} = \hat{z} \times \hat{n}$  of the continuous model even in the limit  $d \rightarrow 0$ . In this limit, the wavelength  $\lambda$  is much larger than the thickness,  $\lambda \gg d$ , and thus modulations in the  $\hat{z}$ -direction are moderated by the boundary condition instead of the bulk physics. Inserting the boundary condition in the  $\hat{z}$ -dependent components of the bulk micromagnetic model yields

$$\frac{1}{2} (\partial_z \hat{n})^2 \rightarrow \frac{1}{2} (\hat{z} \times \hat{n})^2 = \frac{1}{2} (\hat{n}_x^2 + \hat{n}_y^2) \quad (12.5.3)$$

$$\hat{n} \cdot (\hat{z} \times (\partial_z \hat{n})) \rightarrow \hat{n} \cdot (\hat{z} \times (\hat{z} \times \hat{n})) = -(\hat{n}_x^2 + \hat{n}_y^2). \quad (12.5.4)$$

The thin film continuous model for  $d \rightarrow 0$  thus reduces to the two-dimensional continuous model, Eq. 10.2.10, where the surfaces effectively yield an easy-plane anisotropy term  $-K \hat{n}_z^2 = \frac{1}{2} \hat{n}_z^2$ . Note that this interpretation is in a surprisingly precise agreement with the numerical calculations for the two-dimensional model with anisotropy by GÜNGÖRDÜ *et al.*, see Ref. [108], and the three-dimensional numerical calculations for continuous thin films by RYBAKOV *et al.*, see Ref. [111].

### Phase diagrams

When considering the continuous micromagnetic model instead of the discrete atomistic model, we can finally use that the discretizations  $a_i$ ,  $i = x, y, z$ , are not physical but only a property of the numerical mesh. Therefore, they are not necessarily equal and we can apply the simplex minimization from Sec. 12.2 for thin films.

Technically, we initialize sets of different modulated textures on numerical grids that all have  $N_z = 54$  layers. The thickness  $d = N_z a_z$  is then determined by varying  $a_z$ . For the initial textures, we restrict our analysis to texture modulated along only the  $z$ -direction, in the  $(x, z)$ -plane and the skyrmion lattice which we emphasize is only one special candidate for a phase that modulates in all directions. For the current state of discussion, we summarize the final states only according to the number of translation invariant directions that directly corresponds to the chosen initial state.

The convention for names used here is motivated by regarding only one layer of the thin film: Then the *polarized state* refers to all states that are obtained as a result from the first initial set which is translation invariant along both axes in the film. This definition includes the conical phase for perpendicular magnetic fields.

However, we observed that this phase is highly unstable with regard to the alignment of the field: At any finite angle  $\phi > 0$  we observe that the conical phase tilts away from  $\mathbf{q} \parallel \hat{z}$  and

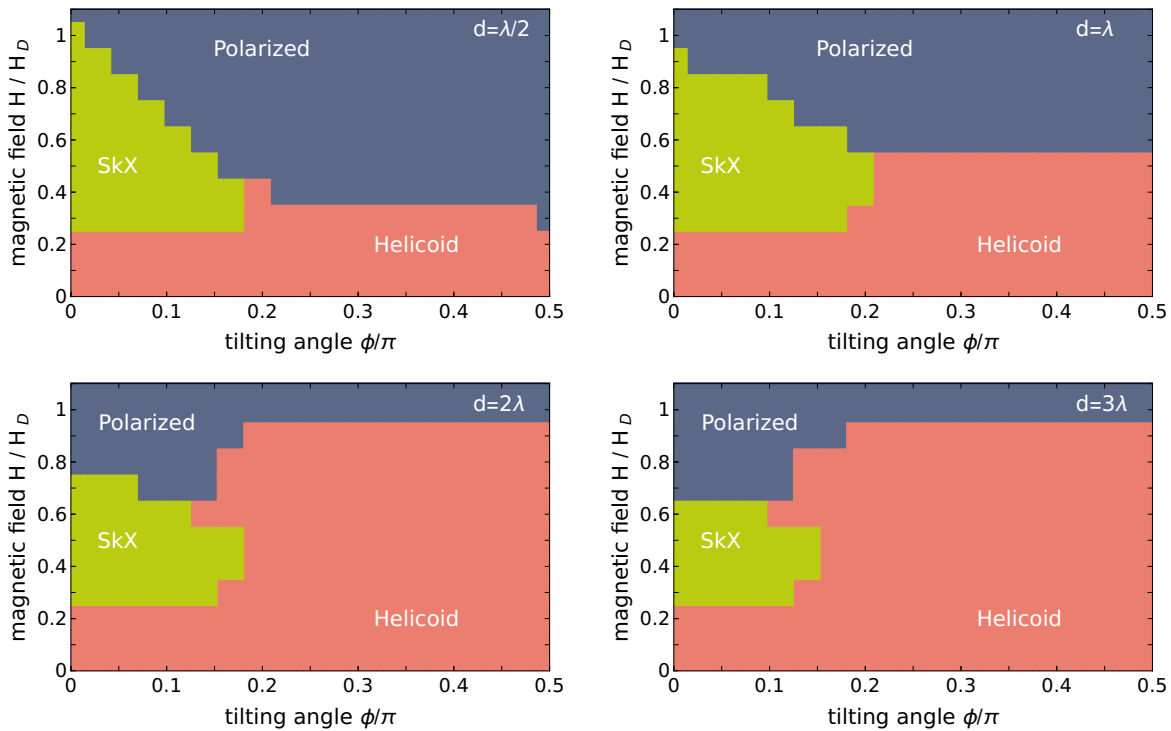


Figure 12.5.8.: Phase diagrams for thin films of a chiral magnet as a function of magnetic field strength  $H$  and tilt angle of the field  $\phi$ . The tilt angle  $\phi$  is defined with respect to the normal of the film. The thickness  $d$  of the films is  $d = \lambda/2, \lambda, 2\lambda, 3\lambda$  as indicated in the top right corner of each panel.  $\lambda = 2\pi$  is the wavelength of the helix. Here, we only distinguish phases according to their number  $N$  of translation invariant directions as *polarized* ( $N = 2$ ), *helicoid* ( $N = 1$ ), and *skyrmion lattice SkX* ( $N = 0$ ).

shows an additional modulation along the in-plane axis of the magnetic field. Note that also the actual polarized phase is not fully polarized at finite angles due to the twists at the surfaces. Accordingly, the *helicoid* phase refers to all states with one translation invariant axis.

The resulting phase diagrams are shown in Fig. 12.5.8 for thicknesses  $d = \lambda/2, \lambda, 2\lambda, 3\lambda$ . In contrast to the previous phase diagrams, we computed the energy densities on a sparse grid with  $\Delta\phi = 5^\circ$  and  $\Delta H = 0.1H_D$  only. In agreement with the results for  $\phi = 0$  by Rybakov *et al.*, Ref. [111], the skyrmion lattice phase (SkX) profits from the surfaces and covers a larger area on the axis  $\phi = 0$  if the film is thinner. For increasing thickness, the impact of the surfaces diminishes and consequently the area with the skyrmion lattice shrinks. For finite tilt angles of the field, the present results suggest that the most stable skyrmion lattice is found for  $d = \lambda$ , while as well thinner and thicker films have a negative impact on the skyrmion lattice in an oblique field.

However, note that the phase diagrams are very coarse, hence, all present statements should be handled with care. Also a broad variety of further initial states has not been considered, such as the in-film skyrmion lattice, c.f. Ref. [104, 248, 249], or helicoid states with surface modulations in other directions than the in-plane component of the field  $\hat{x}$ , c.f. Ref. [111].

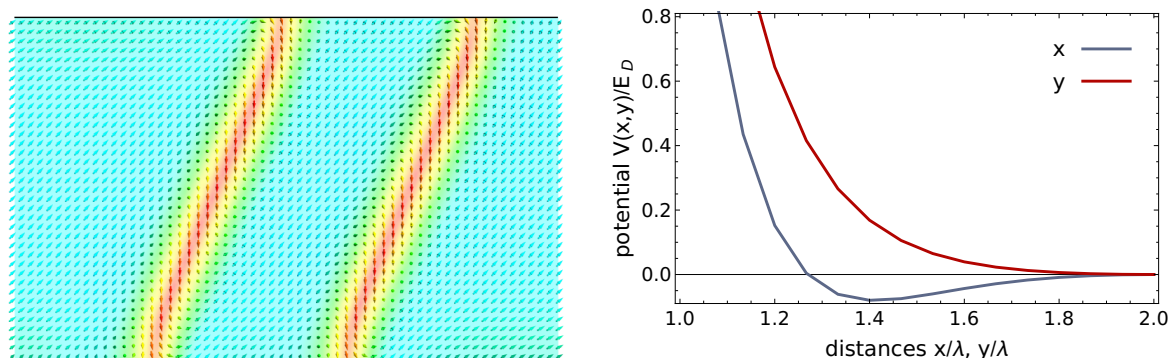


Figure 12.5.9.: Interaction between two isolated Bloch-type skyrmions in a thin film of thickness  $d = 2.5\lambda$ . The external magnetic field  $\mathbf{H}$  is canted by  $\phi = 45^\circ$  in the  $\hat{x}$ -direction and  $|\mathbf{H}| = 1.0H_D$ . Left: Visualization of the magnetization in the  $(x, z)$ -plane on a cut through two skyrmion tubes at a distance  $\Delta x = 1.4\lambda$ . The surfaces of the film are indicated by thin black lines. The color code denotes the component of the magnetization in the direction of the normal of the surface  $\hat{v} = \hat{z}$ . Right: Interaction potential of the two skyrmion tubes as a function of distance along the  $x$ -axis (blue) and the  $y$ -axis, respectively.

### Skyrmion interactions

The calculation of skyrmion interaction potentials in monolayers showed that the energetically optimal state for a fixed number of skyrmions is a chain of these. However, in bulk systems, the skyrmion tubes orient along the external field and are then either repulsive or attractive, dependent on whether the background is polarized or conical [172].

For thin films, a priori, the situation is unclear. Since one can expect that for thick films  $d \gg \lambda$  the bulk limit is recovered, we concentrate on thin films  $d \sim \lambda$  where we expect the bulk repulsion to be small.

When we calculated the interaction potential between two skyrmions, we have simply fixed their centers while running the usual minimization of energy. For thin films, the situation is already more complex since the skyrmion coordinate  $\mathbf{R} \in \mathbb{R}^2$  is not well defined for the skyrmion tube which should rather be described by a line  $\mathbf{R}(z)$ . The full interaction potential between two skyrmion tubes can therefore be arbitrary complex when all possible deformations of the skyrmion tube have to be taken into account.

If we assume, however, that the skyrmion tubes are rigid up to deformation far away from the center  $\mathbf{R}(z)$ , then we can assign a tube a coordinate  $\bar{\mathbf{R}}$ . For the calculation of potentials, we then have to fix the whole line  $\mathbf{R}(z)$  in order to gain consistent results. The resulting interaction potential for two rigid skyrmion tubes in a thin film with a tilted magnetic field,  $H = 1.0H_D$  and  $\phi = 45^\circ$ , is shown in the right panel of Fig. 12.5.9 for the two main axes  $\hat{x}$  and  $\hat{y}$ . The thickness of the film is chosen as  $d = 2.5\lambda$  which is experimentally accessible.

Indeed, the potential for the interaction in a film shows the same features as in monolayer, i.e. an axis with repulsive interaction and an axis where a small potential minimum is present at a finite distance, here  $\Delta x_{\min} = 1.4\lambda$ . The corresponding magnetization texture for the bound state is shown in the left panel of Fig. 12.5.9. Note that the skyrmion tubes are tilted but are not align with the external field  $\mathbf{H}$ .

## 13. Speed-limits for skyrmions

### 13.1. Motivation

The idea to use skyrmions in high-density non-volatile memory devices has been widely discussed since the skyrmion racetrack was proposed by Fert *et al.*, Ref. [140]. A detailed summary of the current status of *skyrmionics* is given in Sec. 1.5. Also in this work, a new possible application of skyrmions in a shift register device is discussed, see Sec. 7, Sec. 8, and the Appendix 15.

Yet, stability and a high density are not the only elements that are necessary for competitive storage devices but also the operational speed must be adequate. The argument that skyrmions couple efficiently to spin-currents and unpin at much lower currents than domain walls, only states that skyrmions could be moved at a lower power consumption. However, a low current density  $\mathbf{v}_s$  still implies a low drift velocity  $\dot{\mathbf{R}}$ .

The Thiele equation allows for arbitrarily high skyrmion velocities

$$0 = \mathbf{G} \times (\dot{\mathbf{R}} - \mathbf{v}_s) + \mathcal{D}(\alpha \dot{\mathbf{R}} - \beta \mathbf{v}_s) \quad (13.1.1)$$

since the equation can be solved for  $\dot{\mathbf{R}}$  and yields a linear relation  $\dot{\mathbf{R}}(\mathbf{v}_s)$ .

For domain walls, nevertheless, it is known that spin-torques lead to a deformation of the internal domain wall angle, i.e., the angle between the normal of the straight domain wall and the rotary plane of the magnetization. Above a critical current density, the domain wall becomes unstable and dissipates energy by continuously emitting spin waves which is known as the Walker breakdown [250]. The new dissipation channel slows down the domain wall.

Small deformations of a skyrmion due to a current have been reported [86]. However, at large currents the deformations strongly influence the shape of a skyrmion, see Fig. 13.1.1.

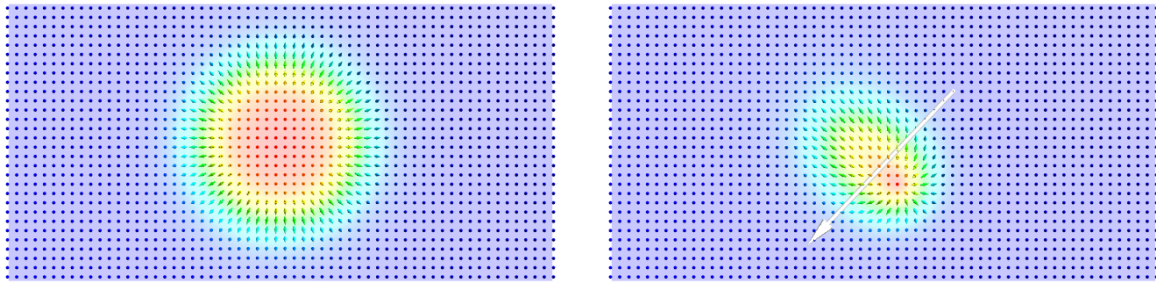


Figure 13.1.1.: The magnetization texture of a Néel-type skyrmion without magnetic field  $\mathbf{H} = 0$  but stabilized by a uniaxial anisotropy  $K = 1.3K_D$  instead. The color code represents the  $z$ -component of the magnetization. The skyrmion at rest (left) is circular and is flat around the core at  $\hat{n} = -\hat{z}$ . The fast drifting skyrmion (right) compressed and elongated in the direction perpendicular to the drift velocity (white arrow). This shooting star skyrmion is obtained for  $\alpha = 0.75$  and  $u = (\alpha - \beta)|\mathbf{v}_s| = 1.8 v_D$ .

## 13.2. Implementation of a co-moving frame

We want to simulate a very fast skyrmion which is described within the continuous micromagnetic model, Sec. 10.2.3. For simplicity, the skyrmion should move in an infinitely large system that is translation invariant, i.e., has not defects or edges.

When we naively start a simulation, we face two problems: (i) The fast change of magnetization requires smaller discretizations  $\Delta t$  of time, thus more iterations  $N$  for the same time-span  $t = N \Delta t$ . (ii) Our simulations with MuMax3 [251] showed that the moving skyrmion gets excited by the tiny energy differences that come from the underlying lattice. The energy of a skyrmion is highest if centered on a spin and lowest if centered in the middle of a square tile. In the continuous micromagnetic model which we consider here, this lattice and thus the potential do not exist. It is only an artifact of the numerical implementation. Choosing a finer mesh for the numerics helps to suppress this issue, but increases the computational effort tremendously.

We therefore need to simulate the skyrmion in a co-moving frame of reference, such that the deformations due to the current are still recovered but the skyrmion stands still on the numerical lattice.

### 13.2.1. The moving frame of reference

Let us first consider a general moving frame of reference. We define the magnetization in a moving frame as

$$\hat{n}(\mathbf{r}, t) = \hat{n}_m(\mathbf{r} - \mathbf{R}_m(t), t) \quad (13.2.2)$$

where  $\mathbf{R}_m(t)$  is the translation of the moving frame with respect to the frame at rest. Since the setup that we consider is translation invariant, we only need to reconsider the derivatives  $\nabla$  and  $\partial_t$  in the LLG equation. We obtain

$$\nabla \hat{n}(\mathbf{r}, t) = \nabla \hat{n}_m(\mathbf{r} - \mathbf{R}_m(t), t) \quad (13.2.3)$$

$$\partial_t \hat{n}(\mathbf{r}, t) = \left( d_t + \left( \dot{\mathbf{R}}_m(t) \cdot \nabla \right) \right) \hat{n}_m(\mathbf{r} - \mathbf{R}_m(t), t) \quad (13.2.4)$$

where  $d_t$  is the time-derivative in the moving frame. These expressions for the derivatives are finally plugged into the LLG equation, Eq. 10.5.40, such that we obtain the general LLG equation in a moving frame  $\mathbf{R}_m(t)$ :

$$d_t \hat{n}_m = -(\mathbf{T}(t) \cdot \nabla) \hat{n}_m + \frac{1}{1 + \alpha^2} (-\hat{n}_m \times \mathbf{B}_{\text{eff}} - \alpha \hat{n}_m \times \hat{n}_m \times \mathbf{B}_{\text{eff}} - (\alpha - \beta) \hat{n}_m \times (\mathbf{v}_s \cdot \nabla) \hat{n}_m) \quad (13.2.5)$$

which is written in the LL form, suitable for numerical implementation. Note that we have summarized all components with a direct translational interpretation in the vector  $\mathbf{T}(t)$ , which reads

$$\mathbf{T}(t) = \dot{\mathbf{R}}_m(t) + \frac{1 + \alpha\beta}{1 + \alpha^2} \mathbf{v}_s \quad (13.2.6)$$

such that the actual moving frame only enters by its velocity,  $\dot{\mathbf{R}}_m(t)$ .

### 13.2.2. The reduced set of parameters

If we want to study the distortion of a moving skyrmion in the following, the distortion in rescaled units can generally depend on the parameters  $\alpha$ ,  $\beta$ , and  $\mathbf{v}_s$ .

In the following we will restrict all discussions to systems without magnetic field,  $\mathbf{H} = 0$ , and where Néel-type skyrmions are stabilized by interfacial DMI  $D$  and a uniaxial anisotropy  $K$ , compare Eq. 10.2.11. With these restrictions, the system is also rotation symmetric. Therefore, the direction of the applied current should not influence the resulting distortion, up to a global rotation.

Furthermore, using the result of the previous section, we can go to the moving frame with  $\mathbf{T}(t) = 0$ , see Eq. 13.2.6. The translation into a moving frame does not change the distortion, but importantly, it changes the number of free parameters: The velocity  $\mathbf{v}_s$  and the non-adiabatic constant  $\beta$  only appear in combination. We therefore define the reduced drive  $\mathbf{u}$  as

$$\mathbf{u} = (\alpha - \beta)\mathbf{v}_s. \quad (13.2.7)$$

After rescaling the time  $t$  by the constant prefactor  $1 + \alpha^2$ , the LLG equation is reduced to

$$d_t \hat{n}_m = -\hat{n}_m \times \mathbf{B}_{\text{eff}} - \alpha \hat{n}_m \times \hat{n}_m \times \mathbf{B}_{\text{eff}} - \hat{n}_m \times (\mathbf{u} \cdot \nabla) \hat{n}_m \quad (13.2.8)$$

where only the two free parameters  $\alpha$  and  $u = |\mathbf{u}|$  remain for influencing the distortion of a skyrmion.

Note that this simple frame of reference with  $\mathbf{T} = 0$  is *not* the co-moving frame. This can easily be seen as this frame moves in the direction of the applied current, whereas a skyrmion does have a perpendicular component for the motion.

### 13.2.3. Thiele revisited

The position of a skyrmion  $\mathbf{R}$  can be both defined and calculated in various ways but in the end only the velocity  $\dot{\mathbf{R}}$  enters the LLG equation for the moving frame of reference. To obtain the velocity as the difference between skyrmion positions in subsequent images is in principle possible but requires very precise tracking algorithms.

An alternative approach is to reconsider the Thiele approach, Sec. 10.3.3. The idea there was to assume a rigid skyrmion and integrate out the static spatial component of the LLG equation. So far, we used the equation mostly for circular skyrmions with a static dissipation constant  $D$ . In the more general case, the dissipative contribution is expressed in the  $2 \times 2$  matrix  $\mathcal{D}$  which is not necessarily time-independent:

$$0 = \mathbf{G} \times (\dot{\mathbf{R}} - \mathbf{v}_s) + \mathcal{D}(t)(\alpha \dot{\mathbf{R}} - \beta \mathbf{v}_s), \quad (13.2.9)$$

with  $\mathbf{G} = 4\pi\mathcal{W}\hat{z}$  the constant gyrocoupling vector if the skyrmion number  $\mathcal{W} = -1$  is a conserved, and the time-dependent dissipation matrix

$$\mathcal{D}_{ij}(t) = \int \left( \frac{d\hat{n}}{dx_i}(t) \cdot \frac{d\hat{n}}{dx_j}(t) \right) d\mathbf{r}^2. \quad (13.2.10)$$

Moreover, this more general equation is invertible and yields a general expression for the skyrmion velocity:

$$\dot{\mathbf{R}}(t) = \frac{1}{\mathbf{G}^2 + \alpha^2 \det(\mathcal{D}(t))} \left( (\alpha - \beta)\mathbf{G} \times (\mathcal{D}(t)\mathbf{v}_s) + (|\mathbf{G}|^2 + \alpha\beta \det(\mathcal{D}(t)))\mathbf{v}_s \right) \quad (13.2.11)$$

with  $\det(\mathcal{D}) = \mathcal{D}_{xx}\mathcal{D}_{yy} - 2\mathcal{D}_{xy}$  the determinant of the dissipation matrix.

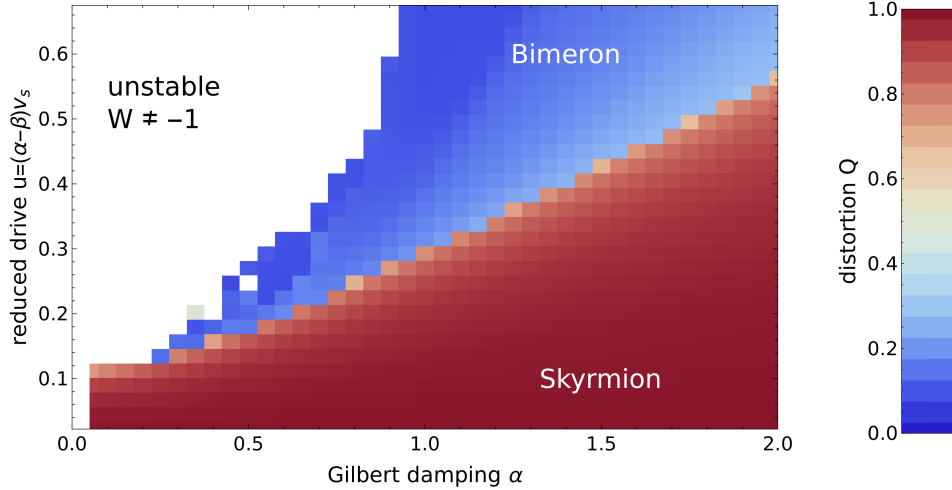


Figure 13.3.2.: Phase diagram for the stability of a skyrmion that is driven by spin-transfer-torque at  $\mathbf{H} = 0$  and  $K = 1.3K_D$  as a function of Gilbert damping  $\alpha$  and the reduced drive  $u = (\alpha - \beta)v_s$ . The color code denotes the distortion  $Q$ , which ranges from a circular skyrmion with  $Q = 1$  (red) to a skyrmion with a maximal elongation  $Q = 0$  (blue) which we refer to as a *bimeron*. Note that a lower bound for  $Q$  is given by the periodic boundary conditions.

This revisited Thiele equation is now able to include changes of the shape of the skyrmion during the simulation. The numerical effort to calculate the dissipation components  $\mathcal{D}_{ij}(t)$  at every time-step is small.

### 13.3. Bimeron instability for current-driven skyrmions

For the following discussion, we initialize a skyrmion on a square lattice with a discretization  $a = 1/3$  and  $60 \times 60$  lattice sites. We let it relax as described in Sec. 10.5.2 with the  $\mathcal{O}(a^8)$  discretization from Sec. 10.5.3 at zero magnetic field  $\mathbf{H} = 0$  and with a uniaxial anisotropy  $K = 1.3K_D$ . The ground state in this parameter regime is the polarized state. Nevertheless, skyrmions exist as metastable excitations, see left panel of Fig. 13.1.1. The following calculations are performed in the Thiele co-moving frame as described in the previous section 13.2.

In order to calculate the skyrmion profile as a function of the two reduced parameters,  $(\alpha, u)$ , we increase the current density continuously from  $v_s = 0$

$$\mathbf{v}_s(t) = \begin{cases} v_0 \sin^2\left(\frac{\pi}{2} \frac{t}{t_0}\right) \hat{x} & \text{for } 0 \leq t < t_0 \\ v_0 \hat{x} & \text{for } t \geq t_0 \end{cases} \quad (13.3.12)$$

where we choose  $v_0 = 0.009v_D$  and the time-scale  $t_0$  sufficiently long. For  $t > t_0$ , the simulation continues until a steady state is reached. In order to map out an entire phase diagram for various values  $(\alpha, u)$ , we vary the Gilbert damping  $\alpha$  and the non-adiabatic parameter  $\beta = \alpha - (u/v_0)$  accordingly. We have checked that the results indeed only depend on  $\alpha$  and the reduced drive  $u = (\alpha - \beta)v_s$  by comparing the results for constant  $u$  but different combinations of  $\beta$  and  $v_s$ .

The resulting phase diagram is shown in Fig. 13.3.2. The skyrmion number  $\mathcal{W}$ , which should remain constant  $\mathcal{W} = -1$ , is an indicator for the stability of the skyrmion. The regime with  $\mathcal{W} \neq -1$  is not further investigated here. We furthermore define the distortion  $0 \leq Q \leq 1$  of

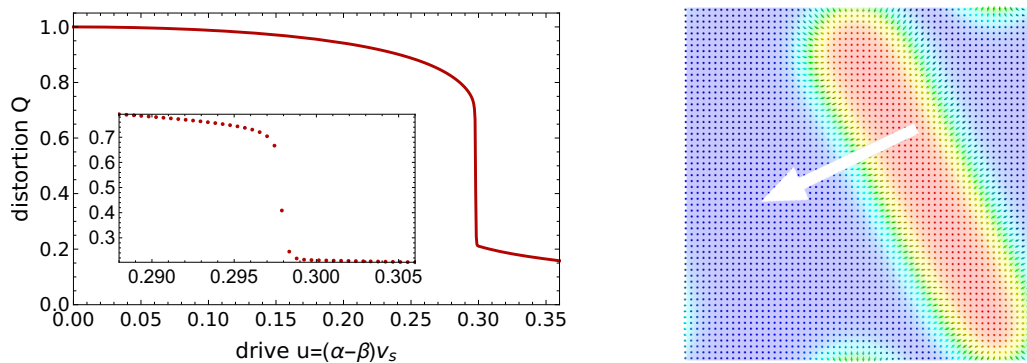


Figure 13.3.3.: Cut through the phase diagram in Fig. 13.3.2 at  $\alpha = 1$ . The left plot shows the distortion  $Q$  as a function of the drive  $u$ . The inset is a zoom to the interval around the bimeron instability. Each red dot in the inset is a bare data point. The right panel shows the magnetization of the bimeron for  $(\alpha, u) = (1, 0.315 v_D)$ . The white arrow indicates the direction of the velocity of the bimeron. The entire simulated grid with periodic boundary conditions is shown.

a skyrmion as the ratio of the smaller and the larger eigenvalue of the dissipation matrix  $\mathcal{D}$ , which is indicated with the red-white-blue color code in the phase diagram:

$$Q = \frac{\mathcal{D}_{xx} + \mathcal{D}_{yy} - \sqrt{4\mathcal{D}_{xy}^2 + (\mathcal{D}_{xx} - \mathcal{D}_{yy})^2}}{\mathcal{D}_{xx} + \mathcal{D}_{yy} + \sqrt{4\mathcal{D}_{xy}^2 + (\mathcal{D}_{xx} - \mathcal{D}_{yy})^2}}. \quad (13.3.13)$$

In a close region to the critical drive  $u_{\text{crit}}(\alpha)$  the deformation drops rapidly with  $u$ . For  $u > u_{\text{crit}}(\alpha)$  the elongation of the skyrmion is infinite within the boundaries of the simulated cell. This elliptical instability is known from the phase diagram at rest as the *bimeron instability*, see Ref. [46]. The data in the phase diagram shows a linear dependence  $u_{\text{crit}}(\alpha) \propto \alpha$  for  $\alpha \gtrsim 0.5$ . For smaller values of  $\alpha$ , unfortunately, the data is too coarse to draw any conclusions.

In practice, however,  $Q$  is bounded from below by the size of the simulated cell. Figure 13.3.3 shows a plot of the distortion  $Q(u)$  as a function of the drive  $u$  for  $\alpha = 1$ . As can be seen here, the transition is very sharp and is not fully resolved, thus, we can not infer from the data if the transition is continuous or if the distortion is also physically bounded. We furthermore performed simulations with 10 times larger  $t_0$  to exclude that the behavior close to the transition is an artifact of the too rapidly increased current. Note also that the data point at  $Q \approx 0.4$  stems from a simulation where the steady state was not yet fully reached.

## 13.4. Current-stabilized shooting star skyrmions

In the previous section we found that above a critical drive  $u_{\text{crit}}(\alpha)$ , the single skyrmion elongates to arbitrary extents and becomes a non-local bimeron. Furthermore, it is expected that above a critical current density the current destabilizes all magnetic textures and the magnetization fluctuates chaotically.

When we simulate the co-moving LLG equation for drives  $u \sim v_D$  of the order of the reduced current, then we indeed observe this phenomenon for Gilbert damping  $\alpha \lesssim 0.7$ . For larger damping, i.e., in the regime where we also observe the bimeron instability, this absolute instability is only found for  $u \gtrsim 2 v_D$ . Interestingly, in between the bimeron phase and the absolute

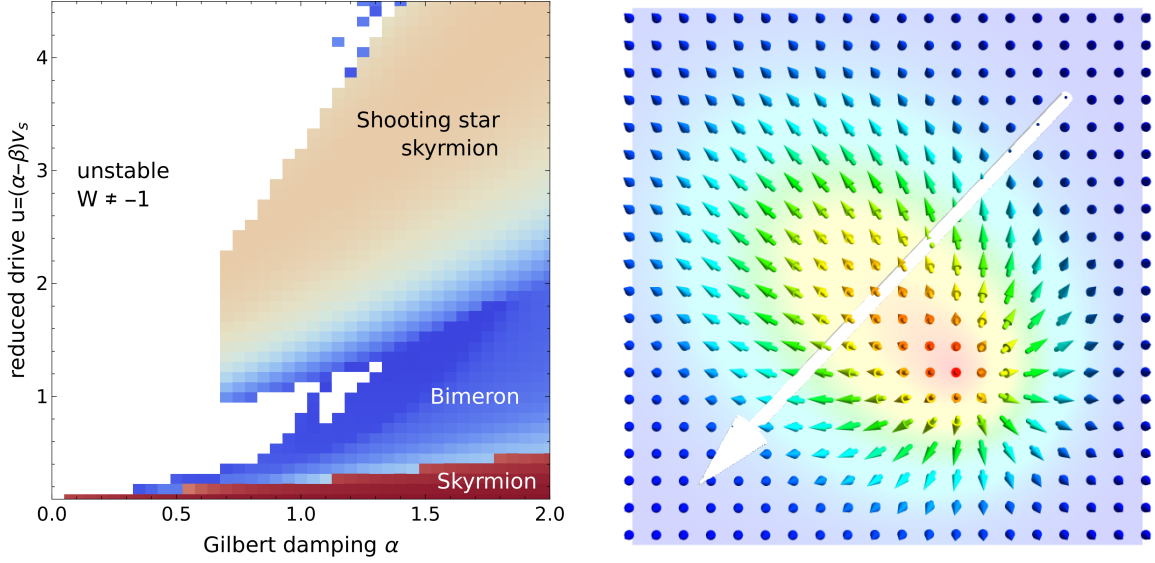


Figure 13.4.4.: Phase diagram for the stability of a skyrmion that is driven by spin-transfer-torque at  $\mathbf{H} = 0$  and  $K = 1.3K_D$  as a function of Gilbert damping  $\alpha$  and the reduced drive  $u = (\alpha - \beta)v_s$ . The color code denotes the distortion  $Q$ , which ranges from a circular skyrmion with  $Q = 1$  (red) to a skyrmion with a maximal elongation  $Q = 0$  (blue), see also Fig. 13.3.2. Note that a lower bound for  $Q$  is given by the periodic boundary conditions. The right panel shows the shooting star skyrmion for  $\alpha = 0.75$  and  $u = 1.8v_D$  which is stabilized in the region indicated in the phase diagram. The white arrow denotes the direction of the skyrmion velocity. The color code represents the  $z$ -component of the magnetization.

instability we find a new skyrmion phase that emerges comparably smooth from the bimeron phase and is stable in a large regime. The phase diagram with the larger range of  $u$  is shown in Fig. 13.4.4.

The newly stabilized skyrmion differs remarkably from the skyrmion that is found below the bimeron instability. The magnetization texture is shown in the right panel of Fig. 13.4.4. In contrast to the skyrmion at rest, see left panel of Fig. 13.1.1, the present skyrmion is strongly compressed and does not show the flat center. Furthermore, it is elongated in the direction perpendicular to the direction of motion which is indicated by the white arrow and it is not rotation symmetric.

In fact, because of the optical similarity, we refer to this asymmetric skyrmion as the shooting star skyrmion. Note that the orientation of the head and the tail of this shooting star are fixed with respect to the direction of motion: In our simulations, the axis  $\hat{v}$  from tail to head points always in the direction  $\hat{z} \times \dot{\mathbf{R}}$ .

Interestingly, the observation  $\hat{v} \propto \hat{z} \times \dot{\mathbf{R}}$  is in agreement with the simple picture that the skyrmion moves so fast that the polarized background becomes as a highly viscous medium which therefore exerts a strong friction  $\mathbf{F}_{\text{fric}} \propto -\dot{\mathbf{R}}$  on the magnetization texture. The Magnus force then turns this force into a velocity contribution  $\mathbf{g}(\mathbf{r}) \times \mathbf{F}_{\text{fric}}$ , where  $\mathbf{g}(\mathbf{r})$  is the local gyrocoupling vector density which is proportional to the topological charge density  $\mathbf{g}(\mathbf{r}) \propto w(\mathbf{r})\hat{z}$ . Since the skyrmion that we consider here has always charge  $\mathcal{W} = -1$ , this results in an agglomeration of (negative) topological charge in the direction  $\hat{z} \times \dot{\mathbf{R}}$  which is precisely what sets  $\hat{v}$ .

Part IV.  
Summary



---

# Summary

The following summary of the diverse results that were obtained in this thesis is structured according to the schematic phase diagram, see Fig. IV, which was also used to guide through the outline, Sec. 2.

## Topological domain walls

Our study of the domain walls that form between patches of the helical phase, Sec. 3, shows that the type of the resulting domain wall is determined by the angle  $\phi = \angle(\mathbf{q}_1, \mathbf{q}_2)$  between the orientations  $\mathbf{q}_i$  of the helices.

While the helical phases are continuously connected by a type-I domain for small angles  $\phi \lesssim 85^\circ$  and separated by a discontinuous type-III wall for  $\phi \gtrsim 140^\circ$ , type-II domain walls are established in the intermediate regime  $85^\circ \lesssim \phi \lesssim 140^\circ$ . These transitions are observed both in experiments and as a result of our numerical calculations in the simple micromagnetic model. Interestingly, the type-II domain wall consists of a sequence of disclinations with alternating sign and henceforth can carry a finite skyrmion number, dependent on the distance between the disclinations.

Due to their non-trivial topology, these novel domain walls will influence macroscopic properties by, e.g., contribute an extra topological Hall effect or tremendously enhance relaxation times due to the topological protection of the disclinations. The possibility of a topological domain wall further adds an interesting new building block to the broad field of spintronics.

The numerical study in Sec. 11 shows that type-II domain walls might also play an important role for the surface reconstruction of the helical phase. Our calculations of the energy as a function of the angle between the normal of the surface  $\hat{\nu}$  and the helical orientation  $\mathbf{q}$  reveal that the energetically optimal geometry is  $\hat{\nu} \perp \mathbf{q}$ , which is in agreement with the experimental observation.

A comparison of the maximal energy gain to the costs of a type-II domain wall indicates that a surface reconstruction is predicted within the micromagnetic model for certain orientations  $\mathbf{q}$  of the helix in the bulk. This simple comparison is in agreement with the results of a more rigorous numerical check which has, however, to be considered with a lot of care due to strong relative anisotropies which spoil the results.

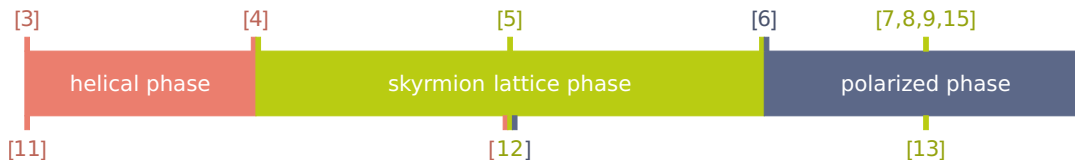


Figure IV.: Schematic representation of how the projects in the different sections are connected via the schematic phase diagram. The colors encode the thermodynamically stable phases and the also possible metastable excitations that were studied therein.

Moreover, for the orientation  $\mathbf{q} \parallel \langle 111 \rangle$  which is pinned in the bulk by the cubic anisotropies, only a small energy gain can come from a realignment at the surface. The type of domain wall which connects this bulk phase to the  $\hat{\nu} \perp \mathbf{q}$ -phase at the surface is a most probably a semi-transparent type-II domain wall which is, however, not included in the calculations in Sec. 3. Future calculations could investigate the energetics of this interface.

Whether the surface reconstruction in the physical system is definitely caused by the bulk-boundary correspondence of the micromagnetic model or if additional modifications have to be taken into account remains to be determined. In any case, the problem of numerical accuracy, both due to relative anisotropies and the calculation of energy contributions in systems with a surface, needs to be controlled for future investigations. Only then one can also consider a finite magnetic which break the time reversal symmetry.

### Skyrmions in the helix

In Sec. 4 we have studied numerically the stability of skyrmions in the helical phase and the interactions among these. It turns out that, besides the topology, skyrmions in the helical phase have little in common with their extensively studied relatives in the polarized background.

The latter is circular and can move in the two-dimensional plane, whereas the motion of the H-shaped helical skyrmion is confined to the lanes provided by the underlying helix. Also the interactions between skyrmions are fundamentally different for the two backgrounds. Skyrmions in the helical phase show a faint repulsive long-range interaction which switches into a strong attractive interaction on small distances, for both scenarios, skyrmions on the same helical lane and skyrmions on neighboring lanes. The skyrmion in a polarized background, in turn, is repulsive to other skyrmions.

Attractive also for possible applications, it turns out that a skyrmion in the helical phase remains metastable down to zero magnetic field and even below, whereas the stability of the skyrmion in a polarized background is limited by the bimeron instability. In this regime, the helical skyrmion and antiskyrmion coexist with equal energy as defects in helical lanes that are shifted by half a wavelength.

This presentation of the stability might, in fact, be misleading since also the skyrmion in the helix has an instability: This zipper instability evolves when skyrmions form a bound chain over multiple neighboring lanes which then might eventually become unstable and decay into the zipper-configuration as pointed out in Sec. 4. Another instability which corresponds more to the bimeron instability, has been observed during our simulations and is not exposed in the paper.

Recall that the bimeron instability occurs as a consequence of the polarized background being only metastable and not the ground state of the system.

For the skyrmion in the helix, the background with a broken translation invariance now becomes crucial because an analogous situation is already created when the helical wavelength is not optimal, for example due to pinning or geometric confinement. Then the skyrmionic defect is the weak spot in the array of hard helical wires and gives way to the pressure of the surrounding helical phase by a decay into two dislocations. Dependent on the sign of the pressure, the two meronic ends of the helical skyrmion either immediately separate in opposite directions and thereby make room for the wavelength to expand, or the merons first pass each other and then separate which adds a helical string at the cost of erasing the skyrmion.

Future studies should investigate the potential of the still underrated helical skyrmions for skyrmionics, since the helical background does not only provide natural tracks for the skyrmions

---

but also waveguides for magnons.

### Stability of skyrmions

According to the Arrhenius law, the temperature-dependent lifetime  $\tau(B, T)$  of a state grows exponentially with the energy barrier  $\Delta E$  associated to its decay,  $\tau(B, T) \approx \tau_0(B)e^{\Delta E/k_B T}$ . This energy barrier is particularly high for a topological object like a skyrmion and makes it ultra stable.

However, our measurements reveal that the decay of the skyrmion lattice does not follow the simple Arrhenius law. This is explained by the Meyer-Neldel rule which states that, for energy barriers significantly larger than the microscopic energy scale, the number of microscopic processes that reach the activation energy grows exponentially. Therefore, instead of the energy barrier, the *free energy barrier* has to be considered for the lifetime:

$$\tau(B) = \tau_{00} \exp\left(-\frac{\Delta S(B)}{k_B}\right) \exp\left(\frac{\Delta E(B)}{k_B T}\right). \quad (13.4.14)$$

Note that, when estimating the lifetime of a skyrmion from its topological energy barrier, the prefactor of the Arrhenius law is usually set to  $\tau_0(B) \sim 10^{-9}$ .

As our findings show, the use of the Arrhenius law is crucial since the prefactor  $\tau_0(B) = \tau_{00} \exp\left(-\frac{\Delta S(B)}{k_B}\right)$ , in fact, changes due to the compensation effect by 30 orders of magnitude. It is therefore important to develop methods that are capable to calculate also the entropy contribution to the topological decay.

The exploration of the magnetic phases under tilted magnetic fields in Sec. 12 required a change of paradigms, so we let go of the constraint that the discretizations  $\{a_i\}$  have to be isotropic and thereby reduced the computational effort with a simplex minimization for the energy density such that three-dimensional phase diagrams can be computed in a reasonable time and with a sufficient accuracy.

Up to now, and with regard to a possible experimental realization, the reliability and the resolution of the preliminary phase diagrams need improvement in terms of more data points but also more starting configurations to ensure that no phase is overlooked. Furthermore, also the role of uniaxial anisotropy is still unclear.

In any case, the preliminary results of this section already hint, that the well-established phases are predominantly stable for misaligned fields. Only more significant tilt angles reveal the differences between the rotation symmetric skyrmions in a perpendicularly polarized background and the asymmetric skyrmions in a canted background.

We find that the asymmetric Néel-type skyrmions do not just pass the asymmetry on to an anisotropic repulsion but instead, the in-plane component of the magnetic field manifests the axis with repulsive interaction whereas the interaction on the perpendicular axis has an oscillating sign. Note that, for Bloch-type skyrmions, the axes are exchanged. Interestingly we could prove that the asymmetric short-range attractive interaction also survives in a thin film with thickness  $d = 2.5\lambda$ .

This observation sounds promising for skyrmionics since the distance between individual skyrmions is often a parameter that should only take discrete values. In setups with tilted fields, these discrete distances are provided by the different minima of the oscillating interaction.

Other proposals require a number of confined channels close to the edge in which the skyrmions move [173], which arises naturally when the external field is canted. We also tried to

replace the energy barrier from the nanostrip in Sec. 7 with a tilted external field that creates attractive edges and thereby divides a racetrack into a two-lane racetrack but the concept fails since the skyrmions are not repulsive.

In any case, the asymmetric interaction can yield interesting new phenomena but unfortunately it is small, therefore it is unclear if the interaction persists at finite temperature in an experiment.

#### Skyrmions in the polarized phase

Our theoretical study in Sec. 6 of the bound magnon modes of the twisted magnetization at the edge of the sample showed interesting features. We found the analytic solution for the magnetization profile of at the edge of a half-infinite system in the micromagnetic model with both magnetic field and uniaxial anisotropy. An expansion in magnon modes around this solution showed that not only the first but also higher order excited modes are bound states of the edge. We further found the instability of the non-reciprocal magnon spectrum which lets magnons condense at the edge until the metastable polarized state is invaded by a chain of merons that enter from the edge, introducing the helical phase.

Finally, upon increasing the magnetic field again, the merons move back towards the edge but instead of leaving, they smoothly pull a second meron into the system and form a chain of skyrmions. This process was already observed in experiments [213]. With a locally confined magnetic field, this process can also be used for the creation of single skyrmion without the need for a singular Bloch point.

The expansion which we used to calculate the excitation of the edge has been applied earlier to a skyrmion in a polarized background which is rotation invariant and therefore again an effectively one-dimensional problem [183]. For less symmetric objects, however, the calculation is more complicated but it would be interesting to find out more about the bound edge modes of other phases, e.g., the a helical phase or skyrmion lattice in a thin film where the magnons bind to the surface twist but get deflected by the periodic modulations of the phases.

In Sec. 7, we introduce the *two-lane racetrack*. This conceptual memory device operates with skyrmions in a racetrack geometry but in contrast to the proposal by Fert *et al.* [140] it aims to exploit the additional degree of (positional) freedom that point-like skyrmions have in contrast to one-dimensional domain walls. The general concept is also described in the appendix, Sec. 15.

The original racetrack is widened such that the skyrmion can slightly shift towards the edges. An energy barrier along then middle of the racetrack separates the track into two close-by lanes. Importantly, the lanes are close enough that skyrmion can not pass by each other. For the memory function, we relate the lane index of a skyrmion to a logical bit value. Here, the height of the central energy barrier and also height of the barrier for exchanging two skyrmions determines the stability of the encoded information.

Note, that this proposal has several advantages over the original proposal, e.g., the distance between skyrmion does not need to be fixed and the close packing of skyrmions makes the whole chain more stable against pinning by defects.

In Sec. 7 we calculate the energy barrier for an additional strip of material on top of a racetrack and show that this geometric solution indeed yields energy barriers suitable for applications. We furthermore show that the calculated potentials and interactions can be used in a Thiele formalism to describe the motion of a skyrmion, even in a setup which is patterned in the third dimension.

---

In the subsequent section, Sec. 8, we have checked if also racetracks with other cross sections than proposed in Sec. 7 can be used for energy barriers. In particular, we have checked that the perturbation of the potential for a smeared-out cross section is surprisingly small. As a side result, we have calculated the confining potentials for the standard racetrack with not sharp edges but a smooth reduction of the height at the edge. For this geometry, our calculation suggest that the edges of the racetrack are only weakly repulsive. In the most extreme case, which assumes a triangular cross section of the racetrack, the edge have completely lost their repulsive character but, instead, become attractive.

The study of magnon-driven skyrmions in Sec. 9 demonstrated that for a small magnonic current, the motion of the skyrmion is still governed by a Thiele description but fails when the internal degrees of freedom of the skyrmion are excited. However, this concept provides an efficient method for moving skyrmions due to the extremely small damping for magnons that be can be achieved in insulator.

The in a sense more classical study in Sec. 13 moves a skyrmion via spin-transfer-torque with an applied electric current. We implement a co-moving Thiele frame of reference to make the study of high-speed moving skyrmions computationally possible.

As part of this implementation it turns out that the deformation due to an applied current is (up to a global rotation) only determined by the reduced parameters  $\alpha$  and  $u$ , where  $\alpha$  is the Gilbert damping and  $u = (\alpha - \beta)|\mathbf{v}_s|$  is the reduced drive as defined in Sec. 13.

With the newly developed method we can calculate a phase diagram for the distortion of a moving skyrmion and find that it exhibits a bimeron instability for drives above the critical drive  $u_{\text{crit}}(\alpha)$ , similar to the instability at low magnetic fields. The critical drive  $u_{\text{crit}}(\alpha)$  is for large damping  $\alpha$  approximately linear in  $\alpha$  is in the interval  $0.1 v_D \lesssim u_{\text{crit}} \lesssim 0.6 v_D$ .

Furthermore, at very high drives  $u > v_D$ , we observe the stabilization of a highly deformed skyrmion solution. This small and asymmetrically elongated skyrmion remains stable within our simulations up to the highest drives  $u_{\text{max}}$ , when the spin-transfer-torque destabilizes all magnetic orders.

We have to stress that the seemingly low speed limit  $0.1 v_D \lesssim u_{\text{crit}} \lesssim 0.6 v_D$  does, however, not mean the end of all ideas about skyrmionics. It is important to notice that the speed limit relates not to the applied current but to the reduced drive which, moreover, depends linearly on the difference  $\alpha - \beta$ . If this difference is kept small, high velocities are possible.

In addition, the skyrmion in this study was chosen particularly large and therefore soft, such already at low drives the deformations become relevant. We do, at present, not know how the critical drive scales with the anisotropy or a magnetic field, nor do we understand the driving mechanism behind the bimeron instability or the stabilization of the shooting star skyrmion at high drives.



Part V.  
Bibliography



- 
- [1] C. Melcher, *A9. Topological solitons in chiral magnetism*, Lecture notes: 48th IFF Spring School *Topological matter - Topological insulators, skyrmions and majoranas*, 2017.
- [2] C. M. Hurd, *Varieties of magnetic order in solids*, Contemporary Physics **23**, 469-493 (1982).
- [3] I. Dzyaloshinsky, *A thermodynamic theory of "weak" ferromagnetism of antiferromagnetics*, Journal of Physics and Chemistry of Solids **4**, 241-255 (1958).
- [4] I. E. Dzyaloshinskii, *Theory of Helicoidal Structures in Antiferromagnets. I. Nonmetals*, Journal of Experimental and Theoretical Physics **19**, 960 (1964).
- [5] I. E. Dzyaloshinskii, *Theory of Helicoidal Structures in Antiferromagnets. II. Metals*, Journal of Experimental and Theoretical Physics **20**, 223 (1965).
- [6] T. Moriya, *Anisotropic Superexchange Interaction and Weak Ferromagnetism*, Physical Review **120**, 91-98 (1960).
- [7] A. Fert and P. M. Levy, *Role of Anisotropic Exchange Interactions in Determining the Properties of Spin-Glasses*, Physical Review Letters **44**, 1538-1541 (1980).
- [8] A. Crépieux and C. Lacroix, *Dzyaloshinskii-Moriya interactions induced by symmetry breaking at a surface*, Journal of Magnetism and Magnetic Materials **182**, 341-349 (1998).
- [9] A. Van Oosterom and J. Strackee, *The Solid Angle of a Plane Triangle*, IEEE Transactions on Biomedical Engineering **30**, 125-126 (1983).
- [10] P. G. de Gennes and J. Prost, *The Physics of Liquid Crystals*, Clarendon, 1993.
- [11] P. Bak and M. H. Jensen, *Theory of helical magnetic structures and phase transitions in MnSi and FeGe.*, Journal of Physics C: Solid State Physics **13**, L881 (1980).
- [12] Y. Ishikawa, K. Tajima, D. Bloch, and M. Roth, *Helical spin structure in manganese silicide MnSi*, Solid State Communications **19**, 525-528 (1976).
- [13] Y. Ishikawa, G. Shirane, J. A. Tarvin, and M. Kohgi, *Magnetic excitations in the weak itinerant ferromagnet MnSi*, Physical Review B **16**, 4956-4970 (1977).
- [14] M. Uchida, Y. Onose, Y. Matsui, and Y. Tokura, *Real-Space Observation of Helical Spin Order*, Science **311**, 359-361 (2006).
- [15] K. von Bergmann, A. Kubetzka, O. Pietzsch, and R. Wiesendanger, *Interface-induced chiral domain walls, spin spirals and skyrmions revealed by spin-polarized scanning tunneling microscopy*, Journal of Physics: Condensed Matter **26**, 394002 (2014).
- [16] I. Kézsmárki, S. Bordács, P. Milde, E. Neuber, L. M. Eng, J. S. White, H. M. Rønnow, C. D. Dewhurst, M. Mochizuki, K. Yanai, H. Nakamura, D. Ehlers, V. Tsurkan, and A. Loidl, *Néel-type skyrmion lattice with confined orientation in the polar magnetic semiconductor GaV<sub>4</sub>S<sub>8</sub>*, Nature Materials **14**, 1116-1122 (2015).
- [17] Y. Togawa, T. Koyama, K. Takayanagi, S. Mori, Y. Kousaka, J. Akimitsu, S. Nishihara, K. Inoue, A. S. Ovchinnikov, and J. Kishine, *Chiral magnetic soliton lattice on a chiral helimagnet*, Physical Review Letters **108**, 107202 (2012).

- [18] K. Tsuruta, M. Mito, Y. Kousaka, J. Akimitsu, J. Kishine, Y. Togawa, and K. Inoue, *Size dependence of discrete change in magnetization in single crystal of chiral magnet Cr<sub>1</sub>/3NbS<sub>2</sub>*, Journal of Applied Physics **120**, 143901 (2016).
- [19] V. Laliena, J. Campo, J.-I. Kishine, A. S. Ovchinnikov, Y. Togawa, Y. Kousaka, and K. Inoue, *Incommensurate-commensurate transitions in the monoaxial chiral helimagnet driven by the magnetic field*, Physical Review B **93**, 134424 (2016).
- [20] V. Laliena, J. Campo, and Y. Kousaka, *Understanding the H-T phase diagram of the monoaxial helimagnet*, Physical Review B **94**, 094439 (2016).
- [21] F. J. T. Goncalves, T. Sogo, Y. Shimamoto, Y. Kousaka, J. Akimitsu, S. Nishihara, K. Inoue, D. Yoshizawa, M. Hagiwara, M. Mito, R. L. Stamps, I. G. Bostrem, V. E. Sinitsyn, A. S. Ovchinnikov, J. Kishine, and Y. Togawa, *Collective resonant dynamics of the chiral spin soliton lattice in a monoaxial chiral magnetic crystal*, Physical Review B **95**, 104415 (2017).
- [22] Y. Ishikawa and M. Arai, *Magnetic Phase Diagram of MnSi near Critical Temperature Studied by Neutron Small Angle Scattering*, Journal of the Physical Society of Japan **53**, 2726-2733 (1984).
- [23] M. L. Plumer and M. B. Walker, *Wavevector and spin reorientation in MnSi*, Journal of Physics C: Solid State Physics **14**, 4689 (1981).
- [24] A. Bauer, A. Chacon, M. Wagner, M. Halder, R. Georgii, A. Rosch, C. Pfleiderer, and M. Garst, *Symmetry breaking, slow relaxation dynamics, and topological defects at the field-induced helix reorientation in MnSi*, Physical Review B **95**, 024429 (2017).
- [25] V. Laliena, J. Campo, and Y. Kousaka, *Nucleation, instability, and discontinuous phase transitions in monoaxial helimagnets with oblique fields*, Physical Review B **95**, 224410 (2017).
- [26] T. H. R. Skyrme, *A non-linear field theory*, Proceedings of the Royal Society A **260**, 127-138 (1961).
- [27] T. H. R. Skyrme, *Particle states of a quantized meson field*, Proceedings of the Royal Society A **262**, 237-245 (1961).
- [28] T. H. R. Skyrme, *A unified field theory of mesons and baryons*, Nuclear Physics **31**, 556-569 (1962).
- [29] G. S. Adkins, C. R. Nappi, and E. Witten, *Static Properties of Nucleons in the Skyrme Model*, Nuclear Physics **B228**, 552 (1983).
- [30] I. Zahed and G.E. Brown, *The Skyrme model*, Physics Reports **142**, 1-102 (1986).
- [31] D. Diakonov, V. Petrov, and M. Polyakov, *Exotic anti-decuplet of baryons: prediction from chiral solitons*, Zeitschrift für Physik A Hadrons and Nuclei **359**, 305-314 (1997).
- [32] E. Chabanat, P. Bonche, P. Haensel, J. Meyer, and R. Schaeffer, *A Skyrme parametrization from subnuclear to neutron star densities*, Nuclear Physics A **627**, 710-746 (1997).

- 
- [33] E. Chabanat, P. Bonche, P. Haensel, J. Meyer, and R. Schaeffer, *A Skyrme parametrization from subnuclear to neutron star densities (Part II. Nuclei far from stabilities)*, Nuclear Physics A **635**, 231-256 (1998).
- [34] S. L. Sondhi, A. Karlhede, S. A. Kivelson, and E. H. Rezayi, *Skyrmions and the crossover from the integer to fractional quantum Hall effect at small Zeeman energies*, Physical Review B **47**, 16419-16426 (1993).
- [35] A. Schmeller, J. P. Eisenstein, L. N. Pfeiffer, and K. W. West, *Evidence for Skyrmions and Single Spin Flips in the Integer Quantized Hall Effect*, Physical Review Letters **75**, 4290-4293 (1995).
- [36] K. Yang, S. Das Sarma, and A. H. MacDonald, *Collective modes and skyrmion excitations in graphene  $SU(4)$  quantum Hall ferromagnets*, Physical Review B **74**, 075423 (2006).
- [37] T.-L. Ho, *Spinor Bose Condensates in Optical Traps*, Physical Review Letters **81**, 742-745 (1998).
- [38] U. Al Khawaja and H. Stoof, *Skyrmions in a ferromagnetic Bose-Einstein condensate*, Nature **411**, 918-920 (2001).
- [39] L. S. Leslie, A. Hansen, K. C. Wright, B. M. Deutsch, and N. P. Bigelow, *Creation and Detection of Skyrmions in a Bose-Einstein Condensate*, Physical Review Letters **103**, 250401 (2009).
- [40] J.-I. Fukuda and S. Žumer, *Quasi-two-dimensional Skyrmion lattices in a chiral nematic liquid crystal*, Nature Communications **2**, 246 (2011).
- [41] J. M. Kosterlitz and D. J. Thouless, *Long range order and metastability in two dimensional solids and superfluids. (Application of dislocation theory)*, Journal of Physics C: Solid State Physics **5**, L124-L126 (1972).
- [42] J. M. Kosterlitz and D. J. Thouless, *Ordering, metastability and phase transitions in two-dimensional systems*, Journal of Physics C: Solid State Physics **6**, 1181-1203 (1973).
- [43] J. M. Kosterlitz, *The critical properties of the two-dimensional  $xy$  model*, Journal of Physics C: Solid State Physics **7**, 1046 (1974).
- [44] A. Fernández-Pacheco, R. Streubel, O. Fruchart, R. Hertel, P. Fischer, and R. P. Cowburn, *Three-dimensional nanomagnetism*, Nature Communications **8**, 15756 (2017).
- [45] N. Nagaosa and Y. Tokura, *Topological properties and dynamics of magnetic skyrmions*, Nature Nanotechnology **8**, 899-911 (2013).
- [46] M. Ezawa, *Compact merons and skyrmions in thin chiral magnetic films*, Physical Review B **83**, 100408 (2011).
- [47] A. N. Bogdanov and D. A. Yablonskii, *Thermodynamically stable "vortices" in magnetically ordered crystals. The mixed state of magnets*, Journal of Experimental and Theoretical Physics **68**, 101 (1989).

- [48] A. N. Bogdanov and A. Hubert, *Thermodynamically stable magnetic vortex states in magnetic crystals*, Journal of Magnetism and Magnetic Materials **138**, 255-269 (1994).
- [49] A. Bogdanov, *New localized solutions of the nonlinear field equations*, JEPT Letters **62**, 247 (1995).
- [50] A. N. Bogdanov and A. Hubert, *The stability of vortex-like structures in uniaxial ferromagnets*, Journal of Magnetism and Magnetic Materials **195**, 182-192 (1999).
- [51] A. N. Bogdanov and U. K. Röföler, *Chiral symmetry breaking in magnetic thin films and multilayers*, Physical Review Letters **87**, 037203 (2001).
- [52] U. K. Röföler, A. N. Bogdanov, and C. Pfeleiderer, *Spontaneous skyrmion ground states in magnetic metals*, Nature **442**, 797-801 (2006).
- [53] S. Mühlbauer, B. Binz, F. Jonietz, C. Pfeleiderer, A. Rosch, A. Neubauer, R. Georgii, and P. Böni, *Skyrmion lattice in a chiral magnet*, Science **323**, 915-919 (2009).
- [54] P. Milde, D. Köhler, J. Seidel, L. M. Eng, A. Bauer, A. Chacon, J. Kindervater, S. Mühlbauer, C. Pfeleiderer, S. Buhbrandt, C. Schütte, and A. Rosch, *Unwinding of a skyrmion lattice by magnetic monopoles*, Science **340**, 1076 (2013).
- [55] A. Neubauer, C. Pfeleiderer, B. Binz, A. Rosch, R. Ritz, P. G. Niklowitz, and P. Böni, *Topological Hall effect in the A phase of MnSi*, Physical Review Letters **102**, 186602 (2009).
- [56] T. Adams, S. Mühlbauer, C. Pfeleiderer, F. Jonietz, A. Bauer, A. Neubauer, R. Georgii, P. Böni, U. Keiderling, K. Everschor, M. Garst, and A. Rosch, *Long-Range Crystalline Nature of the Skyrmion Lattice in MnSi*, Physical Review Letters **107**, 217206 (2011).
- [57] J. Kindervater, S. Mühlbauer, T. Adams, A. Bauer, U. Keiderling, and C. Pfeleiderer, *Kinetic small angle neutron scattering of the skyrmion lattice in MnSi*, New Journal of Physics **18**, 075017 (2016).
- [58] Minhyea Lee, W. Kang, Y. Onose, Y. Tokura, and N. P. Ong, *Unusual Hall Effect Anomaly in MnSi under Pressure*, Physical Review Letters **102**, 186601 (2009).
- [59] R. Ritz, M. Halder, C. Franz, A. Bauer, M. Wagner, R. Bamler, A. Rosch, and C. Pfeleiderer, *Giant generic topological Hall resistivity of MnSi under pressure*, Physical Review B **87**, 134424 (2013).
- [60] A. Chacon, A. Bauer, T. Adams, F. Rucker, G. Brandl, R. Georgii, M. Garst, and C. Pfeleiderer, *Uniaxial pressure dependence of magnetic order in MnSi*, Physical Review Letters **115**, 267202 (2015).
- [61] Y. Nii, T. Nakajima, A. Kikkawa, Y. Yamasaki, K. Ohishi, J. Suzuki, Y. Taguchi, T. Arima, Y. Tokura, and Y. Iwasa, *Uniaxial stress control of skyrmion phase*, Nature Communications **6**, 8539 (2015).
- [62] A. Tonomura, X. Z. Yu, K. Yanagisawa, T. Matsuda, Y. Onose, N. Kanazawa, H. S. Park, and Y. Tokura, *Real-space observation of skyrmion lattice in helimagnet MnSi thin samples*, Nano Letters **12**, 1673 (2012).

- 
- [63] X. Yu, A. Kikkawa, D. Morikawa, K. Shibata, Y. Tokunaga, Y. Taguchi, and Y. Tokura, *Variation of skyrmion forms and their stability in MnSi thin plates*, Physical Review B **91**, 054411 (2015).
- [64] T. Adams, S. Mühlbauer, A. Neubauer, W. Münzer, F. Jonietz, R. Georgii, B. Pedersen, P. Böni, A. Rosch, and C. Pfleiderer, *Skyrmion lattice domains in  $Fe_{1-x}Co_xSi$* , Journal of Physics: Conference Series **200**, 032001 (2010).
- [65] W. Münzer, A. Neubauer, T. Adams, S. Mühlbauer, C. Franz, F. Jonietz, R. Georgii, P. Böni, B. Pedersen, M. Schmidt, A. Rosch, and C. Pfleiderer, *Skyrmion lattice in the doped semiconductor  $Fe_{1-x}Co_xSi$* , Physical Review B **81**, 041203 (2010).
- [66] X. Z. Yu, Y. Onose, N. Kanazawa, J. H. Park, J. H. Han, Y. Matsui, N. Nagaosa, and Y. Tokura, *Real-space observation of a two-dimensional skyrmion crystal*, Nature **465**, 901-904 (2010).
- [67] S. X. Huang and C. L. Chien, *Extended skyrmion phase in epitaxial FeGe(111) thin films*, Physical Review Letters **108**, 267201 (2012).
- [68] X. Z. Yu, N. Kanazawa, Y. Onose, K. Kimoto, W. Z. Zhang, S. Ishiwata, Y. Matsui, and Y. Tokura, *Near room-temperature formation of a skyrmion crystal in thin-films of the helimagnet FeGe*, Nature Materials **10**, 106-109 (2011).
- [69] D. McGrouther, R. J. Lamb, M. Krajenak, S. McFadzean, S. McVitie, R. L. Stamps, A. O. Leonov, A. N. Bogdanov, and Y. Togawa, *Internal structure of hexagonal skyrmion lattices in cubic helimagnets*, New Journal of Physics **18**, 095004 (2016).
- [70] T. Adams, A. Chacon, M. Wagner, A. Bauer, G. Brandl, B. Pedersen, H. Berger, P. Lemmens, and C. Pfleiderer, *Long-wavelength helimagnetic order and skyrmion lattice phase in  $Cu_2OSeO_3$* , Physical Review Letters **108**, 237204 (2012).
- [71] S. Seki, X. Z. Yu, S. Ishiwata, and Y. Tokura, *Observation of skyrmions in a multiferroic material*, Science **336**, 198-201 (2012).
- [72] Y. Okamura, F. Kagawa, S. Seki, and Y. Tokura, *Transition to and from the skyrmion lattice phase by electric fields in a magnetoelectric compound*, Nature Communications **7**, 12669 (2016).
- [73] S. L. Zhang, A. Bauer, H. Berger, C. Pfleiderer, G. van der Laan, and T. Hesjedal, *Resonant elastic x-ray scattering from the skyrmion lattice in  $Cu_2OSeO_3$* , Physical Review B **93**, 214420 (2016).
- [74] S. L. Zhang, A. Bauer, H. Berger, C. Pfleiderer, G. van der Laan, and T. Hesjedal, *Imaging and manipulation of skyrmion lattice domains in  $Cu_2OSeO_3$* , Applied Physics Letters **109**, 192406 (2016).
- [75] S. L. Zhang, A. Bauer, D. M. Burn, P. Milde, E. Neuber, L. M. Eng, H. Berger, C. Pfleiderer, G. van der Laan, and T. Hesjedal, *Multidomain skyrmion lattice state in  $Cu_2OSeO_3$* , Nano Letters **16**, 3285-3291 (2016).

- [76] J. Rajeswari, P. Huang, G. F. Mancini, Y. Murooka, T. Latychevskaia, D. McGrouther, M. Cantoni, E. Baldini, J. S. White, A. Magrez, T. Giamarchi, H. M. Rønnow, and F. Carbone, *Filming the formation and fluctuation of skyrmion domains by cryo-Lorentz transmission electron microscopy*, Proceedings of the National Academy of Science U.S.A. **112**, 14212-14217 (2015).
- [77] K. Karube, J. S. White, N. Reynolds, J. L. Gavilano, H. Oike, A. Kikkawa, F. Kagawa, Y. Tokunaga, H. M. Rønnow, Y. Tokura, and Y. Taguchi, *Robust metastable skyrmions and their triangular-square lattice structural transition in a high-temperature chiral magnet*, Nature Materials **15**, 1237-1242 (2016).
- [78] Y. Tokunaga, X. Z. Yu, J. S. White, H. M. Rønnow, D. Morikawa, Y. Taguchi, and Y. Tokura, *A new class of chiral materials hosting magnetic skyrmions beyond room temperature*, Nature Communications **6**, 7638 (2015).
- [79] S. Heinze, K. von Bergmann, M. Menzel, J. Brede, A. Kubetzka, R. Wiesendanger, G. Bihlmayer, and S. Blügel, *Spontaneous atomic-scale magnetic skyrmion lattice in two dimensions*, Nature Physics **7**, 713-718 (2011).
- [80] R. Wiesendanger, *Nanoscale magnetic skyrmions in metallic films and multilayers: a new twist for spintronics*, Nature Reviews Materials **1**, 16044 (2016).
- [81] N. Romming, C. Hanneken, M. Menzel, J. E. Bickel, B. Wolter, K. von Bergmann, A. Kubetzka, and R. Wiesendanger, *Writing and deleting single magnetic skyrmions*, Science **341**, 636-639 (2013).
- [82] N. Romming, A. Kubetzka, C. Hanneken, K. von Bergmann, and R. Wiesendanger, *Field-dependent size and shape of single magnetic skyrmions*, Physical Review Letters **114**, 177203 (2015).
- [83] L. Schmidt, J. Hagemeister, P.-J. Hsu, A. Kubetzka, K. von Bergmann, and R. Wiesendanger, *Symmetry breaking in spin spirals and skyrmions by in-plane and canted magnetic fields*, New Journal of Physics **18**, 075007 (2016).
- [84] C. Hanneken, A. Kubetzka, K. von Bergmann, and R. Wiesendanger, *Pinning and movement of individual nanoscale magnetic skyrmions via defects*, New Journal of Physics **18**, 055009 (2016).
- [85] C. Moreau-Luchaire, C. MoutaïñAs, N. Reyren, J. Sampaio, C. A. F. Vaz, N. Van Horne, K. Bouzehouane, K. Garcia, C. Deranlot, P. Warnicke, P. Wohlhüter, J.-M. George, M. Weigand, J. Raabe, V. Cros, and A. Fert, *Additive interfacial chiral interaction in multilayers for stabilization of small individual skyrmions at room temperature*, Nature Nanotechnology **11**, 444-448 (2016).
- [86] S. Woo, K. Litzius, B. Krüger, M.-Y. Im, L. Caretta, K. Richter, M. Mann, A. Krone, R. M. Reeve, M. Weigand, P. Agrawal, I. Lemesch, M.-A. Mawass, P. Fischer, M. Kläui, and G. S. D. Beach, *Observation of room-temperature magnetic skyrmions and their current-driven dynamics in ultrathin metallic ferromagnets*, Nature Materials **15**, 501-506 (2016).
- [87] S. Seki, S. Ishiwata, and Y. Tokura, *Magnetoelectric nature of skyrmions in a chiral magnetic insulator  $\text{Cu}_2\text{OSeO}_3$* , Physical Review B **86**, 060403 (2012).

- 
- [88] J. S. White, I. Levatić, A. A. Omrani, N. Egetenmeyer, K. Prša, I. Živković, J. L. Gavilano, J. Kohlbrecher, M. Bartkowiak, H. Berger, and H. M. Rønnow, *Electric field control of the skyrmion lattice in  $\text{Cu}_2\text{OSeO}_3$* , Journal of Physics: Condensed Matter **24**, 432201 (2012).
- [89] P. Milde, E. Neuber, A. Bauer, C. Pfleiderer, H. Berger, and L. M. Eng, *Heuristic description of magnetoelectricity of  $\text{Cu}_2\text{OSeO}_3$* , Nano Letters **16**, 5612-5618 (2016).
- [90] Y. Onose, Y. Okamura, S. Seki, S. Ishiwata, and Y. Tokura, *Observation of Magnetic Excitations of Skyrmion Crystal in a Helimagnetic Insulator  $\text{Cu}_2\text{OSeO}_3$* , Physical Review Letters **109**, 037603 (2012).
- [91] M. Mochizuki, *Spin-wave modes and their intense excitation effects in skyrmion crystals*, Physical Review Letters **108**, 017601 (2012).
- [92] T. Schwarze, J. Waizner, M. Garst, A. Bauer, I. Stasinopoulos, H. Berger, C. Pfleiderer, and D. Grundler, *Universal helimagnon and skyrmion excitations in metallic, semiconducting and insulating chiral magnets*, Nature Materials **14**, 478-483 (2015).
- [93] M. Kugler, G. Brandl, J. Waizner, M. Janoschek, R. Georgii, A. Bauer, K. Seemann, A. Rosch, C. Pfleiderer, P. Böni, and M. Garst, *Band structure of helimagnons in  $\text{MnSi}$  resolved by inelastic neutron scattering*, Physical Review Letters **115**, 097203 (2015).
- [94] Y. Nii, A. Kikkawa, Y. Taguchi, Y. Tokura, and Y. Iwasa, *Elastic Stiffness of a Skyrmion Crystal*, Physical Review Letters **113**, 267203 (2014).
- [95] A. J. Kruchkov and H. M. Rønnow, *Skyrmion Lattices in Electric Fields*, Arxiv e-print (2017), arXiv:1702.08863.
- [96] S. Buhrandt and L. Fritz, *Skyrmion lattice phase in three-dimensional chiral magnets from Monte Carlo simulations*, Physical Review B **88**, 195137 (2013).
- [97] N. Nagaosa, X. Z. Yu, and Y. Tokura, *Gauge fields in real and momentum spaces in magnets: monopoles and skyrmions*, Philosophical Transactions of the Royal Society A **370**, 5806 (2012).
- [98] C. Schütte and A. Rosch, *Dynamics and energetics of emergent magnetic monopoles in chiral magnets*, Physical Review B **90**, 174432 (2014).
- [99] C. Schütte, *Skyrmions and monopoles in chiral magnets and correlated heterostructures*, PhD thesis, University of Cologne, Cologne (2014).
- [100] H. Oike, A. Kikkawa, N. Kanazawa, Y. Taguchi, M. Kawasaki, Y. Tokura, and F. Kagawa, *Interplay between topological and thermodynamic stability in a metastable magnetic skyrmion lattice*, Nature Physics **12**, 62 (2016).
- [101] S. D. Yi, S. Onoda, N. Nagaosa, and J. H. Han, *Skyrmions and anomalous Hall effect in a Dzyaloshinskii-Moriya spiral magnet*, Physical Review B **80**, 054416 (2009).
- [102] J. H. Han, J. Zang, Z. Yang, J.-H. Park, and N. Nagaosa, *Skyrmion lattice in a two-dimensional chiral magnet*, Physical Review B **82**, 094429 (2010).

- [103] A. B. Butenko, A. A. Leonov, U. K. Röfller, and A. N. Bogdanov, *Stabilization of skyrmion textures by uniaxial distortions in noncentrosymmetric cubic helimagnets*, Physical Review B **82**, 052403 (2010).
- [104] M. N. Wilson, A. B. Butenko, A. N. Bogdanov, and T. L. Monchesky, *Chiral skyrmions in cubic helimagnet films: The role of uniaxial anisotropy*, Physical Review B **89**, 094411 (2014).
- [105] S. Banerjee, J. Rowland, O. Erten, and M. Randeria, *Enhanced stability of skyrmions in two-dimensional chiral magnets with Rashba spin-orbit coupling*, Physical Review X **4**, 031045 (2014).
- [106] S.-Z. Lin, A. Saxena, and C. D. Batista, *Skyrmion fractionalization and merons in chiral magnets with easy-plane anisotropy*, Physical Review B **91**, 224407 (2015).
- [107] M. Vousden, M. Albert, M. Beg, M.-A. Bisotti, R. Carey, D. Chernyshenko, D. Cortés-Ortuño, W. Wang, O. Hovorka, C. H. Marrows, and H. Fangohr, *Skyrmions in thin films with easy-plane magnetocrystalline anisotropy*, Applied Physics Letters **108**, 132406 (2016).
- [108] U. Güngördü, R. Nepal, O. A. Tretiakov, K. Belashchenko, and A. A. Kovalev, *Stability of skyrmion lattices and symmetries of quasi-two-dimensional chiral magnets*, Physical Review B **93**, 064428 (2016).
- [109] F. N. Rybakov, A. B. Borisov, and A. N. Bogdanov, *Three-dimensional skyrmion states in thin films of cubic helimagnets*, Physical Review B **87**, 094424 (2013).
- [110] F. N. Rybakov, A. B. Borisov, S. Blügel, and N. S. Kiselev, *New type of stable particlelike states in chiral magnets*, Physical Review Letters **115**, 117201 (2015).
- [111] F. N. Rybakov, A. B. Borisov, S. Blügel, and N. S. Kiselev, *New spiral state and skyrmion lattice in 3D model of chiral magnets*, New Journal of Physics **18**, 045002 (2016).
- [112] A. O. Leonov, Y. Togawa, T. L. Monchesky, A. N. Bogdanov, J. Kishine, Y. Kousaka, M. Miyagawa, T. Koyama, J. Akimitsu, Ts. Koyama, K. Harada, S. Mori, D. McGrouther, R. Lamb, M. Krajenak, S. McVitie, R. L. Stamps, and K. Inoue, *Chiral surface twists and skyrmion stability in nanolayers of cubic helimagnets*, Physical Review Letters **117**, 087202 (2016).
- [113] K. Shibata, J. Iwasaki, N. Kanazawa, S. Aizawa, T. Tanigaki, M. Shirai, T. Nakajima, M. Kubota, M. Kawasaki, H. S. Park, D. Shindo, N. Nagaosa, and Y. Tokura, *Large anisotropic deformation of skyrmions in strained crystal*, Nature Nanotechnology **10**, 589-592 (2015).
- [114] P.-J. Hsu, A. Kubetzka, A. Finco, N. Romming, K. von Bergmann, and R. Wiesendanger, *Electric-field-driven switching of individual magnetic skyrmions*, Nature Nanotechnology **12**, 123-126 (2017).
- [115] A. O. Leonov, T. L. Monchesky, N. Romming, A. Kubetzka, A. N. Bogdanov, and R. Wiesendanger, *The properties of isolated chiral skyrmions in thin magnetic films*, New Journal of Physics **18**, 065003 (2016).

- 
- [116] B. Dupe, M. Hoffmann, C. Paillard, and S. Heinze, *Tailoring magnetic skyrmions in ultra-thin transition metal films*, Nature Communications **5**, 4030 (2014).
- [117] H. Yang, O. Boulle, V. Cros, A. Fert, and M. Chshiev, *Controlling Dzyaloshinskii-Moriya interaction via chirality dependent layer stacking, insulator capping and electric field*, Arxiv e-print (2016), arXiv:1603.01847..
- [118] G. Chen, A. Mascaraque, A. T. N'Diaye, and A. K. Schmid, *Room temperature skyrmion ground state stabilized through interlayer exchange coupling*, Applied Physics Letters **106**, 242404 (2015).
- [119] O. Boulle, J. Vogel, H. Yang, S. Pizzini, D. de Souza Chaves, A. Locatelli, T. O. Mendes, A. Sala, L. D. Buda-Prejbeanu, O. Klein, M. Belmeguenai, Y. Roussigné, A. Stashkevich, S. M. Chérif, L. Aballe, M. Foerster, M. Chshiev, S. Auffret, I. M. Miron, and G. Gaudin, *Room-temperature chiral magnetic skyrmions in ultrathin magnetic nanostructures*, Nature Nanotechnology **11**, 449-454 (2016).
- [120] A. O. Leonov and M. Mostovoy, *Multiply periodic states and isolated skyrmions in an anisotropic frustrated magnet*, Nature Communications **6**, 8275 (2015).
- [121] L. Rózsa, A. Deák, E. Simon, R. Yanes, L. Udvardi, L. Szunyogh, and U. Nowak, *Skyrmions with attractive interactions in an ultrathin magnetic film*, Physical Review Letters **117**, 157205 (2016).
- [122] S.-Z. Lin and S. Hayami, *Ginzburg-Landau theory for skyrmions in inversion-symmetric magnets with competing interactions*, Physical Review B **93**, 064430 (2016).
- [123] X. Zhang, J. Xia, Y. Zhou, X. Liu, H. Zhang, and M. Ezawa, *Skyrmion dynamics in a frustrated ferromagnetic film and current-induced helicity locking-unlocking transition*, Nature Communications **8**, 1717 (2017).
- [124] T. Okubo, S. Chung, and H. Kawamura, *Multiple- $q$  States and the Skyrmion Lattice of the Triangular-Lattice Heisenberg Antiferromagnet under Magnetic Fields*, Physical Review Letters **108**, 017206 (2012).
- [125] H. Velkov, O. Gomonay, M. Beens, G. Schwiete, A. Brataas, J. Sinova, and R. A. Duine, *Phenomenology of current-induced skyrmion motion in antiferromagnets*, New Journal of Physics **18**, 075016 (2016).
- [126] Yufan Li, N. Kanazawa, X. Z. Yu, A. Tsukazaki, M. Kawasaki, M. Ichikawa, X. F. Jin, F. Kagawa, and Y. Tokura, *Robust Formation of Skyrmions and Topological Hall Effect Anomaly in Epitaxial Thin Films of MnSi*, Physical Review Letters **110**, 117202 (2013).
- [127] T. L. Monchesky, J. C. Loudon, M. D. Robertson, and A. N. Bogdanov, *Comment on “Robust formation of skyrmions and topological Hall effect anomaly in epitaxial thin films of MnSi”*, Physical Review Letters **112**, 059701 (2014).
- [128] Y. Li, N. Kanazawa, X. Z. Yu, F. Kagawa, and Y. Tokura, *Reply to comment on “Robust formation of skyrmions and topological Hall effect anomaly in epitaxial thin films of MnSi”*, Physical Review Letters **112**, 059702 (2014).

- [129] F. Jonietz, S. Mühlbauer, C. Pfleiderer, A. Neubauer, W. Münzer, A. Bauer, T. Adams, R. Georgii, P. Böni, R. A. Duine, K. Everschor, M. Garst, and A. Rosch, *Spin Transfer Torques in MnSi at Ultralow Current Densities*, Science **330**, 1648-1651 (2010).
- [130] K. Everschor, M. Garst, R. A. Duine, and A. Rosch, *Current-induced rotational torques in the skyrmion lattice phase of chiral magnets*, Physical Review B **84**, 064401 (2011).
- [131] K. Everschor, M. Garst, B. Binz, F. Jonietz, S. Mühlbauer, C. Pfleiderer, and A. Rosch, *Rotating skyrmion lattices by spin torques and field or temperature gradients*, Physical Review B **86**, 054432 (2012).
- [132] T. Schulz, R. Ritz, A. Bauer, M. Halder, M. Wagner, C. Franz, C. Pfleiderer, K. Everschor, M. Garst, and A. Rosch, *Emergent electrodynamics of skyrmions in a chiral magnet*, Nature Physics **8**, 301-304 (2012).
- [133] N. Nagaosa and Y. Tokura, *Emergent electromagnetism in solids*, Physica Scripta **T146**, 014020 (2012).
- [134] X. Z. Yu, N. Kanazawa, W. Z. Zhang, T. Nagai, T. Hara, K. Kimoto, Y. Matsui, Y. Onose, and Y. Tokura, *Skyrmion flow near room temperature in an ultralow current density*, Nature Communications **3**, 988 (2012).
- [135] J. Zang, M. Mostovoy, J. H.n Han, and N. Nagaosa, *Dynamics of Skyrmion Crystals in Metallic Thin Films*, Physical Review Letters **107**, 136804 (2011).
- [136] C. Chappert, A. Fert, and F. N. Van Dau, *The emergence of spin electronics in data storage*, Nature Materials **6**, 813-823 (2007).
- [137] N. S. Kiselev, A. N. Bogdanov, R. Schäfer, and U. K. Röföler, *Chiral skyrmions in thin magnetic films: new objects for magnetic storage technologies?*, Journal of Physics D: Applied Physics **44**, 392001 (2011).
- [138] S. S. P. Parkin, *U.S. Patents 6,834,005, 6,898,132, 6,920,062, 7,031,178, and 7,236,386 (2004-2007)*,
- [139] S. S. P. Parkin, M. Hayashi, and L. Thomas, *Magnetic domain-wall racetrack memory*, Science **320**, 190-194 (2008).
- [140] A. Fert, V. Cros, and J. Sampaio, *Skyrmions on the track*, Nature Nanotechnology **8**, 152-156 (2013).
- [141] S.-Z. Lin, C. Reichhardt, C. D. Batista, and A. Saxena, *Particle model for skyrmions in metallic chiral magnets: Dynamics, pinning, and creep*, Physical Review B **87**, 214419 (2013).
- [142] S.-Z. Lin, C. Reichhardt, C. D. Batista, and A. Saxena, *Driven skyrmions and dynamical transitions in chiral magnets*, Physical Review Letters **110**, 207202 (2013).
- [143] S.-Z. Lin, C. Reichhardt, C. D. Batista and A. Saxena, *Dynamics of skyrmions in chiral magnets: Dynamic phase transitions and equation of motion*, Journal of Applied Physics **115**, 17D109 (2014).

- 
- [144] C. Reichhardt and C. J. Olson Reichhardt, *Shapiro steps for skyrmion motion on a washboard potential with longitudinal and transverse ac drives*, Physical Review B **92**, 224432 (2015).
- [145] C. Reichhardt and C. J. Olson Reichhardt, *Noise fluctuations and drive dependence of the skyrmion Hall effect in disordered systems*, New Journal of Physics **18**, 095005 (2016).
- [146] J. Sampaio, V. Cros, S. Rohart, A. Thiaville, and A. Fert, *Nucleation, stability and current-induced motion of isolated magnetic skyrmions in nanostructures*, Nature Nanotechnology **8**, 839-844 (2013).
- [147] J. Iwasaki, M. Mochizuki, and N. Nagaosa, *Universal current-velocity relation of skyrmion motion in chiral magnets*, Nature Communications **4**, 1463 (2013).
- [148] J. Iwasaki, M. Mochizuki, and N. Nagaosa, *Current-induced skyrmion dynamics in constricted geometries*, Nature Nanotechnology **8**, 742-747 (2013).
- [149] Y.-H. Liu and Y.-Q. Li, *A mechanism to pin skyrmions in chiral magnets*, Journal of Physics: Condensed Matter **25**, 076005 (2013).
- [150] J. Müller and A. Rosch, *Capturing of a magnetic skyrmion with a hole*, Physical Review B **91**, 054410 (2015).
- [151] E. Barati, M. Cinal, D. M. Edwards, and A. Umerski, *Gilbert damping in magnetic layered systems*, Physical Review B **90**, 014420 (2014).
- [152] I. Stasinopoulos, S. Weichselbaumer, A. Bauer, J. Waizner, H. Berger, S. Maendl, M. Garst, C. Pfleiderer, and D. Grundler, *Low spin wave damping in the insulating chiral magnet  $Cu_2OSeO_3$* , Applied Physics Letters **111**, 032408 (2017).
- [153] R. Tomasello, E. Martinez, R. Zivieri, L. Torres, M. Carpentieri, and G. Finocchio, *A strategy for the design of skyrmion racetrack memories*, Scientific Reports **4**, 6784 EP (2014).
- [154] W. Koshibae, Y. Kaneko, J. Iwasaki, M. Kawasaki, Y. Tokura, and N. Nagaosa, *Memory functions of magnetic skyrmions*, Japanese Journal of Applied Physics **54**, 053001 (2015).
- [155] S. Rohart and A. Thiaville, *Skyrmion confinement in ultrathin film nanostructures in the presence of Dzyaloshinskii-Moriya interaction*, Physical Review B **88**, 184422 (2013).
- [156] M. Beg, M. Vousden, M.-A. Bisotti, M. Albert, D. Chernyshenko, O. Hovorka, R. L. Stamps, R. Carey, W. Wang, D. Cortés-Ortuño, and H. Fangohr, *Ground state search, hysteretic behaviour, and reversal mechanism of skyrmionic textures in confined helimagnetic nanostructures*, Scientific Reports **5**, 17137 (2015).
- [157] R. Keesman, A. O. Leonov, P. van Dieten, S. Buhrandt, G. T. Barkema, L. Fritz, and R. A. Duine, *Degeneracies and fluctuations of Néel skyrmions in confined geometries*, Physical Review B **92**, 134405 (2015).
- [158] W. Koshibae and N. Nagaosa, *Creation of skyrmions and antiskyrmions by local heating*, Nature Communications **5**, 5148 (2014).

- [159] K. Everschor-Sitte, M. Sitte, T. Valet, A. Abanov, and J. Sinova, *Skyrmion production on demand by homogeneous DC currents*, New Journal of Physics **19**, 092001 (2017).
- [160] M. Finazzi, M. Savoini, A. R. Khorsand, A. Tsukamoto, A. Itoh, L. Duò, A. Kirilyuk, Th. Rasing, and M. Ezawa, *Laser-induced magnetic nanostructures with tunable topological properties*, Physical Review Letters **110**, 177205 (2013).
- [161] M. Mochizuki and Y. Watanabe, *Writing a skyrmion on multiferroic materials*, Applied Physics Letters **107**, 0824091 (2015).
- [162] J. Hagemeyer, N. Romming, K. von Bergmann, E. Y. Vedmedenko, and R. Wiesendanger, *Stability of single skyrmionic bits*, Nature Communications **6**, 8455 (2015).
- [163] P. F. Bessarab, V. M. Uzdin, and H. Jónsson, *Method for finding mechanism and activation energy of magnetic transitions, applied to skyrmion and antivortex annihilation*, Computational Physics Communications **196**, 335-347 (2015).
- [164] P. F. Bessarab, G. P. Müller, I. S. Lobanov, F. N. Rybakov, N. S. Kiselev, H. Jónsson, V. M. Uzdin, S. Blügel, L. Bergqvist, and A. Delin, *Lifetime of racetrack skyrmions*, Scientific Reports **8**, 3433 (2018).
- [165] S. von Malottki, B. Dupé, P. F. Bessarab, A. Delin, and S. Heinze, *Enhanced skyrmion stability due to exchange frustration*, Scientific Reports **7**, 12299 (2017).
- [166] N. Kanazawa, M. Kubota, A. Tsukazaki, Y. Kozuka, K. S. Takahashi, M. Kawasaki, M. Ichikawa, F. Kagawa, and Y. Tokura, *Discretized topological Hall effect emerging from skyrmions in constricted geometry*, Physical Review B **91**, 041122(R) (2015).
- [167] K. Hamamoto, M. Ezawa, and N. Nagaosa, *Purely electrical detection of a skyrmion in constricted geometry*, Applied Physics Letters **108**, 112401 (2016).
- [168] C. Hanneken, F. Otte, A. Kubetzka, B. Dupé, N. Romming, K. von Bergmann, R. Wiesendanger, and S. Heinze, *Electrical detection of magnetic skyrmions by tunnelling non-collinear magnetoresistance*, Nature Nanotechnology **10**, 1039-1042 (2015).
- [169] X. Zhang, G. P. Zhao, H. Fangohr, J. P. Liu, W. X. Xia, J. Xia, and F. J. Morvan, *Skyrmion-skyrmion and skyrmion-edge repulsions in skyrmion-based racetrack memory*, Scientific Reports **5**, 7643 (2015).
- [170] A. O. Leonov and I. Kézsmárki, *Asymmetric isolated skyrmions in polar magnets with easy-plane anisotropy*, Physical Review B **96**, 014423 (2017).
- [171] A. O. Leonov and I. Kézsmárki, *Skyrmion robustness in noncentrosymmetric magnets with axial symmetry: The role of anisotropy and tilted magnetic fields*, Physical Review B **96**, 214413 (2017).
- [172] A. O. Leonov, T. L. Monchesky, J. C. Loudon, and A. N. Bogdanov, *Three-dimensional chiral skyrmions with attractive interparticle interactions*, Journal of Physics: Condensed Matter **28**, 35LT01 (2016).
- [173] A. O. Leonov, J. C. Loudon, and A. N. Bogdanov, *Spintronics via non-axisymmetric chiral skyrmions*, Applied Physics Letters **109**, 172404 (2016).

- 
- [174] I. Purnama, W. L. Gan, D. W. Wong, and W. S. Lew, *Guided current-induced skyrmion motion in 1D potential well*, Scientific Reports **5**, 10620 (2015).
- [175] C. Schütte, J. Iwasaki, A. Rosch, and N. Nagaosa, *Inertia, diffusion, and dynamics of a driven skyrmion*, Physical Review B **90**, 174434 (2014).
- [176] K. Everschor-Sitte and M. Sitte, *Real-space Berry phases: skyrmion soccer*, Journal of Applied Physics **115**, 172602 (2014).
- [177] I. Makhfudz, B. Krüger, and O. Tchernyshyov, *Inertia and Chiral Edge Modes of a Skyrmion Magnetic Bubble*, Physical Review Letters **109**, 217201 (2012).
- [178] F. Büttner, C. Moutafis, M. Schneider, B. Krüger, C. M. Gunther, J. Geilhufe, C. v. Korff Schmising, J. Mohanty, B. Pfau, S. Schaffert, A. Bisig, M. Foerster, T. Schulz, C. A. F. Vaz, J. H. Franken, H. J. M. Swagten, M. Kläui, and S. Eisebitt, *Dynamics and inertia of skyrmionic spin structures*, Nature Physics **11**, 225-228 (2015).
- [179] L. Kong and J. Zang, *Dynamics of an insulating skyrmion under a temperature gradient*, Physical Review Letters **111**, 067203 (2013).
- [180] M. Mochizuki, X. Z. Yu, S. Seki, N. Kanazawa, W. Koshibae, J. Zang, M. Mostovoy, Y. Tokura, and N. Nagaosa, *Thermally driven ratchet motion of a skyrmion microcrystal and topological magnon Hall effect*, Nature Materials **13**, 241-246 (2014).
- [181] J. Iwasaki, A. J. Beekman, and N. Nagaosa, *Theory of magnon-skyrmion scattering in chiral magnets*, Physical Review B **89**, 064412 (2014).
- [182] S.-Z. Lin, C. D. Batista, and A. Saxena, *Internal modes of a skyrmion in the ferromagnetic state of chiral magnets*, Physical Review B **89**, 024415 (2014).
- [183] C. Schütte and M. Garst, *Magnon-skyrmion scattering in chiral magnets*, Physical Review B **90**, 094423 (2014).
- [184] S. Schroeter and M. Garst, *Scattering of high-energy magnons off a magnetic skyrmion*, Low Temperature Physics **41**, 817-825 (2015).
- [185] X. Zhang, M. Ezawa, D. Xiao, G. P. Zhao, Y. Liu, and Y. Zhou, *All-magnetic control of skyrmions in nanowires by a spin wave*, Nanotechnology **26**, 225701 (2015).
- [186] F. Garcia-Sanchez, P. Borys, A. Vansteenkiste, J.-V. Kim, and R. L. Stamps, *Nonreciprocal spin-wave channeling along textures driven by the Dzyaloshinskii-Moriya interaction*, Physical Review B **89**, 224408 (2014).
- [187] S. Seki, Y. Okamura, K. Kondou, K. Shibata, M. Kubota, R. Takagi, F. Kagawa, M. Kawasaki, G. Tatara, Y. Otani, and Y. Tokura, *Magneto-chiral nonreciprocity of volume spin wave propagation in chiral-lattice ferromagnets*, Physical Review B **93**, 235131 (2016).
- [188] W. Wang, M. Beg, B. Zhang, W. Kuch, and H. Fangohr, *Driving magnetic skyrmions with microwave fields*, Physical Review B **92**, 020403 (2015).
- [189] J.-V. Kim and M.-W. Yoo, *Current-driven skyrmion dynamics in disordered films*, Applied Physics Letters **110**, 132404 (2017).

- [190] K. Zeissler, M. Mruczkiewicz, S. Finizio, J. Raabe, P. M. Shepley, A. V. Sadovnikov, S. A. Nikitov, K. Fallon, S. McFadzean, S. McVitie, T. A. Moore, G. Burnell, and C. H. Marrows, *Pinning and hysteresis in the field dependent diameter evolution of skyrmions in Pt/Co/Ir superlattice stacks*, Arxiv e-print (2017), arXiv:1706.01065..
- [191] X. Zhang, Y. Zhou, M. Ezawa, G. P. Zhao, and W. Zhao, *Magnetic skyrmion transistor: skyrmion motion in a voltage-gated nanotrack*, Scientific Reports **5**, 11369 (2015).
- [192] H. T. Fook, W. L. Gan, and W. S. Lew, *Gateable skyrmion transport via field-induced potential barrier modulation*, Scientific Reports **6**, 21099 (2016).
- [193] W. Kang, Y. Huang, C. Zheng, W. Lv, N. Lei, Y. Zhang, X. Zhang, Y. Zhou, and W. Zhao, *Voltage controlled magnetic skyrmion motion for racetrack memory*, Scientific Reports **6**, 23164 (2016).
- [194] Y. Zhou, X. Zhang, and M. Ezawa, *Magnetic bilayer-skyrmions without skyrmion Hall effect*, Nature Communications **7**, 10293 (2016).
- [195] S. Parkin and S.-H. Yang, *Memory on the racetrack*, Nature Nanotechnology **10**, 195-198 (2015).
- [196] X. Zhang, Y. Zhou, and M. Ezawa, *Antiferromagnetic Skyrmion: Stability, Creation and Manipulation*, Scientific Reports **6**, 24795 (2016).
- [197] J. Barker and O. A. Tretiakov, *Static and Dynamical Properties of Antiferromagnetic Skyrmions in the Presence of Applied Current and Temperature*, Physical Review Letters **116**, 147203 (2016).
- [198] D. R. Rodrigues, K. Everschor-Sitte, O. A. Tretiakov, J. Sinova, and A. Abanov, *Spin texture motion in antiferromagnetic and ferromagnetic nanowires*, Physical Review B **95**, 174408 (2017).
- [199] W. Jiang, X. Zhang, G. Yu, W. Zhang, X. Wang, B. M. Jungfleisch, J. E. Pearson, X. Cheng, O. Heinonen, K. L. Wang, Y. Zhou, A. Hoffmann, and S. G. E. te Velthuis, *Direct observation of the skyrmion Hall effect*, Nature Physics **13**, 162 (2016).
- [200] F. Zheng, F. N. Rybakov, A. B. Borisov, D. Song, S. Wang, Z.-A. Li, H. Du, N. S. Kiselev, J. Caron, A. Kovács, M. Tian, Y. Zhang, S. Blügel, and R. E. Dunin-Borkowski, *Experimental observation of magnetic bobbars for a new concept of magnetic solid-state memory*, Arxiv e-print (2017), arXiv:1706.04654.
- [201] M. Hoffmann, B. Zimmermann, G. P. Müller, D. Schürhoff, N. S. Kiselev, C. Melcher, and S. Blügel, *Antiskyrmions stabilized at interfaces by anisotropic Dzyaloshinskii-Moriya interactions*, Nature Communications **8**, 308 (2017).
- [202] A. Rosch, *Particles or waves*, Nature Materials **15**, 1231 (2016).
- [203] A. Rosch, *Electric control of skyrmions*, Nature Nanotechnology **12**, 103 (2016).
- [204] C. Heo, N. S. Kiselev, A. K. Nandy, S. Blügel, and T. Rasing, *Switching of chiral magnetic skyrmions by picosecond magnetic field pulses via transient topological states*, Scientific Reports **6**, 27146 (2016).

- 
- [205] Y. Zhou and M. Ezawa, *A reversible conversion between a skyrmion and a domain-wall pair in a junction geometry*, Nature Communications **5**, 4652 (2014).
- [206] X. Zhang, M. Ezawa, and Y. Zhou, *Magnetic skyrmion logic gates: conversion, duplication and merging of skyrmions*, Scientific Reports **5**, 9400 (2015).
- [207] D. Prychynenko, M. Sitte, K. Litzius, B. Krüger, G. Bourianoff, M. Kläui, J. Sinova, and K. Everschor-Sitte, *Magnetic Skyrmion as a Nonlinear Resistive Element: A Potential Building Block for Reservoir Computing*, Physical Review Applied **9**, 014034 (2018).
- [208] F Garcia-Sanchez, J Sampaio, N Reyren, V Cros, and J-V Kim, *A skyrmion-based spin-torque nano-oscillator*, New Journal of Physics **18**, 075011 (2016).
- [209] W. Jiang, P. Upadhyaya, W. Zhang, G. Yu, M. B. Jungfleisch, F. Y. Fradin, J. E. Pearson, Y. Tserkovnyak, K. L. Wang, O. Heinonen, S. G. E. te Velthuis, and A. Hoffmann, *Blowing magnetic skyrmion bubbles*, Science **349**, 283-286 (2015).
- [210] S.-Z. Lin, *Edge instability in a chiral stripe domain under an electric current and skyrmion generation*, Physical Review B **94**, 020402 (2016).
- [211] O. Heinonen, W. Jiang, H. Somaïly, S. G. E. te Velthuis, and A. Hoffmann, *Generation of magnetic skyrmion bubbles by inhomogeneous spin Hall currents*, Physical Review B **93**, 094407 (2016).
- [212] K. Litzius, I. Lemesch, B. Krüger, P. Bassirian, L. Caretta, K. Richter, F. Büttner, K. Sato, O. A. Tretiakov, J. Förster, R. M. Reeve, M. Weigand, I. Bykova, H. Stoll, G. Schütz, G. S. D. Beach, and M. Kläui, *Skyrmion Hall effect revealed by direct time-resolved X-ray microscopy*, Nature Physics **13**, 170 (2016).
- [213] H. Du, R. Che, L. Kong, X. Zhao, C. Jin, C. Wang, J. Yang, W. Ning, R. Li, C. Jin, X. Chen, J. Zang, Y. Zhang, and M. Tian, *Edge-mediated skyrmion chain and its collective dynamics in a confined geometry*, Nature Communications **6**, 8504 (2015).
- [214] P. Schoenherr, J. Müller, L. Köhler, A. Rosch, N. Kanazawa, Y. Tokura, M. Garst, and D. Meier, *Topological domain walls in helimagnets*, Nature Physics , (2018).
- [215] J. Müller, J. Rajeswari, P. Huang, Y. Murooka, H. M. Rønnow, F. Carbone, and A. Rosch, *Magnetic Skyrmions and Skyrmion Clusters in the Helical Phase of Cu<sub>2</sub>OSeO<sub>3</sub>*, Physical Review Letters **119**, 137201 (2017).
- [216] J. Wild, T. N. G. Meier, S. Pöllath, M. Kronseder, A. Bauer, A. Chacon, M. Halder, M. Schowalter, A. Rosenauer, J. Zweck, J. Müller, A. Rosch, C. Pfeiderer, and C. H. Back, *Entropy-limited topological protection of skyrmions*, Science Advances **3**, e1701704 (2017).
- [217] J. Müller, A. Rosch, and M. Garst, *Edge instabilities and skyrmion creation in magnetic layers*, New Journal of Physics **18**, 065006 (2016).
- [218] J. Müller, *Magnetic skyrmions on a two-lane racetrack*, New Journal of Physics **19**, 025002 (2017).
- [219] J. Müller, *Shape-dependence of the barrier for skyrmions on a two-lane racetrack*, Proc. SPIE 9931, Spintronics IX , 993136 (2016).
-

- [220] X. Zhang, J. Müller, J. Xia, M. Garst, X. Liu, and Y. Zhou, *Motion of skyrmions in nanowires driven by magnonic momentum-transfer forces*, New Journal of Physics **19**, 065001 (2017).
- [221] N. S. Kiselev, B. Zimmermann, and J. Chico, *C1. Atomistic and micromagnetic models of magnetism*, Lecture notes: 48th IFF Spring School *Topological matter - Topological insulators, skyrmions and majoranas*, 2017.
- [222] A. Hubert and R. Schäfer, *Magnetic domains: the analysis of magnetic microstructures*, Springer-Verlag, Berlin Heidelberg, 2000.
- [223] K. Everschor, *Current-Induced Dynamics of Chiral Magnetic Structures - Skyrmions, Emergent Electrodynamics and Spin-Transfer Torques*, PhD thesis, University of Cologne, Cologne (2012).
- [224] A. Rosch and L. Heinen, Private communications.
- [225] A. De Lucia, K. Litzius, B. Krüger, O. A. Tretiakov, and M. Kläui, *Multiscale simulations of topological transformations in magnetic-skyrmion spin structures*, Physical Review B **96**, 020405 (2017).
- [226] L. D. Landau and E. M. Lifshitz, *On the Theory of the Dispersion of Magnetic Permeability in Ferromagnetic Bodies*, Physikalische Zeitschrift der Sowjetunion **8**, 153-164 (1935)
- [227] T. L. Gilbert, *A Lagrangian formulation of the gyromagnetic equation of the magnetic field (Abstract only)*, Physical Review **100**, 1235 (1955).
- [228] T. L. Gilbert, *A phenomenological theory of damping in ferromagnetic materials*, IEEE Transactions on Magnetics **40**, 3443-3449 (2004).
- [229] J. L. García-Palacios and F. J. Lázaro, *Langevin-dynamics study of the dynamical properties of small magnetic particles*, Physical Review B **58**, 14937-14958 (1998).
- [230] R. A. Duine, A. S. Núñez, Jairo Sinova, and A. H. MacDonald, *Functional Keldysh theory of spin torques*, Physical Review B **75**, 214420 (2007).
- [231] M. E. Lucassen, H. J. van Driel, C. Morais Smith, and R. A. Duine, *Current-driven and field-driven domain walls at nonzero temperature*, Physical Review B **79**, 224411 (2009).
- [232] H. Kohno, G. Tatara, and J. Shibata, *Microscopic Calculation of Spin Torques in Disordered Ferromagnets*, Journal of the Physical Society of Japan **75**, 113706 (2006).
- [233] A. Manchon, I. M. Miron, T. Jungwirth, J. Sinova, J. Zelezný, A. Thiaville, K. Garello, and P. Gambardella, *Current-induced spin-orbit torques in ferromagnetic and antiferromagnetic systems*, Arxiv e-print (2018), arXiv:1801.09636.
- [234] J. Sinova and T. Jungwirth, *Surprises from the spin Hall effect*, Physics Today **70**, 38 (2017).
- [235] M.I. D'yakonov and V. I. Perel', *Possibility of Orienting Electron Spins with Current*, JETP Letters **13**, 467-469 (1971).

- 
- [236] J. C. Slonczewski, *Current-driven excitation of magnetic multilayers*, Journal of Magnetism and Magnetic Materials **159**, L1-L7 (1996).
- [237] K. Garello, T. M. Miron, C. O. Avci, F. Freimuth, Y. Mokrousov, S. Blügel, S. Auffret, O. Boulle, G. Gaudin, and P. Gambardella, *Symmetry and magnitude of spin-orbit torques in ferromagnetic heterostructures*, Nature Nanotechnology **8**, 587 (2013).
- [238] Y. A. Bychkov and E. I. Rashba, *Properties of a 2d electron-gas with lifted spectral degeneracy*, JETP Letters **39**, 78-81 (1984).
- [239] G. Dresselhaus, *Spin-Orbit Coupling Effects in Zinc Blende Structures*, Physical Review **100**, 580-586 (1955).
- [240] A. V. Khvalkovskiy, V. Cros, D. Apalkov, V. Nikitin, M. Krounbi, K. A. Zvezdin, A. Anane, J. Grollier, and A. Fert, *Matching domain-wall configuration and spin-orbit torques for efficient domain-wall motion*, Physical Review B **87**, 020402 (2013).
- [241] A. A. Thiele, *Steady-state motion of magnetic domains*, Physical Review Letters **30**, 230-233 (1973).
- [242] A. A. Thiele, *Applications of the gyrocoupling vector and dissipation dyadic in the dynamics of magnetic domains*, Journal of Applied Physics **45**, 377 (1974).
- [243] W. H. Press, S. A. Teukolsky, W. T. Vetterling, and B. P. Flannery, *Numerical Recipes 3rd Edition: The Art of Scientific Computing*, Cambridge University Press, New York, NY, USA, 3rd edition, 2007.
- [244] A. Vansteenkiste, J. Leliaert, M. Dvornik, M. Helsen, F. Garcia-Sanchez, and B. Van Waeyenberge, *The design and verification of MuMax3*, AIP Advances **4**, 107133 (2014).
- [245] The calculations with MuMax3 were performed by L. Heinen.
- [246] C. Faber, *Einfluss der Magnetfeldorientierung auf dünne Schichten chiraler Magnete*, Bachelor thesis, University of Cologne, Cologne (2016).
- [247] S.-Z. Lin and A. Saxena, *Noncircular skyrmion and its anisotropic response in thin films of chiral magnets under a tilted magnetic field*, Physical Review B **92**, 180401 (2015).
- [248] M. N. Wilson, E. A. Karhu, A. S. Quigley, U. K. Rößler, A. B. Butenko, A. N. Bogdanov, M. D. Robertson, and T. L. Monchesky, *Extended elliptic skyrmion gratings in epitaxial MnSi thin films*, Physical Review B **86**, 144420 (2012).
- [249] M. N. Wilson, E. A. Karhu, D. P. Lake, A. S. Quigley, S. Meynell, A. N. Bogdanov, H. Fritzsche, U. K. Rößler, and T. L. Monchesky, *Discrete helicoidal states in chiral magnetic thin films*, Physical Review B **88**, 214420 (2013).
- [250] N. L. Schryer and L. R. Walker, *The motion of 180° domain walls in uniform dc magnetic fields*, Journal of Applied Physics **45**, 5406-5421 (1974).
- [251] The calculations with MuMax3 were performed by B. McKeever.



Part VI.  
Appendix



## 14. Discretization of derivatives

### 14.1. Getting the prefactors

Consider, for simplicity, an infinite square lattice with lattice constant  $a$ . We restrict our analysis to only one spatial dimension and denote the spin  $\hat{n}(\mathbf{r} + ma\hat{e}_i)$  simply by  $\hat{n}^m$ . Then, most generally, the discretized derivatives that consider  $N$  neighbors on each side are given by

$$\partial_x^i \hat{n}^0 = \frac{1}{a^i} \left( \sum_{m=-N}^N g_{m,i} \hat{n}^m \right) + \mathcal{O}(a^{2N}) \quad (14.1.1)$$

where the prefactors  $g_{m,i}$  have to be chosen accordingly.

The correct choice of prefactors is achieved by a Taylor expansion of the spin  $\hat{n}_m$  at site  $m \neq 0$  around the site  $m = 0$ :

$$\hat{n}^m = \hat{n}^0 + ma \partial_x \hat{n}^0 + \frac{m^2 a^2}{2} \partial_x^2 \hat{n}^0 + \frac{m^3 a^3}{3!} \partial_x^3 \hat{n}^0 + \dots = \sum_{k=0}^{\infty} \frac{(ma)^k}{k!} \partial_x^k \hat{n}^0 \quad (14.1.2)$$

with the factorial notation  $k! = (k-1)! \cdot k$  with  $0! = 1$ . Using this expansion in the formula for the derivative leads to the following condition:

$$\partial_x^i \hat{n}^0 \stackrel{!}{=} \sum_{m=-N}^N \sum_{k=0}^{2N} g_{m,i} \frac{(ma)^{k-i}}{k!} \left( \partial_x^k \hat{n}^0 \right). \quad (14.1.3)$$

Since all orders  $k$  of derivatives  $\partial_x^k$  are linearly independent, the equation has to hold for all  $k$  independently. This single equation corresponds therefore to a system of  $2N$  (the number of addends in the sum over  $k$ ) coupled linear equations which have to be fulfilled simultaneously:

$$\delta_{i,k} \stackrel{!}{=} \sum_{m=-N}^N g_{m,i} \frac{(ma)^{k-i}}{k!}. \quad (14.1.4)$$

Here  $\delta_{i,k}$  is the Kronecker Delta with  $\delta_{i,k} = 1$  if  $i = k$  and  $\delta_{i,k} = 0$  otherwise. Dividing both sides by  $a^{k-i}/k!$  and further exploiting the Kronecker Delta leads to the matrix equation

$$i! \hat{e}_i \stackrel{!}{=} \mathcal{G} \mathbf{g}_i \quad (14.1.5)$$

with the matrix  $\mathcal{G}$  that includes the Taylor coefficients and the vector  $\mathbf{g}_i$  that summarizes the prefactors that we desire

$$(\mathcal{G})_{k,m} = \begin{cases} m^{k-i} & \text{if } m \neq 0 \\ \delta_{k,0} & \text{if } m = 0 \end{cases} \quad \text{and} \quad (\mathbf{g}_i)_m = g_{m,i}. \quad (14.1.6)$$

Finally, the matrix is inverted and due to the unit vector  $\hat{e}_i$  on the left-hand-side we only need the  $i$ -th component of the inverse matrix:

$$\mathbf{g}_i \stackrel{!}{=} i! \mathcal{G}^{-1} \hat{e}_i \quad (14.1.7)$$

which can be computed, e.g. using Mathematica. This method can as well be applied for asymmetric discretizations and also discretizations with inhomogeneous lattice spacing  $a$  as needed for the higher order discretization of boundary conditions, see Sec. 10.5.4. In the following, the factors  $g_{m,i}$  are provided for the most frequent applications.

## 14.2. Symmetric discretizations

The general formula for the symmetric discretization of the  $i$ -th derivative in the arbitrary direction  $x$  with  $N$  sites on each side reads

$$\partial_x^i \hat{n}^0 = \frac{1}{a^i} \left( \sum_{m=-N}^N g_{m,i} \hat{n}^m \right) + \mathcal{O}(a^{2N}). \quad (14.2.8)$$

The factors  $g_{m,i}$  are computed as described in Sec. 14.1 and are provided in the following.

### First order derivatives

The values for  $g_{m,1}$  as defined in Eq. 14.2.8:

$N$	$m = -4$	$m = -3$	$m = -2$	$m = -1$	$m = 0$	$m = 1$	$m = 2$	$m = 3$	$m = 4$
1	–	–	–	$-\frac{1}{2}$	0	$\frac{1}{2}$	–	–	–
2	–	–	$\frac{1}{12}$	$-\frac{8}{12}$	0	$\frac{8}{12}$	$-\frac{1}{12}$	–	–
3	–	$-\frac{1}{60}$	$\frac{9}{60}$	$-\frac{45}{60}$	0	$\frac{45}{60}$	$-\frac{9}{60}$	$\frac{1}{60}$	–
4	$\frac{3}{840}$	$-\frac{32}{840}$	$\frac{168}{840}$	$-\frac{672}{840}$	0	$\frac{672}{840}$	$-\frac{168}{840}$	$\frac{32}{840}$	$-\frac{3}{840}$

### Second order derivatives

The values for  $g_{m,2}$  as defined in Eq. 14.2.8:

$N$	$m = -4$	$m = -3$	$m = -2$	$m = -1$	$m = 0$	$m = 1$	$m = 2$	$m = 3$	$m = 4$
1	–	–	–	1	–2	1	–	–	–
2	–	–	$-\frac{1}{12}$	$\frac{16}{12}$	$-\frac{30}{12}$	$\frac{16}{12}$	$-\frac{1}{12}$	–	–
3	–	$\frac{2}{180}$	$-\frac{27}{180}$	$\frac{270}{180}$	$-\frac{490}{180}$	$\frac{270}{180}$	$-\frac{27}{180}$	$\frac{2}{180}$	–
4	$-\frac{9}{5040}$	$\frac{128}{5040}$	$-\frac{1008}{5040}$	$\frac{8064}{5040}$	$-\frac{14350}{5040}$	$\frac{8064}{5040}$	$-\frac{1008}{5040}$	$\frac{128}{5040}$	$-\frac{9}{5040}$

### 14.3. Asymmetric discretizations

The general formula for an asymmetric discretization of the  $i$ -th derivative in the arbitrary direction  $x$  with  $N_0$  sites on the left side and  $2N - N_0$  sites on the right side reads

$$\partial_x^i \hat{n}^0 = \frac{1}{a} \left( \sum_{m=-N_0}^{2N-N_0} g_{m,i}^{N_0} \hat{n}^m \right) + \mathcal{O}(a^{2N}) \quad (14.3.9)$$

The factors  $g_{m,i}^{N_0}$  are computed as described in Sec. 14.1 and are provided in the following.

#### First order derivatives

The values for  $g_{m,1}^{N_0}$  as defined in Eq. 14.3.9. Note that the value for  $-N_0$  is the value of the index  $m$  in the first occupied column.

$N$	$m = -8$	$m = -7$	$m = -6$	$m = -5$	$m = -4$	$m = -3$	$m = -2$	$m = -1$	$m = 0$
4	$\frac{105}{840}$	$-\frac{960}{840}$	$\frac{3920}{840}$	$-\frac{9408}{840}$	$\frac{14700}{840}$	$-\frac{15680}{840}$	$\frac{11760}{840}$	$-\frac{6720}{840}$	$\frac{2283}{840}$
$N$	$m = -7$	$m = -6$	$m = -5$	$m = -4$	$m = -3$	$m = -2$	$m = -1$	$m = 0$	$m = 1$
3	–	$\frac{10}{60}$	$-\frac{72}{60}$	$\frac{225}{60}$	$-\frac{400}{60}$	$\frac{450}{60}$	$-\frac{360}{60}$	$\frac{147}{60}$	–
4	$-\frac{15}{840}$	$\frac{140}{840}$	$-\frac{588}{840}$	$\frac{1470}{840}$	$-\frac{2450}{840}$	$\frac{2940}{840}$	$-\frac{2940}{840}$	$\frac{1338}{840}$	$\frac{105}{840}$
$N$	$m = -6$	$m = -5$	$m = -4$	$m = -3$	$m = -2$	$m = -1$	$m = 0$	$m = 1$	$m = 2$
2	–	–	$\frac{3}{12}$	$-\frac{16}{12}$	$\frac{36}{12}$	$-\frac{48}{12}$	$\frac{25}{12}$	–	–
3	–	$-\frac{2}{60}$	$\frac{15}{60}$	$-\frac{50}{60}$	$\frac{100}{60}$	$-\frac{150}{60}$	$\frac{77}{60}$	$\frac{10}{60}$	–
4	$\frac{5}{840}$	$-\frac{48}{840}$	$\frac{210}{840}$	$-\frac{560}{840}$	$\frac{1050}{840}$	$-\frac{1680}{840}$	$\frac{798}{840}$	$\frac{240}{840}$	$-\frac{15}{840}$
$N$	$m = -5$	$m = -4$	$m = -3$	$m = -2$	$m = -1$	$m = 0$	$m = 1$	$m = 2$	$m = 3$
1	–	–	–	$\frac{1}{2}$	$-\frac{4}{2}$	$\frac{3}{2}$	–	–	–
2	–	–	$-\frac{1}{12}$	$\frac{6}{12}$	$-\frac{18}{12}$	$\frac{10}{12}$	$\frac{3}{12}$	–	–
3	–	$\frac{1}{60}$	$-\frac{8}{60}$	$\frac{30}{60}$	$-\frac{80}{60}$	$\frac{35}{60}$	$\frac{24}{60}$	$-\frac{2}{60}$	–
4	$-\frac{3}{840}$	$\frac{30}{840}$	$-\frac{140}{840}$	$\frac{420}{840}$	$-\frac{1050}{840}$	$\frac{378}{840}$	$\frac{420}{840}$	$-\frac{60}{840}$	$\frac{5}{840}$
$N$	$m = -4$	$m = -3$	$m = -2$	$m = -1$	$m = 0$	$m = 1$	$m = 2$	$m = 3$	$m = 4$
1	–	–	–	$-\frac{1}{2}$	0	$\frac{1}{2}$	–	–	–
2	–	–	$\frac{1}{12}$	$-\frac{8}{12}$	0	$\frac{8}{12}$	$-\frac{1}{12}$	–	–
3	–	$-\frac{1}{60}$	$\frac{9}{60}$	$-\frac{45}{60}$	0	$\frac{45}{60}$	$-\frac{9}{60}$	$\frac{1}{60}$	–
4	$\frac{3}{840}$	$-\frac{32}{840}$	$\frac{168}{840}$	$-\frac{672}{840}$	0	$\frac{672}{840}$	$-\frac{168}{840}$	$\frac{32}{840}$	$-\frac{3}{840}$
$N$	$m = -3$	$m = -2$	$m = -1$	$m = 0$	$m = 1$	$m = 2$	$m = 3$	$m = 4$	$m = 5$
1	–	–	–	$-\frac{3}{2}$	$\frac{4}{2}$	$-\frac{1}{2}$	–	–	–
2	–	–	$-\frac{3}{12}$	$-\frac{10}{12}$	$\frac{18}{12}$	$-\frac{6}{12}$	$\frac{1}{12}$	–	–
3	–	$\frac{2}{60}$	$-\frac{24}{60}$	$-\frac{35}{60}$	$\frac{80}{60}$	$-\frac{30}{60}$	$\frac{8}{60}$	$-\frac{1}{60}$	–
4	$-\frac{5}{840}$	$\frac{60}{840}$	$-\frac{420}{840}$	$-\frac{378}{840}$	$\frac{1050}{840}$	$-\frac{420}{840}$	$\frac{140}{840}$	$-\frac{30}{840}$	$\frac{3}{840}$

VI. Appendix

$N$	$m = -2$	$m = -1$	$m = 0$	$m = 1$	$m = 2$	$m = 3$	$m = 4$	$m = 5$	$m = 6$
2	–	–	$-\frac{25}{12}$	$\frac{48}{12}$	$-\frac{36}{12}$	$\frac{16}{12}$	$-\frac{3}{12}$	–	–
3	–	$-\frac{10}{60}$	$-\frac{77}{60}$	$\frac{150}{60}$	$-\frac{100}{60}$	$\frac{50}{60}$	$-\frac{15}{60}$	$\frac{2}{60}$	–
4	$\frac{15}{840}$	$-\frac{240}{840}$	$-\frac{798}{840}$	$\frac{1680}{840}$	$-\frac{1050}{840}$	$\frac{560}{840}$	$-\frac{210}{840}$	$\frac{48}{840}$	$-\frac{5}{840}$

$N$	$m = -1$	$m = 0$	$m = 1$	$m = 2$	$m = 3$	$m = 4$	$m = 5$	$m = 6$	$m = 7$
3	–	$-\frac{147}{60}$	$\frac{360}{60}$	$-\frac{450}{60}$	$\frac{400}{60}$	$-\frac{225}{60}$	$\frac{72}{60}$	$-\frac{10}{60}$	–
4	$-\frac{105}{840}$	$-\frac{1338}{840}$	$\frac{2940}{840}$	$-\frac{2940}{840}$	$\frac{2450}{840}$	$-\frac{1470}{840}$	$\frac{588}{840}$	$-\frac{140}{840}$	$\frac{15}{840}$

$N$	$m = 0$	$m = 1$	$m = 2$	$m = 3$	$m = 4$	$m = 5$	$m = 6$	$m = 7$	$m = 8$
4	$-\frac{2283}{840}$	$\frac{6720}{840}$	$-\frac{11760}{840}$	$\frac{15680}{840}$	$-\frac{14700}{840}$	$\frac{9408}{840}$	$-\frac{3920}{840}$	$\frac{960}{840}$	$-\frac{105}{840}$

Second order derivatives

The values for  $g_{m,2}^{N_0}$  as defined in Eq. 14.3.9. Note that the value for  $-N_0$  is the value of the index  $m$  in the first occupied column.

$N$	$m = -8$	$m = -7$	$m = -6$	$m = -5$	$m = -4$	$m = -3$	$m = -2$	$m = -1$	$m = 0$
4	$\frac{3267}{5040}$	$-\frac{29664}{5040}$	$\frac{120008}{5040}$	$-\frac{284256}{5040}$	$\frac{435330}{5040}$	$-\frac{448672}{5040}$	$\frac{312984}{5040}$	$-\frac{138528}{5040}$	$\frac{29531}{5040}$

$N$	$m = -7$	$m = -6$	$m = -5$	$m = -4$	$m = -3$	$m = -2$	$m = -1$	$m = 0$	$m = 1$
3	–	$\frac{137}{180}$	$-\frac{972}{180}$	$\frac{2970}{180}$	$-\frac{5080}{180}$	$\frac{5265}{180}$	$-\frac{3132}{180}$	$\frac{812}{180}$	–
4	$-\frac{261}{5040}$	$\frac{2396}{5040}$	$-\frac{9828}{5040}$	$\frac{23688}{5040}$	$-\frac{37030}{5040}$	$\frac{38556}{5040}$	$-\frac{20916}{5040}$	$\frac{128}{5040}$	$\frac{3267}{5040}$

$N$	$m = -6$	$m = -5$	$m = -4$	$m = -3$	$m = -2$	$m = -1$	$m = 0$	$m = 1$	$m = 2$
2	–	–	$\frac{11}{12}$	$-\frac{56}{12}$	$\frac{114}{12}$	$-\frac{104}{12}$	$\frac{35}{12}$	–	–
3	–	$-\frac{13}{180}$	$\frac{93}{180}$	$-\frac{285}{180}$	$\frac{470}{180}$	$-\frac{255}{180}$	$-\frac{147}{180}$	$\frac{137}{180}$	–
4	$\frac{47}{5040}$	$-\frac{432}{5040}$	$\frac{1764}{5040}$	$-\frac{4144}{5040}$	$\frac{5670}{5040}$	$\frac{1008}{5040}$	$-\frac{9268}{5040}$	$\frac{5616}{5040}$	$-\frac{261}{5040}$

$N$	$m = -5$	$m = -4$	$m = -3$	$m = -2$	$m = -1$	$m = 0$	$m = 1$	$m = 2$	$m = 3$
1	–	–	–	1	–2	1	–	–	–
2	–	–	$-\frac{1}{12}$	$\frac{4}{12}$	$\frac{6}{12}$	$-\frac{20}{12}$	$\frac{11}{12}$	–	–
3	–	$\frac{2}{180}$	$-\frac{12}{180}$	$\frac{15}{180}$	$\frac{200}{180}$	$-\frac{420}{180}$	$\frac{228}{180}$	$-\frac{13}{180}$	–
4	$-\frac{9}{5040}$	$\frac{72}{5040}$	$-\frac{196}{5040}$	$-\frac{252}{5040}$	$\frac{6930}{5040}$	$-\frac{13216}{5040}$	$\frac{7308}{5040}$	$-\frac{684}{5040}$	$\frac{47}{5040}$

$N$	$m = -4$	$m = -3$	$m = -2$	$m = -1$	$m = 0$	$m = 1$	$m = 2$	$m = 3$	$m = 4$
1	–	–	–	1	–2	1	–	–	–
2	–	–	$-\frac{1}{12}$	$\frac{16}{12}$	$-\frac{30}{12}$	$\frac{16}{12}$	$-\frac{1}{12}$	–	–
3	–	$\frac{2}{180}$	$-\frac{27}{180}$	$\frac{270}{180}$	$-\frac{490}{180}$	$\frac{270}{180}$	$-\frac{27}{180}$	$\frac{2}{180}$	–
4	$-\frac{9}{5040}$	$\frac{128}{5040}$	$-\frac{1008}{5040}$	$\frac{8064}{5040}$	$-\frac{14350}{5040}$	$\frac{8064}{5040}$	$-\frac{1008}{5040}$	$\frac{128}{5040}$	$-\frac{9}{5040}$

$N$	$m = -3$	$m = -2$	$m = -1$	$m = 0$	$m = 1$	$m = 2$	$m = 3$	$m = 4$	$m = 5$
1	–	–	–	1	–2	1	–	–	–
2	–	–	$\frac{11}{12}$	$-\frac{20}{12}$	$\frac{6}{12}$	$\frac{4}{12}$	$-\frac{1}{12}$	–	–
3	–	$-\frac{13}{180}$	$\frac{228}{180}$	$-\frac{420}{180}$	$\frac{200}{180}$	$\frac{15}{180}$	$-\frac{12}{180}$	$\frac{2}{180}$	–
4	$\frac{47}{5040}$	$-\frac{684}{5040}$	$\frac{7308}{5040}$	$-\frac{13216}{5040}$	$\frac{6930}{5040}$	$-\frac{252}{5040}$	$-\frac{196}{5040}$	$\frac{72}{5040}$	$-\frac{9}{5040}$

$N$	$m = -2$	$m = -1$	$m = 0$	$m = 1$	$m = 2$	$m = 3$	$m = 4$	$m = 5$	$m = 6$
2	–	–	$\frac{35}{12}$	$-\frac{104}{12}$	$\frac{114}{12}$	$-\frac{56}{12}$	$\frac{11}{12}$	–	–
3	–	$\frac{137}{180}$	$-\frac{147}{180}$	$-\frac{255}{180}$	$\frac{470}{180}$	$-\frac{285}{180}$	$\frac{93}{180}$	$-\frac{13}{180}$	–
4	$-\frac{261}{5040}$	$\frac{5616}{5040}$	$-\frac{9268}{5040}$	$\frac{1008}{5040}$	$\frac{5670}{5040}$	$-\frac{4144}{5040}$	$\frac{1764}{5040}$	$-\frac{432}{5040}$	$\frac{47}{5040}$
$N$	$m = -1$	$m = 0$	$m = 1$	$m = 2$	$m = 3$	$m = 4$	$m = 5$	$m = 6$	$m = 7$
3	–	$\frac{812}{180}$	$-\frac{3132}{180}$	$\frac{5265}{180}$	$-\frac{5080}{180}$	$\frac{2970}{180}$	$-\frac{972}{180}$	$\frac{137}{180}$	–
4	$\frac{3267}{5040}$	$\frac{128}{5040}$	$-\frac{20916}{5040}$	$\frac{38556}{5040}$	$-\frac{37030}{5040}$	$\frac{23688}{5040}$	$-\frac{9828}{5040}$	$\frac{2396}{5040}$	$-\frac{261}{5040}$
$N$	$m = 0$	$m = 1$	$m = 2$	$m = 3$	$m = 4$	$m = 5$	$m = 6$	$m = 7$	$m = 8$
4	$\frac{29531}{5040}$	$-\frac{138528}{5040}$	$\frac{312984}{5040}$	$-\frac{448672}{5040}$	$\frac{435330}{5040}$	$-\frac{284256}{5040}$	$\frac{120008}{5040}$	$-\frac{29664}{5040}$	$\frac{3267}{5040}$

## 14.4. Asymmetric discretizations with boundary conditions

For the discretization of derivatives that take the boundary condition properly into account, we have derived a method which uses a discretization scheme that does not rely on equidistant sites anymore: The distance from the last site in the sample to the edge is only half the distance between lattice sites.

Here, the general formula for the  $i$ -th derivative on the  $k$ -th site with in total  $2N$  physical sites contributing reads

$$\partial_x^i \hat{n}^k = \frac{1}{a^i} \sum_{m=0}^{2N} \left( f_{m,i}^k \mathbf{1} + f_{B,i}^k f_m^B (a\mathcal{M}_B^x - f_B^B \mathbf{1})^{-1} \right) \hat{n}^m \quad (14.4.10)$$

where the factors  $f_m^B$  and  $f_B^B$  are coefficients from the first derivative at site  $m = B$ , i.e. precisely at the edge. Thus we will in the following write them as  $f_{m,1}^B = f_m^B$  and  $f_{B,1}^B = f_B^B$  and collect them in the list of first derivatives.

The factors  $f_{m,i}^k$  are computed as described in Sec. 14.1 and are provided in the following. Note that due to the restricted space on this page, the coefficients for  $N = 4$  have been separated from the rest.

### First order derivatives

The values for  $f_{m,1}^k$  as defined in Eq. 14.4.10 for all combinations of  $(N, k)$  for an edge at  $m = B = -1/2$ , i.e. the sites are at  $m > B$ . The corresponding factors for an edge on the other side, thus sites taken into account with  $m < B$ , are obtained by simply changing the sign.

$(N, k)$	$m = B$	$m = 0$	$m = 1$	$m = 2$	$m = 3$	$m = 4$
(1, B)	$-\frac{184}{60}$	$\frac{225}{60}$	$-\frac{50}{60}$	$\frac{9}{60}$	–	–
(1, 0)	$-\frac{32}{30}$	$\frac{15}{30}$	$\frac{20}{30}$	$-\frac{3}{30}$	–	–
(2, B)	$-\frac{72064}{23063040}$	$\frac{99225}{23063040}$	$-\frac{44100}{23063040}$	$\frac{23814}{23063040}$	$-\frac{8100}{23063040}$	$\frac{1225}{23063040}$
(2, 0)	$-\frac{1024}{1260}$	$-\frac{105}{1260}$	$\frac{1680}{1260}$	$-\frac{756}{1260}$	$\frac{240}{1260}$	$-\frac{35}{1260}$
(2, 1)	$\frac{256}{1260}$	$-\frac{945}{1260}$	$-\frac{210}{1260}$	$\frac{1134}{1260}$	$-\frac{270}{1260}$	$\frac{35}{1260}$

VI. Appendix

$(N, k)$	$m = B$	$m = 0$	$m = 1$	$m = 2$	$m = 3$	$m = 4$	$m = 5$	$m = 6$
$(3, B)$	$-\frac{90182656}{23063040}$	$\frac{135270135}{23063040}$	$-\frac{90180090}{23063040}$	$\frac{81162081}{23063040}$	$-\frac{55212300}{23063040}$	$\frac{25050025}{23063040}$	$-\frac{6707610}{23063040}$	$\frac{800415}{23063040}$
$(3, 0)$	$-\frac{40960}{60060}$	$-\frac{27027}{60060}$	$\frac{120120}{60060}$	$-\frac{90090}{60060}$	$\frac{57200}{60060}$	$-\frac{25025}{60060}$	$\frac{6552}{60060}$	$-\frac{770}{60060}$
$(3, 1)$	$\frac{20480}{180180}$	$-\frac{90090}{180180}$	$-\frac{111111}{180180}$	$\frac{270270}{180180}$	$-\frac{128700}{180180}$	$\frac{50050}{180180}$	$-\frac{12285}{180180}$	$\frac{1386}{180180}$
$(3, 2)$	$-\frac{8192}{180180}$	$\frac{30030}{180180}$	$-\frac{120120}{180180}$	$-\frac{33033}{180180}$	$\frac{171600}{180180}$	$-\frac{50050}{180180}$	$\frac{10920}{180180}$	$-\frac{1155}{180180}$

$(N, k)$	$m = B$	$m = 0$	$m = 1$	$m = 2$	$m = 3$	$m = 4$
$(4, B)$	$-\frac{52208238592}{12546293760}$	$\frac{83770862175}{12546293760}$	$-\frac{74462988600}{12546293760}$	$\frac{93823365636}{12546293760}$	$-\frac{95738128200}{12546293760}$	$\frac{72394572250}{12546293760}$
$(4, 0)$	$-\frac{3670016}{6126120}$	$-\frac{4397679}{6126120}$	$\frac{16336320}{6126120}$	$-\frac{17153136}{6126120}$	$\frac{16336320}{6126120}$	$-\frac{11911900}{6126120}$
$(4, 1)$	$\frac{458752}{6126120}$	$-\frac{2297295}{6126120}$	$-\frac{5673954}{6126120}$	$\frac{12864852}{6126120}$	$-\frac{9189180}{6126120}$	$\frac{5955950}{6126120}$
$(4, 2)$	$-\frac{131072}{6126120}$	$\frac{546975}{6126120}$	$-\frac{2917200}{6126120}$	$-\frac{3369366}{6126120}$	$\frac{8751600}{6126120}$	$-\frac{4254250}{6126120}$
$(4, 3)$	$-\frac{65536}{6126120}$	$-\frac{255255}{6126120}$	$\frac{1021020}{6126120}$	$-\frac{4288284}{6126120}$	$-\frac{1006434}{6126120}$	$\frac{5955950}{6126120}$

$(N, k)$	$m = 5$	$m = 6$	$m = 7$	$m = 8$
$(4, B)$	$-\frac{38769985800}{12546293760}$	$\frac{13879196100}{12546293760}$	$-\frac{2978519544}{12546293760}$	$\frac{289864575}{12546293760}$
$(4, 0)$	$\frac{6237504}{6126120}$	$-\frac{2199120}{6126120}$	$\frac{466752}{6126120}$	$-\frac{45045}{6126120}$
$(4, 1)$	$-\frac{2923830}{6126120}$	$\frac{989604}{6126120}$	$-\frac{204204}{6126120}$	$\frac{19305}{6126120}$
$(4, 2)$	$\frac{1856400}{6126120}$	$-\frac{589050}{6126120}$	$\frac{116688}{6126120}$	$-\frac{10725}{6126120}$
$(4, 3)$	$-\frac{1949220}{6126120}$	$\frac{549780}{6126120}$	$-\frac{102102}{6126120}$	$\frac{9009}{6126120}$

Second order derivatives

The values for  $f_{m,2}^k$  as defined in Eq. 14.4.10 for all combinations of  $(N, k)$  for an edge at  $m = B = -1/2$ , i.e. the sites are at  $m > B$ . The corresponding factors for an edge on the other side, thus sites taken into account with  $m < B$ , are the same. The special case  $k = B$  can be considered but is not relevant and thus not provided.

$(N, k)$	$m = B$	$m = 0$	$m = 1$	$m = 2$	$m = 3$	$m = 4$	$m = 5$	$m = 6$
$(1, 0)$	$\frac{16}{5}$	$-\frac{25}{5}$	$\frac{10}{5}$	$\frac{1}{5}$	-	-	-	-
$(2, 0)$	$\frac{2560}{756}$	$-\frac{4095}{756}$	$\frac{1848}{756}$	$-\frac{378}{756}$	$\frac{72}{756}$	$-\frac{7}{756}$	-	-
$(2, 1)$	$-\frac{256}{756}$	$\frac{1323}{756}$	$-\frac{2100}{756}$	$\frac{1134}{756}$	$-\frac{108}{756}$	$\frac{7}{756}$	-	-
$(3, 0)$	$\frac{86016}{25740}$	$-\frac{136136}{25740}$	$\frac{56628}{25740}$	$-\frac{3861}{25740}$	$-\frac{5720}{25740}$	$\frac{4290}{25740}$	$-\frac{1404}{25740}$	$\frac{187}{25740}$
$(3, 1)$	$-\frac{2048}{7020}$	$\frac{11349}{7020}$	$-\frac{17745}{7020}$	$\frac{8073}{7020}$	$\frac{1170}{7020}$	$-\frac{1105}{7020}$	$\frac{351}{7020}$	$-\frac{45}{7020}$
$(3, 2)$	$\frac{4096}{77220}$	$-\frac{17589}{77220}$	$\frac{121836}{77220}$	$-\frac{216216}{77220}$	$\frac{120120}{77220}$	$-\frac{13585}{77220}$	$\frac{1404}{77220}$	$-\frac{66}{77220}$

$(N, k)$	$m = B$	$m = 0$	$m = 1$	$m = 2$	$m = 3$	$m = 4$	$m = 5$
$(4, 0)$	$\frac{199491584}{61261200}$	$-\frac{307047455}{61261200}$	$\frac{92183520}{61261200}$	$\frac{74738664}{61261200}$	$-\frac{125634080}{61261200}$	$\frac{111461350}{61261200}$	$-\frac{64602720}{61261200}$
$(4, 1)$	$-\frac{14614528}{61261200}$	$\frac{88500555}{61261200}$	$-\frac{128551280}{61261200}$	$\frac{18990972}{61261200}$	$\frac{78326820}{61261200}$	$-\frac{70620550}{61261200}$	$\frac{39541320}{61261200}$
$(4, 2)$	$\frac{2490368}{61261200}$	$-\frac{11486475}{61261200}$	$\frac{90433200}{61261200}$	$-\frac{159211052}{61261200}$	$\frac{78764400}{61261200}$	$\frac{4254250}{61261200}$	$-\frac{8044400}{61261200}$
$(4, 3)$	$-\frac{589824}{61261200}$	$\frac{2540395}{61261200}$	$-\frac{13564980}{61261200}$	$\frac{99855756}{61261200}$	$-\frac{176393360}{61261200}$	$\frac{99549450}{61261200}$	$-\frac{13087620}{61261200}$

$(N, k)$	$m = 6$	$m = 7$	$m = 8$
(4, 0)	$\frac{24242680}{61261200}$	$-\frac{5367648}{61261200}$	$\frac{534105}{61261200}$
(4, 1)	$-\frac{14372820}{61261200}$	$\frac{3101956}{61261200}$	$-\frac{302445}{61261200}$
(4, 2)	$\frac{3534300}{61261200}$	$-\frac{816816}{61261200}$	$\frac{82225}{61261200}$
(4, 3)	$\frac{1858780}{61261200}$	$-\frac{175032}{61261200}$	$\frac{6435}{61261200}$



## 15. German patent application for a memory device based on skyrmions

On the following pages, the German patent application for a memory device with skyrmions is copied. The official release note (*Offenlegungsschrift*) is also online accessible on the website of the German patent register:

<https://register.dpma.de/DPMAreger/pat/register?AKZ=1020162001612>

Note that the release note only informs about the application and its content. The proof is still in process.

Briefly, the idea is to split a racetrack via an energy barrier in two close-by lanes. This concept is worked out in more detail in Sec. 7 and 8, where in this case, the energy barrier is provided by the extra material barrier in the geometry of the racetrack. However, the application remains more general since the material barrier is just one possible realization for an energetic barrier. The first considerations that led to the two-lane concept were on lines with modified micromagnetic parameters. In particular, Fig. 5 in the following application shows a plot of an energy landscape with two degenerate lanes that was obtained as the interaction between a skyrmion and a line with lowered uniaxial anisotropy.



(10) **DE 10 2016 200 161 A1** 2017.07.13

(12) **Offenlegungsschrift**

(21) Aktenzeichen: **10 2016 200 161.2**  
 (22) Anmeldetag: **08.01.2016**  
 (43) Offenlegungstag: **13.07.2017**

(51) Int Cl.: **G11C 11/16 (2006.01)**  
**G11C 19/02 (2006.01)**

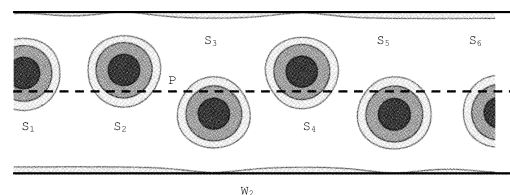
<p>(71) Anmelder: <b>Universität zu Köln, 50931 Köln, DE</b></p> <p>(74) Vertreter: <b>RCD-PATENT, 52134 Herzogenrath, DE</b></p> <p>(72) Erfinder: <b>Müller, Jan, 50354 Hürth, DE</b></p>	<p>(56) Ermittelter Stand der Technik:</p> <p><b>Koshibae, Wataru, et al. Memory functions of magnetic skyrmions. Japanese Journal of Applied Physics, 2015, 54. Jg., Nr. 5, S. 053001.</b></p>
---	---

Rechercheantrag gemäß § 43 PatG ist gestellt.

**Die folgenden Angaben sind den vom Anmelder eingereichten Unterlagen entnommen.**

(54) Bezeichnung: **Logischer Speicher mit einer Vielzahl von magnetischen Skyrmionen**

(57) Zusammenfassung: Die Erfindung betrifft einen logischen Speicher mit einer Vielzahl von magnetischen Skyrmionen ( $S_1, S_2, S_3, S_4, S_5, S_6, \dots, S_N$ ), wobei je ein magnetisches Skyrmion ( $S_1, S_2, S_3, S_4, S_5, S_6, \dots, S_N$ ) als eine Speicherzelle dient, wobei die Vielzahl von Skyrmionen ( $S_1, S_2, S_3, S_4, S_5, S_6, \dots, S_N$ ) zwischen einer oder mehreren Systemwänden ( $W_1, W_2$ ) eines magnetischen Nanodrahtes hintereinander angeordnet sind, wobei die Systemwände ( $W_1, W_2$ ) abschnittsweise parallel zueinander angeordnet sind, wobei ein Skyrmion ( $S_1, S_2, S_3, S_4, S_5, S_6, \dots, S_N$ ) versetzt zur Mitte der abschnittsweise parallelen Systemwände ( $W_1, W_2$ ) angeordnet ist, wobei die relative Lage des Skyrmions ( $S_1, S_2, S_3, S_4, S_5, S_6, \dots, S_N$ ) zur Mitte den Wert der Speicherzelle bestimmt.



Unser Zeichen: UKO 01262 DE

Anmelder.: NN

Titel: Logischer Speicher mit einer Vielzahl von magnetischen Skyrmionen

---

Logischer Speicher mit einer Vielzahl von magnetischen Skyrmionen

---

5 Universität Köln, Köln

Die vorliegende Erfindung betrifft einen logischen Speicher und insbesondere einen Speicher, der eine Vielzahl von magnetischen Skyrmionen zur Speicherung aufweist.

10 Hintergrund der Erfindung

Die Speicherung von Daten – sei es zur längerfristigen Ablage oder sei es nur zur kurzfristigen Zwischenspeicherung – ist ein allgegenwärtiger Vorgang.

15 Dabei haben sich im Wesentlichen zwei Zweige herausgebildet. Zum einen existieren magnetisch basierte Speicher, wie z.B. Festplatten, die verglichen mit ihren Herstellungskosten eine hohe Speicherdichte bieten, allerdings nur sehr mäßige Zugriffszeiten aufweisen, zum anderen existieren Halbleiter basierte Speicher, die mittels Transistoren eine schnelle Zugriffszeit bei allerdings vergleichsweise hohen  
20 Herstellungskosten bieten.

Festplattenspeicher können dabei mittlerweile einige Terabyte Daten speichern. Dennoch sind Festplattenspeicher inhärent unzuverlässig. Dies ist z.B. in den Schreib/Leseköpfen und den beweglichen Speicherplatten angelegt, denn bewegliche Teile neigen zu Verschleiß und  
25 damit ist der Ausfall lediglich eine Frage der Zeit.

Unser Zeichen: UKO 01262 DE

Anmelder.: NN

Titel: Logischer Speicher mit einer Vielzahl von magnetischen Skyrmionen

Zwischenzeitlich konnten sich sogenannte Flash-Speicher etablieren, die bei leicht höheren Herstellungskosten als Festplatten und geringeren Kosten als Halbleiterspeicher bei moderaten Zugriffsgeschwindigkeiten einen Ersatz für Festplatten darstellen. Allerdings neigen Flash-Speicher dazu abhängig vom Einsatz die Speicherwirkung zu verlieren, sodass  
5 sie nicht für häufige Lese/Schreib-Zugriffe geeignet sind.

Andere Halbleiter basierte Speicher sind z.B. FRAM, bei denen Daten in Form von Richtungen einer ferroelektrischen Domäne gespeichert wird. Zwar stellen diese Speicher bessere Zugriffszeiten als Flash-Speicher zur Verfügung, sie sind jedoch immer noch  
10 vergleichsweise langsam und schwer herzustellen.

Andere Halbleiter basierte Speicher sind z.B. Semiconductor magnetoresistive RAM (MRAM), welches Daten als magnetisches Moment in einem ferromagnetischen Material speichern.

15 Zwar wurden in der Vergangenheit Versuche unternommen die Speicherdichte bisheriger magnetischer Speicher und der Zugriffszeiten zu erhöhen, so z.B. mittels sogenannte Racetracks siehe z.B. die US Patentanmeldung US 2004 / 252 539 A1, jedoch waren diese Speicher aufgrund unterschiedlicher Probleme nicht langzeitstabil sondern metastabil.

20 In den von der vorgenannten Anmeldung angedachten Racetracks wurden, um eine hohe Packungsdichte zu erreichen, Skyrmionen als logische Einheit verwendet, d.h. das Vorhandensein oder Fehlen eines Skyrmions an einer bestimmten Stelle kodierte den jeweiligen binären Wert. Dies ist beispielhaft in Figur 1 wiedergegeben. Dort stellt z.B. ein Skyrmion dargestellt als dunklerer Kreis einen logischen Zustand dar, während ein fehlendes  
25 Skyrmion einen anderen logischen Zustand darstellt. Wenn ein vorhandenes Skyrmion den Zustand 1 repräsentiert, dann wäre in dem Ausschnitt der Figur 1 die Datenfolge 011010 dargestellt. Um diese Werte auszulesen, ist eine komplizierte Ausleselogik nötig. Zudem muss ein erheblicher Aufwand in das Schreiben eines Zustands, d.h. das Erzeugen bzw. Vernichten eines Skyrmions gesetzt werden. Weiterhin ist die Temperaturbeständigkeit  
30 problematisch, da Skyrmionen Temperatur- und Nachbarschaftsempfindlich sich bewegen.

Unser Zeichen: UKO 01262 DE

Anmelder.: NN

Titel: Logischer Speicher mit einer Vielzahl von magnetischen Skyrmionen

#### Aufgabe

Es ist daher eine Aufgabe der Erfindung einen verbesserten Speicher zur Verfügung zu stellen, der erheblich verbesserte Zugriffszeiten bei hoher Speicherdichte zur Verfügung  
5 stellen kann.

#### Kurzdarstellung der Erfindung

Die Aufgabe wird gelöst durch einen Logischer Speicher mit einer Vielzahl von magnetischen  
10 Skyrmionen, wobei je ein magnetisches Skyrmion als eine Speicherzelle dient, wobei die  
Vielzahl von Skyrmionen zwischen Systemwänden eines magnetischen Nanodrahtes  
hintereinander angeordnet sind, wobei die Systemwände abschnittsweise parallel  
zueinander angeordnet sind, wobei ein Skyrmion versetzt zur Mitte der abschnittsweise  
parallelen Systemwände angeordnet ist, wobei die relative Lage des Skyrmions zur Mitte den  
15 Wert der Speicherzelle bestimmt.

Weitere vorteilhafte Ausgestaltungen sind Gegenstand der abhängigen Ansprüche und der ausführlichen Beschreibung.

#### 20 Kurzdarstellung der Figuren

Nachfolgend wird die Erfindung näher unter Bezugnahme auf die Figuren erläutert werden.  
In diesen zeigt:

25 Fig. 1 einen beispielhaften Speicherinhalt eines simulierten Racetracks gemäß Stand der Technik,

Fig. 2 einen beispielhaften Speicherinhalt in einem logischen Speicher gemäß Ausführungsformen der Erfindung,

Unser Zeichen: UKO 01262 DE

Anmelder.: NN

Titel: Logischer Speicher mit einer Vielzahl von magnetischen Skyrmionen

Fig. 3 3D-Form eines Skyrmions,

Fig. 4 die Abbildung des Stachelballs in die Ebene

Fig. 5 eine perspektivische Darstellung eines Potentialverlaufes bei einer Potentiallinie P .

#### 5 Detaillierte Beschreibung

Nachfolgend wird die Erfindung eingehender unter Bezugnahme auf die Figur dargestellt werden. Dabei ist anzumerken, dass unterschiedliche Aspekte beschrieben werden, die jeweils einzeln oder in Kombination zum Einsatz kommen können. D.h. jeglicher Aspekt kann  
10 mit unterschiedlichen Ausführungsformen der Erfindung verwendet werden soweit nicht explizit als reine Alternative dargestellt.

Weiterhin wird nachfolgend der Einfachheit halber in aller Regel immer nur auf eine Entität  
15 Bezug genommen werden. Soweit nicht explizit vermerkt, kann die Erfindung aber auch jeweils mehrere der betroffenen Entitäten aufweisen. Insofern ist die Verwendung der Wörter „ein“, „eine“ und „eines“ nur als Hinweis darauf zu verstehen, dass in einer einfachen Ausführungsform zumindest eine Entität verwendet wird.

In der theoretischen Physik wird ein stabiler Wirbel in Feldern nach dem Physiker Skyrme als  
20 Skyrmion bezeichnet.

Mit Skyrmionen wird in der sogenannten Spintronics gearbeitet. Dabei können Skyrmionen als Abbildung einer 3-dimensionalen spin-Stachelballs (ähnlich einem eingerollten Igel) – siehe Figur 3 - in eine 2 dimensionale Ebene dargestellt werden, bei der z.B. der Spin entsprechend eines positive Nord-Pols auf das äußere einer Scheibe projiziert wird während  
25 der Spin entsprechend dem negativen Süd-Pol auf den Mittelpunkt der Scheibe projiziert wird. Diese Abbildung ist in Fig. 4 gezeigt.

Spezielle Formen von Skyrmionen werden z.B. in magnetischen Materialien angetroffen, die die Inversionssymmetrie brechen und bei denen bestimmte Interaktionen (z.B.

Unser Zeichen: UKO 01262 DE

Anmelder.: NN

Titel: Logischer Speicher mit einer Vielzahl von magnetischen Skyrmionen

Dzyaloshinskii-Moriya Interaction) eine Rolle spielen. Diese können z.B. Domänen von wenigen nm bilden (z.B. Fe auf Ir(111)).

5 Als Materialsysteme sind alle Magnete mit gebrochener Inversionssymmetrie (= chirale Magnete) geeignet. Eine gebrochene Inversionssymmetrie kann z.B. durch einen Symmetriebruch in der Einheitszelle der Gitterstruktur bereitgestellt werden, oder aber auch durch ein asymmetrisches Stapeln von Layern aus unterschiedlicher Materialien.

10 Von Vorteil ist, dass Skyrmionen in der Anordnung der Erfindung mit geringem Aufwand erstellt und verschoben werden können.

Ein beispielhafter logischer Speicher gemäß der Erfindung ist in Figur 2 als Ausschnitt dargestellt.

15 Dieser beispielhafte logische Speicher besitzt eine Vielzahl von magnetischen Skyrmionen  $S_1, S_2, S_3, S_4, S_5, S_6$ . Diese können bereits vorhanden sein oder aber durch geeignete Einrichtungen erzeugt werden. Natürlich können eine erheblich höhere Zahl  $N$  von Skyrmionen vorhanden sein. Nachfolgend werden wir nur Bezug auf die dargestellten Skyrmionen nehmen.

20

In der Erfindung dient nun je ein magnetisches Skyrmion  $S_1, S_2, S_3, S_4, S_5, S_6$  als eine Speicherzelle, wobei die Vielzahl von Skyrmionen  $S_1, S_2, S_3, S_4, S_5, S_6, \dots S_N$  zwischen einer oder mehreren Systemwänden  $W_1, W_2$  eines magnetischen Nanodrahtes hintereinander angeordnet sind.

25

Nanodraht ist dabei nicht als zylindrische Ausgestaltung limitierend zu verstehen sondern als Ausgestaltung eines langegezogenen Elements, dass nicht notwendigerweise frei schwebend ist, sondern auch abschnittsweise auf einem Substrat angeordnet sein kann.

Unser Zeichen: UKO 01262 DE

Anmelder.: NN

Titel: Logischer Speicher mit einer Vielzahl von magnetischen Skyrmionen

Die Systemwände sind in der Figur 2 als schwarze Linie oberhalb und unterhalb der Skyrmionen angedeutet.

Die Systemwände  $W_1$ ,  $W_2$  sind abschnittsweise parallel zueinander angeordnet.

- 5 Abschnittsweise bedeutet hier, dass lediglich in einem infinitesimal kleinen Bereich die Systemwände jeweils zueinander parallel sind. D.h. die Systemwände können auch gebogen sein und können so für verschiedene Schreib/Lese-Systeme angepasst werden. Der Einfachheit halber ist in den Figuren nur eine parallele Anordnung gezeigt.

- 10 Ein Skyrmion  $S_1$ ,  $S_2$ ,  $S_3$ ,  $S_4$ ,  $S_5$ ,  $S_6$  ist nun jeweils versetzt zur Mitte der abschnittsweise parallelen Systemwände  $W_1$ ,  $W_2$  angeordnet. Diese Mitte ist als gestrichelte Linie P in Figur 2 eingezeichnet.

- 15 Die relative Lage des Skyrmions  $S_1$ ,  $S_2$ ,  $S_3$ ,  $S_4$ ,  $S_5$ ,  $S_6$  zur Mitte bestimmt dann den Wert der Speicherzelle. Beispielsweise könnte  $S_1$ ,  $S_4$ , und  $S_6$  der Zustand einer logischen 1 bedeuten während  $S_2$ ,  $S_3$ ,  $S_5$  den Zustand einer logischen 0 bedeuten könnte.

Da hier die Skyrmionen in relativ enger Nachbarschaft angeordnet sind kann dieser Zustand nahe am energetisch günstigen Skyrmiongitterzustand ausgerichtet sein, wodurch die

- 20 Langzeit-Stabilität erheblich verbessert werden kann. D.h. die sonst vorhanden negativen Effekte von Temperatur und Abstoßung können nahezu vollständig unterdrückt werden, da kein Raum zur Verfügung steht, in den die Skyrmionen entweichen könnten.

In einer Ausführungsform der Erfindung ist vorgesehen, dass die Mitte der abschnittsweise

- 25 parallelen Systemwände einer Potentiallinie P entspricht.

In diesem Fall kann z.B. ein einfaches Energie-Maximum (z.B. durch ein effektives Magnetfeld) bereitgestellt werden, sodass die Skyrmionen mit gleicher Energie entweder in der oberen Hälfte oder in der unteren Hälfte angeordnet sein können.

Unser Zeichen: UKO 01262 DE

Anmelder.: NN

Titel: Logischer Speicher mit einer Vielzahl von magnetischen Skyrmionen

Ein solcher Fall ist in Figur 5 dargestellt. Dort ist in perspektivischer Sichtweise das Potential aufgezeichnet, wobei die Systemwände und die Potentiallinie zu zwei Wellentälern führen (Energiminima), in denen die Skyrmionen gehalten werden. Hieraus wird auch ersichtlich,  
5 dass es für einen Wechsel von einem Zustand zwischen  $W_1$  und P in einen Zustand zwischen P und  $W_2$  lediglich so viel Energie bedarf, dass die Potentiallinie überwunden werden kann.

Offensichtlich erlaubt es diese Anordnung auch mehrere (parallele) Potentiallinien zwischen  
10 den Systemwänden vorzusehen, sodass auch mehr Zustände kodiert werden könnten.

Besonders einfach lässt sich jedoch die Erfindung mit binären Speicherzellen verwenden.

Mit der vorgestellten Erfindung können benachbarte Speicherzellen einen Abstand von 25  
15 nm und weniger aufweisen, insbesondere von weniger als 15 nm aufweisen. Hiermit können erhebliche Mengen an Daten auf geringstem Raum gespeichert werden.

Die Potentiallinie P kann unterschiedlich ausgestaltet sein. Lediglich beispielhaft sei erwähnt, dass eine solche Potentiallinie durch eine mechanischen Riefe, Dotierungsatome, zusätzlich aufgebrachtene Atome, etc. aufweist. Insbesondere eignen sich hierfür Atome mit einem  
20 hohen magnetischen Moment, sodass auf der Potentiallinie ein höheres Magnetfeld als oberhalb bzw. unterhalb der Potentiallinie herrscht. D.h. die Skyrmionen werden abgestoßen. Alternativ oder zusätzlich kann jedoch auch vorgesehen sein, dass mittels Fremdatomen an den Außenseiten (d.h. versetzt zur Potentiallinie) eine anziehende Wirkung erzeugt wird.

25 Zum Schreiben der Speicherzellen können unterschiedliche Techniken verwendet werden. Lediglich beispielhaft seien ein spin-polarisierter Strom, Spinwellen, magnetische oder elektrische Felder hierfür benannt. Natürlich können auch mehrere Techniken miteinander kombiniert Anwendung finden.

Unser Zeichen: UKO 01262 DE

Anmelder.: NN

Titel: Logischer Speicher mit einer Vielzahl von magnetischen Skyrmionen

In gleicher Weise kann vorgesehen sein, dass die Speicherzellen des logischen Speichers mittels eines spin-polarisierten Stroms, eines Magnetkraft-Sensors oder Detektion über einen Tunnelstrom gelesen werden können.

- 5 Mit der Erfindung ist es nunmehr möglich eine stabile Speicherung bei gleichzeitig hoher Dichte zur Verfügung zu stellen. Ohne weiteres können mit der vorgestellten Erfindung unterschiedliche Speichersysteme realisiert werden, die einen schnellen Zugriff ermöglichen. Damit wird es möglich Speicherdichten mit bisher unerreichten Transfer-Geschwindigkeiten von mehreren GByte zu ermöglichen.

10

Skyrmionen können dabei innerhalb des Drahtes, d.h zwischen den Systemwänden bzw. einer Systemwand und einer Potentiallinie parallel verschoben werden. Hierzu kann ein Strom verwendet werden, der die entsprechenden Skyrmionen verschiebt. D.h. mittels der Stromrichtung kann auch die Verschieberichtung festgelegt werden. Somit können auf  
15 einfache Weise schnelle Speicher bereitgestellt werden, die keinerlei bewegliche Teile mehr aufweisen, wodurch die Langzeitstabilität erhöht wird. D.h. ein Schreibkopf und/oder Lesekopf kann ortsfest bleiben ebenso wie der Nanodraht. Lediglich durch Anlegen eines Stromes werden die entsprechenden Speicherzellen zum und über den Schreib- oder Lesekopf bewegt.

20

Insbesondere ist es möglich parallel auslesbare Speicher bereitzustellen. Auch ist es möglich Schieberegister zur Verfügung zu stellen.

Unser Zeichen: UKO 01262 DE

Anmelder.: NN

Titel: Logischer Speicher mit einer Vielzahl von magnetischen Skyrmionen

### Ansprüche

1. Logischer Speicher mit einer Vielzahl von magnetischen Skyrmionen ( $S_1, S_2, S_3, S_4, S_5, S_6, \dots S_N$ ), wobei je ein magnetisches Skyrmion ( $S_1, S_2, S_3, S_4, S_5, S_6, \dots S_N$ ) als  
5 eine Speicherzelle dient, wobei die Vielzahl von Skyrmionen ( $S_1, S_2, S_3, S_4, S_5, S_6, \dots S_N$ ) zwischen einer oder mehreren Systemwänden ( $W_1, W_2$ ) eines magnetischen Nanodrahtes hintereinander angeordnet sind, wobei die Systemwände ( $W_1, W_2$ ) abschnittsweise parallel zueinander angeordnet sind, wobei ein Skyrmion ( $S_1, S_2, S_3, S_4, S_5, S_6, \dots S_N$ ) versetzt zur Mitte der abschnittsweise parallelen Systemwände ( $W_1, W_2$ )  
10 angeordnet ist, wobei die relative Lage des Skyrmions ( $S_1, S_2, S_3, S_4, S_5, S_6, \dots S_N$ ) zur Mitte den Wert der Speicherzelle bestimmt.
2. Logischer Speicher nach Anspruch 1, dadurch gekennzeichnet, dass die Mitte der abschnittsweise parallelen Systemwände einer Potentiallinie (P) entspricht.  
15
3. Logischer Speicher nach Anspruch 1 oder 2, dadurch gekennzeichnet, dass der Wert der Speicherzelle binär ist.
4. Logischer Speicher nach einem der vorhergehenden Ansprüche, dadurch  
20 gekennzeichnet, dass die Systemwände ( $W_1, W_2$ ) parallele Linien sind.
5. Logischer Speicher nach einem der vorhergehenden Ansprüche, dadurch gekennzeichnet, dass benachbarte Speicherzellen einen Abstand von 25 nm und weniger aufweisen.  
25
6. Logischer Speicher nach einem der vorhergehenden Ansprüche 2 bis 5, dadurch gekennzeichnet, dass die Potentiallinie (P) zumindest eines aus einer mechanischen Riefe, Dotierungsatome, zusätzlich aufgebrauchten Atome, etc. aufweist.

Unser Zeichen: UKO 01262 DE

Anmelder.: NN

Titel: Logischer Speicher mit einer Vielzahl von magnetischen Skyrmionen

7. Logischer Speicher nach einem der vorhergehenden Ansprüche, dadurch gekennzeichnet, dass eine Speicherzelle mittels eines spin-polarisierten Stroms, Spinwellen, magnetischen oder elektrische Felder geschrieben werden kann.

5

8. Logischer Speicher nach einem der vorhergehenden Ansprüche, dadurch gekennzeichnet, dass eine Speicherzelle mittels eines spin-polarisierten Stroms, eines Magnetkraft-Sensors oder Detektion über einen Tunnelstrom gelesen werden kann.

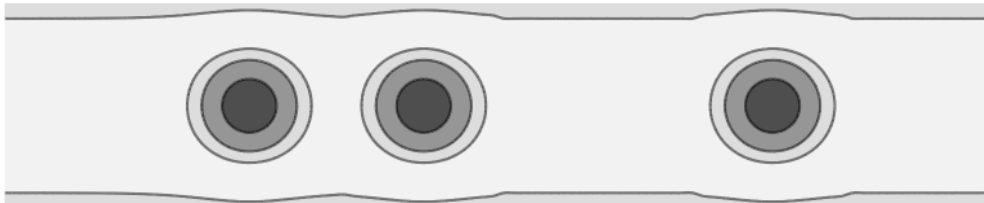
10

Unser Zeichen: UKO 01262 DE

Anmelder.: NN

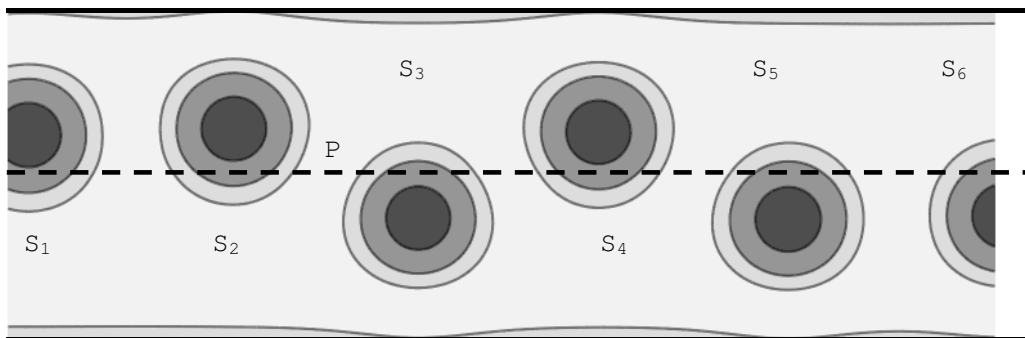
Titel: Logischer Speicher mit einer Vielzahl von magnetischen Skyrmionen

Figuren



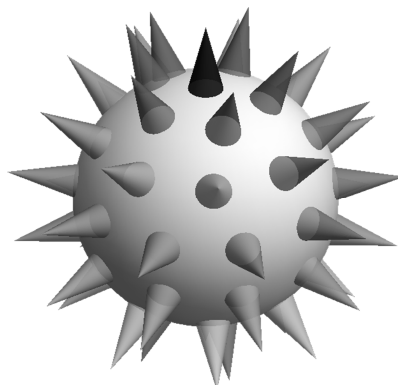
Figur 1

5



$W_2$

Figur 2



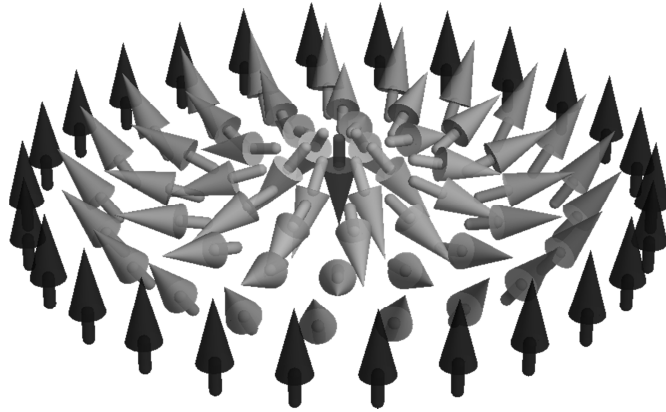
10

Figur 3

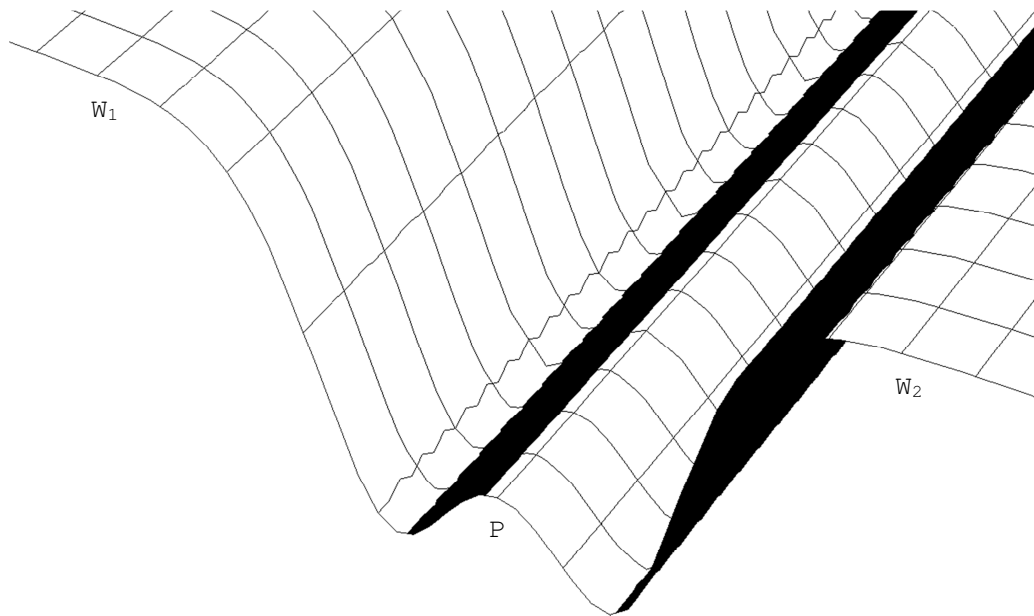
Unser Zeichen: UKO 01262 DE

Anmelder.: NN

Titel: Logischer Speicher mit einer Vielzahl von magnetischen Skyrmionen



Figur 4



Figur 5

5

Unser Zeichen: UKO 01262 DE

Anmelder.: NN

Titel: Logischer Speicher mit einer Vielzahl von magnetischen Skyrmionen

### Zusammenfassung

Die Erfindung betrifft einen logischen Speicher mit einer Vielzahl von magnetischen Skyrmionen ( $S_1, S_2, S_3, S_4, S_5, S_6, \dots S_N$ ), wobei je ein magnetisches Skyrmion ( $S_1, S_2, S_3, S_4,$   
5  $S_5, S_6, \dots S_N$ ) als eine Speicherzelle dient, wobei die Vielzahl von Skyrmionen ( $S_1, S_2, S_3, S_4,$   
 $S_5, S_6, \dots S_N$ ) zwischen einer oder mehreren Systemwänden ( $W_1, W_2$ ) eines magnetischen  
Nanodrahtes hintereinander angeordnet sind, wobei die Systemwände ( $W_1, W_2$ )  
abschnittsweise parallel zueinander angeordnet sind, wobei ein Skyrmion ( $S_1, S_2, S_3, S_4, S_5,$   
 $S_6, \dots S_N$ ) versetzt zur Mitte der abschnittsweise parallelen Systemwände ( $W_1, W_2$ )  
10 angeordnet ist, wobei die relative Lage des Skyrmions ( $S_1, S_2, S_3, S_4, S_5, S_6, \dots S_N$ ) zur Mitte  
den Wert der Speicherzelle bestimmt.

Fig. 2

15



# Acknowledgments

Now, the point has come where I would like to thank all the people who supported me during this work.

Let me start by saying thank you to my supervisor, *Achim Rosch*, for all the support already since my Bachelor, for the endless discussions full of enthusiasm for physics, for giving me the freedom to follow my own ideas and giving me support when I didn't know how to proceed, and for giving me the opportunity to travel to so many conferences in the world where I enjoyed the uncountable discussions with almost everyone who is somewhere cited or referenced in this work.

Next, I thank *Markus Garst* with whom I've spent so many hours working together on these projects.

Further, I enjoyed an inspiring stay in Paris in the group of the fabulous *Vincent Cros* who I have to thank for the wonderful time, for encouraging me to the patent application, and for the people who I got to know there, in particular *Albert Fert* and *Joo-Von Kim* but also all the other members of the group who I seem to periodically meet on conferences.

I would like to also thank all our collaborators for the numerous projects, in particular those who I discussed most with who are in order of appearance in this thesis *Peggy Schoenherr*, *Laura Köhler*, *Dennis Meier*, *Raji Jayaraman*, *Yoshie Murooka*, *Henrik Rønnow*, *Simon Pöhlath*, *Alfonso Chacon*, *Christian Pfeleiderer*, *Christian Back*, *Xichao Zhang*, *Christian Faber*, *Ben McKeever*, *Karin Everschor-Sitte*, and all those whose names are not in the titles but who contributed with their discussions as *Nikolai Kiselev*, *Gideon Müller*, *Pavel Bessarab*, *Stefan Blügel*, *Kai Litzius*, *Mathias Kläui*, *Shilei Zhang*, *Thorsten Hesjedal*, *Junichi Iwasaki*, and so many more.

Special thanks goes also to *Christoph Schütte* for the nice and clean code of which I've successfully made a huge mess but also to *Thomas Nattermann* who kept telling me in his lectures that I should always have a simple picture of what I am doing. He is probably the reason for the many illustrations in this thesis.

I have to thank also all the people who I have around me every five days per week. Let me truncate this endless list in the traditional way by only mentioning those with whom I've shared an office, in order of appearance *Mario*, *Jonathan*, *Michael*, *Christopher*, *Kevin*, *Mathieu*, *Samh*, *Florian*, *Terenz*, *Lukas*, *Philipp*, *Dennis*, *Johannes*, *Christian*, *Matthias*, *Junichi*, *Bernd*, *Benni*, but most importantly *Finn*, *Tim*, and *Max* for the lazy 5 minutes after lunch.

Let me also thank *Petra Neubauer-Günther* for being a great organizer in the Bonn-Cologne Graduate School of Physics and Astronomy BCGS, *Christiane Frense-Heck* for being a great organizer in the Deutsche Telekom Stiftung DTS, and *Andreas Sindermann* who always stayed friendly even if after so many years I still don't know how to fill out official forms.

I acknowledge the financial support which I had from both BCGS and DTS where I was, unfortunately, the very last scholar. I also thank the team of the RRZK for keeping CHEOPS running (and restoring my files when I've accidentally hit the wrong button and deleted everything).

Ich danke außerdem meiner Familie und meinen Freunden, die in der ganzen Zeit immer für mich da waren und mich voller Vertrauen unterstützt haben.

And as always, the first person on the list is the one who did most of the work while the last person is the one who coordinates everything and keeps things running: Yvonne.

Anhänge gemäß Prüfungsordnung



# Anhang zur Eigenbeteiligung an den Publikationen

- P. Schoenherr, J. Müller, L. Köhler, A. Rosch, N. Kanazawa, Y. Tokura, M. Garst, and D. Meier,  
*Topological domain walls in helimagnets*,  
Nature Physics, DOI: 10.1038/s41567-018-0056-5 (2018)

Für dieses Projekt habe ich die numerischen Daten produziert und die zugehörigen Texte und Grafiken erstellt.

- J. Müller, J. Rajeswari, P. Huang, Y. Murooka, H. M. Rønnow, F. Carbone, and A. Rosch,  
*Magnetic skyrmions and skyrmion clusters in the helical phase of  $\text{Cu}_2\text{OSeO}_3$* ,  
Phys. Rev. Lett. 119, 137201 (2017)

Für dieses Projekt habe ich alle numerischen und analytischen Berechnungen durchgeführt. Die theoretischen Abbildungen habe ich erstellt. An dem Text habe ich maßgeblich mitgewirkt.

- J. Wild, T.N.G. Meier, S. Pöllath, M. Kronseder, A. Bauer, A. Chacon, M. Halder, M. Schowalter, A. Rosenauer, J. Zweck, J. Müller, A. Rosch, C. Pfeiderer, and C. H. Back,  
*Entropy-limited topological protection of skyrmions*,  
Science Advances 3 (9), e1701704 (2017)

In diesem Projekt geht die Idee auf mich zurück, anstelle der Energie die freie Energie zu betrachten. Zusammen mit A. Rosch habe ich diesen theoretischen Beitrag ausgearbeitet. Die Daten aus den Teil-Grafiken (C) und (D) aus Figur 5.1.1 habe ich simuliert und daraus die dargestellten Bilder produziert.

- J. Müller, A. Rosch, and M. Garst,  
*Edge instabilities and skyrmion creation in magnetic layers*,  
New Journal of Physics 18, 065006 (2016)

Für dieses Projekt habe ich die analytischen und numerischen Rechnungen durchgeführt. Ich habe die Bilder erstellt und von mir stammt die Idee für das Protokoll, das zur Erzeugung der Skyrmionkette führt.

- J. Müller,  
*Magnetic Skyrmions on a Two-Lane Racetrack*,  
New Journal of Physics 19, 025002 (2017)

Die Idee zu diesem Artikel stammt von mir. Die Daten habe ich erzeugt und den Artikel geschrieben.

- J. Müller,  
*Shape-dependence of the barrier for skyrmions on a two-lane racetrack*,  
Proc. SPIE 9931, Spintronics IX, 993136 (2016)

Die Idee zu diesem Konferenzbeitrag stammt von mir. Die Daten habe ich erzeugt und den Artikel geschrieben.

- X. Zhang, J. Müller, J. Xia, M. Garst, X. Liu, and Y. Zhou,  
*Motion of skyrmions in nanowires driven by magnonic momentum-transfer forces*,  
New Journal of Physics 19, 065001 (2017)

Die Idee zur Beschreibung der Skyrmiontrajektorien mittels der Thiele-Gleichung stammt von mir. Ich habe die Rechnungen durchgeführt und zusammen mit M. Garst diesen Teil des Manuskripts geschrieben. An der Auswertung der Ergebnisse war ich maßgeblich beteiligt.

# Erklärung

Ich versichere, dass ich die von mir vorgelegte Dissertation selbständig angefertigt, die benutzten Quellen und Hilfsmittel vollständig angegeben und die Stellen der Arbeit – einschließlich Tabellen, Karten und Abbildungen –, die anderen Werken im Wortlaut oder dem Sinn nach entnommen sind, in jedem Einzelfall als Entlehnung kenntlich gemacht habe; dass diese Dissertation noch keiner anderen Fakultät oder Universität zur Prüfung vorgelegen hat; dass sie – abgesehen von unten angegebenen Teilpublikationen – noch nicht veröffentlicht worden ist, sowie, dass ich eine solche Veröffentlichung vor Abschluss des Promotionsverfahrens nicht vornehmen werde. Die Bestimmungen der Promotionsordnung sind mir bekannt. Die von mir vorgelegte Dissertation ist von Prof. Dr. Achim Rosch betreut worden.

Köln, den 19. März 2018

## Teilpublikationen

- J. Müller, A. Rosch, and M. Garst,  
*Edge instabilities and skyrmion creation in magnetic layers*,  
New Journal of Physics 18, 065006 (2016)
- J. Müller,  
*Shape-dependence of the barrier for skyrmions on a two-lane racetrack*,  
Proc. SPIE 9931, Spintronics IX, 993136 (2016)
- J. Müller,  
*Magnetic Skyrmions on a Two-Lane Racetrack*,  
New Journal of Physics 19, 025002 (2017)
- X. Zhang, J. Müller, J. Xia, M. Garst, X. Liu, and Y. Zhou,  
*Motion of skyrmions in nanowires driven by magnonic momentum-transfer forces*,  
New Journal of Physics 19, 065001 (2017)
- J. Müller, J. Rajeswari, P. Huang, Y. Murooka, H. M. Rønnow, F. Carbone, and A. Rosch,  
*Magnetic skyrmions and skyrmion clusters in the helical phase of  $\text{Cu}_2\text{OSeO}_3$* ,  
Phys. Rev. Lett. 119, 137201 (2017)

- J. Wild, T.N.G. Meier, S. Pöllath, M. Kronseder, A. Bauer, A. Chacon, M. Halder, M. Schowalter, A. Rosenauer, J. Zweck, J. Müller, A. Rosch, C. Pfeiderer, and C. H. Back, *Entropy-limited topological protection of skyrmions*, Science Advances 3 (9), e1701704 (2017)
- P. Schoenherr, J. Müller, L. Köhler, A. Rosch, N. Kanazawa, Y. Tokura, M. Garst, and D. Meier, *Topological domain walls in helimagnets*, Nature Physics, DOI: 10.1038/s41567-018-0056-5 (2018)